



Copyright © 1981, by John Wiley & Sons, Inc.

All rights reserved. Published simultaneously in Canada.

Reproduction or translation of any part of this work beyond that permitted by Sections 107 and 108 of the 1976 United States Copyright Act without the permission of the copyright owner is unlawful. Requests for permission or further information should be addressed to the Permissions Department, John Wiley & Sons.

Library of Congress Cataloging in Publication Data:

Stutzman, Warren L.
Antenna theory and design.

Includes bibliographies and index.

I. Antennas (Electronics) I. Thiele, Gary A., joint author. II. Title.
TK7871.6.S77 621.38'0283 80-23498
ISBN 0-471-04458-X

Printed in the United States of America

10 9 8 7 6 5



PREFACE

This book is the result of several years of classroom teaching, research investigations, and experiences with operating antennas. It is primarily intended for use at the introductory and intermediate levels by seniors and graduate students of electrical engineering. Introductory course work in static and dynamic electromagnetics is required background but an effort is made, particularly in Chapters 2 to 6, not to rely heavily on the mathematics of electromagnetic theory. Instead, the engineering aspects of antenna theory are emphasized.

The book covers the topic of antennas from roughly three vantage points: antenna fundamentals, antenna techniques, and the design of various antenna types. In the first four chapters fundamental material is stressed. Since the beginning student typically has had very little exposure to antennas, many details are found in Chapter 1. In that chapter the emergence of antenna theory from Maxwell's equations is established, along with many definitions of terms used in antenna practice. At the end of Chapter 1 are discussions of how antennas are used in operating systems, so that the student can develop an immediate appreciation for the uses of antennas. Chapter 2 examines a few simple antenna systems to solidify the principles developed in Chapter 1 and to provide specific antenna types for the discussion of arrays in Chapter 3. The discrete approach (arrays) to antennas is considered early because the general relationship between current distributed in space and radiation is more easily understood in that setting. Then the continuous distribution of current follows naturally in the discussion of line sources in Chapter 4.

A survey of most of the antenna types encountered in practice is presented in Chapter 5 (Wire Antennas), Chapter 6 (Broadband Antennas), and Chapter 8 (Aperture Antennas). These discussions are bound together with the analysis principles described in the introductory material. Emphasis is placed on the understanding of how antennas operate and on illustrating commonality among antenna types. However, design principles are included for the various antenna types, and "rules of thumb" are often given to simplify design calculations.

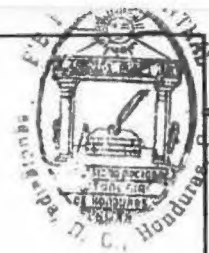
Specialized techniques are also presented. In Chapter 7, moment methods are used to analyze wire antennas of practically any configuration. High frequency techniques are detailed in Chapter 9 with applications to aperture antennas and antennas in the presence of ground surfaces. In Chapter 10 the topic of antenna synthesis for line sources and linear arrays is introduced.

This book can be readily adapted to various curricula. After the first five chapters are covered, any of the remaining five chapters could be selected. The first six chapters are ideally suited to a one-quarter, senior course. For a semester course, Chapter 8 is the logical addition to the first six chapters. Follow-on courses at the graduate level in a quarter system could include a course using Chapters 8 and 10 and a course using Chapters 7 and 9. An alternative would be a course based on Chapters 7 and 10 and a course based on Chapters 8 and 9.

Several features have been incorporated into the text as aids to learning. Defined terms follow the official IEEE (Institute of Electrical and Electronics Engineers) standard definitions of terms. Specific references to the literature are listed at the end of each chapter so that the reader may locate further source material on topics of particular interest. The appendices provide useful data on frequency designations and conductors, and many mathematical relationships. Computer programs are also presented in Appendix G. These programs are useful in solving many of the problems included at the end of each chapter.

We are appreciative of the assistance received during the writing of the manuscript. In particular, we are grateful to the many students who provided comments during the long classroom testing phase and to the publisher's reviewers for their valuable suggestions. Gary A. Thiele acknowledges colleagues at The Ohio State University and friends from Australia who reviewed Chapters 7 and 9 and who contributed to the computer programs in Appendices G.7, G.8, and G.9. Also, we express our deep appreciation to Cynthia Will for her expert typing of several manuscript versions. Finally, we must recognize our families for the many hours of neglect they endured. In particular, our wives, Claudia and Jo Ann are to be commended for their patience.

Warren L. Stutzman
Gary A. Thiele



CONTENTS

1	ANTENNA FUNDAMENTALS AND DEFINITIONS	1
1.1	INTRODUCTION	1
1.2	ELECTROMAGNETIC FUNDAMENTALS	4
1.3	SOLUTION OF MAXWELL'S EQUATIONS FOR RADIATION PROBLEMS	9
1.4	THE IDEAL DIPOLE	13
1.5	RADIATION PATTERN	17
1.6	DIRECTIVITY AND GAIN	32
1.7	RECIPROCITY AND ANTENNA PATTERN MEASUREMENTS	40
1.8	ANTENNA IMPEDANCE AND RADIATION EFFICIENCY	47
1.9	ANTENNA POLARIZATION	53
1.10	ANTENNAS IN COMMUNICATION LINKS AND RADAR	57
1.11	RECEIVING PROPERTIES OF ANTENNAS	64
	REFERENCES	71
	PROBLEMS	72
2	SOME SIMPLE RADIATING SYSTEMS	79
2.1	ELECTRICALLY SMALL DIPOLES	79
2.2	THE HALF-WAVE DIPOLE	84
2.3	ANTENNAS ABOVE A PERFECT GROUND PLANE	87
2.3.1	Image Theory	87
2.3.2	Monopoles	92

2.4	SMALL LOOP ANTENNAS	95
2.4.1	Duality	95
2.4.2	The Small Loop Antenna	99
2.5	SOME PRACTICAL CONSIDERATIONS	104
	REFERENCES	106
	PROBLEMS	106
3	ARRAYS	108
3.1	THE ARRAY FACTOR FOR LINEAR ARRAYS	109
3.2	UNIFORMLY EXCITED, EQUALLY SPACED LINEAR ARRAYS	124
3.2.1	The Array Factor Expression	124
3.2.2	Main Beam Scanning and Beamwidth	128
3.2.3	The Ordinary Endfire Array	130
3.2.4	The Hansen-Woodyard Endfire Array	130
3.3	PATTERN MULTIPLICATION	134
3.4	DIRECTIVITY OF UNIFORMLY EXCITED, EQUALLY SPACED LINEAR ARRAYS	141
3.5	NONUNIFORMLY EXCITED, EQUALLY SPACED LINEAR ARRAYS	145
3.6	MUTUAL IMPEDANCE	154
3.7	PHASED ARRAYS	160
3.8	PERSPECTIVE	167
	REFERENCES	167
	PROBLEMS	168
4	LINE SOURCES	173
4.1	THE UNIFORM LINE SOURCE	174
4.2	TAPERED LINE SOURCES	184
	REFERENCES	189
	PROBLEMS	189
5	WIRE ANTENNAS	192
5.1	DIPOLE ANTENNAS	193
5.1.1	Straight Wire Dipoles	193
5.1.2	The Vee Dipole	204
5.2	FOLDED DIPOLE ANTENNAS	205
5.3	FEEDING WIRE ANTENNAS	212
5.4	YAGI-UDA ANTENNAS	220
5.5	WIRE ANTENNAS ABOVE AN IMPERFECT GROUND PLANE	229
5.5.1	Pattern Effects of a Real Earth Ground Plane	229
5.5.2	Ground Plane Construction	235
5.6	TRAVELING-WAVE WIRE ANTENNAS	239

5.7	SQUARE LOOP ANTENNAS	244
	REFERENCES	252
	PROBLEMS	253
6	BROADBAND ANTENNAS	260
6.1	HELICAL ANTENNAS	261
6.1.1	Normal Mode of Radiation	262
6.1.2	Axial Mode of Radiation	264
6.2	BICONICAL ANTENNAS	270
6.2.1	The Infinite Biconical Antenna	270
6.2.2	The Finite Biconical Antenna	273
6.2.3	The Discone Antenna	274
6.3	SLEEVE ANTENNAS	278
6.3.1	Sleeve Monopoles	278
6.3.2	Sleeve Dipoles	280
6.4	SPIRAL ANTENNAS	281
6.5	LOG-PERIODIC ANTENNAS	287
	REFERENCES	303
	PROBLEMS	304
7	MOMENT METHODS	306
7.1	POCKLINGTON'S INTEGRAL EQUATION	307
7.2	INTEGRAL EQUATIONS AND KIRCHHOFF'S NETWORK EQUATIONS	310
7.3	WEIGHTED RESIDUALS AND THE MOMENT METHOD	315
7.4	REACTION INTEGRAL EQUATION	321
7.5	PIECEWISE SINUSOIDAL GALERKIN METHOD	323
7.5.1	Two-Segment Solution	325
7.5.2	Four-Segment Solution	327
7.5.3	<i>N</i> -Segment Solution	329
7.6	CALCULATION OF ANTENNA AND SCATTERER CHARACTERISTICS	332
7.7	SOURCE MODELING	336
7.8	SOME COMPUTATIONAL CONSIDERATIONS	339
7.8.1	Computer Time Considerations	340
7.8.2	Toeplitz Matrices	341
7.8.3	Block Toeplitz Matrices	342
7.8.4	Compressed Matrices	343
7.9	THE WIRE ANTENNA OR SCATTERER AS AN <i>N</i> -PORT NETWORK	344
7.9.1	Series Connections	344
7.9.2	Parallel Connections	345

7.10	ANTENNA ARRAYS	349	9.10	EQUIVALENT CURRENT CONCEPTS	492
7.10.1	The Linear Array	349	9.11	A MULTIPLE DIFFRACTION FORMULATION	495
7.10.2	The Circular Array	350	9.12	DIFFRACTION BY CURVED SURFACES	498
7.10.3	Two-Dimensional Planar Array of Dipoles	354	9.13	EXTENSION OF MOMENT METHODS USING THE GTD	500
7.10.4	Summary	356	9.14	SUMMARY	510
7.11	MODELING OF SOLID SURFACES	356		REFERENCES	510
7.11.1	Wire-Grid Model	358		PROBLEMS	512
7.11.2	Continuous Surface Model	365			
7.12	SUMMARY	370	10	ANTENNA SYNTHESIS	520
	REFERENCES	370	10.1	THE SYNTHESIS PROBLEM	520
	PROBLEMS	372	10.2	LINE SOURCE METHODS	522
8	APERTURE ANTENNAS	375	10.2.1	The Fourier Transform Method	523
8.1	RADIATION FROM APERTURES AND HUYGENS PRINCIPLE	375	10.2.2	The Woodward-Lawson Sampling Method	526
8.2	RECTANGULAR APERTURES	385	10.3	LINEAR ARRAY METHODS	530
8.2.1	The Uniform Rectangular Aperture	385	10.3.1	The Fourier Series Method	531
8.2.2	Tapered Rectangular Apertures	391	10.3.2	The Woodward-Lawson Sampling Method	534
8.3	GAIN CALCULATIONS FOR APERTURE ANTENNAS	392	10.3.3	Comparison of Shaped Beam Synthesis Methods	535
8.4	RECTANGULAR HORN ANTENNAS	397	10.4	LOW SIDE LOBE, NARROW MAIN BEAM METHODS	537
8.4.1	The <i>H</i> -Plane Sectoral Horn Antenna	399	10.4.1	The Dolph-Chebyshev Linear Array Method	537
8.4.2	The <i>E</i> -Plane Sectoral Horn Antenna	406	10.4.2	The Taylor Line Source Method	543
8.4.3	The Pyramidal Horn Antenna	411		REFERENCES	550
8.5	CIRCULAR APERTURES	415		PROBLEMS	551
8.5.1	The Uniform Circular Aperture	415			
8.5.2	Tapered Circular Apertures	418	APPENDIX A	VECTORS	555
8.6	REFLECTOR ANTENNAS	422	A.1	UNIT VECTOR REPRESENTATIONS	555
8.6.1	Prime-Focus Parabolic Reflector Systems	422	A.2	VECTOR IDENTITIES	555
8.6.2	Cassegrain Reflector Systems	430	A.3	VECTOR DIFFERENTIAL OPERATORS	556
8.6.3	Gain Calculations for Reflector Antennas	433			
8.6.4	Other Reflector Antennas	437	APPENDIX B	TRIGONOMETRIC RELATIONS	558
	REFERENCES	440			
	PROBLEMS	441	APPENDIX C	HYPERBOLIC RELATIONS	560
9	HIGH-FREQUENCY METHODS	446			
9.1	GEOMETRICAL OPTICS	447	APPENDIX D	TABLES OF COMMONLY USED FREQUENCIES	561
9.2	PHYSICAL OPTICS	454	D.1	RADIO FREQUENCY BANDS	561
9.3	WEDGE DIFFRACTION THEORY	458	D.2	TELEVISION CHANNEL FREQUENCIES	561
9.4	THE RAY-FIXED COORDINATE SYSTEM	469	D.3	RADAR BANDS	562
9.5	A UNIFORM THEORY OF WEDGE DIFFRACTION	472			
9.6	<i>E</i> -PLANE ANALYSIS OF HORN ANTENNAS	479	APPENDIX E	CONDUCTOR DATA	563
9.7	CYLINDRICAL PARABOLIC ANTENNA	482	E.1	CONDUCTIVITIES OF GOOD CONDUCTORS	563
9.8	RADIATION BY A SLOT ON A FINITE GROUND PLANE	485	E.2	WIRE DATA	564
9.9	RADIATION BY A MONOPOLE ON A FINITE GROUND PLANE	489			

APPENDIX F	SOME USEFUL MATHEMATICAL RELATIONS	565
F.1	DIRAC DELTA FUNCTION	565
F.2	BINOMIAL THEOREM	566
F.3	BESSEL FUNCTIONS	566
F.4	SOME USEFUL INTEGRALS	566
APPENDIX G	COMPUTER PROGRAMS	568
G.1	LINE PRINTER POLAR PLOT SUBROUTINE—PLOT	568
G.2	LINE PRINTER RECTANGULAR PLOT SUBROUTINE—PROFIL	569
G.3	EQUALLY SPACED, UNIFORMLY EXCITED ARRAY FACTOR PROGRAM—ARRFAC	571
G.4	COMPLETE PATTERN PROGRAM FOR AN ARBITRARY ARRAY—ARRPAT	572
G.5	NONUNIFORMLY EXCITED, (UN)EQUALLY SPACED LINEAR ARRAY PROGRAM—NEESLAP	575
G.6	SAMPLING PATTERN ANTENNA PROGRAM—SPAP	576
G.7	MOMENT METHOD PROGRAM FOR A CENTER-FED DIPOLE	577
G.8	MOMENT METHOD PROGRAM FOR AN ARRAY OF EQUALLY SPACED, PARALLEL DIPOLES	582
G.9	DIFFRACTION COEFFICIENT COMPUTER PROGRAM	591
INDEX		595

1

ANTENNA FUNDAMENTALS AND DEFINITIONS

1.1 INTRODUCTION

Since the dawn of civilization communications has been of primary importance to human beings. At first, communication was achieved by sound through voice. As the distances of communicating increased, various devices were introduced, such as drums, horns, and so forth. For even greater distances visual methods were introduced, for example, signal flags and smoke signals in the daytime and fireworks at night. These optical communication devices, of course, utilize the light portion of the electromagnetic spectrum. It has been only very recently in human history that the electromagnetic spectrum, outside the visible region, has been employed for communication, through the use of radio.

The radio antenna is an essential component in any radio system. A radio antenna is a device that provides a means for radiating or receiving radio waves. In other words, it provides a transition from a guided wave on a transmission line to a "free-space" wave (and vice versa in the receiving case). Thus, information can be transferred between different locations without any intervening structures. The possible frequencies of the electromagnetic waves carrying this information form the electromagnetic spectrum (the radio frequency bands are given in Appendix D.1). One of human kind's greatest natural resources is the electromagnetic spectrum and the antenna has been instrumental in harnessing

this resource. A brief history of antenna technology [1, 2, 3, 4] and a discussion of the uses of antennas follow.

The theoretical foundations for antennas rest on Maxwell's equations. James Clark Maxwell (1831–1879) before the Royal Society in 1864 presented his results, which showed that light and electromagnetics were one in the same physical phenomenon. He also predicted that light and electromagnetic disturbances both can be explained by waves traveling at the same speed.

In 1886 the German physicist Heinrich Hertz (1857–1894) was able to verify experimentally the claim of Maxwell that electromagnetic actions are propagated through air. Hertz discovered that electrical disturbances could be detected with a secondary circuit of the proper dimensions for resonance and containing an air gap for sparks to occur. The primary source of electrical disturbances studied by Hertz consisted of two metal plates in the same plane, each with a wire connected to an induction coil; this earliest antenna is similar to the capacitor-plate dipole antenna described in Section 2.1. Hertz constructed dipole and loop antennas, as well as relatively sophisticated parabolic cylinder reflector antennas fed with dipoles along the focal line.

Guglielmo Marconi (1874–1937), an Italian electrical engineer, also built a microwave parabolic cylinder at a wavelength of 25 cm for his original code transmissions. But his subsequent work was at longer wavelengths for improved communication range. The transmitting antenna for the first transatlantic radio communication in 1901 consisted of a spark transmitter connected between the ground and a system of 50 vertical wires. The wires were fanned out and supported on the top by a horizontal wire between two masts. The receiving antenna was supported by kites. Marconi realized the importance of elevating antennas at these low frequencies, which were around 60 kHz.

The Russian physicist Alexander Popov (1859–1905) also recognized the importance of Hertz's discovery of radio waves, and began working on ways of receiving them a year before Marconi. He is sometimes credited with using the first antenna in the first radio system by sending a signal from ship to shore for three miles in 1897. However, it was Marconi who developed radio commercially and followed through to the impressive level of transoceanic radio communication. Marconi may be considered to be the father of amateur radio.

Antenna developments in the early years were limited by the availability of signal generators. About 1920 resonant length antennas (such as a half-wavelength dipole) were possible after the De Forest triode tube was used to produce continuous wave signals up to 1 MHz. At these higher frequencies antennas could be built with a physical size in the resonance region (e.g., a half-wavelength). Before World War II microwave (about 1 GHz) klystron and magnetron signal generators were developed along with hollow pipe waveguides. These lead to the development of horn antennas, although Chunder Bose (1858–1937) in India produced the first electromagnetic horn antenna many years

earlier. The first commercial microwave radiotelephone system in 1934 was between England and France and operated at 1.8 GHz. During the war an intensive development effort [5] primarily directed toward radar, spawned many "modern" antenna types, such as large reflectors, lenses, and waveguide slot arrays.

Let us now direct our attention to the uses of antennas. The transmission of electromagnetic energy may employ some type of guiding structure (a transmission line) or can be accomplished with transmit and receive antennas with no guiding structure in between. If a transmitter and receiver are spaced a distance r apart, the power loss when using a transmission line is proportional to $(e^{-\alpha r})^2$ where α is the attenuation constant of the transmission line. If antennas are used in a line of sight configuration, the power loss is proportional to $1/r^2$. Many factors enter into the decision of whether to use transmission lines or antennas. Generally speaking, at low frequencies and short distances transmission lines are practical. High frequencies are often used because of the available bandwidth. As distances become large and the frequency high, the signal losses and the costs of using transmission lines become large, and thus the use of antennas is favored. A notable exception to this is the fiber optic transmission line in the visible region.

In several applications antennas *must* be used. For example, in mobile communications involving aircraft, spacecraft, ships, or land vehicles antennas are required. Antennas are also popular in broadcast situations where one transmit terminal can serve an unlimited number of receivers, which can be mobile (e.g., car radio). Nonbroadcast radio applications such as municipal radio (police, fire, rescue) and amateur radio also require antennas. In noncommunication applications such as radar, antennas are also necessary.

Other factors that influence the choice of the type of transmission system include historical reasons, security, and reliability. Telephone companies began interconnecting multiple transmit and receiver terminals with transmission lines before radio technology was available. Recently the telephone companies have employed radio more heavily; well over half of all long distance telephone calls are now carried over microwave radio links. Transmission lines also provide a certain degree of security. When radio is used, anyone with an adequate receiving system can listen to a transmission. With transmission lines a "wire-tap" is required to violate privacy. For more sophisticated systems coding may be employed to secure a radio link. Also, security is a concern for only a small fraction of the communication situations. Another factor to be considered is reliability. For example, radio signals are affected by environmental conditions such as structures along the signal path, the ionosphere, and weather. Furthermore, interference is always a threat to radio systems. All of these factors must be examined together with a cost comparison of systems using transmission lines and antennas. Every year radio equipment decreases in cost and increases in

reliability. This tends to tip the scale in favor of radio systems. Thus, the demand for antennas and a knowledge of their operation will be ever present.

The following two sections of this first chapter present a brief review of electromagnetic field principles and the solution of Maxwell's equations for radiation problems. After a few basic relationships are derived, direct application of Maxwell's equations is required only in a few special situations. The remainder of this chapter is devoted to antenna terminology and some simple examples. Also included are discussions of antenna applications in communication systems and radar.

1.2 ELECTROMAGNETIC FUNDAMENTALS

The fundamental electromagnetic equations are¹

$$\nabla \times \mathcal{E} = -\frac{\partial \mathcal{B}}{\partial t} \quad (1-1)$$

$$\nabla \times \mathcal{H} = \frac{\partial \mathcal{D}}{\partial t} + \mathcal{J}_T \quad (1-2)$$

$$\nabla \cdot \mathcal{D} = \rho_T(t) \quad (1-3)$$

$$\nabla \cdot \mathcal{B} = 0 \quad (1-4)$$

$$\nabla \cdot \mathcal{J}_T = -\frac{\partial}{\partial t} \rho_T(t) \quad (1-5)$$

The first four of these differential equations are frequently referred to as Maxwell's equations and the last as the continuity equation. The curl equations together with the continuity equation are equivalent to the curl and divergence equations. In time-varying field problems the curl equations with the continuity equation is the most convenient formulation. Each of these differential equations has an integral counterpart.²

If the sources $\rho_T(t)$ and $\mathcal{J}_T(t)$ vary sinusoidally with time at radian frequency ω , the fields will also vary sinusoidally and are frequently called time-harmonic fields. The fundamental electromagnetic equations and their solutions are considerably simplified if phasor fields are introduced as follows:³

$$\mathcal{E} = \text{Re}(\mathbf{E}e^{j\omega t}), \mathcal{H} = \text{Re}(\mathbf{H}e^{j\omega t}), \text{etc.} \quad (1-6)$$

¹ Time-varying quantities will be denoted with script quantities, for example, $\mathcal{E} = \mathcal{E}(x, y, z, t)$.

² For a thorough discussion of the fundamental electromagnetic equations see [6].

³ The student is cautioned that some authors use $e^{-j\omega t}$ which leads to sign differences in subsequent developments.

where phasor quantities \mathbf{E} , \mathbf{H} , \mathbf{D} , \mathbf{B} , ρ_T , and \mathbf{J}_T are complex-valued functions of spatial coordinates only (i.e., time dependence is not shown). Using the phasor definitions of the electromagnetic quantities from (1-6) in (1-1) to (1-5) and eliminating the $e^{j\omega t}$ factors that appear on both sides of the equations yields

$$\nabla \times \mathbf{E} = -j\omega \mathbf{B} \quad (1-7)$$

$$\nabla \times \mathbf{H} = j\omega \mathbf{D} + \mathbf{J}_T \quad (1-8)$$

$$\nabla \cdot \mathbf{D} = \rho_T \quad (1-9)$$

$$\nabla \cdot \mathbf{B} = 0 \quad (1-10)$$

$$\nabla \cdot \mathbf{J}_T = -j\omega \rho_T \quad (1-11)$$

The time derivatives in (1-1) to (1-5) have been replaced by a $j\omega$ factor in (1-7) to (1-11) and time-varying electromagnetic quantities have been replaced by their phasor counterpart. This process is similar to the solution of network equations where the time dependent differential equations are Laplace transformed and the time derivatives are thus replaced by $j\omega$ (or s). Equations (1-7) to (1-10) are often referred to as the time-harmonic form of Maxwell's equations, because they apply to sinusoidally varying (i.e., time-harmonic) fields.

If more than one frequency is present the time-varying forms of the electromagnetic quantities can be found by inverse transforms after (1-7) to (1-11) have been solved for the phasor quantities as a function of radian frequency ω . This is again analogous to the procedure used to solve network problems. Fortunately this is not usually necessary in antenna problems since the bandwidth of the signals is usually very small. In the typical case a carrier frequency is accompanied by some form of modulation giving a spread of frequencies around the carrier. For analysis purposes we use a single frequency equal to the carrier frequency. Thus, all subsequent material in this book will assume time-harmonic fields.

The total current density \mathbf{J}_T is composed of an impressed, or source, current \mathbf{J} and a conduction current density term $\sigma\mathbf{E}$, which occurs in response to the impressed current:

$$\mathbf{J}_T = \sigma\mathbf{E} + \mathbf{J} \quad (1-12)$$

The role played by the impressed current density is that of a known quantity. It is quite frequently an assumed current density on an antenna, but as far as the field equations are concerned it is a known function. The current density $\sigma\mathbf{E}$ is a current density flowing on a nearby conductor due to the fields created by source \mathbf{J} and may be computed after the field equations are solved for \mathbf{E} . In

addition to conductivity σ , a material is further characterized by permittivity ϵ and permeability μ , where⁴

$$\mathbf{D} = \epsilon \mathbf{E} \quad (1-13)$$

and

$$\mathbf{B} = \mu \mathbf{H}. \quad (1-14)$$

We will now rewrite the field equations in preparation for their solution. Substituting (1-12) and (1-13) into (1-8) gives

$$\nabla \times \mathbf{H} = j\omega \left(\epsilon + \frac{\sigma}{j\omega} \right) \mathbf{E} + \mathbf{J} = j\omega \epsilon' \mathbf{E} + \mathbf{J} \quad (1-15)$$

where we have defined $\epsilon' = \epsilon - j(\sigma/\omega)$. Let ρ be the source charge density corresponding to the source current density \mathbf{J} . Then using (1-12) to (1-14) in (1-7) and (1-9) to (1-11), and repeating (1-15) we have [see Prob. 1.2-2 for (1-18)]:

$$\nabla \times \mathbf{E} = -j\omega \mu \mathbf{H} \quad (1-16)$$

$$\nabla \times \mathbf{H} = j\omega \epsilon' \mathbf{E} + \mathbf{J} \quad (1-17)$$

$$\nabla \cdot \mathbf{E} = \frac{\rho}{\epsilon'} \quad (1-18)$$

$$\nabla \cdot \mathbf{H} = 0 \quad (1-19)$$

$$\nabla \cdot \mathbf{J} = -j\omega \rho. \quad (1-20)$$

These are the time-harmonic electromagnetic field equations with source current density \mathbf{J} and source charge density ρ shown explicitly. Sometimes it is convenient to introduce a fictitious magnetic current density \mathbf{M} . Then (1-16) becomes

$$\nabla \times \mathbf{E} = -j\omega \mu \mathbf{H} - \mathbf{M}. \quad (1-21)$$

Magnetic currents are useful as equivalent sources that replace complicated electric currents.

The solution of the fundamental electromagnetic equations is not complete until the boundary conditions are satisfied. A sufficient set of boundary conditions (in the time-harmonic form) is

$$\hat{\mathbf{n}} \times (\mathbf{H}_2 - \mathbf{H}_1) = \mathbf{J}_s \quad (1-22)$$

$$(\mathbf{E}_2 - \mathbf{E}_1) \times \hat{\mathbf{n}} = \mathbf{M}_s \quad (1-23)$$

⁴ In general ϵ and μ can be complex, but in many antenna problems they can be approximated as real constants.

where the electric and magnetic surface currents, \mathbf{J}_s and \mathbf{M}_s , flow on the boundary between two homogeneous media with constitutive parameters $\epsilon_1, \mu_1, \sigma_1$, and $\epsilon_2, \mu_2, \sigma_2$. \mathbf{M}_s is zero unless an equivalent magnetic current sheet is used. The unit normal to the boundary surface $\hat{\mathbf{n}}$ is directed from medium 1 into medium 2. The cross products with the unit normal form the tangential components to the boundary, and these equations can be written as

$$H_{\tan 2} = H_{\tan 1} + J_s \quad (1-24)$$

$$E_{\tan 2} = E_{\tan 1} + M_s. \quad (1-25)$$

These boundary conditions are derived from the integral form of (1-17) and (1-21). If one side is a perfect electrical conductor, the boundary conditions become

$$H_{\tan} = J_s \quad (1-26)$$

$$E_{\tan} = 0. \quad (1-27)$$

The tangential boundary conditions on the magnetic field intensity are illustrated in Fig. 1-1 for the general case and for the case where medium 1 is a perfect conductor. It is important to note that all field quantities in the boundary condition equations are evaluated at the boundary and that the equations apply to each point along the boundary.

Also derivable from Maxwell's curl equations is a conservation of power equation, or Poynting's theorem [7]. Consider a volume v bounded by a closed surface s . The complex power P_s delivered by the sources in v equals the sum of

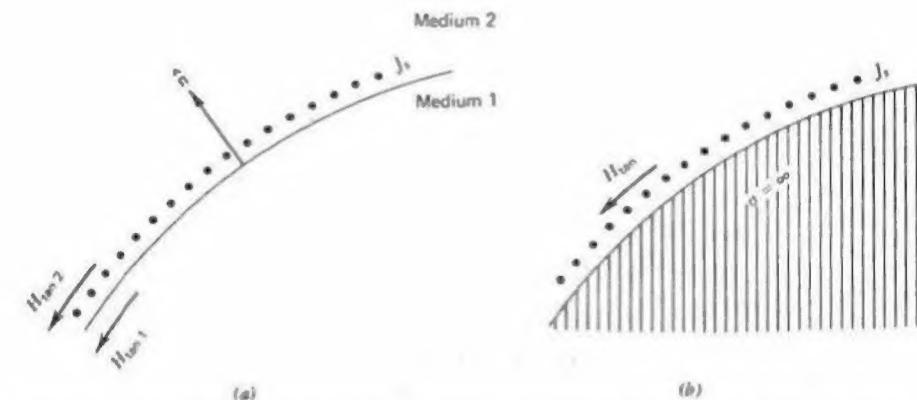


Figure 1-1 Magnetic field intensity boundary condition. (a) General case. (b) One medium a perfect conductor.

the power P_f flowing out of s , the time-average power $P_{d_{av}}$ dissipated in v , plus the time-average stored power in v ,

$$P_s = P_f + P_{d_{av}} + j2\omega(W_{m_{av}} - W_{e_{av}}). \quad (1-28)$$

The complex power flowing out through closed surface s is found from

$$P_f = \frac{1}{2} \oint_s \mathbf{E} \times \mathbf{H}^* \cdot d\mathbf{s} \quad (1-29)$$

where $d\mathbf{s} = ds\hat{\mathbf{n}}$ and $\hat{\mathbf{n}}$ is the unit normal to the surface directed *out* from the surface. The quantity $\mathbf{S} = \frac{1}{2}\mathbf{E} \times \mathbf{H}^*$ is the complex Poynting vector. The time-average dissipated power in volume v bounded by closed surface s is

$$P_{d_{av}} = \frac{1}{2} \iiint_v \sigma |E|^2 dv. \quad (1-30)$$

The time-average stored magnetic energy is

$$W_{m_{av}} = \frac{1}{2} \iiint_v \frac{1}{2} \mu |H|^2 dv. \quad (1-31)$$

The time-average stored electric energy is

$$W_{e_{av}} = \frac{1}{2} \iiint_v \frac{1}{2} \epsilon |E|^2 dv. \quad (1-32)$$

If the source power is not known explicitly, it may be calculated from the volume current density as follows:

$$P_s = -\frac{1}{2} \iiint_v \mathbf{E} \cdot \mathbf{J}^* dv. \quad (1-33)$$

If magnetic current density is used, a term $\mathbf{H}^* \cdot \mathbf{M}$ is added to the integrand in the preceding equation.

From (1-29) we see that the integral of the complex Poynting vector $\frac{1}{2}\mathbf{E} \times \mathbf{H}^*$ over a closed surface s gives the total complex power flowing out through the surface s . It is natural to assume that the complex Poynting vector represents the complex power density in watts per square meter at a point. Then the complex power through any surface s (not necessarily closed) can be found by integrating the complex Poynting vector over that surface. We are particularly interested in real power (the real component of the complex power which represents the

electric and magnetic field intensities being in-phase). The real power flowing through surface s is

$$P_{av} = \frac{1}{2} \operatorname{Re} \left(\oint_s \mathbf{E} \times \mathbf{H}^* \cdot d\mathbf{s} \right). \quad (1-34)$$

The reference direction for this average power flow is that of the specified unit normal $\hat{\mathbf{n}}$ contained in $d\mathbf{s} = ds\hat{\mathbf{n}}$.

1.3 SOLUTION OF MAXWELL'S EQUATIONS FOR RADIATION PROBLEMS

The antenna problem consists of solving for the fields that are created by an impressed current distribution \mathbf{J} . In the simplest approach this current distribution is obtained during the solution process. How to obtain the current distribution will be discussed at various points in the book, but for the moment suppose we have the current distribution and wish to determine the fields \mathbf{E} and \mathbf{H} . As mentioned in the previous section, we need only work with the two curl equations of Maxwell's equations as given by (1-16) and (1-17). These are two coupled, linear, first-order differential equations. They are coupled because the unknown functions, \mathbf{E} and \mathbf{H} , appear in both equations. Thus, these equations must be solved simultaneously. In order to simplify the solution for \mathbf{E} and \mathbf{H} with a given \mathbf{J} we introduce the scalar and vector potential functions Φ and \mathbf{A} .

The vector potential is introduced by noting from (1-19) that the divergence of \mathbf{H} is zero,

$$\nabla \cdot \mathbf{H} = 0. \quad (1-35)$$

Therefore the vector field \mathbf{H} has only circulation; for this reason it is often called a solenoidal field. Because it possesses only a circulation it can be represented by the curl of some other vector function as follows

$$\mathbf{H} = \nabla \times \mathbf{A} \quad (1-36)$$

where \mathbf{A} is the (*magnetic*) *vector potential*. To be more precise, (1-36) is possible because it satisfies (1-35) identically, that is, from (A-9) $\nabla \cdot \nabla \times \mathbf{A} \equiv 0$ for any \mathbf{A} . The curl of \mathbf{A} is defined by (1-36), but its divergence is yet to be specified for a complete definition of \mathbf{A} .

The scalar potential is introduced by substituting (1-36) into (1-16), which gives

$$\nabla \times (\mathbf{E} + j\omega\mu\mathbf{A}) = 0. \quad (1-37)$$

The expression in parentheses is an electric field, and since its curl is zero, it is a conservative field and behaves as a static electric field. The (electric) scalar potential Φ is defined from

$$\mathbf{E} + j\omega\mu\mathbf{A} = -\nabla\Phi \quad (1-38)$$

because this definition satisfies (1-37) identically, that is, from (A-10) $\nabla \times \nabla\Phi \equiv 0$ for any Φ . Solving (1-38) for the total electric field gives

$$\mathbf{E} = -j\omega\mu\mathbf{A} - \nabla\Phi \quad (1-39)$$

which may be a familiar result.

The fields \mathbf{E} and \mathbf{H} are now expressed in terms of potential functions by (1-36) and (1-39). If we knew the potential functions then the fields could be obtained. We shall now discuss the solution for the potential functions. Substituting (1-36) into (1-17) gives

$$\nabla \times \mathbf{H} = \nabla \times \nabla \times \mathbf{A} = j\omega\epsilon\mathbf{E} + \mathbf{J} \quad (1-40)$$

Using the following vector identity, from (A-17),

$$\nabla \times \nabla \times \mathbf{A} \equiv \nabla(\nabla \cdot \mathbf{A}) - \nabla^2 \mathbf{A} \quad (1-41)$$

and (1-39) in (1-40) yields

$$\nabla(\nabla \cdot \mathbf{A}) - \nabla^2 \mathbf{A} = j\omega\epsilon(-j\omega\mu\mathbf{A} - \nabla\Phi) + \mathbf{J} \quad (1-42)$$

or

$$\nabla^2 \mathbf{A} + \omega^2\mu\epsilon\mathbf{A} - \nabla(j\omega\epsilon\Phi + \nabla \cdot \mathbf{A}) = -\mathbf{J} \quad (1-43)$$

As we mentioned previously, the divergence of \mathbf{A} is yet to be specified. A convenient choice would be one that eliminates the third term of (1-43). It is the Lorentz condition

$$\nabla \cdot \mathbf{A} = -j\omega\epsilon\Phi \quad (1-44)$$

Then (1-43) reduces to

$$\nabla^2 \mathbf{A} + \omega^2\mu\epsilon\mathbf{A} = -\mathbf{J} \quad (1-45)$$

The choice of (1-44) leads to a decoupling of variables, that is, (1-45) involves \mathbf{A} and not Φ . This is the *vector wave equation*. It is a differential equation which can be solved for \mathbf{A} after the impressed current \mathbf{J} has been specified. The fields are easily found then from (1-36) and

$$\mathbf{E} = -j\omega\mu\mathbf{A} + \frac{\nabla(\nabla \cdot \mathbf{A})}{j\omega\epsilon} \quad (1-46)$$

where this equation was obtained from (1-39) and (1-44). Notice that only a knowledge of \mathbf{A} is required. A more cumbersome approach would be to solve the scalar wave equation

$$\nabla^2\Phi + \omega^2\mu\epsilon'\Phi = -\frac{\rho}{\epsilon'} \quad (1-47)$$

in addition to the vector wave equation. [It is left as a problem to derive (1-47).] If this approach is used, \mathbf{E} is found from (1-39). Note that ρ in (1-47) is related to \mathbf{J} in (1-45) by the continuity equation; see (1-20).

The vector wave equation (1-45) is solved by first forming three scalar equations. This is done by decomposing \mathbf{A} into rectangular components:

$$\nabla^2 \mathbf{A} = \hat{x} \nabla^2 A_x + \hat{y} \nabla^2 A_y + \hat{z} \nabla^2 A_z \quad (1-48)$$

Rectangular components are used because the unit vectors in rectangular components can be factored out of the Laplacian, since they are not themselves functions of coordinates. This feature is unique to the rectangular coordinate system. The Laplacian of \mathbf{A} is always performed for \mathbf{A} decomposed into rectangular components; however, the Laplacian of each component of \mathbf{A} may be expressed in any coordinate system. Proceeding with the solution, we substitute (1-48) into (1-45) and equate rectangular components, and we get

$$\begin{aligned} \nabla^2 A_x + \beta^2 A_x &= -J_x \\ \nabla^2 A_y + \beta^2 A_y &= -J_y \\ \nabla^2 A_z + \beta^2 A_z &= -J_z \end{aligned} \quad (1-49)$$

where $\beta^2 = \omega^2\mu\epsilon'$. At this point we will assume that $\sigma = 0$ so that $\epsilon' = \epsilon$, which is also assumed to be real. Then

$$\beta = \omega\sqrt{\mu\epsilon} \quad (1-50)$$

which is a real number, may be recognized as the phase constant for a plane wave.

The three equations of (1-49) are identical in form. Thus if we solve one of them, the other two are easily solved. We first find the solution for a point source, that is, the unit impulse response. The general solution is then the sum of weighted point source responses. The differential equation for a point source is

$$\nabla^2\psi + \beta^2\psi = -\delta(x)\delta(y)\delta(z) \quad (1-51)$$

where ψ is the response to a point source at the origin, and δ is the unit impulse function, or dirac delta function (see Appendix F.1). If the current is in the z -direction, for example, then $\psi = A_z$. For all points except at the origin

$$\nabla^2\psi + \beta^2\psi = 0 \quad (1-52)$$

This is the complex scalar wave equation or *Helmholtz equation*. Because of spherical symmetry the Laplacian is written in spherical coordinates and ψ has only radial dependence. The two solutions to (1-52) are $e^{-j\beta r}/r$ and $e^{+j\beta r}/r$. These correspond to waves propagating radially outward and inward, respectively. The physically meaningful solution is the one for waves traveling away from the point source. Evaluating the constant of proportionality (see Prob. 1.3-2) we have for the point source solution

$$\psi = \frac{e^{-j\beta r}}{4\pi r} \quad (1-53)$$

This is the solution to (1-51) and gives the effect of a point source at distance r away from a point source located at the origin. If the source were positioned at an arbitrary location, we must compute the distance R between the source location and observation point P (see Fig. 1-2). Then

$$\psi = \frac{e^{-j\beta R}}{4\pi R} \quad (1-54)$$

The point source solution is actually that of an ideal dipole and will be discussed more fully in the next section.

For an arbitrary z -directed current density, the vector potential is z -directed. If we consider the source to be a collection of point sources weighted by the distribution J_z , the response A_z is a sum of the point source responses of (1-54). This is expressed by the integral over the source volume v' :

$$A_z = \iiint_{v'} J_z \frac{e^{-j\beta R}}{4\pi R} dv' \quad (1-55)$$

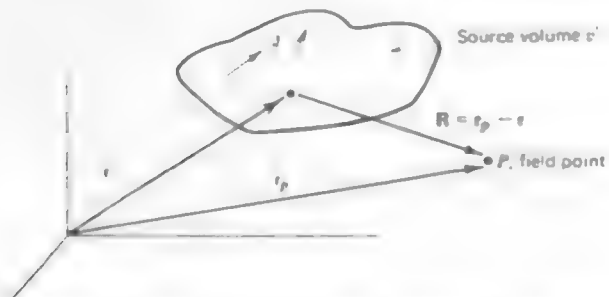


Figure 1-2 Vectors used to solve radiation problems

Similar equations hold for the x - and y -components. The total solution is then the sum of all components:

$$\mathbf{A} = \iiint_{v'} \mathbf{J} \frac{e^{-j\beta R}}{4\pi R} dv' \quad (1-56)$$

This is the solution to the vector wave equation (1-45). The geometry is shown in Fig. 1-2. The coordinate system shown is used to describe both the source point and field point. \mathbf{r}' is the vector from the coordinate origin to the source point, and \mathbf{r}_p is the vector from the coordinate origin to the field point P . The vector \mathbf{R} is the vector from the source point to the field point and is given by $\mathbf{r}_p - \mathbf{r}'$. This geometry will be used henceforth.

We can summarize rather simply the procedure for finding the fields generated by a current distribution \mathbf{J} . First \mathbf{A} is found from (1-56). The \mathbf{H} field is found from (1-36). The \mathbf{E} field may be found from (1-46), but frequently it is simpler to find \mathbf{E} from (1-17) as

$$\mathbf{E} = \frac{1}{j\omega\epsilon} (\nabla \times \mathbf{H} - \mathbf{J}) \quad (1-57)$$

if we are in the source region, or from just

$$\mathbf{E} = \frac{1}{j\omega\epsilon} \nabla \times \mathbf{H} \quad (1-58)$$

if the field point is removed in distance from the source, that is, if $\mathbf{J} = 0$ at point P .

1.4 THE IDEAL DIPOLE

In this section the principles presented in the previous section are used to find the fields of an infinitesimal element of current. We shall use the term *ideal dipole* for a piece of uniform amplitude current which is of infinitesimal length or of very small finite length, $\Delta z \ll \lambda$. It does not exist by itself, but it may be considered to be a piece of a larger current on an actual antenna. The ideal dipole concept is also useful because its fields approximate those of electrically small dipoles to be discussed in Chapter 2.

Consider an element of current of length Δz along the z -axis centered on the

coordinate origin. It is of constant amplitude I . In this case the volume integral of (1-56) for vector potential reduces to the one-dimensional integral⁵

$$\mathbf{A} = \hat{\mathbf{z}} I \int_{-\Delta z/2}^{\Delta z/2} \frac{e^{-j\beta R}}{4\pi R} dz' \quad (1-59)$$

The length Δz is very small compared to a wavelength and to the distance R . See Fig. 1-3. Since Δz is very small, the distance R from points on the current element to the field point approximately equals the distance r from the origin to the field point. Substituting r for R in (1-59) and integrating gives

$$\mathbf{A} = \frac{I e^{-j\beta r}}{4\pi r} \Delta z \hat{\mathbf{z}} \quad (1-60)$$

This is exactly true for an infinitesimal current element and is approximately true for a small ($\Delta z \ll \lambda$ and $\Delta z \ll R$) but finite uniform current element. The vector potential A_z for an infinitesimal current was also derived in the previous section; see (1-53) in which $I \Delta z = 1$. For many current sources we can readily make the substitution of r for R in the denominator of the integrand in (1-59) but usually cannot make the same substitution in the exponent. However, in the case of a very small source, we can use r for R in both the denominator and exponent.

We are now ready to calculate the electromagnetic fields created by the ideal dipole. The magnetic field is found from (1-36) as

$$\mathbf{H} = \nabla \times \mathbf{A} = \nabla \times (A_z \hat{\mathbf{z}}) \quad (1-61)$$

If we apply the vector identity (A-16), the preceding equation becomes

$$\mathbf{H} = (\nabla A_z) \times \hat{\mathbf{z}} + A_z (\nabla \times \hat{\mathbf{z}}) = (\nabla A_z) \times \hat{\mathbf{z}} \quad (1-62)$$

The second term is zero because the curl of a constant vector is zero. Substituting (1-60) into (1-62) we have

$$\mathbf{H} = \nabla \left(\frac{I \Delta z e^{-j\beta r}}{4\pi r} \right) \times \hat{\mathbf{z}} \quad (1-63)$$

⁵ The result in (1-59) could also be obtained by representing the current density as

$$\mathbf{J} = I \delta(x') \delta(y') \hat{\mathbf{z}} \quad \text{for} \quad -\frac{\Delta z}{2} < z' < \frac{\Delta z}{2}$$

Substituting this into (1-56) yields

$$\mathbf{A} = \hat{\mathbf{z}} I \int_{-\infty}^{\infty} \delta(x') dx' \int_{-\infty}^{\infty} \delta(y') dy' \int_{-\Delta z/2}^{\Delta z/2} \frac{e^{-j\beta R}}{4\pi R} dz'$$

from which (1-59) follows

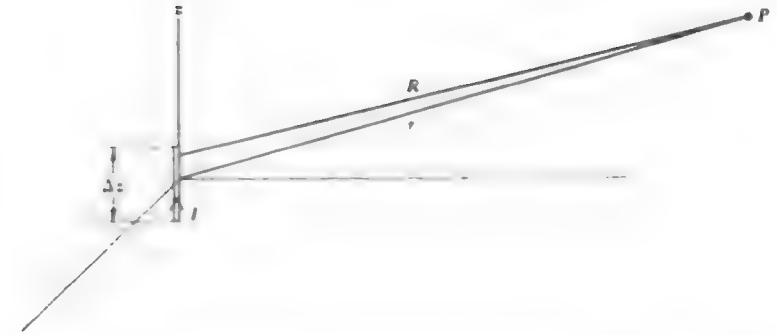


Figure 1-3 The ideal dipole. The current I is uniform, $\Delta z \ll \lambda$, and $R \approx r$.

Applying the gradient in spherical coordinates from (A-33) gives

$$\begin{aligned} \mathbf{H} &= \frac{I \Delta z}{4\pi} \frac{\partial}{\partial r} \left(\frac{e^{-j\beta r}}{r} \right) \hat{\mathbf{r}} \times \hat{\mathbf{z}} \\ &= \frac{I \Delta z}{4\pi} \left[-\frac{j\beta e^{-j\beta r}}{r} - \frac{e^{-j\beta r}}{r^2} \right] \hat{\mathbf{r}} \times \hat{\mathbf{z}} \end{aligned} \quad (1-64)$$

From (A-3) we have

$$\hat{\mathbf{r}} \times \hat{\mathbf{z}} = \hat{\mathbf{r}} \times (\hat{\mathbf{r}} \cos \theta - \hat{\boldsymbol{\theta}} \sin \theta) = -\hat{\boldsymbol{\phi}} \sin \theta \quad (1-65)$$

Substituting (1-65) into (1-64) gives

$$\mathbf{H} = \frac{I \Delta z}{4\pi} \left[\frac{j\beta}{r} + \frac{1}{r^2} \right] e^{-j\beta r} \sin \theta \hat{\boldsymbol{\phi}} \quad (1-66)$$

The electric field can be obtained from (1-58) as

$$\begin{aligned} \mathbf{E} &= \frac{I \Delta z}{4\pi} \left[\frac{j\omega\mu}{r} + \sqrt{\frac{\mu}{\epsilon}} \frac{1}{r^2} + \frac{1}{j\omega\epsilon r^3} \right] e^{-j\beta r} \sin \theta \hat{\boldsymbol{\theta}} \\ &\quad + \frac{I \Delta z}{2\pi} \left[\sqrt{\frac{\mu}{\epsilon}} \frac{1}{r^2} + \frac{1}{j\omega\epsilon r^3} \right] e^{-j\beta r} \cos \theta \hat{\mathbf{r}} \end{aligned} \quad (1-67)$$

where we still have

$$\beta = \omega \sqrt{\mu\epsilon} \quad (1-68)$$

Note that if the medium surrounding the dipole is air or free space, $\beta = \omega \sqrt{\mu_0 \epsilon_0}$.

Equations (1-66) and (1-67) may be written as

$$\mathbf{H} = \frac{I \Delta z}{4\pi} j\beta \left(1 + \frac{1}{j\beta r}\right) \frac{e^{-j\beta r}}{r} \sin \theta \hat{\phi} \quad (1-69)$$

$$\begin{aligned} \mathbf{E} = & \frac{I \Delta z}{4\pi} j\omega\mu \left[1 + \frac{1}{j\beta r} + \frac{1}{(j\beta r)^2}\right] \frac{e^{-j\beta r}}{r} \sin \theta \hat{\theta} \\ & + \frac{I \Delta z}{2\pi} j\omega\mu \left[\frac{1}{j\beta r} + \frac{1}{(j\beta r)^2}\right] \frac{e^{-j\beta r}}{r} \cos \theta \hat{r}. \end{aligned} \quad (1-70)$$

If βr is large (i.e., $\beta r \gg 1$, or $r \gg \lambda$ since $\beta = 2\pi/\lambda$), then all terms having inverse powers of $j\beta r$ are small compared to unity, and (1-69) and (1-70) reduce to

$$\mathbf{E} = \frac{I \Delta z}{4\pi} j\omega\mu \frac{e^{-j\beta r}}{r} \sin \theta \hat{\theta} \quad (1-71)$$

$$\mathbf{H} = \frac{I \Delta z}{4\pi} j\beta \frac{e^{-j\beta r}}{r} \sin \theta \hat{\phi}. \quad (1-72)$$

These are the fields of an ideal dipole at large distances from the dipole. The ratio of these electric and magnetic field components is

$$\frac{E_\theta}{H_\phi} = \frac{\omega\mu}{\beta} = \frac{\omega\mu}{\omega\sqrt{\mu\epsilon}} = \sqrt{\frac{\mu}{\epsilon}} = \eta \quad (1-73)$$

where $\eta = \sqrt{\mu/\epsilon}$ is the intrinsic impedance of the medium (for free space $\eta_0 = 376.7 \text{ ohms} \approx 120\pi \text{ ohms}$). This is a property of plane waves. Also we shall see that at large distances from any antenna, the fields are related in this manner.

Using the fields of (1-71) and (1-72), we can find an expression for the complex power flowing out of a sphere of radius r surrounding the ideal dipole from (1-29) as follows

$$\begin{aligned} P_f &= \frac{1}{2} \oint \mathbf{E} \times \mathbf{H}^* \cdot d\mathbf{s} \\ &= \frac{1}{2} \left(\frac{I \Delta z}{4\pi} \right)^2 \int_0^{2\pi} \int_0^\pi j\omega\mu \frac{e^{-j\beta r}}{r} \sin \theta \hat{\theta} \times (-j\beta) \frac{e^{+j\beta r}}{r} \sin \theta \hat{\phi} \cdot d\mathbf{s} \\ &= \frac{1}{2} \left(\frac{I \Delta z}{4\pi} \right)^2 \omega\mu\beta \int_0^{2\pi} \int_0^\pi \frac{\sin^2 \theta}{r^2} \hat{r} \cdot r^2 \sin \theta d\theta d\phi \\ &= \frac{1}{2} \left(\frac{I \Delta z}{4\pi} \right)^2 \omega\mu\beta \int_0^{2\pi} d\phi \int_0^\pi \sin^3 \theta d\theta \\ &= \frac{1}{2} \left(\frac{I \Delta z}{4\pi} \right)^2 \omega\mu\beta 2\pi \frac{4}{3} \\ &= \frac{\omega\mu\beta}{12\pi} (I \Delta z)^2. \end{aligned} \quad (1-74)$$

This is a real quantity, and real power indicates dissipated power. It is dissipated in the sense that it travels away from the source and can never be recovered. In fact, the average power going out through a sphere of radius r can be found [see (1-34)] by taking the real part of (1-74), which leaves it unchanged. This power expression is independent of r , and thus if we integrate over a sphere of larger radius, we still have the same total power streaming through it. We refer to this type of power as *radiated power*. The fields in (1-71) and (1-72) are called *radiation fields*. The region in which the radiation fields are the most significant portion of all fields arising from the antenna is called the *far-field region*, or simply the far field or far zone. The distance away from an antenna where the far field begins is discussed further in Section 1.5.

In the *near-field region* of an antenna, terms of the field expressions with powers of inverse r greater than one are significant compared to the radiation fields. The complex Poynting vector $\frac{1}{2} \mathbf{E} \times \mathbf{H}^*$ will then contain terms with powers of $(1/r)$ of three and higher in addition to the radiation field term, that varies as $1/r^2$. It turns out that these terms are pure imaginary, indicating reactive power. Thus, in the near field of an antenna there is stored energy.

The input impedance of an antenna is, in general, complex. The real part (neglecting ohmic losses on the antenna structure) represents radiation, while the imaginary part corresponds to the reactive near-field power. Antenna impedance will be discussed further in Section 1.8.

1.5 RADIATION PATTERN

A *radiation pattern* is a graphical representation of the radiation (far-field) properties of an antenna. It can be measured by moving a probe antenna around the test antenna at a constant distance from it, noting the response as a function of angular coordinates. The probe antenna is usually maintained in a given orientation. For example, consider an ideal dipole along the z -axis at the origin as shown in Fig. 1-4a. Its radiation fields are given by (1-71) and (1-72). Since the electric field is totally θ -directed we would choose a probe antenna that responds to this field. Another ideal dipole oriented as shown in Fig. 1-4a will serve as a probe and it responds to E_θ . As this probe is moved over the spherical surface its output (terminal voltage) varies and is recorded. The variation of E_θ over the sphere, from (1-71), is $\sin \theta$; remember r is constant during this measurement. Any plane containing the z -axis has the same radiation pattern since there is no ϕ variation in the fields. A pattern taken in one of these planes is called an *E-plane pattern* because it contains the electric vector. A pattern taken in a plane perpendicular to an *E-plane* and cutting through the test antenna (the xy -plane in this case) is called an *H-plane pattern* because it contains the magnetic field vector (H_ϕ). The *E*- and *H*-plane patterns for the ideal dipole are shown in Fig. 1-4b and 1-4c. These are polar plots in which the distance from the

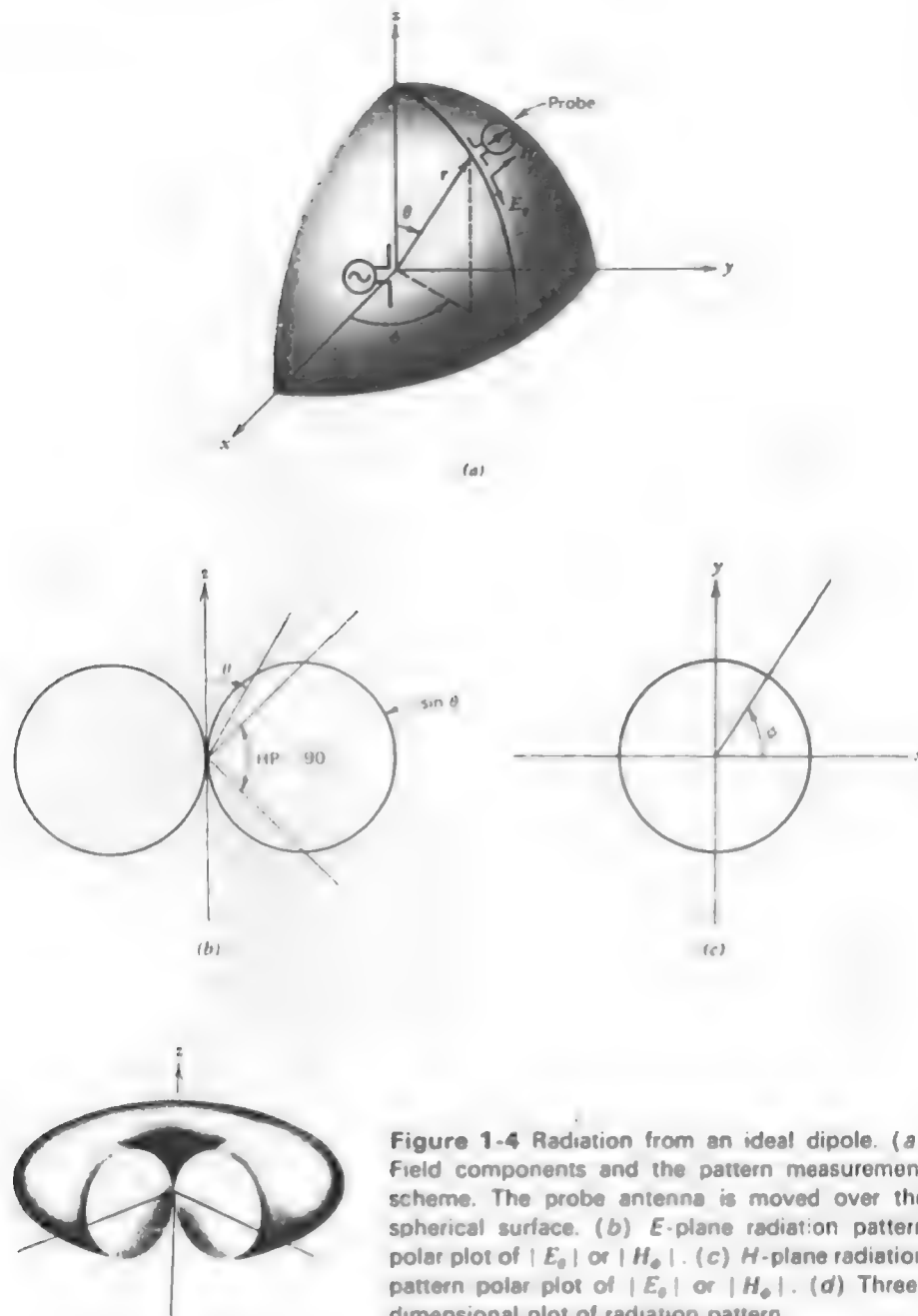


Figure 1-4 Radiation from an ideal dipole. (a) Field components and the pattern measurement scheme. The probe antenna is moved over the spherical surface. (b) E -plane radiation pattern polar plot of $|E_\theta|$ or $|H_\phi|$. (c) H -plane radiation pattern polar plot of $|E_\theta|$ or $|H_\phi|$. (d) Three-dimensional plot of radiation pattern.

origin to the curve is proportional to the field intensity. The E - and H -plane patterns, in general, are referred to as *principal plane patterns*.

The complete pattern for the ideal dipole is shown in isometric view with a slice removed in Fig. 1-4d. It resembles a "holeless doughnut," and is often referred to as an *omnidirectional pattern* since it is uniform in the xy -plane. When encountering new antennas the reader should attempt to visualize the complete pattern in three dimensions.

Radiation patterns in general may be calculated in a manner similar to that used for the ideal dipole if the current distribution on the antenna is known. This is done by first finding the vector potential given in (1-56). As a simple example consider a filament of current along the z -axis and located near the origin. Many antennas may be modeled by this *line source*; straight wire antennas are good examples. In this case the vector potential has only a z -component and the vector potential integral is one-dimensional⁶

$$A_z = \int I(z') \frac{e^{-j\beta R}}{4\pi R} dz'. \quad (1-75)$$

Due to the symmetry of the source we expect that the radiation fields will not vary with ϕ . This is because as the observer moves around the source such that r and z are constant, the appearance of the source remains the same; thus, its radiation fields are also unchanged. Therefore, for simplicity we will confine the observation point to a fixed ϕ in the yz -plane ($\phi = 90^\circ$) as shown in Fig. 1-5. Then from Fig. 1-5 we see that

$$r^2 = y^2 + z^2 \quad (1-76)$$

$$z = r \cos \theta \quad (1-77)$$

$$y = r \sin \theta. \quad (1-78)$$

Also $\mathbf{r}_p = r \hat{y} + z \hat{z}$ and $\mathbf{r}' = z' \hat{z}$ lead to $\mathbf{R} = \mathbf{r}_p - \mathbf{r}' = y \hat{y} + (z - z') \hat{z}$ and then

$$\begin{aligned} R &= \sqrt{y^2 + (z - z')^2} \\ &= \sqrt{y^2 + z^2 - 2zz' + (z')^2}. \end{aligned} \quad (1-79)$$

Substituting (1-76) and (1-77) into (1-79), to put all field point coordinates into the spherical coordinate system, gives

$$R = \{r^2 + [-2r \cos \theta z' + (z')^2]\}^{1/2}. \quad (1-80)$$

⁶ This result could also be obtained by using $J_z(\mathbf{r}') = I(z') \delta(x') \delta(y')$ in (1-55) where $d\mathbf{r}' = dx' dy' dz'$.

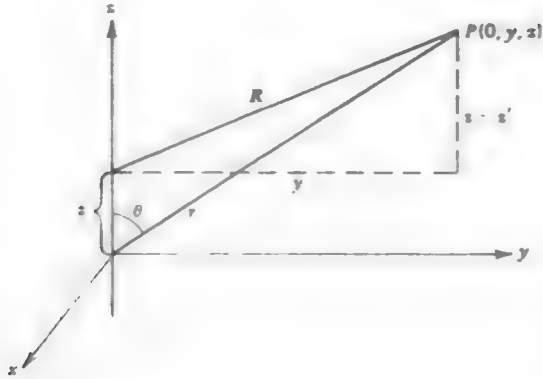


Figure 1-5 Geometry used for field calculations of a line source along the z -axis

In order to develop approximate expressions for R , we expand (1-80) using the binomial theorem (F-4):

$$\begin{aligned}
 R &= (r^2)^{1/2} + \frac{1}{2} (r^2)^{-1/2} [-2r \cos \theta z' + (z')^2] + \frac{\frac{1}{2}(-\frac{1}{2})}{2} (r^2)^{-3/2} \\
 &\quad \cdot [-2r \cos \theta z' + (z')^2]^2 + \dots \\
 &= r - z' \cos \theta + \frac{(z')^2}{2r} - \frac{(z')^2 \cos^2 \theta}{2r} + \text{terms of order } \left(\frac{1}{r^2}\right) + \dots \\
 &= r - z' \cos \theta + \frac{(z')^2 \sin^2 \theta}{2r} + \dots
 \end{aligned} \quad (1-81)$$

The terms in this series decrease as the power of z' increases if z' is small compared to r . This expression for R is used in the radiation integral (1-75) to different degrees of approximation. In the denominator (which affects only the amplitude) we let

$$R \approx r. \quad (1-82)$$

We can do this because in the far field r is very large compared to the antenna size, so $r \gg z' \geq z' \cos \theta$. In the phase term $-\beta R$ we must be more accurate when computing the distance from points along the line source to the observation point. The integral (1-75) sums the contributions from all the points along the line source. Although the amplitude of waves due to each source point is essentially the same, the phase may be different if the path length differences are

a sizable fraction of a wavelength. We, therefore, include the first two terms of the series in (1-81) for the R in the numerator of (1-75) giving

$$R \approx r - z' \cos \theta. \quad (1-83)$$

Using the far-field approximations (1-82) and (1-83) in (1-75) yields

$$\begin{aligned}
 A_z &= \int I(z') \frac{e^{-j\beta r - z' \cos \theta}}{4\pi r} dz' \\
 &= \frac{e^{-j\beta r}}{4\pi r} \int I(z') e^{j\beta z' \cos \theta} dz'
 \end{aligned} \quad (1-84)$$

where the integral is over the extent of the line source. This may be recognized as a Fourier transform type integral. Next the magnetic field is found from

$$\begin{aligned}
 \mathbf{H} &= \nabla \times \mathbf{A} = \nabla \times (A_z \hat{\mathbf{z}}) \\
 &= \nabla \times (-A_z \sin \theta \hat{\mathbf{r}} + A_z \cos \theta \hat{\boldsymbol{\theta}})
 \end{aligned} \quad (1-85)$$

where (A-3) was used. Since A_z is a function of r and θ , the curl in spherical coordinates, as given by (A-35), leads to

$$\mathbf{H} = \hat{\boldsymbol{\phi}} \frac{1}{r} \left[\frac{\partial}{\partial r} (-r A_z \sin \theta) - \frac{\partial}{\partial \theta} (A_z \cos \theta) \right]. \quad (1-86)$$

Substitution of (1-84) into the above gives

$$\begin{aligned}
 \mathbf{H} &= \hat{\boldsymbol{\phi}} \left\{ \frac{-\sin \theta}{4\pi r} \int I(z') e^{j\beta z' \cos \theta} dz' \frac{\partial}{\partial r} e^{-j\beta r} - \frac{e^{-j\beta r}}{4\pi r^2} \frac{\partial}{\partial \theta} \right. \\
 &\quad \left. \cdot \left[\cos \theta \int I(z') e^{j\beta z' \cos \theta} dz' \right] \right\} \\
 &= \hat{\boldsymbol{\phi}} \frac{e^{-j\beta r}}{4\pi r} \left\{ j\beta \sin \theta \int I(z') e^{j\beta z' \cos \theta} dz' \right. \\
 &\quad \left. - \frac{1}{r} \frac{\partial}{\partial \theta} \left[\cos \theta \int I(z') e^{j\beta z' \cos \theta} dz' \right] \right\}.
 \end{aligned} \quad (1-87)$$

The ratio of the first term to the second term above is of the order βr . If $\beta r \gg 1$ the second term is small compared to the first and may be neglected, as we did for the far-field approximation of the ideal dipole in Section 1.4. Thus (1-87) becomes

$$\mathbf{H} = \hat{\boldsymbol{\phi}} j\beta \sin \theta \frac{e^{-j\beta r}}{4\pi r} \int I(z') e^{j\beta z' \cos \theta} dz' = \hat{\boldsymbol{\phi}} j\beta \sin \theta A_z. \quad (1-88)$$

The electric field is found from (1-46), which is

$$\mathbf{E} = -j\omega\mu\mathbf{A} + \frac{\nabla(\mathbf{V} \cdot \mathbf{A})}{j\omega\epsilon} \quad (1-89)$$

Using (1-75) in (1-89) and retaining only the r^{-1} term (and assuming $\beta r \gg 1$) leads to the far-field approximation

$$\mathbf{E} = -j\omega\mu A_\theta \hat{\theta} = \hat{\theta} j\omega\mu \sin \theta A_z \quad (1-90)$$

Note that (1-90) is the portion of the first term of (1-89) which is transverse to \hat{r} because $-j\omega\mu\mathbf{A} = -j\omega\mu(-A_z \sin \theta \hat{\theta} + A_z \cos \theta \hat{r})$. This is a general feature that may be exploited to simplify radiation calculations.

The radiation fields from a z -directed line source (any z -directed current source in general) are H_ϕ and E_θ , and are found from (1-88) and (1-90). The only remaining problem is to calculate A_z , which is given by (1-55) in general and by (1-84) for z -directed line sources. Calculation of A_z is the focal point of antenna analysis. We shall return to this topic after pausing to further examine the characteristics of the far-field region.

The ratio of the radiation field components as given by (1-88) and (1-90) yields

$$\begin{aligned} E_\theta &= \frac{\omega\mu}{\beta} H_\phi = \frac{\omega\mu}{\omega\sqrt{\mu\epsilon}} H_\phi \\ &= \eta H_\phi \end{aligned} \quad (1-91)$$

where $\eta = \sqrt{\mu/\epsilon}$ = intrinsic impedance of the medium. An interesting conclusion can be made at this point. The radiation fields are perpendicular to each other and to the direction of propagation \hat{r} and their magnitudes are related by (1-91). These are the properties of a plane wave except that the phase is not constant over a plane, and from (1-88) the magnitude dependence is $1/r$. However, at large distances the wave appears to an observer to be a plane wave over a small region. This is called "local plane wave behavior," or more formally a TEM (transverse electromagnetic) wave. Thus, having found any one component of a radiation field the other may be found by plane wave relationships. These are general properties of radiating systems. If we get far enough away from any source the fields exhibit local plane wave behavior and have a magnitude dependence of $1/r$.

These far-field approximations have a simple geometric interpretation. If we draw the rays from each point on the source as parallel lines, then (1-83) is easily verified as indicated in Fig. 1-6. The parallel ray assumption is exact only when the observation point is at infinity, but it is a good approximation in the far field. Radiation calculations are frequently begun by assuming parallel rays and then

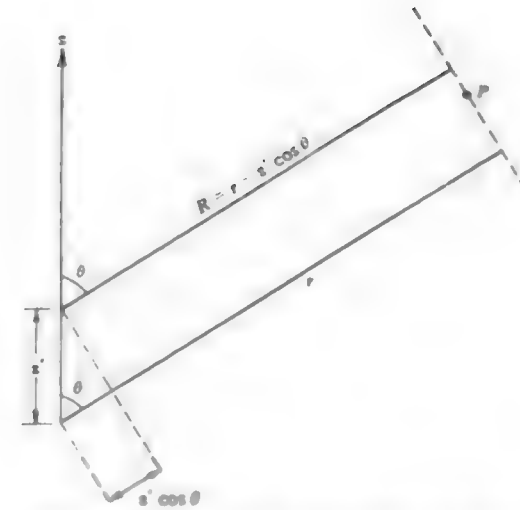


Figure 1-6 Parallel ray approximation for far-field calculations of a line source.

determining R for the phase by geometrical techniques. Consider a general source shown in Fig. 1-7. From the figure we see that

$$R = r - r' \cos \alpha \quad (1-92)$$

Using the definition of dot product, we have

$$R = r - r' \frac{\mathbf{r} \cdot \mathbf{r}'}{rr'}$$

or

$$R = r - \hat{r} \cdot \mathbf{r}' \quad (1-93)$$

Notice that if $\mathbf{r}' = z'\hat{z}$, as for line sources along the z -axis, (1-93) reduces to (1-83). Equation (1-93) provides a general method for obtaining the far-field approximation to R for the phase factor in the radiation integral.

The definition of the distance from the source where the far field begins is taken to be where the parallel ray approximation begins to breakdown. To be precise the distance where the far field begins, r_{ff} , is that value of r for which the path length deviation due to neglecting the third term of (1-81) is a sixteenth of a wavelength. This corresponds to a phase error (by neglecting the third term) of $2\pi/\lambda \cdot \lambda/16 = \pi/8 \text{ rad} = 22.5^\circ$.

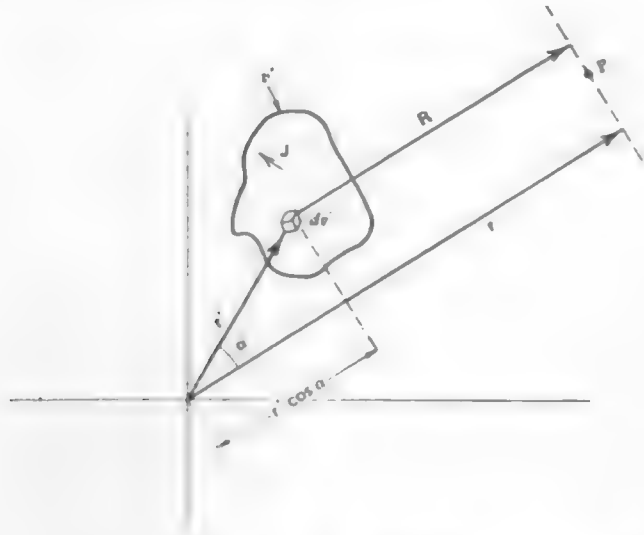


Figure 1-7 Parallel ray approximation for far-field calculations of a general source.

If D is the length of the line source, r_{ff} is found by equating the maximum value of the third term of (1-81), that is, for $z' = D/2$ and $\theta = 90^\circ$, to a sixteenth of a wavelength as

$$\frac{(D/2)^2}{2r_{ff}} = \frac{\lambda}{16} \quad (1-94)$$

Solving for r_{ff} gives

$$r_{ff} = \frac{2D^2}{\lambda} \quad (1-95)$$

The far-field region is $r \geq r_{ff}$.

The far-field conditions are summarized as follows.

$r > \frac{2D^2}{\lambda}$	
$r \gg D$	far-field conditions
$r \gg \lambda$	

$$(1-96)$$

$$(1-97)$$

$$(1-98)$$

The condition $r \gg D$ was mentioned in association with (1-82) for the amplitude approximation. The condition $r \gg \lambda$ follows from $\beta r = (2\pi r/\lambda) \gg 1$ which was used to reduce (1-87) to (1-88). Usually the far field is taken to begin at a distance given by (1-95) where D is the maximum dimension of the antenna. This is usually a sufficient condition for antennas operating in the VHF region and above. At lower frequencies, where the antenna may be small compared to the wavelength, the far-field distance may have to be greater than $2D^2/\lambda$ in order that the conditions (1-97) and (1-98) be satisfied.

So far in this section we have derived expressions for radiation fields and have defined the region over which they are valid. Fortunately it is not necessary to repeat these derivations every time the radiation fields from an antenna are to be calculated. The procedure for obtaining the radiation fields can be reduced to three steps.

1. **Find A.** Select a coordinate system most compatible with the geometry of the antenna, using the notation of Fig. 1-2. In general, use (1-56) with $R \approx r$ and the parallel ray approximation of (1-93) for determining phase differences over the antenna. These yield

$$A = \frac{e^{-j\beta r}}{4\pi r} \iiint_{V'} J e^{j\beta \mathbf{r}' \cdot \mathbf{r}} dv' \quad (1-99)$$

For z -directed sources

$$A = \hat{z} \frac{e^{-j\beta r}}{4\pi r} \iint_{V'} J_z e^{j\beta \mathbf{r}' \cdot \mathbf{r}} dv' \quad (1-100)$$

For z -directed line sources on the z -axis

$$A = \hat{z} \frac{e^{-j\beta r}}{4\pi r} \int I(z') e^{j\beta z' \cos \theta} dz' \quad (1-101)$$

2. **Find E.** In general, use the component of

$$\mathbf{E} = -j\omega\mu\mathbf{A} \quad (1-102)$$

which is transverse to the direction of propagation, \mathbf{f} . This is expressed formally as

$$\mathbf{E} = -j\omega\mu\mathbf{A} - (-j\omega\mu\mathbf{A} \cdot \hat{\mathbf{r}})\hat{\mathbf{r}} \quad (1-103)$$

For z -directed sources

$$\mathbf{E} = j\omega\mu \sin \theta A_z \hat{\theta} \quad (1-104)$$

3. Find \mathbf{H} . In general, use the plane wave relation

$$\mathbf{H} = \frac{1}{\eta} \hat{\mathbf{r}} \times \mathbf{E} \quad (1-105)$$

This equation expresses the fact that in the far field the directions of \mathbf{E} and \mathbf{H} are perpendicular to each other and to the direction of propagation, and also that their magnitudes are related by η . For z -directed sources

$$H_\phi = \frac{E_\theta}{\eta} \quad (1-106)$$

The most difficult step is the first, calculating the radiation integral. This topic will be discussed many times throughout the book, but to immediately develop an appreciation for the process we will present an example. This uniform line source example will also serve to provide a specific setting for introducing general radiation pattern concepts and definitions.

Example 1-1. The Uniform Line Source

The **uniform line source** is a line source for which the current is constant along its extent. If we use a z -directed uniform line source centered on the origin and along the z -axis, the current is

$$I(z') = \begin{cases} I_0 & z' = 0, \quad y' = 0, \quad |z'| \leq \frac{L}{2} \\ 0 & \text{elsewhere} \end{cases} \quad (1-107)$$

where L is the length of the line source. See Fig. 1-8. We first find A_z from (1-101) as follows.

$$\begin{aligned} A_z &= \frac{e^{-j\beta r}}{4\pi r} \int_{-L/2}^{L/2} I_0 e^{j\beta r' \cos \theta} dz' \\ &= \frac{e^{-j\beta r}}{4\pi r} I_0 \left[\frac{e^{j\beta L/2 \cos \theta} - e^{-j\beta L/2 \cos \theta}}{j\beta \cos \theta} \right] \\ &= \frac{I_0 L e^{-j\beta r}}{4\pi r} \frac{\sin[(\beta L/2) \cos \theta]}{(\beta L/2) \cos \theta} \end{aligned} \quad (1-108)$$

The electric field from (1-104) is then

$$\mathbf{E} = j\omega\mu \sin \theta A_z \hat{\boldsymbol{\theta}} = \frac{j\omega\mu I_0 L e^{-j\beta r}}{4\pi r} \sin \theta \frac{\sin[(\beta L/2) \cos \theta]}{(\beta L/2) \cos \theta} \hat{\boldsymbol{\theta}} \quad (1-109)$$

The magnetic field is simply found from this using $H_\phi = E_\theta/\eta$.

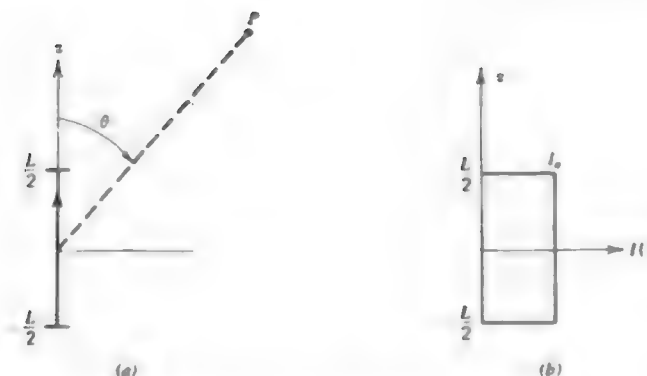


Figure 1-8 The uniform line source (Example 1-1). (a) Antenna geometry. (b) Current distribution.

Since the radiation pattern is the variation over a sphere centered on the antenna, r is constant and we have only θ and ϕ variation of the field. It is convenient to normalize the field expression such that its maximum value is unity. This is accomplished as follows for a z -directed source which has only a θ -component of \mathbf{E}

$$F(\theta, \phi) = \frac{E_\theta}{E_\theta(\max)} \quad (1-110)$$

where $F(\theta, \phi)$ is the *normalized field pattern* and $E_\theta(\max)$ is the maximum value of E_θ over a sphere of radius r . This variation is, of course, independent of r . An element of current on the z -axis has a normalized field pattern from (1-71) of

$$F(\theta) = \frac{(I \Delta z / 4\pi) j\omega\mu (e^{-j\beta r}/r) \sin \theta}{(I \Delta z / 4\pi) j\omega\mu (e^{-j\beta r}/r)} = \sin \theta \quad (1-111)$$

and there is no ϕ variation. The normalized field pattern for the uniform line source is from (1-109) in (1-110)

$$F(\theta) = \sin \theta \frac{\sin[(\beta L/2) \cos \theta]}{(\beta L/2) \cos \theta} \quad (1-112)$$

and again there is no ϕ variation. The second factor of this expression is the function $\sin(u)/u$ and we shall be encountering it frequently. It has a maximum value of unity at $u = 0$; this corresponds to $\theta = 90^\circ$ where $u = (\beta L/2) \cos \theta$. Substituting $\theta = 90^\circ$ in (1-112) gives unity and we see that $F(\theta)$ is normalized.

In general, a normalized field pattern can be written as the product

$$F(\theta, \phi) = g(\theta, \phi) f(\theta, \phi) \quad (1-113)$$

where $g(\theta, \phi)$ is the *element factor* and $f(\theta, \phi)$ is *pattern factor*. The pattern factor comes from the integral over the current and is strictly due to the distribution of current in space. The element factor is the pattern of an infinitesimal current element in the current distribution. For example, we found for a z -directed current element that $F(\theta) = \sin \theta$. This is, obviously, also the element factor, so

$$g(\theta) = \sin \theta \quad (1-114)$$

for a z -directed current element. Actually this factor originates from (1-90) and can be interpreted as the projection of the current element in the θ -direction. In other words, at $\theta = 90^\circ$ we see the maximum length of the current, whereas at $\theta = 0^\circ$ or 180° we see the endview of an infinitesimal current which yields no radiation. The $\sin \theta$ factor expresses the fraction of the size of the current as seen from the observation angle θ . On the other hand, the pattern factor $f(\theta, \phi)$ expresses the fractional change in the radiation due to the total effect of parallel rays emanating from the source. These rays arrive with different phases and the radiation integral (1-99) sums all of these rays. For a source with constant phase all rays arrive in-phase in the direction normal to the antenna and the pattern is maximum there. For the ideal dipole we have said that the source is so small that there are essentially no phase differences for rays along the source and thus the pattern factor is unity.

For the z -directed uniform line source pattern of (1-112) we can identify the factors as

$$g(\theta) = \sin \theta \quad (1-115)$$

and

$$f(\theta) = \frac{\sin[(\beta L/2) \cos \theta]}{(\beta L/2) \cos \theta} \quad (1-116)$$

For long line sources ($L \gg \lambda$) the pattern factor of (1-116) is much sharper than the element factor $\sin \theta$, and the total pattern is approximately that of (1-116), that is, $F(\theta) \approx f(\theta)$. Hence, in many cases we need only work with $f(\theta)$, which is obtained from (1-101). If we allow the beam to be scanned (this will be discussed below) the element factor becomes important as the pattern maximum approaches the z -axis.

Frequently the directional properties of the radiation from an antenna are described by another form of radiation pattern, the power pattern. The *power pattern* gives the power density angular dependence and is found from the θ, ϕ variation of the r -component of the Poynting vector. For z -directed sources

$H_\phi = E_\theta/\eta$ so the r -component of the Poynting vector is $\frac{1}{2} E_\theta H_\phi^* = |E_\theta|^2/2\eta$ and the normalized power pattern is simply the square of its field pattern

$$P(\theta) = |F(\theta)|^2 \quad (1-117)$$

The normalized power pattern for a z -directed current element is

$$P(\theta) = \sin^2 \theta \quad (1-118)$$

and for a z -directed uniform line source is

$$P(\theta) = \left[\sin \theta \frac{\sin[(\beta L/2) \cos \theta]}{(\beta L/2) \cos \theta} \right]^2 \quad (1-119)$$

Frequently patterns are plotted in decibels. It is important to recognize that the field (magnitude) pattern and power pattern are the same when plotted in decibels. This follows directly from the definitions. For field intensity in decibels

$$|F(\theta)|_{dB} = 20 \log |F(\theta)| \quad (1-120)$$

and for power in decibels

$$P(\theta)_{dB} = 10 \log P(\theta) = 10 \log |F(\theta)|^2 = 20 \log |F(\theta)| \quad (1-121)$$

and we see that $P(\theta)_{dB} = |F(\theta)|_{dB}$.

Radiation Pattern Parameters. Now we will discuss the structure of an antenna pattern. A typical antenna power pattern is shown in Fig. 1-9 as a polar plot in linear units (rather than decibels). The *main lobe* (or main beam or major lobe) is the lobe containing the direction of maximum radiation. There are also usually a series of lobes smaller than the main lobe. Any lobe other than the main lobe is called a *minor lobe*. Also we can define a *side lobe* as a radiation lobe in any direction other than that of the intended lobe. In most cases the main lobe is the intended lobe and thus the minor lobes are side lobes; we shall assume this is the case. Typically the side lobes are alternately positive and negative valued. In fact, a pattern in its most general form may be complex-valued. Then we use the magnitude of the field pattern $|F(\theta)|$ or the power pattern $P(\theta)$.

A measure of how well the power is concentrated into the main lobe is the (relative) *side lobe level* which is the ratio of the pattern value of a side lobe peak to the pattern value of the main lobe. The largest side lobe level for the whole pattern is the *maximum (relative) side lobe level*, frequently abbreviated as SLL. In decibels it is given by

$$SLL_{dB} = 20 \log \frac{|F(SLL)|}{|F(\max)|} \quad (1-122)$$

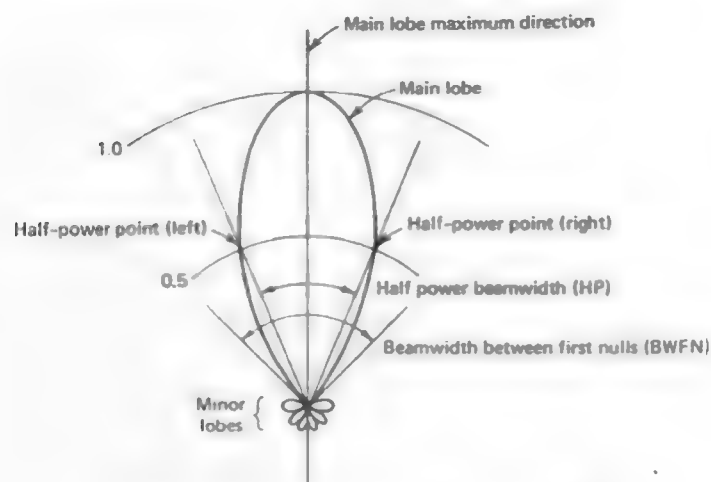


Figure 1-9 A typical power pattern polar plot.

where $|F(\max)|$ is the maximum value of the pattern magnitude and $|F(\text{SLL})|$ is the pattern value of the maximum of the highest side lobe magnitude. For a normalized pattern $F(\max) = 1$.

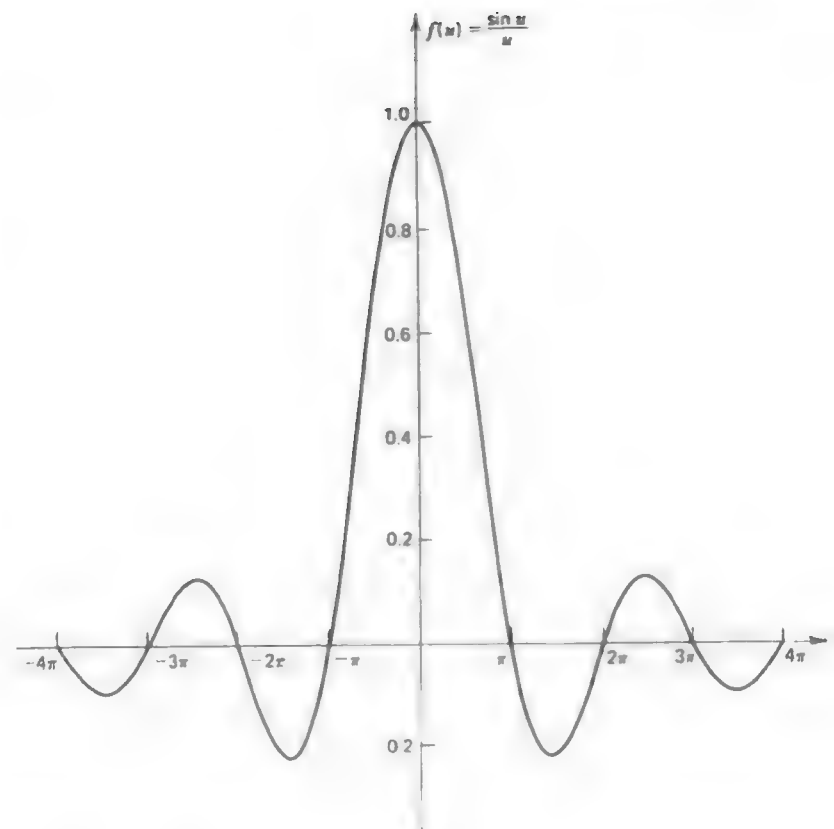
For a specific example the pattern factor for a uniform line source is plotted in a linear, rectangular form in Fig. 1-10. The smaller lobes are the side lobes and they are alternately positive and negative. Note that to convert the plot in Fig. 1-10 to a polar plot in terms of θ we must specify the source length L . This will be discussed further in Chapter 4.

Another meaningful parameter is the *half-power beamwidth*, HP. It is the angular separation of the points where the main beam of the power pattern equals one-half. Hence

$$\text{HP} = |\theta_{\text{HP left}} - \theta_{\text{HP right}}| \quad (1-123)$$

where $\theta_{\text{HP left}}$ and $\theta_{\text{HP right}}$ are points to the "left" and "right" of the main beam maximum for which the power pattern has a value of one-half (see Fig. 1-9). On the field pattern $|F(\theta)|$ these points correspond to the value $1/\sqrt{2}$. For example, the $\sin \theta$ pattern of an ideal dipole has a value of $1/\sqrt{2}$ for θ values of $\theta_{\text{HP left}} = 135^\circ$ and $\theta_{\text{HP right}} = 45^\circ$. Then $\text{HP} = |135^\circ - 45^\circ| = 90^\circ$. This is shown in Fig. 1-4b. Note that the definition of HP is the magnitude of the difference of the half-power points and the assignment of left and right may be interchanged without changing HP.

We often refer to antennas as being broadside or endfire. A *broadside antenna* is one for which the main beam maximum is in a direction normal to the plane containing the antenna. An *endfire antenna* is one for which the main beam is in

Figure 1-10 Pattern factor for a uniform line source of length L and $u = (BL/2) \cos \theta$.

a direction parallel to the plane containing the antenna. For a linear current on the z -axis, the broadside direction is $\theta = 90^\circ$ and the endfire directions are 0° and 180° . For example, an ideal dipole is a broadside antenna. For z -directed line sources several patterns are possible. Figure 1-11 illustrates a few $|f(\theta)|$ patterns. The entire pattern (in three dimensions) is imagined by holding the z -axis and spinning it. The full pattern can then be generated from the E -plane patterns shown. The broadside pattern of Fig. 1-11a is called a *fan beam*. The full (in three dimensions) endfire pattern of Fig. 1-11c has a single lobe in the endfire direction. This single lobe is referred to as a *pencil beam*. Note that the $\sin \theta$ element factor, which must multiply these patterns to obtain the total pattern, will have a significant effect on the endfire pattern.

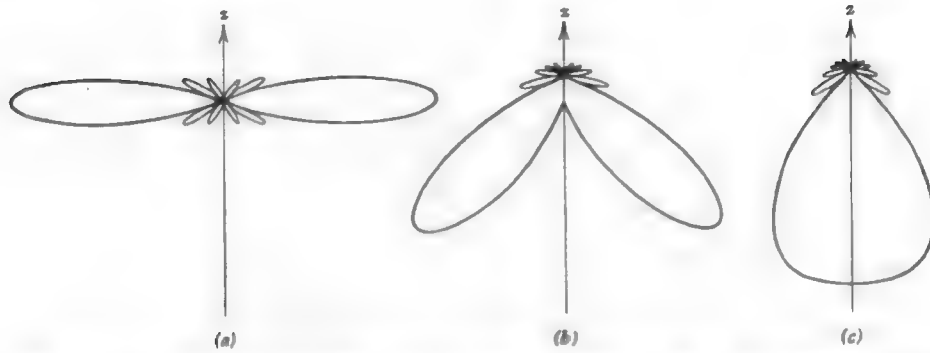


Figure 1-11 Polar plots of uniform line source patterns $|f(\theta)|$. (a) Broadside. (b) Intermediate. (c) Endfire.

1.6 DIRECTIVITY AND GAIN

One very important description of an antenna is how much it concentrates energy in one direction in preference to radiation in other directions. This characteristic of an antenna is called its directivity and is equal to its power gain if the antenna is 100% efficient. Usually power gain is expressed relative to a reference such as an isotropic radiator or half-wavelength dipole.

Toward the definition of directivity, let us begin by recalling that the power radiated by an antenna from (1-29) is

$$P_r = \frac{1}{2} \operatorname{Re} \iint (\mathbf{E} \times \mathbf{H}^*) \cdot d\mathbf{s} \quad (1-124)$$

$$= \frac{1}{2} \operatorname{Re} \iint (E_\theta H_\phi^* - E_\phi H_\theta^*) r^2 \sin \theta d\theta d\phi. \quad (1-125)$$

In general there will be both θ - and ϕ -components of the radiation fields. From (1-105) we find that

$$H_\phi = \frac{E_\theta}{\eta} \quad \text{and} \quad H_\theta = -\frac{E_\phi}{\eta}. \quad (1-126)$$

Using these in (1-125) gives

$$P_r = \frac{1}{2\eta} \iint (|E_\theta|^2 + |E_\phi|^2) r^2 d\Omega \quad (1-127)$$

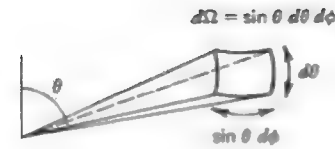


Figure 1-12 Element of solid angle $d\Omega$.

where $d\Omega = \text{element of solid angle} = \sin \theta d\theta d\phi$ which is shown in Fig. 1-12. The integral may be evaluated over any surface enclosing the antenna, however, for simplicity a spherical surface centered on the origin is usually used. Since the amplitude variations of the radiation fields are $1/r$ we find it convenient to introduce *radiation intensity*, which is defined from

$$U(\theta, \phi) = \frac{1}{2} \operatorname{Re}(\mathbf{E} \times \mathbf{H}^*) \cdot r^2 \hat{\mathbf{r}}. \quad (1-128)$$

Radiation intensity is the power radiated in a given direction per unit solid angle and has units of watts per square radian (or steradian, sr). It is independent of distance r . Introducing the normalized electric field $F(\theta, \phi)$ leads to

$$U(\theta, \phi) = U_m |F(\theta, \phi)|^2 \quad (1-129)$$

where U_m is the maximum radiation intensity, and $|F(\theta, \phi)|^2$ expresses the θ and ϕ variation with a maximum value of unity in the direction $(\theta_{\max}, \phi_{\max})$, that is,

$$U_m = U(\theta_{\max}, \phi_{\max}). \quad (1-130)$$

The total power radiated is obtained by integrating the radiation intensity over all angles around the antenna.

$$\begin{aligned} P_r &= \iint U(\theta, \phi) d\Omega \\ &= U_m \iint |F(\theta, \phi)|^2 d\Omega. \end{aligned} \quad (1-131)$$

An isotropic source with uniform radiation in all directions is only hypothetical but is sometimes a useful concept. The radiation intensity of an isotropic source is constant over all space, at a value of U_{ave} . Then $P_r = \iint U_{\text{ave}} d\Omega = U_{\text{ave}} \iint d\Omega = 4\pi U_{\text{ave}}$ since there are 4π sr in all space (see Prob. 1.6-1). For nonisotropic sources the radiation intensity is not constant throughout space, but an average power per steradian can be defined as

$$U_{\text{ave}} = \frac{1}{4\pi} \iint U(\theta, \phi) d\Omega = \frac{P_r}{4\pi}. \quad (1-132)$$

The average radiation intensity, U_{ave} , may also be considered as the radiation intensity of an isotropic source which radiates the same total power, P_r , as our real antenna, which produces $U(\theta, \phi)$.

As an example consider the ideal dipole again; we find from (1-71), (1-72), and (1-128) that

$$U(\theta, \phi) = \frac{1}{2} \left(\frac{I \Delta z}{4\pi} \right)^2 \beta \omega \mu \sin^2 \theta \quad (1-133)$$

so

$$U_m = \frac{1}{2} \left(\frac{I \Delta z}{4\pi} \right)^2 \beta \omega \mu \quad (1-134)$$

and

$$F(\theta, \phi) = \sin \theta. \quad (1-135)$$

The average radiation intensity follows from the total radiated power expression (1-74) for an ideal dipole as

$$\begin{aligned} U_{ave} &= \frac{P_r}{4\pi} = \frac{(\beta \omega \mu / 12\pi)(I \Delta z)^2}{4\pi} \\ &= \frac{1}{3} \left(\frac{I \Delta z}{4\pi} \right)^2 \beta \omega \mu \\ &= \frac{2}{3} U_m \quad (\text{ideal dipole}). \end{aligned} \quad (1-136)$$

Thus, $U_m = 1.5U_{ave}$ for the ideal dipole which means that in the direction of maximum radiation, the radiation intensity is 50% more than that which would occur from an isotropic source radiating the same total power.

Directive Gain. *Directive gain* is defined as the ratio of the radiation intensity in a certain direction to the average radiation intensity, or

$$D(\theta, \phi) = \frac{U(\theta, \phi)}{U_{ave}}. \quad (1-137)$$

If we divide the numerator and denominator by r^2 then we would have power densities. So directive gain is also the ratio of the power density in a certain direction at a given range, r , to the average power density at that range, or

$$\begin{aligned} D(\theta, \phi) &= \frac{U(\theta, \phi)/r^2}{U_{ave}/r^2} \\ &= \frac{\frac{1}{2} \operatorname{Re}(\mathbf{E} \times \mathbf{H}^*) \cdot \mathbf{f}}{P_r/4\pi r^2} \end{aligned} \quad (1-138)$$

Substitution of (1-132) for U_{ave} in (1-137) yields

$$\begin{aligned} D(\theta, \phi) &= \frac{U(\theta, \phi)}{\frac{1}{4\pi} \iint U(\theta, \phi) d\Omega} \\ &= \frac{|F(\theta, \phi)|^2}{\frac{1}{4\pi} \iint |F(\theta, \phi)|^2 d\Omega} \\ &= \frac{4\pi}{\Omega_A} |F(\theta, \phi)|^2 \end{aligned} \quad (1-139)$$

where Ω_A is the *antenna beam solid angle* defined by

$$\Omega_A = \iint |F(\theta, \phi)|^2 d\Omega. \quad (1-140)$$

The antenna beam solid angle is the solid angle through which all the power would be radiated if the power per unit solid angle (radiation intensity) equaled the maximum value over the beam area. This is illustrated in Fig. 1-13. From (1-131) and (1-140) we see that

$$P_r = U_m \Omega_A. \quad (1-141)$$

This may also be inferred from Fig. 1-13b.



Figure 1-13 Antenna beam solid angle Ω_A . (a) Plot of radiation intensity $U(\theta, \phi)$ from an actual antenna. (b) Plot of radiation intensity with all radiation from the actual antenna concentrated into a cone of solid angle Ω_A with constant radiation intensity equal to the maximum of the actual pattern.

Directivity. Directivity is now simply defined as the maximum value of directive gain, or

$$D = \frac{U_m}{U_{ave}} \quad (1-142)$$

Using (1-132) and (1-141) in (1-142) gives

$$D = \frac{U_m}{P_r/4\pi} = \frac{4\pi U_m}{\Omega_A}$$

or

$$D = \frac{4\pi}{\Omega_A} \quad (1-143)$$

Also from (1-129) in (1-137) we see that

$$D(\theta, \phi) = \frac{U_m |F(\theta, \phi)|^2}{U_{ave}} = D |F(\theta, \phi)|^2 \quad (1-144)$$

and since $|F(\theta, \phi)|^2$ has a maximum value of unity the maximum value of directive gain is the directivity D . There is D times as much power density in the direction $(\theta_{max}, \phi_{max})$ as there would be if the same total power were radiated by an isotropic source. Directivity is determined entirely by pattern shape.

The concept of directivity is illustrated in Fig. 1-14. If the radiated power were distributed isotropically over all of space, the radiation intensity would have a maximum value equal to its average value as shown in Fig. 1-14a, that is, $U_m = U_{ave}$ or $\Omega_A = 4\pi$. Thus, the directivity of this isotropic pattern is unity. The distribution of radiation intensity $U(\theta, \phi)$ for an actual antenna is shown in

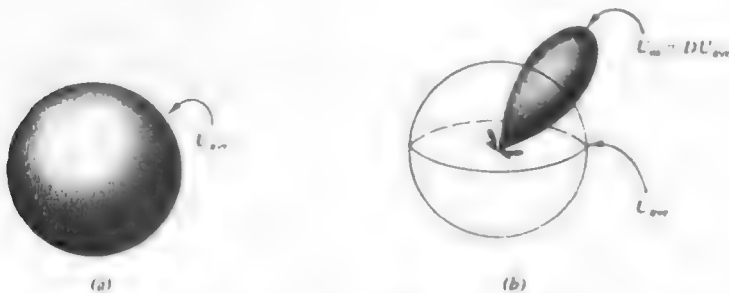


Figure 1-14 Illustration of directivity. (a) Radiation intensity distributed isotropically. (b) Radiation intensity from an actual antenna.

Fig. 1-14b. It has a maximum radiation intensity in the direction $(\theta_{max}, \phi_{max})$ of $U_m = DU_{ave}$ and an average radiation intensity of $U_{ave} = P_r/4\pi$. By directing the radiated power P_r in a preferred direction we can increase the radiation intensity in that direction by a factor of D over what it would be if the same radiated power had been isotropically radiated.

The directivity of an ideal dipole may now be calculated easily. Using (1-136) in (1-142) gives

$$D = \frac{U_m}{U_{ave}} = \frac{U_m}{\frac{1}{3}U_m} = \frac{3}{2} \quad (\text{ideal dipole}). \quad (1-145)$$

Usually directivity is calculated directly from (1-143), and the directivity calculation reduces to one of finding the beam solid angle. To illustrate we will use the ideal dipole example; substituting (1-135) in (1-140) gives

$$\Omega_A = \int_0^{2\pi} \int_0^\pi |\sin \theta|^2 \sin \theta \, d\theta \, d\phi = 2\pi \cdot \frac{4}{3} = \frac{8\pi}{3} \quad (1-146)$$

and we obtain the same value of directivity from

$$D = \frac{4\pi}{\Omega_A} = \frac{4\pi}{8\pi/3} = \frac{3}{2}. \quad (1-147)$$

Thus, the directivity of an ideal dipole is 50% greater than that of an isotropic source, which has a directivity of 1.

Gain. As noted above, directivity is solely determined by the radiation pattern of an antenna. When an antenna is used in a system (say as a transmitting antenna) we are actually interested in how efficiently the antenna transforms available power at its input terminals to radiated power, together with its directive properties. To quantify this, *power gain* (or simply *gain*) is defined as 4π times the ratio of the radiation intensity in a given direction to the net power accepted by the antenna from the connected transmitter, or

$$G(\theta, \phi) = \frac{4\pi U(\theta, \phi)}{P_{in}} \quad (1-148)$$

where $G(\theta, \phi)$ is the gain and $U(\theta, \phi)$ is the radiation intensity of the antenna in the direction (θ, ϕ) including the effect of any losses on the antenna, and P_{in} is the input power accepted by the antenna. This definition does not include losses due to mismatches of impedance or polarization. The maximum value of power gain is the maximum of (1-148), so

$$G = \frac{4\pi U_m}{P_{in}} \quad (1-149)$$

Thus, power gain may be expressed as a function of θ and ϕ and may also be given as a value in a specific direction. If no direction is specified and the power gain value is not given as a function of θ and ϕ , it is assumed to be the maximum power gain.

Directivity can be written as $D = 4\pi U_m / P_r$. Comparing this with (1-149) we see that the only difference between maximum power gain and directivity is the power value used. Directivity may be viewed as the power gain an antenna would have if all input power appeared as radiated power, that is, $P_{in} = P_r$. Power gain reflects the fact that real antennas do not behave in this fashion and some of the input power is lost. The portion of input power P_{in} which does not appear as radiated power is absorbed on the antenna and nearby structures. This prompts us to define *radiation efficiency*, e , as

$$e = \frac{P_r}{P_{in}}. \quad (1-150)$$

Note that

$$0 \leq e \leq 1. \quad (1-151)$$

Using (1-150) in (1-148) gives

$$G(\theta, \phi) = e \frac{4\pi U(\theta, \phi)}{P_r} = e \frac{U(\theta, \phi)}{U_{ave}} = eD(\theta, \phi). \quad (1-152)$$

Similarly, for maximum power gain

$$G = eD. \quad (1-153)$$

Thus, maximum power gain of an antenna is equal to its purely directional characteristic of directivity reduced by its radiation efficiency.

The terminology found in the literature is inconsistent and often incorrect on the topics of directive gain, directivity, and power gain. Current usage is slanted toward using only the terms directivity and gain. Then directivity and gain can be a function of angle or be maximum values, that is, $D(\theta, \phi)$ or D , and $G(\theta, \phi)$ or G . If no other information is given during a discussion of directivity or gain it can safely be assumed that the maximum value is intended. More importantly, the concepts of directivity and gain are often confused and abused, so be on the lookout in future reading.

Since gain is a power ratio it can be calculated in decibels as follows

$$G_{dB} = 10 \log G. \quad (1-154)$$

Similarly for directivity

$$D_{dB} = 10 \log D. \quad (1-155)$$

For example, the directivity in decibels of an ideal dipole is

$$D_{dB} = 10 \log 1.5 = 1.76 \text{ dB (ideal dipole)} \quad (1-156)$$

Frequently gain is used to describe the performance of the antenna relative to some standard reference antenna. In that case maximum power gain is defined as the ratio of the maximum radiation intensity from the antenna U_m to the maximum radiation intensity from a reference antenna $U_{m \text{ ref}}$ with the same input power, or

$$G_{\text{ref}} = \frac{U_m}{U_{m \text{ ref}}}. \quad (1-157)$$

This is a convenient definition from a measurement standpoint. The previous definition of gain employs a lossless isotropic antenna as a reference antenna. This can be shown by noting that the lossless isotropic reference antenna has a maximum radiation intensity of $P_{in}/4\pi$ since all of its input power is radiated, and substituting this into (1-157) for $U_{m \text{ ref}}$ leads to (1-149).

Gain Measurement. Power pattern measurement (to be discussed in Section 1.7) is a relative measurement and does not require an accurate knowledge of the gain of the antenna used to measure the pattern of the test antenna. However, power gain measurement (either maximum or as a function of angle) is an absolute measurement and thus, is more difficult. One method of maximum power gain measurement is illustrated in Fig. 1-15. A source antenna is driven by a constant power transmitter. First a standard gain antenna with a known maximum power gain G_s is used as the receiving antenna as shown in Fig. 1-15a.

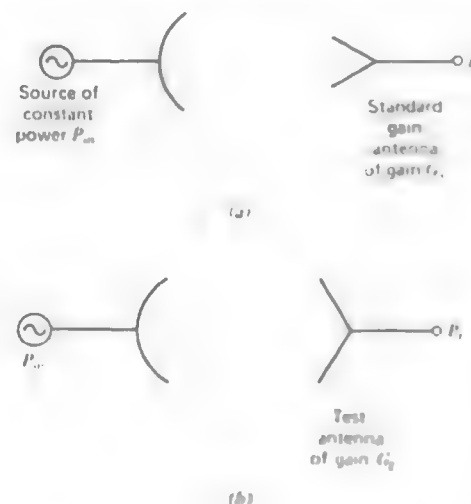


Figure 1-15 Measurement of maximum power gain by comparison to an antenna of known maximum power gain. $G_t = (P_t/P_s)G_s$. (a) Measurement of power output P_s from a standard gain antenna. (b) Measurement of power output P_t from the test antenna.

It is oriented such that its output power P_t is maximum. Next the test antenna replaces the standard gain antenna and is oriented for maximum power output P_r . Since the absolute maximum power gain (relative to an isotropic lossless antenna) of the standard gain antenna is known, the absolute maximum power gain of the test antenna can be calculated from the differences in the measured received powers. The ratio P_r/P_s is the increase in received power from the test antenna over that of the standard gain antenna. The gain of the test antenna must then have that much more gain, that is,

$$G_r = \frac{P_r}{P_s} G_s. \quad (1-158)$$

As an example suppose that a standard gain antenna has a gain of 63, or 18 dB. Following the measurement technique of Fig. 1-15 the measured powers are $P_s = 3.16$ mW, or 5 dBm (5 dB above a milliwatt), and $P_r = 31.6$ mW, or 15 dBm. The gain of the test antenna is then $G_r = (31.6/3.16)63 = 630$, or in terms of decibels

$$G_r(\text{dB}) = P_r(\text{dBm}) - P_s(\text{dBm}) + G_s(\text{dB}) = 15 - 5 + 18 = 28 \text{ dB}.$$

1.7 RECIPROCITY AND ANTENNA PATTERN MEASUREMENTS

In this section we show that the radiation pattern of an antenna is the same whether it is used as a transmitting antenna or receiving antenna. Reciprocity allows the calculation or measurement of an antenna pattern in either the transmit or receive case. Practical considerations for the measurement of antenna patterns are also discussed in this section.

In order to show the reciprocity of the transmit and receive patterns for an antenna it is necessary to discuss some reciprocity theorems. There are several forms reciprocity theorems take for electromagnetic field problems. We will consider two forms of reciprocity for use in antenna problems. First the Lorentz reciprocity theorem will be discussed. Let sources \mathbf{J}_a and \mathbf{M}_a produce fields \mathbf{E}_a and \mathbf{H}_a and sources \mathbf{J}_b and \mathbf{M}_b produce fields \mathbf{E}_b and \mathbf{H}_b . See Fig. 1-16. The frequencies of all quantities are identical. The Lorentz reciprocity theorem that is derivable from Maxwell's equations (see Prob. 1.7-1) states that for isotropic media

$$\iiint_{v_a} (\mathbf{E}_b \cdot \mathbf{J}_a - \mathbf{H}_b \cdot \mathbf{M}_a) dv' = \iiint_{v_b} (\mathbf{E}_a \cdot \mathbf{J}_b - \mathbf{H}_a \cdot \mathbf{M}_b) dv'. \quad (1-159)$$

The left-hand side is the reaction (a measure of the coupling) of the fields from source b on the sources a , and the right-hand side is the reaction of the fields



Figure 1-16 Source configuration for the Lorentz reciprocity theorem.

from source a on the sources b . This is a very general expression but it can be put into a more usable form. Let sources b consist of only an ideal electric dipole of vector length \mathbf{p} located at point (x_p, y_p, z_p) . Since the ideal dipole can be represented as an infinitesimal source and \mathbf{M}_b is zero, (1-159) becomes⁷

$$\mathbf{E}_a(x_p, y_p, z_p) \cdot \mathbf{p} = \iiint_{v_a} (\mathbf{E}_b \cdot \mathbf{J}_a - \mathbf{H}_b \cdot \mathbf{M}_a) dv'. \quad (1-160)$$

This expression allows us to calculate the electric field from sources a by evaluating the integral using known sources \mathbf{J}_a and \mathbf{M}_a and known ideal dipole fields \mathbf{E}_b and \mathbf{H}_b of (1-67) and (1-66), evaluated at the location of sources a . This may be performed for various orientations \mathbf{p} of the ideal dipole, which is acting as a field probe.

The Lorentz reciprocity theorem can also be used to derive a reciprocity theorem using terminal voltages and currents. Suppose sources a and b are antennas excited with ideal (infinite impedance) current generators I_a and I_b . Since no magnetic sources are present (1-159) reduces to

$$\iiint_{v_a} \mathbf{E}_b \cdot \mathbf{J}_a dv' = \iiint_{v_b} \mathbf{E}_a \cdot \mathbf{J}_b dv'. \quad (1-161)$$

For perfectly conducting antennas the electric fields will be zero over the antennas; however, voltages will be produced across the terminals. Taking the current to be constant in the terminal region and using the concept of $\int \mathbf{E} \cdot d\mathbf{l} = -V$, we see that (1-161) becomes

$$V_a^{\text{oc}} I_a = V_b^{\text{oc}} I_b \quad (1-162)$$

where V_a^{oc} is the open circuit voltage across the terminals of antenna a due to the field \mathbf{E}_b generated by antenna b and similarly V_b^{oc} is the open circuit voltage at

⁷ The ideal dipole current could be written as $\mathbf{J}_b = \delta(x - x_p) \delta(y - y_p) \delta(z - z_p) \mathbf{p}$. This together with $\mathbf{M}_b = 0$ in (1-159) yields (1-160).

antenna b due to antenna a . Open circuit voltages have been used because of the infinite impedances of the generators. Rearranging (1-162) leads to a statement of reciprocity in circuit form

$$\frac{V_a^{\text{oc}}}{I_b} = \frac{V_b^{\text{oc}}}{I_a} \quad (1-163)$$

Several factors affect the voltage appearing at one antenna due to another antenna which is excited: the specific antennas used, the medium between the antennas with perhaps other objects present, and the relative orientation of the antennas. We can represent the general situation entirely in terms of circuit parameters as follows

$$V_a = Z_{aa} I_a + Z_{ab} I_b \quad (1-164)$$

$$V_b = Z_{ba} I_a + Z_{bb} I_b \quad (1-165)$$

where V_a , V_b , I_a , and I_b are the terminal voltages and currents of antennas a and b . If antenna a is excited with a generator of current I_a , the open circuit voltage appearing at the terminals of antenna b is $V_b|_{I_b=0}$. The transfer impedance Z_{ba} is from (1-165) with I_b zero,

$$Z_{ba} = \frac{V_b}{I_a} \bigg|_{I_b=0} \quad (1-166)$$

If antenna b is excited with a generator of current I_b the open circuit voltage appearing at the terminals of antenna a is $V_a|_{I_a=0}$. The transfer impedance Z_{ab} is, from (1-164) with I_a zero,

$$Z_{ab} = \frac{V_a}{I_b} \bigg|_{I_a=0} \quad (1-167)$$

Comparing (1-166) and (1-167) to (1-163) we see that

$$Z_{ab} = Z_{ba} = Z_m \quad (1-168)$$

where Z_m is the transfer (or mutual) impedance between the antennas. This can also be shown from the circuit formulation of (1-164) and (1-165) if the individual impedances are linear, passive, and bilateral. (See Probs. 1.7-3, 1.7-4). This, in turn, is true if the medium and the antennas are linear, passive, and isotropic.

If an ideal current source of current I excites antenna a , the open circuit voltage at the terminals of b from (1-166) is

$$V_b|_{I_b=0} = I Z_{ba} \quad (1-169)$$

If the same source is now applied to the terminals of antenna b , the open circuit voltage appearing at the terminals of antenna a is from (1-167)

$$V_a|_{I_a=0} = I Z_{ab} \quad (1-170)$$

But $Z_{ab} = Z_{ba}$, so the preceding two equations yield

$$V_a|_{I_a=0} = V_b|_{I_b=0} = V \quad (1-171)$$

Thus the same excitation current will produce the same terminal voltage independent of which port is excited, as illustrated in Fig. 1-17. In other words, reciprocity states that the source and the measurer can be interchanged without changing the system response. The same is true of an ideal voltage source and short circuit terminal currents. These are familiar results from network theory.

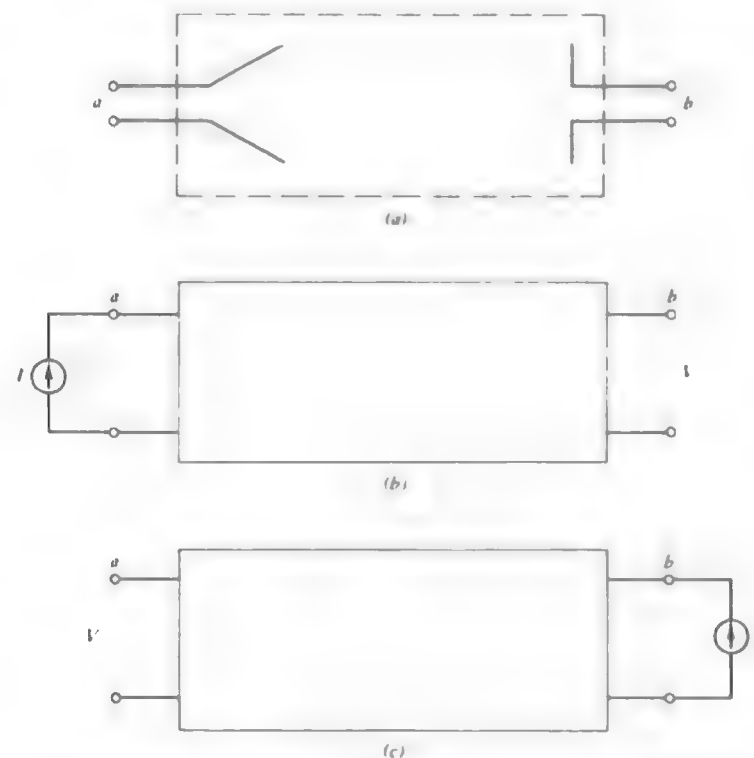


Figure 1-17 Reciprocity for antennas The output voltage V is the same in (b) and (c) for the same input current I . (a) Two-port representation of a two-antenna system. (b) Antenna a excited with current source I . (c) Antenna b excited with current source I

The self-impedances of the antennas from (1-164) and (1-165) are

$$Z_{aa} = \frac{V_a}{I_a} \bigg|_{I_b=0} \quad (1-172)$$

$$Z_{bb} = \frac{V_b}{I_b} \bigg|_{I_a=0} \quad (1-173)$$

If an antenna is isolated so that all objects including other antennas are far away and the antenna is lossless, the self-impedance equals its input impedance [8].

Suppose antenna a is excited (i.e., acting as a transmitter) and the voltage produced at the terminals of antenna b is measured with an ideal voltmeter. If the antennas are separated so that they are in each others far field, the transfer impedance Z_{ba} is actually the far-field (or radiation) pattern of antenna a if antenna b is moved around a on a constant radius as shown in Fig. 1-18a. It is normally assumed that as antenna b is moved it is maintained with the same orientation and polarization relative to antenna a . The output voltage of b as a function of angle around antenna a gives the relative angular variation of the radiation from antenna a , that is, its radiation pattern. Examining (1-166) we see that this is really Z_{ba} (I_a is constant). Thus Z_{ba} as a function of angle is the transmitting pattern of antenna a . If now antenna b is excited and antenna a acts as a receiver, the terminal voltage of antenna a is the receiving pattern of antenna a as antenna b is again moved around at a constant distance from antenna a ; see Fig. 1-18b. Thus Z_{aa} as a function of angle is the receiving pattern of antenna a . Since the transfer impedances are identical we can conclude that *the transmit and receive patterns of an antenna are identical*. This is an important consequence of reciprocity.

It is important to note that reciprocity as illustrated in Fig. 1-17 (or equivalently $Z_{ab} = Z_{ba}$) is true even if the antennas are not far removed from each other. In that case though, $Z_{aa}(\theta, \phi)$ is not the far-field pattern.

Antenna Pattern Measurement. An antenna pattern is a graphical representation of the radiation properties of an antenna as a function of the direction from the antenna. With the antenna centered on the origin of a spherical coordinate system, the radiation fields \mathbf{E} and \mathbf{H} are perpendicular to each other and both are transverse to the direction of propagation, $\hat{\mathbf{r}}$. Also the field intensities vary as r^{-2} . In antenna pattern discussions the electric field is used, but the magnetic field behavior follows directly since its intensity is found from $\mathbf{H} = \mathbf{E}/\eta$ and its direction is perpendicular to \mathbf{E} and $\hat{\mathbf{r}}$; see (1-105).

The electric field is both a vector and a phasor. In general it has two orthogonal components, frequently decomposed into E_θ and E_ϕ . These components are complex-valued having an amplitude and phase. The relative amplitude and phase of these components determines the polarization that is discussed further

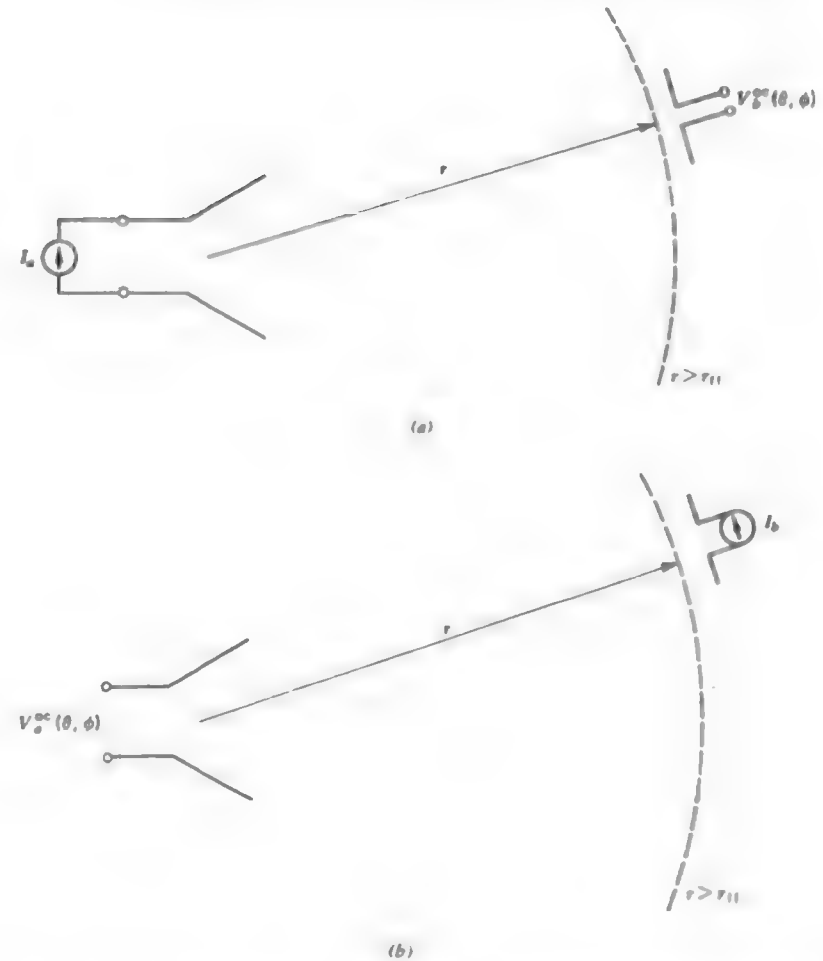


Figure 1-18 Antenna pattern reciprocity. The transmitting and receiving patterns of an antenna are identical because $Z_{ba}(\theta, \phi) = Z_{ab}(\theta, \phi) = Z_{aa}(\theta, \phi)$.
 (a) The transmitting pattern of antenna a is $Z_{ba}(\theta, \phi) = V_b^{oc}(\theta, \phi)/I_a$.
 (b) The receiving pattern of antenna a is $Z_{aa}(\theta, \phi) = V_a^{oc}(\theta, \phi)/I_b$.

in Section 1.9. Separate antenna patterns may be given for each component of the electric field. For simple antennas only one component is present. For example, the ideal dipole on the z -axis has only an E_θ component. It may be noted that for actual antennas a small component of electric field perpendicular to that

predicted from the ideal case always exists. This is referred to as the cross-polarized component and arises from currents flowing on the antenna or supporting structures, which are not accounted for in a simple mathematical model.

A complete representation of the radiation properties of an antenna would, of course, require measuring the radiation at all possible angles (θ, ϕ). This is rarely attempted and fortunately is also rarely necessary. For most applications the principal plane patterns are sufficient. Figure 1-4 illustrates the principal plane patterns for an ideal dipole.

There are many ways of displaying antenna patterns. For example, a principal plane pattern could be plotted in polar or rectangular form. In addition, the scale could be either linear or logarithmic (decibel). All combinations of plot type and scale type are used: polar-linear, polar-log, rectangular-linear, and rectangular-log. Figure 1-9 illustrates a polar-linear pattern plot. A polar-log pattern plot example is found in Fig. 5-9. Figure 1-10 shows a rectangular-linear plot. Figure 4-1 is the same pattern as the last (a uniform line source) but in rectangular-log form. Generally speaking log plots are used for high-gain, low-side lobe patterns and linear plots are used when the main beam structure is of primary interest. These various antenna pattern representations can be recorded directly using commercially available measurement and recording equipment. When more detailed information is required the results of several planar cuts can be put together to make a contour plot.

Although we have conceptualized the measurement of a radiation pattern by moving a receiver over a sphere of constant radius, this is obviously an impractical way of making such measurements. The important feature is to maintain the distance between the antennas constant (but large enough so the antennas are in each others far field) and to vary the observation angle. For example, to measure the pattern of antenna *a* we could rotate it about its axis and keep antenna *b* fixed. By reciprocity it makes no difference if we operate antenna *a* as a receiver or as a transmitter, but usually the antenna whose pattern is desired is used as a receiving antenna. In Fig. 1-19 the incident fields of transmit antenna *b* on receive antenna *a* are constant and the output of antenna *a* varies with its angular position. Thus, the antenna that is rotated is the pattern being measured; in this case antenna *a*. Antenna positioners of many types together with required control systems, receivers, and recording devices are available for such rotation pattern measurements.⁸

Antenna pattern measuring equipment varies with frequency range and the size of the antennas. If the antenna size is not extremely large in terms of a wavelength, the far-field distance ($2D^2/\lambda$) is small enough to permit indoor tests in anechoic chambers, which are lined with special absorbing material to minimize reflections. In other situations antenna test ranges are set up outdoors. In this case the antennas are elevated on towers or hills to avoid ground reflections.

⁸Perhaps the most complete discussion of antenna measurements is found in [9]. Also see [10].



Figure 1-19 Radiation pattern measurement. The pattern of antenna *a* is proportional to the terminal voltage V_a which is a function of the angular position of antenna *a* during rotation.

For very large antennas such as satellite ground station or radio astronomy antennas, the far-field distance may be extremely large necessitating special techniques for pattern measurement. For example, a satellite or airplane platform can be used for the source antenna. Also, the sun or a "radio star" can be employed as sources.

1.8 ANTENNA IMPEDANCE AND RADIATION EFFICIENCY

The input impedance of an antenna is the impedance presented by the antenna at its terminals. Thus, suitable terminals must be defined for an antenna. The input impedance will be affected by other antennas or objects that are nearby, but for this discussion we will assume that the antenna is isolated. The input impedance is composed of real and imaginary parts.

$$Z_{in} = R_{in} + jX_{in} \quad (1-174)$$

The input resistance, R_{in} , represents dissipation. Power can be dissipated in two ways. There are heating losses on the antenna structure and associated hardware. Also power that leaves the antenna and never returns (radiation) is a form of dissipation. On many antennas ohmic losses are small compared to radiation losses. The input reactance, X_{in} , represents power stored in the near field of the antenna.

First we shall discuss the input resistance. The average power dissipated in an antenna is

$$P_{in} = \frac{1}{2} R_{in} |I_{in}|^2 \quad (1-175)$$

where I_{in} is the current at the input terminals. Note that a factor of one-half appears in (1-175) because current is defined as a peak value. Separating the dissipated power into radiative and ohmic losses we have

$$\begin{aligned} P_{in} &= P_r + P_{ohmic} \\ &= \frac{1}{2} R_r |I_{in}|^2 + \frac{1}{2} R_{ohmic} |I_{in}|^2 \end{aligned} \quad (1-176)$$

where we define radiation resistance of an antenna referred to the input terminals as

$$R_{ri} = \frac{2P_r}{|I_{in}|^2} \quad (1-177)$$

and ohmic resistance of an antenna as

$$R_{ohmic} = \frac{2P_{ohmic}}{|I_{in}|^2} = \frac{2(P_{in} - P_r)}{|I_{in}|^2}. \quad (1-178)$$

From (1-34) the radiated power is

$$P_r = \frac{1}{2} \iint_{s_{ff}} (\mathbf{E} \times \mathbf{H}^*) \cdot d\mathbf{s} \quad (1-179)$$

where s_{ff} is a surface in the far field, usually spherical. Also the power density $\mathbf{S} = \frac{1}{2} \mathbf{E} \times \mathbf{H}^*$ will be real in the far field. Radiation resistance can be defined relative to the current at any point on the antenna. It is customary to use the maximum current; in other words the current in the denominator of (1-177), in general, is the maximum current. The symbol R_r will be reserved for radiation resistance relative to the maximum current that occurs on the antenna. The radiation resistance R_{ri} is referred to the input terminals. In this section we will be dealing with electrically short antennas which always have a current maximum at the input, if fed in the center, and thus there is no chance for confusion. In those cases $R_{ri} = R_r$, and the symbol R_r will be used. In Section 5.1 we will discuss this topic again.

As an example consider the ideal dipole antenna. The radiated power for an ideal dipole of length $\Delta z \ll \lambda$ and input current I is given by (1-74). The radiation resistance is then

$$\begin{aligned} R_r &= \frac{2P_r}{|I_{in}|^2} = \frac{2}{I^2} \frac{\omega \mu \beta}{12\pi} (I \Delta z)^2 = \frac{\sqrt{\mu \omega} \sqrt{\mu} \sqrt{\epsilon}}{\sqrt{\epsilon} 6\pi} \beta (\Delta z)^2 \\ &= \eta \frac{\beta^2}{6\pi} (\Delta z)^2 = \frac{120\pi}{6\pi} \left(\frac{2\pi}{\lambda} \Delta z \right)^2 \\ R_r &= 80\pi^2 \left(\frac{\Delta z}{\lambda} \right)^2 \approx 800 \left(\frac{\Delta z}{\lambda} \right)^2 \text{ ohms (ideal dipole).} \end{aligned} \quad (1-180)$$

Since $\Delta z \ll \lambda$, R_r for ideal dipoles is very small.

The relative amounts of input power dissipated by radiation and ohmic losses determine the efficiency of the antenna. This is expressed by the radiation

efficiency ϵ which was introduced in Section 1.6 and defined in (1-150) as the ratio of total radiated power to the net power accepted by the antenna, so

$$\epsilon = \frac{P_r}{P_{in}} = \frac{P_r}{P_r + P_{ohmic}}. \quad (1-181)$$

Substituting (1-176) and (1-177) into (1-181) yields

$$\begin{aligned} \epsilon &= \frac{\frac{1}{2} R_{ri} |I_{in}|^2}{\frac{1}{2} R_{ri} |I_{in}|^2 + \frac{1}{2} R_{ohmic} |I_{in}|^2} \\ &= \frac{R_{ri}}{R_{ri} + R_{ohmic}} = \frac{R_{ri}}{R_{in}}. \end{aligned} \quad (1-182)$$

For many antennas radiation efficiency is nearly 100%. For electrically small antennas, however, the radiation efficiency may be extremely small. A quick calculation will show this. Consider an ideal dipole operating at 1 MHz and of length $\Delta z = 1 \text{ m} = 0.0033\lambda$. It has a radiation resistance from (1-180) of

$$R_r = 80\pi^2 \left(\frac{1}{300} \right)^2 = 0.0088 \text{ ohm}. \quad (1-183)$$

The ohmic resistance for an antenna that carries a uniform current is

$$R_{ohmic} \approx \frac{L}{2\pi a} R_s \quad (1-184)$$

where L is the length of the wire, a is the wire radius, and R_s is the surface resistance [11]

$$R_s = \sqrt{\frac{\omega \mu}{2\sigma}}. \quad (1-185)$$

At 1 MHz for copper wire

$$R_s = \sqrt{\frac{4\pi \times 10^{-7} \cdot 2\pi \times 10^6}{2 \cdot 5.7 \times 10^7}} = 2.63 \times 10^{-4} \text{ ohm}. \quad (1-186)$$

Assuming that the wire is No. 20 AWG of radius $a = 4.06 \times 10^{-4} \text{ m}$ and evaluating (1-184) gives

$$R_{ohmic} = \frac{1}{2\pi \cdot 4.06 \times 10^{-4}} 2.63 \times 10^{-4} = 0.103 \text{ ohm}. \quad (1-187)$$

The radiation efficiency from (1-182), (1-183), and (1-187) is

$$\epsilon = \frac{0.0088}{0.0088 + 0.103} = 7.87\%. \quad (1-188)$$

This is a low efficiency. Since the radiation resistance increases with length squared and ohmic resistance increases linearly with length, the radiation efficiency could be increased by lengthening the antenna. For broadcast receiving antennas, low efficiency is frequently overcome by using high-power transmitters operating into tall antennas that are efficient. Thus cost and complexity are concentrated into a few transmitting stations allowing inexpensive and simple receiving antennas.

The ideal dipole model is a uniform current element, as shown in Fig. 1-20a. In reality the current on a straight wire antenna must smoothly go to zero at the ends. The current distribution on a center fed wire dipole of length $\Delta z \ll \lambda$, called a **short dipole**, is approximately triangular in shape as illustrated in Fig. 1-20b. If end loading such as with metal plates (see Fig. 2-3) is added to the short dipole, there is a place for charge to accumulate at the wire ends giving a nearly uniform current on the dipole itself which permits use of the ideal dipole model. More will be said about short dipoles in Section 2.1.

The triangular current distribution of the short dipole leads to an equivalent length which is one-half that of its physical length. This is true because the equivalent length is proportional to the total charge on the wire at any instant, which is proportional to the area under the current versus distance curves shown in Fig. 1-20. This follows directly from the fact that the radiation integral [see (1-101)] reduces to $\int I(z') dz'$ since $\exp(j\beta z' \cos \theta) \approx 1$ for short dipoles. The

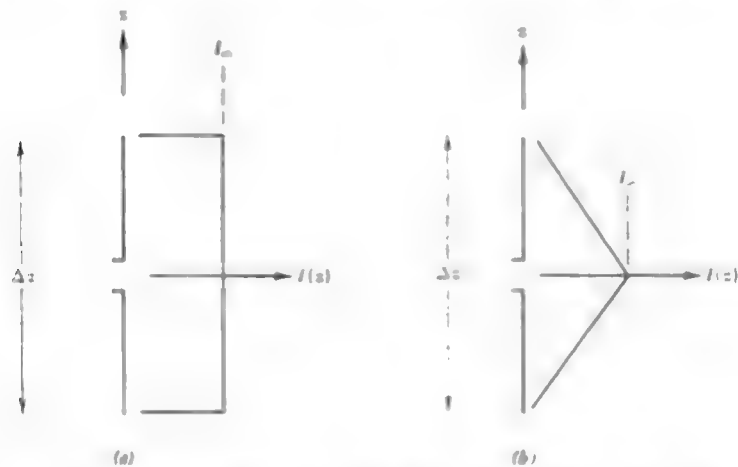


Figure 1-20 The ideal dipole model and short dipole with current distributions. $\Delta z \ll \lambda$. I_m is the value of the input current at the terminals in the center of each antenna. The short dipole of (b) is that which is encountered in practice for a wire segment as shown. (a) Ideal dipole. (b) Short dipole.

radiated fields are, in turn, proportional to this equivalent length. Since the radiation resistance is proportional to the integral of the far-zone electric field squared and the patterns of the ideal and short dipoles are the same as will be shown below, the radiation resistances are proportional to the equivalent lengths squared. The area of the short dipole current triangle shape is one-half that of the uniform current shape. This reduced equivalent length for the short dipole leads to a reduction in the radiation resistance. Since the length is effectively one-half for the short dipole, the radiation resistance is reduced by a factor of four from that of the ideal dipole. Thus dividing (1-180) by four yields

$$R_r = 20\pi^2 \left(\frac{\Delta z}{\lambda} \right)^2 \text{ ohms (short dipole).} \quad (1-189)$$

In the pattern calculations for the ideal dipole (see Section 1.4) we assumed that the phase and amplitude differences of rays coming from different points on the wire due to different path lengths were negligible. These effects influence the pattern shape. Since the short dipole also satisfies $\Delta z \ll \lambda$ the pattern is calculated in the same fashion and will, thus, have the same $\sin \theta$ radiation pattern as the ideal dipole. To be more specific, the vector potential of (1-60) is used for both the uniform and triangular current models except $\Delta z/2$ is used in place of Δz in the triangular current case because its equivalent length is one-half that of the uniform current. The patterns are then the same since A is the same, except for a constant factor of one-half. The ideal dipole and short dipole will also have the same directivity value of 1.5 because the pattern shape completely determines directivity.

Not only is the radiation resistance of the short dipole reduced from that of the ideal dipole, but the ohmic resistance is also reduced. The reduction is, however, not the same, and as can be seen from (1-182), if R_r and R_{ohmic} change differently, e will be different from the ideal dipole case. First we will find an expression for the ohmic resistance of a short dipole. Since the power dissipation from ohmic losses at any point along the antenna is proportional to the current squared at that point, the total power dissipated can, in general, be found from

$$P_{ohmic} = \frac{R_s}{2\pi a} \int_{-L/2}^{L/2} \frac{1}{2} |I(z)|^2 dz. \quad (1-190)$$

It is easy to show that this reduces to (1-184) for a uniform current of length $L = \Delta z$. The triangular current of Fig. 1-20b for the short dipole can be written as a function of position along the wire as

$$I(z) = I_m \left(1 - \frac{2|z|}{\Delta z} \right) \quad |z| \leq \frac{\Delta z}{2}. \quad (1-191)$$

Using this in (1-190) yields

$$R_{\text{ohmic}} = \frac{\Delta z}{2\pi a} \frac{R_s}{3} \quad (\text{short dipole}) \quad (1-192)$$

for a short dipole of length Δz with a triangular current distribution. Notice that this is one-third that for an ideal dipole. Since the radiation resistance for the short dipole is one-fourth that of an ideal dipole, the radiation resistance is decreased more relative to the ohmic resistance and thus the efficiency is lower for the short dipole than it is for an ideal dipole of the same length.

We now return to the example presented earlier in this section and redo it for the case of a short dipole. This antenna now closely approximates the dipole antenna found in the windshield of some automobiles. The wavelength at 1 MHz (in the AM broadcast band) is 300 m and the length Δz is 1 m. Then from (1-189)

$$R_r = 20\pi^2 \left(\frac{1}{300} \right)^2 = 0.0022 \text{ ohm.} \quad (1-193)$$

and from (1-186) and (1-192)

$$R_{\text{ohmic}} = \frac{1}{2\pi \cdot 4.06 \times 10^{-4}} \frac{2.63 \times 10^{-4}}{3} = 0.0344 \text{ ohm.} \quad (1-194)$$

The radiation efficiency is then

$$\epsilon = \frac{0.0022}{0.0022 + 0.0344} = 6.01\%, \quad (1-195)$$

which is slightly less than the 7.87% for the corresponding ideal dipole.

In addition to loss of efficiency, ohmic losses on antennas have another undesirable effect. Any resistive element in an electrical system is a source of noise. Thus ohmic losses on antennas are sources of noise. Large ohmic resistances on receiving antennas introduce noise into the receiver. It turns out, though, that for frequencies around 1 MHz and below, external noise (mainly due to lightning) is significant and always present. This external noise picked up by the antenna is proportional to the antenna radiation resistance and is usually larger than the noise arising from the ohmic resistance.

We now return to the reactive part of the input impedance. Radiated power contributes to the real part of the input impedance whereas power stored in the near field is represented by the reactive part of the input impedance. This behavior is very similar to a complex load impedance in circuit theory. Antennas that are electrically small (much smaller than a wavelength) have a large input reactance, in addition to a small radiation resistance. For example, the short dipole has a capacitive reactance whereas an electrically small loop antenna has

an inductive reactance. This is an expected result from low-frequency circuit theory.

Antenna impedance is important to the transfer of power from a transmitter to an antenna or from an antenna to a receiver. For example, to maximize the power transferred from a receiving antenna the antenna impedance should be a conjugate match (equal resistances, equal magnitude and opposite sign reactances). Usually the receiver has a real impedance so it is necessary to "tune out" the antenna reactance with a matching network of variable inductances and capacitances adjusted to cancel antenna reactance. It would at first appear to be no problem if antenna impedances were reactive because they could always be tuned. There are, however, two disadvantages to using matching networks. They are always somewhat inefficient because there are ohmic losses in tuning coils. Second, a matching network can provide a match only over a narrow band of frequencies thus reducing the operational bandwidth. Impedance matching techniques are discussed in Section 5.3.

Finally, we note that as a consequence of reciprocity, antenna impedance for receiving and transmitting is the same.

1.9 ANTENNA POLARIZATION

We will first discuss the possible polarizations of an electromagnetic wave and then antenna polarization will follow directly from wave polarization.⁹ In fact, the polarization of an antenna is the polarization of the wave radiated by the antenna in a given direction.

If the electric and magnetic field vectors of an electromagnetic wave lie in a fixed plane at all times, it is called a *plane polarized wave*. The tip of the instantaneous electric field vector traces out a figure with time; we refer to this phenomena simply as the polarization of the electric field vector. There may be a random component to this figure (a nonperiodic behavior), but we will not consider such randomly polarized wave components because antennas cannot generate them. For a completely polarized wave the figure traced out is, in general, an ellipse.

There are some important special cases of the polarization ellipse. If the path of the electric field vector is back and forth along a line, it is said to be *linearly polarized*. See Figs. 1-21a and 1-21b. An example is the electric field from an ideal dipole or any linear current. If the electric field vector remains constant in length but rotates around in a circular path, it is *circularly polarized*. The rotation radian frequency is ω and occurs in one of two directions, referred to as the sense of rotation. If the wave is traveling toward the observer and the vector

⁹ For a complete discussion of wave polarization see [12]

Using this in (1-190) yields

$$R_{\text{ohmic}} = \frac{\Delta z R_s}{2\pi a^3} \quad (\text{short dipole}) \quad (1-192)$$

for a short dipole of length Δz with a triangular current distribution. Notice that this is one-third that for an ideal dipole. Since the radiation resistance for the short dipole is one-fourth that of an ideal dipole, the radiation resistance is decreased more relative to the ohmic resistance and thus the efficiency is lower for the short dipole than it is for an ideal dipole of the same length.

We now return to the example presented earlier in this section and redo it for the case of a short dipole. This antenna now closely approximates the dipole antenna found in the windshield of some automobiles. The wavelength at 1 MHz (in the AM broadcast band) is 300 m and the length Δz is 1 m. Then from (1-189)

$$R_r = 20\pi^2 \left(\frac{1}{300} \right)^2 = 0.0022 \text{ ohm.} \quad (1-193)$$

and from (1-186) and (1-192)

$$R_{\text{ohmic}} = \frac{1}{2\pi \cdot 4.06 \times 10^{-4}} \frac{2.63 \times 10^{-4}}{3} = 0.0344 \text{ ohm.} \quad (1-194)$$

The radiation efficiency is then

$$\epsilon = \frac{0.0022}{0.0022 + 0.0344} = 6.01\%, \quad (1-195)$$

which is slightly less than the 7.87% for the corresponding ideal dipole.

In addition to loss of efficiency, ohmic losses on antennas have another undesirable effect. Any resistive element in an electrical system is a source of noise. Thus ohmic losses on antennas are sources of noise. Large ohmic resistances on receiving antennas introduce noise into the receiver. It turns out, though, that for frequencies around 1 MHz and below, external noise (mainly due to lightning) is significant and always present. This external noise picked up by the antenna is proportional to the antenna radiation resistance and is usually larger than the noise arising from the ohmic resistance.

We now return to the reactive part of the input impedance. Radiated power contributes to the real part of the input impedance whereas power stored in the near field is represented by the reactive part of the input impedance. This behavior is very similar to a complex load impedance in circuit theory. Antennas that are electrically small (much smaller than a wavelength) have a large input reactance, in addition to a small radiation resistance. For example, the short dipole has a capacitive reactance whereas an electrically small loop antenna has

an inductive reactance. This is an expected result from low-frequency circuit theory.

Antenna impedance is important to the transfer of power from a transmitter to an antenna or from an antenna to a receiver. For example, to maximize the power transferred from a receiving antenna the antenna impedance should be a conjugate match (equal resistances, equal magnitude and opposite sign reactances). Usually the receiver has a real impedance so it is necessary to "tune out" the antenna reactance with a matching network of variable inductances and capacitances adjusted to cancel antenna reactance. It would at first appear to be no problem if antenna impedances were reactive because they could always be tuned. There are, however, two disadvantages to using matching networks. They are always somewhat inefficient because there are ohmic losses in tuning coils. Second, a matching network can provide a match only over a narrow band of frequencies thus reducing the operational bandwidth. Impedance matching techniques are discussed in Section 5.3.

Finally, we note that as a consequence of reciprocity, antenna impedance for receiving and transmitting is the same.

1.9 ANTENNA POLARIZATION

We will first discuss the possible polarizations of an electromagnetic wave and then antenna polarization will follow directly from wave polarization.⁹ In fact, the polarization of an antenna is the polarization of the wave radiated by the antenna in a given direction.

If the electric and magnetic field vectors of an electromagnetic wave lie in a fixed plane at all times, it is called a *plane polarized wave*. The tip of the instantaneous electric field vector traces out a figure with time; we refer to this phenomena simply as the polarization of the electric field vector. There may be a random component to this figure (a nonperiodic behavior), but we will not consider such randomly polarized wave components because antennas cannot generate them. For a completely polarized wave the figure traced out is, in general, an ellipse.

There are some important special cases of the polarization ellipse. If the path of the electric field vector is back and forth along a line, it is said to be *linearly polarized*. See Figs. 1-21a and 1-21b. An example is the electric field from an ideal dipole or any linear current. If the electric field vector remains constant in length but rotates around in a circular path, it is *circularly polarized*. The rotation radian frequency is ω and occurs in one of two directions, referred to as the sense of rotation. If the wave is traveling toward the observer and the vector

⁹ For a complete discussion of wave polarization see [12].

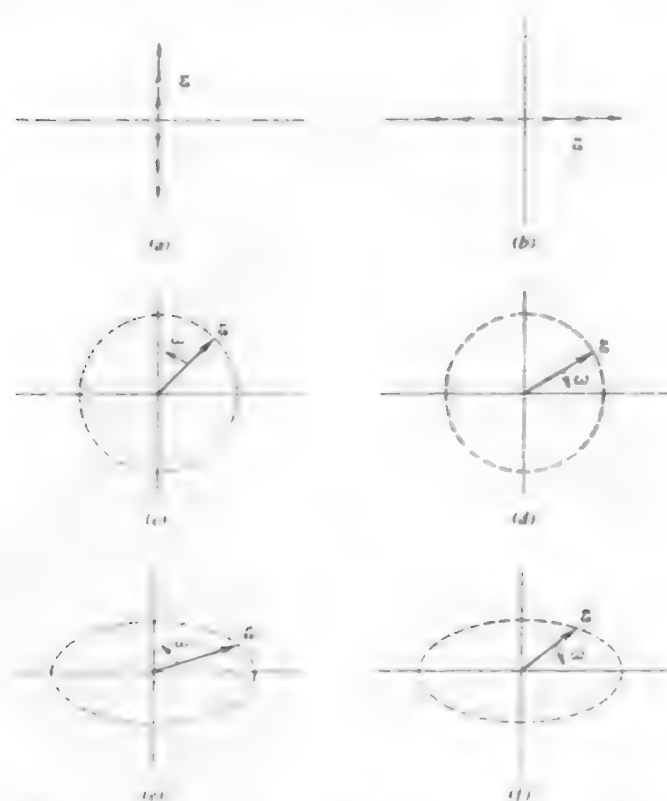


Figure 1-21 Some wave polarization states. The wave is approaching. (a) Linear (vertical) polarization. (b) Linear (horizontal) polarization. (c) Right-hand circular polarization. (d) Left-hand circular polarization. (e) Right-hand elliptical polarization. (f) Left-hand elliptical polarization.

rotates counterclockwise, it is *right-hand polarized*. The right-hand rule applies here: with the thumb of the right hand in the direction of propagation, the fingers will curl in the direction of rotation of the instantaneous electric field \mathcal{E} . If it rotates clockwise, it is *left-hand polarized*. Right- and left-hand circularly polarized waves are shown in Figs. 1-21c and 1-21d. A helix antenna produces circularly polarized waves (see Section 6.1) and the sense of rotation of the wave is the same as the sense of the helix windings, for example, a right-hand wound helix produces a right-hand circularly polarized wave. Finally, a wave may be *elliptically polarized*, with either right- or left-hand sense of rotation, as shown in Figs. 1-21e and 1-21f.

A general polarization ellipse is shown in Fig. 1-22 with a reference axis system. The wave associated with this polarization ellipse is traveling in the $+z$ -direction. The sense of rotation can be either left or right. The instantaneous electric field vector \mathcal{E} has components \mathcal{E}_x and \mathcal{E}_y along the x and y axes. The peak values of these components are E_1 and E_2 . The angle γ describes the relative values of E_1 and E_2 from

$$\gamma = \tan^{-1} \frac{E_2}{E_1} \quad 0^\circ \leq \gamma \leq 90^\circ \quad (1-196)$$

The tilt angle of the ellipse, τ , is the angle between the x -axis (horizontal) and the major axis of the ellipse. The angle τ is seen from Fig. 1-22 to be

$$\tau = \cot^{-1}(\text{AR}) \quad 1 \leq |\text{AR}| \leq \infty, \quad -45^\circ \leq \tau \leq 45^\circ \quad (1-197)$$

where the axial ratio of the ellipse, $|\text{AR}|$, is the ratio of the major axis electric field component to that along the minor axis. The sign of AR is positive for left-hand sense and negative for right-hand sense.

The instantaneous electric field for the wave of Fig. 1-22 can be written as (with $z = 0$ for simplicity)

$$\mathcal{E} = \mathcal{E}_x \hat{x} + \mathcal{E}_y \hat{y} = E_1 \cos \omega t \hat{x} + E_2 \cos(\omega t + \delta) \hat{y} \quad (1-198)$$

where δ is the phase by which the y -component leads the x -component. This representation describes the ellipse shape as time t progresses. If the components



Figure 1-22 The general polarization ellipse. The associated wave direction is out of the page in the $+z$ -direction. The tip of the instantaneous electric field vector \mathcal{E} traces out the ellipse.

are in phase ($\delta = 0$) the net vector is linearly polarized. The orientation of the linear polarization depends on the relative values of E_1 and E_2 . For example, if $E_1 = 0$ vertical linear polarization results; if $E_2 = 0$ horizontal linear results; if $E_1 = E_2$ the polarization is linear at 45° with respect to the axes. Linear polarization is a collapsed ellipse with infinite axial ratio. If δ is nonzero the axial ratio is finite. When $\delta > 0$, ϵ_1 leads ϵ_2 in phase and the sense of rotation is left hand. For $\delta < 0$ the sense is right hand. If $E_1 = E_2$ and $\delta = \pm 90^\circ$ the polarization is circular ($+90^\circ$ is left and -90° is right). The axial ratio of a circularly polarized wave is unity.

The phasor form of (1-198) is

$$\mathbf{E} = E_1 \hat{\mathbf{x}} + E_2 e^{j\delta} \hat{\mathbf{y}} \quad (1-199)$$

which can be written as (see Prob. 1.9-3)

$$\mathbf{E} = \sqrt{E_1^2 + E_2^2} (\cos \gamma \hat{\mathbf{x}} + \sin \gamma e^{j\delta} \hat{\mathbf{y}}) \quad (1-200)$$

The factor $\sqrt{E_1^2 + E_2^2}$ is the field magnitude and the remaining factor is the complex unit vector for the field. Thus γ and δ completely specify the polarization state of the wave. In fact, either pair of angles (ϵ , τ) or (γ , δ) uniquely define the polarization state of a wave. The transformations between these angles are

$$\gamma = \frac{1}{2} \cos^{-1}(\cos 2\epsilon \cos 2\tau) \quad (1-201)$$

$$\delta = \tan^{-1} \left(\frac{\tan 2\epsilon}{\sin 2\tau} \right) \quad (1-202)$$

The *polarization of an antenna* is the polarization of the wave radiated by the antenna in a given direction. Therefore, all of the discussions on wave polarization apply directly to antenna polarization. Usually the polarization characteristics of an antenna remain relatively constant over its main beam. However, the radiation from some side lobes may differ greatly in polarization from that of the main beam. When measuring the radiation from an antenna both E_H and E_V should be measured to be complete. The principal plane patterns of a linearly polarized antenna, such as a line source on the z -axis, are completely specified when a linearly polarized probe antenna is oriented to E_H .

The polarization of an antenna is determined by the wave radiated from the antenna, which must, of course, be in the far field where local plane wave behavior exists. Therefore, the plane polarized wave discussions given earlier apply. Furthermore, since the pattern (i.e., the radiation field) is reciprocal, the polarization of an antenna is reciprocal. In other words, an antenna responds best (gives maximum output) for an incident wave of given intensity when the polarization ellipse of the incident electric field has the same axial ratio, the same sense of polarization, and the same spatial orientation of the major axis

as that of the receiving antenna for that direction. For example, a right-hand circularly polarized receiving antenna is polarization matched to a right circularly polarized wave. As a mechanical analogy, let a right-hand threaded rod represent a right-hand circularly polarized (RHCP) wave and a right-hand tapped hole represent a RHCP antenna. The rod and hole are matched when screwed either in or out, corresponding to reception or transmission.

1.10 ANTENNAS IN COMMUNICATION LINKS AND RADAR

It is important to have an appreciation for the role played by antennas when they are employed in their two primary application areas, communication links and radar. First, consider a simple transmit-receive communication link as shown in Fig. 1-23. The transmitting antenna transmits power P_T . It is of primary interest to be able to calculate how much of this power we can pick up with the receive antenna. In the far field of the transmit antenna the waves are essentially plane and of uniform amplitude over any small region. The total power incident on the receiving antenna is found by summing up the incident power density (Poynting vector) over the "area" of the receive antenna; see (1-34). How an antenna converts this incident power into available power at its terminals depends on the type of antenna used, its pointing direction, and polarization.

Let us define *maximum effective aperture* A_{em} of an antenna using the following relationship

$$P_R = S_{av} A_{em} \quad (1-203)$$

where P_R is the time-average available power at the antenna terminals for a lossless antenna aligned to pick up maximum power (i.e., beam maximum in the direction of the incoming wave and its polarization state aligned with that of the incoming wave), and S_{av} is the time-average power density of the incoming wave. A_{em} (in square meters) is a measure of how effectively the antenna converts incident power density S_{av} (in watts per square meter) into received power P_R (in watts). If $Z_L = R_L + jX_L$ is the load impedance of the receiver at the antenna terminals and Z_{in} is the impedance of the antenna, we may model the antenna



Figure 1-23 A communication link.

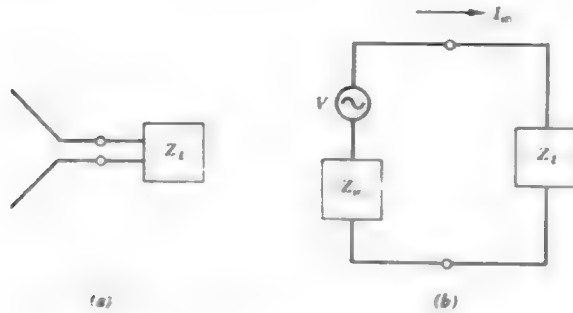


Figure 1-24 Equivalent circuit for a receiving antenna. (a) Receive antenna connected to a receiver with load impedance Z_L . (b) Equivalent circuit.

and receiver in Fig. 1-24a with the equivalent circuit of Fig. 1-24b. The terminal current is

$$I_{in} = \frac{V}{Z_{in} + Z_L} \quad (1-204)$$

The average power transferred to the load (receiver) is

$$P_R = \frac{1}{2} |I_{in}|^2 R_L \quad (1-205)$$

Our definition of A_{em} is based on power available to the terminals and maximum transfer of this power occurs for a conjugate matched load impedance $Z_L = R_{in} - jX_{in}$. Then (1-204) becomes

$$I_{in} = \frac{V}{2R_{in}} \quad (1-206)$$

where we have neglected losses on the antenna and thus $R_{in} = R_{r1}$. Substituting (1-206) into (1-205) and using $R_L = R_{r1}$ (for maximum power transfer) yields

$$P_R = \frac{1}{2} \frac{|V|^2}{4R_{r1}} = \frac{V_{rms}^2}{4R_{r1}} \quad (1-207)$$

Then A_{em} follows from its definition in (1-203) as

$$A_{em} = \frac{P_R}{S_{av}} = \frac{V_{rms}^2}{4R_{r1}S_{av}} \quad (1-208)$$

As an example we can calculate the maximum effective aperture of an ideal dipole of length Δz by noting that if the dipole is oriented parallel to the incoming electric field with rms value E_{rms} we have

$$V_{rms} = E_{rms} \Delta z \quad (1-209)$$

The power density of the incoming wave is

$$S_{av} = \frac{E_{rms}^2}{\eta} \quad (1-210)$$

The radiation resistance for the ideal dipole from (1-180) can be written as $\eta \frac{4}{3} \pi (\Delta z / \lambda)^2$; this with (1-209) and (1-210) in (1-208) gives

$$A_{em} = \frac{(E_{rms} \Delta z)^2}{4[\eta \frac{4}{3} \pi (\Delta z^2 / \lambda^2)](E_{rms}^2 / \eta)} = \frac{3}{8\pi} \lambda^2 = 0.119 \lambda^2 \quad (1-211)$$

The maximum effective aperture of an ideal dipole is independent of its length Δz (as long as $\Delta z \ll \lambda$). However, it is important to note that R_r is proportional to $(\Delta z / \lambda)^2$ so that even though A_{em} remains constant as the dipole is shortened, its radiation resistance is decreasing rapidly and it is more difficult to realize this maximum effective aperture because of the required conjugate impedance match of the receiver to the antenna.

The directivity of the ideal dipole is $\frac{3}{2}$ and can be written in the following manner

$$D = \frac{3}{2} = \frac{4\pi}{\lambda^2} \frac{3}{8\pi} \lambda^2 \quad (1-212)$$

Grouping factors this way permits identification of A_{em} from (1-211). Thus

$$D = \frac{4\pi}{\lambda^2} A_{em} \quad (1-213)$$

Although we derived this for an ideal dipole *this relationship is true for any antenna*. Comparing this to $D = 4\pi / \Omega_A$ we see that

$$\lambda^2 = A_{em} \Omega_A \quad (1-214)$$

which is also a general relationship. We can extract some interesting concepts from this relation. For a fixed wavelength A_{em} and Ω_A are inversely proportional: as the maximum effective aperture increases (as a result of increasing its physical size) the beam solid angle decreases which means power is more concentrated (i.e., directivity goes up, which also follows from $D = 4\pi / \Omega_A$). For a fixed maximum effective aperture (i.e., antenna size), as wavelength decreases

(frequency increases) the beam solid angle also decreases which means increased directivity.

Communication Links. We are now ready to completely describe the power transfer in the communication link of Fig. 1-23. If the transmit antenna were isotropic it would have power density at distance r of¹⁰

$$S_{av} = \frac{U_{ave}}{r^2} = \frac{P_T}{4\pi r^2} \quad (1-215)$$

where P_T is the time-average radiated power from the transmit antenna and (1-128) and (1-132) have been used. For a transmit antenna that is not isotropic but has directivity D_T and is pointed for maximum power density in the direction of the receiver, we have

$$S_{av} = \frac{U_m}{r^2} = \frac{D_T U_{ave}}{r^2} = \frac{D_T P_T}{4\pi r^2} \quad (1-216)$$

for the average power density incident on the receiver antenna, because $U_m = D_T U_{ave}$ and $U_{ave} = P_T/4\pi$. Using this in (1-203) gives

$$P_R = \frac{D_T P_T A_{emR}}{4\pi r^2} \quad (1-217)$$

where A_{emR} is the maximum effective aperture of the receive antenna and we assume it to be pointed and polarized for maximum response. Now from (1-213) $A_{emR} = D_R \lambda^2/4\pi$, so (1-217) becomes

$$P_R = P_T \frac{D_T D_R \lambda^2}{(4\pi r)^2} \quad (1-218)$$

which gives the available received power in terms of the transmitted power, antenna directivities, and the wavelength. Or, we could use $D_T = 4\pi A_{emT}/\lambda^2$ in (1-217) giving

$$P_R = P_T \frac{A_{emT} A_{emR}}{r^2 \lambda^2} \quad (1-219)$$

which is called the *Friis transmission formula*.

In the practical case antennas are not lossless. In Section 1.6 we saw that power available at the terminals of a transmitting antenna was not all transformed into radiated power, but rather the fraction e (radiation efficiency) of the available power. The power received by a receiving antenna is also reduced by the fraction e from what it would be if the antenna were lossless. The concept of

¹⁰ Note that U_{ave} is a spatial average of the time-average radiation intensity

gain was introduced to account for losses on an antenna, that is, $G = eD$. We can form a gain expression from the directivity expression (1-213) by multiplying both sides by e giving

$$G = \frac{4\pi}{\lambda^2} e A_{em} \quad (1-220)$$

We now define *effective aperture* (or *effective area*) A_e as

$$A_e = e A_{em} \quad (1-221)$$

Effective aperture is then a measure of the ability of an antenna to collect power from an incident wave and deliver it to its terminals. Combining these two equations gives the important result

$$G = \frac{4\pi}{\lambda^2} A_e \quad (1-222)$$

We shall show in Section 8.3 that effective aperture is equal to or less than the physical aperture area of the antenna.

The power transfer equation we have developed is now easily modified to include lossy antennas. We merely replace directivities by gains. Then, (1-218) becomes

$$P_R = P_T \frac{G_T G_R \lambda^2}{(4\pi r)^2} \quad (1-223)$$

This power transmission formula is very useful for calculating signal power levels in communication links. It assumes that there are no impedance mismatches at the transmit and receive antenna terminals, and that the transmit and receive antennas have identical polarizations and are aligned for polarization match. It also assumes the antennas are pointed toward each other for maximum gain. If any of the above conditions are not met, it is a simple matter to correct for the loss introduced by impedance mismatch, polarization mismatch, or antenna misalignment. The mismatch effects are discussed in the next section. The antenna misalignment effect is easily included by using the power gain value in the appropriate direction.

Communication link signal power calculations are usually computed in a decibel form. For example, (1-223) may be written as

$$P_R(\text{dBm}) = P_T(\text{dBm}) + G_T(\text{dB}) + G_R(\text{dB}) - 20 \log r(\text{km}) - 20 \log f(\text{MHz}) - 32.44 \quad (1-224)$$

where $P_T(\text{dBm})$ and $P_R(\text{dBm})$ are the transmit and receive powers in decibels above a milliwatt, dBm; for example, 30 dBm is 1 W. The transmit and receive

powers in this equation could also be expressed in units of decibels above a watt (dBW). $G_T(\text{dB})$ and $G_R(\text{dB})$ are the transmit and receive antenna gains in decibels, $r(\text{km})$ is the distance between the transmitter and receiver in kilometers, and $f(\text{MHz})$ is the frequency in megahertz.

Example 1-2. The ATS-6 Satellite.

The 20-GHz transmitter on board the ATS-6 (Application Technology Satellite-6) satellite has 2 W of power into a 37-dB gain, 45.7-cm diameter parabolic antenna. The 1.22-m diameter parabolic ground station antenna at the Virginia Tech earth terminal has 45.8-dB gain. Thus, $P_T(\text{dBm}) = 10 \log 2000 = 33.0$, $G_T(\text{dB}) = 37.0$, $G_R(\text{dB}) = 45.8$, and $f(\text{MHz}) = 2 \times 10^4$. The satellite to earth distance for this synchronous satellite is $r = 36,941.031 \text{ km}$. Using these values in (1-224) yields

$$P_R(\text{dBm}) = -94.0 \quad \text{or} \quad P_R = 3.98 \times 10^{-10} \text{ mW.} \quad (1-225)$$

High-gain antennas are extremely important for the successful operation of long communication links such as encountered with satellites. The available power at the ground station antenna terminals as calculated above is typical for satellite systems. If the combined antenna gain, $G_T(\text{dB}) + G_R(\text{dB}) = 82.8 \text{ dB}$, were not present then P_R would be $1.57 \times 10^{-21} \text{ W}$. A signal of this power level would be hopelessly lost in noise.

EIRP. A frequently used concept in communication systems is that of *effective (or equivalent) isotropically radiated power, EIRP*. It is formally defined as the power gain of a transmitting antenna in a given direction multiplied by the net power accepted by the antenna from the connected transmitter. Sometimes it is denoted as ERP, but this term may also be used for effective radiated power relative to a half-wave dipole. As an example, suppose an observer is located in the direction of maximum radiation from a transmitting antenna with input power P_T . Then

$$\text{EIRP} = P_T G_T. \quad (1-226)$$

The radiation intensity there is U_m as illustrated in Fig. 1-25a and $G_T = 4\pi U_m / P_T$, so

$$\text{EIRP} = P_T \frac{4\pi U_m}{P_T} = 4\pi U_m. \quad (1-227)$$

The same radiation intensity could be obtained from a lossless isotropic antenna (with power gain $G_i = 1$) if it had an input power P_{in} equal to $P_T G_T$ as illustrated in Fig. 1-25b. In other words, to obtain the same radiation intensity produced by the directional antenna in its pattern maximum direction, an isotropic antenna would have to have an input power G_T times greater. Effective radiated power is a parameter frequently used in the broadcast business. FM radio stations often give their effective radiated power when they sign off at night.

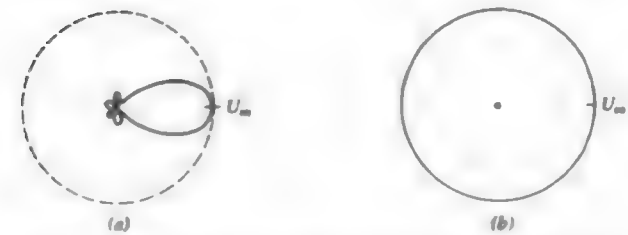


Figure 1-25 Illustration of effective isotropically radiated power. In both cases shown $\text{EIRP} = 4\pi U_m$ is the same. (a) Directional antenna with input power P_T and gain G_T . (b) Isotropic antenna with input power $P_T G_T$ and unity gain.

Radar. We now turn our attention to the radar problem. Suppose an airplane is the radar target as shown in Fig. 1-26. We shall assume that the transmit and receive antennas are pointed such that the pattern maxima are directed toward the target. The power density incident on the target is then

$$S_{\text{inc}} = \frac{P_T}{4\pi r^2} G_T = \frac{P_T A_{eT}}{\lambda^2 r^2} \quad (1-228)$$

where (1-216) was used with directivity D_T replaced by gain G_T to include losses on the transmit antenna; (1-222) was used to obtain the last of (1-228). The power intercepted by the target is proportional to the incident power density, so

$$P_{\text{inc}} = \sigma S_{\text{inc}} \quad (1-229)$$

where the proportionality constant σ has the units of area— σ is the *radar cross section* and is the equivalent area of the target as if the target reradiated the incident power isotropically. Although the power P_{inc} is not really scattered isotropically, the receiver is sampling scattered power in only one direction and

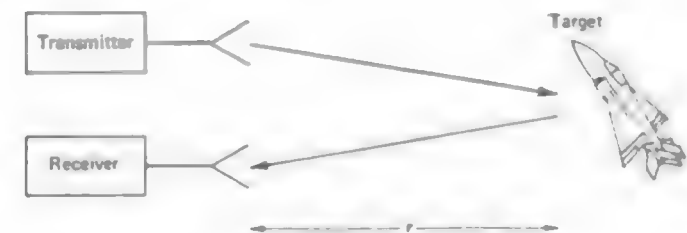


Figure 1-26 Radar example.

we are only concerned about that direction and assume the target scatters isotropically. Because P_{inc} appears to be scattered isotropically, the power density arriving at the receiver is

$$S_{scat} = \frac{P_{inc}}{4\pi r^2}. \quad (1-230)$$

The power available at the receiver is then

$$P_R = A_{eR} S_{scat}. \quad (1-231)$$

Combining the above four equations gives

$$P_R = A_{eR} \frac{\sigma S_{inc}}{4\pi r^2} = P_T \frac{A_{eR} A_{eT} \sigma}{4\pi r^4 \lambda^2}. \quad (1-232)$$

which is referred to as the *radar equation*. Usually the transmit and receive antennas are one and the same, that is, $A_{eR} = A_{eT}$. Using (1-222) we can rewrite this equation in a convenient form as

$$P_R = P_T \frac{\lambda^2 G_R G_T \sigma}{(4\pi)^3 r^4}. \quad (1-233)$$

If the transmit and receive antennas are identical $G_R G_T = G^2$.

Combining (1-229) and (1-230) actually forms the definition of radar cross section:

$$\sigma = \frac{4\pi r^2 S_{scat}}{S_{inc}} \quad (1-234)$$

which is the ratio of 4π times the radiation intensity, $r^2 S_{scat}$, in the receiver direction to the incident power density from the transmitter direction.

1.11 RECEIVING PROPERTIES OF ANTENNAS

In the preceding section we defined effective aperture from

$$A_e = \frac{\lambda^2}{4\pi} G. \quad (1-235)$$

The power available at the terminals of a receiving antenna with effective aperture A_e and an incident wave of time-average power density S_{av} is

$$P_R = A_e S_{av}. \quad (1-236)$$

It is assumed that the polarization of the receiving antenna is perfectly matched to that of the incoming wave. Also the load must be a conjugate impedance

match to the antenna in order to realize this available power. In general, the antenna and the wave are not exactly matched in polarization and the antenna and its load are not impedance matched. These two mismatches will reduce the power delivered to the transmission line. Let P_D be the power delivered to a transmission line with input impedance Z_L . Now we modify the effective aperture definition to include the mismatches as follows

$$P_D = A_R S_{av} \quad (1-237)$$

where A_R is the *effective receiving aperture*. This effective receiving aperture is the effective aperture A_e reduced by the mismatch effects, or

$$A_R = pq A_e \quad (1-238)$$

where p is the factor representing polarization mismatch and q is the factor for impedance mismatch. Using (1-235) in (1-238) gives

$$A_R = pq \frac{\lambda^2}{4\pi} G. \quad (1-239)$$

With power gain as a function of angle of arrival this becomes

$$A_R(\theta, \phi) = pq \frac{\lambda^2}{4\pi} G(\theta, \phi). \quad (1-240)$$

Impedance Mismatch. The *impedance mismatch factor* q is the fraction of power transmitted across the antenna terminal-transmission line junction, that is, the power transmission coefficient. From transmission line theory we have

$$\begin{aligned} q &= 1 - |\Gamma|^2 \\ &= 1 - \frac{|Z_L - Z_{ant}|^2}{|Z_L + Z_{ant}|^2} = 1 - \left| \frac{VSWR - 1}{VSWR + 1} \right|^2 \end{aligned} \quad (1-241)$$

where Γ is the voltage reflection coefficient, Z_L is the load impedance seen at the antenna terminals, Z_{ant} is the antenna input impedance, and VSWR is the voltage standing wave ratio on the transmission line. The possible values of q are from 0 to 1, with 1 being a perfect impedance match ($VSWR = 1$).

Polarization Mismatch. The factor p is the *polarization mismatch factor*, or polarization efficiency, and it also varies from 0 to 1 in value. It is unity when the wave and the antenna have the same polarization state. It is zero when they are orthogonal; for example, horizontal and vertical linear polarizations, and right- and left-hand circular polarizations. The determination of p is facilitated by introducing the concept of the *effective length* h of an antenna. It is defined from

$$V_{oc} = h^* \cdot E \quad (1-242)$$

where V_{oc} is the open circuit voltage produced at the terminals of an antenna of effective length \mathbf{h} with an electric field \mathbf{E} incident upon it. The complex conjugate is used because \mathbf{h} is that arising from the antenna when transmitting and (1-242) is a receiving relationship. In other words, the complex conjugate acts to reverse the reference direction, so that the components of antenna polarization and wave polarization are referenced to the same reference axes. In general \mathbf{h} may be a complex vector. If \mathbf{h} and \mathbf{E} are, for example, both linear vectors and are parallel, maximum voltage will result.

As an example consider the radiation electric field of an ideal dipole, which from (1-71) is

$$\mathbf{E} = \frac{j\omega\mu I}{4\pi} \frac{e^{-j\beta r}}{r} \Delta z \sin \theta \hat{\theta}. \quad (1-243)$$

If we let \mathbf{h} be determined by the size of the antenna and the angular dependence of the radiation pattern, then we may write

$$\mathbf{E} = \frac{j\omega\mu I}{4\pi} \frac{e^{-j\beta r}}{r} \mathbf{h} \quad (1-244)$$

where

$$\mathbf{h} = \Delta z \sin \theta \hat{\theta}. \quad (1-245)$$

Note that the dimension of \mathbf{h} is length and observe that, for the ideal dipole, the effective length is the same as the projection of the physical length viewed from the angle θ . This is not, however, true in general.

Now consider an arbitrary receiving antenna with effective length \mathbf{h}_R and an incident wave field \mathbf{E} . The power received is proportional to $|V_{oc}|^2$ which from (1-242) is $|\mathbf{h}_R^* \cdot \mathbf{E}|^2$. By normalizing this we can obtain the fraction of power lost due to polarization mismatch as

$$p = \frac{|\mathbf{h}_R^* \cdot \mathbf{E}|^2}{|\mathbf{h}_R|^2 |\mathbf{E}|^2} \quad (1-246)$$

because $|\mathbf{h}_R|^2 |\mathbf{E}|^2$ in the denominator is the maximum possible value of the numerator. We can write this as

$$p = \left| \frac{\mathbf{h}_R^*}{|\mathbf{h}_R|} \cdot \frac{\mathbf{E}}{|\mathbf{E}|} \right|^2 = |\hat{\mathbf{h}}_R^* \cdot \hat{\mathbf{e}}|^2 \quad (1-247)$$

where $\hat{\mathbf{h}}_R$ and $\hat{\mathbf{e}}$ are the complex unit vectors for the effective length of the antenna and for the wave. Equation (1-247) is usually the most convenient form for computing p . Note that $\hat{\mathbf{e}}$ represents the polarization state of the incoming wave. It is equal to the polarization state of the transmitting antenna, that is, $\hat{\mathbf{h}}_T$, if the intervening propagation medium does not alter the wave polarization state.

It now remains to show how the complex unit vectors $\hat{\mathbf{h}}_R$ and $\hat{\mathbf{e}}$ are determined. To do this it is most convenient to set up an xy -coordinate system perpendicular to the direction of arrival of the wave. Then we can use the polarization ellipse definitions of Section 1.9. Also since we are only interested in normalized values, the magnitude of the effective length [even though it is a function of arrival angle as seen by (1-245)] does not enter into the problem. From (1-200) we can write the required complex unit vectors as

$$\hat{\mathbf{h}}_R = \cos \gamma_R \hat{\mathbf{x}} + \sin \gamma_R e^{j\delta_R} \hat{\mathbf{y}} \quad (1-248)$$

and

$$\hat{\mathbf{e}} = \cos \gamma \hat{\mathbf{x}} + \sin \gamma e^{j\delta} \hat{\mathbf{y}} \quad (1-249)$$

where (γ_R, δ_R) and (γ, δ) describe the polarization state of the antenna and the wave. Summarizing, p is calculated by using (1-248) and (1-249) in (1-247).

To illustrate, consider a transmitting antenna that is vertically polarized, that is, produces a linearly polarized wave along the y -axis as shown in Fig. 1-27a, and a linearly polarized receiving antenna as shown in Fig. 1-27b. If the wave from the transmitter arrives at the receiver without being depolarized by the propagation path we see from Fig. 1-27 that

$$\hat{\mathbf{e}} = \hat{\mathbf{y}} \quad (1-250)$$

and

$$\hat{\mathbf{h}}_R = \cos \tau_R \hat{\mathbf{x}} + \sin \tau_R \hat{\mathbf{y}} \quad (1-251)$$

since $\gamma_R = \tau_R$ in this case of linear polarization. Then from (1-247)

$$p = |(\cos \tau_R \hat{\mathbf{x}} + \sin \tau_R \hat{\mathbf{y}})^* \cdot \hat{\mathbf{y}}|^2 = \sin^2 \tau_R. \quad (1-252)$$

When $\tau_R = 90^\circ$ both the wave and the antenna are vertically polarized and $p = 1$; the wave and the antenna are said to be *copolarized*, or polarization matched. If $\tau_R = 0^\circ$ the wave and the antenna states are orthogonal and (1-252) yields $p = 0$; the wave and antenna are referred to as being *cross-polarized* when $p = 0$.

As a further illustration suppose the receiving antenna is now circularly polarized; Fig. 1-27c shows how this may be accomplished. For circular polarization the x - and y -components are equal in amplitude and 90° out-of-phase. Suppose it is left-hand sense circular polarization. Then $AR = +1$ and $\epsilon_R = +45^\circ$ from (1-197) and $\gamma_R = +45^\circ$, $\delta_R = +90^\circ$ from (1-201) and (1-202). Then (1-248) yields

$$\hat{\mathbf{h}}_R = \cos 45^\circ \hat{\mathbf{x}} + \sin 45^\circ e^{j90^\circ} \hat{\mathbf{y}} = \frac{1}{\sqrt{2}} (\hat{\mathbf{x}} + j\hat{\mathbf{y}}) \quad (1-253)$$

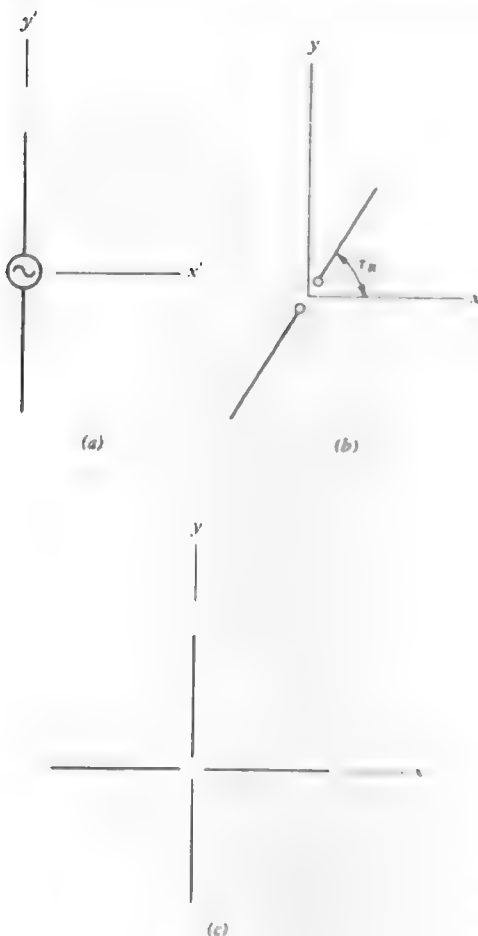


Figure 1-27 A vertical linearly polarized transmit antenna and two cases of receive antennas. (a) Transmitting antenna along y' -axis. (b) Linearly polarized receiving antenna in xy -plane. (c) Circularly polarized receiving antenna: two crossed dipoles whose outputs are combined with a 90° phase difference.

and

$$\rho = \left| \frac{1}{\sqrt{2}} (\hat{x} + j\hat{y})^* \cdot \hat{y} \right|^2 = \frac{1}{2} \quad (1-254)$$

Thus half the power is lost in this case. In fact, for any linearly polarized wave incident on any circularly polarized antenna (or vice versa) the power loss is one-half. In many situations a 3-dB loss may be significant and the antenna configuration must be altered to produce a better match, for example, by making both antennas vertical linear or both same sense circular. On the other hand,

there are situations when operating with one antenna linear and the other circular is desired. For example, if a spacecraft has a linearly polarized antenna the effects due to spacecraft motion or Faraday rotation in the ionosphere on the incoming linearly polarized wave orientation angle will not lead to power level fluctuations if a circularly polarized receive antenna is used. Thus, even though a 3-dB signal loss is encountered this loss is constant. If two linearly polarized antennas were used for this example, there is the possibility of significant polarization loss (ρ varies from 1 to 0 as τ_R varies from 90° to 0°) or a polarization tracking system must be used to maintain alignment.

Power Budget Calculations Including Mismatches. The effects of mismatch factors p and q can be included in power budget calculations for communication links rather simply. For example, the received power expression of (1-224) is modified to give the power delivered to the load as follows

$$P_R(\text{dBm}) = P_A(\text{dBm}) + 10 \log p + 10 \log q. \quad (1-255)$$

Field Intensity Measurements. A very small receiving antenna can be used as a *field probe*. Probes are used when it is necessary to measure the spatial amplitude distribution of electromagnetic fields. The probe must be small relative to the structure whose fields are being measured in order to minimize the disturbance of the fields introduced by the probe itself. The electrically small dipole, in any of its practical forms discussed in Section 2.1, is used to probe electric fields.

Receiving antennas are also used to measure absolute field intensity. For example, it is often necessary to know the field intensity at a fixed distance from a transmit antenna. The antenna pattern can, of course, be measured also by moving around the transmitter at a fixed distance from it in the far field; this is the relative field intensity variation. Measurements are often required because the effects of terrain and the real earth surface are difficult to calculate. If the gain of the measuring antenna is known (it usually is) and the voltage developed across its terminals is measured, the field intensity incident upon the measuring antenna can be calculated. We shall now discuss this.

Suppose the receiving antenna for field intensity measurements is matched to its transmission line and the input impedance of the antenna is essentially its radiation resistance. Then the antenna/receiver can be modeled as shown in Fig. 1-28. From the figure we see that

$$I_{in} = \frac{V_{in}}{R_r} \quad (1-256)$$

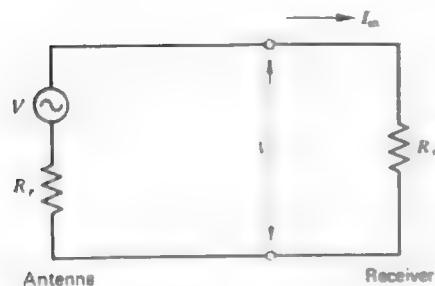


Figure 1-28 Equivalent circuit model for an antenna-receiver combination used to measure field intensity.

The time-average power received is then

$$P_R = \frac{1}{2} I_{in}^2 R_r$$

$$= \frac{1}{2} \left(\frac{V_{in}}{R_r} \right)^2 R_r = \frac{1}{2} \frac{V_{in}^2}{R_r} = \frac{V_{in, rms}^2}{R_r} \quad (1-257)$$

where $V_{in, rms} = V_{in}/\sqrt{2}$ since V_{in} is a peak quantity. Using (1-203) and (1-210) the received power can also be expressed in terms of the electric field intensity incident upon the antenna as

$$P_R = S_{av} A_e = \frac{E_{rms}^2}{\eta} A_e \quad (1-258)$$

Then using (1-222) this becomes

$$P_R = \frac{E_{rms}^2}{\eta} G \frac{\lambda^2}{4\pi} \quad (1-259)$$

Equating the two power expressions (1-257) and (1-259) yields

$$E_{rms}^2 = \eta \frac{V_{in, rms}^2}{R_r} \frac{4\pi}{G\lambda^2} = f^2 \frac{1}{G} V_{in, rms}^2 \frac{\eta 4\pi}{R_r c^2} \quad (1-260)$$

where wavelength λ was converted to frequency f by $\lambda = c/f$ with c the velocity of light. From this equation the rms electric field intensity can be calculated if the voltage $V_{in, rms}$ is measured. The decibel form of this equation is obtained by taking 10 log of both sides of (1-260) giving

$$20 \log E_{rms} = 20 \log f \text{ (MHz)} - G \text{ (dB)}$$

$$+ 20 \log V_{in, rms} - 10 \log R_r - 12.8. \quad (1-261)$$

A conventional unit for the electric field intensity is dB μ V/m which is decibels above a microvolt per meter. Then (1-261) is

$$E_{rms} \text{ (dB}\mu\text{V/m)} = 20 \log f \text{ (MHz)} - G \text{ (dB)}$$

$$+ V_{in, rms} \text{ (dB}\mu\text{V)} - 10 \log R_r - 12.8 \quad (1-262)$$

where $V_{in, rms}$ (dB μ V) is the antenna terminal rms voltage in units of decibels above a microvolt.

As an example suppose the antenna and transmission line input impedances are both 300 ohms. Then (1-262) becomes [13]

$$E_{rms} \text{ (dB}\mu\text{V/m)} = 20 \log f \text{ (MHz)} - G \text{ (dB)} + V_{in, rms} \text{ (dB}\mu\text{V)} - 37.6. \quad (1-263)$$

To be specific consider a typical FM broadcast receiver with a sensitivity of 1 μ V, that is, minimum satisfactory performance is produced when the value of $V_{in, rms}$ is 1 μ V, or 0 dB μ V. The most popular receiving antenna for FM receivers is the half-wave folded dipole (see Section 5.2) which has a real impedance of about 300 ohms and a gain of 2.15 dB. At a frequency of 100 MHz the incident field intensity required for minimum satisfactory performance from (1-263) is 0.25 dB μ V/m or 1.03 μ V/m.

If impedance or polarization mismatches are present in the field intensity measuring antenna, (1-262) is modified by including the terms $-10 \log p$ and $-10 \log q$ on the right-hand side, as well as replacing R_r by the transmission line characteristic impedance R_o . Gain loss due to mispointing can also be accounted for. If, for example, a 10-dB gain antenna is pointed such that the incoming wave approaches in a direction of the receiving antenna pattern where the gain is 4 dB below its maximum, then 6-dB gain is used in (1-262) rather than 10 dB.

REFERENCES

1. W. L. Weeks, *Antenna Engineering*, McGraw-Hill, New York, 1968; Section 1.1.
2. Sir Edmund Whittaker, *A History of the Theories of Aether and Electricity*, vol. 1: *The Classical Theories*, Harper Torchbooks, New York, 1960.
3. R. C. Hansen, Editor, *Microwave Scanning Antenna*, vol. 1: *Apertures*, Academic Press, New York, 1964; Chapter 2.
4. E. Larsen, *Telecommunications—A History*, Frederick Muller Ltd., London, 1977.
5. S. Silver, Editor, *Microwave Antenna Theory and Design*, M.I.T. Radiation Laboratory Series, vol. 12, McGraw-Hill, New York, 1949.
6. J. D. Kraus and K. R. Carver, *Electromagnetics*, Second Edition, McGraw-Hill, New York, 1973.
7. D. T. Paris and F. K. Hurd, *Basic Electromagnetic Theory*, McGraw-Hill, New York, 1969; p. 313.
8. J. D. Kraus, *Antennas*, McGraw-Hill, New York, 1950, p. 251.
9. J. S. Hollis, T. J. Lyon, and L. Clayton, *Microwave Antenna Measurements*, Scientific Atlanta, Inc., Atlanta, 1970.

10. W. K. Kummer and E. S. Gillespie, "Antenna measurements—1978," *Proc. IEEE*, vol. 66, pp. 483–507, April 1978.
11. J. D. Kraus and K. R. Carver, *Electromagnetics*, Second Edition, McGraw-Hill, New York, 1973, p. 411.
12. *Ibid.*, Chapter 11.
13. H. V. Carnagan, "Measure that field using any antenna," *Microwaves*, vol. 14, pp. 45–47, July 1975.

PROBLEMS

- 1.2-1 Use (1-6) in (1-1) to derive (1-7).
- 1.2-2 Use (1-13) in (1-9) together with (1-11), (1-12), and (1-20) to derive (1-18).
- 1.2-3 Assuming ϵ and μ are real and $M = 0$, derive (1-28) through (1-33) using the identity (A-19).
- 1.2-4 Write the complex power equation for a series *RLC* network driven by a voltage generator in a form analogous to the Poynting theorem.
- 1.4-1 Derive (1-47) starting with (1-18).
- 1.4-2 (a) Show that $\psi = Ce^{-j\beta r}/r$ satisfies (1-52) at all points except the origin.
(b) By integrating (1-51) over a small volume containing the origin, substituting $\psi = Ce^{-j\beta r}/r$, and letting r approach zero, show that $C = (4\pi)^{-1}$, thus proving (1-53).
- 1.4-3 Show that (1-70) follows from (1-67).
- 1.4-2 The expression for the electric field intensity of an ideal dipole can be derived in two ways:
(a) Derive (1-70) using the magnetic field intensity expression (1-69) in (1-58).
(b) Derive (1-70) using the vector potential expression (1-60) in (1-46) and $\mathbf{r}' = \mathbf{r}$.
- 1.4-3 For a z -directed current element $I \Delta z$ in free space and located at the origin of a spherical coordinate system:
(a) Calculate the complex Poynting vector in the general case, where r can be in the far-field region. Use the fields of (1-69) and (1-70).
(b) Then find the expression for the time-average power flowing out through a sphere of radius r enclosing the current element. Your answer will be that of (1-74). Why?
- 1.4-4 Show that the electric field for the ideal dipole in (1-70) satisfies Maxwell's equation $\nabla \cdot \mathbf{E} = 0$.
- 1.5-1 Prove (1-90) by using (1-84) in (1-89) and retaining only $1/r$ terms; that is, using $\nabla \cdot \mathbf{E} = 0$.
- 1.5-2 Uniform line source.
(a) Find the half-power beamwidth of the uniform line source pattern factor $|f(\theta)|$ of (1-16). Your answer should be in the form

$$HP = K\lambda/L \quad \text{for } L \gg \lambda.$$

Determine the constant K . *Hint:* First find the values u_{HP} of $u = (\beta L/2)\cos\theta$ for which $|f(u)| = 1/\sqrt{2}$. Then use the approximation $\cos^{-1}(\pm x) \approx \pi/2 \mp x$ for x small.
(b) Calculate the maximum side lobe level for the pattern in decibels relative to the main beam maximum. The side lobe maximum can be located by differentiating $f(u)$ with respect to u , setting equal to zero, and solving for u .

- (c) Suppose now that the current has a linear phase taper across it so that

$$I(z') = I_0 e^{j\beta z'}.$$

What is $f(\theta)$ now? If we let $\beta_0 = -\beta \cos\theta_0$, where is the pattern maximum (main beam pointing direction)? This is how the scanned beams of Fig. 1-11 are generated.

1.5-3 Equation (1-93) can be derived without initially assuming that the rays are parallel. Derive (1-93) by writing $R = [(r - r') \cdot (r - r')]^{1/2}$, expanding, factoring out an r , neglecting the smallest term, and using the first two terms of the binomial expansion.

1.5-4 Using the inner boundary of the far-field to be $r_{ff} = 2L^2/\lambda$ for a linear antenna of length L , find r_{ff} for the following three antennas: $L = 5\lambda$, a half-wave dipole ($L = \lambda/2$), and a short dipole ($L = 0.01\lambda$). Is the far-field boundary you have computed valid for each of these; if not, why not?

1.5-5 It can be shown that criteria for the far-field distance corresponding to (1-97) and (1-98) are more accurately given by $r > 5D$ and $r > 1.6\lambda$. Using these together with (1-96) plot a single graph of r/λ (vertical axis) versus D/λ for the far-field boundary. Indicate which region of the graph corresponds to the far field.

1.5-6 A car radio antenna is 1 m long and operates at a frequency of 1 MHz. Use the graph of Prob. 1.5-5 to find the far-field distance.

1.6-1 Show that there are 4π sr in all of space by evaluating $\iint d\Omega$ over a spherical surface.

1.6-2 A source has a power pattern of $|\cos^2\theta|$ for $0 \leq \theta \leq \pi/2$ and is zero for $\pi/2 < \theta \leq \pi$.

- (a) Calculate the directivity for $n = 1, 2$, and 3.

(b) Sketch the pattern in each case and comment on the general relationship between directivity and beamwidth.

(c) By physical reasoning alone, state the directivity for the $n = 0$ case. Check your answer mathematically.

1.6-3 An antenna has a far-field pattern which is independent of ϕ but which varies with θ as follows:

$$\begin{aligned} F &= 1 & \text{for } 0^\circ \leq \theta \leq 30^\circ \\ F &= 0.5 & \text{for } 60^\circ \leq \theta \leq 120^\circ \\ F &= 0.707 & \text{for } 150^\circ \leq \theta \leq 180^\circ \\ F &= 0 & \text{for } 30^\circ < \theta < 60^\circ \\ & & \text{and } 120^\circ < \theta < 150^\circ \end{aligned}$$

Find the directivity. Also find the directivity in the direction $\theta = 90^\circ$.

1.6-4 For a single-lobed pattern the beam solid angle is approximately given by

$$\Omega_b \approx HP_E HP_H$$

where HP_E and HP_H are the half-power beamwidths in radians of the main beam in the E and H planes. Show that

$$D \approx \frac{41.253}{HP_E HP_H}$$

where HP_E and HP_H are the E and H plane half-power beamwidths in degrees.

1.6-5 A horn antenna with low side lobes has half-power beamwidths of 29° in both principal planes. Use the approximate expression in Prob. 1.6-4 to compute the directivity of the horn in decibels.

1.6-6 A sector pattern has uniform radiation intensity over a specified angular region and is zero elsewhere. An example is

$$F(\theta) = \begin{cases} 1 & \frac{\pi}{2} - \alpha < \theta < \frac{\pi}{2} + \alpha \\ 0 & \text{elsewhere} \end{cases}$$

Derive an expression for the directivity corresponding to this pattern.

1.6-7 An airplane is flying parallel to the ground (in the z -direction). For a surface search radar an antenna is required which uniformly illuminates the ground over some region. The so-called cosecant pattern will do this. From the figure we see that

$$h = r \cos\left(\frac{\pi}{2} - \theta\right)$$

or

$$r = \frac{h}{\sin \theta} = h \csc \theta.$$

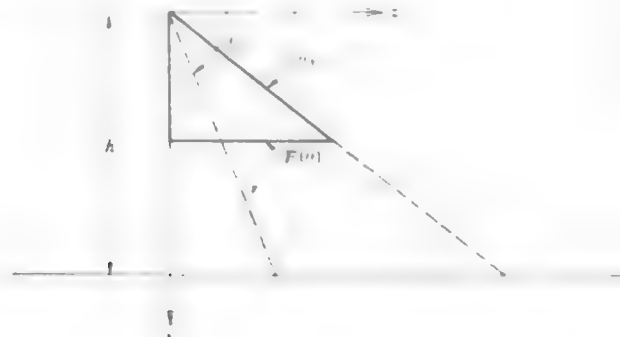
Thus the radiation must travel farther to reach the ground as θ is decreased. The factor $\csc \theta$ expresses the increase in this distance. If the angular variation in the radiation pattern is

$$F(\theta) = \csc \theta,$$

this will just compensate for the $1/r$ field variation with distance. Further assume that the ϕ variation is a sector pattern of small angular extent ϕ_0 . The whole pattern is then,

$$F(\theta, \phi) = \begin{cases} \csc \theta & \theta_1 < \theta < \frac{\pi}{2}, 0 < \phi < \phi_0 \\ 0 & \text{elsewhere.} \end{cases}$$

Derive an expression for the directivity.



1.6-8 An antenna has a directivity of 20 and a radiation efficiency of 90%. Compute the gain of the antenna in decibels.

1.7-1 Let sources \mathbf{J}_a , \mathbf{M}_a , \mathbf{J}_b , and \mathbf{M}_b all be of the same frequency in a linear medium. The following steps lead to the Lorentz reciprocity theorem:

(a) Maxwell's equations for sources a are

$$\nabla \times \mathbf{E}_a = -j\omega\mu\mathbf{H}_a - \mathbf{M}_a$$

$$\nabla \times \mathbf{H}_a = j\omega\epsilon\mathbf{E}_a + \mathbf{J}_a.$$

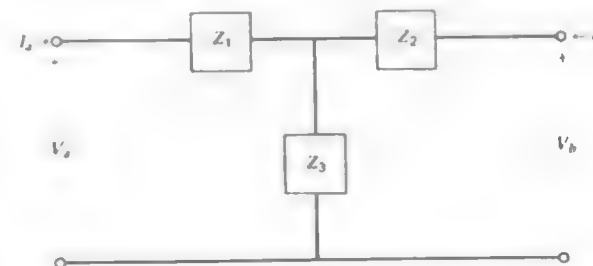
Similar equations can be written for sources b . Manipulate these four equations and use the vector identity (A-19) to show that

$$\nabla \cdot (\mathbf{E}_b \times \mathbf{H}_a - \mathbf{E}_a \times \mathbf{H}_b) = \mathbf{E}_b \cdot \mathbf{J}_a + \mathbf{H}_a \cdot \mathbf{M}_b - \mathbf{H}_b \cdot \mathbf{M}_a - \mathbf{E}_a \cdot \mathbf{J}_b.$$

(b) Integrate the above equation over a volume v enclosing all sources, employ the divergence theorem (A-23) for the left-hand side, and let the volume extend to infinity. Then the fields arriving at the surface of the volume behave like spherical waves, and the TEM wave relationships can be employed to show that the left-hand side is zero, leading to a proof of (1-159).

1.7-2 Use the reciprocity theorem form of (1-160) to show that the distant field of any finite electric current distribution in free space can have no radial component.

1.7-3 Since any two port network can be reduced to an equivalent T section, the general antenna system of Fig. 1-17a can be modeled as shown in the figure. First excite terminals a with a current source I_a and find the open circuit output voltage $V_b|_{I_b=0}$. Then excite terminals b with a current source I_b and find the open circuit output voltage $V_a|_{I_a=0}$. From these relationships find Z_{aa} and Z_{bb} ; they will, of course, be equal.



1.7-4 Write the voltage equations for the network representation of Prob. 1.7-3, and compare to (1-164) and (1-165) to show that the T network impedances are $Z_1 = Z_{aa} - Z_m$, $Z_2 = Z_{bb} - Z_m$, and $Z_3 = Z_m$.

1.7-5 If antennas a and b are identical, how is the network of Probs. 1.7-3 and 1.7-4 simplified?

1.7-6 Reciprocity can also be shown with voltage generators and short circuit currents:

(a) Drive terminals a of the network in Prob. 1.7-3 with a voltage generator V_a and short circuit terminals b . Find the expression of $V_a/I_a|_{I_b=0}$ in terms of Z_1 , Z_2 , and Z_3 . Then drive terminals b with voltage source V_b while short circuiting terminals a . Find $V_b/I_b|_{V_a=0}$. It should equal $V_a/I_a|_{V_b=0}$.

(b) Find the same transfer impedance expressions in terms of Z_{aa} , Z_{bb} , Z_{ab} , and Z_{ba} from (1-164) and (1-165). Show that they are equal if $Z_{ab} = Z_{ba}$.

(c) Using $Z_1 = Z_{aa} - Z_{aa}$, $Z_2 = Z_{bb} - Z_{aa}$, and $Z_3 = Z_{aa}$ from Prob. 1.7-4, show that the transfer impedance expressions of (a) are the same as those of (b).

1.8-1 A 2-m-long dipole made of 6.35-mm (0.25-in.) diameter aluminum is operated at 500 KHz. Compute its radiation efficiency, assuming

- (a) the current is uniform
- (b) the current is triangular.

1.8-2 A citizen's band radio at 27 MHz uses a half-wavelength long antenna that has a radiation resistance of 70 ohms. Compute the radiation efficiency if the antenna is made with 6.35-mm-diameter aluminum. As a rough approximation assume that the current is triangular.

1.8-3 Use the ohmic resistance formula of (1-190) to verify the expression for R_{ohmic} for

- (a) a uniform current given by (1-184)
- (b) a triangular current given by (1-192).

1.9-1 The instantaneous electric field components of an elliptically polarized wave are $E_x = E_1 \cos(\omega t - \beta z)$ and $E_y = E_2 \cos(\omega t - \beta z + \delta)$. Specify E_1 , E_2 , and δ for the following polarizations:

- (a) Linear with $E_1 \neq 0$ and $E_2 \neq 0$.
- (b) Right circular.
- (c) Left circular.
- (d) Elliptical with $E_1 = E_2$.
- (e) Elliptical with $\delta = 90^\circ$.

1.9-2 Write the frequency domain form of the total vector electric fields given in Prob. 1.9-1.

1.9-3 Start with (1-199) and prove (1-200). Use the fact that the magnitude of \mathbf{E} follows from $|\mathbf{E}|^2 = \mathbf{E} \cdot \mathbf{E}^*$. Also note that γ in Fig. 1-22 is in a triangle with sides E_1 and E_2 and hypotenuse $|\mathbf{E}|$.

1.10-1 Calculate the beam solid angle Ω_A for an ideal dipole in steradians (square radians) and in square degrees. Use the fact that $A_{em} = 0.119\lambda^2$ for an ideal dipole.

1.10-2 A half-wavelength dipole has a directivity of 2.15 dB. Derive an expression for its maximum effective aperture in terms of wavelength squared.

1.10-3 A certain parabolic reflector antenna 3.66 m (12 ft) in diameter has an effective aperture of 6.30 m². Compute the gain in decibels at 11.7 GHz.

1.10-4 A parabolic reflector antenna is circular with a diameter of 1.22 m (4 ft). If the effective aperture equals 55% of the physical aperture area, compute the gain of the antenna in decibels at 20 GHz.

1.10-5 Suppose a transmitting antenna produces a maximum far-zone electric field in a certain direction given by

$$E = 90I \frac{e^{-j\beta r}}{r}$$

where I is the peak value of the terminal current. The input resistance of the lossless antenna is 50 ohms. Find the maximum effective aperture of the antenna, A_{em} . Your answer will be a number times wavelength squared.

1.10-6 Derive the decibel form of the power transmission equation (1-224) from (1-223).

1.10-7 Write a power transfer equation similar to (1-224) but with distance r in units of miles.

1.10-8 Calculate the received power in watts for the ATS-6 system of Example 1-2 using (1-223).

1.10-9 The CTS (Communications Technology Satellite) satellite had an 11.7-GHz transmitter on board which provided 200 mW to a 19.3-dB gain antenna. Use (1-224) to determine the received power (in watts) available from the terminals of a ground station antenna with 50.4-dB gain (3.66 m diameter parabolic reflector). The satellite is in synchronous orbit 36,941 km away from the ground station.

1.10-10 A VHF transmitter at 150 MHz delivers 20 W into an antenna with 10-dB gain. Compute the power in watts available from a 3-dB gain receiving antenna 50 km away from the transmitter.

1.10-11 Let us compare the performance of the radio system of Prob. 1.10-10 to a transmission line. Suppose an RG-8 coaxial cable were used instead of the antenna. The attenuation is 0.1 dB/m.

- (a) Calculate the cable loss in decibels for the 50 km distance.
- (b) What is the net loss for the radio system of Prob. 1.10-10; that is, the net loss encountered between the transmit antenna input and the receive antenna output?
- (c) Would repeater amplifiers be necessary in the cable system?
- (d) Repeat parts (a) and (b) for the case of a 500-m path length.
- (e) Repeat (d) using a frequency of 300 MHz where the cable attenuation is 0.14 dB/m.

Assume the antenna gains are the same.

(f) Current fiber-optic cables have a loss of 1 dB/km. Compute the loss in decibels for the 50 km and 500-m paths.

(g) Tabulate results.

1.10-12 Derive a power transfer equation in a form involving the effective isotropically radiated power of the transmitter, the effective aperture of the receiving antenna and free space spreading loss, $1/4\pi r^2$. Start with (1-223).

1.10-13 The maximum radar cross section for a resonant half-wavelength dipole is approximately $0.85\lambda^2$. The frequency is 10 GHz, the range is 1000 m, the gain of the transmit and receive antennas is 20 dB, and the transmit power is 1000 W. Compute the received power if the receiver is in the same location as the transmitter (i.e., monostatic radar case).

1.10-14 An FM broadcast radio station has a 2-dB gain antenna system and 100-kW transmit power. Calculate the effective isotropically radiated power in kilowatts.

1.11-1 Suppose a transmitting antenna is not impedance matched to its input transmission line. The radiation intensity, or equivalently the power density at a specified distance, will be reduced from the perfect impedance match case. Compute this reduction in decibels, in a fixed direction, for the mismatch conditions which give voltage standing wave ratios on the transmission line of 1.01, 1.2, 2, and 10.

1.11-2 The magnitude of the axial ratio of a polarization ellipse is often given in decibels, where $AR(\text{dB}) = 20 \log |AR|$. For a right-hand elliptically polarized wave with an axial ratio of 2 dB and a tilt angle τ of 45° , find the complex unit vector \hat{e} .

1.11-3 For the wave of Prob. 1.11-2 compute the polarization mismatch factor for the following receiving antennas:

- (a) Horizontal linear.
- (b) Vertical linear.
- (c) Right-hand circular.
- (d) Left-hand circular.
- (e) Right-hand elliptical with $AR(dB) = 2$ and tilt angle $\tau = 45^\circ$.
- (f) Left-hand elliptical with $AR(dB) = 2$ and tilt angle $\tau = 135^\circ$.

1.11-4 Derive (1-261) from (1-260).

1.11-5 To receive a certain FM radio station properly a terminal voltage of $200 \mu V$ (peak) is required at the receiver terminals. The input impedance of the FM receiver is 300 ohms (pure real). The receiving antenna is a linearly polarized folded dipole whose directive gain in the direction of the station is 1.64. The input impedance of the folded dipole is $300 + j0$ ohms. The radiation resistance of the folded dipole is 300 ohms. The FM receiver is connected to the folded dipole by a 300-ohm transmission line.

- (a) Determine the radiation efficiency ϵ and q .
 - (b) If the radio station transmitting antenna is circularly polarized, find the minimum electric field strength (peak) required for proper reception by the FM receiver at 100 MHz.
- 1.11-6 Justify the complex conjugate which appears in (1-242). To do this recall that the polarization state of an antenna is the polarization of the wave radiated by the antenna when transmitting. Set up a fixed xy -coordinate system with z directed toward the antenna. Refer h and E to those x - and y -axes.

BIBLIOTECA NACIONAL AUTONOMA DE MEXICO
DEPARTAMENTO DE BIBLIOTECAS
BIBLIOTECA CENTRAL
Toluca, B. C., Honduras C. A.

2

SOME SIMPLE RADIATING SYSTEMS

In this chapter we consider a few simple radiating systems such as electrically small dipoles, the half-wave dipole, and small loop antennas. Also we show how the presence of a perfect ground plane affects the performance of an antenna.

These simple antennas are introduced here so that the treatment of arrays in the next chapter will be more meaningful. In Chapter 5 we return to the analysis and design of antenna structures.

2.1 ELECTRICALLY SMALL DIPOLES

An antenna whose dimensions are much smaller than a wavelength is referred to as an *electrically small antenna*. One possible definition for electrically small is that the antenna must fit inside a "radiansphere" (i.e., a sphere whose diameter is $\lambda/2\pi$, or about one-sixth of a wavelength) [1, 2]. Such antennas are inherently inefficient. However, considerations of size, weight, cost, and mobility frequently require that an antenna be physically small. For low frequencies this means that the antenna will be electrically small as well. The simplest of the electrically small antennas are the electrically small dipoles. In Section 1.4 we discussed the ideal dipole which is a small linear piece of uniform current. The ideal dipole does not exist but can be approximated in practice.

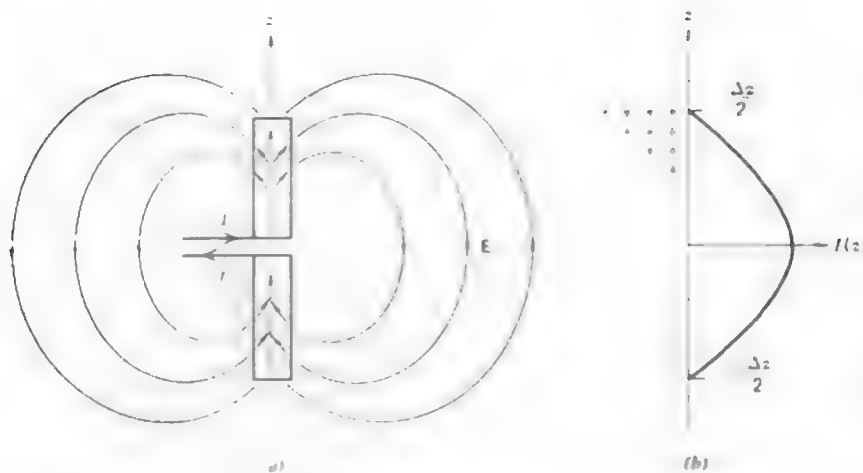


Figure 2-1 Short dipole, $\Delta z \ll \lambda$. (a) Current on the antenna and the electric fields surrounding it. (b) Current and charge distributions.

First consider an (actual) short dipole shown in Fig. 2-1a. In this real antenna the current must smoothly go to zero at the ends of the wire as indicated in Fig. 2-1b. For a thin wire (diameter $\ll \lambda$) this current distribution is approximately sinusoidal. The decreasing current toward the wire ends requires that charges peel off and appear on the wire surface as shown in Fig. 2-1a. This charge accumulation leads to a displacement current density $j\omega\epsilon\mathbf{E}$ in the space surrounding the dipole. The displacement current density in turn gives rise to an electromagnetic wave which propagates outward from the source. This is one visualization of the phenomena of radiation. Displacement current in space couples a transmitting antenna to a receiving antenna, much as a conduction current provides coupling between lumped elements in a circuit.

The current and charge distributions shown in Fig. 2-1b are for an instant of time when the input current at the dipole terminals is maximum. Since the input current is changing sinusoidally with time, the current and charge distributions on the dipole will also. As Δz becomes extremely small the sinusoidal type current distribution is well approximated by the triangular distribution of Fig. 1-20b. The radiation resistance using the triangular current distribution is from (1-189)

$$R_r = 20\pi^2 \left(\frac{\Delta z}{\lambda} \right)^2 \text{ ohms (short dipole).} \quad (2-1)$$

The input reactance of the actual short dipole is capacitive. This can be seen by visualizing the antenna as an open circuited transmission line. The distance

$\Delta z/2$ from the end of the antenna to the feed point is much less than a quarter wavelength and thus the input impedance is capacitive. (Recall from transmission line theory that the impedance a distance s from an open circuit termination is $-jZ_0 \cot \beta s$. Loading coils are frequently used to tune out this capacitance. They are sometimes seen on automobile radio antennas. A more complete discussion of dipole impedance will be presented in Chapter 5.)

In the ideal dipole all charge accumulates at the ends of the antenna. In fact, the ideal dipole may be analyzed as either a uniform current or two point charges (see Prob. 2.1-1), all oscillating at radian frequency ω . See Fig. 2-2. The charge dipole model shows that charge accumulates at the ends of the antenna. Thus to realize a uniform current distribution in practice a mechanism must be provided for charge storage at the ends of the short wire. One method of accomplishing this is to place metal plates at the ends of the wire. This is called a **capacitor-plate antenna**, or top-hat-loaded dipole antenna. Figure 2-3 shows the construction of the antenna and the current and charges on it. If $\Delta z \ll \lambda$ the radial currents on the plates will produce fields that almost cancel in the far field, since the currents are opposite directed and the phase difference due to separation is small ($\beta \Delta z \ll 2\pi$). If, in addition, $\Delta z \ll \Delta r$ the plates will provide for charge storage such that the current on the wire is constant. The capacitor-plate antenna then closely approximates the uniform current ideal dipole model. Frequently in practice radial wires are used for the top loading in place of the solid plates.

Another small antenna used to approximate the ideal dipole is the **transmission line loaded antenna** as shown in Fig. 2-4a. The results of transmission line theory can be borrowed to determine the current distribution. The current is essentially sinusoidal along the wire with a zero at the ends. This current distribution is sketched in Fig. 2-4b for $L < \lambda/4$. If $\Delta z \ll \lambda$ the fields from the currents



Figure 2-2 Ideal dipole models. (a) Uniform current model. (b) Charge dipole model.

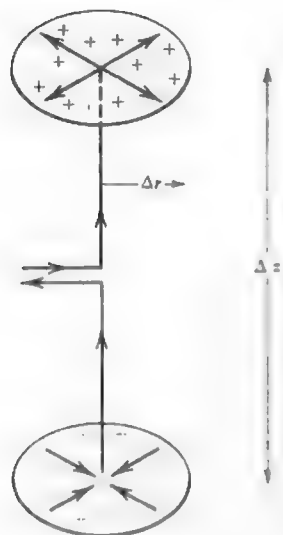


Figure 2-3 Capacitor-plate antenna. The arrows on the antenna indicate current. The charges on the plates are also shown.

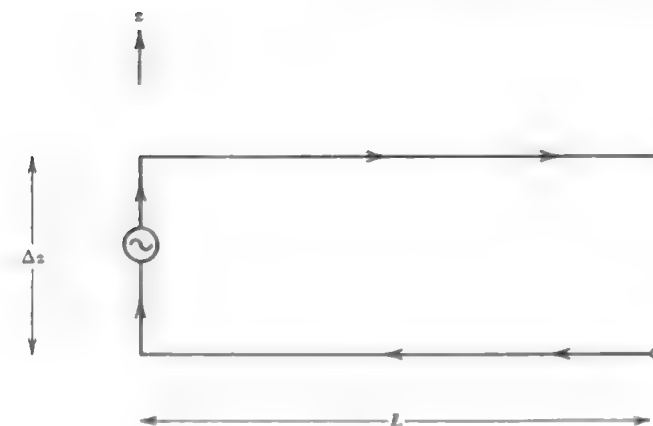
on the horizontal wires will almost cancel in the far field. If also $\Delta z \ll L$, the horizontal wires will provide an effective place for the charge to be stored and the current on the vertical section will be nearly constant as illustrated in the Fig. 2-4b. Then most radiation comes from a short section over which the current is nearly constant and the antenna approximates an ideal dipole.

Transmission line loading ideas may be extended and several horizontal wires can be attached to the ends of the short vertical section. If the transmission lines of Fig. 2-4a are extended in opposite directions the reactance is one-half its former value (by paralleling identical capacitive elements). As more wires are added the reactance is further reduced and the structure approaches that of a capacitor-plate antenna.

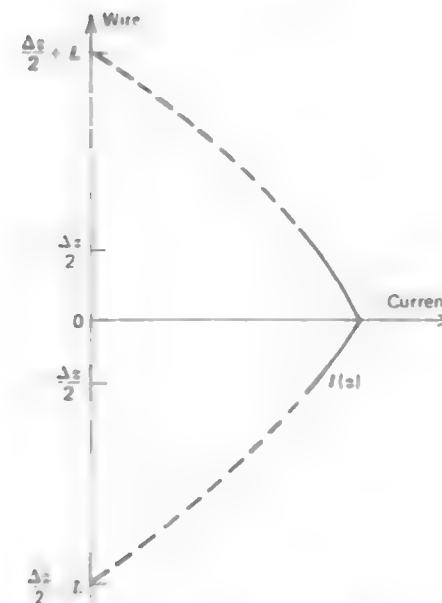
For the small dipoles discussed in this section, if the current on the vertical wire is nearly uniform the radiation resistance is given approximately by (1-180), or

$$R_r = 80\pi^2 \left(\frac{\Delta z}{\lambda} \right)^2 \text{ ohms} \quad (2-2)$$

where Δz is the length of uniform current section. The input reactance is capacitive. If end loading is added this reactance is reduced as the loading (in the form of wires or plates) is increased. This is because the distance from the open



(a)



(b)

Figure 2-4 The transmission line loaded antenna. (a) The antenna structure. Arrows indicate the current. (b) Current distribution on the antenna if imagined to be bent back straight. The solid line is the current on vertical section of (a) and the dashed line is the current on the horizontal transmission line section.

circuit in the transmission line analog is increased. (See Prob. 2.1-3.) The radiation pattern of all forms of the small dipole is that of the ideal dipole shown in Fig. 1-4.

At different portions of the frequency spectrum electrically small antennas are used for different reasons. For instance, in the VLF region where wavelength is very large, an electrically short vertical radiator is used with a large top hat load. The top hat loading makes the antenna appear like the capacitor-plate antenna of Fig. 2-3. Further up the spectrum, such as in the AM broadcast band, receiving antennas are usually small electrically, as we saw in Section 1.8. The transmitting antennas are not small, but are of resonant size as discussed in the next section. At VHF frequencies and above, electrically small antennas are only used in special situations.

2.2 THE HALF-WAVE DIPOLE

A very widely used antenna is the **half-wave dipole** antenna. It is a linear current whose amplitude varies as one-half of a sine wave with a maximum at the center. For simplicity we will assume this to be a filament of current. Also it could be imagined to flow on an infinitely thin, perfectly conducting, half-wavelength long wire. This is a good approximation to a wire half-wave dipole which has a diameter much smaller than its length. The advantage of a half-wave dipole is that it can be made to resonate and present a zero input reactance, thus eliminating the need for tuning to achieve a conjugate impedance match. Input impedance of dipole antennas is discussed in detail in Section 5.1, but for now we will just say that to obtain a resonant condition for a half-wave dipole the physical length must be somewhat shorter than a free space half-wavelength and as the antenna wire thickness is increased the length must be reduced more to achieve resonance.

As usual the current distribution is placed along the z -axis and for the half-sine wave current on the half-wave dipole the current distribution is written as

$$I(z) = I_m \sin \left| \beta \left(\frac{\lambda}{4} - |z| \right) \right| \quad |z| \leq \frac{\lambda}{4}. \quad (2-3)$$

Recall that $\beta = 2\pi/\lambda$. This current goes to zero at the ends (for $z = \pm\lambda/4$) and its maximum value I_m occurs at the center ($z = 0$) as shown in Fig. 2-5a. From this current we can calculate the radiation pattern. Since it is a z -directed line source we can use (1-101) in (1-104) to find the electric field as

$$E_\theta = j\omega\mu \sin \theta \frac{e^{-j\beta r}}{4\pi r} \int I(z') e^{j\beta z' \cos \theta} dz'. \quad (2-4)$$

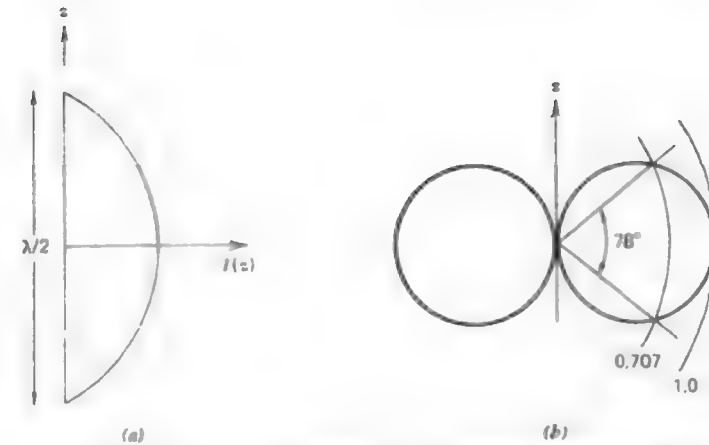


Figure 2-5 The half-wave dipole. (a) Current distribution $I(z)$. (b) Radiation pattern $F(\theta)$.

Substituting (2-3) into the integral of (2-4) and evaluating,

$$\begin{aligned} f_{un} &= \int I(z') e^{j\beta z' \cos \theta} dz' = \int_{-\lambda/4}^{\lambda/4} I_m \sin \left(\frac{\pi}{2} - \beta |z'| \right) e^{j\beta z' \cos \theta} dz' \\ &= I_m \int_{-\lambda/4}^0 \sin \left(\frac{\pi}{2} + \beta z' \right) e^{j\beta z' \cos \theta} dz' + I_m \int_0^{\lambda/4} \sin \left(\frac{\pi}{2} - \beta z' \right) e^{j\beta z' \cos \theta} dz' \quad (2-5) \end{aligned}$$

where f_{un} is the unnormalized pattern factor. Using the integral (F-5)

$$\int \sin(a + bx) e^{cx} dx = \frac{e^{cx}}{b^2 + c^2} [c \sin(a + bx) - b \cos(a + bx)] \quad (2-6)$$

in (2-5) we have

$$\begin{aligned} f_{un} &= I_m \frac{e^{j\beta z' \cos \theta}}{\beta^2 - \beta^2 \cos^2 \theta} \left[j\beta \cos \theta \sin \left(\frac{\pi}{2} + \beta z' \right) - \beta \cos \left(\frac{\pi}{2} + \beta z' \right) \right]_{-\lambda/4}^0 \\ &\quad + I_m \frac{e^{j\beta z' \cos \theta}}{\beta^2 - \beta^2 \cos^2 \theta} \left[j\beta \cos \theta \sin \left(\frac{\pi}{2} - \beta z' \right) + \beta \cos \left(\frac{\pi}{2} - \beta z' \right) \right]_{0}^{\lambda/4} \\ &= \frac{I_m}{\beta^2 \sin^2 \theta} [j\beta \cos \theta - e^{-j\beta \lambda/2 \cos \theta}(-\beta) + e^{j\beta \lambda/2 \cos \theta}(\beta) - j\beta \cos \theta] \\ &= \frac{I_m}{\beta \sin^2 \theta} 2 \cos \left(\frac{\pi}{2} \cos \theta \right). \quad (2-7) \end{aligned}$$

Substituting this into (2-4) gives

$$E_\theta = j\omega\mu \frac{2I_m}{\beta} \frac{e^{-j\beta r}}{4\pi r} \sin\theta \frac{\cos[(\pi/2)\cos\theta]}{\sin^2\theta} \quad (2-8)$$

In this expression we can identify the element factor $g(\theta) = \sin\theta$ and the normalized pattern factor

$$f(\theta) = \frac{\cos[(\pi/2)\cos\theta]}{\sin^2\theta} \quad (2-9)$$

Both $g(\theta)$ and $f(\theta)$ are maximum for $\theta = \pi/2$ and have a value of unity there. The complete (normalized) far-field pattern is then, see (1-113),

$$F(\theta) = g(\theta)f(\theta) = \frac{\cos[(\pi/2)\cos\theta]}{\sin\theta} \quad (\text{half-wave dipole}). \quad (2-10)$$

This pattern is plotted in Fig. 2-5b in linear, polar form. The half-power beamwidth is 78° . For comparison, the half-power beamwidth of an ideal dipole pattern is 90° ; see Fig. 1-4b. Thus, there is a small increase in the directivity of the half-wave dipole over the short dipole. In fact, the directivity for a short dipole is 1.5; see (1-145). We shall show in Section 5.1 that it is 1.64 for a half-wave dipole. The input impedance of an infinitely thin half-wavelength long dipole is $73 + j42.5$ ohms. If it is slightly reduced in length to achieve resonance, the input impedance is about $70 + j0$ ohms.

In Section 2.1 we briefly discussed one viewpoint on the phenomena of radiation. We are now ready to discuss another viewpoint in which the fields in space are considered to be produced by currents and charges on the antenna as sources. We know that in a complete system there must at any instant of time be equal numbers of positive and negative charges, and, if these were static fields (i.e., zero frequency and infinite wavelength), then the fields at a great distance from the positive and negative sources would practically cancel. However, when the distance between positive and negative sources becomes comparable with wavelength, the phase shift (or retardation) due to different path lengths from positive and negative sources to an observation point may keep the effects from canceling. In the case of the half-wave dipole when the current is essentially in phase (either positive or negative), this means that radiation will be strongest in a direction normal to the dipole and weakest along the axis of the dipole. For longer dipoles (e.g., see Section 5.1), where the current is not in phase along the entire length of the dipole, the phase shift between sources due to distance will cause the radiation from the various sources (i.e., different parts of the dipole) to add in certain directions and cancel in others, depending on whether the dis-

tances between plus and minus sources is an odd or even multiple of a half-wavelength, respectively. This picture of radiation suggests why practical antennas are comparable with a wavelength in size. It also tells us something about the shape of the far-field pattern and will be useful to us in qualitative thinking about arrays in the next chapter.

2.3 ANTENNAS ABOVE A PERFECT GROUND PLANE

Antennas are frequently operated in the presence of other structures. One such structure that is commonly encountered is a ground plane. A ground plane in its ideal form is infinite in extent and perfectly conducting, often referred to as a *perfect ground plane*. A solid metal sheet or a planar wire grid system that is large compared to the antenna size is, in most cases, well approximated as a perfect ground plane. In this section we discuss the effect of a perfect ground plane on some simple antennas. The problem is most easily solved by employing image theory, which will be discussed first. Antennas over a real earth ground are covered in Section 5.5.

2.3.1 Image Theory

Most of the theory developed thus far is for antennas in a homogeneous medium characterized by ϵ and μ . In other words, no other objects are present. This is often a poor approximation to reality. But, by using image theory the fields of an antenna operating in the presence of materials of simple geometric shape may be determined.

Consider first an ideal dipole in front of an infinite plane perfect conductor and oriented perpendicular to the plane as shown in Fig. 2-6. We wish to find the fields \mathbf{E} and \mathbf{H} above the plane PP' . By the uniqueness of the solution to a differential equation (the wave equation) plus its boundary conditions, we may introduce an equivalent system that is different below PP' but satisfies the same boundary conditions on PP' and has the same sources above PP' . Such an equivalent system, which produces the same fields above PP' as the original system, has an image source the same distance below the plane PP' and similarly directed. In this case, the image source is another ideal dipole as shown in Fig. 2-6b. It is a simple matter to prove that the boundary condition of zero tangential electric field along plane PP' is satisfied by this source configuration. To do this we examine the electric field expression for an ideal dipole given by (1-70). The complete expression must be used because the ground plane can be, and usually is, in the near field of the antenna. The radial component varies as $\cos\theta$ and the θ -component varies as $\sin\theta$, where θ is the angle from the axis

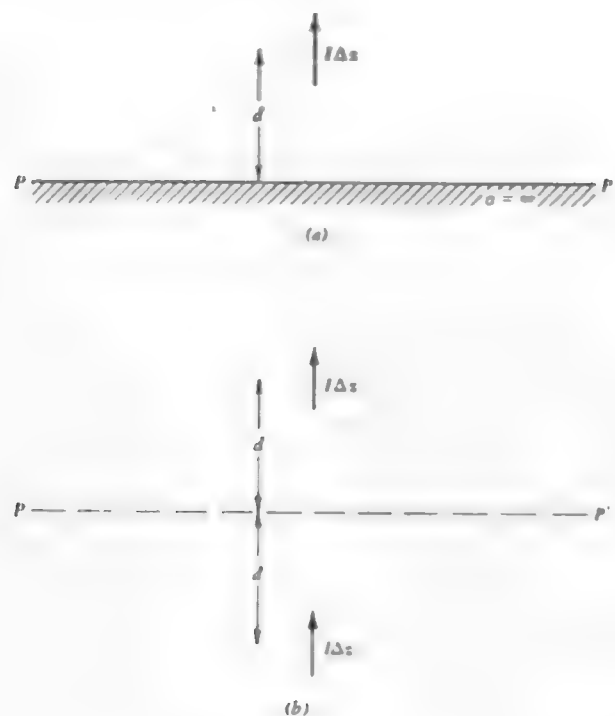


Figure 2-6 Ideal dipole above and perpendicular to a perfectly conducting ground plane. (a) Physical model. (b) Equivalent model using image theory.

along the direction of the current element. Let θ_1 and θ_2 be the angles from the line of the current elements to a point on the plane PP' for the primary source and its image, respectively. The radial components from the sources are then

$$E_{r1} = C \cos \theta_1 \quad (2-11)$$

$$E_{r2} = C \cos \theta_2. \quad (2-12)$$

The constant C is the same for each field component since the amplitude of the sources is the same and points on the boundary are equidistant from the current elements. From Fig. 2-7a we see that

$$\theta_1 + \theta_2 = 180^\circ. \quad (2-13)$$

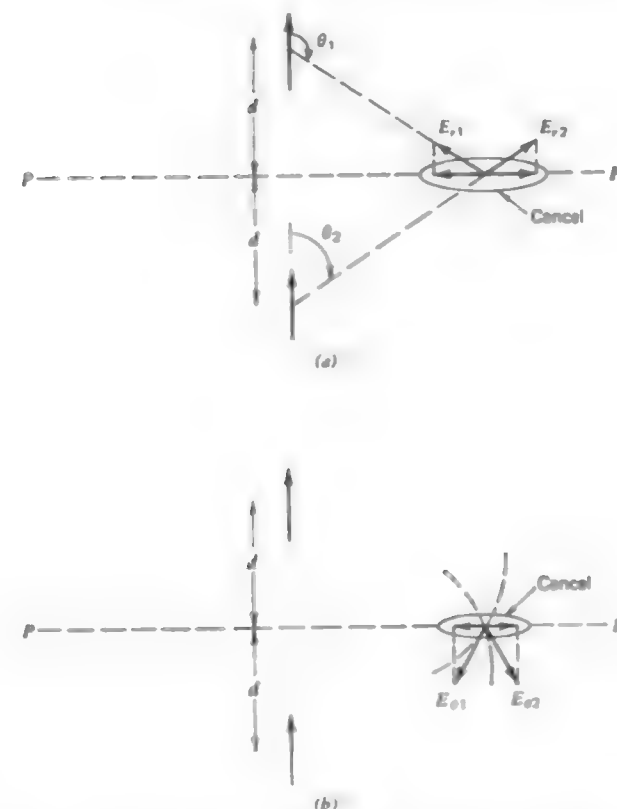


Figure 2-7 The ideal dipole and its image in a ground plane as in Fig. 2-6. The source and its image acting together give zero tangential electric field intensity along the plane PP' where the original perfect ground plane was located. (a) Radial components. (b) Theta components.

So

$$E_{r1} = C \cos(180^\circ - \theta_2) = -C \cos \theta_2. \quad (2-14)$$

Comparing this to (2-12) we see that

$$E_{r1} = -E_{r2} \text{ along boundary.} \quad (2-15)$$

Thus along the plane PP' the radial components are equal in magnitude and opposite in phase. E_{r2} is directed radially out from the image source since θ_2 is

less than 90° , and then $\cos \theta_2$ is positive. On the other hand, E_{r1} is radially inward toward the primary source since (2-14) is negative. Figure 2-7a illustrates this and shows that the projections of each along PP' will cancel. A similar line of reasoning for the θ -components leads to

$$E_{\theta 1} = D \sin \theta_1 = D \sin \theta_2 \quad (2-16)$$

$$E_{\theta 2} = D \sin \theta_2 \quad (2-17)$$

where θ is a constant and thus

$$E_{\theta 1} = E_{\theta 2} \text{ along boundary.} \quad (2-18)$$

Figure 2-7b demonstrates that the net projection of these θ -components along plane PP' is zero.

We have shown that the total tangential electric field intensity is zero along the image plane PP' for an ideal dipole perpendicular to the plane and its image acting together. Therefore, since the source configuration above the plane and the boundary conditions were not altered, the system of Fig. 2-6b is equivalent to the original problem of Fig. 2-6a. The systems are equivalent in the sense that the fields above the plane PP' are identical. The above derivation may be reversed by starting with the two sources of Fig. 2-6b and then introducing a perfect ground plane with its surface along plane PP' , thus arriving at Fig. 2-6a. The essential feature to remember is that the fields above a perfect ground plane from a primary source acting in the presence of the perfect ground plane are found by summing the contributions of the primary source and its image, each acting in free space.

An ideal dipole oriented parallel to a perfect ground plane has an image that again is equidistant below the image plane, but in this case the image is oppositely directed as shown in Fig. 2-8. The equivalent model of Fig. 2-8b, which gives the same fields above plane PP' as the physical model of Fig. 2-8a, may be proven by simple sketches similar to those of Fig. 2-7.

The image of a current element oriented in any direction with respect to a perfect ground plane may be found by decomposing it into perpendicular and parallel components, forming the images of the components, and constructing the image from these image components. An example is shown in Fig. 2-9. The image of an arbitrary current distribution is obtained in a similar fashion. The current is decomposed into perpendicular and parallel current elements whose images are readily found. The image current distribution is then the vector sum of these image current elements.

The perfectly-conducting infinite ground plane is, of course, an idealization. The perfectly conducting assumption is valid when good conductors such as aluminum or copper are used. The infinitely large assumption is more severe,

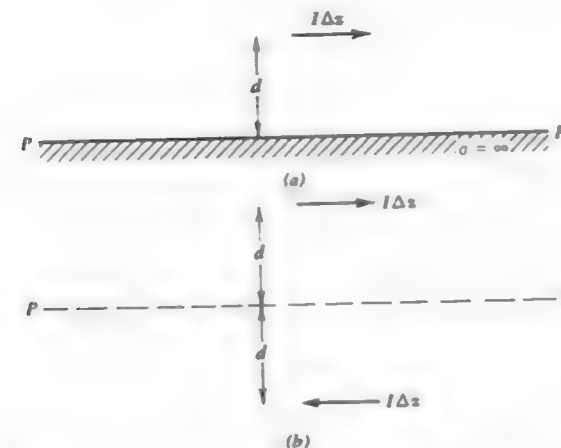


Figure 2-8 Ideal dipole above and parallel to a perfect ground plane. (a) Physical model. (b) Equivalent model using image theory

however. It is difficult to give specific rules as to when this assumption is good. Generally speaking, though, if the conducting plane extends beyond the source by several times the length of the source and if the source is not too far away from the conducting plane, this assumption is also valid.

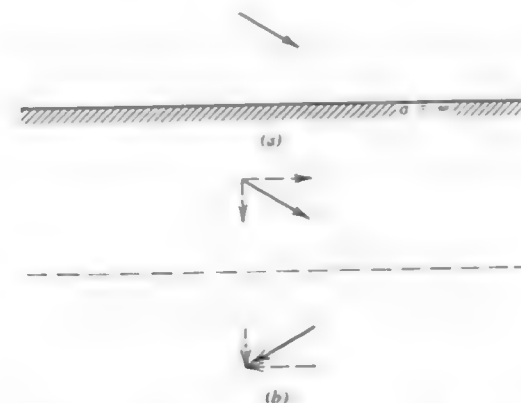


Figure 2-9 Ideal dipole above and obliquely oriented relative to a perfect ground plane. (a) Physical model. (b) Equivalent model using image theory.

2.3.2 Monopoles

The principles of image theory are illustrated in this section with several forms of the monopole antenna. A **monopole** is a dipole divided in half at its center feed point and fed against a ground plane. Three monopoles and their images in a perfect ground plane are shown in Fig. 2-10. High-frequency monopoles are often fed from coaxial cables behind the ground plane as shown in Fig. 2-11.

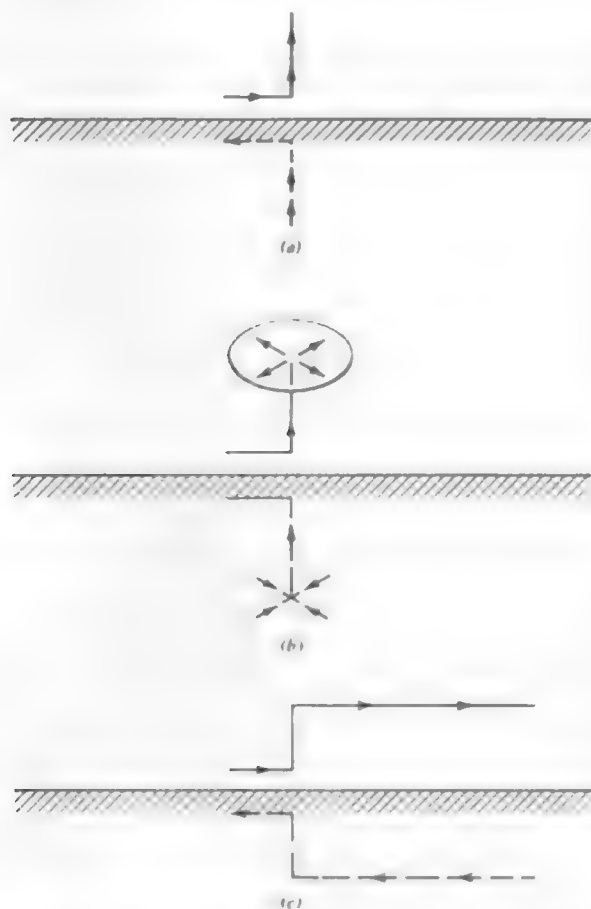


Figure 2-10 Monopole antennas over perfect ground planes with their images (dashed). (a) Monopole antenna. (b) Capacitor plate monopole. (c) Transmission line monopole.

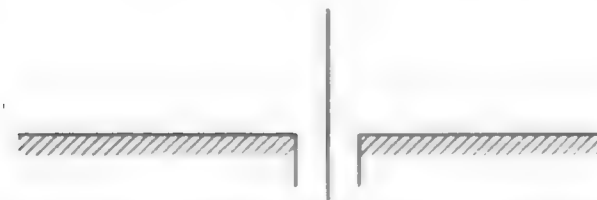


Figure 2-11 Monopole antenna fed from a coaxial cable.

The currents and charges on a monopole are the same as on the upper half of its dipole counterpart, but the terminal voltage is only half that of the dipole. The voltage is half because the gap width of the input terminals is half that of the dipole, and the same electric field over half the distance gives half the voltage. The input impedance for a monopole is therefore half that of its dipole counterpart, or

$$Z_{in, mono} = \frac{V_{in, mono}}{I_{in, mono}} = \frac{\frac{1}{2}V_{in, dipole}}{I_{in, dipole}} = \frac{1}{2}Z_{in, dipole}. \quad (2-19)$$

This is easily demonstrated for the radiation resistance. Since the fields only extend over a hemisphere the power radiated is only half that of a dipole with the same current. Therefore, the radiation resistance of a monopole is given by

$$R_{r, mono} = \frac{P_{rad, mono}}{\frac{1}{2}|I_{in, mono}|^2} = \frac{\frac{1}{2}P_{rad, dipole}}{\frac{1}{2}|I_{in, dipole}|^2} = \frac{1}{2}R_{r, dipole}. \quad (2-20)$$

For example, the radiation resistance of an ideal monopole is from (2-2)

$$R_{r, mono} = 160\pi^2 \left(\frac{h}{\lambda}\right)^2 \approx 1600 \left(\frac{h}{\lambda}\right)^2 \quad \text{for } h \ll \lambda \quad (2-21)$$

where h is the length of the monopole and $\Delta z = 2h$.

The radiation pattern of a monopole above a perfect ground plane, as in Fig. 2-11, is the same as that of a dipole similarly positioned in free space since the fields above the image plane are the same. Therefore, a monopole above a perfect ground plane radiates one-half the total power of a similar dipole in free space because the power is distributed in the same fashion but only over half as much space. Equivalently, the beam solid angle of a monopole above a perfect ground plane is one-half that of a similar dipole in free space. This leads to the fact that the directivity doubles for a monopole since

$$D_{mono} = \frac{4\pi}{\Omega_{A, mono}} = \frac{4\pi}{\frac{1}{2}\Omega_{A, dipole}} = 2D_{dipole}. \quad (2-22)$$

This can be shown in another way. If a dipole in free space has a maximum radiation intensity of U_m , a monopole of half the length above a perfect ground plane with the same current will have same value of U_m since the fields are the same. The total radiated power for the dipole is P_r , so the power radiated from the monopole is $\frac{1}{2}P_r$. The directivity from (1-142) for the two antennas is

$$D_{\text{dipole}} = \frac{U_m}{U_{\text{ave}}} = \frac{U_m}{P_r/4\pi} \quad (2-23)$$

and

$$D_{\text{mono}} = \frac{U_m}{\frac{1}{2}P_r/4\pi} = 2D_{\text{dipole}} \quad (2-24)$$

The directivity increase does not come from an increase in the radiation intensity (and, hence, field intensity) but rather from a decrease in average radiation intensity. This, in turn, comes about because only half the power radiated by a dipole is radiated by a monopole. The directivity of a short monopole, for example, is $2(1.5) = 3$.

At low frequencies a monopole that is a quarter wavelength long or less may be rather large physically. For example, in the standard AM broadcast band (say 1 MHz) the wavelength is 300 m, so a quarter-wave monopole would be 75 m tall. Such a large structure is usually not self-supporting, and guy wires are employed for support. Currents may exist in these guy wires in a downward direction tending to cancel the effect of the vertical element. Insulators are added to break up these currents, as in Fig. 2-12a.

If currents are allowed to continue from the monopole out onto the guys, a partial top-loading effect for towers shorter than a quarter wavelength may be achieved, thereby increasing the radiation resistance. See Fig. 2-12b. The loading is usually not enough to give uniform current on the vertical member. Secondly, the downward angle of the guys gives a slight canceling of the fields from the vertical current. For a comparable length monopole the umbrella loaded version has a lower radiation resistance than the capacitor-plate monopole. Experimental data are available in the literature for umbrella-loaded monopoles [3].



Figure 2-12 Monopoles with supporting guy wires. (a) Insulators added to reduce currents in guys. (b) Umbrella-loaded monopole.

2.4 SMALL LOOP ANTENNAS

A closed loop of current whose maximum dimension is less than about a tenth of a wavelength is called a **small loop antenna**. So again small is to be interpreted as meaning electrically small, or small compared to a wavelength. In this section we will use two methods to solve for the radiation properties of small loop antennas. First we will show that the small loop is the dual of an ideal dipole, and by observing the duality contained in Maxwell's equations we can use the results previously derived for the ideal dipole to write the fields of a small loop. Next we will derive the fields of a small loop directly and show that the results are the same as obtained using duality.

2.4.1 Duality

Frequently an antenna problem arises for which the structure is the dual of an antenna whose solution is known. If antenna structures are duals it is possible to write the fields for one antenna from the field expressions of the other by interchanging parameters using the principle of duality. Before examining the small loop we will discuss the general principle of duality as applied to antennas.

Dual antenna structures are similar to dual networks. For example, consider a simple network of a voltage source applied to a series connection of a resistor R and an inductor L as in Fig. 2-13a. The dual network of Fig. 2-13b is a current source $I (=) V$ applied to the parallel combination of conductance $G (=) R$ and capacitance $C (=) L$.¹ Since the networks are duals the solutions are duals. In this example the original series network can be described by the mesh equation

$$V = RI + j\omega LI. \quad (2-25)$$

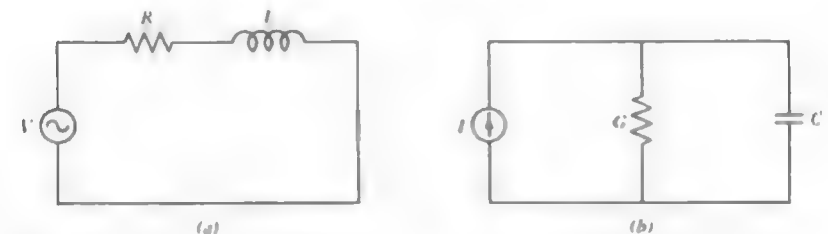


Figure 2-13 Dual networks: $I (=) V$, $G (=) R$, $C (=) L$. (a) Original network. (b) Dual network.

¹ In discussions of duality the symbol " $(=)$ " means replace the quantity on the left with the quantity on the right, much as the equal sign in a computer program statement.

The dual to this mesh equation is a node equation obtained by replacing V by I , R by G , and L by C . The node equation for the dual parallel network is then

$$I = GV + j\omega CV. \quad (2-26)$$

Returning to the antenna problem, suppose we have an electric current source with current density \mathbf{J}_1 and boundary conditions on materials present ($\epsilon_1, \mu_1, \sigma_1$). Maxwell's equations for this system from (1-16) and (1-17) are

$$\nabla \times \mathbf{E}_1 = -j\omega\mu_1\mathbf{H}_1 \quad (2-27)$$

$$\nabla \times \mathbf{H}_1 = j\omega\epsilon_1'\mathbf{E}_1 + \mathbf{J}_1 \quad (2-28)$$

where \mathbf{E}_1 and \mathbf{H}_1 are the fields generated by \mathbf{J}_1 with materials ($\epsilon_1, \mu_1, \sigma_1$) present. Now suppose a fictitious magnetic current source with magnetic current density \mathbf{M}_2 exists with materials ($\epsilon_2, \mu_2, \sigma_2$) present. Maxwell's equations for this system from (1-17) and (1-21) are

$$\nabla \times \mathbf{H}_2 = j\omega\epsilon_2'\mathbf{E}_2 \quad (2-29)$$

$$\nabla \times \mathbf{E}_2 = -j\omega\mu_2\mathbf{H}_2 - \mathbf{M}_2 \quad (2-30)$$

where \mathbf{E}_2 and \mathbf{H}_2 are the fields arising from \mathbf{M}_2 .

The electric and magnetic systems are duals if the procedure in Table 2-1 can be performed. This is easy to demonstrate. To see if (2-29) and (2-30) are the duals of (2-27) and (2-28) we substitute the quantities in left-hand column of Table 2-1 into (2-29) and (2-30) for the corresponding quantities of the right-hand column. This yields

$$\nabla \times \mathbf{E}_1 = j\omega\mu_1(-\mathbf{H}_1) \quad (2-31)$$

$$\nabla \times (-\mathbf{H}_1) = -j\omega\epsilon_1'\mathbf{E}_1 - \mathbf{J}_1. \quad (2-32)$$

These equations are (2-27) and (2-28). In other words, using the parameter substitutions of Table 2-1, the equations of the electric system, (2-27) and (2-28),

Table 2-1 Dual Radiating Systems.
Radiating system #1 with electric currents and system #2 with magnetic currents are duals if one can:

Replace the following in system #2	By the following in system #1
\mathbf{M}_2	\mathbf{J}_1
ϵ_2'	μ_1
μ_2	ϵ_1'
\mathbf{E}_2	$-\mathbf{H}_1$
\mathbf{H}_2	\mathbf{E}_1

are dual to the equations of the magnetic system, (2-29) and (2-30), just as (2-25) and (2-26) are dual equations. Since the equations of the systems are dual, the solutions will be also. Before illustrating this we will summarize the principle of duality.

If the sources of two systems are duals, that is,

$$\mathbf{M}_2 (=) \mathbf{J}_1 \quad (2-33)$$

and if the boundary conditions are also dual,² that is,

$$\mu_2 (=) \epsilon_1' \quad \epsilon_2' (=) \mu_1, \quad (2-34)$$

then the fields of system #2 can be found from the solution of system #1 by the substitutions

$$\mathbf{E}_2 (=) -\mathbf{H}_1 \quad \mathbf{H}_2 (=) \mathbf{E}_1 \quad (2-35)$$

in the field expressions for system #1 along with the substitutions in (2-34).

Now we will use duality to find the fields of a small current loop from a knowledge of the fields of an ideal electric dipole. A current loop may be represented as a fictitious (ideal) magnetic dipole with uniform magnetic current I^m and length Δz . The sources are duals as required by (2-33) if we let

$$I^m (=) I^e \quad (2-36)$$

where I^e is the current of an ideal electric dipole of length Δz . Since no materials are present there are no boundary conditions. The ideal electric dipole has field solutions of the form

$$\mathbf{E}_1 = E_{\theta 1}\hat{\theta} + E_{r1}\hat{r} \quad (2-37)$$

$$\mathbf{H}_1 = H_{\phi 1}\hat{\phi}. \quad (2-38)$$

The fields of the dual magnetic dipole are then found from (2-35) as

$$\mathbf{E}_2 (=) -\mathbf{H}_1 = -H_{\phi 1}\hat{\phi} \quad (2-39)$$

$$\mathbf{H}_2 (=) \mathbf{E}_1 = E_{\theta 1}\hat{\theta} + E_{r1}\hat{r} \quad (2-40)$$

if we make the substitutions

$$\mu_2 = \mu (=) \epsilon_1' = \epsilon \quad \text{and} \quad \epsilon_2' = \epsilon (=) \mu_1 = \mu \quad (2-41)$$

which follow from (2-34) and the fact that in both systems the surrounding medium is a homogeneous material of μ and ϵ . Note that β remains the same since replacing μ by ϵ and ϵ by μ in $\omega\sqrt{\mu\epsilon}$ yields $\omega\sqrt{\epsilon\mu}$. Now, using (2-36) and

² Note that $\epsilon_1' = \epsilon_1 - j(\sigma_1/\omega)$. If magnetic conductors of magnetic conductivity σ_2^m were assumed to exist in system #2, then μ_2 would become $\mu_2' = \mu_2 - j(\sigma_2^m/\omega)$ in the equations above. Thus ϵ_1' is replaced by μ_2' , or equivalently σ_1 is replaced by σ_2^m .

(2-41) in the ideal electric dipole field expressions of (1-69) and (1-70) together with (2-39) and (2-40) give

$$E_z = -\frac{I^m \Delta z}{4\pi} j\beta \left(1 + \frac{1}{j\beta r} \right) \frac{e^{-j\beta r}}{r} \sin \theta \hat{\phi} \quad (2-42)$$

$$H_z = \frac{I^m \Delta z}{4\pi} j\omega \epsilon \left[1 + \frac{1}{j\beta r} + \frac{1}{(j\beta r)^2} \right] \frac{e^{-j\beta r}}{r} \sin \theta \hat{\theta} + \frac{I^m \Delta z}{2\pi} j\omega \epsilon \left[\frac{1}{j\beta r} + \frac{1}{(j\beta r)^2} \right] \frac{e^{-j\beta r}}{r} \cos \theta \hat{r}. \quad (2-43)$$

These are the complete field expressions (valid in the near-field region) for a small loop of electric current. The far-field components are obtained by retaining only those terms that vary as r^{-1} , giving

$$E_z = -I^m \Delta z j\beta \frac{e^{-j\beta r}}{4\pi r} \sin \theta \hat{\phi} \quad (2-44)$$

$$H_z = I^m \Delta z j\omega \epsilon \frac{e^{-j\beta r}}{4\pi r} \sin \theta \hat{\theta} \quad (2-45)$$

These radiation fields as well as those of the ideal electric dipole are shown in Fig. 2-14. Both antennas have the same radiation pattern, $\sin \theta$. The magnetic field component H_ϕ of the ideal electric dipole is easily remembered by use of the right-hand rule. Place the thumb of your right hand along the current of the dipole and pointing in the direction of current flow. Your fingers will then curl in the direction of the magnetic field. This statement is implicit in Ampere's law of

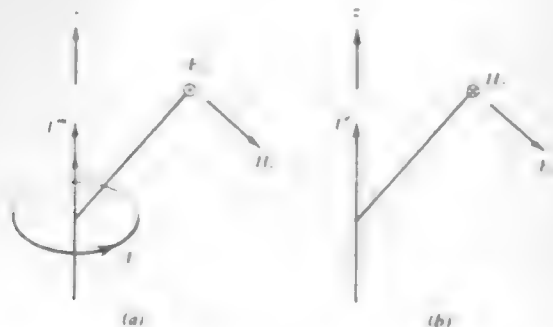


Figure 2-14 Radiation field components of ideal magnetic and electric dipoles. (a) Small current loop and equivalent magnetic dipole. (b) Ideal electric dipole

(2-28). A similar relationship holds for the magnetic dipole, except the left-hand rule is used and the field obtained is the electric field component $-E_\phi$. This follows from (2-30).

2.4.2 The Small Loop Antenna

Using duality we found the field expressions for a small loop of uniform current. However, these expressions contain the equivalent magnetic dipole current amplitude I^m . By solving the small loop problem directly we can establish the relationship between the current I in the loop and I^m . This can be accomplished by dealing only with the far-field region.

It turns out that the radiation fields of small loops are independent of the shape of the loop and depend only on the area of the loop. Therefore we will select a square loop as shown in Fig. 2-15 to simplify the mathematics. The current has constant amplitude I and zero phase around the loop. Each side of the square loop is a short uniform electric current segment which is modeled as an ideal dipole. The two sides parallel to the x -axis have a total vector potential which is x -directed and is given by

$$A_x = \frac{I}{4\pi} \left(\frac{e^{-j\beta R_1}}{R_1} - \frac{e^{-j\beta R_3}}{R_3} \right) \quad (2-46)$$

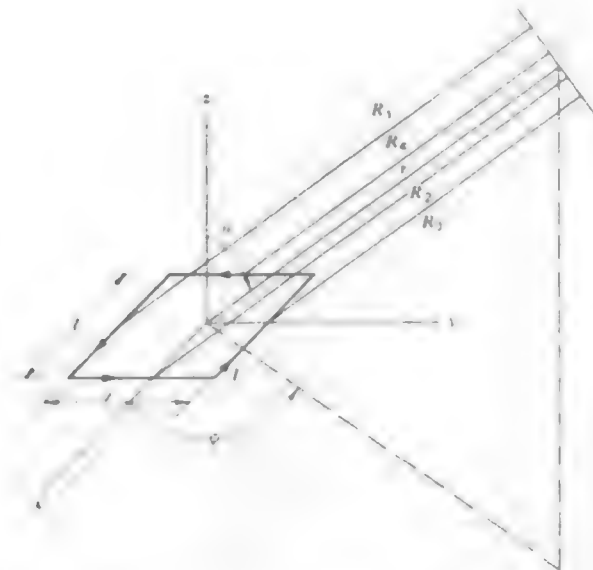


Figure 2-15 Geometry for calculating the radiation fields from a small square loop antenna.

which follows from (1-60). The minus sign in the second term arises because the current in side 3 is negative x -directed. Similarly for sides 2 and 4 we find

$$A_y = \frac{I}{4\pi} \left(\frac{e^{-j\beta R_2}}{R_2} - \frac{e^{-j\beta R_4}}{R_4} \right) \quad (2-47)$$

The far-field approximation is that the distances used for amplitude variations are nearly equal (i.e., $R_1 \approx R_2 \approx R_3 \approx R_4 \approx r$) and the phase differences are found from assuming parallel rays emanating from each side. By comparing the parallel path lengths we find from geometrical considerations that

$$R_1 = r + \frac{l}{2} \sin \theta \sin \phi, \quad R_2 = r - \frac{l}{2} \sin \theta \cos \phi \quad (2-48)$$

$$R_3 = r - \frac{l}{2} \sin \theta \sin \phi, \quad R_4 = r + \frac{l}{2} \sin \theta \cos \phi.$$

Substituting these into the exponents and r into the denominators of (2-46) and (2-47) we have

$$A_x = \frac{I e^{-j\beta r}}{4\pi r} (e^{-j\beta l/2 \sin \theta \sin \phi} - e^{+j\beta l/2 \sin \theta \sin \phi})$$

$$A_y = \frac{I e^{-j\beta r}}{4\pi r} (e^{+j\beta l/2 \sin \theta \cos \phi} - e^{-j\beta l/2 \sin \theta \cos \phi})$$

or

$$A_x = -2j \frac{I e^{-j\beta r}}{4\pi r} \sin \left(\frac{\beta l}{2} \sin \theta \sin \phi \right) \quad (2-49)$$

$$A_y = 2j \frac{I e^{-j\beta r}}{4\pi r} \sin \left(\frac{\beta l}{2} \sin \theta \cos \phi \right).$$

Since the loop is small compared to a wavelength, $\beta l = 2\pi l/\lambda$ is also small and the sine functions in (2-49) may be replaced by their arguments giving

$$A_x \approx -j \frac{I e^{-j\beta r}}{4\pi r} \beta l^2 \sin \theta \sin \phi \quad (2-50)$$

$$A_y \approx j \frac{I e^{-j\beta r}}{4\pi r} \beta l^2 \sin \theta \cos \phi.$$

Combining components to form the total vector potential gives

$$\mathbf{A} = A_x \hat{x} + A_y \hat{y} = j\beta l^2 \frac{I e^{-j\beta r}}{4\pi r} \sin \theta (-\sin \phi \hat{x} + \cos \phi \hat{y}). \quad (2-51)$$

The term in parentheses is the unit vector $\hat{\phi}$ in (A-6), so

$$\mathbf{A} = j\beta S \frac{I e^{-j\beta r}}{4\pi r} \sin \theta \hat{\phi} \quad (2-52)$$

where S is the area of the loop. All of \mathbf{A} is transverse to the direction of propagation, so the radiation electric field from (1-102) is $-j\omega\mu\mathbf{A}$ giving

$$\mathbf{E} = \eta\beta^2 S \frac{I e^{-j\beta r}}{4\pi r} \sin \theta \hat{\phi} \quad (2-53)$$

since $\omega\mu\beta = \omega^2\mu\sqrt{\mu\epsilon} = \sqrt{\mu/\epsilon}\omega^2\mu\epsilon = \eta\beta^2$. The radiation magnetic field is

$$\mathbf{H} = \frac{1}{\eta} \hat{r} \times \mathbf{E} = -\beta^2 S \frac{I e^{-j\beta r}}{4\pi r} \sin \theta \hat{\theta}. \quad (2-54)$$

Comparing (2-53) or (2-54) to the magnetic dipole radiation fields of (2-44) or (2-45) we find that

$$I^m \Delta z = j\omega\mu IS. \quad (2-55)$$

This completes the relationship between the small current loop and its equivalent magnetic dipole. The complete field expressions for a small loop of magnetic moment IS are found from (2-42) and (2-43) using (2-55). The fields depend only on the magnetic moment (current and area) and not the loop shape. And the radiation pattern for a small loop, independent of its shape, equals that of an ideal electric dipole. Thus if the small current loop is in the xy -plane its pattern is $\sin \theta$. The radiation fields from a large loop are derived in Section 5.7.

The impedance of a small loop antenna is quite different from its ideal dipole dual. While the ideal dipole is capacitive, the small loop is inductive. But first we will discuss the input resistance. The radiation resistance is found by calculating the power radiated using the small loop radiation fields with (1-125) which yields

$$P_r = 10I^2(\beta^2 S)^2. \quad (2-56)$$

The radiation resistance is then

$$R_r = \frac{2P_r}{I^2} = 20(\beta^2 S)^2 \approx 31,200 \left(\frac{S}{\lambda^2} \right)^2 \text{ ohms}. \quad (2-57)$$

This result provides a reasonable approximation to the radiation resistance of an actual small loop antenna for a loop perimeter less than about three-tenths of a wavelength.

The radiation resistance of a loop antenna may be increased significantly by using several turns. The magnetic moment of an n turn loop is nIS where S is the area of a single turn. The radiation resistance is then

$$R_r = 20(\beta^2 nS)^2 \approx 31,200 \left(n \frac{S}{\lambda^2} \right)^2 \text{ ohms.} \quad (2-58)$$

The radiation resistance thus goes up as n^2 . Another way to enhance the radiation resistance is to wind the loop turns around a ferrite core. For a ferrite core of effective relative permeability μ_{eff} , rays from different parts of the loop, as in Fig. 2-15, encounter a phase constant of $\beta = \omega\sqrt{\mu\epsilon} = \omega\sqrt{\mu_0\epsilon_0}\sqrt{\mu_{eff}} = (2\pi/\lambda)\sqrt{\mu_{eff}}$ where λ is the free-space wavelength. The relative effective permeability³ depends on the core size and shape and is usually less than the relative permeability of the core material. The radiation resistance of a coil of n turns wound on a ferrite core is then

$$R_r \approx 31,200 \left(n\mu_{eff} \frac{S}{\lambda^2} \right)^2 \text{ ohms.} \quad (2-59)$$

A ferrite core multiturn loop antenna is often referred to as a **loop-stick antenna**. It is a commonly used low-frequency receiving antenna. For example, it is used with most AM broadcast receivers.

Small loop antennas also have considerable ohmic resistance. For a rectangular loop of wire ℓ_1 by ℓ_2 the ohmic resistance is given approximately by

$$R_{ohmic} = \frac{2\ell_1\ell_2}{\pi d^2} R_s \left[\frac{1}{[(\ell_1/d)^2 - 1]^{1/2}} + \frac{1}{[(\ell_2/d)^2 - 1]^{1/2}} \right] \quad (2-60)$$

where d is the wire diameter and R_s is the surface resistance of (1-185). If ℓ_1 and ℓ_2 are much larger than d (i.e., the wire is thin) then (2-60) reduces to

$$R_{ohmic} = \frac{2(\ell_1 + \ell_2)}{\pi d} R_s. \quad (2-61)$$

This formula may be generalized to loops of arbitrary shape as follows

$$R_{ohmic} = \frac{\ell}{w} R_s \quad (2-62)$$

where ℓ is the mean length of the wire loop and w is the perimeter of the wire cross section. For a circular loop this becomes

$$R_{ohmic} = \frac{2\pi b}{\pi d} R_s = \frac{2b}{d} R_s \quad (\text{circular loop}) \quad (2-63)$$

where b is the mean loop radius and d is the wire diameter.

³ See [4] for a discussion of relative effective permeability.

As mentioned previously, the small loop antenna is inherently inductive. The inductance of a small ℓ_1 by ℓ_2 rectangular loop is given by

$$L = \frac{\mu}{\pi} \left(\ell_2 \cosh^{-1} \frac{\ell_1}{d} + \ell_1 \cosh^{-1} \frac{\ell_2}{d} \right) \quad (2-64)$$

where d is the wire diameter. For a small circular loop of radius b the inductance is [5]

$$L = b\mu \left[\ln \left(\frac{16b}{d} \right) - 1.75 \right] \quad (\text{circular loop}) \quad (2-65)$$

for $d \ll b$.

Example 2-1. A Small Circular Loop Antenna

To illustrate the impedance calculations for small loop antennas, consider a circular loop with a mean loop circumference of 0.2λ and a wire radius of 0.001λ . Then $b = 0.1\lambda/\pi$ and $d = 0.002\lambda$ in (2-57) yields the radiation resistance as

$$R_r = 31,200 \left(\frac{\pi b^2}{\lambda^2} \right)^2 = 31,200 \left(\frac{0.01}{\pi} \right)^2 = 0.316 \text{ ohm.} \quad (2-66)$$

The reactance from (2-65) is

$$X_{in} = \omega L = 2\pi \frac{c}{\lambda} b\mu \left[\ln \left(\frac{16b}{d} \right) - 1.75 \right] \quad (2-67)$$

where c is the velocity of light. For an air-filled loop $\mu = \mu_0$ and then

$$X_{in} = 2\pi \frac{3 \times 10^8 \cdot 0.1\lambda}{\lambda} \frac{4\pi \times 10^{-7}}{\pi} \left[\ln \frac{1.6}{0.002\pi} - 1.75 \right] = 285.8 \text{ ohms.} \quad (2-68)$$

To determine the ohmic resistance a frequency must be specified; suppose it is 1 MHz. Further suppose the wire is copper, and then $\mu = \mu_0$ and $\sigma = 5.7 \times 10^7$ mhos/m in (1-185) gives

$$R_s = \sqrt{\frac{\mu_0 2\pi f}{2\sigma}} = \sqrt{\frac{4\pi \times 10^{-7} \cdot 2\pi \times 10^6}{2 \cdot 5.7 \times 10^7}} = 2.63 \times 10^{-4} \text{ ohm.} \quad (2-69)$$

And from (2-63)

$$R_{ohmic} = \frac{2b}{d} R_s = \frac{0.2}{0.002\pi} 2.63 \times 10^{-4} = 8.38 \times 10^{-3} \text{ ohm.} \quad (2-70)$$

Adding this to (2-66) gives the total input resistance

$$R_{in} = R_r + R_{ohmic} = 0.324 \text{ ohm.} \quad (2-71)$$

The input impedance is thus

$$Z_{in} = R_{in} + jX_{in} = 0.324 + j285.8 \text{ ohms.} \quad (2-72)$$

The radiation efficiency of this loop is

$$\epsilon = \frac{R_r}{R_{in}} = \frac{0.316}{0.324} = 97.5\% \quad (2-73)$$

2.5 SOME PRACTICAL CONSIDERATIONS

In this chapter we have examined several simple but basic radiators. Some of these were electrically small radiators while one (the half-wave dipole) was of resonant size. We say more about resonant antennas in Chapter 5 and 6 but not much more will be said about electrically small antennas. Thus, it is appropriate at this point to consider the practical limitations of electrically small antennas.

Recall that an electrically small antenna is one that is smaller than a radian-sphere. It is characterized by a radiation resistance that is much less than its self-reactance and by a far-field pattern that is independent of the antenna size. An electrically small antenna is usually a simple electric or magnetic dipole. The electric dipole is physically realizable, while the magnetic dipole is a flux element simulated by a current loop. While the radiation pattern and the directivity of a small antenna are independent of size or frequency, the radiation resistance and especially the self-reactance are not. This makes it difficult to transfer power from the antenna to a load or from a generator to the antenna as the frequency changes. An antenna with this characteristic is said to have a high Q . We can define antenna Q as 2π times the peak energy stored-average power radiated, but conceptually a high Q means that the input impedance is very sensitive to small changes in frequency.

The Q of an ideal (lossless) antenna is shown in Fig. 2-16 versus βa , where a is the radius of a sphere that would enclose the antenna [2]. While the Q of a practical electrically small antenna may be less than this, the curve does serve to show rather clearly what happens to the Q as the antenna size diminishes. The increasing Q with diminishing size in turn implies a fundamental limitation on the usable bandwidth of an electrically small antenna. The concept of bandwidth will be considered more formally in Chapter 5, but for our purposes here let it simply be the frequency range over which the antenna is usable without retuning to a resonant condition (i.e., tuning out the self-reactance). Thus, the higher the Q , the smaller the bandwidth. To reduce the Q , damping (resistance) can be added to the antenna at the expense of efficiency. High Q and small bandwidth are characteristic limitations of electrically small antennas [6, 7].

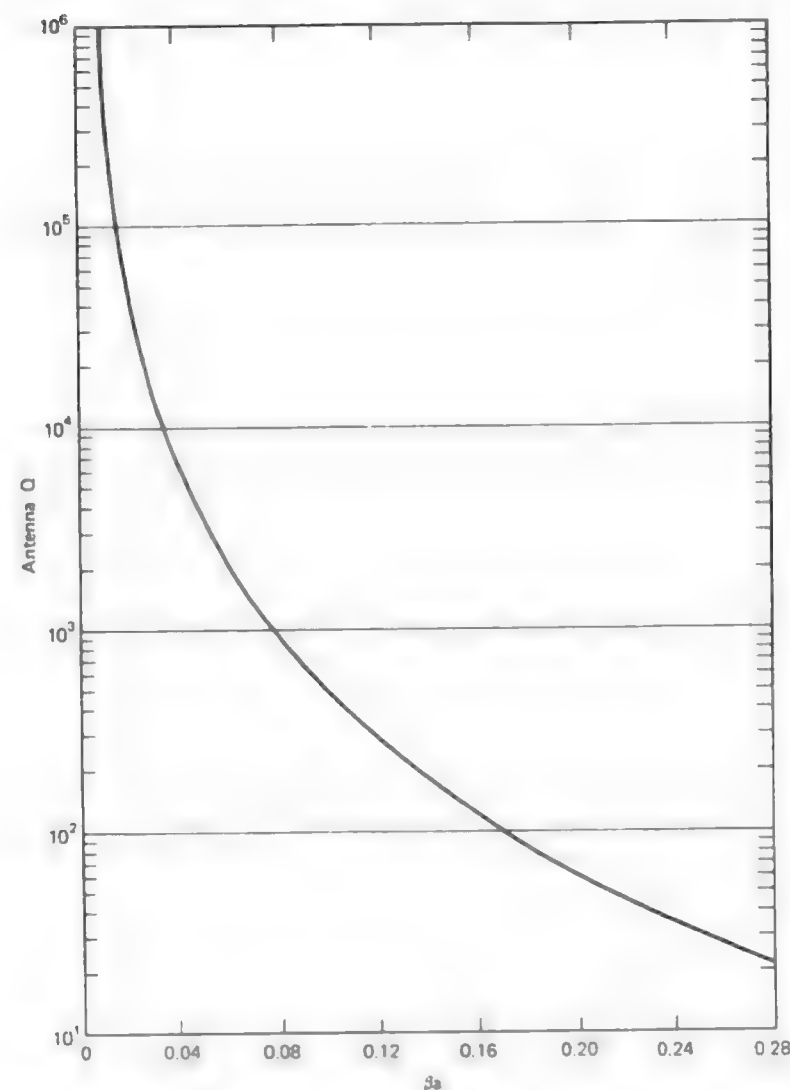


Figure 2-16 The Q of an ideal (lossless) antenna as a function of βa , where a is the radius of a sphere enclosing the antenna.

REFERENCES

1. H. A. Wheeler, "The radiansphere around a small antenna," *Proc. of IRE*, vol. 47, pp. 1325-1331, Aug. 1959.
2. E. H. Newman, P. Bohley, and C. H. Walter, "Two methods for the measurement of antenna efficiency," *IEEE Transactions on Antennas and Propagation*, vol. AP-23, pp. 457-461, July 1975.
3. A. F. Gangi, S. Sensiper, and G. R. Dunn, "The characteristics of electrically short, umbrella top-loaded antennas," *IEEE Transactions on Antennas and Propagation*, vol. AP-13, pp. 864-871, Nov. 1965. Also see W. Weeks, *Antenna Engineering*, McGraw-Hill, New York, 1968; pp. 44-46.
4. W. J. Polydoroff, *High-Frequency Magnetic Materials*, Wiley, New York, 1960; Chapter 5.
5. R. Plonsey and R. E. Collin, *Principles and Applications of Electromagnetic Fields*, McGraw-Hill, New York, 1961, p. 280.
6. Harold A. Wheeler, "Fundamental limitations of small antennas," *Proc. IRE*, vol. 35, pp. 1479-1484, Dec. 1947.
7. L. J. Chu, "Physical limitations of omni-directional antennas," *J. Appl. Phys.*, vol. 19, pp. 1163-1175, Dec. 1948.

PROBLEMS

2.1-1 Use the oscillating charge model for an ideal dipole as shown in Fig. 2-2b to derive the electric field expressions of (1-70). *Hints:* The far-field scalar potential function for this problem is

$$\Phi = \frac{q}{4\pi\epsilon_0} \left| \frac{e^{-j\beta r - (l\Delta z/2)\cos\theta}}{r - (\Delta z/2)\cos\theta} - \frac{e^{-j\beta r + (l\Delta z/2)\cos\theta}}{r + (\Delta z/2)\cos\theta} \right|$$

where the parallel ray approximation was used and the $e^{j\omega t}$ time dependence was suppressed. Use $r \gg \Delta z$, $z \gg \Delta z$, and $l = j\omega q$ to show that

$$\Phi \approx \frac{e^{-j\beta r}}{4\pi\epsilon_0} \frac{l \Delta z}{j\omega r^2} (1 + j\beta r) \cos\theta.$$

Then make use of (1-39)

2.1-2 The current density on an actual short dipole antenna of Fig. 2-1 can be written as

$$\mathbf{J} = \hat{\mathbf{z}} J_0 \sin \left| \beta \left(\frac{\Delta z}{2} - |z| \right) \right|$$

Find an expression for the associated charge density. The relative variation of your answer is indicated in Fig. 2-1b.

2.1-3 Show that the capacitance of the capacitor of the capacitor-plate antenna of Fig. 2-3 is given by

$$C = \frac{\pi(\Delta r)^2 \epsilon_0}{\Delta z}$$

Assume that capacitance is entirely due to the end plates and neglect fringing.

2.1-4 (a) Using the capacitance formula in Prob. 2.1-3 calculate the capacitive reactance of a capacitor-plate dipole for which $\Delta r = 0.01\lambda$ and $\Delta z = 0.02\lambda$.

(b) Calculate the radiation resistance of this antenna.

2.2-1 Sketch the current distribution on a half-wave dipole for various instants during the cycle of the current oscillation.

2.2-2 Show that the pattern factor for half-wave dipole in (2-9) is normalized to unity at $\theta = \pi/2$.

2.2-3 Calculate and plot the radiation pattern $F(\theta)$ for a half-wave dipole in (2-10) for $0 \leq \theta \leq 180^\circ$. Plot in linear, polar form as shown in Fig. 2-5b.

2.2-4 (a) Show that the ohmic resistance of a half-wave dipole from (1-190) is given by

$$R_{\text{ohmic}} = \frac{R_s \lambda}{2\pi a^4}$$

(b) Compare this to the result one would obtain if the current were assumed to be uniform on the half-wave dipole.

2.2-5 Use the results of Prob. 2.2-4(a) to calculate the radiation efficiency of a half-wave dipole at 100 MHz if it is made of aluminum wire 6.35 mm (0.25 in.) in diameter. Assume the radiation resistance to be 70 ohms.

2.3-1 Show that the image theory model of Fig. 2-8b for an ideal dipole parallel to a perfect ground plane yields zero tangential electric field along plane PP' .

2.3-2 If a thin monopole as shown in Fig. 2-11 is a quarter wavelength long:

(a) Rough sketch the radiation pattern in polar form as a function of θ , if the monopole is along the z -axis.

(b) What is the directivity?

(c) What is the input impedance?

2.4-1 Use (1-93) to derive the far-field distance expressions (2-48) for the small square loop.

2.4-2 Verify that the power radiated from a small loop is given by (2-56)

2.4-3 Show that (2-61) follows from (2-60)

2.4-4 Compute the radiation efficiency of a small single turn loop antenna at 1 MHz if it is made of No. 20 AWG copper wire and has a loop radius of 0.2 m.

2.4-5 Compute the inductance of the loop antenna in Prob. 2.4-4.

2.4-6 A single turn circular loop 15 cm in radius is made of 3-mm-diameter copper wire. Calculate the radiation resistance, ohmic resistance, input impedance, and radiation efficiency at 1 MHz.

2.4-7 A ferrite core loop antenna is 20 cm long and 1 cm in diameter. It has 22 turns of wire and an effective relative permeability of 38. Compute its radiation resistance at a frequency of 1 MHz.

2.4-8 A single turn square loop antenna that is 1 m on a side operates at 30 MHz. The wire is aluminum with a diameter of 2 cm. Compute (a) the radiation resistance, (b) the input reactance, and (c) the radiation efficiency.

3

ARRAYS

Several antennas can be arranged in space and interconnected to produce a directional radiation pattern. Such a configuration of multiple radiating elements is referred to as an **array antenna**, or simply, an **array**. The introduction of shortwave radio equipment in the 1920s made possible the use of reasonably sized antenna arrays, thereby providing a convenient way to achieve a directive radiation pattern for radio communications. During World War II UHF and microwave array antennas were introduced for use in radar systems. Today arrays at microwave frequencies and above are used extensively in satellite communication systems.

Many small antennas can be used in an array to obtain a level of performance similar to that of a single large antenna. The mechanical problems associated with a single large antenna are traded for the electrical problems of feeding several small antennas. With the advancements in solid state technology, the feed network required for array excitation is of improved quality and reduced cost. Arrays offer the unique capability of electronic scanning of the main beam. By changing the phase of the exciting currents in each element antenna of the array, the radiation pattern can be scanned through space. The array is then called a **phased array**. Phased arrays have many applications, particularly in radar.

Arrays are found in many geometrical configurations. The most elementary is that of a **linear array** in which the array element centers lie along a straight line. The elements may be equally or unequally spaced. When the array element centers are located in a plane it is said to be a **planar array**. Examples of planar

arrays are circular and rectangular arrays in which the element centers are disposed on a circle, or are contained within a rectangular area, respectively. A class of arrays which is just emerging is that of **conformal arrays**. In this application the array element locations must conform to some nonplanar surface such as found on an aircraft or missile.

The radiation pattern of an array is determined by the type of individual elements used, their orientations, their positions in space, and the amplitude and phase of the currents feeding them. To simplify our discussion of arrays we will begin by letting each element of the array be an isotropic point source. The resulting radiation pattern is called the **array factor**. In this chapter the array factors for several simple arrays will be examined before considering general uniformly excited linear arrays. The principle of pattern multiplication will then be introduced in Section 3.3 for the purpose of including the effect of the array element type. Array directivity is discussed in Section 3.4. By controlling the current amplitudes in an array, the pattern can be shaped for special applications. The relationship between the radiation pattern of an array and its element current amplitudes is illustrated by several linear array examples in Section 3.5. The effects of mutual coupling between elements of a real array on impedance are detailed in Section 3.6. The scanning of the array pattern by element phase control is discussed in Section 3.7. The chapter is closed with a perspective discussion in Section 3.8.

3.1 THE ARRAY FACTOR FOR LINEAR ARRAYS

A typical linear array composed of similar element antennas is shown in Fig. 3-1. The output of each array element may be controlled in amplitude and phase as indicated by the phase shifters and attenuators. In addition to the amplitude and phase control imposed on each element represented by I_n , there is relative phase shift between the waves arriving at the antenna elements due to their positions in space and the angle of arrival of the wave. Furthermore, the pattern of each element leads to a response that varies with the arrival angle of the incoming plane wave. If it is the same for each element, the principle of pattern multiplication allows us to consider it as one multiplicative factor in the total pattern. This is discussed in detail in Section 3.3. The remaining angular dependence of the pattern is called the array factor, and it is determined solely by the element positions and their amplitudes and phases represented by I_n . The array of Fig. 3-1 is shown as a receiving array; however, the receiving pattern is the same as the transmitting pattern by reciprocity. In our discussions of arrays either the receiving or transmitting viewpoint will be used depending upon which is more convenient.

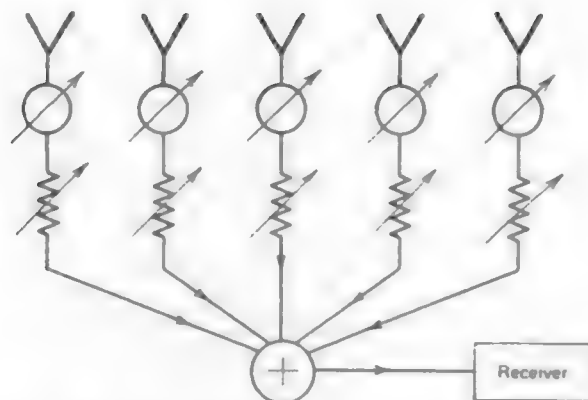


Figure 3-1 A typical linear array. The symbols ϕ and γ indicate variable phase shifters and attenuators. The output currents are summed in a summing device before entering the receiver.

Since the pattern of an array obtained by neglecting the patterns of the individual elements of the array is the array factor, if we replace each element of the array (without disturbing the relative currents or the positions) with an isotropic point source, the resulting pattern is the array factor. An isotropic point source is a hypothetical antenna occupying just a point in space and radiating uniformly in all directions. It is referred to frequently as a point source. The radiation fields of a point source at the origin of a spherical coordinate system are proportional to

$$I_0 \frac{e^{-jkr}}{4\pi r} \quad (3-1)$$

where I_0 is the current of the point source. This can be seen by examining the radiation field expressions, (1-71) and (1-72), for an ideal dipole and dropping the angular dependence. The far-field pattern is obtained from the angular dependence (i.e., at constant r) of the radiation fields, thus the pattern of a point source, from (3-1), is constant and is given by

$$AF = I_0 \quad (3-2)$$

where AF is the array factor for this "array" of only one point source. Since I_0 is constant the array factor in (3-2) could have been written as unity, but as elements are added to the array, each with a different current, it is necessary to account for their relative field strengths as determined by their element currents.

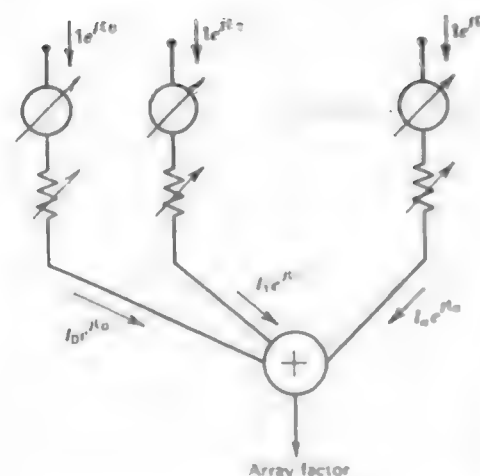


Figure 3-2 Equivalent configuration of the array in Fig. 3-1 for determining the array factor. The elements of the array are replaced by isotropic point sources

The array factor for the array of Fig. 3-1 is found from the array of Fig. 3-2 which has point sources for array elements in place of the actual elements. The array factor for this receiving array is then the sum of the point source receiving antenna responses $\{e^{j\xi_0}, e^{j\xi_1}, \dots\}$ weighted by the amplitude and phase shift $\{I_0, I_1, \dots\}$ introduced in the transmission line connected to each element. The array factor of the array shown in Fig. 3-2 is thus

$$AF = I_0 e^{j\xi_0} + I_1 e^{j\xi_1} + I_2 e^{j\xi_2} + \dots \quad (3-3)$$

where ξ_0, ξ_1, \dots are the phases of an incoming plane wave at the element locations designated 0, 1, Usually these phases are relative to the coordinate origin, that is, the phase of the wave arriving at n th element leads the phase of the wave arriving at the origin by ξ_n .

Before going any further with general expressions such as (3-3), some specific examples are in order to get a feel for what pattern effects can be achieved through the use of arrays. These examples will be kept simple so that a rough pattern can be obtained by inspection.

Example 3-1. Two Isotropic Point Sources with Identical Amplitude and Phase Currents, and Spaced One-Half Wavelength Apart (Fig. 3-3)

Figure 3-3a shows how the pattern of this example may be approximated by inspection. It is easier in the inspection method to consider the array to be transmitting. At points (in the far field) along the perpendicular bisector of the line joining the point sources (x -axis), path lengths from each point source are equal. Since the amplitudes and phases of each source are also equal, the waves arrive in phase and equal in amplitude in the far field

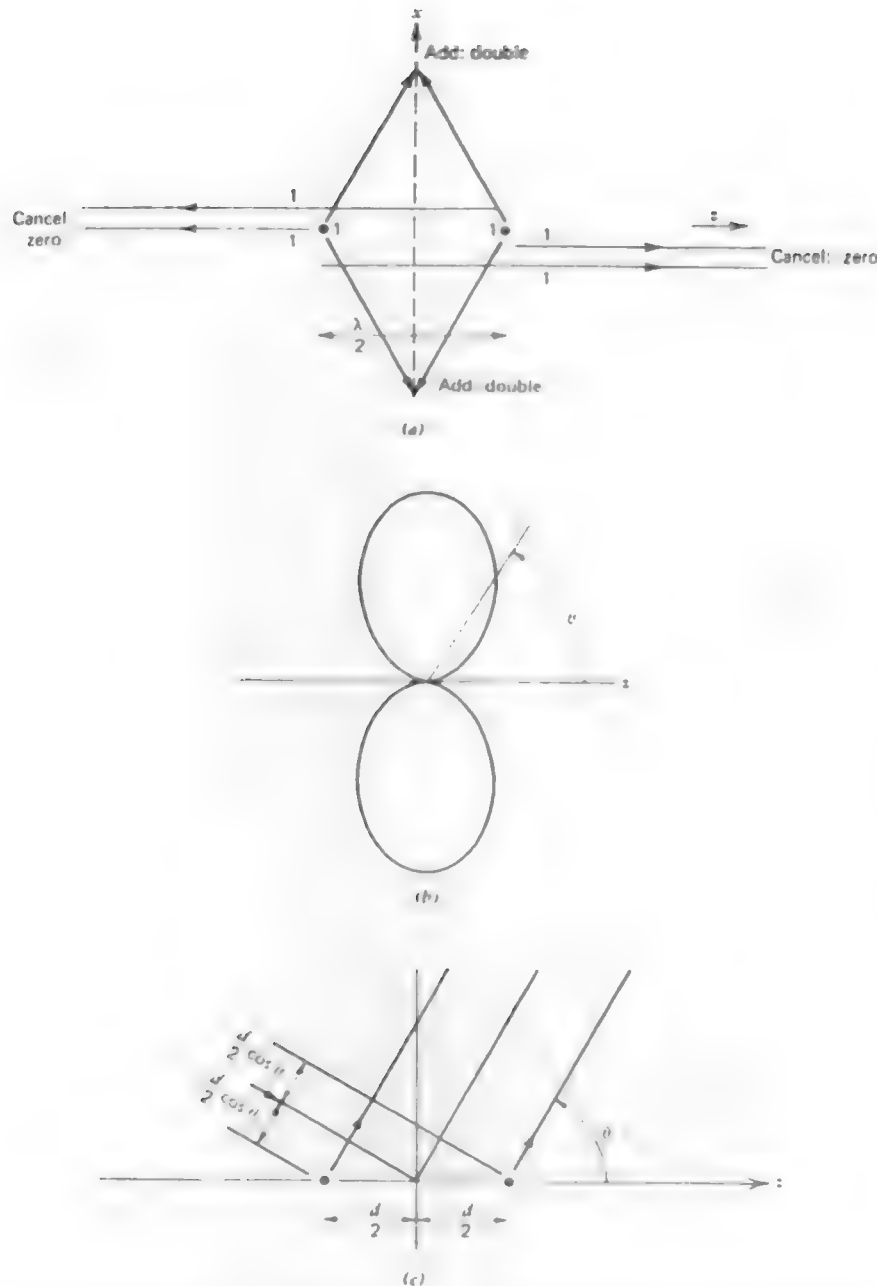


Figure 3-3 Two isotropic point sources with identical amplitude and phase currents, and spaced one-half wavelength apart (Example 3-1). (a) Inspection method. (b) Polar plot of the array factor $f(\theta) = \cos[(\pi/2) \cos \theta]$. (c) Calculation method

along the x -axis, and the total field is double that for one source. The situation is different along the axis of the array (z -axis). Looking to the right along the $+z$ -axis, waves coming from the left source must travel one-half wavelength before reaching the source on the right. This amounts to a 180° phase lag. The waves then continue traveling to the right along the $+z$ -axis and maintain this same phase relationship on out to the far field. Thus, in the far field, waves from the two sources traveling in $+z$ -direction arrive 180° out-of-phase (due to the one-half wavelength separation of the sources) and are equal in amplitude (since the sources are). Therefore, there is perfect cancellation and the total field is zero. The same reasoning can be used to see the effect in the $-z$ -direction. The total pattern has a relative value of two in the $\pm x$ -directions, zero in the $\pm z$ -directions, and a smooth variation in between (because the phase difference between waves from two sources changes smoothly from 0 to 180° as the observer moves from the broadside direction to the axial direction along a constant radius from the array center). This pattern is sketched in Fig. 3-3b. The pattern in three dimensions can be imagined by holding the z -axis in your finger tips and spinning the pattern shown to sweep out the total pattern.

We can also calculate the array factor exactly. Using phases corresponding to the path length differences shown in Fig. 3-3c in (3-3) the array factor is

$$AF = 1e^{-j\beta d/2 \cos \theta} + 1e^{j\beta d/2 \cos \theta} = 2 \cos\left(\beta \frac{d}{2} \cos \theta\right). \quad (3-4)$$

The distance between the elements is $d = \lambda/2$, so $\beta d/2 = \pi/2$ and (3-4) becomes

$$AF = 2 \cos\left(\frac{\pi}{2} \cos \theta\right). \quad (3-5)$$

Normalizing the array factor for a maximum value of unity gives

$$f(\theta) = \cos\left(\frac{\pi}{2} \cos \theta\right). \quad (3-6)$$

This is maximum for $\theta = \pi/2$ since $\cos[(\pi/2) \cdot 0] = 1$ and zero for $\theta = 0$ since $\cos[(\pi/2) \cdot 1] = 0$. This result agrees with the inspection method that leads to Fig. 3-3b.

Example 3-2. Two Isotropic Point Sources with Identical Amplitudes and Opposite Phases, and Spaced One-Half Wavelength Apart (Fig. 3-4)

If we consider the array to be transmitting the gross features of the pattern may be determined by inspection as shown in Fig. 3-4a. The path lengths from each point source to a point on the x -axis are the same. But the left source is 180° out-of-phase with respect to the right source, thus, waves arriving at points on the x -axis are 180° out-of-phase and equal in amplitude giving a zero field. Along the z -axis (in both directions) the 180° phase difference in the currents is compensated for by the half-wavelength path difference between waves from the two sources. For example, in the $+z$ -direction the waves from the left source arrive at the location of the right source lagging the phase of waves from the right source by 360° (180° from distance traveled and 180° from excitation lag). This is an in-phase condition and thus the waves add in the far field giving a relative maximum.

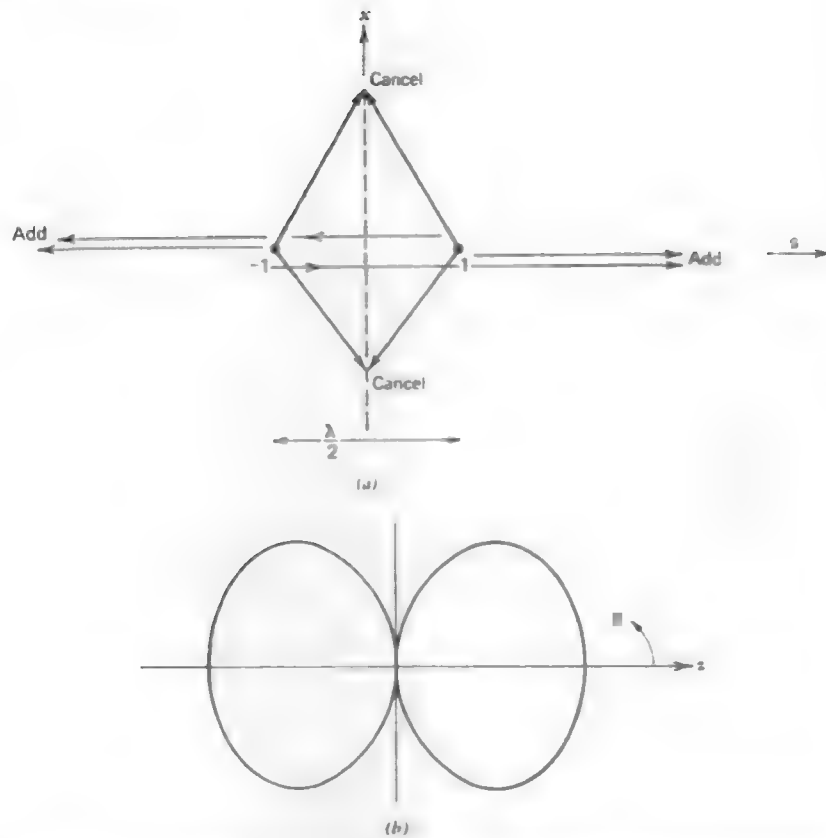


Figure 3-4 Two isotropic point sources with identical amplitudes and opposite phases, and spaced one-half wavelength apart (Example 3-2). (a) Inspection method. (b) Polar plot of the array factor magnitude $|f(\theta)| = |\sin[(\pi/2) \cos \theta]|$.

From these few pattern values the entire pattern can be sketched yielding a plot similar to that of Fig. 3-4b.

We calculate the array factor exactly using (3-3) and Fig. 3-3c as

$$AF = -1e^{-j\beta d/2 \cos \theta} + 1e^{j\beta d/2 \cos \theta} = 2j \sin\left(\beta \frac{d}{2} \cos \theta\right) \quad (3-7)$$

Using $d = \lambda/2$ and normalizing we have

$$f(\theta) = \sin\left(\frac{\pi}{2} \cos \theta\right) \quad (3-8)$$

Plotting this pattern we obtain the same result as with the inspection method (see Fig. 3-4b).

Example 3-3. Two Isotropic Point Sources with Identical Amplitudes and 90° Out-of-Phase, and Spaced a Quarter-Wavelength Apart (Fig. 3-5)

Waves leaving the left source of the transmitting array in Fig. 3-5 and traveling in the $+z$ -direction arrive at the right source delayed by 90° due to the quarter-wavelength path. But the excitation of the right source lags the left source by 90° so waves in the $+z$ -direction are in step and add in the far field. For waves leaving the right-hand source and traveling in the $-z$ -direction, the phase at the location of the left source is 180° lagging with respect to the wave from the left source (90° from path difference and 90° from excitation). See Fig. 3-5b. At angles between $\theta = 0^\circ$ ($+z$ -direction) and 180° ($-z$ -direction) there is a smooth pattern variation from two (perfect addition) to zero (perfect cancellation). This pattern is shown in Fig. 3-5c and is the so-called *cardioid*

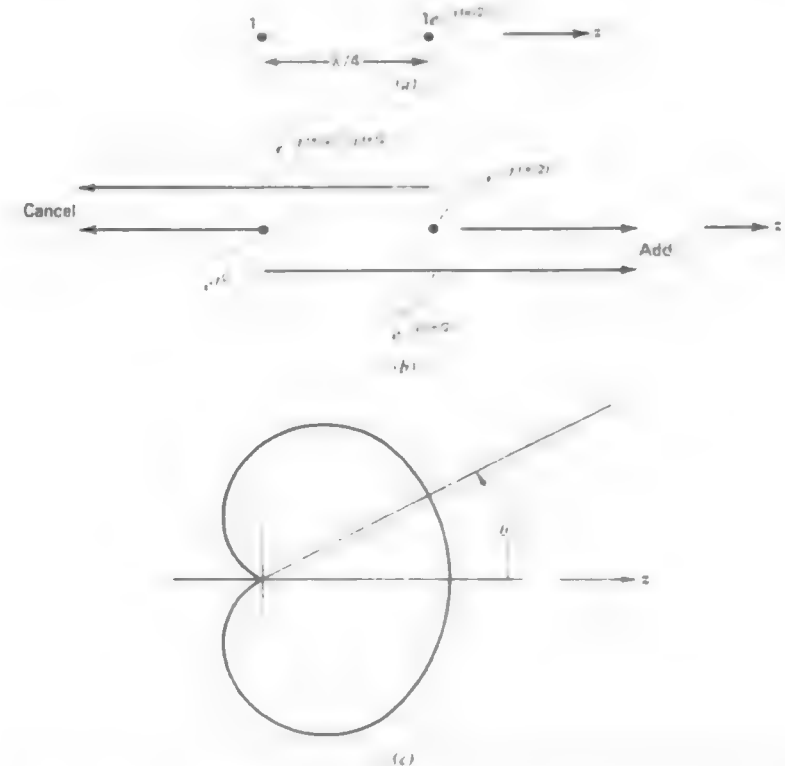


Figure 3-5 Two isotropic point sources with identical amplitudes and the right element lagging the left by 90° , and spaced a quarter-wavelength apart (Example 3-3). (a) Array configuration. (b) Inspection method. (c) Polar plot of the array factor $f(\theta) = \cos[(\pi/4)(\cos \theta - 1)]$. This pattern shape is called a *cardioid* pattern.

pattern. It is used frequently in the area of acoustics for microphone patterns. The response is strong in the direction of the microphone input and weak in the direction where the speakers are aimed to reduce feedback.

Using these excitations in (3-3) and Fig. 3-3c we can calculate the array factor expression as follows

$$\begin{aligned} AF &= 1e^{-j\beta d/2 \cos \theta} + 1e^{-j(\pi/2)}e^{j\beta d/2 \cos \theta} \\ &= e^{-j\pi/4} [e^{-j\beta d/2 \cos \theta - \pi/4} + e^{j\beta d/2 \cos \theta - \pi/4}] \\ &= e^{-j\pi/4} 2 \cos \left(\frac{\beta d}{2} \cos \theta - \frac{\pi}{4} \right). \end{aligned} \quad (3-9)$$

Substituting $d = \lambda/4$ and normalizing gives

$$f(\theta) = \cos \left[\frac{\pi}{4} (\cos \theta - 1) \right]. \quad (3-10)$$

This function has a maximum value of unity for $\theta = 0^\circ$, $1/\sqrt{2}$ for $\theta = 90^\circ$, and zero for $\theta = 180^\circ$. Again, this agrees with the pattern of Fig. 3-5c obtained by inspection.

Example 3-4. Two Identical Isotropic Point Sources Spaced One Wavelength Apart (Fig. 3-6)

Since the currents are in phase the fields of each element add perfectly (i.e., double) in the $\pm x$ -directions. Also, since the phase lag of the field from one element is 360° (one wavelength additional path length) with respect to the other in either the $+z$ or $-z$ direction, their effects add perfectly in the far field. However, with the one-wavelength spacing there are directions of perfect cancellation as indicated in Fig. 3-6b. To determine these directions we reason as follows. For perfect cancellation the waves from the two sources must be 180° out-of-phase. This means a path length difference of one-half wavelength. Since the path length difference as a function of θ is $\lambda \cos \theta$ (see Fig. 3-3c) we must solve for the values of θ such that

$$\lambda \cos \theta = \pm \frac{\lambda}{2} \quad \text{or} \quad \cos \theta = \pm \frac{1}{2} \quad (3-11)$$

The solutions are 60° and 120° . By filling in smooth variations between the maxima and zeros indicated in Fig. 3-6b, the pattern of Fig. 3-6c results.

The exact array factor calculation parallels that of Example 3-1 except that with $d = \lambda$ in (3-4)

$$AF = 2 \cos \left(\beta \frac{d}{2} \cos \theta \right) = 2 \cos(\pi \cos \theta). \quad (3-12)$$

The normalized array factor is

$$f(\theta) = \cos(\pi \cos \theta). \quad (3-13)$$

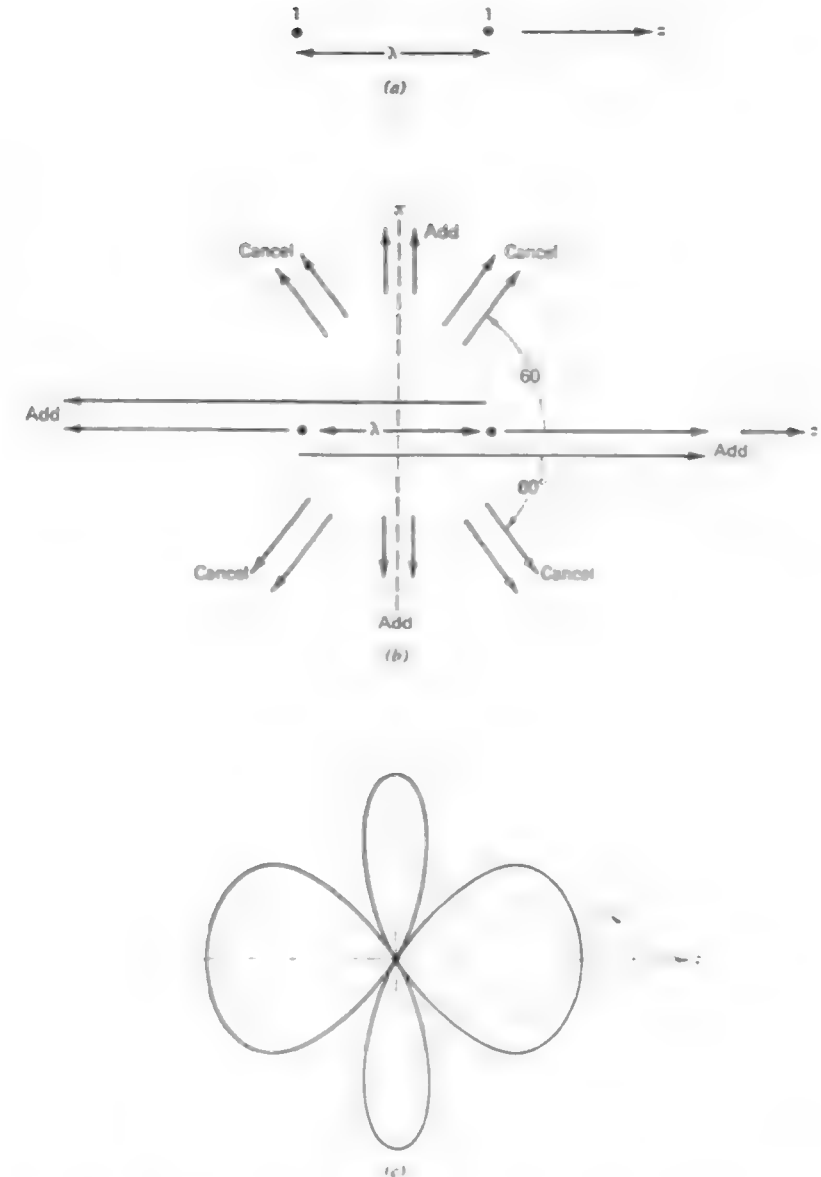


Figure 3-6 Two isotropic point sources with identical amplitude and phase currents, and spaced one wavelength apart (Example 3-4). (a) Array configuration. (b) Inspection method. (c) Polar plot of array factor magnitude $|f(\theta)| = |\cos \pi \cos \theta|$.

Note that $|f(\theta)|$ has a maximum value of unity for $\theta = 0^\circ, 90^\circ$, and 180° and is zero for $\theta = 60^\circ$ and 120° . These are the same results we obtained by inspection in Fig. 3-6c. This example illustrates the fact that multiple lobes will appear for spacings greater than a half-wavelength.

The inspection method is difficult to use in all but the simplest arrays. Therefore, we shall examine the general array factor given by (3-3) for the case of equally spaced arrays. We will study its properties and develop a method to obtain a quick sketch of the radiation pattern.

Suppose we have a linear array of several elements. If the elements are equally spaced as shown in Fig. 3-7, the array factor expression (3-3) may be simplified. The angle θ is that of an incoming plane wave relative to the axis of the receiving array. The isotropic sources respond equally in all directions but when their outputs are added together (each weighted according to I_n), a directional response is obtained. The phase of the wave arriving at the origin is set arbitrarily to zero, so $\xi_0 = 0$. The incoming waves at element 1 arrive before those at the origin since the distance is shorter by an amount $d \cos \theta$. The corresponding phase lead of waves at element 1 relative to those at 0 is $\xi_1 = \beta d \cos \theta$. This process continues and (3-3) becomes

$$AF = I_0 + I_1 e^{j\beta d \cos \theta} + I_2 e^{j\beta 2d \cos \theta} + \dots = \sum_{n=0}^{N-1} I_n e^{j\beta n d \cos \theta} \quad (3-14)$$

Now consider the array to be transmitting. If the current has a linear phase progression (i.e., relative phase between adjacent elements is the same), we will separate out this phase explicitly as

$$I_n = A_n e^{jn\alpha} \quad (3-15)$$

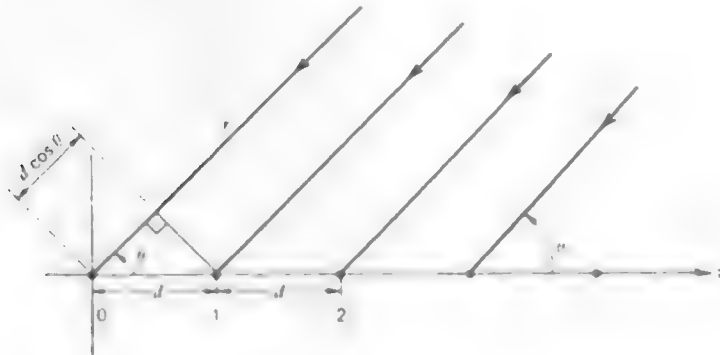


Figure 3-7 Equally spaced linear array of isotropic point sources

where the $n + 1$ th element leads the n th element in phase by α . Then (3-14) becomes

$$AF = \sum_{n=0}^{N-1} A_n e^{j\beta n d \cos \theta + jn\alpha} \quad (3-16)$$

Define

$$\psi = \beta d \cos \theta + \alpha \quad (3-17)$$

Then

$$AF = \sum_{n=0}^{N-1} A_n e^{jn\psi} \quad (3-18)$$

This array factor is a function of ψ and may be recognized as a Fourier series. This form is convenient for calculations, but we usually want field plots in terms of the polar angle θ . The nonlinear transformation from ψ to θ given by (3-17) can be accomplished graphically.

For example, consider two elements spaced one-half wavelength apart and with identical currents as in Example 3-1. We found the normalized array factor in (3-6) to be $f(\theta) = \cos[(\pi/2)\cos \theta]$. In this case ψ from (3-17) is

$$\psi = \beta d \cos \theta + \alpha = \pi \cos \theta \quad (3-19)$$

since $d = \lambda/2$ and $\alpha = 0$. Now f may be expressed in terms of ψ as

$$f(\psi) = \cos \frac{\psi}{2} \quad (3-20)$$

This is a rather simple function to plot. From it we wish to obtain a plot of $|f|$ as a function of θ . To do this first plot $|f(\psi)|$ from (3-20) as shown in Fig. 3-8. Then draw a circle of radius $\psi = \pi$ below it as shown, since (3-19) is a polar equation of a circle. For an arbitrary value of ψ , say ψ_1 , drop a line straight down until it intersects the circle. The values of $\theta = \theta_1$ and $|f| = f_1$ corresponding to $\psi = \psi_1$ are indicated on the figure. Locating several points taken in this fashion will lead to the desired sketch. Note that as θ ranges from 0 to π , ψ goes from π to $-\pi$ in this case. The resulting polar plot is shown in Fig. 3-10b. It is the same as the result obtained using inspection in Fig. 3-3.

Before proceeding with more specific examples, let us consider a general array factor and how a polar pattern is obtained from it. The magnitude of a typical array factor is plotted as a function of ψ in Fig. 3-9. Below it a circle is constructed with a radius equal to βd and its center located at $\psi = \alpha$. The angle θ is as shown. It is very simple to use this plot. For a given value of θ locate the intersection of a radial line from the origin of the circle and the perimeter, point a . The corresponding value of ψ , at point b , is on a vertical line from a . The array

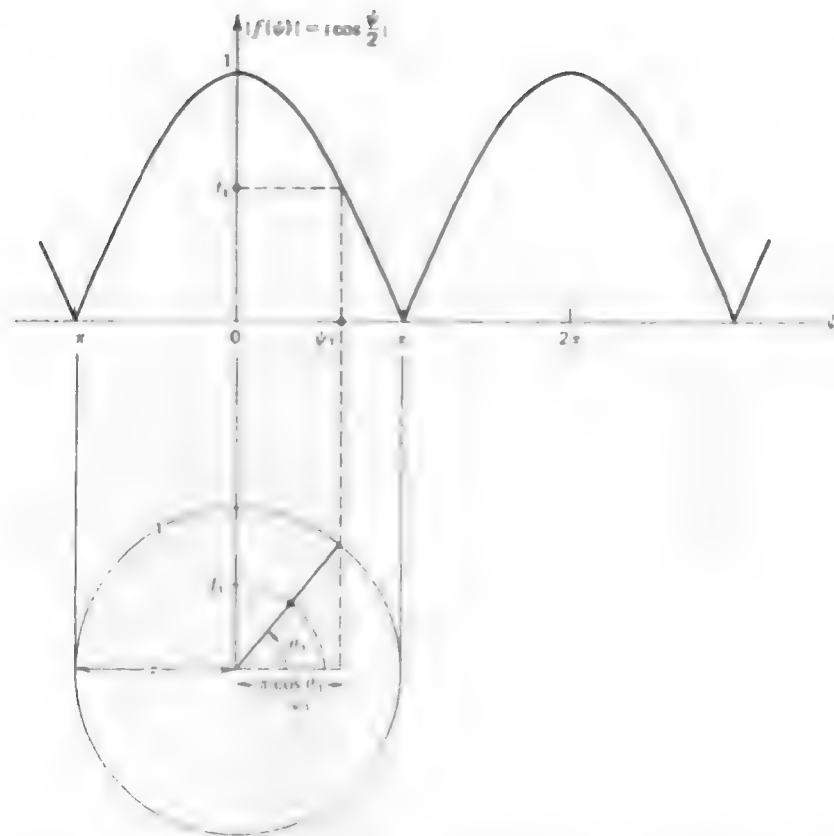


Figure 3-8 Procedure for obtaining the polar plot of the array factor of two elements spaced one-half wavelength apart with identical currents.

factor value corresponding to these values of ψ and θ is then point c , also on the vertical line from a . Notice that the distance from the $\psi = 0$ axis to a point, say at a , can be written as $\psi = \alpha + \beta d \cos \theta$, which is (3-17).

To illustrate the procedure further we will find the polar plots of the array factors for some two element arrays with equal current amplitudes which were discussed earlier in this section. The array factor as a function of ψ , from (3-18) with $N = 2$, is

$$AF = 1 + e^{j\psi} = e^{j\psi/2}(e^{-j\psi/2} + e^{j\psi/2}) = 2e^{j\psi/2} \cos \frac{\psi}{2} \quad (3-21)$$

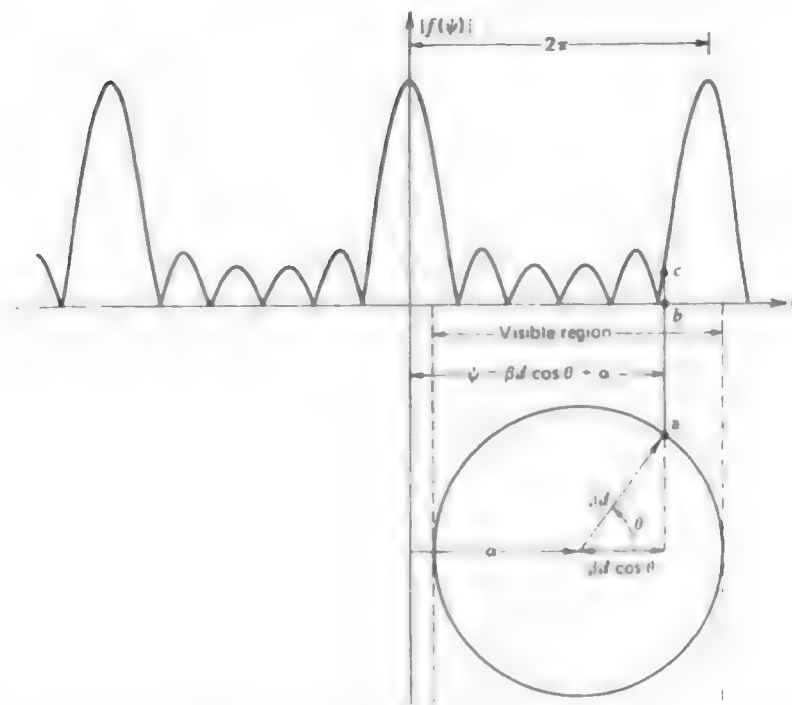


Figure 3-9 Construction technique for finding the array factor as a function of polar angle θ .

where $A_0 = A_1 = 1$. Taking the magnitude eliminates the exponential factor and normalization removes the factor of two. The normalized array factor magnitude is

$$|f(\psi)| = \left| \cos \frac{\psi}{2} \right| \quad (3-22)$$

which also follows from (3-20). The array factor $|f(\psi)|$ is the same for all two element arrays with the same current amplitudes, and is plotted in Fig. 3-10a. Of course, ψ changes with element spacing and phasing. For example, if the spacing is a half-wavelength and the phases of each element are zero ($\alpha = 0$), the pattern is obtained as shown in Fig. 3-8 with the resulting pattern plotted in Fig. 3-10b. This is Example 3-1 discussed earlier. For Example 3-2, $d = \lambda/2$ and $\alpha = \pi$. The resulting polar plot of the array factor using the procedures of Fig. 3-9 is shown

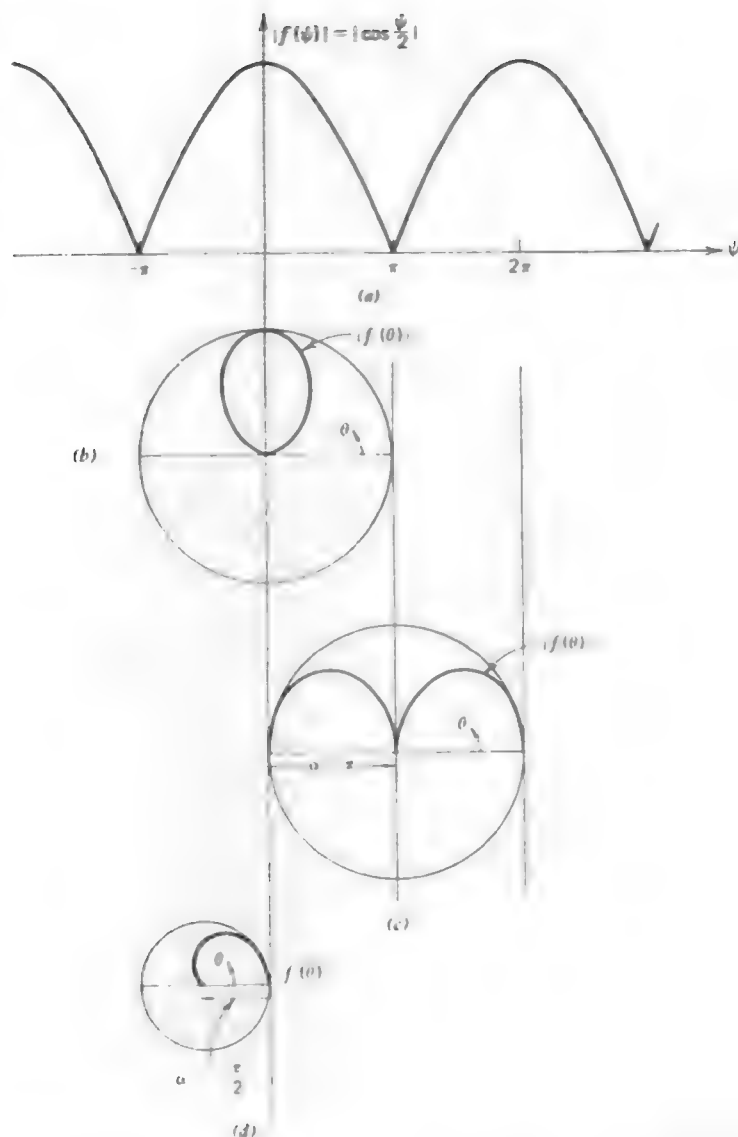


Figure 3-10 Array factors for two-element arrays with equal amplitude currents. (a) Universal array factor. (b) Polar plot for $d = \lambda/2$, $\beta d = \pi$, $\alpha = 0$ (Example 3-1). (c) Polar plot for $d = \lambda/2$, $\beta d = \pi$, $\alpha = \pi$ (Example 3-2). (d) Polar plot $d = \lambda/4$, $\beta d = \pi/2$, $\alpha = -\pi/2$ (Example 3-3)

in Fig. 3-10c. The array factor for Example 3-3 with $d = \lambda/4$ and $\alpha = -\pi/2$ is shown in Fig. 3-10d.

By examining the general array factor expression in (3-18) some general properties may be derived which aid in the construction of pattern plots. First, the array factor is periodic in the variable ψ with period 2π . This is easily shown as follows.

$$AF(\psi + 2\pi) = \sum A_n e^{j n (\psi + 2\pi)} = \sum A_n e^{j n \psi} e^{j n 2\pi} = \sum A_n e^{j n \psi} = AF(\psi). \quad (3-23)$$

The array factor of a linear array along the z -axis is a function of θ but not of ϕ (the element pattern may be though). In other words, the array factor is a pattern that has rotational symmetry about the line of the array. Therefore, its complete structure is determined by its values for

$$0 < \theta < \pi. \quad (3-24)$$

This is called the *visible region*. This corresponds to $-1 < \cos \theta < 1$ or $-\beta d < \beta d \cos \theta < \beta d$ or

$$\alpha - \beta d < \psi < \alpha + \beta d. \quad (3-25)$$

Hence, the visible region in terms of θ and ψ are given by (3-24) and (3-25), respectively. The element spacing of the array in terms of a wavelength, d/λ , determines the size of the circle in Fig. 3-9 and thus how much of the array factor appears in the visible region. The visible region in the variable ψ is of length $2\beta d$, as seen from (3-25). This is the diameter of the circle in Fig. 3-9. Suppose that exactly one period appears in the visible region. Since the period is 2π we have $2\pi = 2\beta d = 2(2\pi/\lambda)d$ or $d/\lambda = \frac{1}{2}$. Thus, *exactly one period of the array factor appears in the visible region when the element spacing is one-half wavelength*. Less than one period is visible if $2\beta d < 2\pi$ which corresponds to $d/\lambda < \frac{1}{2}$, that is, for spacings less than one-half wavelength. For spacings greater than one-half wavelength more than one period will be visible. For one-wavelength spacings two periods will be visible. For spacings larger than a half-wavelength there may be more than one major lobe in the visible region, depending on the element phasings. Additional major lobes which rise to an intensity equal to that of the main lobe are called *grating lobes*. In the one-wavelength spaced, two-element array factor of Fig. 3-6c there are grating lobes at $\theta = 0$ and 180° , assuming that the lobe in the $\theta = 90^\circ$ direction is the desired lobe. In most situations, it is undesirable to have grating lobes. As a result, most arrays are designed such that the element spacing is less than one wavelength, usually close to a half-wavelength.

3.2 UNIFORMLY EXCITED, EQUALLY SPACED LINEAR ARRAYS

3.2.1 The Array Factor Expression

A very important special case of equally spaced linear arrays is that of the uniformly excited array. This is an array whose element current amplitudes are identical, so

$$A_0 = A_1 = A_2 = \dots \quad (3-26)$$

In this section we will consider only element phasings of a linear form accounted for by interelement phase shift α . The array factor from (3-18) is then

$$AF = A_0 \sum_{n=0}^{N-1} e^{jn\psi} = A_0(1 + e^{j\psi} + \dots + e^{j(N-1)\psi}). \quad (3-27)$$

Only a few short steps are required to sum this geometric series. First multiply (3-27) by $e^{j\psi}$ to obtain

$$AF e^{j\psi} = A_0(e^{j\psi} + e^{j2\psi} + \dots + e^{jN\psi}). \quad (3-28)$$

Subtracting this from (3-27) gives

$$AF(1 - e^{j\psi}) = A_0(1 - e^{jN\psi})$$

or

$$AF = \frac{1 - e^{jN\psi}}{1 - e^{j\psi}} A_0. \quad (3-29)$$

This may be rewritten in a more convenient form as follows.

$$\begin{aligned} AF &= A_0 \frac{e^{jN\psi/2} - 1}{e^{j\psi/2} - 1} = A_0 \frac{e^{jN\psi/2} - e^{-jN\psi/2}}{e^{j\psi/2} - e^{-j\psi/2}} \\ &= A_0 e^{j(N-1)\psi/2} \frac{\sin(N\psi/2)}{\sin(\psi/2)}. \end{aligned} \quad (3-30)$$

The phase factor $e^{j(N-1)\psi/2}$ is not important (unless one is going to further combine the array output signal with the output from another antenna). In fact, if the array were centered about the origin, the phase factor would not be present since it represents the phase shift of the array phase center relative to the origin. Neglecting the phase factor in (3-30) gives

$$AF = A_0 \frac{\sin(N\psi/2)}{\sin(\psi/2)}. \quad (3-31)$$

This expression is maximum for $\psi = 0$ and has a maximum value most easily seen from (3-27) as

$$AF(\psi = 0) = A_0(1 + 1 + \dots + 1) = A_0 N. \quad (3-32)$$

Dividing this into (3-31) gives the normalized array factor

$$f(\psi) = \frac{\sin(N\psi/2)}{N \sin(\psi/2)}. \quad (3-33)$$

This is the normalized array factor for an N element, uniformly excited, equally spaced array which is centered about the coordinate origin. This function is similar to a $(\sin u)/u$ function with a major difference that the side lobes do not die off without limit for increasing argument. In fact, the function (3-33) is periodic in 2π , which is true in general as we showed in (3-23).

In Fig. 3-11 are sketched the array factors for three values of N .¹ A number of trends can be seen by examining the plots in Fig. 3-11.

1. As N increases the main lobe narrows.
2. As N increases there are more side lobes in one period of $f(\psi)$. In fact, the number of full lobes (one main lobe and the side lobes) in one period of $f(\psi)$ equals $N - 1$. Thus there will be $N - 2$ side lobes and one main lobe in each period.
3. The minor lobes are of width $2\pi/N$ in the variable ψ and the major lobes (main and grating) are twice this width.
4. The side lobe peaks decrease with increasing N . A measure of the side lobe peaks is the *side lobe level* which we have defined as

$$SLL = \frac{|\text{maximum value of largest side lobe}|}{|\text{maximum value of main lobe}|} \quad (3-34)$$

and it is often expressed in decibels. The side lobe level of the array factor for $N = 5$ is -12 dB and it is -13 dB for $N = 20$. It approaches the value of a uniform line source, -13.3 dB, as N is increased.

5. $|f(\psi)|$ is symmetric about π . It is left as an exercise to show this.

The radiation field polar plots in the variable θ can be obtained from $f(\psi)$ as discussed in Section 3.1. For example, consider the two-element case. Then (3-33) becomes

$$f(\psi) = \frac{\sin \psi}{2 \sin(\psi/2)}. \quad (3-35)$$

¹ A comprehensive set of array factor plots for many values of N is found in [1].

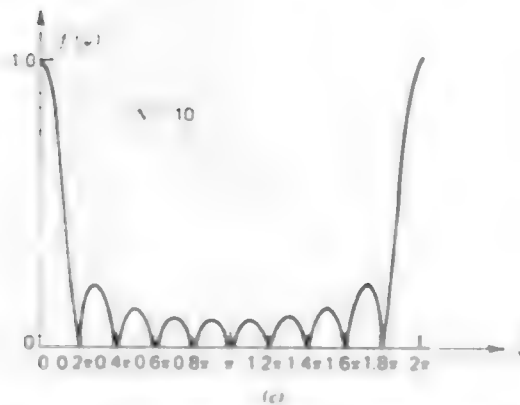
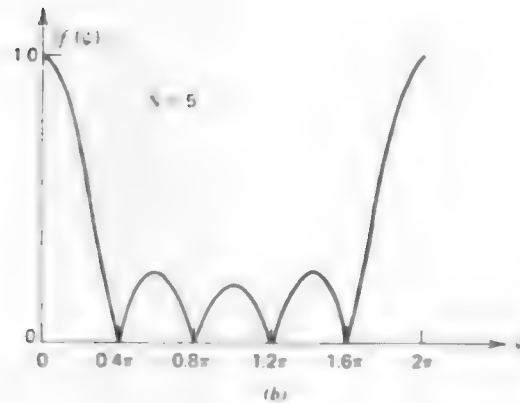
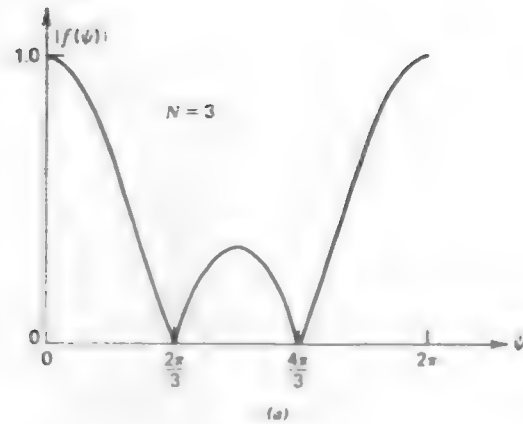


Figure 3-11 Array factor of an equally spaced, uniformly excited linear array for a few array numbers. (a) Three elements. (b) Five elements. (c) Ten elements

This is a universal pattern function for all equal amplitude two element arrays and is plotted in Fig. 3-10a. Note that by the techniques used in Section 3.1 we found that the array factor for a two element array was $\cos(\psi/2)$; see (3-20). It can be shown that this is identical to (3-35).

The universal array factor for a four-element, uniformly excited, equally spaced array is plotted in Fig. 3-12b. Let us find the array factor polar plot for

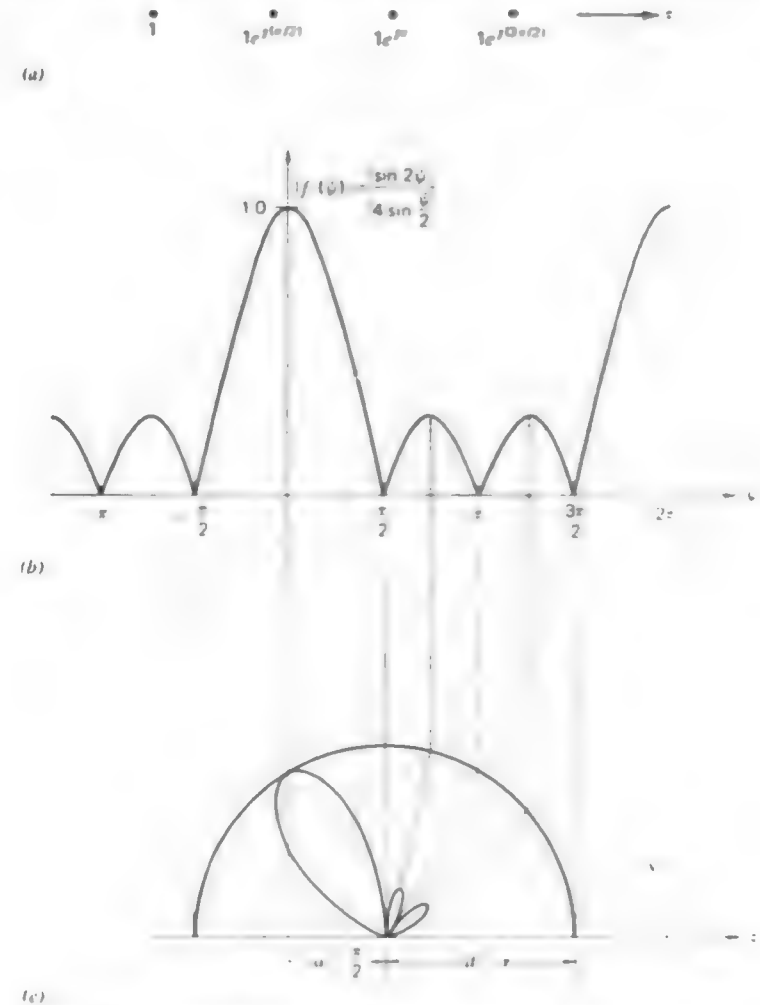


Figure 3-12 Array factor for a four-element, uniformly excited, equally spaced phased array. (a) The array excitations (b) Universal pattern for $N=4$. (c) Polar plot for $d = \lambda/2$ and $\alpha = \pi/2$.

the special case of half-wavelength spacing and 90° interelement phasing (i.e., $\alpha = \pi/2$). The array excitations are shown in Fig. 3-12a. The pattern plot can be sketched quickly by locating prominent features such as maxima and zeros. Then vertical lines are dropped down from these points to the circle below. From the intersection points with the circle, straight lines are drawn in to the center of the circle. The perimeter of the circle has a pattern value of unity and the center a value of zero. For linear polar plots such as this one, the magnitude of the pattern factor is linearly proportional to the distance from the origin. For example, if the circle radius is 4 cm and the pattern value to be plotted is 0.25, the pattern point is 1 cm from the origin along a radial line at the appropriate angle θ . After locating the relative maxima and the zeros a smooth curve is drawn joining these points. The complete polar plot is shown in Fig. 3-12c. Note that a polar plot can be made larger or smaller by expanding or contracting the construction circle.

3.2.2 Main Beam Scanning and Beamwidth

A maximum of an array factor occurs for $\psi = 0$. Let θ_o be the corresponding value of θ for which the array factor is maximum. Then from (3-17) we have $0 = \beta d \cos \theta_o + \alpha$, or

$$\alpha = -\beta d \cos \theta_o. \quad (3-36)$$

This is the element-to-element phase shift in the excitation currents required to produce an array factor main beam maximum in a direction θ_o relative to the line along which the array elements are disposed. Thus, if we want an array factor maximum in the $\theta = \theta_o$ direction, the required element currents from (3-15) with (3-36) are

$$I_n = e^{jn\alpha} = e^{-jn\beta d \cos \theta_o} \quad (3-37)$$

for a uniformly excited, equally spaced linear array. For the broadside case ($\theta_o = 90^\circ$) $\alpha = 0$. For the endfire case ($\theta_o = 0^\circ$ or 180°) $\alpha = -\beta d$ or βd . In the example illustrated in Fig. 3-12, $\alpha = \pi/2$ and $d = \lambda/2$ so $\theta_o = \cos^{-1}(-\alpha/\beta d) = \cos^{-1}(-\frac{1}{2}) = 120^\circ$. This main beam scanning by phase control feature can be explicitly incorporated into ψ by substituting (3-36) into (3-17) giving

$$\psi = \beta d (\cos \theta - \cos \theta_o). \quad (3-38)$$

Scanning is discussed further in Section 3.7.

A measure of the width of the main beam of a uniformly excited, equally spaced linear array is given by the *beamwidth between first nulls*, BWFN, which is illustrated in Fig. 1-9 for a general pattern. The main beam nulls are where the array factor (3-33) first goes to zero in a plane containing the linear array. The zeros of the numerator of (3-33) occur for $N\psi/2 = \pm n\pi$. When the denomina-

tor also goes to zero ($\frac{1}{2}\psi_{FN} = \pm n\pi$) the pattern factor is unity, corresponding to the main beam ($n = 0$) and grating lobes. The first nulls associated with the main beam occur for $N\psi_{FN}/2 = \pm \pi$. For a broadside array ($\alpha = 0^\circ$) $\psi = \beta d \cos \theta$, so the angles θ for the first nulls are found from

$$\pm \pi = \frac{N}{2} \frac{2\pi}{\lambda} d \cos \theta_{FN} \quad (3-39)$$

or

$$\theta_{FN} = \cos^{-1} \left(\pm \frac{\lambda}{Nd} \right). \quad (3-40)$$

The BWFN is then

$$\text{BWFN} = |\theta_{FN \text{ left}} - \theta_{FN \text{ right}}| \quad (3-41)$$

$$= \left| \cos^{-1} \left(-\frac{\lambda}{Nd} \right) - \cos^{-1} \left(+\frac{\lambda}{Nd} \right) \right|. \quad (3-42)$$

For long arrays (length $L = Nd \gg \lambda$) we can approximate (3-42) as follows

$$\text{BWFN} \approx \left| \frac{\pi}{2} + \frac{\lambda}{Nd} - \left(\frac{\pi}{2} - \frac{\lambda}{Nd} \right) \right| = \frac{2\lambda}{Nd} \quad (\text{near broadside}). \quad (3-43)$$

For an endfire array (a typical endfire pattern is shown in Fig. 1-11c) the beamwidth between first nulls is twice that from the main beam maximum to the first null. It is given approximately by

$$\text{BWFN} \approx 2 \sqrt{\frac{2\lambda}{Nd}} \quad (\text{endfire}) \quad (3-44)$$

for long arrays.

The half-power beamwidth (HP) is perhaps a more popular measure of the main beam size than is BWFN. Both depend on the array length Nd and main beam pointing angle θ_o . For a long ($Nd \gg \lambda$) uniformly excited linear array the HP is approximately [2]

$$\text{HP} \approx 0.886 \frac{\lambda}{Nd} \csc \theta_o \quad (\text{near broadside}) \quad (3-45)$$

and

$$\text{HP} \approx 2 \sqrt{0.886 \frac{\lambda}{Nd}} \quad (\text{endfire}). \quad (3-46)$$

By comparing the formulas for HP and BWFN it is seen that HP is roughly one-half of the corresponding BWFN value for long, uniformly excited linear arrays.

3.2.3 The Ordinary Endfire Array

In many applications antennas are required to produce a single pencil beam. The array factor for a broadside array produces a fan beam, although proper selection of array elements may yield a total pattern that has a single pencil beam. Another way to achieve a single pencil beam is by proper design of an endfire array. We have said that an endfire condition results when $\theta_o = 0^\circ$ or 180° , which corresponds to $\alpha = -\beta d$ or $+\beta d$. Such arrays for which $\alpha = \pm \beta d$ are referred to as *ordinary endfire* arrays. If the spacing d is a half-wavelength there will be two identical endfire lobes (see Fig. 3-10c, for example). There are several ways to eliminate one of these lobes, thus leaving a single pencil beam. The most obvious way is to reduce the spacing below a half-wavelength. The visible region is $2\beta d$ wide in the variable ψ , and to eliminate the unwanted major lobe (grating lobe) we should reduce the visible region (and thus the spacing d) below the half-wavelength spacing value of 2π . Since the grating lobe half-width (maximum to null) is $2\pi/N$, we can eliminate most of it by reducing the visible region by at least π/N , that is,

$$2\beta d \leq 2\pi - \frac{\pi}{N} \quad (\text{ordinary endfire}). \quad (3-47)$$

Dividing this by 2β gives the condition on the spacings as

$$d \leq \frac{\lambda}{2} \left(1 - \frac{1}{2N} \right) \quad (\text{ordinary endfire}). \quad (3-48)$$

An ordinary endfire array with spacing d satisfying (3-48) will produce a single endfire beam at $\theta = 0^\circ$ for $\alpha = -\beta d$ or at $\theta = 180^\circ$ for $\alpha = \beta d$. A five-element array example is shown in Fig. 3-13. From (3-48) we must have $d \leq (\lambda/2)(1 - 1/10) = 0.45\lambda$. Selecting $d = 0.45\lambda$ with a main beam direction $\theta_o = 180^\circ$, the required element-to-element phase shift is $\alpha = -\beta d \cos \theta_o = \beta d = (2\pi/\lambda)(0.45\lambda) = 0.9\pi$.

3.2.4 The Hansen-Woodyard Endfire Array

In the ordinary endfire case the interelement excitation phase, $\alpha = \pm \beta d$, exactly equals the spatial phase delay of waves in the endfire direction. It is possible to make the main beam narrower and thus increase directivity by increasing the interelement phase shift, thereby moving some of the main beam outside of the visible region. If the phase shift is increased over the ordinary endfire case such that

$$\alpha = \pm \left(\beta d + \frac{\pi}{N} \right) \quad (\text{Hansen-Woodyard}) \quad (3-49)$$

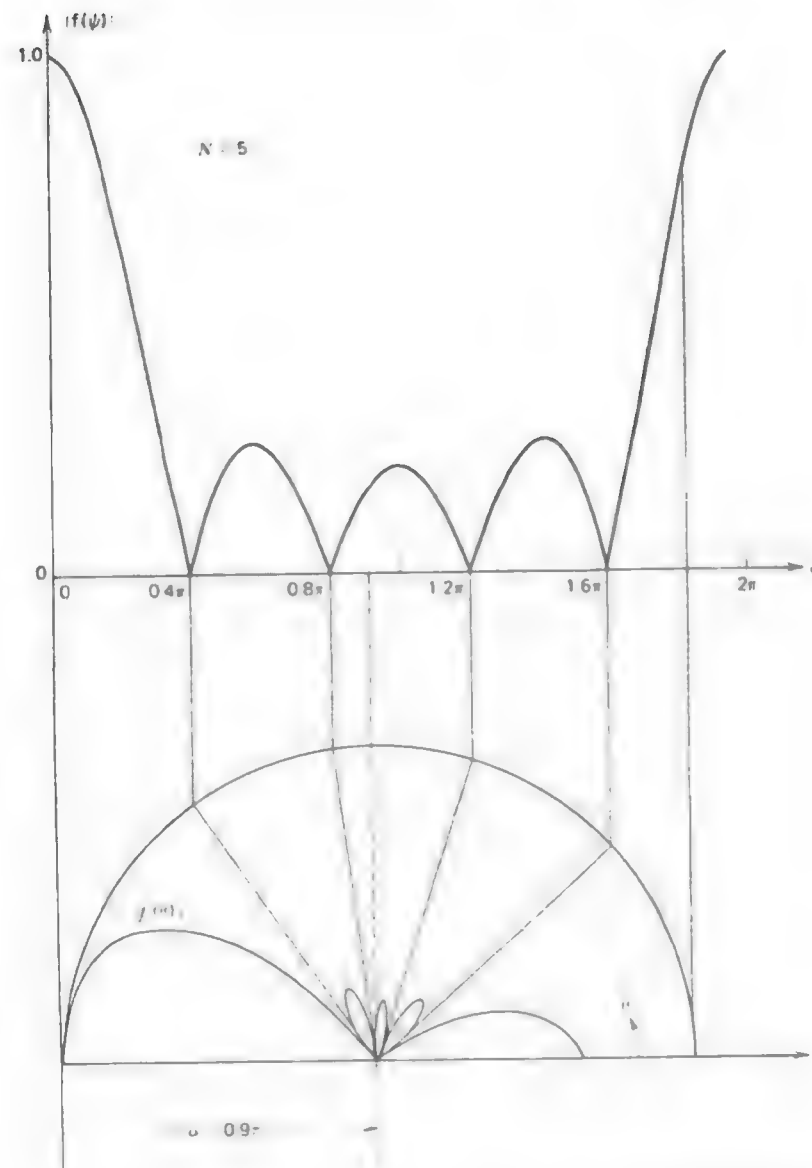


Figure 3-13 A single main beam ordinary endfire array of five elements that are uniformly excited, equally spaced with $d = 0.45\lambda$, and phased with $\alpha = 0.9\pi$.

it is called the *Hansen-Woodyard condition* for increased directivity [3]. This condition was obtained by studying several long line sources, but also applies to long arrays.

To illustrate the Hansen-Woodyard condition, return to Fig. 3-13 and notice that as α is increased the circle will move to the right but the radius of the circle will remain the same for βd unchanged. This will cause the main beam to narrow since part of the main lobe of the $|f(\psi)|$ plot does not appear in the visible region. However, the side lobes will become larger relative to the main beam and the back lobe will increase in magnitude. To prevent the back lobe from

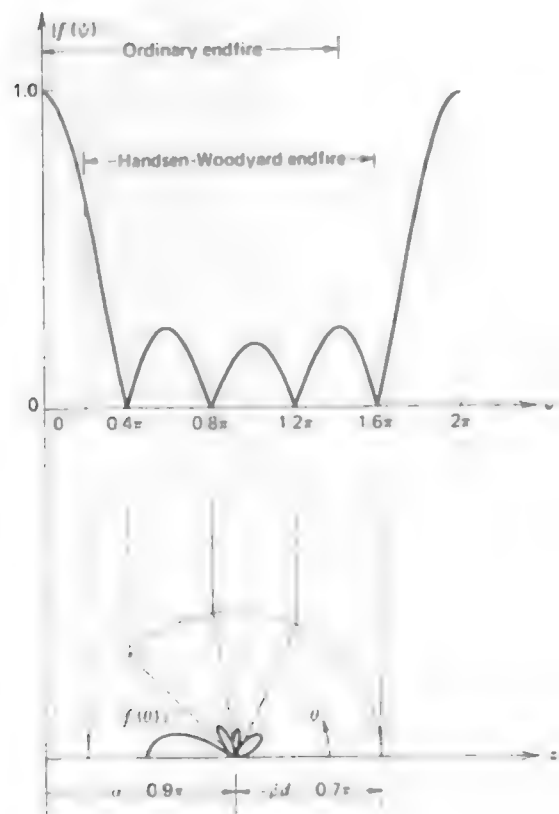


Figure 3-14 Single endfire beam for a five-element Hansen-Woodyard increased directivity array with $\alpha = 0.9\pi$ and $d = 0.35\lambda$.

becoming equal to or larger than the main beam it is necessary that the phase α be less than π . Using this fact with (3-49) yields

$$\alpha = \beta d + \frac{\pi}{N} < \pi \quad (3-50)$$

or

$$d < \frac{\lambda}{2} \left(1 - \frac{1}{N} \right) \quad (\text{Hansen-Woodyard}). \quad (3-51)$$

Therefore, to achieve a single main beam in the Hansen-Woodyard case, it is necessary that the elements be more closely spaced than for the ordinary endfire condition of (3-48).

An example of a Hansen-Woodyard increased directivity array is shown in Fig. 3-14. The array has five elements, so from (3-51) we must have $d < (\lambda/2)(1 - 1/5) = 0.4\lambda$. Choosing $d = 0.35\lambda$ leads to $\alpha = \beta d + \pi/N = 0.7\pi + 0.2\pi = 0.9\pi$. The main beam is narrower than if the ordinary endfire condition were used (see Fig. 3-13), but the side lobes are higher. Nevertheless, the array exhibits increased directivity. The directivity as a function of spacing is compared to that of an ordinary endfire five-element array in Fig. 3-15.

The Hansen-Woodyard example of an increased directivity array is important for it is one of the very few instances where it is *practical* to obtain more directivity than would normally be obtainable from an array of a given size.

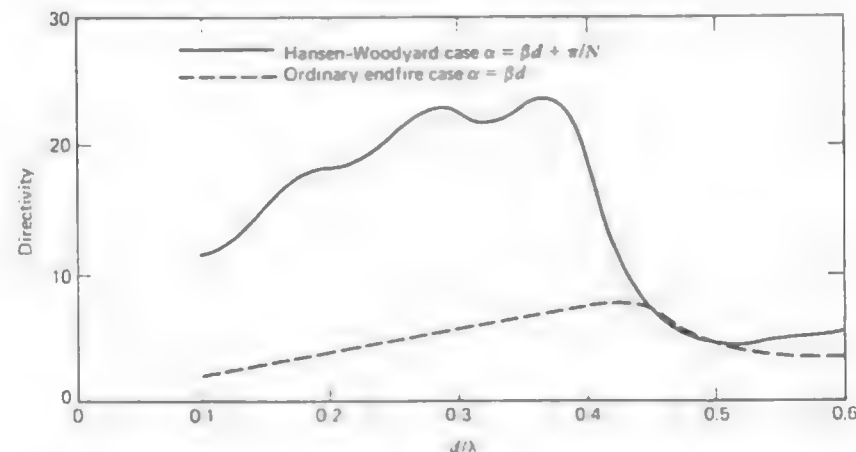


Figure 3-15 Comparison of directivities for two five-element equally spaced, uniformly excited endfire arrays. From (3-48), $d \leq 0.45\lambda$ for ordinary endfire; and from (3-51), $d < 0.4\lambda$ for Hansen-Woodyard endfire.

Such arrays are said to be *superdirective*. Generally, the advantages of superdirectivity are illusory since superdirectivity does not usually lead to supergain. A measure of supergain is a quantity called the *supergain ratio*, which is the ratio of the total power in all pattern space (visible and invisible) to the power in the visible region only. Supergain ratio is equal to one plus the antenna Q . Thus, a large value of antenna Q accompanies superdirective antenna arrays. The large stored energy in turn requires that the element currents be exceptionally large with a corresponding increase in ohmic losses. As a result, superdirectivity can be achieved without supergain.

We will encounter the Hansen-Woodyard condition again when we study the Yagi-Uda antenna in Section 5.4 and the helix in Section 6.1.2.

3.3 PATTERN MULTIPLICATION

So far in our study of arrays we have discussed only arrays of isotropic point sources. Actual arrays are usually made up of nearly identical element antennas which, of course, are not isotropic. In this section we discuss how to compute the radiation pattern from such arrays. We will find that the array factor still plays a major role in these pattern calculations.

When the elements of an array are placed along a line and the currents in each element also flow in the direction of that line, the array is said to be *collinear*. As a simple example of a collinear array suppose we have N short dipoles as shown in Fig. 3-16. The elements are equally spaced a distance d apart and have currents $I_0, I_1, I_2, \dots, I_{N-1}$. The total current is the sum of the z -directed short dipole currents and thus is z -directed and the vector potential is also. The vector potential integral in (1-101) reduces to a sum over the element currents (modeled as ideal dipoles) as²

$$A_z = \frac{e^{-j\beta r}}{4\pi r} \Delta z [I_0 + I_1 e^{j\beta d \cos \theta} + I_2 e^{j\beta 2d \cos \theta} + \dots + I_{N-1} e^{j\beta (N-1)d \cos \theta}] = \frac{e^{-j\beta r}}{4\pi r} \Delta z \sum_{n=0}^{N-1} I_n e^{j\beta n d \cos \theta} \quad (3-52)$$

² This result could also be obtained by writing the z -directed current density as

$$J_z = \delta(x') \delta(y') [I_0 \delta(z') + I_1 \delta(z' - d) + I_2 \delta(z' - 2d) + \dots + I_{N-1} \delta(z' - (N-1)d)] \Delta z$$

and substituting this into (1-100) giving

$$A_z = \frac{e^{-j\beta r}}{4\pi r} \Delta z \int_{-\infty}^{\infty} [I_0 \delta(z') + I_1 \delta(z' - d) + \dots] e^{j\beta z' \cos \theta} dz'$$

from which (3-52) follows

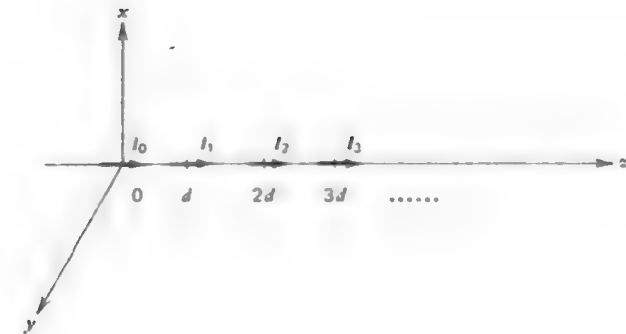


Figure 3-16 A collinear array of short dipoles.

in the far field. Then from (1-104)

$$E_\theta = j\omega\mu \frac{e^{-j\beta r}}{4\pi r} \Delta z \sin \theta \sum_{n=0}^{N-1} I_n e^{j\beta n d \cos \theta} \quad (3-53)$$

From this expression we can identify $\sin \theta$ as the pattern of a single element by itself, called the *element pattern*. The remaining factor

$$AF = \sum_{n=0}^{N-1} I_n e^{j\beta n d \cos \theta} \quad (3-54)$$

is the array factor of (3-14). The array factor may be thought of as a sum of isotropic point sources located at the center of each array element. The array factor is that factor of the radiation pattern which is found from the element currents (amplitudes and phases) and their locations. On the other hand, the element pattern is that factor of the radiation pattern determined by the individual properties of an element (its current distribution and orientation in space). We shall see that this factoring process holds in general if the elements have the same pattern and are similarly oriented.

Let us now consider a slightly more complicated case. Suppose for the sake of explanation we have N identical element antennas forming a collinear array along the z -axis. The n th element is centered at $z = z_n$ and has a current distribution $i_n(z')$. We are now relaxing the equal spacing constraint. The total current along the z -axis is

$$I(z') = \sum_{n=0}^{N-1} i_n(z'). \quad (3-55)$$

The vector potential is then

$$A_z = \frac{e^{-j\beta r}}{4\pi r} \int_{-\infty}^{\infty} \sum_{n=0}^{N-1} i_n(z') e^{j\beta z' \cos \theta} dz' \quad (3-56)$$

The far-field electric field from this and (1-104) is

$$E = j\omega\mu \frac{e^{-j\beta r}}{4\pi r} \sum_{n=0}^{N-1} E_n(\theta) \quad (3-57)$$

where

$$E_n(\theta) = \sin \theta \int_{-\ell/2}^{\ell/2} i_n(z') e^{j\beta z' \cos \theta} dz' \quad (3-58)$$

is the pattern of the n th element.

If the array possesses no symmetry (3-57) cannot be simplified. But if the array elements are similar, a great deal of simplification is possible. By *similar* we mean that the currents of each antenna element are in the same direction, of the same length, and have the same distribution (although there may be different current amplitudes and phases for each element). Then the patterns of (3-58) will be similar, that is, have the same spatial variation but may have different amplitudes and phases. In the example at hand the currents are all z -directed. Now assume that each element is of length ℓ , has a normalized current distribution over its length of $i(z')$, and an input current of I_n . Then

$$i_n(z') = I_n i(z' - z_n) \quad (3-59)$$

where z_n is the position of the n th element center along the z -axis. Substituting this into (3-58) gives

$$E_n(\theta) = \sin \theta I_n \int_{z_n - \ell/2}^{z_n + \ell/2} i(\xi - z_n) e^{j\beta \xi \cos \theta} d\xi \quad (3-60)$$

where ξ replaces z' . Let $\tau = \xi - z_n$, then (3-60) becomes

$$\begin{aligned} E_n(\theta) &= \sin \theta I_n \int_{-\ell/2}^{\ell/2} i(\tau) e^{j\beta(\tau + z_n) \cos \theta} d\tau \\ &= \sin \theta \left[\int_{-\ell/2}^{\ell/2} i(\tau) e^{j\beta \tau \cos \theta} d\tau \right] I_n e^{j\beta z_n \cos \theta} \end{aligned} \quad (3-61)$$

To maintain consistent notation, we replace τ by z' yielding

$$E_n(\theta) = \sin \theta \left[\int_{-\ell/2}^{\ell/2} i(z') e^{j\beta z' \cos \theta} dz' \right] I_n e^{j\beta z_n \cos \theta} \quad (3-62)$$

The pattern for each element of an array of similar elements given by (3-62) is a product of the pattern of the current distribution, and the amplitude and phase of excitation I_n , and the last factor represents the spatial phase due to the separation from the origin. Substituting (3-62) into (3-57) gives

$$E_\theta = j\omega\mu \frac{e^{-j\beta r}}{4\pi r} \left[\sin \theta \int_{-\ell/2}^{\ell/2} i(z') e^{j\beta z' \cos \theta} dz' \right] \sum_{n=0}^{N-1} I_n e^{j\beta z_n \cos \theta} \quad (3-63)$$

The factor

$$\sin \theta \int_{-\ell/2}^{\ell/2} i(z') e^{j\beta z' \cos \theta} dz' \quad (3-64)$$

when normalized is the element pattern, $g_n(\theta)$, of any element in the array of similar elements. The sum

$$AF = \sum_{n=0}^{N-1} I_n e^{j\beta z_n \cos \theta} \quad (3-65)$$

is the unnormalized array factor.

In going from (3-57) to (3-63) it was necessary to assume that the elements of the array were similar. When this is true the electric field may be written as a product of an element pattern, as in (3-64), and an array factor, as in (3-65). Note that the array factor of (3-65) is the pattern of a linear array of N point sources located at positions $\{z_n\}$ on the z -axis. If the elements are equally spaced (3-14) results. If further, they are uniformly excited the array factor reduces to (3-31). This result is not restricted to collinear elements but may be applied to any array of similar elements. This will be discussed below.

The process of factoring the pattern of an array into an element pattern and an array factor is referred to as the *principle of pattern multiplication*. It is stated as follows: The electric field pattern of an array consisting of similar elements is the product of the pattern of one of the elements (the element pattern) and the pattern of an array of isotropic point sources with the same locations, relative amplitudes and phases as the original array (the array factor).

In Section 1.5 we wrote the normalized electric field pattern of a single antenna as a product of a normalized element factor g and a normalized pattern factor f . For array antennas we expand this concept and call the pattern of one element antenna in the array an element pattern g_n . It in turn is composed of an element factor which is the pattern of an infinitesimal piece of current on the array element (i.e., an ideal dipole) and a pattern factor which is the pattern due to its current distribution. The complete (normalized) pattern of an array antenna is then

$$F(\theta, \phi) = g_n(\theta, \phi) f(\theta, \phi) \quad (3-66)$$

where $g_a(\theta, \phi)$ is the normalized pattern of a single element antenna of the array (the element pattern) and $f(\theta, \phi)$ is the normalized array factor.

To illustrate pattern multiplication, consider two collinear short dipoles spaced a half-wavelength apart and equally excited. The element pattern is $\sin \theta$ for an element along the z -axis and the array factor was found in (3-6) to be $\cos[(\pi/2)\cos \theta]$. The total pattern is then $\sin \theta \cos[(\pi/2)\cos \theta]$. The patterns are illustrated in Fig. 3-17.

The principle of pattern multiplication can be used directly for many different geometries. For example, suppose line sources positioned along the z -axis are not z -directed, as in a collinear array, but are parallel as shown in Fig. 3-18. Let γ be the spherical polar angle from the x -axis. Note $0^\circ \leq \gamma \leq 180^\circ$. The element pattern is then found from the following expression which is analogous to (3-64)

$$\sin \gamma \int_{-l_0/2}^{l_0/2} i(x') e^{j\beta x' \cos \gamma} dx'. \quad (3-67)$$

Note that $\cos \gamma = \sin \theta \cos \phi$. The array factor of (3-65) is unchanged. For example, if two short dipoles are parallel as shown in Fig. 3-19a, the total pattern is found by pattern multiplication as indicated in Fig. 3-19b and 3-19c.

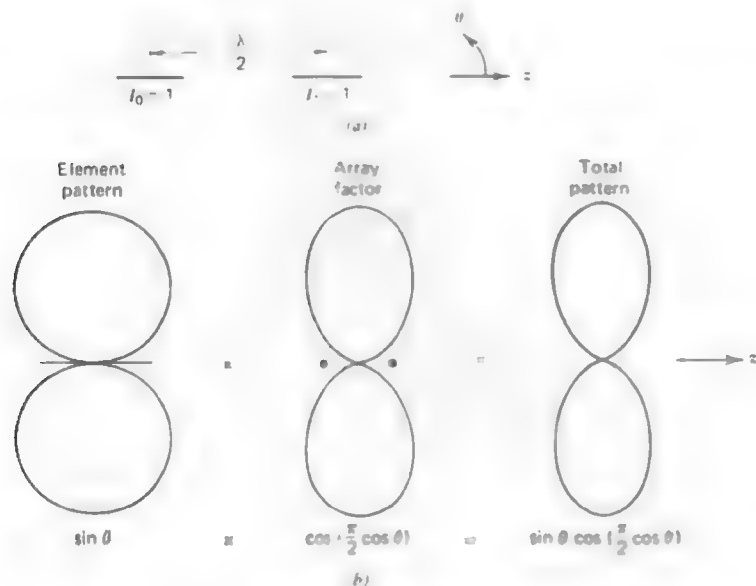


Figure 3-17 Array of two half-wavelength spaced, equal amplitude, equal phase, collinear short dipoles. (a) The array. (b) The pattern.

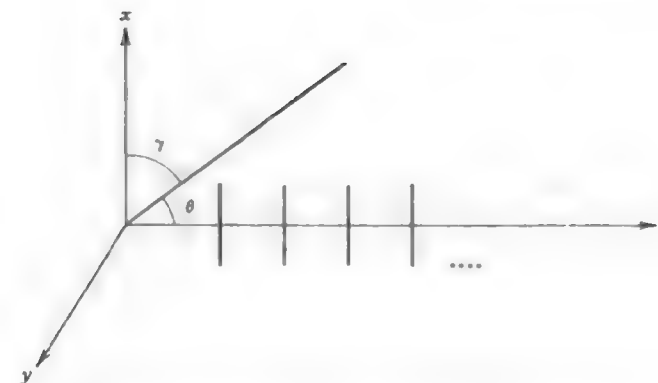


Figure 3-18 A linear array of parallel line sources.

To illustrate parallel element arrays further, suppose the element antennas of Fig. 3-18 are half-wave dipoles. Also suppose there are five elements arranged and excited for ordinary endfire as in Fig. 3-13. The complete pattern is the product of the single half-wave dipole element pattern and the array factor found from five isotropic sources. The element pattern for a half-wave dipole element in the array is

$$g_a(\gamma) = \frac{\cos[(\pi/2)\cos \gamma]}{\sin \gamma} \quad (3-68)$$

which is (2-10) with θ replaced by γ . Since $\cos \gamma = \sin \theta \cos \phi$ then

$$\sin \gamma = \sqrt{1 - \sin^2 \theta \cos^2 \phi}$$

and (3-68) becomes

$$g_a(\theta, \phi) = \frac{\cos[(\pi/2)\sin \theta \cos \phi]}{\sqrt{1 - \sin^2 \theta \cos^2 \phi}} \quad (3-69)$$

The array factor is (3-33) with $N = 5$, or

$$f(\psi) = \frac{\sin(\frac{5}{2}\psi)}{5 \sin(\frac{1}{2}\psi)} \quad (3-70)$$

For this example $\alpha = 0.9\pi$ and $d = 0.45\lambda$ so $\psi = \beta d \cos \theta + \alpha = 0.9\pi \cos \theta + 0.9\pi$, and (3-70) is

$$f(\theta) = \frac{\sin(2.25\pi \cos \theta + 2.25\pi)}{5 \sin(0.45\pi \cos \theta + 0.45\pi)} \quad (3-71)$$

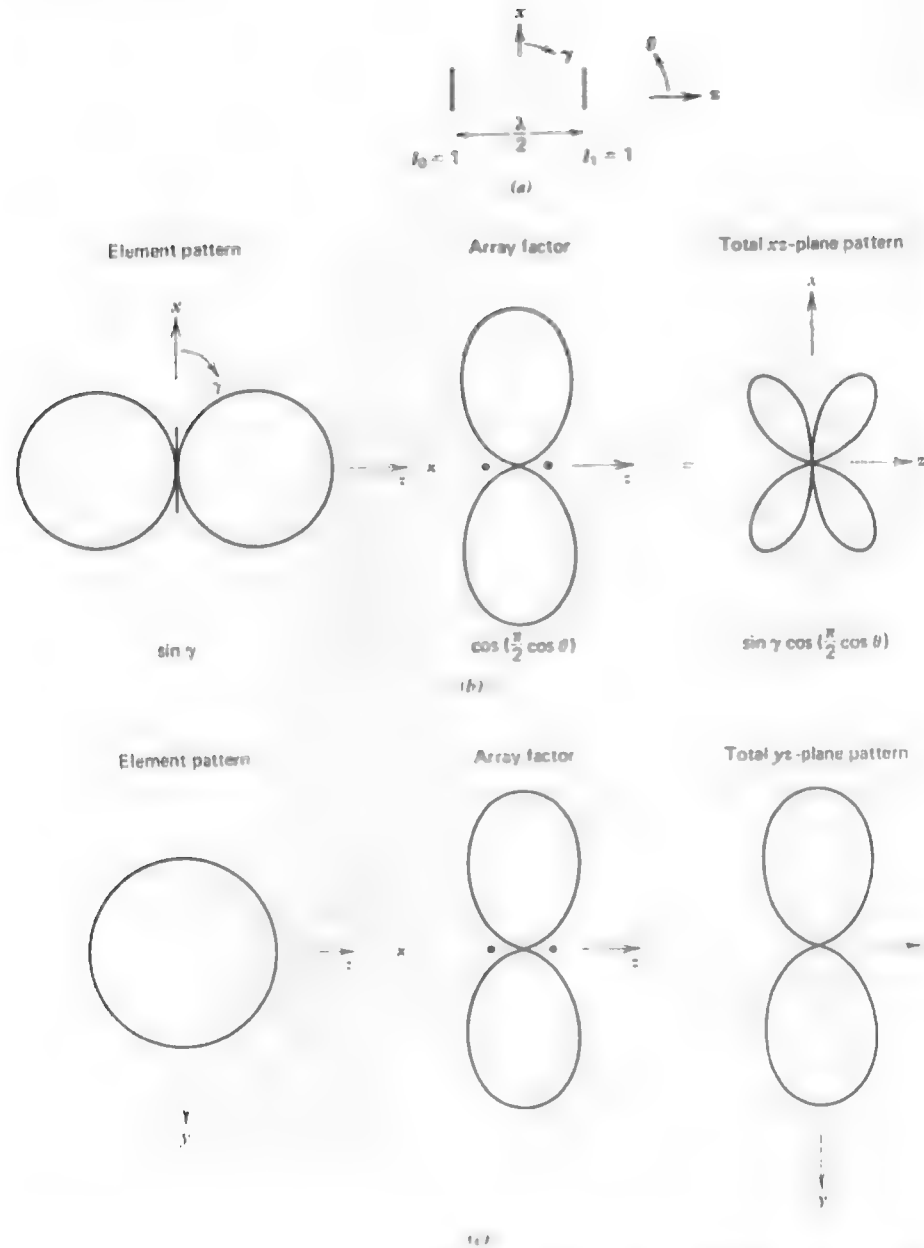


Figure 3-19 Array of two half-wavelength spaced, equal amplitude, equal phase, parallel short dipoles. (a) The array. (b) The xz -plane pattern. (c) The yz -plane pattern.

The total pattern of the array in terms of θ and ϕ is then the product of (3-69) and (3-71)

$$F(\theta, \phi) = \frac{\cos[(\pi/2)\sin \theta \cos \phi] \sin(2.25\pi \cos \theta + 2.25\pi)}{\sqrt{1 - \sin^2 \theta \cos^2 \phi} \sin(0.45\pi \cos \theta + 0.45\pi)} \quad (3-72)$$

The polar plot of this pattern is easily obtained by multiplying the plot in Fig. 2-5b, where the axis of symmetry is now the x -axis instead of the z -axis, times the polar plot of Fig. 3-13. This will be a polar plot similar to the array factor plot except that the endfire lobes will be slightly narrower, and there will be a pattern zero in the $\gamma = 0^\circ$ direction caused by the element pattern.

3.4 DIRECTIVITY OF UNIFORMLY EXCITED, EQUALLY SPACED LINEAR ARRAYS

Now that we have developed a method for obtaining the entire pattern expression for an antenna array we can discuss directivity of various arrays. The directivity is, of course, determined entirely from the radiation pattern. The array gain can be found by multiplying the array directivity by the radiation efficiency of one element (assuming all elements are alike).

To derive directivity expressions we use $D = 4\pi\Omega_A$, first finding the beam solid angle as

$$\Omega_A = \iint |F(\theta, \phi)|^2 d\Omega = \iint |g_a(\theta, \phi)|^2 |f(\theta)|^2 d\Omega \quad (3-73)$$

where $g_a(\theta, \phi)$ and $f(\theta)$ are the normalized element pattern and linear array factor and $d\Omega = \sin \theta d\theta d\phi$.

Let us begin by assuming the elements are equally spaced, uniformly excited, and isotropic. This assumption leads to approximate results for situations where the element pattern is much broader than the array factor and the main beams of both are aligned. The appropriate array factor from (3-33) can be written as

$$|f|^2 = \left| \frac{\sin(N\psi/2)}{N \sin(\psi/2)} \right|^2 \quad (3-74)$$

$$= \frac{1}{N} + \frac{2}{N^2} \sum_{m=1}^{N-1} (N-m) \cos m\psi \quad (3-75)$$

where (3-75) is another form for (3-74). This identity can be shown to be true for $N = 2$ since from (3-75) $|f(\psi)|^2 = \frac{1}{2} + \frac{1}{2} \cos \psi \approx \cos^2(\psi/2)$ as in (3-20). With the simple expression in (3-75) it is easier to perform the integration in (3-73) in

terms of the variable ψ . Using $g_a(\theta, \phi) = 1$, $\psi = \beta d \cos \theta + \alpha$, and $\sin \theta d\theta = -(1/\beta d) d\psi$ in (3-73) gives

$$\begin{aligned}\Omega_A &= \int_0^{2\pi} d\phi \int_0^\pi |f(\theta)|^2 \sin \theta d\theta = 2\pi \int_{-\beta d + \alpha}^{-\beta d + \pi} |f(\psi)|^2 \left(-\frac{1}{\beta d}\right) d\psi \\ &= \frac{2\pi}{\beta d} \int_{-\beta d + \alpha}^{-\beta d + \pi} |f(\psi)|^2 d\psi.\end{aligned}\quad (3-76)$$

Substituting (3-75) in the above yields

$$\begin{aligned}\Omega_A &= \frac{2\pi}{\beta d} \left[\frac{1}{N} \int_{-\beta d + \alpha}^{-\beta d + \pi} d\psi + \frac{2}{N^2} \sum_{m=1}^{N-1} (N-m) \int_{-\beta d + \alpha}^{-\beta d + \pi} \cos m\psi d\psi \right] \\ &= \frac{2\pi}{\beta d} \left[\frac{1}{N} \psi \Big|_{-\beta d + \alpha}^{-\beta d + \pi} + \frac{2}{N^2} \sum_{m=1}^{N-1} (N-m) \frac{\sin m\psi}{m} \Big|_{-\beta d + \alpha}^{-\beta d + \pi} \right] \\ &= \frac{2\pi}{\beta d} \left[\frac{1}{N} (2\beta d) + \frac{2}{N^2} \sum_{m=1}^{N-1} \frac{N-m}{m} [\sin m(\beta d + \alpha) - \sin m(-\beta d + \alpha)] \right] \\ &= \frac{4\pi}{N} + \frac{4\pi}{N^2} \sum_{m=1}^{N-1} \frac{N-m}{m\beta d} 2 \cos m\alpha \sin m\beta d\end{aligned}\quad (3-77)$$

where (B-6) was used in the last step. The directivity is then

$$D = \frac{4\pi}{\Omega_A} = \frac{1}{\frac{1}{N} + \frac{2}{N^2} \sum_{m=1}^{N-1} \frac{N-m}{m\beta d} \sin m\beta d \cos m\alpha} \quad (3-78)$$

for a linear array of N isotropic sources spaced a distance d apart with interelement phase shift α .

The directivity expression becomes extremely simple for a broadside array of half-wavelength spaced elements. For half-wavelength spacings $d = n\lambda/2$ with n an integer and $\beta d = n\pi$, so $\sin m\beta d = 0$. The array gives a broadside pattern when all elements are in-phase, or $\alpha = 0$. These conditions simplify (3-78) to

$$D = N \quad \left(d = n \frac{\lambda}{2}, \quad \alpha = 0 \right) \quad (3-79)$$

The directivity of a broadside array of isotropic elements as a function of the spacing in terms of a wavelength, d/λ , is plotted in Fig. 3-20 for several element numbers N . Notice that the directivity equals N at integer multiples of a half-wavelength. Also the directivity curves for each N take a sharp dip for spacings near one and two wavelengths. This is caused by the emergence of grating lobes into the visible region. For example, see Fig. 3-6 where full grating lobes appear for one-wavelength spacing

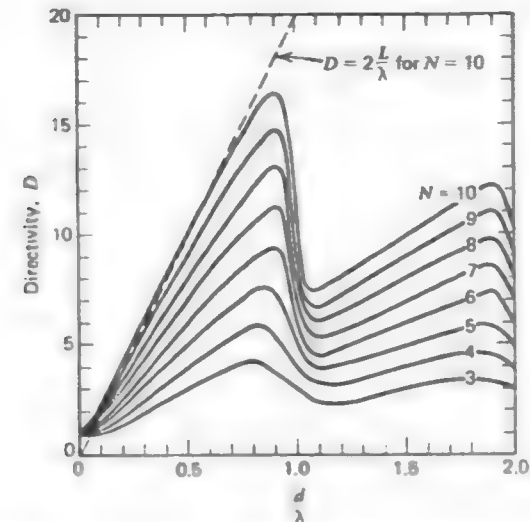


Figure 3-20 Directivity as a function of element spacing for a broadside array of isotropic elements for several element numbers, N .

The directivity of a broadside array of isotropic elements is approximated by

$$D \approx 2 \frac{L}{\lambda} = 2 \frac{Nd}{\lambda} \quad (\text{broadside}) \quad (3-80)$$

where $L = Nd$ is the array length. This is a straight line approximation to the curves in Fig. 3-20, being very accurate in the region from d slightly less than one-half wavelength to nearly one wavelength. This approximation is shown in Fig. 3-20 for $N = 10$; note the excellent agreement over a limited, but important, range of spacings. Note that (3-80) is exact for $d = \lambda/2$, since then (3-80) equals N as in (3-79). Similar approximations exist for endfire arrays of isotropic elements. For an ordinary endfire array with $\alpha = \pm \beta d$ and the spacing satisfying (3-48), the directivity is

$$D \approx 4 \frac{L}{\lambda} \quad (\text{ordinary endfire}) \quad (3-81)$$

and for an endfire array of the Hansen-Woodyard type it is given by

$$D \approx 7.28 \frac{L}{\lambda} \quad (\text{Hansen-Woodyard}). \quad (3-82)$$

These approximations improve as L increases. The increased directivity claimed for the Hansen-Woodyard endfire array over that of the ordinary endfire array is apparent from these directivity expressions.

It is also interesting to examine the directivity expression of (3-78) for various scan angles. A few cases are given in Fig. 3-21. From the figure it is apparent that $d = n\lambda/2$ with n an integer is again a special case since the directivity is independent of scan angle. This will be shown mathematically in Section 3.5. For the four cases shown, the greatest directivity in the broadside direction ($\theta_0 = 90^\circ$) is for the largest spacing. In fact we would obtain even higher directivities for spacings up to $d = 0.8\lambda$ in the $N = 5$ case (see Fig. 3-20). As can be seen from this example, the directivity of linear arrays remains constant over a wide range of scan angles near broadside; this will be explained in Section 3.7. The greatest directivity in the endfire direction ($\theta_0 = 0$ or 180°) is for the largest spacing that satisfies the single main beam criterion of (3-48), which is $d \leq 0.45\lambda$ for $N = 5$. For the four spacings shown $d = 0.4\lambda$ is the largest spacing satisfying this single endfire beam condition, and thus displays the largest endfire directivity.

If the element pattern is included in the directivity calculation, the appropriate directivity expression is

$$D = \frac{1}{\frac{a_0}{N} + \frac{2}{N^2} \sum_{m=1}^{N-1} \frac{N-m}{m\beta d} (a_1 \sin m\beta d + a_2 \cos m\beta d) \cos m\alpha} \quad (3-83)$$

where a_0 , a_1 , and a_2 are given in Table 3-1 for various element patterns [5, 6]. The directivity of long arrays ($L \gg \lambda$) is primarily controlled by the array factor if the element pattern is of low directivity and its major lobe is aligned with that of the array factor. In cases such as these, the approximate formulas of (3-80) to (3-82) can be used.

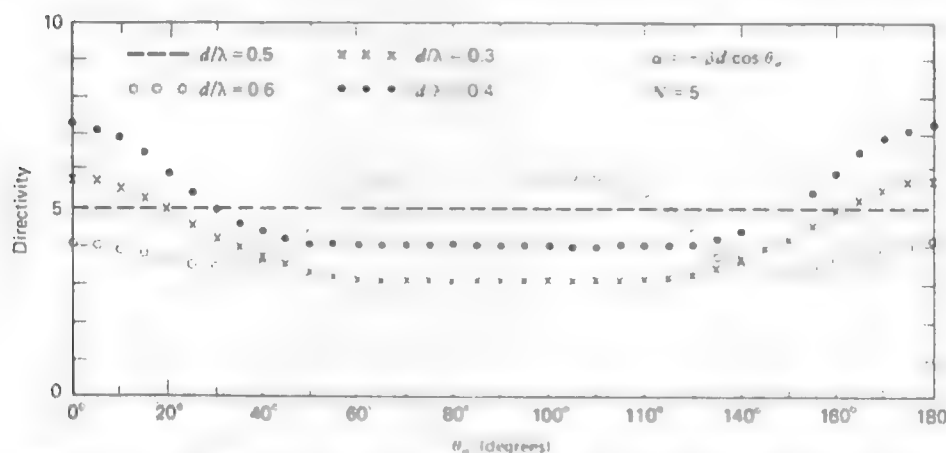


Figure 3-21 Variation of directivity with scan angle for five-element uniformly excited arrays of various element spacings. The elements are isotropic.

Table 3-1 Parameters for Use in Computing the Directivity of Uniform Current Amplitude, Equally Spaced Linear Arrays; see (3-83).

Element type	$ g_e(\theta, \phi) ^2$	a_0	a_1	a_2
Isotropic	1	1	1	0
Collinear short dipoles (Fig. 3-16)	$\sin^2 \theta$	2	2	-2
		3	$(m\beta d)^2$	$m\beta d$
Parallel short dipoles (Fig. 3-18)	$1 - \sin^2 \theta \cos^2 \phi$ $= \sin^2 \gamma$	2	$1 - \frac{1}{(m\beta d)^2}$	$\frac{1}{m\beta d}$
		3		

It is important to note that array directivity represents the increase in the radiation intensity in the direction of maximum radiation over that of a single element. Consider a single isotropic element and an array of N equally excited isotropic elements as shown in Fig. 3-22. The input power to the array is assumed to divide equally among the array elements; thus, if the element powers are $1/N$ of the input power, the element currents are $1/\sqrt{N}$ of its input current. The radiation intensity U_0 for the isotropic element is proportional to its input power, which in turn is proportional to the input current squared, I_0^2 . The maximum radiation intensity U_{\max} of the array in Fig. 3-22b is proportional to $(AF_{\max})^2 = [N(I_0/\sqrt{N})]^2 = NI_0^2$. Thus, $U_{\max} = NU_0 = DU_0$, since $D = N$ for the array.

3.5 NONUNIFORMLY EXCITED, EQUALLY SPACED LINEAR ARRAYS

We have seen that the main beam of an endfire array could be narrowed by changing the phase from that which is required for the ordinary endfire case. We can also shape the beam and control the level of the side lobes by adjusting the amplitudes of the current in an array. General synthesis procedures for achieving a specified pattern are presented in Chapter 10. In this section a few simple techniques for controlling side lobe levels and beamwidth are introduced. Several examples are given which reveal the array current distribution-radiation pattern relationship. The directivity for arrays with nonuniform excitation will also be examined.

The array factor of (3-18) can be written as a polynomial in terms of $Z = e^{j\psi}$ as follows

$$AF = \sum_{n=0}^{N-1} A_n e^{jn\psi} = \sum_{n=0}^{N-1} A_n Z^n \quad (3-84)$$

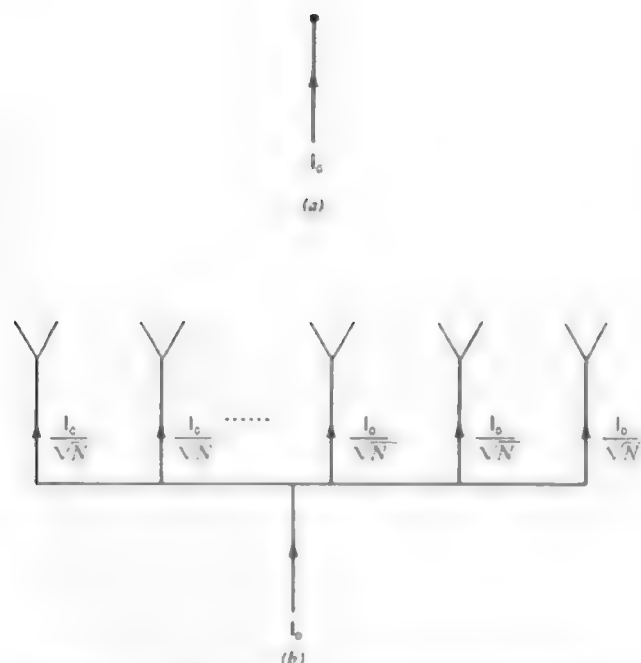


Figure 3-22 Array directivity may be viewed as the ratio of radiation intensity in the maximum radiation direction for an array with total input current I_0 to that of an isotropic element with the same input current. (a) Reference isotropic antenna with input current I_0 . (b) Equally excited array with total input current I_0 . The power is assumed to divide equally among the elements.

where the current amplitudes A_n are real and can be different for each n . S. A. Schelkunoff [7] applied the existing knowledge about the algebra of polynomials to array factors. He showed the connection between placement in the complex plane of the $N - 1$ zeros (roots) of the array polynomial in (3-84) and the radiation pattern and element currents. However, we shall examine the relationship between the element excitation and the array factor in a direct fashion. It is a simple matter to investigate element current distributions by utilizing a digital computer to perform the array factor summation.³ We will present the results of several such calculations. The influence of the element current amplitudes will become apparent if we use the same array configuration. Thus for purposes of comparison we will use a five-element, broadside linear array with a half-wavelength element spacing throughout this section

³ See the program NEESLAP in Appendix G.5

The basic array to which we will compare all others is the uniform array with all current amplitudes equal. The pattern in linear, polar form is plotted in Fig. 3-23a and the element currents are shown in Fig. 3-24a. If the element current amplitude forms a triangle as shown in Fig. 3-24b, the radiation pattern of Fig. 3-23b results. Notice that the side lobes are considerably smaller than those of the uniformly illuminated array, but at the expense of increased beamwidth. This increased beamwidth (from 20.8° to 26.0°) is responsible for reduced directivity (from 5 to 4.26).

The side lobe reduction introduced by the triangular amplitude taper suggests that perhaps an amplitude distribution exists such that all side lobes are completely eliminated. Indeed this is possible if the ratios of the currents are equal to the coefficients of the binomial series. To see how this comes about, first consider a two-element array with equal amplitudes and spacing d . The array factor from (3-84) is $AF = 1 + e^{j\psi}$ which can be written in terms of $Z = e^{j\psi}$ as

$$AF = 1 + Z. \quad (3-85)$$

If the spacing for this broadside array is less than, or at most equal to, a half-wavelength, the array factor will have no side lobes (see Fig. 3-3). Now consider an array formed by taking the product of two array factors of this type,

$$AF = (1 + Z)(1 + Z) = 1 + 2Z + Z^2. \quad (3-86)$$

This corresponds to a three-element array with the current amplitudes in the ratio 1 : 2 : 1. Since this array is simply the square of one which had no side lobes, the three-element array also has no side lobes. This process can also be viewed as arraying of two of the two-element arrays such that the centers of each subarray are spaced d apart. This leads to a coincidence of two elements in the middle of the total array, thus giving a current of two there. The total array factor is the product of the "element pattern," which is a two-element subarray pattern, and the array factor which is again a two-element, equal amplitude array. Thus the total array factor is the square of one subarray pattern. Continuing this process for an N element array we obtain

$$AF = (1 + Z)^{N-1} \quad (3-87)$$

which is a binomial series: see (F-4). For $N = 5$

$$AF = (1 + Z)^4 = 1 + 4Z + 6Z^2 + 4Z^3 + Z^4. \quad (3-88)$$

Therefore the ratios of the current amplitudes are 1 : 4 : 6 : 4 : 1. This current distribution is shown in Fig. 3-24c and the resulting pattern is shown in

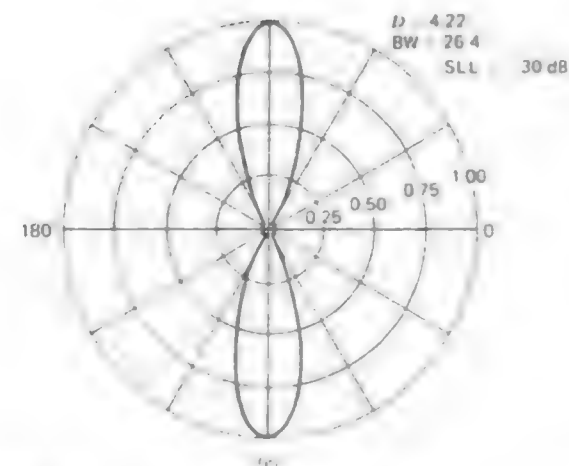
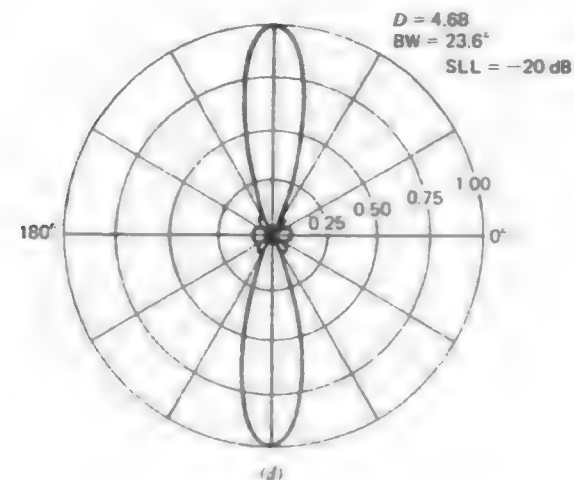
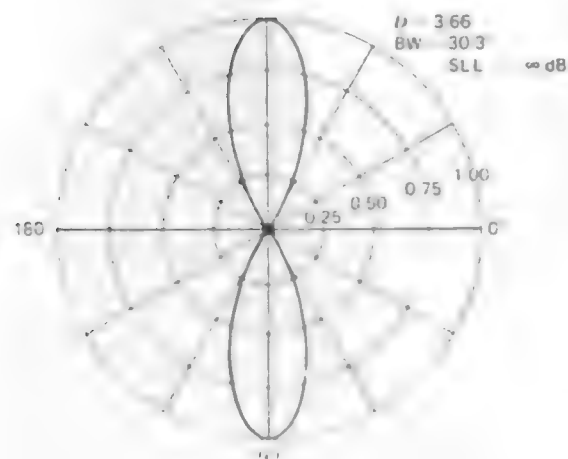
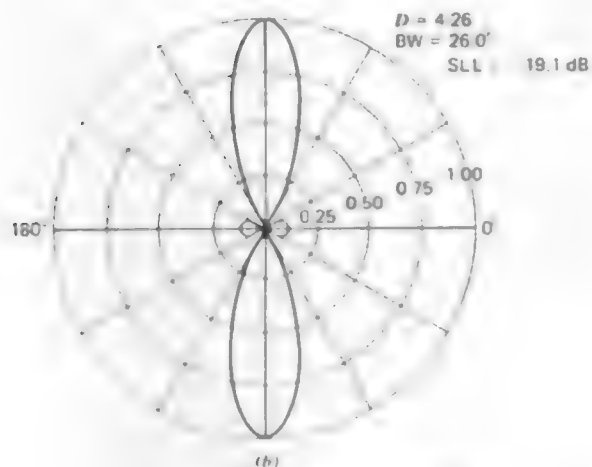
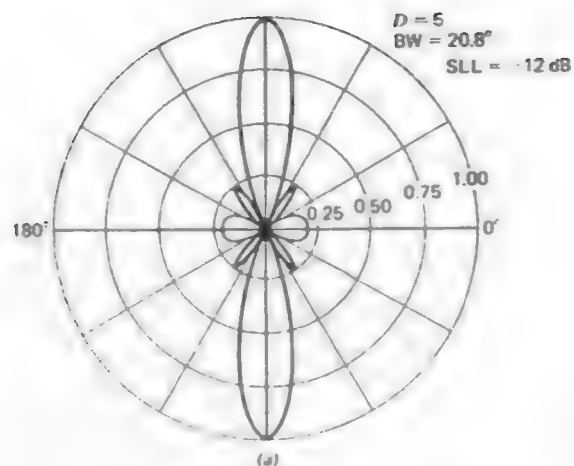


Figure 3-23 Patterns of several uniform phase ($\theta_0 = 90^\circ$), equally spaced ($d = \lambda/2$) linear arrays with various amplitude distributions. The currents are plotted in Fig. 3-24. (a) Uniform currents, 1:1:1:1:1. (b) Triangular current amplitude distribution, 1:2:3:2:1. (c) Binomial current amplitude distribution, 1:4:6:4:1. (d) Dolph-Chebyshev current amplitude distribution, 1:1.61:1.94:1.61:1, for a side lobe level of -20 dB . See Example 10-5. (e) Dolph-Chebyshev current amplitude distribution, 1:2.41:3.14:2.41:1, with a side lobe level of -30 dB .

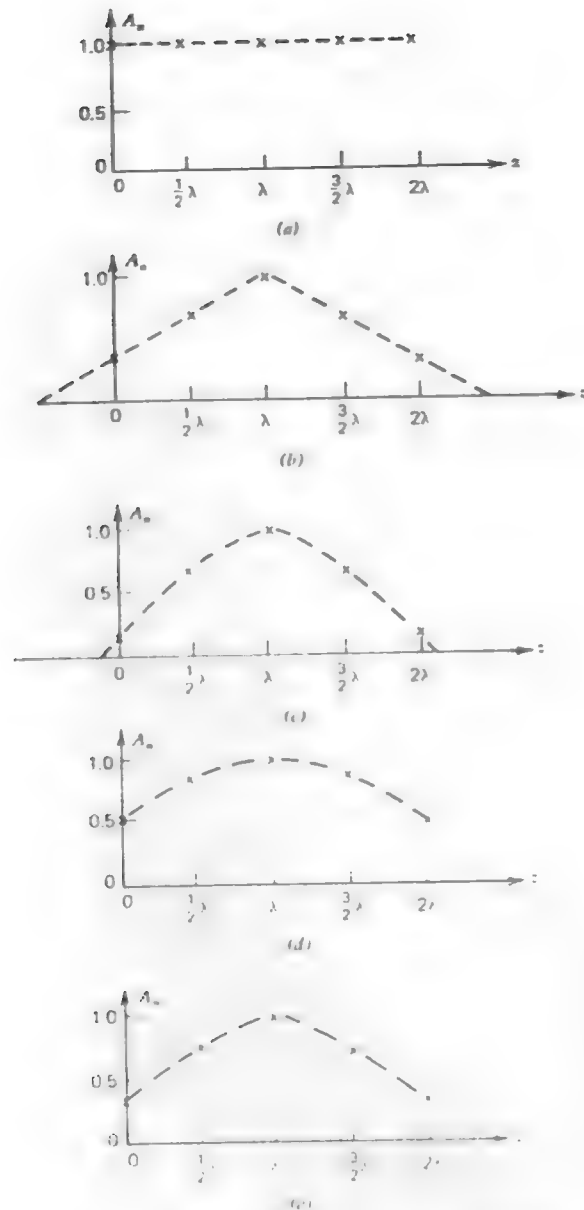


Figure 3-24 Current distributions corresponding to the patterns of Fig. 3-23. The current phases are zero ($\alpha = 0$). Currents are normalized to unity at the array center. (a) Uniform. (b) Triangular. (c) Binomial. (d) Dolph-Chebyshev (SLL = -20 dB). (e) Dolph-Chebyshev (SLL = -30 dB).

Fig. 3-23c. This pattern is broader than either the uniform or triangular distribution cases and has a lower directivity, but it has no side lobes.

From these three five-element array examples a trend has already emerged: As the current amplitude is tapered more toward the edges of the array, the side lobes tend to decrease and the beamwidth increases. This beamwidth/side lobe level tradeoff can be optimized. In other words, it is possible to determine the element current amplitudes such that the beamwidth is minimum for a specified side lobe level, or conversely to specify the beamwidth and obtain the lowest possible side lobe level. This array is referred to as a Dolph-Chebyshev array and it provides a pattern with all side lobes of the same level. The Dolph-Chebyshev array synthesis procedure will be explained in detail in Section 10.4.1. For a five-element array with an element spacing of a half-wavelength and a specified side lobe level of -20 dB, the Dolph-Chebyshev current distribution is plotted in Fig. 3-24d and the corresponding pattern is shown in Fig. 3-23d. If the side lobe level for the Dolph-Chebyshev array is specified to be -30 dB, the distribution is that of Fig. 3-24e and the corresponding pattern is shown in Fig. 3-23e. We note that the main beam is slightly broader than in the previous case where the side lobe level was 10 dB higher.

The discussion of nonuniformly excited arrays has, thus far, been concerned with amplitude tapers that become small near the ends of the linear array. If the amplitude distribution becomes larger at the ends of the array (called an inverse taper), we can expect the opposite effect, that is, that the side lobe level increases and the beamwidth decreases. Suppose, for example, that we invert the triangular distribution such that the amplitudes are 3 : 2 : 1 : 2 : 3. The resulting pattern shown in Fig. 3-25 demonstrates the expected decrease in beamwidth and increase in side lobe level. Although the directivity for the inverse triangular tapered current is greater than that for the triangular taper of Fig. 3-23b, it is still not as large as that produced by the uniform distribution.

The directivity values have been given for each of the examples in this section. We shall close this section by developing the directivity expression. With little additional complexity the treatment can be expanded to include unequal element spacings as well as nonuniform excitation. The element positions along the z -axis are z_n and the element current amplitudes are A_n . If the element phasings are linear with distance, then $\alpha_n = -\beta z_n \cos \theta_0$, where θ_0 is the angle of the pattern maximum; the applications of this type of phasing will be discussed in Section 3.7. The array factor of (3-65) is then appropriate and when normalized is

$$f(\theta) = \frac{\sum_{n=0}^{N-1} A_n e^{j\beta z_n \cos \theta}}{\sum_{n=0}^{N-1} A_n} \quad (3-89)$$

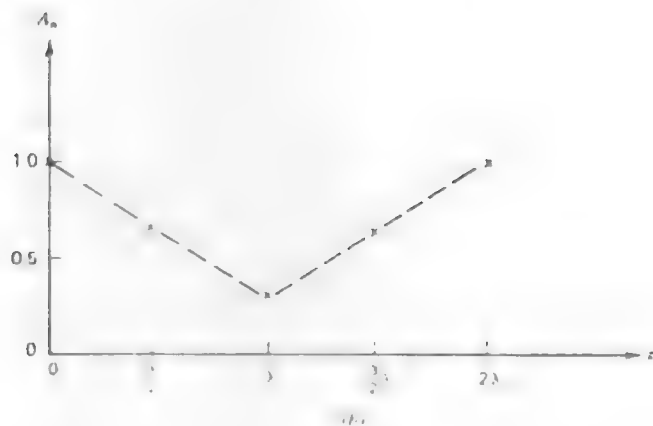
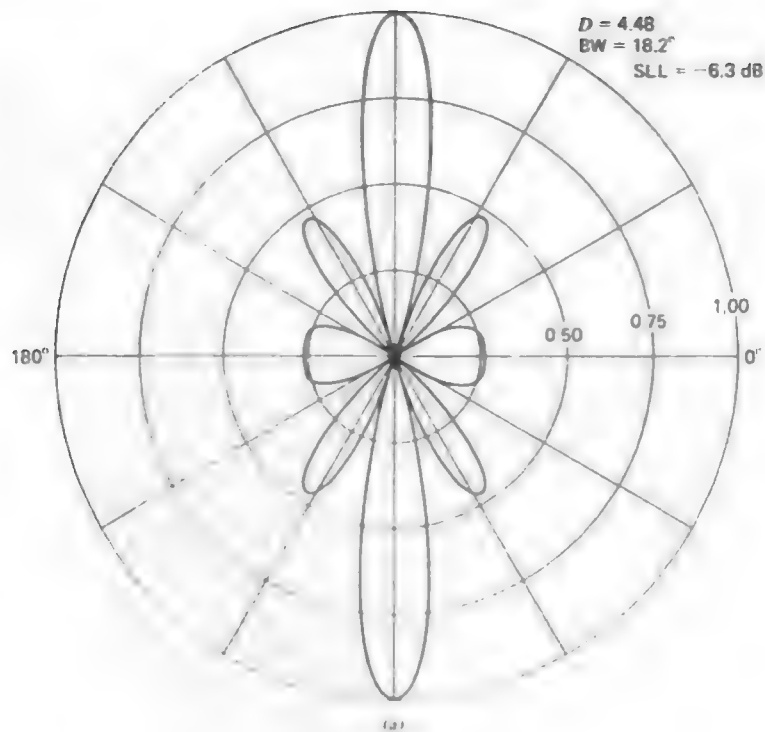


Figure 3-25 The inverse triangular tapered linear array with $d = \lambda/2$ and $\theta_0 = 90^\circ$. (a) The array factor (b) The current distribution, 3:2:1:2:3

And the appropriate beam solid angle expression is

$$\Omega_A = 2\pi \int_0^\pi |f(\theta)|^2 \sin \theta d\theta$$

$$= \frac{2\pi}{\left(\sum_{k=0}^{N-1} A_k\right)^2} \sum_{m=0}^{N-1} \sum_{p=0}^{N-1} A_m A_p e^{j\alpha_m - \alpha_p} \int_0^\pi e^{j\beta(z_m - z_p) \cos \theta} \sin \theta d\theta. \quad (3-90)$$

Evaluating the integral in the above expression and applying the result to $D = 4\pi/\Omega_A$ yields

$$D = \frac{\left(\sum_{k=0}^{N-1} A_k\right)^2}{\sum_{m=0}^{N-1} \sum_{p=0}^{N-1} A_m A_p \frac{\sin[\beta(z_m - z_p)]}{\beta(z_m - z_p)}} \quad (3-91)$$

where $\alpha_n = -\beta z_n \cos \theta_0$ and the elements can have any positions z_n and current amplitudes A_n . This general result can be simplified. For a broadside, equally spaced array

$$D = \frac{\left(\sum_{k=0}^{N-1} A_k\right)^2}{\sum_{m=0}^{N-1} \sum_{p=0}^{N-1} A_m A_p \frac{\sin[(m-p)\beta d]}{(m-p)\beta d}} \quad (\alpha_n = 0, \quad z_n = nd). \quad (3-92)$$

As another special case, when the spacings are a multiple of a half-wavelength (3-91) reduces to

$$D = \frac{\left(\sum_{n=0}^{N-1} A_n\right)^2}{\sum_{n=0}^{N-1} (A_n)^2} \quad \left(d = \frac{\lambda}{2}, \lambda, \dots\right). \quad (3-93)$$

Note that this is independent of scan angle θ_0 , as indicated in Fig. 3-21 for $d = \lambda/2$. Also, if the amplitudes are uniform (3-93) yields $D = N$ as given by (3-79). For a further example, consider the triangular excitation with the pattern of Fig. 3-23b. The directivity value from (3-93) is $[2(1) + 2(2) + 3]^2 / [2(1)^2 + 2(2)^2 + (3)^2] = 4.26$. Equation (3-93) is a very instructive formula for it tells us that the directivity is a measure of the coherent radiation from the linear array. The numerator is proportional to the square of the *total* coherent field, whereas the denominator is proportional to the *sum* of the squares of the field from each of the elements.

In conclusion, we have shown that the side lobe levels of a linear array can be altered by controlling the amplitude distribution. To achieve low side lobe levels it is necessary to taper the distribution such that the largest excitation occurs at the center of the array. However, we pay a price for the smaller side lobe levels in the form of reduced directivity associated with the corresponding increase in beamwidth.

3.6 MUTUAL IMPEDANCE

When antennas are in close proximity they interact in a complicated manner. This interaction is called *mutual coupling* and the effect is to change the current on an antenna from that which it would have if it were isolated in free space. Often it is the phase change of the current which is most noticeable, although the amplitude may be different as well. Thus, the current in a given element depends not only on the voltage source at its own terminals, but also on the current in all other nearby antennas. Therefore the impedance at the terminals of an array element depends on the array configuration and excitations. Obviously, if a designer is to accurately predict the pattern and especially the input impedance of an array he or she must be able to take into account such mutual coupling effects.

In general, it has been very difficult in the past to calculate mutual coupling effects, and so analysis and design of arrays were initially based on the assumption of constant current generators at the terminals of the array elements, as was done in the preceding sections of this chapter. However, as we shall see in Chapter 7, present day numerical procedures now make it possible to more or less routinely take into account mutual coupling effects. Although the subject of mutual effects will be taken up more fully in Chapter 7, in this section we will attempt to impart some physical understanding to aid, for example, in the explanation of phased arrays in the following section and in the study of wire antennas such as the Yagi-Uda array in Chapter 5.

To begin a discussion of mutual coupling effects, consider the input impedance, or driving point impedance, of any element in an array of N elements. The relationship between the various currents and voltages are given by the familiar network relationships

$$\begin{aligned} V_1 &= Z_{11}I_1 + Z_{12}I_2 + \cdots + Z_{1N}I_N \\ V_2 &= Z_{21}I_1 + Z_{22}I_2 + \cdots + Z_{2N}I_N \end{aligned} \quad (3-94)$$

$$V_N = Z_{N1}I_1 + Z_{N2}I_2 + \cdots + Z_{NN}I_N$$

where V_n and I_n are the impressed current and voltage in the n th element, Z_{nn} is the self-impedance of the n th element when all other elements are open circuited, and $Z_{mn}(=Z_{nm}$ by reciprocity) is the mutual impedance between the m th and n th elements. The *mutual impedance* Z_{mn} between the two terminal pairs of elements m and n is the open circuit voltage produced at the first terminal pair divided by the current supplied to the second when all other terminals are open circuited, that is,

$$Z_{mn} = \left. \frac{V_m}{I_n} \right|_{I_i=0} \quad \text{for all } i \text{ except } i = n. \quad (3-95)$$

The *active impedance* of an element is the input impedance of that element when all other elements are excited. For example, from (3-94) the active impedance of element 1 is

$$Z_{1, \text{in}} = \frac{V_1}{I_1} = Z_{11} + \frac{I_2}{I_1}Z_{12} + \cdots + \frac{I_N}{I_1}Z_{1N}. \quad (3-96)$$

We note that the active impedance is not merely the sum of the self-impedance and all the mutual impedances, but depends on the various currents as well.

Intuitively, one can suggest gross guidelines for estimating the degree of mutual coupling.

1. To a first-order approximation, the strength of the coupling decreases as spacing increases.
2. Considering the free-space pattern of each element, if the elements are oriented such that they are illuminated by a pattern maximum then the coupling will be appreciable. If, on the other hand, the individual patterns exhibit a null in the direction of the coupled antennas, the coupling will be small. For example, two similar parallel elements such as dipoles will couple much more strongly than two collinear elements.

Figures 3-26, 3-27, and 3-28 illustrate these points for the cases of two resonant (when isolated) half-wave dipoles which are parallel, collinear, and staggered.

Next, let us consider how we might measure the mutual impedance between two antennas. Suppose an antenna when isolated in free space has a voltage V_1 and a current I_1 , so the input impedance is

$$Z_{in} = Z_{11} = \frac{V_1}{I_1} \quad (3-97)$$

If a second antenna is brought into proximity with the first then radiation from the first antenna will induce currents on the second, which in turn will radiate by virtue of that induced current and influence the current on the first antenna. The

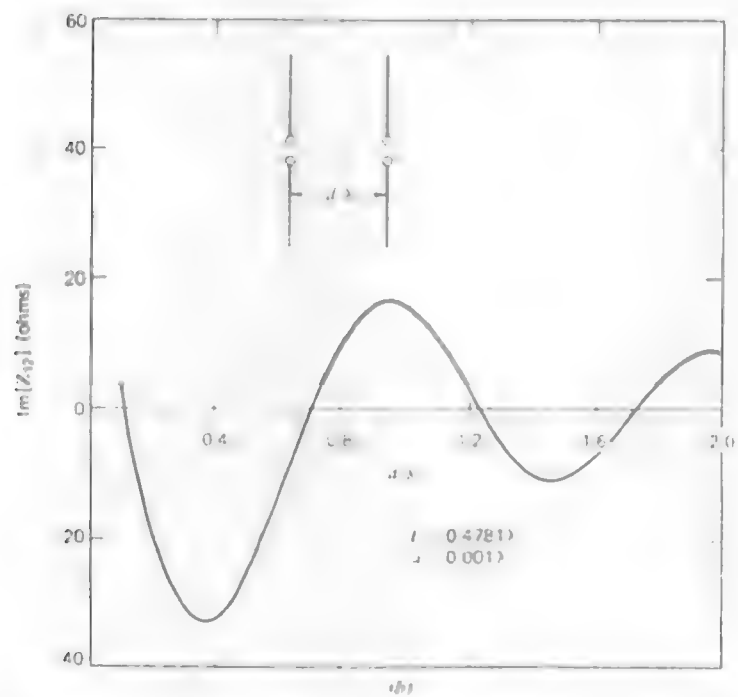
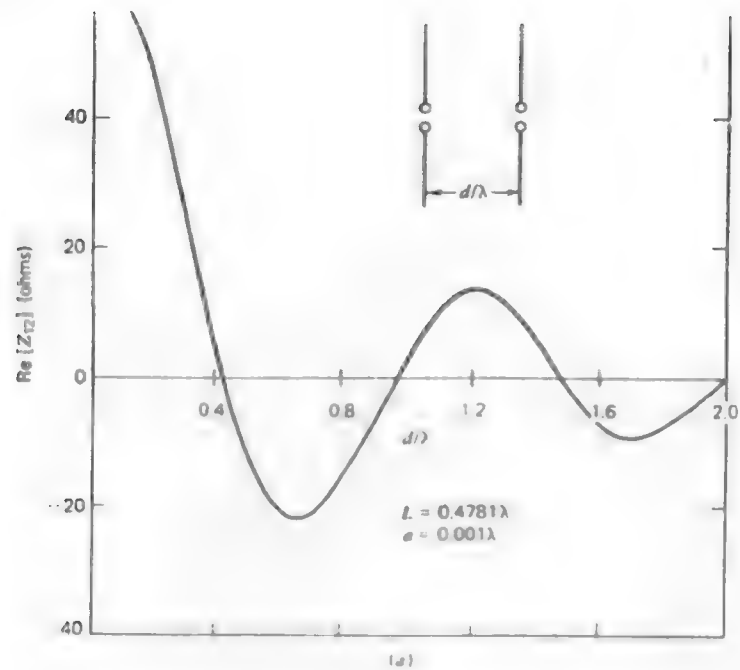


Figure 3-26 The mutual impedance between two resonant parallel dipoles as a function of their spacing relative to a wavelength. (a) The real part. (b) The imaginary part.

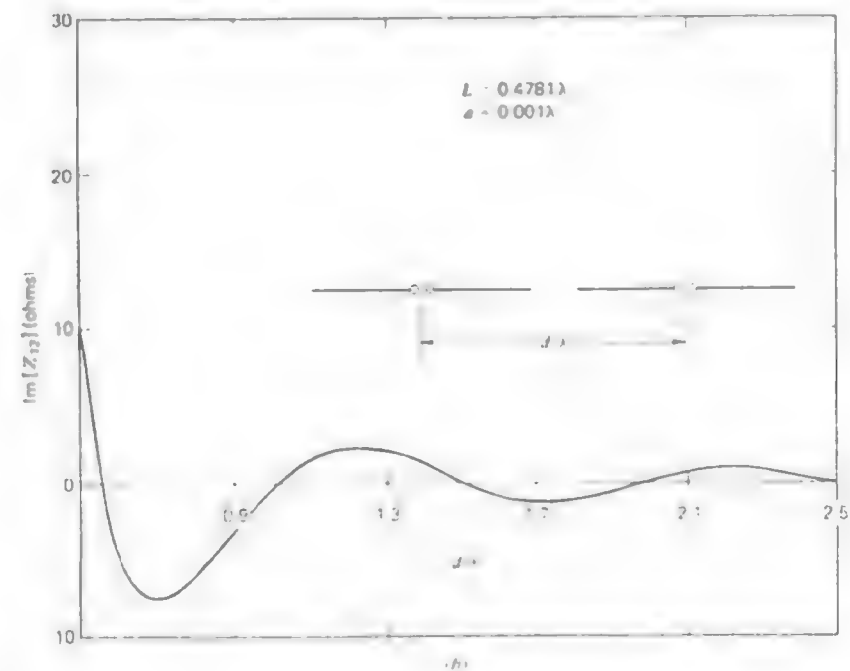
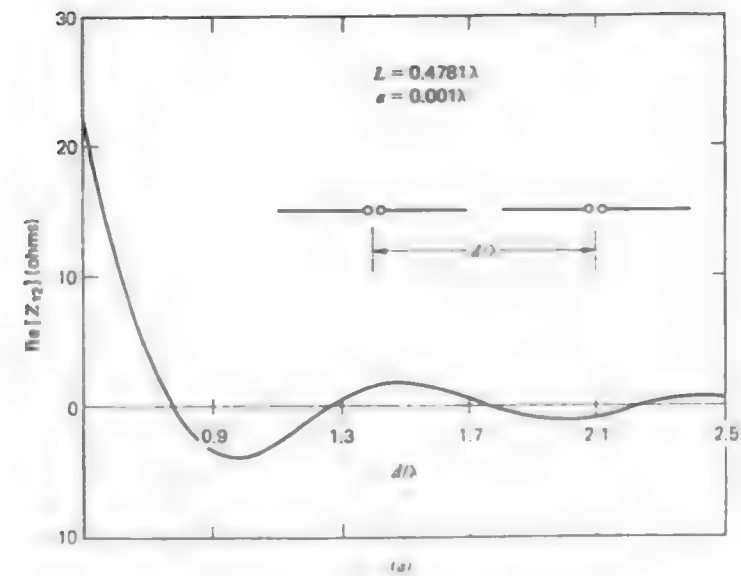


Figure 3-27 The mutual impedance between two resonant collinear dipoles as a function of spacing relative to a wavelength. (a) The real part. (b) The imaginary part.

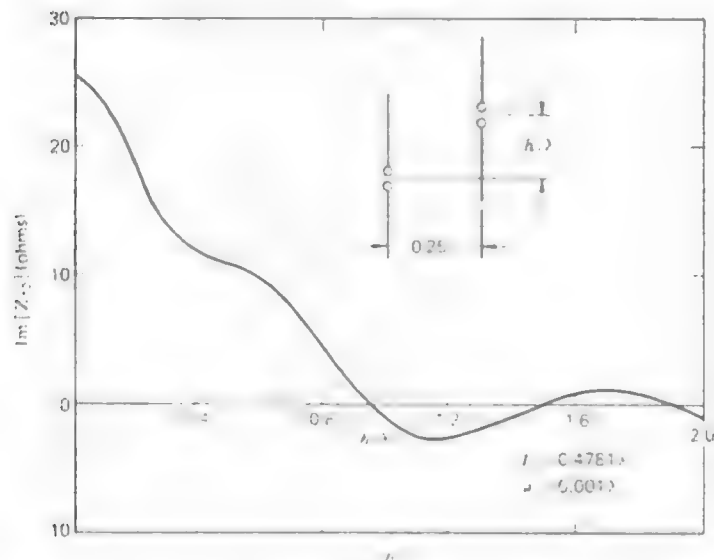
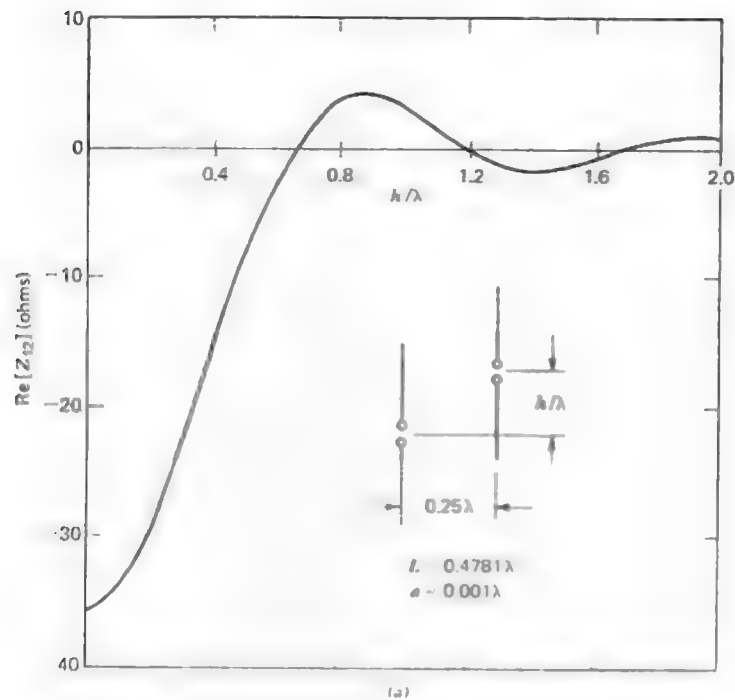


Figure 3-28 The mutual impedance between two resonant staggered dipoles as a function of spacing relative to a wavelength. (a) The real part. (b) The imaginary part

second antenna may either be excited or unexcited (parasitic), but in any case it has terminal current I_2 . Then the total voltage at the first antenna is

$$V_1 = Z_{11}I_1 + Z_{12}I_2. \quad (3-98)$$

Similarly, the voltage at the terminals of the second antenna is expressed by

$$V_2 = Z_{21}I_1 + Z_{22}I_2. \quad (3-99)$$

Note that (3-94) is a generalization of (3-98) and (3-99) and of (1-164) and (1-165).

Now suppose the second antenna has a load impedance Z_2 across its terminals such that $V_2 = -Z_2I_2$; see Fig. 7-21. We may write (3-99) as

$$-Z_2I_2 = Z_{21}I_1 + Z_{22}I_2. \quad (3-100)$$

Solving for I_2 we obtain

$$I_2 = \frac{-Z_{21}I_1}{Z_{22} + Z_2} = \frac{-Z_{12}I_1}{Z_{22} + Z_2} \quad (3-101)$$

Substituting this into (3-98) and dividing by I_1 , we find that

$$\frac{V_1}{I_1} = Z_{11, \text{in}} = Z_{11} - \frac{(Z_{12})^2}{Z_{22} + Z_2}. \quad (3-102)$$

This expresses the input impedance in terms of the two self-impedances (Z_{11} and Z_{22}), the mutual impedance (Z_{12}) and the load (Z_2) at the unexcited terminals of antenna 2. For example, if the two antennas in question are half-wave dipoles and if the terminals of the second dipole are open circuited, then $Z_{1, \text{in}} = Z_{11}$ because $Z_2 = \infty$. Physically this means that very little current is induced on each of the arms of the second dipole. As a consequence, one could measure the self-impedance of the first dipole in the presence of the second simply by open circuiting the second dipole thereby rendering it nonresonant and reducing the current on it. Clearly one could not do this if the second dipole were, say, one wavelength long (see Fig. 5-3).

The above discussion suggests the equivalent circuit of Fig. 3-29 for the coupling between two resonant antennas (see Prob. 1.7-4). Note that if the terminals on the right are open circuited $Z_{1, \text{in}} = Z_{11}$.

In general, to determine the mutual impedance between two antennas, we perform the following three measurements [7].

1. Measure Z_{11} at the terminals of antenna 1 with antenna 2 either removed or open circuited
2. Measure Z_{22} in a similar manner to that for Z_{11}

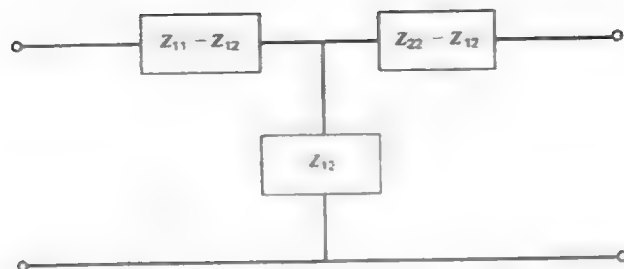


Figure 3-29 Network representation of the coupling between two antennas

3. Measure $Z_{1, \text{in}}$ when antenna 2 is short circuited, that is, $Z_2 = 0$. From (3-102) we find that

$$Z_{12} = \sqrt{Z_{22}(Z_{11} - Z_{1, \text{in}})} \quad (3-103)$$

All quantities on the right are known from the three measurements and thus Z_{12} can be computed. Knowing the mutual impedance we can then use (3-96) to calculate the active impedance. In turn, knowing the active impedance, we can determine the voltage necessary to establish the current required for the proper array radiation pattern. Of course this procedure is only valid for a two-element array. In general, it is necessary to use the system of equations given by (3-94) in an antenna synthesis procedure.

3.7 PHASED ARRAYS

An array antenna whose main beam maximum direction or pattern shape is controlled primarily by the relative phase of the element excitation currents is referred to as a **phased array**. Phased arrays⁴ are finding increasing application in radar where extremely fast tracking is required, in direction finding, and communications where the radiation pattern must be adjusted to accommodate varying traffic conditions. In this section the scanning of the pattern main beam by element current phase control is discussed. Pattern shaping by element current amplitude and phase control is found in Chapter 10.

Consider an array of similar elements with centers at arbitrary locations on the z -axis. The currents are

$$I_n = I_0 e^{j\alpha_n} \quad (3-104)$$

If the elements are phased so that

$$\alpha_n = -\beta z_n \cos \theta_0, \quad (3-105)$$

the array is said to be of *linear phase*, or *uniform progressive phase*. The phase shift is linear with the element positions z_n and the slope, or proportionality constant, is $\beta \cos \theta_0$. The array factor (3-65) then becomes

$$AF = \sum_{n=0}^{N-1} A_n e^{j\beta z_n (\cos \theta - \cos \theta_0)}. \quad (3-106)$$

The array factor is maximum when the far-field contributions from the elements add in-phase. This occurs for $\cos \theta = \cos \theta_0$, or $\theta = \theta_0$. In other words, the main beam maximum direction is θ_0 . For an equally spaced array $z_n = nd$ and $\alpha_n = n\alpha$ where $\alpha = -\beta d \cos \theta_0$.

If the phase of each element is changed with time according to (3-105) the pattern is scanned and thus the main beam pointing direction θ_0 changes with time. Figure 3-30 shows the patterns of a linear array with different linear phase shifts. Note that as the beam is scanned from broadside ($\theta_0 = 90^\circ$) the main beam broadens. This is called *beam broadening*. Remember that the entire pattern is formed by rotating the pattern shown around the z -axis. It turns out that as the main beam is scanned away from broadside the main beam broadening is just about compensated by the reduced volume contained in the total pattern (formed by rotation about the array axis). The directivity as a function of scan angle is found in Fig. 3-21 for five element arrays. For equally spaced arrays with spacings less than a half-wavelength, as the beam approaches endfire it is not broadening as rapidly as is the pattern volume decreasing. Therefore, the directivity remains nearly constant for wide scan angles about broadside but increases near endfire. For slightly greater than half-wavelength spacings, a grating lobe begins to appear for scan angles near endfire and the directivity decreases. Again, refer to Fig. 3-21.

If an equally spaced array has half-wavelength spacings, there is exactly one period of the array factor in the visible region. At endfire then, there will be two endfire main lobes. For spacings greater than a half-wavelength, part or all of a grating lobe will become visible before endfire is reached. When large interelement spacings are used and many grating lobes appear in the visible region the array is called an *interferometer*. Each major lobe has a narrow beamwidth but there are many of them. If large element antennas are used, the element pattern will also have a relatively narrow beam which will decrease the size of the grating lobes.

Occasionally array element currents have a phase that is nonlinear with distance along the array. Nonlinear phase arises in certain shaped-beam synthesis cases. The pattern, of course, can still be scanned by applying a linear phase. Then α_n would contain both a linear part as in (3-105) and a nonlinear part.

⁴ An excellent review of microwave phased arrays is found in [9].

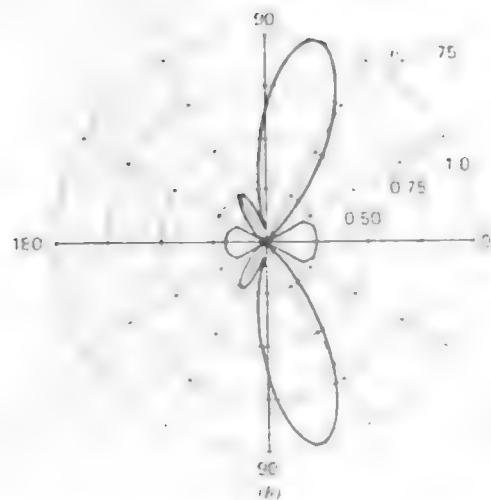
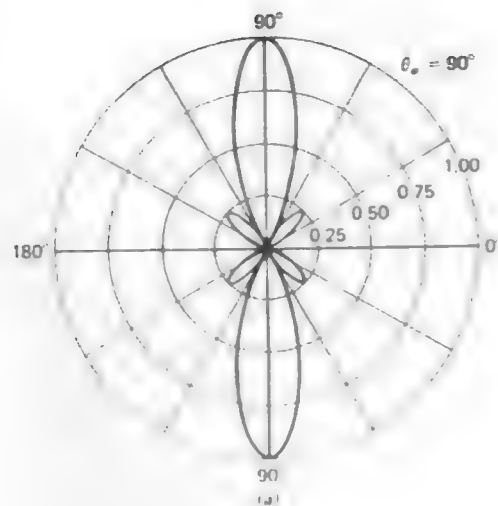
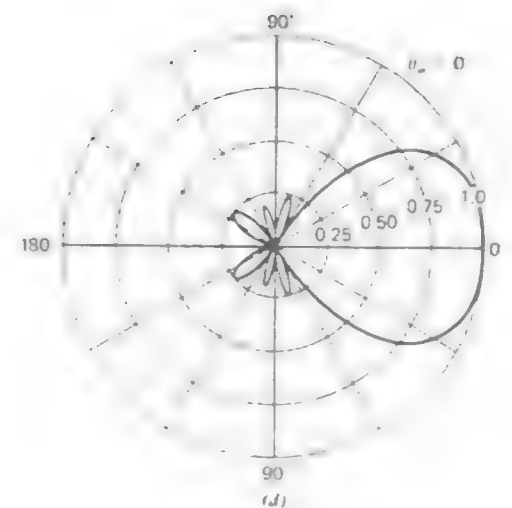
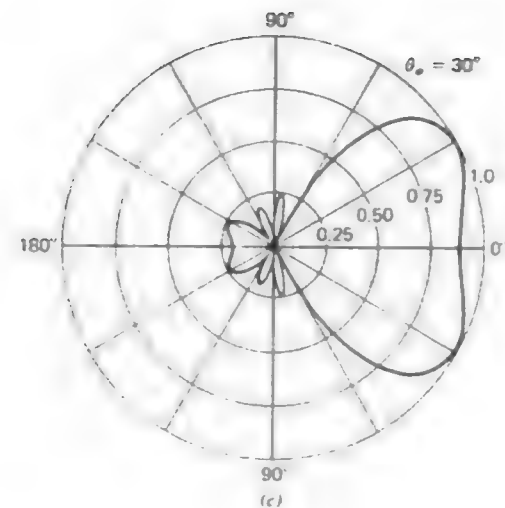


Figure 3-30 Scanned patterns of a uniformly excited, equally spaced ($d = 0.4\lambda$), five-element, linear phased array. The patterns are linear, polar plots. The element phases are found from (3-105) with $\alpha_n = n\theta_0$. (a) Broadside case; $\theta_0 = 90^\circ$ (b) $\theta_0 = 75^\circ$



(c) Bifurcated pattern; $\theta_0 = 30^\circ$. (d) Endfire case; $\theta_0 = 0^\circ$

In ordinary array theory as described in Section 3.3, the principle of pattern multiplication allows us to factor the total pattern as

$$F(\theta, \phi) = g_a(\theta, \phi) f(\theta, \phi). \quad (3-107)$$

Here $g_a(\theta, \phi)$ is the pattern of a single element of the array when physically far removed from all other elements of the array. The array factor $f(\theta, \phi)$ is the pattern of an array with the elements replaced by point sources with the same current amplitudes and phases. This idealization is used when the element antennas are similar; that is, each element of the array has an element pattern given by $g_a(\theta, \phi)$. In practice, the performance of an element operating in the array environment is different from its performance when isolated. Each element of the array is affected by the presence of other elements as discussed in the previous section. Since this mutual coupling depends on the array geometry, the performance of the elements in the array will vary with location in the array as well as scan angle. This is because in a (finite) array each element operates in a different environment. For example, an element on the end of a linear array "sees" all of elements in one direction and none in opposite direction, whereas the center element of the array "sees" half of the elements in each direction.

The effect of mutual coupling between array elements is threefold. First, the impedance of an element when operated in the array differs from its impedance when it is far removed from any objects, as we saw in the previous section. The impedance depends both on the location within the array and also the main beam scan angle, that is, element phasing; see (3-96). Second, the radiation pattern of an element when operated in the presence of the other array elements is different from its pattern when isolated. Again the pattern of an individual element in the array depends on its location in the array. Finally, the polarization characteristics of an array of similar elements may be different from that of a single isolated element.

The (unnormalized) pattern of an array which includes the effects of mutual coupling is found as follows

$$F_{un}(\theta, \phi) = \sum_n g_a(\theta, \phi, n) I_n e^{j\mathbf{r}_n' \cdot \hat{\mathbf{r}}} \quad (3-108)$$

where $g_a(\theta, \phi, n)$ is the pattern of the n th element of the array when operated at its appropriate position in the array. The vector \mathbf{r}_n' is a position vector from the coordinate origin to the element position, and $\hat{\mathbf{r}}$ is unit spherical radius vector for the same coordinate system; see (1-93). This formulation does not restrict the element centers to be located along a line, but permits arbitrary locations in space. In general, a knowledge of the patterns $g_a(\theta, \phi, n)$ is not available. However, in many cases it is possible to obtain an approximate pattern expression. If the array is large so that edge effects are small, the elements and their generator impedances are nominally identical, and the elements are regularly

spaced so that each element "sees" about the same environment, then we can obtain an *array-element factor* $g_{ae}(\theta, \phi)$. This factor is an element pattern of a "typical" element in the array and it contains the pattern effects of the element type plus interaction effects between elements. It may be obtained by exciting a typical element and match loading the remaining elements of the array. Since the array-element factor is typical of element performance, (3-108) can be approximated as

$$F_{un}(\theta, \phi) \approx g_{ae}(\theta, \phi) \sum_n I_n e^{j\mathbf{r}_n' \cdot \hat{\mathbf{r}}}. \quad (3-109)$$

Note that the summation is now the array factor, that is, the pattern of point sources with position vectors \mathbf{r}_n' and currents I_n .

So far we have not discussed how power is distributed to elements of an array. There are many techniques employed in practice but they can be broadly classified into three types: parallel, series, or space feed networks. Figure 3-31 shows examples of each. The *parallel feed* of Fig. 3-31a is also called a *corporate feed* because it is similar to a corporate structure diagram of a large corporation. Note that the path length to each element is equal, thus the amplitude and phase of the currents will also be equal. Variable attenuators and phase shifters may be inserted to adjust the amplitude and phase if desired.

The array of Fig. 3-31b employs a *series feed*, which is easy to construct but may be difficult to design. As the wave travels down the transmission line it is attenuated because of power radiated by the antenna elements. This must be accounted for in the design by determining the fraction of power radiated by each element. The load impedance is usually a matched load to prevent reflections. The relative phase between each pair of adjacent elements is determined by the transmission line electrical length and the effects of mutual coupling. By changing the frequency, the electrical length, and thus the phase between each element, is changed. The resulting phase control via frequency control can be used to steer the pattern main beam. This is referred to as *frequency scanning*. In all series fed arrays the relative phases of the antenna elements are affected by changes in frequency, whereas in parallel fed arrays they are not. One example of a series fed array is a waveguide with milled slots which act as radiating elements.

A way to avoid a complicated feed structure is to use a *space feed*. An example is shown in Fig. 3-31c. One primary radiating antenna is excited by the transmitter and is used to illuminate several pickup antennas. The relative current amplitudes in each pickup antenna is determined by the radiation properties of the primary antenna. Phase differences may arise due to the different path lengths from the primary antenna to the pickup antennas. Each pickup antenna is connected, through perhaps a variable attenuator and/or phase shifter, to a secondary transmitting antenna. These secondary transmitting antennas then form the array.

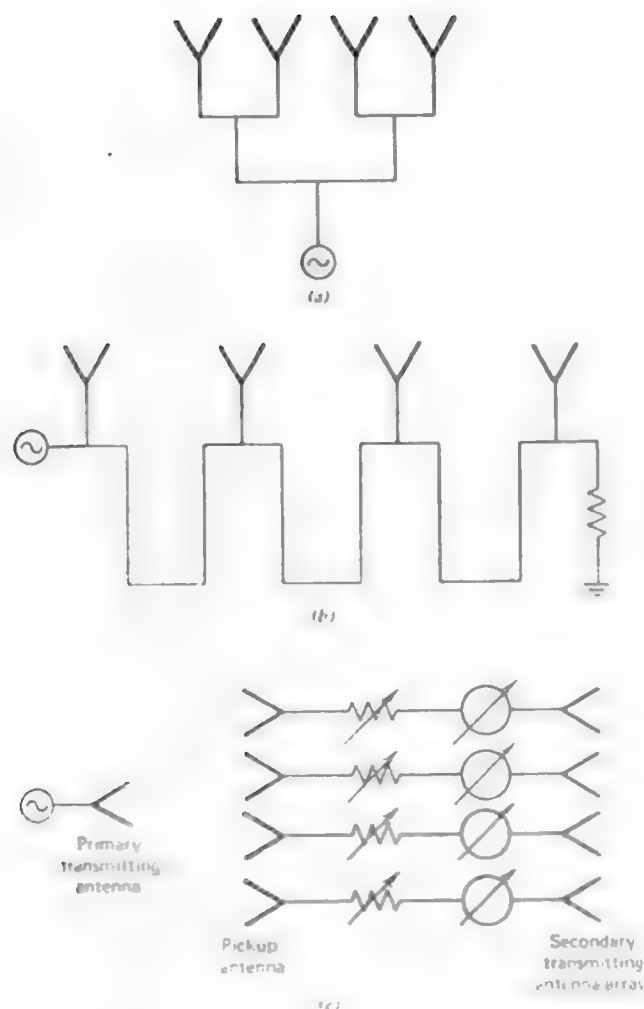


Figure 3-31 Various types of feeding structures for arrays
(a) The corporate (or parallel) feed (b) The series feed. (c)
The space feed

Array antennas are encountered in practice with many element types and configurations. For example, a very popular antenna system is one employing an array of antennas (usually horns) feeding a reflector antenna. This utilizes the large aperture of the reflector as well as the scanning capabilities of the feed array. Also, practical array antenna feed networks are of many hybrid forms. For example, the Hostile Weapons Locator System (HOWLS) experimental radar

system for use in small Remotely Piloted Vehicles is a linear phased array which combines corporate and series feeds [10]. The input is divided 16 ways with a corporate feed and then each corporate feed output is connected to a series fed subarray with 13 microstrip dipole radiating elements. The amplitudes to each of the 208 elements is that of the 25-dB ($\bar{n} = 3$) Taylor line source (see Section 10.4.2), which is similar to the Dolph-Chebyshev array. The array has a half-power beamwidth of 0.45° at 16 GHz, is 2.5 m long, can be scanned $\pm 30^\circ$, has a gain of 27.5 dB and a side lobe level of -18.5 dB. This array architecture yields an array system that can be mass produced without individual optimization of each element after production.

3.8 PERSPECTIVE

The first five sections of this chapter dealt with the analysis of linear arrays of elements having known currents. From this analysis it was possible to learn many things about arrays, such as how to scan a main beam and how to control side lobe levels. Of necessity, the analysis ignored mutual coupling. In some simple design situations it may be valid to do so. In more complex design settings mutual coupling must be taken into account, often quite accurately. This is not an easy task. One of the real challenges in the design of arrays for the creation of a desired pattern is the actual establishment of the current on the elements dictated by the analysis procedure. The mutual coupling aspect of array design will be addressed further in subsequent chapters.

Also in this chapter the relationship between a current distribution in space and its radiation pattern was established. We found that for a uniformly spaced array the array factor takes the mathematical form of a Fourier series; see (3-18). In the next chapter we will see that the pattern factor of a continuous current source in the form of a line source is related to the current distribution by a Fourier transform. In both cases (discrete or continuous current distributions) the same general principles apply. That is, as the current amplitude taper toward the ends of the source is increased, the side lobes are reduced and the beamwidth is increased. Also, the main beam pointing direction can be scanned by applying a phase shift along the source which is linear with distance. These general features which we have demonstrated for linear arrays will be seen to hold true for all types of antennas.

REFERENCES

1. J. D. Kraus, *Antennas*, McGraw-Hill, New York, 1950; Appendix 17
2. R. C. Hansen, Editor, *Microwave Scanning Antennas, vol. II, Array Theory and Practice*, Academic Press, 1966; pp. 23-29

3. W. W. Hansen and J. R. Woodyard, "A new principle in directional antenna design," *Proc. IRE*, vol. 26, pp. 333-345, March 1938.
4. C. T. Tai, "The optimum directivity of uniformly spaced broadside arrays of dipoles," *IEEE Trans. on Antennas and Propagation*, vol. AP-12, pp. 447-454, July 1964.
5. H. Bach, "Directivity diagrams for uniform linear arrays," *Microwave Journal*, vol. 15, pp. 41-44, Dec. 1972.
6. H. Bach, "Directivity of basic linear arrays," *IEEE Trans. on Antennas and Propagation*, vol. AP-18, pp. 107-110, Jan. 1970.
7. S. A. Schelkunoff, "A mathematical theory of linear arrays," *Bell System Technical Journal*, vol. 22, pp. 80-107, Jan. 1943.
8. R. C. Hansen, Editor, *Microwave Scanning Antennas*, vol. 11, *Array Theory and Practice*, Academic Press, 1977; Chapter 2.
9. L. Stark, "Microwave theory of phase-array antennas - a review," *Proceedings of the IEEE*, vol. 62, pp. 1661-1701, Dec. 1974.
10. J. Barker and M. E. Davis, "Ku band linear phased array," *Microwave Journal*, vol. 20, pp. 44-46, 58, Oct. 1966.
11. N. A. McDonald, "Approximate relationship between directivity and beamwidth for broadside collinear arrays," *IEEE Trans. on Antennas and Propagation*, vol. AP-26, pp. 240-241, March 1978.

PROBLEMS

3.1-1 Consider an array of two elements spaced one wavelength apart with currents that are equal in amplitude and 180° out-of-phase.

- (a) Use the inspection method to rough sketch the polar plot of the array factor.
- (b) Derive the exact array factor as a function of θ if the elements are on the z -axis.
- (c) For what angles of θ is this array factor maximum?
- (d) What is the expression for the normalized array factor $|f(\theta)|^2$?
- (e) Show that (3-20) reduces to your answer in (d).

3.1-2 Use the techniques of Fig. 3-9 to obtain a polar plot of the array factor of the array given in Prob. 3.1-1.

3.1-3 Use the techniques of Fig. 3-9 to obtain a polar plot of the array factor of a two-element, one-wavelength spaced array with equal amplitude and equal phase currents (Example 3-4).

3.1-4 Usually the interelement spacing of an array is about one-half wavelength. Spacings much greater than this produce major lobes in undesired directions. To illustrate this point use the techniques of Fig. 3-9 to sketch the array factor for a two-element array with equal amplitude, in-phase elements in polar form for the following spacings: (a) $d = 3\lambda/4$, and (b) $d = 2\lambda$. Examples 3-1 and 3-4 and this problem show the effects of spacing on an array of fixed excitation.

3.1-5 Using the array factor for a two-element broadside array ($\tau = 0$) with equal current amplitude point source elements, show that the directivity expression is

$$D = \frac{1}{1 + (\sin \beta d)^2}$$

Hint: Change from variable θ to $\psi = \beta d \cos \theta$

3.1-6 Plot the directivity expression of Prob. 3.1-5 as a function of d from zero to two wavelengths.

3.2-1 Prove that the array factor magnitude $|f(\psi)|$ for a uniformly excited, equally spaced linear array is symmetric about $\psi = \pi$.

3.2-2 Show that the array factor expressions (3-20) and (3-35) for a two-element uniformly excited array are identical.

3.2-3 Derive (3-44).

3.2-4 The expression for the half-power beamwidth of the array factor for a broadside, uniformly excited, equally spaced, linear array may be approximated as

$$HP \approx K \frac{\lambda}{Nd}$$

for $Nd \gg \lambda$. Determine K for $N = 10$ and 20 , and compare to (3-45).

3.2-5 In this problem the effects of phasings and spacings on a simple array are illustrated. Consider an equally spaced five-element array with uniform current amplitudes. Sketch the array factors for:

- (a) $d = \lambda/2$, broadside case ($\theta_0 = 90^\circ$)
- (b) $d = \lambda$, broadside case.
- (c) $d = 2\lambda$, broadside case
- (d) $d = \lambda/2$, $\theta_0 = 45^\circ$.
- (e) $d = \lambda/2$, $\theta_0 = 0^\circ$.

These five plots can be obtained from one universal pattern plot as discussed in Sections 3.1 and 3.2. For the last two cases determine the interelement phase shift α required to steer the main beam as specified.

3.2-6 Repeat Prob. 3.2-5 using the ARRFAC and PLOT computer programs in Appendix G.

3.2-7 Design a five-element uniformly excited, equally spaced linear array for:

- (a) Main beam maximum at broadside.
- (b) Main beam maximum at 45° from broadside ($\theta_0 = 45^\circ$)

In each case select the element spacing and linear phasing such that the beamwidth is as small as possible and also so that no part of a grating lobe appears in the visible region. Sketch the polar plots of the patterns.

3.2-8 Design and plot the array factor for an ordinary endfire, five-element, uniformly excited linear array with spacings $d = 0.35\lambda$. Use $\theta_0 = 180^\circ$ and find α . Compare the polar pattern to the one in Fig. 3-14 which is of a similar array with increased directivity.

3.3-1 Two collinear half-wave dipoles are spaced a half-wavelength apart (but not quite touching) with equal amplitude and equal phase terminal currents. What is the expression for the far-field pattern $F(\theta)$ if the element centers are along the z -axis? Use pattern multiplication ideas to rough sketch the pattern.

3.3-2 (a) Repeat Prob. 3.3-1 for one-wavelength spacing.

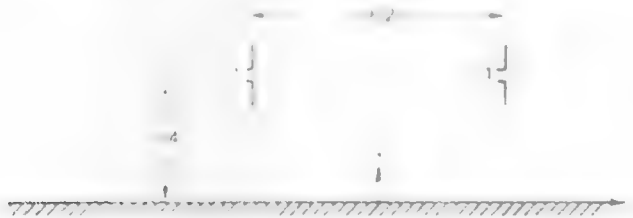
- (b) Plot $F(\theta)$ directly to check your pattern multiplication result.

3.3-3 Two parallel half-wave dipoles are spaced one wavelength apart with equal amplitude and equal phase terminal currents. The element centers are along the z -axis and the dipoles are parallel to the x -axis. Write the expressions for the far-field pattern $F(\theta, \phi)$. Rough sketch this pattern, using pattern multiplication ideas, in both the xz -plane and the yz -plane.

3.3-4 A linear array of three, quarter-wavelength long, vertical monopoles are operated against an infinite, perfectly conducting ground plane. Let the element feeds be along the z -axis, the ground plane in the yz -plane, and the monopoles in the x -direction.

- Design the array as a Hansen-Woodyard increased directivity endfire array, that is, determine the element spacings and phasings (choose $d = 0.3\lambda$).
- Use the universal array factor plot for three uniformly excited elements to obtain a polar plot of the array factor for this problem.
- Write the expression for the complete pattern.
- Using pattern multiplication ideas rough sketch the complete far-field patterns in the xz -plane and the yz -plane.

3.3-5 A two-element array of vertical short dipoles is operated a quarter-wavelength above a perfect ground plane as shown. The elements are a half-wavelength apart and are excited with equal amplitude and opposite phase. Obtain polar plots for the radiation pattern of this radiating system in the xz - and yz -planes. Carefully explain how you obtain these plots



3.3-6 Prove that $\cos \gamma = \sin \theta \cos \phi$. See Fig. 3-18

3.3-7 A four-element linear array of parallel, in-phase, half-wave dipoles is located $\lambda/4$ in front of a large planar reflector located in the yz -plane. Assume the reflector to be a perfect ground plane. If the dipoles are parallel to the z -axis and spaced $\lambda/2$ apart, sketch the complete pattern in the xy - and xz planes. Show your reasoning.

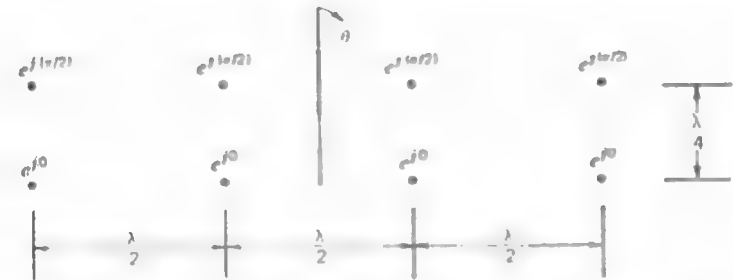
3.3-8 Use the ARRPAI and PPLOT computer programs to generate the principal plane far-field plots of:

- The array in Prob. 3.3-4
- The array of Prob. 3.3-5
- The array in Prob. 3.3-2
- The array in Prob. 3.3-3
- The array of Prob. 3.3-7

3.3-9 A uniformly excited, unequally spaced linear array of four isotropic sources is shown below. Using the principle of pattern multiplication sketch the array pattern, showing your intermediate steps. Can (3-35) and the graphical procedure be used to verify your final result? Why?



3.3-10 A two-dimensional, uniformly excited array is shown below. Using the principle of pattern multiplication sketch the pattern of the eight-element array, showing your intermediate steps.



3.4-1 Calculate the directivities in decibels for the following broadside arrays of point sources:

- $N = 2$, $d = \lambda/2$.
- $N = 10$, $d = \lambda/2$.
- $N = 15$, $d = \lambda$.

3.4-2 Evaluate (3-78) for $d = 3\lambda/8$ and $N = 10$ for:

- Broadside, and compare result to that of (3-80).
- Ordinary endfire, and compare result to that of (3-81).

3.4-3 Evaluate (3-78) and plot D as a function of d/λ for $N = 5$ and endfire operation. Compare to Fig. 3-21.

3.4-4 The approximate directivity formula of (3-80) for long, broadside linear arrays of isotropic elements can be checked in the following two ways using $HP \approx 0.886 \lambda/L$ from (3-45)

- Use $D = 4\pi \Omega_A$ to find D in terms of λ/L .
- It has been shown [11] that the following formula gives good results for broadside collinear arrays

$$D = \frac{101}{HP_A - 0.0027(HP_A)^2}$$

where HP_A is the half-power beamwidth of the array pattern in degrees. Use $HP \approx 0.886 \lambda/L$ and $L = \lambda$ to find D . $K = \lambda/L$, find K .

3.4-5 Write a computer program to calculate the directivity for the arrays given in Table 3-1. Treat N , D/λ , and γ as input variables.

3.4-6 Show that $D = N$ for an ordinary endfire linear array of equally excited isotropic elements with spacing $d = \lambda/4$.

3.4-7 Evaluate the directivity (in decibels) of a uniformly excited, broadside array of eight isotropic elements spaced 0.7λ apart in two ways: (a) from Fig. 3-20, and (b) using (3-80).

3.5-1 Use the NEISLAP and PPLOT computer programs to plot the array factors shown in Figs. 3-23 and 3-25. Verify the side lobe levels and beamwidth values.

3.5-2 (a) Show that (3-91) follows from (3-90).

(b) Show that (3-93) follows from (3-91).

3.5-3 Verify the directivity values given in Figs. 3-23c, 3-23d, 3-23e, and Fig. 3-25a.

3.6-1 Two antennas have the following self- and mutual impedances:

$$Z_{11} = 70 \angle 0^\circ, \quad Z_{22} = 100 \angle 45^\circ, \quad Z_{12} = 60 \angle -10^\circ$$

(a) Find the input impedances to antenna 1, if antenna 2 is short circuited.

(b) Find the voltage induced at the open circuited terminals of antenna 2 when the voltage applied to antenna 1 is $1 \angle 0^\circ$ V.

3.7-1 Compute the phases (in degrees) for each element current required to produce the pattern of Fig. 3-30. Choose the center element to have zero phase.

3.7-2 Obtain a family of plots similar to those of Fig. 3-30 for (a) $d = 0.5\lambda$ and (b) $d = 0.6\lambda$. You can use ARRFAC.

3.7-3 An interferometer is constructed from five collinear halfwave dipoles spaced two wavelengths apart. Sketch the polar plot of the complete array pattern. You can use ARRPAT.

3.7-4 Show how the general phase term $\beta \mathbf{r} \cdot \mathbf{r}'_n$ of (3-108) reduces to that of (3-65), $\beta z_n \cos \theta$, for a linear array.

3.7-5 A parallel fed, uniform array of five half-wave dipole elements has half-wavelength spacing at 300 MHz. The five dipoles are located along the z -axis as shown in Fig. 3-18, and they all have the same phase. If the array is operated at 360 MHz, compare the pattern in the yz -plane at 360 MHz with that at 300 MHz.

3.7-6 Repeat Prob. 3.7-5 if the array is series fed, starting with the element closest to the coordinate origin. Assume all elements have the same amplitudes and that there is 1 m of transmission line between adjacent elements which are a half-wavelength apart at 300 MHz.

4

LINE SOURCES

In Chapter 1 we found that far-zone fields are obtained by a radiation integral over the current distribution. For a line source along the z -axis the far-zone electric field intensity from (1-101) and (1-104) is

$$\mathbf{E} = \hat{\theta} j\omega\mu \frac{e^{-j\beta r}}{4\pi r} \sin \theta \int_{-L/2}^{L/2} I(z') e^{j\beta z' \cos \theta} dz' \quad (4-1)$$

where the line source current distribution $I(z')$ is of length L centered symmetrically about the origin as shown in Fig. 1-8. The far-zone magnetic field intensity is then simply $H_\phi = E_\theta/\eta$. The element factor is $\sin \theta$. The pattern factor is $f(\theta)$ and is obtained by normalizing the integral in (4-1). This pattern factor is solely determined by the current distribution $I(z')$.

In Chapter 3 we found that the far-zone fields of an array are obtained by summing over the individual element currents. For an array of collinear short dipoles the far-zone electric field intensity from (3-53) is

$$\mathbf{E} = \hat{\theta} j\omega\mu \frac{e^{-j\beta r}}{4\pi r} \sin \theta \sum_{n=0}^{N-1} I_n e^{j\beta nd \cos \theta} \quad (4-2)$$

The factor $\sin \theta$ is, in this case, the element pattern and the summation is the array factor. Note the similarities between (4-1) and (4-2); the integral in (4-1) is replaced by a summation in (4-2), z' is replaced by nd , and $I(z')$ is replaced by I_n . The line source is, in a sense, a continuous array. It will become apparent to us

in the discussion of the line source which follows that much of what we know about the pattern characteristics of discrete arrays is also true of line sources. Line sources are important because many antennas can be modeled as a line source or combination of line sources.

4.1 THE UNIFORM LINE SOURCE

We begin our discussion of line sources by considering an important special case, that of the uniform line source. A uniform line source has a current distribution with uniform amplitude and linear phase progression given by

$$I(z') = \begin{cases} I_0 e^{j\beta_0 z'} & -\frac{L}{2} < z' < \frac{L}{2} \\ 0 & \text{elsewhere} \end{cases} \quad (4-3)$$

where β_0 is the phase shift per unit length along the line source. The unnormalized pattern factor of the uniform line source is

$$f_{un}(u) = \int_{-L/2}^{L/2} I(z') e^{j\beta_0 z' \cos \theta} dz' = I_0 L \frac{\sin u}{u} \quad (4-4)$$

where

$$u = (\beta \cos \theta + \beta_0) \frac{L}{2}. \quad (4-5)$$

The evaluation of (4-4) is similar to that given in (1-108) for a broadside uniform line source.

It is convenient to introduce an angle θ_0 such that

$$\beta_0 = -\beta \cos \theta_0. \quad (4-6)$$

Then (4-5) becomes

$$u = \frac{\beta L}{2} (\cos \theta - \cos \theta_0). \quad (4-7)$$

The far-zone electric field from (4-1) and (4-4) is

$$E_\theta = \frac{j\omega\mu e^{-j\beta r}}{4\pi r} I_0 L \sin \theta \frac{\sin u}{u}. \quad (4-8)$$

The pattern factor of this uniform line source field expression is

$$f(u) = \frac{\sin u}{u}. \quad (4-9)$$

The linear, rectangular plot of this pattern is given in Fig. 1-10. It is shown in Fig. 4-1 as a logarithmic (dB), rectangular plot. The maximum occurs for $u = 0$ and is unity (0 dB) there. The nulls occur at multiples of π and are separated by π , except for the beamwidth between first nulls which is 2π .

The half-power beamwidth of the uniform line source pattern factor is found from solving

$$\frac{1}{\sqrt{2}} = \frac{\sin u_{HP}}{u_{HP}}. \quad (4-10)$$

The solutions to this are $u_{HP} = \pm 1.39$. Then from (4-7)

$$\theta_{HP} = \cos^{-1} \left(\frac{2}{\beta L} u_{HP} + \cos \theta_0 \right) = \cos^{-1} \left(\pm 0.443 \frac{\lambda}{L} + \cos \theta_0 \right). \quad (4-11)$$

The plus sign corresponds to the half-power point on the right of the main beam maximum and the minus sign to the left half-power point. So from (1-123)

$$\begin{aligned} HP &= |\theta_{HP \text{ left}} - \theta_{HP \text{ right}}| \\ &= \left| \cos^{-1} \left(-0.443 \frac{\lambda}{L} + \cos \theta_0 \right) - \cos^{-1} \left(0.443 \frac{\lambda}{L} + \cos \theta_0 \right) \right|. \end{aligned} \quad (4-12)$$

This formula is general but useful only when both half-power points appear in the visible region ($0 \leq \theta \leq 180^\circ$) which in turn requires that the arguments of the

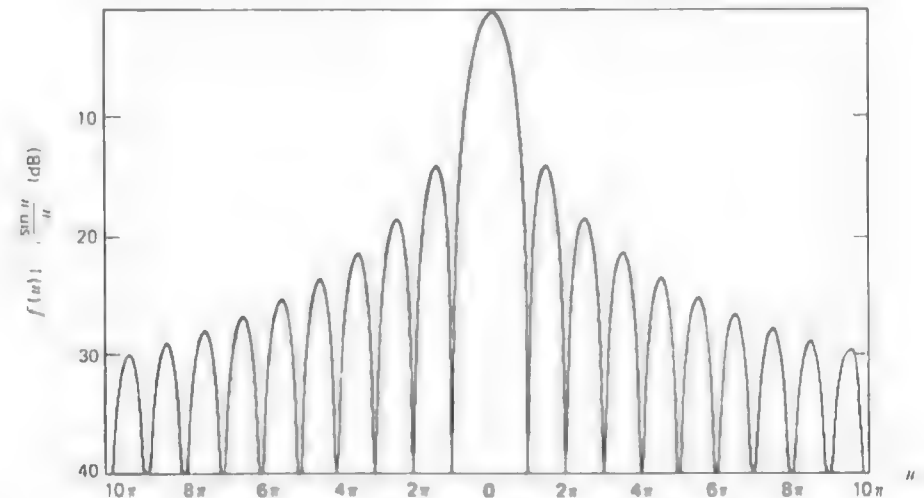


Figure 4-1 Pattern factor of a uniform line source

arccosines in (4-12) are between -1 and $+1$. For a broadside uniform line source $\theta_0 = 90^\circ$ and (4-12) reduces to (see Prob. 4.1-1)

$$\text{HP} = 2 \sin^{-1} \left(0.443 \frac{\lambda}{L} \right) \quad (\theta_0 = 90^\circ). \quad (4-13)$$

For long ($L \gg \lambda$) line sources this is approximately

$$\text{HP} \approx 0.886 \frac{\lambda}{L} \text{ rad} = 50.8 \frac{\lambda}{L} \text{ degrees} \quad (\theta_0 = 90^\circ) \quad (4-14)$$

since $\sin^{-1}(x) \approx x$ for $x \ll 1$. For an endfire uniform line source only one half-power point appears in the visible region and then

$$\text{HP} = 2 \cos^{-1} \left(1 - 0.443 \frac{\lambda}{L} \right) \quad (\theta_0 = 0^\circ \text{ or } 180^\circ). \quad (4-15)$$

For long ($L \gg \lambda$) line sources this may be approximated as (see Prob. 4.1-2)

$$\text{HP} \approx 2 \sqrt{0.886 \frac{\lambda}{L}} \text{ rad} \quad (\theta_0 = 0^\circ \text{ or } 180^\circ). \quad (4-16)$$

Since (4-16) leads to wider beamwidths than does (4-14), we conclude that beamwidth increases as the pattern is scanned away from broadside (see Fig. 4-3).

The half-power beamwidth expression $\text{HP} = 0.886(\lambda/L)$ for the broadside uniform line source was developed using two approximations. The effect of the element factor $\sin \theta$ was neglected and also it was assumed that the line source was long. With a few examples we can see how these approximations affect the beamwidth. In Table 4-1 half-power beamwidth values for three uniform line sources are presented for various levels of approximation. The first column is the HP found from the complete pattern expression

$$F(\theta) = \sin \theta \frac{\sin[(\beta L/2) \cos \theta]}{(\beta L/2) \cos \theta} \quad (\theta_0 = 90^\circ). \quad (4-17)$$

The second column is the HP obtained from only the pattern factor of (4-9). The third column is that of (4-14). Note that even for five wavelengths all values are in very close agreement. We can also see that as the length increases the approximations improve.

The largest side lobe is the first one (i.e., the one closest to the main beam).

Table 4-1 Half-Power Beamwidth Evaluation for Broadside Uniform Line Sources

Length L	Exact value from complete pattern F of (4-17)	Value from pattern factor $f = \frac{\sin u}{u}$	Value from $\text{HP} = 0.886 \frac{\lambda}{L}$
2 λ	24.766°	25.591°	25.382°
5 λ	10.112°	10.166°	10.153°
10 λ	5.071°	5.080°	5.076°

The side lobe maxima locations are found by differentiating (4-9) and setting it equal to zero. This leads to

$$u_{\text{SL}} = \tan u_{\text{SL}}. \quad (4-18)$$

The intersections of the straight line curve u_{SL} with the curve $\tan u_{\text{SL}}$ give the side lobe maximum locations (the main beam maximum is at $u_{\text{SL},0} = 0$). The first side lobe maximum occurs for $u_{\text{SL},1} = \pm 1.43\pi$. This is not precisely midway between the pattern nulls at π and 2π . The side lobe maxima are slightly closer to the main beam than midway between their nulls. Evaluating (4-9) at the first side lobe maximum location gives 0.217 or -13.3 dB.

The polar plot of the pattern factor of a uniform line source can be obtained from a universal pattern factor in a manner very similar to that used for linear arrays. The uniform line source universal pattern factor is shown in Fig. 4-2a. It is used for all source lengths L and scan angles θ_0 . A typical case is shown in Fig. 4-2b. The transformation (4-7) between u and θ is illustrated graphically by the dashed lines. Pattern values for a given value of θ can be found from the universal pattern factor using this graphical transformation. The radius of the circle used in the transformation is $\beta L/2$ and its origin is at the value of u equal to $-(\beta L/2) \cos \theta_0$.

As an example consider a three-wavelength uniform line source. The universal pattern factor is shown in Fig. 4-3a. The polar plot for the broadside case is shown in Fig. 4-3b. The pattern factor for a main beam maximum angle of 45° is polar plotted in Fig. 4-3c. The endfire case is shown in Fig. 4-3d. Notice that the main beam (and also the side lobes) widen near endfire, as pointed out earlier. The current distributions required to produce those patterns are shown in Fig. 4-4. The amplitudes are constant in all cases, as illustrated in Fig. 4-4a. The required linear phase distributions for main beam scanning are shown in Fig. 4-4b.

The effects of the element factor on the total pattern are shown in Fig. 4-5 for the three-wavelength uniform line source. In the broadside case of Fig. 4-5a the

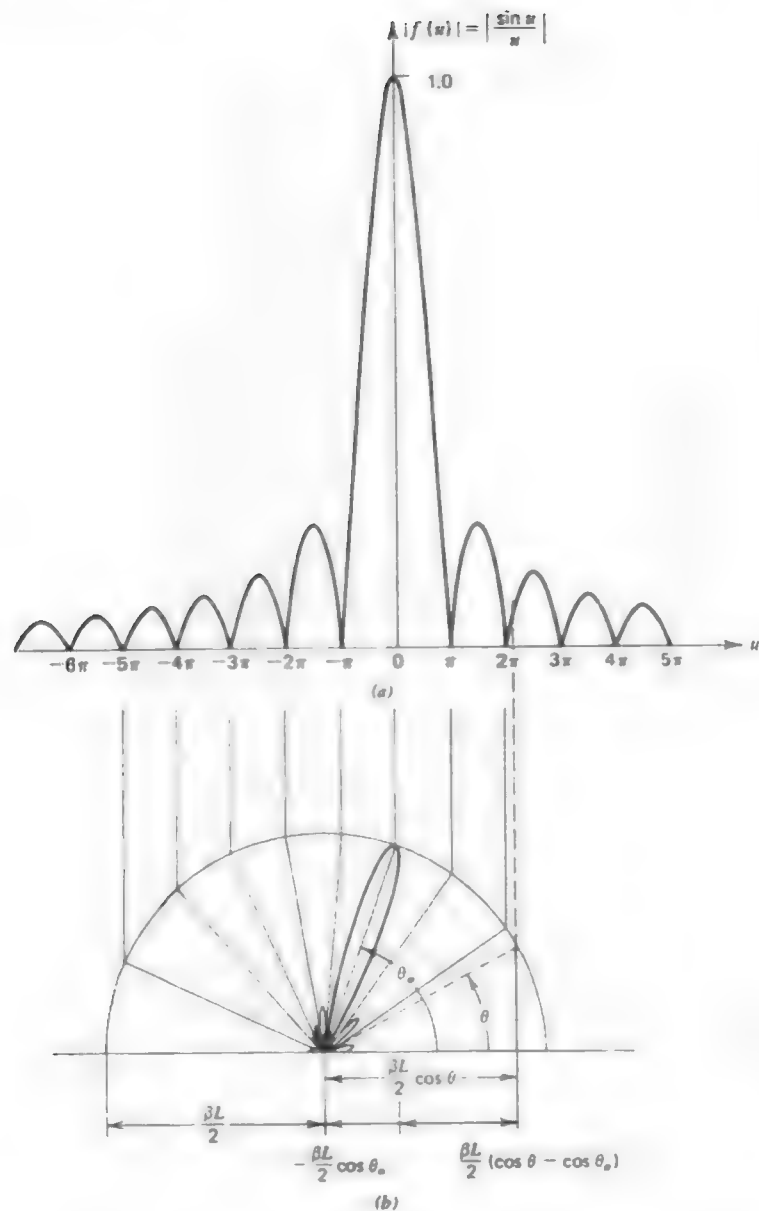


Figure 4-2 Illustration of obtaining a polar plot from the universal pattern factor of a uniform line source. (a) Universal pattern factor. (b) Polar plot of pattern factor for $L = 4\lambda$.

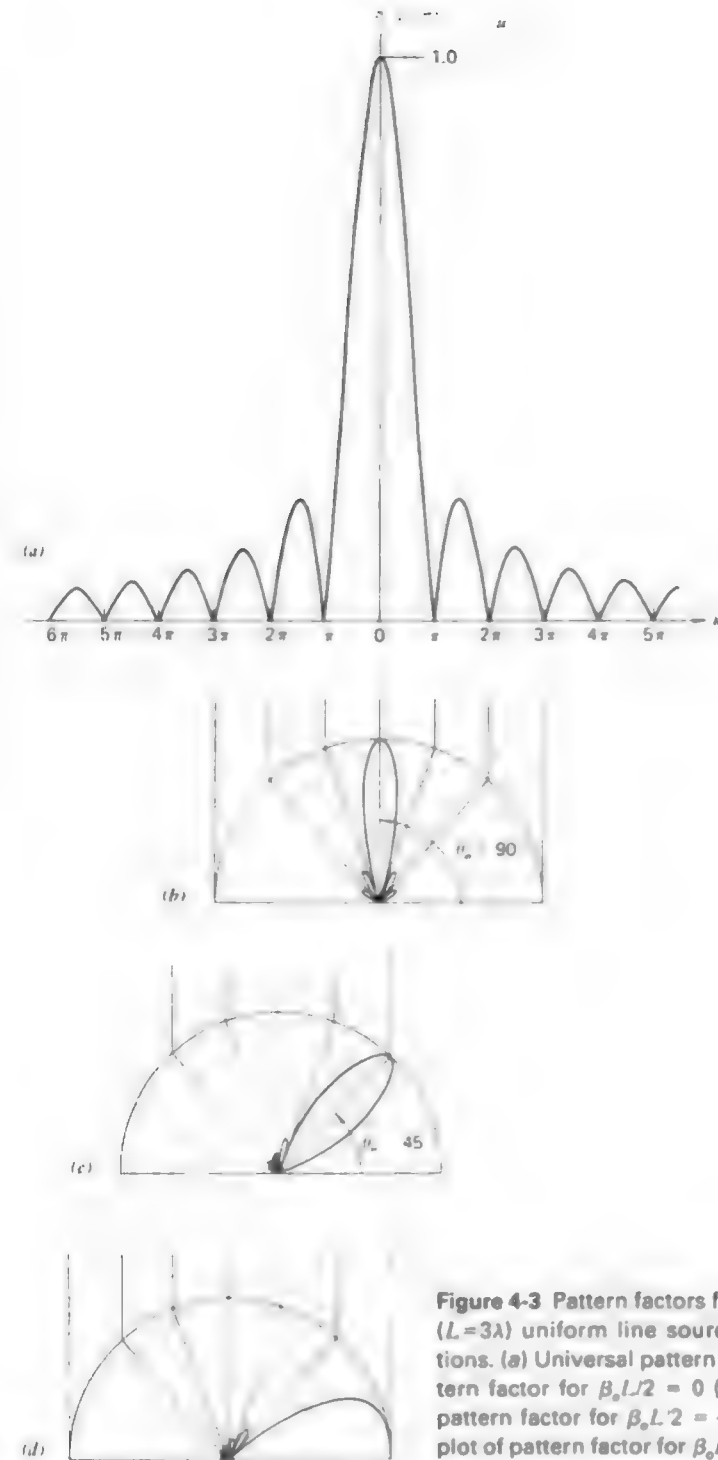


Figure 4-3 Pattern factors for a three-wavelength long ($L = 3\lambda$) uniform line source for various scan conditions. (a) Universal pattern factor. (b) Polar plot of pattern factor for $\beta_0 L/2 = 0$ ($\theta_0 = 90^\circ$). (c) Polar plot of pattern factor for $\beta_0 L/2 = -2.12\pi$ ($\theta_0 = 45^\circ$). (d) Polar plot of pattern factor for $\beta_0 L/2 = -\beta L/2 = -3\pi$ ($\theta_0 = 0^\circ$).

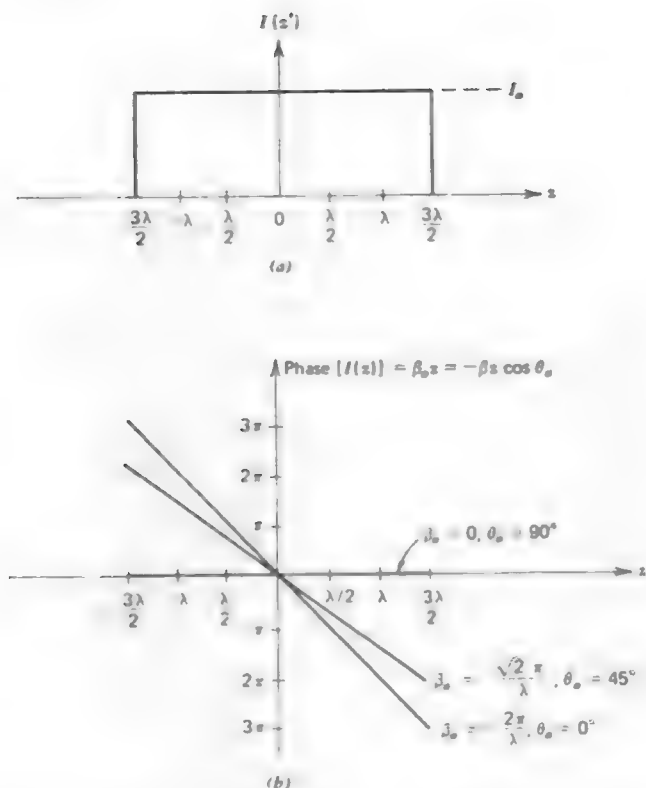


Figure 4-4 Current distributions for the three-wavelength uniform line source patterns of Fig. 4-3. (a) Current amplitude distribution. (b) Current phase distributions.

element factor has a relatively minor effect. However, in the endfire case of Fig. 4-5b where the pattern factor alone produces a single endfire beam, the element factor effect on the total pattern produces a null in the endfire direction, thus bifurcating the main beam.

Next we consider the directivity of the uniform line source. The directivity can be found easily if the element factor is assumed to have a negligible effect on the pattern. Then, we can work with the pattern factor f alone. First, the beam solid angle is from (1-140) and (4-9)

$$\Omega_A = \int_0^{2\pi} \int_0^\pi \left| \frac{\sin u}{u} \right|^2 \sin \theta \, d\theta \, d\phi. \quad (4-19)$$

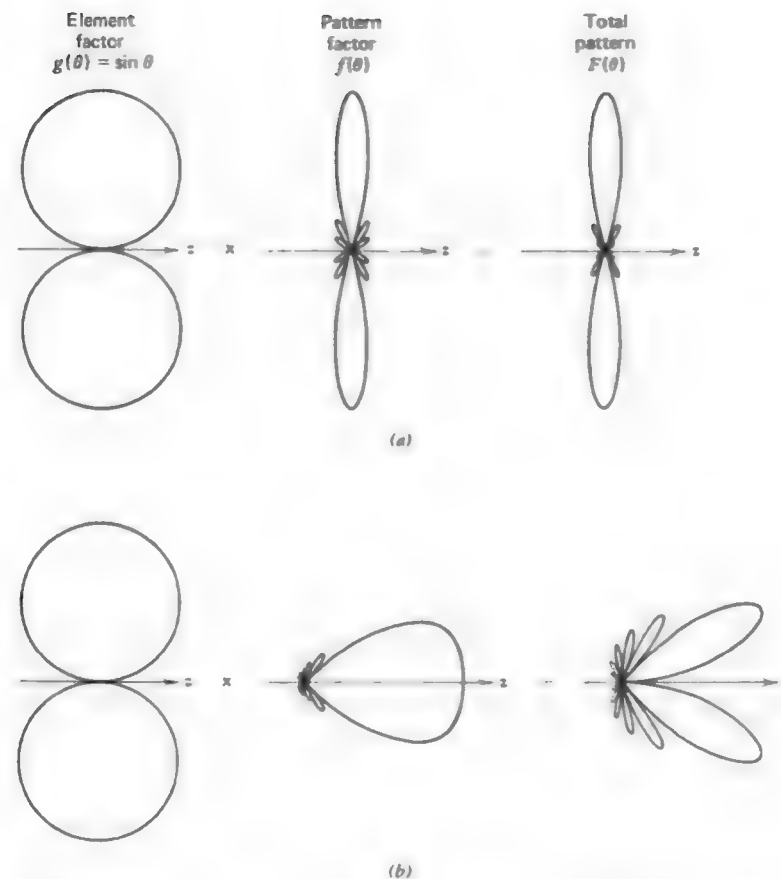


Figure 4-5 Total patterns for a three-wavelength uniform line source. (a) Broadside case ($\theta_0 = 90^\circ$, $\beta_0 = 0$). Pattern factor is from Fig. 4-3b. (b) Endfire case ($\theta_0 = 0^\circ$, $\beta_0 L/2 = -3\pi$). Pattern factor is from Fig. 4-3d.

with the element factor g set to unity. If we change the θ integration variable to u as given by (4-5) then $du = -(\beta L/2) \sin \theta \, d\theta$ and (4-19) becomes

$$\begin{aligned} \Omega_A &= \int_0^{2\pi} d\phi \int_{\theta_0 + \beta L/2}^{\pi - \beta + \beta L/2} \frac{\sin^2 u}{u^2} \frac{du}{-(\beta L/2)} \\ &= 2 \frac{\lambda}{L} \int_{\theta_0 - \beta L/2}^{\theta_0 + \beta L/2} \frac{\sin^2 u}{u^2} du. \end{aligned} \quad (4-20)$$

Evaluation of this expression for the general case is discussed in Prob. 4.1-7. For the broadside case ($\beta_o = 0$) the limits on the integral are $-\beta L/2$ to $\beta L/2$. If further $L \gg \lambda$, then $\beta L/2 \gg 1$ and we approximate the limits as $-\infty$ to $+\infty$, and using (F-12) the definite integral has a value of π . Thus $\Omega_A \approx 2\lambda\pi/L$ and $D = 4\pi/\Omega_A$ yields

$$D_u = 2 \frac{L}{\lambda} \quad (\text{broadside, } L \gg \lambda). \quad (4-21)$$

where the subscript u indicates a uniform line source. For the endfire case ($\beta_o = \pm\beta$) the integral limits are 0 and $\beta L/2$ which are approximated as 0 and ∞ when $L \gg \lambda$; this yields a value of $\pi/2$ for the integral. So $\Omega_A \approx \lambda\pi/L$ and

$$D_u = 4 \frac{L}{\lambda} \quad (\text{endfire, } L \gg \lambda). \quad (4-22)$$

These are the same directivity results we obtained for linear arrays; see (3-80) and (3-81). The uniform line source exhibits the most directivity that can be obtained from a linear phase source of fixed length. Other current distributions will yield lower directivities. We found this principle to hold true in Section 3.5 for discrete current distributions (arrays).

From the beamwidth and directivity relationships presented here for the uniform line source we can begin to get a feel for the pattern changes as a function of source length and scan angle. First consider the pattern factor alone. As the length increases, the beamwidth decreases and the directivity increases. The side lobe level (if the line source is long enough for the first side lobe maximum to be visible) remains constant with length variations: it is always -13.3 dB for a uniform line source. For a scanned line source the beamwidth increases as the main beam is scanned away from broadside. However, the total main beam volume (obtained by rotating E -plane pattern about z -axis) decreases and consequently Ω_A decreases which in turn leads to an increase in directivity. The beamwidth and directivity change slowly for scan angles near broadside but change rapidly near endfire. The complete pattern must include the element factor effects. For long sources ($L \gg \lambda$) the pattern factor $f(\theta)$ has a much narrower pattern than the element factor $g(\theta) = \sin \theta$ and the total pattern obtained from $g(\theta)f(\theta)$ is closely approximated by $f(\theta)$. The side lobe level, beamwidth, and directivity values are then accurately determined from the pattern factor $f(\theta)$ alone, except near endfire where the element factor becomes significant since it forces the total pattern to zero in the $\theta = 0$ and 180° directions, as illustrated in Fig. 4-5b.

Example 4-1. Plane Wave Incident on a Slit

A simple physical example of a uniform line source is a long narrow slit in a good conductor which has a uniform plane wave incident on it, as illustrated in Fig. 4-6. Phase

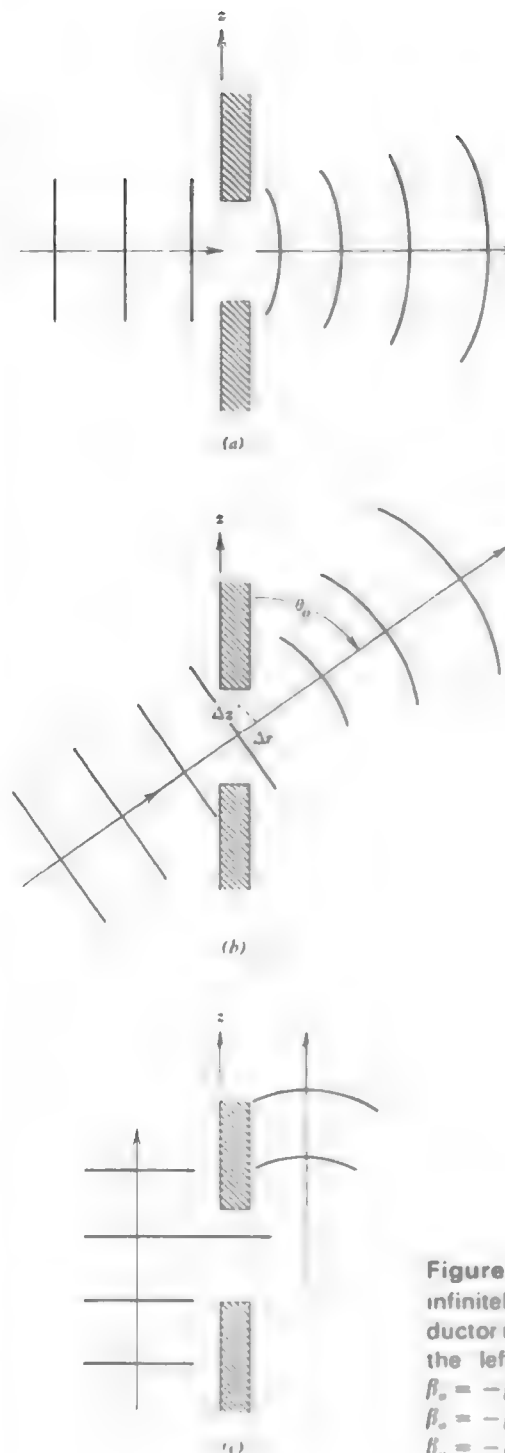


Figure 4-6 Example of a uniform line source: an infinitely long slit of width L in a good conductor illuminated by a uniform plane wave from the left. (a) Broadside case: $\theta_o = 90^\circ$ and $\beta_o = -\beta \cos 90^\circ = 0$. (b) Intermediate case: $\beta_o = -\beta \cos \theta_o$. (c) Endfire case: $\theta_o = 0$ and $\beta_o = -\beta$.

fronts (planes of constant phase) are indicated by the parallel lines. In Fig. 4-6a the wave is normally incident on the slit. Thus, the slit has a uniform amplitude excitation and also has uniform phase since the phase fronts are parallel to the slit. The slit then behaves as a uniform line source with uniform phase across it. This equivalence of a field distribution to a current distribution will be discussed further in Section 8.1. It is obvious, however, that the maximum radiation on the right-hand side of the slit will be primarily in the direction of propagation of the incident wave coming from the left, that is, $\theta_0 = 90^\circ$. For a line source the phase shift along the source is related to the direction of maximum radiation θ_0 by $\beta_0 = -\beta \cos \theta_0$, where in this case β is the phase constant of the incident plane wave. Since $\theta_0 = 90^\circ$, $\beta_0 = -\beta \cos 90^\circ = 0$. This says that there is no phase shift along the slit. We already observed that this must be true for a plane wave normally incident on the slit.

If the direction of propagation of the plane wave makes an angle θ_0 with the slit plane, there will be a phase shift along the slit due to different arrival times of the wave. In fact, this phase shift is given by $\beta_0 z'$ where β_0 is the phase shift per meter along the slit and we have assumed zero phase at $z' = 0$. But the phase shifts β rad/m in the direction of propagation, so the phase shift for distance Δr along the direction of propagation is $\Delta\phi = -\beta\Delta r$ (since the wave propagates as $e^{-j\phi}$). The same phase shift is encountered in the distance Δz along the slit, or $\Delta\phi = \beta_0 \Delta z$ (see Fig. 4-6b). But $\Delta r = \Delta z \cos \theta_0$, and since the phase shifts are equal we have $\Delta\phi = -\beta\Delta z \cos \theta_0 = \beta_0 \Delta z$. Thus $\beta_0 = -\beta \cos \theta_0$ as given by (4-6), which was then a convenient definition. It is obvious from Fig. 4-6b that the maximum radiation from the slit or its equivalent line source will occur in the direction of propagation of the wave $\theta = \theta_0$.

In Fig. 4-6c the incident wave is traveling parallel to the slit. The phase shift per meter along the slit is obviously equal to the negative of the wave phase constant. This also follows from $\beta_0 = -\beta \cos \theta_0 = -\beta$ for $\theta_0 = 0^\circ$. The radiated wave on the right side is endfire in this case.

4.2 TAPERED LINE SOURCES

Many antennas that can be modeled by line sources are designed to have tapered distributions. This is because if the current amplitude decreases toward the ends of a line source, the pattern side lobes are lowered and the main beam widens. In many applications low side lobes are necessary and a wider main beam is accepted as a consequence. This tradeoff between side lobe level and half-power beamwidth is a major consideration to the antenna engineer.

As an example, consider a current distribution with the so-called cosine taper, where

$$I(z') = \begin{cases} I_0 \cos\left(\frac{\pi}{L} z'\right) e^{j\beta_0 z'} & -\frac{L}{2} < z' < \frac{L}{2} \\ 0 & \text{elsewhere.} \end{cases} \quad (4-23)$$

The shape of this current distribution is plotted in Fig. 4-7a. The unnormalized pattern factor is then found as follows

$$\begin{aligned} f_{un}(\theta) &= I_0 \int_{-L/2}^{L/2} \cos\left(\frac{\pi}{L} z'\right) e^{j\beta \cos \theta + j\beta_0 z'} dz' \\ &= \frac{I_0}{2} \int_{-L/2}^{L/2} [e^{j\pi z'/L + j\beta \cos \theta + j\beta_0 z'} + e^{-j\pi z'/L - j\beta \cos \theta - j\beta_0 z'}] dz' \\ &= \frac{I_0}{2} \left[\frac{e^{j\pi L/2 + j\beta \cos \theta + j\beta_0 L/2}}{j(\pi/L + \beta \cos \theta + \beta_0)} + \frac{e^{-j\pi L/2 - j\beta \cos \theta - j\beta_0 L/2}}{-j(\pi/L - \beta \cos \theta - \beta_0)} \right]_{-L/2}^{L/2} \end{aligned} \quad (4-24)$$

Evaluating the above expression leads to

$$f_{un}(\theta) = I_0 \frac{2L \cos[(\beta \cos \theta + \beta_0)L/2]}{\pi [1 - ((\beta \cos \theta + \beta_0)L/\pi)^2]} \quad (4-25)$$

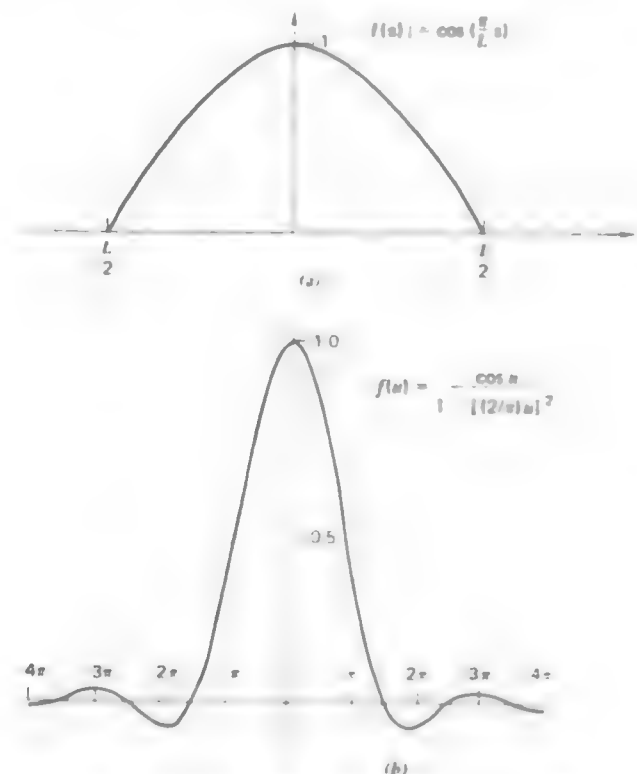


Figure 4-7 Current distribution and pattern factor for a cosine-tapered line source. (a) The current distribution amplitude. (b) The pattern factor.

Using $\beta_o = -\beta \cos \theta_o$ as in (4-6) and normalizing such that the pattern factor is unity for $\theta = \theta_o$ gives

$$f(\theta) = \frac{\cos[(\beta L/2)(\cos \theta - \cos \theta_o)]}{1 - [(\beta L/\pi)(\cos \theta - \cos \theta_o)]^2} \quad (4-26)$$

This pattern can be written in terms of u using (4-7) as

$$f(u) = \frac{\cos u}{1 - (2u/\pi)^2} \quad (4-27)$$

This pattern is plotted in Fig. 4-7b. Compare it to that of the Fig. 1-10 for the uniform line source.

The side lobe level for the cosine-tapered line source is -23.0 dB and the beamwidth is given by

$$\text{HP} \approx 1.19 \frac{\lambda}{L} \text{ rad} = 68.2 \frac{\lambda}{L} \text{ degrees} \quad (4-28)$$

for the broadside case. The side lobe level is 10 dB lower and the beamwidth is 38% greater than a uniform line source of the same length. Although the side lobes are reduced from those of the uniform line source, the main beam widening leads to smaller directivity than obtained from a uniform line source. The ratio D/D_u is used to compare the directivity of a tapered line source to that of a uniform line source of the same length. For the cosine taper $D/D_u = 0.810$. The actual directivity D from (4-21) is then

$$D = 0.810 D_u = 1.620 \frac{L}{\lambda} \quad (\text{broadside, } L \gg \lambda). \quad (4-29)$$

If the current amplitude taper is increased as in the case of a cosine-squared taper, the side lobes are reduced even more and the beamwidth is further widened. The pattern parameters of the cosine-squared case, as well as many other important cases, are summarized in Table 4-2 [1, 2, 3].

As a further example, consider the triangular current taper given in Table 4-2a. The pattern $(\sin u/u)^2$ is the square of the uniform line source pattern. This property is apparent when the pattern of Fig. 4-8 for the triangular line source is compared to that of the uniform line source in Fig. 4-1. The first nulls of the triangular line source are twice as far out as for the uniform line source pattern. Thus the beamwidth between first nulls is twice as large. The half-power beamwidth is 44% larger (from $0.886\lambda/L$ to $1.28\lambda/L$). Also, the side lobes of the triangular line source are twice as wide in the variable u and the side lobe level in decibels is twice as small, -13.3 dB for the uniform line source and -26.6 dB for the triangular line source. The directivity (from Table 4-2a) is 75% of the uniform line source value.

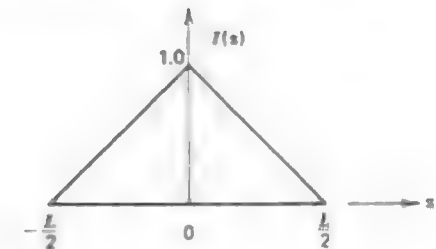
Table 4-2 Characteristics of Tapered Line Source Distributions

(a) Triangular taper

$$I(z) = 1 - \frac{2}{L} |z| \quad |z| \leq \frac{L}{2}$$

$$f(u) = \left| \frac{\sin(u/2)}{u/2} \right|^2$$

HP (rad)	Side lobe level (dB)	D/D_u
$1.28(\lambda/L)$	-26.6	0.75



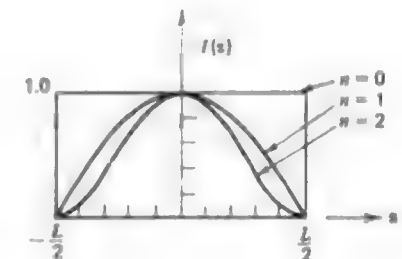
(b) Cosine tapers

$$I(z) = \cos^n \left(\frac{\pi z}{L} \right) \quad |z| \leq \frac{L}{2}$$

$$f(u) = \frac{\sin u}{u} \quad n=0$$

$$f(u) = \frac{\cos u}{1 - (2u/\pi)^2} \quad n=1$$

$$f(u) = \frac{1}{1 - (u/\pi)^2} \frac{\sin u}{u} \quad n=2$$

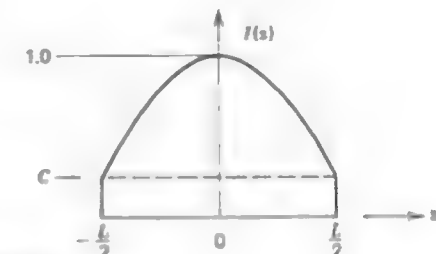


n	HP (rad)	Side lobe level (dB)	D/D_u	Type
0	$0.886 \frac{\lambda}{L}$	-13.3	1.00	Uniform line source
1	$1.19 \frac{\lambda}{L}$	-23.0	0.810	Cosine taper
2	$1.44 \frac{\lambda}{L}$	-31.7	0.667	Cosine-squared taper

(c) Cosine on a pedestal

$$I(z) = C + (1 - C) \cos^2 \frac{\pi z}{L}$$

$$f(u) = \frac{C \frac{\sin u}{u} + (1 - C) \frac{2}{\pi} \frac{\cos u}{1 - (2u/\pi)^2}}{C + (1 - C) \frac{2}{\pi}}$$



(continued)

Table 4.2 (continued)

Edge illumination		HP (rad)	Side lobe level (dB)	D/D_0
C	$20 \log C$ (dB)			
0.3162	-10	$1.03 \frac{\lambda}{L}$	-20	0.92
0.1778	-15	$1.08 \frac{\lambda}{L}$	-22	0.88
0	$-\infty$	$1.19 \frac{\lambda}{L}$	-23	0.81

Note 1: The pattern expressions are valid for any value of $u = (\beta L/2)(\cos \theta - \cos \theta_0)$. However, the half-power beamwidth values and directivities are approximations for broadside line sources ($\theta_0 = 90^\circ$ and $u = (\beta L/2)\cos \theta$) and $L \gg \lambda$.

Note 2: The directivity for each line source is found from the ratio D/D_0 as

$$D = \frac{D}{D_0} D_0 = \frac{D}{D_0} \frac{2L}{\lambda}$$

for broadside line sources with $L \gg \lambda$.

Note 3: The element factor $\sin \theta$ has been neglected in the calculations leading to the values in this table. For long, broadside line sources its effect is minimal.

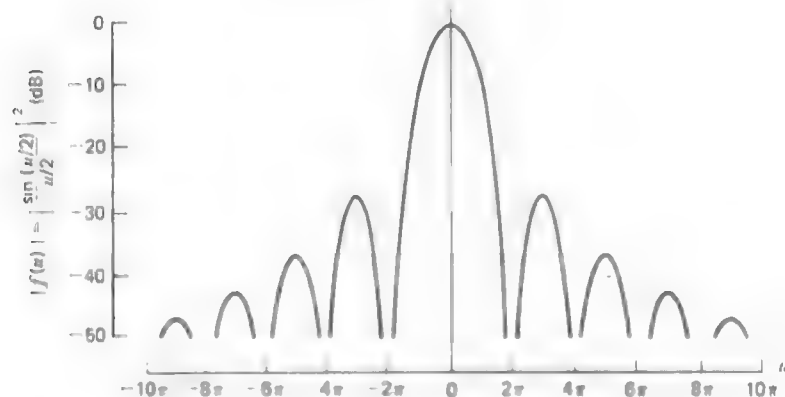


Figure 4-8 Pattern factor of a triangular tapered line source.

From Table 4-2 we can generalize and make some statements about current amplitude distributions and their influence on the far-field pattern. We assume that the current is of constant phase. *As the taper of the current amplitude from the center to the edges of a line source becomes more severe, the side lobes decrease and the beamwidth increases.* Consequently, the directivity decreases. There is then a tradeoff between the side lobe level and the beamwidth for the continuous source just as there was for discrete sources (see Section 3.5). The antenna engineer must decide on a compromise between beamwidth and side lobe level for each specific design problem.

Example 4-2. A Parabolic Reflector Antenna

A circular parabolic reflector antenna (see Section 8.6) can be modeled for some purposes as a line source. Suppose the reflector is 5 m in diameter and operates at 14 GHz. Further suppose the field distribution across the aperture of the reflector is circularly symmetric and can be modeled as a cosine on a pedestal line source with a -10-dB edge illumination. Then from Table 4-2c the half-power beamwidth is

$$\text{HP} = 1.03 \frac{\lambda}{L} = 1.03 \frac{0.0214}{5} = 0.00441 \text{ rad} = 0.25^\circ$$

and the side lobe level is -20 dB. Due to the circular symmetry of the aperture distribution, these results are valid for any pattern plane containing the normal to the reflector aperture, that is, the pattern is also circularly symmetric. Directivity cannot be calculated from line source formulas since this is a two-dimensional aperture. Much more will be said about aperture antennas in Chapter 8 where, as in this example, line source results will play an important role.

REFERENCES

1. J. F. Ramsay, "Lambda functions describe antenna/diffraction patterns," *Microwave Journal*, vol. 6, pp. 69-107, June 1967.
2. R. C. Hansen, Editor, *Microwave Scanning Antennas*, vol. I, Academic Press, 1964; Chapter 1.
3. S. Silver, Editor, *Microwave Antenna Theory and Design*, vol. 12, MIT Radiation Laboratory Series, Boston Technical Publishers, Inc., Lexington, Mass., 1964; p. 187.

PROBLEMS

4.1-1 Show that

$$\cos^{-1}(-x) - \cos^{-1}(x) = 2 \sin^{-1}(x)$$

and thereby proving (4-13). To do this introduce α such that $x = \sin \alpha$ and use $\cos(\alpha \pm \pi/2) = \mp \sin \alpha$

4.1-2 Prove the half-power beamwidth expression for an endfire, uniform line source. Start with (4-15) and derive (4-16). *Hint:* let $x = \cos^{-1}(1 - y)$ where $y = 0.443(\lambda/L)$, then form $\cos^2 \alpha$, neglect y^2 , expand 1 as $\cos^2 \alpha + \sin^2 \alpha$, and use $\sin \alpha \approx \alpha$.

4.1-3 Show that the far-zone electric field expression E_θ for a broadside, uniform line source approximates that of an ideal dipole for short line sources ($L \ll \lambda$).

4.1-4 Compute the half-power beamwidths (in degrees) and the directivities (in decibels) for the following uniform line sources:

- Eight-wavelength broadside, uniform line source.
- Eight-wavelength endfire, uniform line source.
- Sixteen-wavelength broadside, uniform line source.
- Sixteen-wavelength endfire, uniform line source.

4.1-5 (a) Use the universal pattern factor for a uniform line source to obtain polar plots of a four-wavelength uniform line source for two cases: broadside and endfire ($\theta_0 = 0^\circ$).

(b) Measure the half-power beamwidths from the polar plots obtained in part (a).

(c) Calculate the half-power beamwidths in degrees using (4-14) and (4-16). The agreement between these results and those of (b) depends mainly upon how accurately you constructed the polar plot.

4.1-6 Verify the half-power beamwidth values in Table 4-1 for the three levels of approximation for uniform line sources with the following lengths: (a) 2λ , (b) 5λ , and (c) 10λ .

4.1-7 *Uniform line source directivity.*

(a) Show that (4-20) leads to the expression

$$\frac{\beta L}{D_u} = \frac{\cos a - 1}{a} + \frac{\cos b - 1}{b} + \text{Si}(a) + \text{Si}(b)$$

where D_u is the directivity of a uniform line source with excitation phase shift per unit length of β , $a = (\beta - \beta_0)L$, $b = (\beta + \beta_0)L$, and Si is the sine integral function defined in (F-13).

(b) Plot the directivity relative to that of the broadside, very long, uniform line source case, that is, $D_u/(2L/\lambda)$, for $\beta L = 10$ and $\beta L = 100$ as a function of θ_0 from 90° to 0° .

(c) What does the expression in part (a) reduce to for the broadside case ($\theta_0 = 90^\circ$)?

(d) As L becomes much larger than a wavelength show that your result in part (c) gives (4-21).

(e) Use the result from part (c) and plot the directivity relative to that of a broadside, very long, uniform line source (i.e., $\lambda D_u/2L$) for βL from 1 to 10. This result shows how well the long line-source directivity approximation behaves.

4.2-1 Verify for the cosine-tapered line source pattern of (4-27) that (a) HP = $1.19(\lambda/L)$ in the broadside case for $L \gg \lambda$, and (b) the side lobe level is -23.0 dB.

4.2-2 Construct the linear, polar plot of the pattern factor for a broadside cosine-tapered line source which is three wavelengths long. Proceed as in Fig. 4-3.

4.2-3 A 3-m long, broadside line source operating at 1 GHz has a cosine-squared tapered current distribution.

(a) Compute the half-power beamwidth in degrees.

(b) Compute the directivity in decibels.

4.2-4 Evaluate the half-power beamwidths in degrees and the directivities in decibels of 10λ long line sources with the following current distributions: (a) uniform, (b) triangular,

(c) cosine, (d) cosine squared, and (e) cosine on a -10 -dB pedestal.

4.2-5 *Triangular current-tapered line source.*

(a) From the current distribution in Table 4-2a derive the normalized pattern factor $f(u)$.

(b) Verify that the half-power beamwidth is given by $1.28(\lambda/L)$ for $L \gg \lambda$ and that the side lobe level is -26.6 dB. You may do this by substitution, and also you may find some of the results from the uniform line source helpful.

4.2-6 The pattern from a triangular-tapered current distribution is the square of that of the uniform current distribution. From Fourier transform theory, how are the current distributions related?

4.2-7 Dipole antennas with lengths less than a half-wavelength have current distributions that are nearly triangular (see Fig. 1-20b).

(a) Write the complete electric field expression E_θ in the far field for a broadside line source with a triangular current distribution.

(b) Approximate the expression of part (a) for short dipoles ($L \ll \lambda$).

(c) Compare this to the far-field expression for E_θ of an ideal dipole. Discuss.

4.2-8 Derive the pattern factor expression in Table 4-2 for a cosine-squared line source current distribution. Also verify the half-power beamwidth expression.

4.2-9 A broadside line source has a cosine on a -10 -dB pedestal current distribution. It operates at 200 MHz and has a length of 20 m. Compute (a) the half-power beamwidth in degrees, and (b) the directivity in decibels.

4.2-10 Derive the pattern factor expression in Table 4-2 for a cosine on a pedestal current distribution for a line source.

4.2-11 The directivity of a line source can be calculated from

$$D = \frac{2 \left| \int_{-L/2}^{L/2} I(z) dz \right|^2}{\int_{-L/2}^{L/2} |I(z)|^2 dz}$$

This is the one-dimensional analogy of (8-65). Use this formula to:

(a) Derive $D_u = 2L/\lambda$, the directivity of a uniform line source.

(b) Derive an expression for D/D_u of a cosine on a pedestal current distribution. Evaluate for $C = 1, 0.3162, 0.1778$, and 0.

5

WIRE ANTENNAS

In this chapter we discuss the important topic of wire antennas. Wire antennas are the oldest and still the most prevalent of all antenna forms. Just about every imaginable shape and configuration of wires have a useful antenna application. Wire antennas can be made from either solid wire or tubular conductors. They are relatively simple in concept, are easy to construct, and are very inexpensive.

To obtain completely accurate solutions for wire antennas the current on the wire must be solved for, subject to the boundary condition that the tangential electric field is zero along the wire. This approach gives rise to an integral equation, for which many approximate solutions have been reported over the last several decades [1]. These classical solutions are rather tedious and are limited to a few simple wire shapes. On the other hand, modern numerical methods implemented on the digital computer are rather simple in concept and are applicable to many wire antenna configurations. These numerical (moment method) techniques are discussed in Chapter 7. In this chapter we adopt a simple approach to solving for the properties of wire antennas. This affords a conceptual understanding of how wire antennas operate, as well as yielding surprisingly accurate engineering results. For example, during the discussion of the loop antenna in Section 5.7 a detailed comparison of results from simple theory and the more exact numerical methods demonstrates the accuracy of simple theory.

In this chapter we discuss several resonant wire antennas such as straight wire dipoles, vee dipoles, folded dipoles, Yagi-Uda arrays, and loops. Selected

traveling-wave antennas are also discussed, but broadband wire antennas such as the helix and log-periodic are presented in the next chapter. Methods of feeding wire antennas and their performance in the presence of an imperfect ground plane are included too. Most of the developments in this chapter utilize the principles set forth thus far. Design data and guidelines for the construction and use of wire antennas are emphasized.

5.1 DIPOLE ANTENNAS

We have discussed the short dipole in Sections 1.8 and 2.1 and the half-wave dipole in Section 2.2. In this section dipoles of arbitrary length are examined. The dipole antenna has received intensive study [1, 2, 3]. We will use a simple but effective approach which involves an assumed form for the current distribution. The radiation integral may then be evaluated and thus also the pattern parameters. For dipoles we assume that the current distribution is sinusoidal. This is a good approximation verified by measurements. The current must, of course, be zero at the ends. We are, in effect, using the current distribution which is found on an open-circuited parallel wire transmission line. It is assumed that if the end of such a transmission line is bent out to form a wire antenna, the current distribution along the bent portion is essentially unchanged. Although this is not strictly true it is a good approximation for thin antennas, for which the conductor diameter is on the order of 0.01λ or smaller [4].

5.1.1 Straight Wire Dipoles

A straight dipole antenna is shown in Fig. 5-1 oriented along the z -axis. It is fed at the center from a balanced two-wire transmission line, that is, the currents on each wire are equal in magnitude and opposite in direction. The current distribution along the antenna is assumed to be sinusoidal and can be written as

$$I(z) = I_m \sin \left| \beta \left(\frac{L}{2} - |z| \right) \right| \quad |z| < \frac{L}{2} \quad (5-1)$$

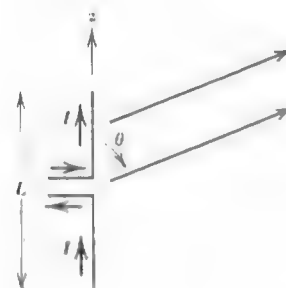


Figure 5-1 The dipole antenna

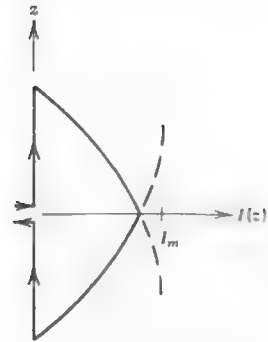


Figure 5-2 Current distribution on a dipole of length $L < \lambda/2$.

The dipole is surrounded by free space, thus the phase constant is that of free space, β .

It is helpful to visualize the current distribution on an antenna. Figure 5-2 shows the current on a dipole for $L < \lambda/2$. The solid lines indicate actual currents on the antenna and the dotted lines indicate extensions of the sine wave function. As a note of caution with this visualization, the dotted portion of the current distribution does not appear on the transmission line [5]. For this case I_m in (5-1) is not the maximum current attained on the antenna. The maximum current on the antenna shown in Fig. 5-2 is at the input terminals where $z = 0$ and is of a value $I_m \sin(\beta L/2)$. The arrows in Fig. 5-2 show the current direction. The currents on the top and bottom halves of the antenna are in the same direction at any instant of time, and thus the radiation effects from each half reinforce. The transmission line, however, has oppositely directed currents which have canceling radiation effects, for typical close conductor spacings.

In Fig. 5-3 current distributions on various dipoles are plotted together with the antennas used to generate them. The sinusoidal curves superimposed on the antennas indicate the intensity of the current on the wire, that is, the value of the curve at point z is the current value on the wire at the same point z . Again the arrows indicate current directions. To construct plots such as these, begin on the z -axis at one end of the wire where the current is zero and draw a sine wave while moving toward the feed point. The current on the other half is then the mirror image. For dipoles longer than one wavelength the currents on the antenna are not all in the same direction. Over a half-wave section the current is in-phase and adjacent half-wave sections are of opposite phase. We would then expect to see some large canceling effects in the radiation pattern. This will be shown later to be precisely what happens. For all of the current distributions presented, the plots represent the maximum excitation state. It is assumed that a sinusoidal waveform generator of radian frequency $\omega = 2\pi c/\lambda$ is connected to the input transmission line. The standing wave pattern of the current at any

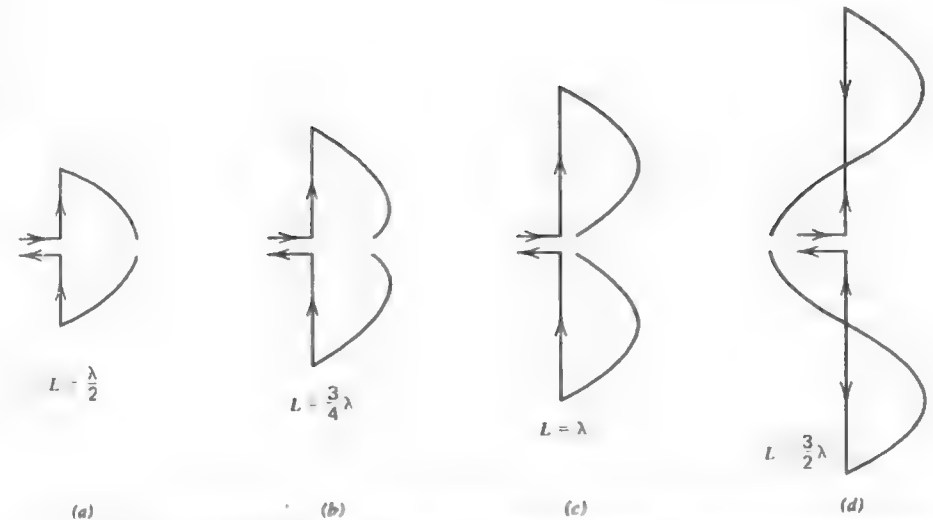


Figure 5-3 Current distributions for various center-fed dipoles. Arrows indicate relative current directions for these maximum current conditions. (a) $L = \lambda/2$. (b) $L = \frac{3}{4}\lambda$. (c) $L = \lambda$. (d) $L = \frac{3}{2}\lambda$.

instant of time is obtained by multiplying (5-1) by $\cos \omega t$, which follows from (1-6).

To obtain the dipole radiation pattern we first evaluate the radiation integral

$$f_{\text{un}} = \int_{-L/2}^{L/2} I(z') e^{j\beta z' \cos \theta} dz'. \quad (5-2)$$

Substituting the current expression from (5-1) gives

$$f_{\text{un}} = \int_{-L/2}^0 I_m \sin \left[\beta \left(\frac{L}{2} + z' \right) \right] e^{j\beta z' \cos \theta} dz' + \int_0^{L/2} I_m \sin \left[\beta \left(\frac{L}{2} - z' \right) \right] e^{j\beta z' \cos \theta} dz'. \quad (5-3)$$

Evaluating these integrals (see Prob. 5.1-1) gives the unnormalized pattern

$$f_{\text{un}} = \frac{2I_m \cos[(\beta L/2) \cos \theta] - \cos(\beta L/2)}{\beta \sin^2 \theta}. \quad (5-4)$$

Using this in (4-1) leads to the complete far-zone electric field

$$E_\theta = j\omega\mu \sin \theta \frac{e^{-j\beta r}}{4\pi r} \frac{2I_m \cos[(\beta L/2) \cos \theta] - \cos(\beta L/2)}{\beta \sin^2 \theta}. \quad (5-5)$$

Noting that $\omega\mu/\beta = \eta$, this expression simplifies to

$$E_\theta = j\eta \frac{e^{-j\beta r}}{2\pi r} I_m \frac{\cos[(\beta L/2)\cos\theta] - \cos(\beta L/2)}{\sin\theta} \quad (5-6)$$

The θ -variation of this function determines the far-field pattern. For $L = \lambda/2$ it is

$$F(\theta) = \frac{\cos[(\pi/2)\cos\theta]}{\sin\theta} \quad (L = \lambda/2). \quad (5-7)$$

This expression was also derived in Section 2.2; see (2-10). This is the normalized electric field pattern of a **half-wave dipole**. The half-power beamwidth is 78° and its pattern plot is shown in Fig. 5-4a.

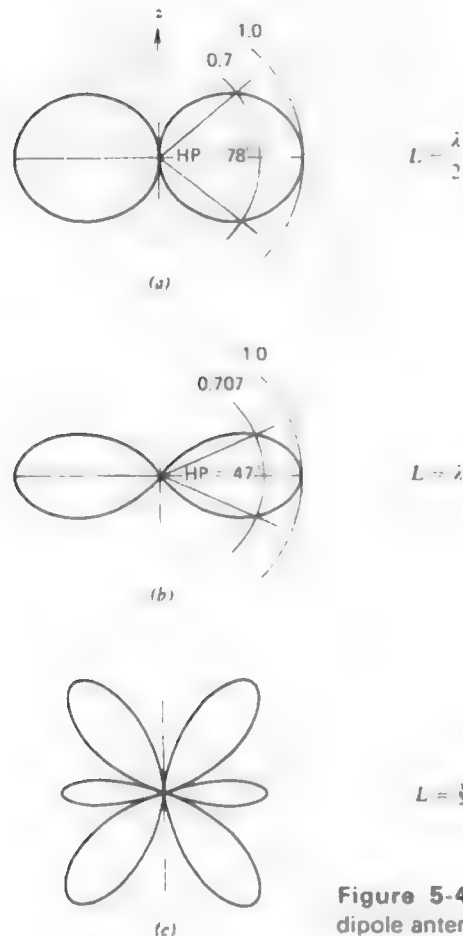


Figure 5-4 Radiation patterns of center-fed straight dipole antennas. (a) $L = \lambda/2$. (b) $L = \lambda$. (c) $L = \frac{3}{2}\lambda$.

For $L = \lambda$ the normalized electric field pattern from (5-6) is

$$F(\theta) = \frac{\cos(\pi \cos\theta) + 1}{2 \sin\theta} \quad (L = \lambda). \quad (5-8)$$

The half-power beamwidth for this **full-wave dipole** is 47° . Its pattern is shown in Fig. 5-4b. If $L = \frac{3}{2}\lambda$, the pattern function is

$$F(\theta) = 0.7148 \frac{\cos(\frac{3}{2}\pi \cos\theta)}{\sin\theta} \quad (L = \frac{3}{2}\lambda). \quad (5-9)$$

The factor 0.7148 is the normalization constant. As predicted earlier, for dipoles of length greater than one wavelength, the pattern of the three-halves wavelength dipole shown in Fig. 5-4c has a multiple lobe structure due to the canceling effect of oppositely directed currents on the antenna.

As L/λ becomes very small the dipole pattern variation in (5-6) approaches $\sin\theta$. Thus we see again that the pattern of a short dipole along the z -axis is $\sin\theta$. Recall that the short dipole pattern has a 90° half-power beamwidth; see Fig. 1-4b.

To obtain the radiation resistance, first the radiated power must be found. Substituting (5-6) into (1-127) gives

$$\begin{aligned} P_r &= \frac{1}{2} \int_0^{2\pi} \int_0^\pi \eta^2 \frac{I_m^2}{(2\pi r)^2} \left| \frac{\cos[(\beta L/2)\cos\theta] - \cos(\beta L/2)}{\sin\theta} \right|^2 r^2 \sin\theta \, d\theta \, d\phi \\ &= \frac{\eta}{8\pi^2} I_m^2 \int_0^{2\pi} d\phi \int_0^\pi \frac{[\cos[(\beta L/2)\cos\theta] - \cos(\beta L/2)]^2}{\sin\theta} \, d\theta. \end{aligned} \quad (5-10)$$

Changing the integration variable to $\tau = \cos\theta$, so $d\tau = -\sin\theta \, d\theta$, gives

$$\begin{aligned} P_r &= \frac{\eta}{2\pi} I_m^2 \int_1^{-1} \frac{[\cos[(\beta L/2)\tau] - \cos(\beta L/2)]^2}{1 - \tau^2} (-d\tau) \\ &= \frac{\eta}{4\pi} I_m^2 \int_0^1 \left(\frac{[\cos[(\beta L/2)\tau] - \cos(\beta L/2)]^2}{1 + \tau} + \frac{[\cos[(\beta L/2)\tau] - \cos(\beta L/2)]^2}{1 - \tau} \right) d\tau \end{aligned} \quad (5-11)$$

where in the last expression the identity

$$\frac{1}{1 - u^2} = \frac{1}{2} \left(\frac{1}{1 + u} + \frac{1}{1 - u} \right) \quad (5-12)$$

was used. Equation (5-11) can be evaluated in terms of sine and cosine integral functions; see (F-13) and (F-14). A simpler expression for the special case of the half-wave dipole is obtainable in terms of a single cosine integral function. Thus, when $\beta L/2 = \pi/2$, (5-11) becomes

$$P_r = \frac{\eta}{4\pi} I_m^2 \int_0^1 \left| \frac{\cos^2(\pi\tau/2)}{1+\tau} + \frac{\cos^2(\pi\tau/2)}{1-\tau} \right| d\tau. \quad (5-13)$$

Changing variables again as $v = 1 - \tau$ and $w = 1 + \tau$ and substituting into (5-13) gives

$$\begin{aligned} P_r &= \frac{\eta}{4\pi} I_m^2 \left[\int_1^0 \frac{-\sin^2(\pi v/2)}{v} dv + \int_1^2 \frac{\sin^2(\pi w/2)}{w} dw \right] \\ &= \frac{\eta}{4\pi} I_m^2 \int_0^2 \frac{\sin^2(\pi v/2)}{v} dv = \frac{\eta}{4\pi} I_m^2 \int_0^2 \frac{1 - \cos \pi v}{2v} dv. \end{aligned} \quad (5-14)$$

Changing the variable of integration to $t = \pi v$ leads to

$$P_r = \frac{\eta}{8\pi} I_m^2 \int_0^{2\pi} \frac{1 - \cos t}{t} dt = \frac{\eta}{8\pi} I_m^2 \text{Cin}(2\pi) = \frac{\eta}{8\pi} I_m^2 (2.44) \quad (5-15)$$

where $\text{Cin}(x)$ is related to the cosine integral function by (F-16) and is tabulated in [6]. In this case $\text{Cin}(2\pi) = 2.44$. Using this and $\eta = 120\pi$ in (5-15) leads to the radiation resistance for a half-wave dipole as

$$R_r = \frac{2P_r}{I_m^2} = \frac{2(15I_m^2 \cdot 2.44)}{I_m^2} = 73 \text{ ohms} \quad \left(L = \frac{\lambda}{2} \right). \quad (5-16)$$

The infinitely thin dipole antenna also has a reactive impedance component. For the half-wave dipole the reactance is inductive, and the complete input impedance is

$$Z_{in} = 73 + j42.5 \text{ ohms} \quad \left(L = \frac{\lambda}{2} \right). \quad (5-17)$$

This can be calculated for an infinitely thin dipole by a classical procedure known as the induced emf method [7]. However, the input impedance of dipoles with finite wire diameter can be calculated using the numerical methods of Chapter 7, where the form of the current is not assumed. The results of such a calculation for the input resistance and reactance of a small diameter, center-fed dipole are given in Figs. 5-5 and 5-6. The resonance effects are evident in these

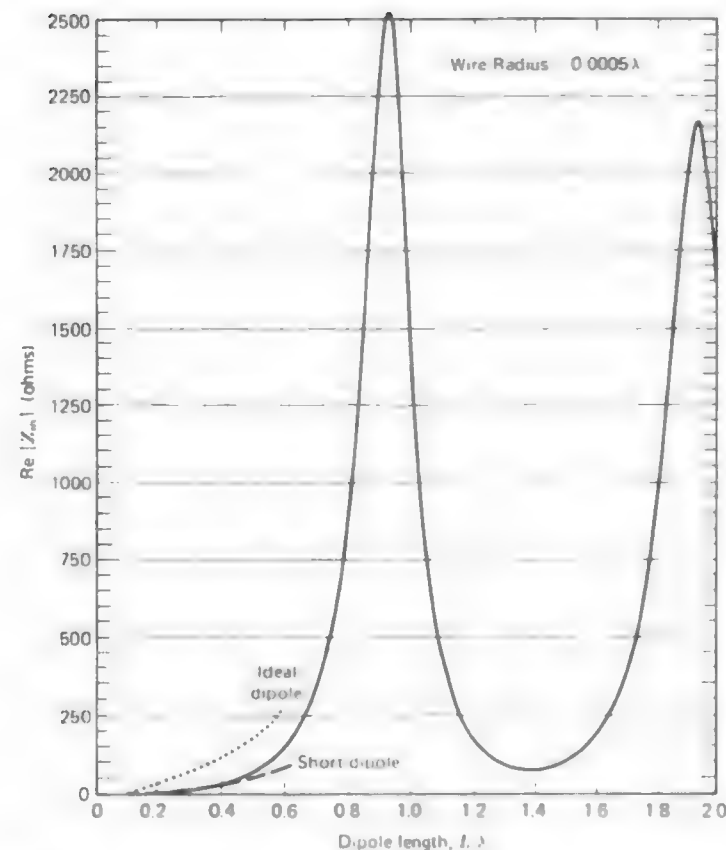


Figure 5-5 Calculated input resistance of a center-fed wire dipole of 0.0005λ radius as a function of length L (solid curve). Also shown is the input resistance $R_{in} = 80\pi^2(L/\lambda)^2$ of an ideal dipole with a uniform current distribution (dotted curve) and the input resistance $R_{in} = 20\pi^2(L/\lambda)^2$ of a short dipole with a triangular current distribution approximation (dashed curve)

plots. Note that the input reactance is capacitive for small lengths, as we pointed out in Section 2.1.

The dotted curve in Fig. 5-5 is the input resistance from (1-180) for an ideal dipole with uniform current. It does not give good results for an actual wire dipole as shown by the solid curve of Fig. 5-5. However, the triangular current approximation with $R_{in} = 20\pi^2(L/\lambda)^2$ from (1-189) does give a good approximation to the input resistance for short dipoles as demonstrated by the dashed curve of Fig. 5-5. Some simple formulas that approximate the input resistance of

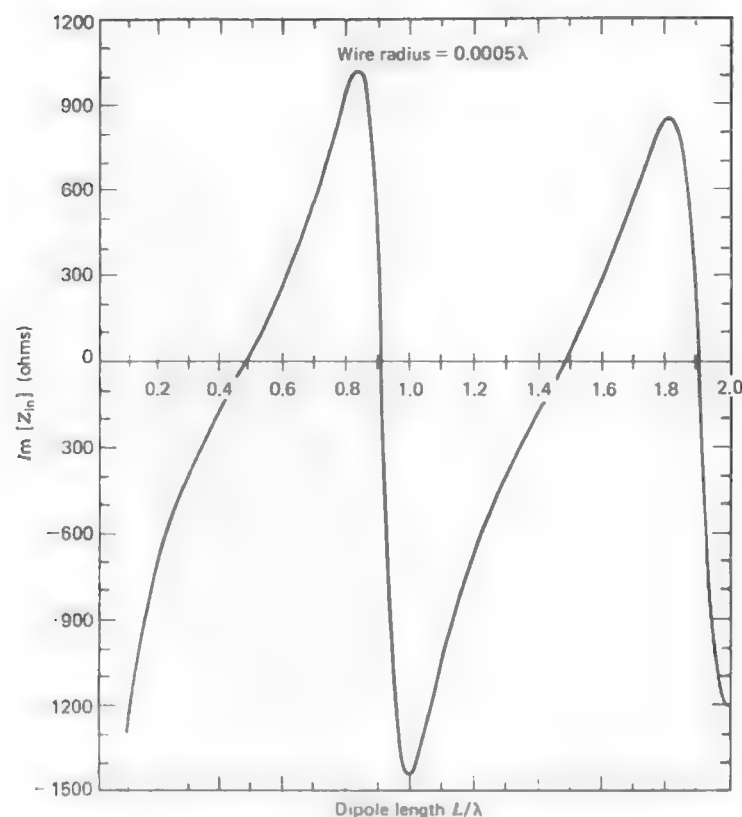


Figure 5-6 Calculated input reactance of center-fed wire dipole of radius 0.0005λ as a function of length L .

wire dipoles are given in Table 5-1 [8]. For example, using the second formula for $L = \lambda/2$ gives $R_{in} = 24.7(\pi/2)^{2.4} = 73.0$ ohms which agrees with (5-17). The values obtained from Table 5-1 also agree closely with those of Fig. 5-5.

Input resistance can be related to radiation resistance. There are several ways to define radiation resistance by using different current reference points. Usually radiation resistance is defined using the current distribution maximum I_m , whether or not it actually occurs on the antenna. We shall use the symbol R_{rm} for this definition. It is also useful to refer the radiation resistance to the input terminal point. In this case the symbol R_{ri} is used. These definitions can be related by writing the radiated power as

$$P_r = \frac{1}{2} I_m^2 R_{rm} = \frac{1}{2} I_{in}^2 R_{ri}. \quad (5-18)$$

Table 5-1 Simple Formulas for the Input Resistance of Dipoles

Length L	Input resistance R_{in} (ohms)
$0 < L < \frac{\lambda}{4}$	$20\pi^2 \left(\frac{L}{\lambda}\right)^2$
$\frac{\lambda}{4} < L < \frac{\lambda}{2}$	$24.7 \left(\pi \frac{L}{\lambda}\right)^{2.4}$
$\frac{\lambda}{2} < L < 0.637\lambda$	$11.14 \left(\pi \frac{L}{\lambda}\right)^{4.17}$

For dipoles that are odd integer multiples of a half-wavelength long, $I_m = I_{in}$ and $R_{rm} = R_{ri}$. A third radiation resistance, denoted by R_r , is often used; it is the radiation resistance relative to the maximum current that occurs on the antenna. For dipoles less than a half-wavelength long the current maximum on the antenna always occurs at the center, and then $R_{ri} = R_r$ for center-fed dipoles; this was discussed in Section 1.8. In practice we are interested in input resistance, so R_{ri} is of primary importance. It is related to R_{rm} for center-fed dipoles by setting $z = 0$ in (5-1) giving

$$I_{in} = I_m \sin \frac{\beta L}{2} \quad (5-19)$$

and substituting into (5-18), which yields

$$R_{ri} = \frac{I_m^2}{I_{in}^2} R_{rm} = \frac{R_{rm}}{\sin^2(\beta L/2)}. \quad (5-20)$$

R_{ri} is the component of input resistance due to radiation and equals the total input resistance R_{in} if ohmic losses are neglected, which we shall do unless otherwise indicated.

For dipole lengths $L = \lambda, 2\lambda, 3\lambda, \dots$, $\beta L/2 = \pi, 2\pi, 3\pi, \dots$, and R_{ri} from (5-20) is infinite. For example, the one-wavelength dipole of Fig. 5-3c has a current zero at its feed point and thus has an infinite input impedance. This, of course, is based on the perfect sine wave current distribution. Dipoles of finite thickness have large but finite values of input impedance for lengths near integer multiples of wavelength, as seen in Fig. 5-5. This effect arises from the deviation of the current distribution from that of (5-1) for dipole lengths near integer multiples

of a wavelength: there is always a finite input current on an actual dipole. For other length dipoles the sinusoidal current distribution is a good approximation for thin wire dipole antennas.

By reducing the length of the half-wave dipole slightly the antenna can be made to resonate ($X_{in} = 0$). The input impedance of the infinitely thin half-wave dipole is then about $70 + j0$ ohms. In Fig. 5-6 the dipole of radius 0.0005λ resonates for lengths corresponding to the intersections with the horizontal ($X_{in} = 0$) axis. The first intersection is the half-wave dipole case and the resonant length is slightly less than $\lambda/2$. It turns out that as the wire thickness increases the dipole must be shortened more to obtain resonance. Approximate length values for resonance are given in Table 5-2. For the dipole of 0.0005λ wire radius the length-to-diameter ratio, $L/2a$, is 500 for the half-wave case. From Table 5-2 we see that about 4% shortening ($L = 0.48\lambda$) would be required to produce resonance. This agrees closely with the resonance point from Fig. 5-6. In practice, wire antennas are constructed slightly longer than required. Then a transmitter is connected to the antenna and the standing wave ratio (or reflected power) is monitored on the feed transmission line. The ends of the antenna are trimmed until a low value of standing wave ratio is obtained. Note that as the length is reduced to obtain resonance the input resistance also decreases. For example, for a thick dipole with $L/2a = 50$ and $L = 0.475\lambda$, the second formula of Table 5-1 gives $R_{in} = 64.5$ ohms; the reactance is, of course, zero.

Since dipoles are resonant type structures their bandwidth is low. The VSWR as a function of frequency for a half-wave dipole is shown in Fig. 5-7. In general bandwidth is defined as "the range of frequencies within which the performance of the antenna, with respect to some characteristic, conforms to a specified standard" [9]. In this case let the specified standard be a VSWR less than 2.0: 1. From Fig. 5-7 we see that the bandwidths are $310 - 262 = 48$ MHz and $304 - 280 = 24$ MHz, respectively for $a = 0.005$ m ($L/2a = 50$) and $a = 0.0001$ m ($L/2a = 2500$). In terms of percent relative to the design frequency (300 MHz)

Table 5-2 Wire Lengths Required To Produce a Resonant Half-Wave Dipole for a Wire Diameter of $2a$ and Length L

Length to diameter ratio, $L/2a$	Percent shortening required	Resonant length L	Dipole thickness class
5000	2	0.49λ	very thin
50	5	0.475λ	thin
10	9	0.455λ	thick

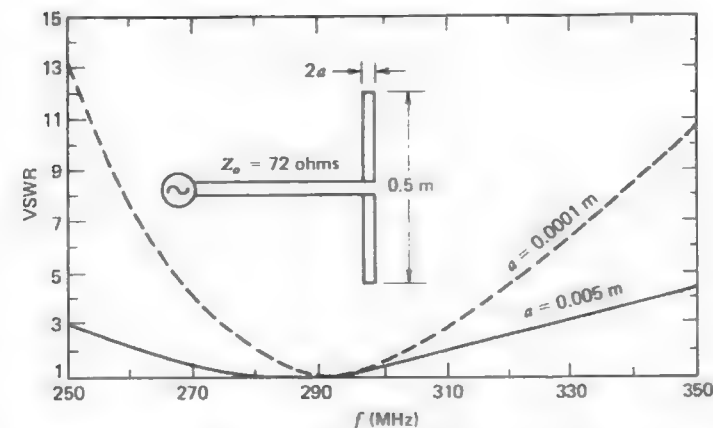


Figure 5-7 Calculated VSWR as a function of frequency for dipoles of different wire diameters.

the bandwidths are 16 and 8%. It is a general principle that the thicker the dipole, the wider is its bandwidth. Also, note that the minimum VSWR for the thicker dipole occurs at a lower frequency than for the thinner one. In fact, using the rules in Table 5-2 the resonant frequencies are calculated to be 285 and 294 MHz for wire radii of 0.005 and 0.0001 m. These values agree well with the minimum points of the curves in Fig. 5-7.

Finally, we compute the directivity of a half-wave dipole. It is found from $D = 4\pi U_m / P_r$. The radiated power P_r was evaluated in (5-15). Using the far-zone electric field of (5-6) leads to the maximum radiation intensity as

$$U_m = \frac{r^2}{2\eta} |E_\theta|_{\max}^2 = \frac{1}{2\eta} \frac{\eta^2 I_m^2}{(2\pi)^2} = \frac{\eta}{8\pi^2} I_m^2. \quad (5-21)$$

So

$$D_{(\lambda/2) \text{ dipole}} = \frac{4\pi U_m}{P_r} = \frac{4\pi(\eta/8\pi^2)I_m^2}{(\eta/8\pi)I_m^2(2.44)} = 1.64 = 2.15 \text{ dB}. \quad (5-22)$$

This is only slightly greater than the directivity value of 1.5 for an ideal dipole with uniform current. So for very short dipoles the directivity is 1.5 and increases to 1.64 as the length is increased to a half-wavelength. As length is increased further directivity also increases. A full-wave dipole has a directivity of 2.41. Even more directivity is obtained for a length of about 1.25λ . As the length is increased further the pattern begins to break up (see Fig. 5-4c) and directivity drops sharply. See Prob. 5.1-12.

5.1.2 The Vee Dipole

Wire dipole antennas that are not straight also appear in practice. One such antenna is the **vee dipole** shown in Fig. 5-8. This antenna may be visualized as an open circuited transmission line that has been bent so that ends of length h have an included angle of γ . The angle γ for which the directivity is greatest in the direction of the bisector of γ , is given by

$$\gamma = 152\left(\frac{h}{\lambda}\right)^2 - 388\left(\frac{h}{\lambda}\right) + 324, \quad 0.5 \leq \frac{h}{\lambda} < 1.5 \quad (5-23)$$

$$\gamma = 11.5\left(\frac{h}{\lambda}\right)^2 - 70.5\left(\frac{h}{\lambda}\right) + 162, \quad 1.5 \leq \frac{h}{\lambda} \leq 3.0$$

where the resulting angle γ is in degrees. The corresponding directivity is

$$D = 2.94\left(\frac{h}{\lambda}\right) + 1.15. \quad (5-24)$$

These equations have been empirically derived for antennas with $0.5 \leq h/\lambda \leq 3.0$ using the computational methods of Chapter 7.

The directivity of a vee dipole can be greater than that of a straight dipole. This can be seen from the pattern in Fig. 5-9 where $h = 0.75\lambda$ and γ from (5-23) is 118.5° . Notice that the direction of maximum radiation is $\phi = 90^\circ$ while radiation in the $\phi = 270^\circ$ direction is about 2 dB less. Even more significant is the low level of the side lobes. For the most part it is the reduced side lobe levels of the vee dipole which give it a greater directivity than the straight dipole version (see Fig. 5-4c). The directivity for the vee dipole of Fig. 5-9 from (5-24) is $D = 2.94(0.75) + 1.15 = 3.355 = 5.26$ dB. The directivity of a 1.5λ long straight wire dipole is about 2.2, or 3.4 dB.

The input impedance of a vee dipole antenna is generally less than that of a straight dipole of the same length. For example, the input impedance of the vee dipole in Fig. 5-9 is $102 + j14$ ohms which is less than for the straight dipole version ($L = 1.5\lambda$) as found from Figs. 5-5 and 5-6.

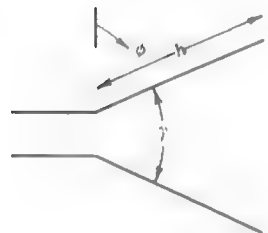


Figure 5-8 The vee dipole antenna.

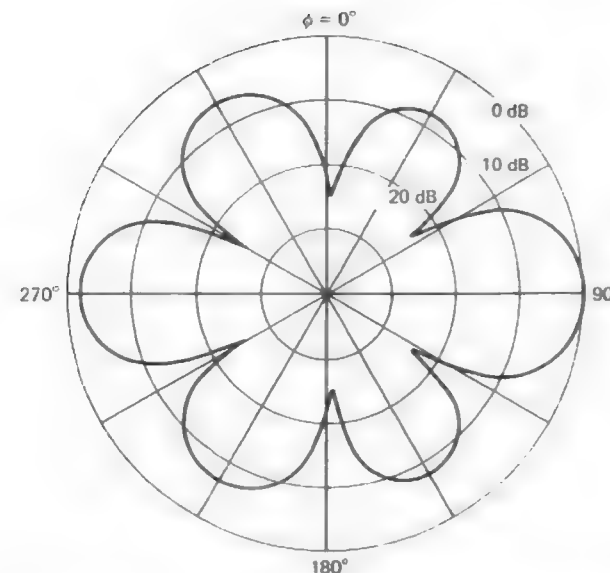


Figure 5-9 Far-field pattern of a vee dipole shown in Fig. 5-8 with arm length $h = 0.75\lambda$ and $\gamma = 118.5^\circ$. The plot is in decibels.

5.2 FOLDED DIPOLE ANTENNAS

An extremely practical wire antenna is the **folded dipole**. It consists of two parallel dipoles connected at the ends forming a narrow wire loop, as shown in Fig. 5-10, with dimension d much smaller than L and much smaller than a wavelength. The feed point is at the center of one side. The folded dipole is essentially an unbalanced transmission line with unequal currents. Its operation

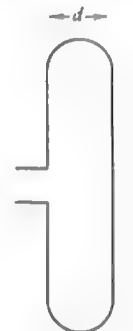


Figure 5-10 The folded dipole antenna.

is analyzed by considering the current to be composed to two modes: the transmission line mode and the antenna mode. The currents for these modes are illustrated in Fig. 5-11.

The currents in the transmission line mode have fields that tend to cancel in the far field since d is small. The input impedance for this mode is given by the equation for a transmission line with a short circuit load

$$Z_T = jZ_0 \tan \beta \frac{L}{2} \quad (5-25)$$

where Z_0 is the characteristic impedance of the transmission line.

In the antenna mode the fields from the currents in each vertical section reinforce in the far field since they are similarly directed. In this mode the charges "go around the corner" at the end, instead of being reflected back toward the input as in an ordinary dipole, which leads to a doubling of the input current for resonant lengths. The result of this is that the antenna mode has an input current that is half that of a dipole for resonant lengths.

Suppose a voltage V is applied across the input terminals. The total behavior is determined by the superposition of the equivalent circuits for each mode in Fig. 5-12. Note that if the figures for each mode are superimposed and the voltages are added, the total on the left is V and on the right is zero as it should be. The transmission line mode current is

$$I_T = \frac{V/2}{Z_T} = \frac{V}{2Z_T} \quad (5-26)$$

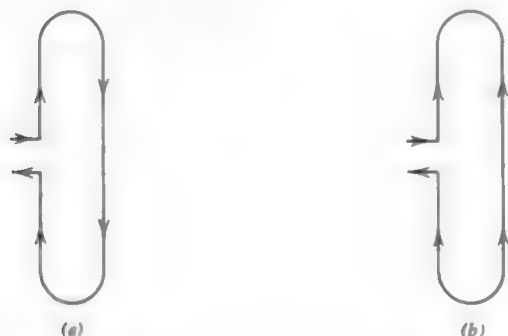


Figure 5-11 The current modes on a folded dipole antenna. (a) Transmission line mode. (b) Antenna mode.

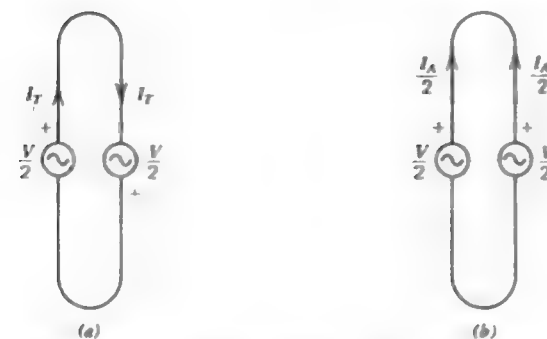


Figure 5-12 Mode excitation and current for a voltage V applied to the terminals of a folded dipole. Superposition of these modes gives the complete folded dipole model. (a) Transmission line mode. (b) Antenna mode.

For the antenna mode, the total current is the sum of each side, or I_A . The excitation for this current is $V/2$, thus the antenna current is

$$I_A = \frac{V/2}{Z_D} = \frac{V}{2Z_D} \quad (5-27)$$

where to a first-order approximation Z_D is the input impedance for an ordinary dipole of the same wire size [10]. The total current on the left is $I_T + \frac{1}{2}I_A$, and the total voltage is V , so the input impedance of the folded dipole is

$$Z_{in} = \frac{V}{I_T + \frac{1}{2}I_A} \quad (5-28)$$

Substituting (5-26) and (5-27) in (5-28) yields

$$Z_{in} = \frac{4Z_T Z_D}{Z_T + 2Z_D} \quad (5-29)$$

As an example consider the popular **half-wave folded dipole**. From (5-25) with $L = \lambda/2$, $Z_T = jZ_0 \tan[(2\pi/\lambda)(\lambda/4)] = jZ_0 \tan(\pi/2) = \infty$. Then (5-29) gives

$$Z_{in} = 4Z_D \quad \left(L = \frac{\lambda}{2}\right) \quad (5-30)$$

Thus the half-wave folded dipole provides a four fold increase in impedance over its dipole version. Since the half-wave dipole (at resonance) has a real input impedance, the half-wave folded dipole will also.

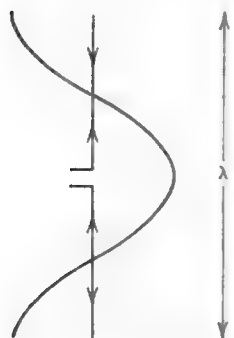


Figure 5-13 Current for the antenna mode of a half-wave folded dipole that has been folded out without disturbing the current.

The current on the half-wave folded dipole is particularly easy to visualize. We will discuss this current and also rederive the impedance. If the vertical wire section on the right in Fig. 5-10 were cut directly across from the feed point and the wire folded out without disturbing the current, it would appear as shown in Fig. 5-13. The current is not zero at the ends because they are actually connected. Perhaps a better way to view this is to fold the current back down and note that currents on the folded part are now upside down as shown in Fig. 5-14a. The same total current (and thus same pattern) is obtained with both the folded and the ordinary dipoles in Fig. 5-14. The difference is that the folded dipole has two closely spaced currents equal in value, whereas in the ordinary dipole they are combined on one wire. From this it is easy to see that the input currents in the two cases are related as

$$I_F = \frac{1}{2} I_D \quad \left(L = \frac{\lambda}{2} \right) \quad (5-31)$$

The input powers are

$$P_F = \frac{1}{2} Z_{in} I_F^2 \quad (\text{folded dipole}) \quad (5-32)$$

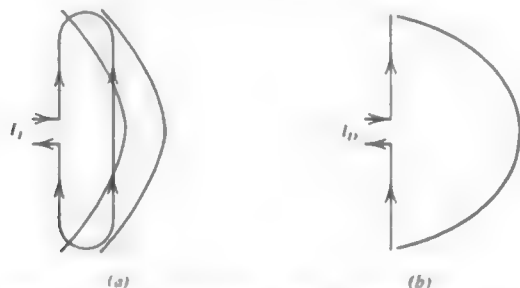


Figure 5-14 Currents on half-wave dipoles. (a) Folded dipole. (b) Dipole.

and

$$P_D = \frac{1}{2} Z_D I_D^2 \quad (\text{dipole}). \quad (5-33)$$

Since the total currents are the same in the half-wave case, the radiated powers are also. Equating (5-32) and (5-33) and using (5-31) gives

$$\frac{1}{2} Z_D I_D^2 = \frac{1}{2} Z_{in} \frac{1}{4} I_D^2$$

or

$$Z_{in} = 4Z_D \quad \left(L = \frac{\lambda}{2} \right). \quad (5-34)$$

This result is an independent confirmation of the result in (5-30).

The input impedance of a half-wave folded dipole (at resonance) is four times that of an ordinary dipole. A resonant half-wave dipole has about 70 ohms input resistance, so a half-wave folded dipole then has an input impedance of

$$Z_F = 4(70) = 280 \text{ ohms} \quad (\text{half-wave}). \quad (5-35)$$

This impedance is very close to the 300 ohms of common twin-lead transmission line.

The input impedance curves for a folded dipole of finite wire thickness are given in Fig. 5-15 as a function of folded dipole length. The solid curves were obtained from the transmission line model. The wire spacing $d = 12.5a$ is such that the characteristic impedance corresponds to a 300-ohm transmission line [$Z_o = (\eta/\pi) \ln(d/a) = 120 \ln(12.5a/a) \approx 300$ ohms]. The folded dipole input impedance is then found from (5-25) and (5-29). As an example consider a folded dipole of length $L = 0.8\lambda$, spacing $d = 12.5a$, and radius $a = 0.0005\lambda$. From (5-25)

$$Z_T = j300 \tan 0.8\pi = -j218 \text{ ohms}. \quad (5-36)$$

From Figs. 5-5 and 5-6

$$Z_D = 950 + j950. \quad (5-37)$$

Using these in (5-29) yields

$$Z_{in} = 28 - j461 \text{ ohms} \quad (L = 0.8\lambda). \quad (5-38)$$

This result agrees with the values shown in Fig. 5-15.

Also shown in Fig. 5-15 as dashed curves is the input impedance calculated using the more exact methods of Chapter 7. The agreement between the simple transmission line model and the numerical method results is quite good. Both methods show that the real part of the input impedance is slightly less than

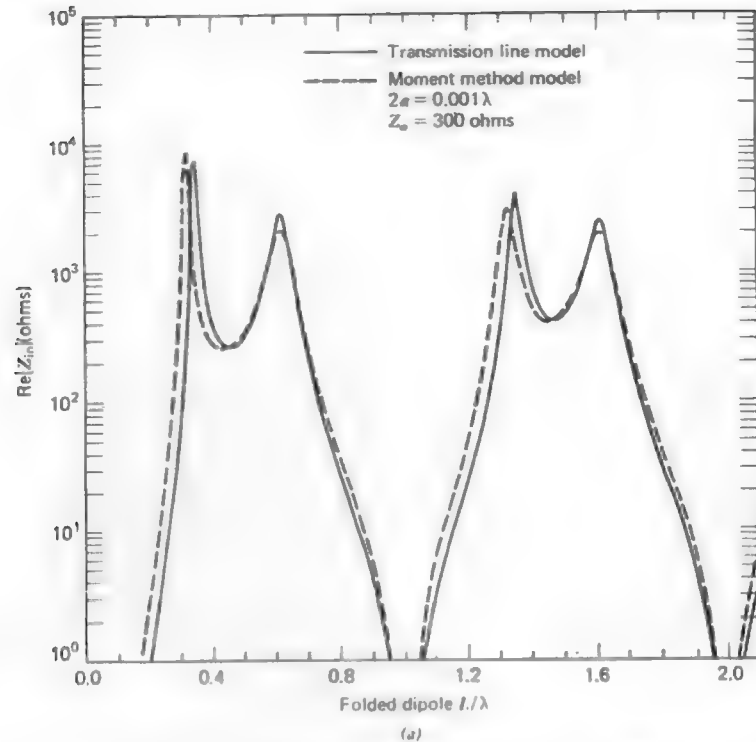


Figure 5-15 Input impedance of a folded dipole. The solid curves are calculated from the transmission line model. The dashed curves are calculated from more accurate numerical methods. The wire radius a is 0.0005λ and wire spacing d is $12.5a$. (a) Input resistance.

300 ohms at the first resonance ($L \approx 0.48\lambda$) and slightly larger than 300 ohms at the second resonance ($L \approx 1.47\lambda$). It is this characteristic of the folded dipole that makes it useful at harmonically related frequencies. Note too the very low value of Z_{in} when $L \approx \lambda, 2\lambda, \dots$. This can easily be explained from the transmission line model, since then $\tan(\beta L/2) \approx \tan \pi = 0$ and thus $Z_T = 0$ and Z_{in} from (5-29) is zero.

The folded dipole is used as an FM broadcast band receiving antenna, and it can be simply constructed by cutting a piece of 300 ohm twin-lead transmission line about a half-wavelength long (1.5 m at 100 MHz). The ends are soldered together such that the overall length L is slightly less than a half-wavelength at the desired frequency (usually 100 MHz). One wire is then cut in the middle and connected to the twin-lead transmission line feeding the receiver.

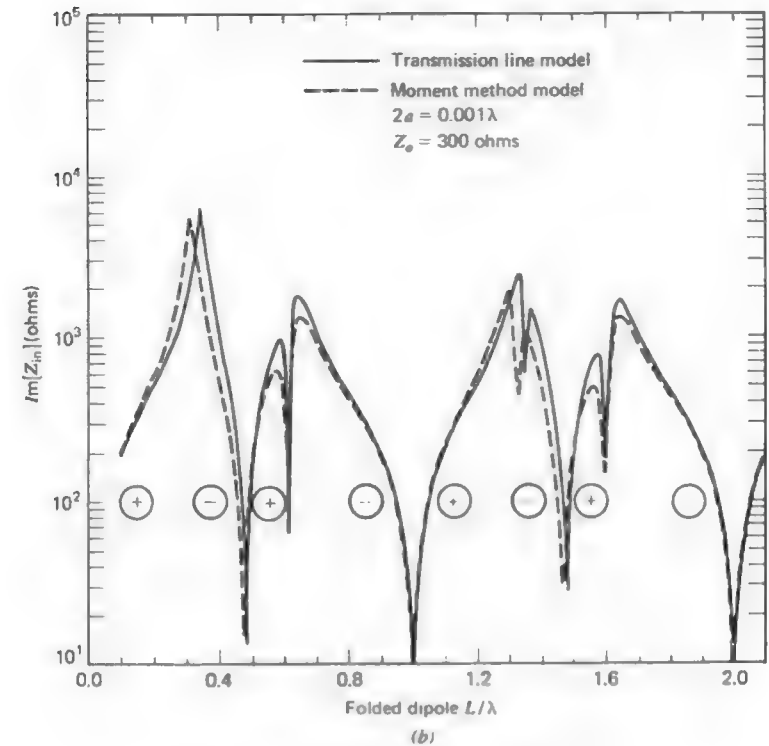


Figure 5-15 (b) Input reactance.

Occasionally two different wire sizes are used for a folded dipole as shown in Fig. 5-16. The input impedance for the half-wave case is given by

$$Z_{in} = (1 + c)^2 Z_D \quad \left(L = \frac{\lambda}{2} \right) \quad (5-39)$$

For given values of d , a_1 , and a_2 the value of c can be found [10, 11]. As is frequently the case, if a_1 and a_2 are much less than d , c is approximately given by

$$c \approx \frac{\ln(d/a_1)}{\ln(d/a_2)} \quad (5-40)$$

The folded dipole antenna is a very popular wire antenna. The reasons for this are its impedance properties and ease of construction. The equal size conductor half-wave folded dipole has an input impedance very close to that of a 300-ohm

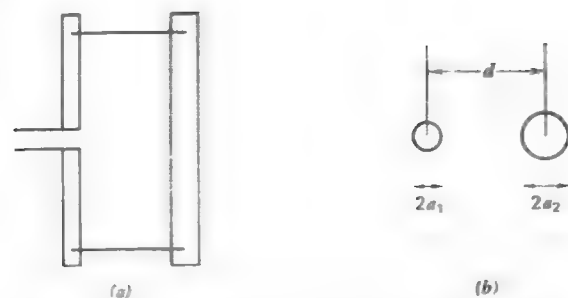


Figure 5-16 Folded dipole antenna constructed from two different size conductors. (a) Side view. (b) End view.

twin-lead type transmission line as seen from Fig. 5-15. Also, by changing the conductor radii the input impedance can be changed. In addition to having desirable impedance properties, the half-wave folded dipole has wider bandwidth than an ordinary half-wave dipole [12]. For these reasons a folded dipole is frequently used as a feed antenna for Yagi-Uda arrays and other popular antennas.

5.3 FEEDING WIRE ANTENNAS

When connecting an antenna to a transmission line it is important to make effective use of all available power from the transmitter in the transmit case and from the antenna in the receive case. There are two primary considerations: the impedance match between the antenna and transmission line, and the excitation of the current distribution on the antenna. In this section these general topics are discussed along with specific applications to wire antennas.

First, consider impedance matching. A typical transmitter or receiver circuit is shown in Fig. 5-17. Usually the transmitter or receiver has an impedance equal to that of the transmission line, Z_o . However, the antenna impedance, Z_{ant} , is frequently quite different from Z_o . The question is whether this is a problem. The answer depends upon the application. In some cases corrective measures such as a matching network are necessary. Let us examine the effects created by a mismatch. It is well known that maximum power is transferred when there is a conjugate impedance match. Also, if the system were operated with a poor match at the antenna there would be reflections set up along the transmission line; that is, the voltage standing wave ratio (VSWR) is much greater than one. If the transmission line is of high quality (low loss) these reflections represent low-dissipative losses. For many applications an extremely low VSWR is a

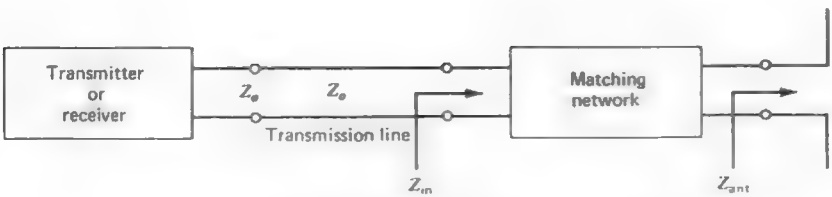


Figure 5-17 Typical transmitter/receiver configuration.

luxury and not a necessity. This is demonstrated in Table 5-3, which follows from (1-241). For example, a VSWR of 2 : 1 leads to 89% power transmission. On the other hand, if the VSWR is very high, power is traveling back and forth along the transmission line, and if the line is lossy and/or of long length, dissipative losses may be significant.

High VSWR has other undesirable effects on a system. In high power applications very high voltages will be developed between the conductors at certain points along a transmission line. These are called “hot spots” and may cause arcing. Also a high VSWR means that the impedance varies along the transmission line and further that the impedance at any point varies as the frequency is changed. This may affect transmitter operation. For example, the frequency of the transmitter can be changed by severe input impedance mismatch; this is called “frequency pulling.”

If the impedance mismatch is unacceptable there are several methods for improving the performance. Usually the characteristic impedance Z_o is nearly

Table 5-3 VSWR and Transmitted Power for a Mismatched Antenna

VSWR	Percent reflected power $= \Gamma ^2 \times 100$ $= \left(\frac{\text{VSWR} - 1}{\text{VSWR} + 1} \right)^2 \times 100$	Percent transmitted power $= q \times 100$ $= (1 - \Gamma ^2) \times 100$
1.0	0.0	100.0
1.1	0.2	99.8
1.2	0.8	99.2
1.5	4.0	96.0
2.0	11.1	88.9
3.0	25.0	75.0
4.0	36.0	64.0
5.0	44.4	55.6
5.83	50.0	50.0
10.0	66.9	33.1

real since low-loss transmission lines are used. For a match then the antenna should have an input impedance equal to $Z_0 + j0$. Sometimes it is possible to select an antenna that achieves this. If this is not possible a matching network can be employed as shown in Fig. 5-17. Such matching networks take many forms. One example is the quarter-wave transformer, which is a quarter-wavelength long transmission line with characteristic impedance $\sqrt{Z_0 R_{ant}}$ where R_{ant} is the antenna input resistance. If the antenna impedance has a reactive component other devices may be used. At high frequencies tuning devices such as stub tuners and irises are introduced to transform the real part of the impedance to that of the transmission line as well as tuning out the reactive component. At low frequencies reactive tuning is accomplished with variable capacitors and coils.

There are disadvantages to using matching networks. The match is maintained only over a narrow band of frequencies. Also matching networks introduce loss; for example, the current in tuning coils leads to ohmic loss.

On the other hand, there are several ways to change the input impedance of an antenna without using a matching network. For example, the input resistance of a dipole can be changed by displacing the feed point off center. If the feed point is a distance z_{in} from the center of the dipole the current at the input terminals is

$$I_{in} = I_m \sin \left[\beta \left(\frac{L}{2} - |z_{in}| \right) \right] \quad (5-41)$$

In the case of a half-wave dipole as shown in Fig. 5-18 $\beta L/2 = \pi/2$ and this reduces to

$$I_{in} = I_m \cos \beta z_{in} \quad (5-42)$$

The input resistance (not including ohmic losses) is found from (5-42) in (5-20) giving

$$R_{in} = \frac{I_m^2}{I_{in}^2} R_{rm} = \frac{R_{rm}}{\cos^2 \beta z_{in}} \quad \left(L = \frac{\lambda}{2} \right) \quad (5-43)$$

As the feed point approaches the end of the wire this result indicates that the input resistance increases toward infinity. In practice, the input resistance be-

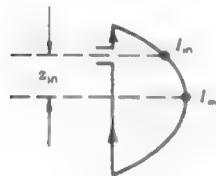


Figure 5-18 Half-wave dipole with displaced feed.

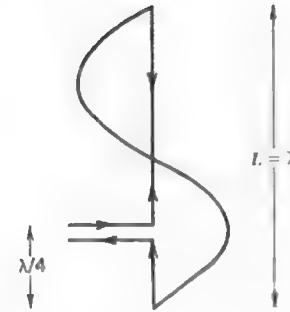


Figure 5-19 Current distribution on a full wave dipole for an off-center feed.

comes very large as the feed point moves out. The pattern is essentially unchanged as the feed point shifts. For longer dipoles the pattern and impedance differ significantly from the center-fed case as the feed point is displaced. For example, a full-wave dipole fed a quarter-wavelength from one end, as shown in Fig. 5-19, will have a current distribution which is significantly different from the center fed full-wave dipole of Fig. 5-3c.

The off-center feed arrangement is unsymmetrical and can lead to undesirable phase reversals in the antenna, as shown in Fig. 5-19. A symmetrical feed that increases the input resistance with increasing distance from the center point of the wire antenna is the *shunt feed*. A few forms of shunt matching are shown in Fig. 5-20. We will discuss the operation of the tee match and the remaining shunt matches behave in a similar fashion. The center section of the tee match may be viewed as being a shorted transmission line in parallel with a dipole of wide feed gap spacing. The shorted transmission line is less than a quarter-wavelength long and thus its impedance is inductive. Capacitance can be introduced to tune out this inductance by either shortening the dipole length or by placing variable capacitors in the shunt legs. As the distance D is increased the input impedance increases and peaks for a D of about half of the dipole length. As D is increased further the impedance decreases and finally equals the folded dipole value when D equals the dipole length. The exact impedance value

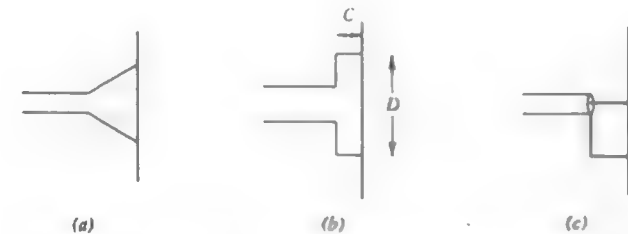


Figure 5-20 Shunt matching configurations. (a) Delta match. (b) Tee match. (c) Gamma match.

depends on the distances C and D , and the ratio of the dipole wire diameter to the shunt arm wire diameter (similar to the folded dipole behavior). In practice, sliding contacts are made between the shunt arms and the dipole for impedance adjustment. Shunt matches will radiate and do so in an undesirable fashion.

We now turn our attention to a separate but related problem of balancing currents on wire antennas. Many wire antennas are symmetrical in nature and, thus, the currents should also be symmetrical (or balanced). An example of balanced and unbalanced operation of a half-wave dipole is shown in Fig. 5-21. In the balanced case the currents on the transmission line are equal in magnitude and opposite in direction, which yields very small radiation from the transmission line for closely spaced conductors. For unbalanced operation, as illustrated in Fig. 5-21b, the current I_1 is greater than I_2 and there is a net current flow on the transmission line leading to uncontrolled radiation, that is, not in the desired direction or of the desired polarization. Also, the unbalanced current on the antenna will change the radiation pattern from the balanced case. Thus, it is clear that balanced operation is necessary.

Transmission lines are referred to as balanced and unbalanced. Parallel wire lines are inherently balanced in that if an incident wave (with balanced currents) is launched down the line it will excite balanced currents on a symmetrical antenna. On the other hand, a coaxial transmission line is not balanced. A wave traveling down the coax may have a balanced current mode, that is, the currents on the inner conductor and the inside of the outer conductor are equal in magnitude and opposite in direction. However, when this wave reaches a symmetrical antenna a current may flow back on the outside of the outer conductor which unbalances the antenna and transmission line. This is illustrated in Fig. 5-22. Note that the currents on the two halves of the dipole are unbalanced. The current I_3 flowing on the outside of the coax will radiate. The currents I_1 and I_2 in the coax are shielded from the external world by the thickness of the outer conductor. They could actually be unbalanced with no resulting radiation; it is the current on the outside surface of the outer conductor which must be



Figure 5-21 Balanced and unbalanced operation of a center-fed half-wave dipole. (a) Balanced currents, $I_1 = I_2$. (b) Unbalanced currents, $I_1 > I_2$.

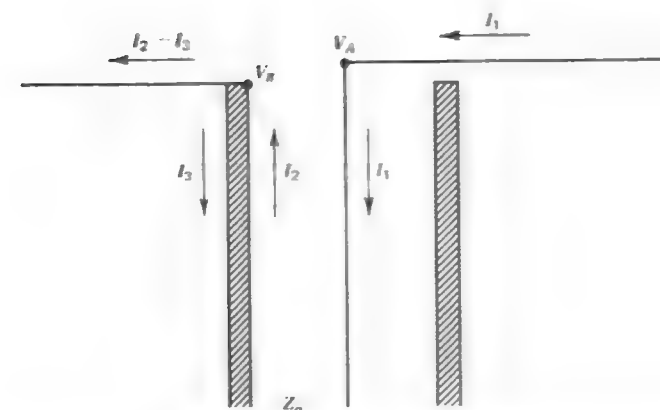


Figure 5-22 Cross section of a coaxial transmission line feeding a dipole antenna at its center.

suppressed. To suppress this outside surface current, a *balun* (contraction for "balanced to unbalanced") is used.

The situation in Fig. 5-22 may be understood by examining the voltages that exist at the terminals of the antenna. These voltages are equal in magnitude but opposite in phase (i.e., $V_A = -V_B$). Both voltages act to cause a current to flow on the outside of the coaxial line. If the magnitude of the currents on the outside of the coax produced by both voltages were equal, the net current would be zero. However, since one antenna terminal is directly connected to the outer conductor, its voltage V_B produces a much stronger current than does the other voltage V_A . A balun is used to transform the balanced input impedance of the dipole to

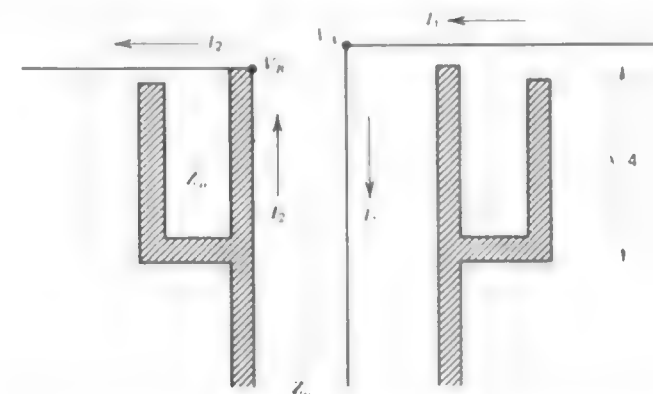


Figure 5-23 Cross-section of a sleeve balun feeding a dipole at its center.

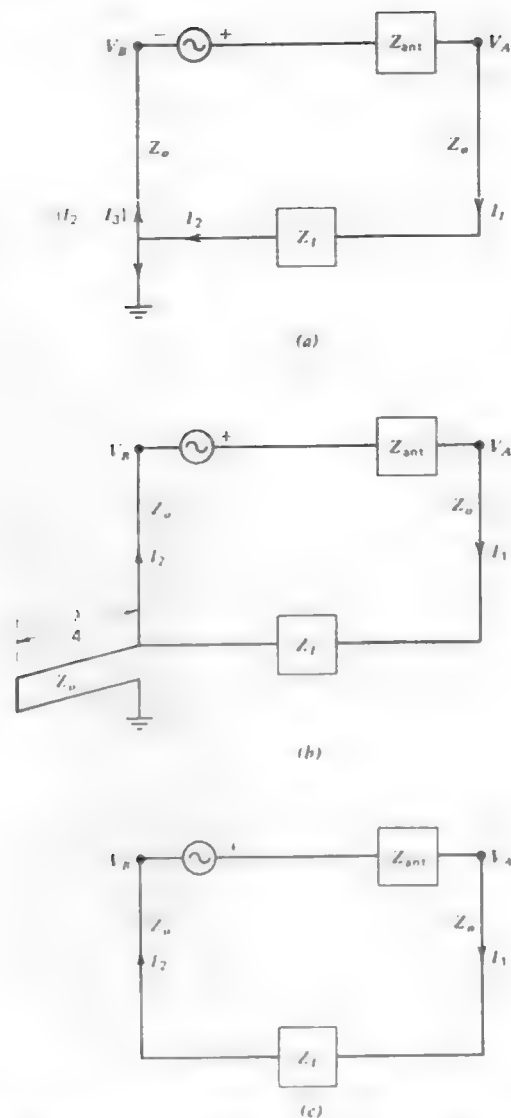


Figure 5-24 Equivalent circuits for a dipole fed from a coaxial transmission line of characteristic impedance Z_o and load impedance Z_L . (a) Equivalent circuit of coax-fed dipole in Fig. 5-22. (b) Equivalent circuit of sleeve balun-fed dipole in Fig. 5-23. (c) Final equivalent circuit for Fig. 5-23 with quarter-wave transmission line removed, $I_1 = I_2$.

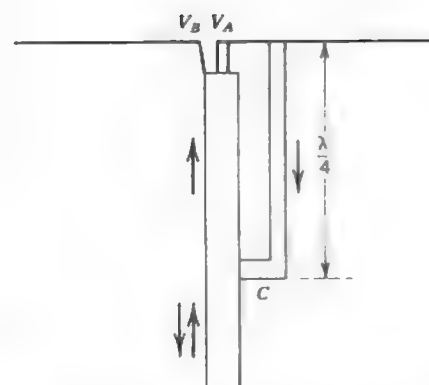


Figure 5-25 The split coax balun.

the unbalanced coaxial line such that there is no net current on the outer conductor of the coax.

To illustrate how a balun works, consider the *sleeve (or bazooka) balun* in Fig. 5-23. The sleeve and outer conductor of the coaxial line form another coaxial line of characteristic impedance Z_o' which is shorted a quarter-wavelength away from its input at the antenna terminals. The equivalent circuit for Fig. 5-22 is that of Fig. 5-24a. The equivalent circuit of Fig. 5-23 is that of Fig. 5-24b, which shows that both terminals see a very high impedance to ground. Thus, the situation in Fig. 5-24b is equivalent to the balanced condition of Fig. 5-24c wherein the currents I_1 and I_2 are equal.

The sleeve balun appears in practice in several forms. An easily constructed

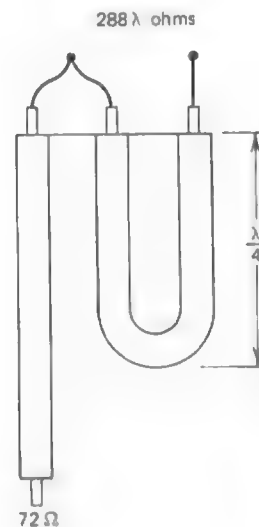


Figure 5-26 A balun that provides an impedance stepup ratio of 4:1.

form is the *split coax balun* shown in Fig. 5-25. The quarter-wavelength of coax from the A terminal to the outer conductor of the transmission line does not affect the antenna impedance Z_{ant} . The extra quarter-wavelength of coax together with the outer conductor of the main transmission line form another equivalent transmission line, which is a quarter-wavelength long and is shorted at C . Therefore, the short circuit at C is (ideally) transformed to an infinite impedance at the antenna terminals, which is in parallel with Z_{ant} leaving the input impedance unchanged. The quarter-wavelength line induces a cancelling current on the outside of the coaxial transmission line, so that the net current on the outside of the main coax below point C is zero as shown in Fig. 5-25. The sleeve balun is, of course, not broadband because of the quarter-wavelength involved in its construction. Broadband baluns can be constructed by coiling a coaxial line in a symmetrical fashion. If the coil is wound around a toroidal ferrite core, a bandwidth of as much as 10:1 is possible.

Impedance transformation may also be included in a balun for matching purposes. For example, the "four-to-one" balun in Fig. 5-26, will transform an unbalanced 72-ohm impedance to one that is 288-ohm balanced. Such a balun is useful with a folded dipole antenna. A balun that leaves the impedance unchanged is frequently referred to as a "one-to-one" balun.

5.4 YAGI-UDA ANTENNAS

We saw in Chapter 3 that array antennas can be used to increase directivity. The arrays we have examined have had all elements active, requiring a direct connection to each element by a feed network. The feed networks for arrays are considerably simplified if only a few elements are fed directly. Such an array is referred to as a *parasitic array*. The elements that are not directly driven (called parasites) receive their excitation by near-field coupling from the driven elements. A parasitic linear array of parallel dipoles is called a **Yagi-Uda antenna**, a Yagi-Uda array, or simply "Yagi." Yagi-Uda antennas are very popular because of their simplicity and relatively high gain. In this section the principles of operation and design data for Yagis will be presented.

The first research done on the Yagi-Uda antenna was performed by Shintaro Uda at Tohoku University in Sendai, Japan, in 1926 and was published in Japanese in 1926 and 1927; see [13]. The work of Uda was reviewed in an article written in English by Uda's professor, H. Yagi, in 1928 [14].

The basic unit of a Yagi consists of three elements. To understand the principles of operation for a three-element Yagi we will begin with a driven element (or "driver") and add parasites to the array. Consider a driven element that is a resonant half-wave dipole. If a parasitic element is spaced very close to it, it is

excited by the driven element with roughly equal amplitude, so the field incident on the parasite is

$$E_{\text{incident}} = E_{\text{driver}} \quad (5-44)$$

A current is excited on the parasite and the resulting radiated electric field, also tangent to the wire, is equal in amplitude and opposite in phase to the incident wave. This is because the electric field arriving at the parasite from the driver is tangential to it and the total electric field tangential to a good conductor is zero. Thus the field radiated by the parasite is such that the total tangential field on the parasite is zero, or $0 = E_{\text{incident}} + E_{\text{parasite}}$. Combining this fact with (5-44) gives

$$E_{\text{parasite}} = -E_{\text{incident}} = -E_{\text{driver}} \quad (5-45)$$

From array theory we know that two closely spaced, equal amplitude, opposite phase elements will have an endfire pattern; for example see Fig. 3-4. The pattern of this simple two-element parasitic array for 0.04λ spacing is shown in Fig. 5-27b.

The simplistic beauty of the Yagi is revealed by lengthening the parasite. The dual endfire beam is changed to a more desirable single endfire beam. This effect is illustrated for the two-element parasitic array of Fig. 5-28. The driver is a dipole of length 0.4781λ , which is a half-wave resonant length when operated in free space. The parasite is a straight wire of length 0.49λ and spaced a distance 0.04λ away from the driver. The H -plane pattern in Fig. 5-28b obtained from the numerical methods of Chapter 7 demonstrates the general trend of a parasite which is longer than the driver: a single main beam occurs in the endfire direction from the parasite to the driver along the line of the array. Such a parasite is called a *reflector* because it appears to reflect radiation from the driver.

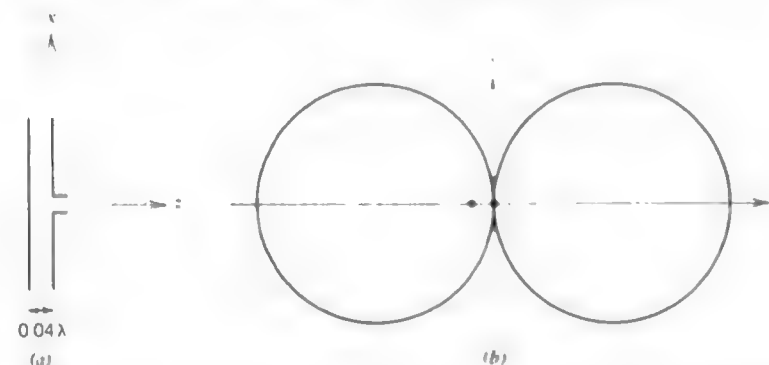


Figure 5-27 A two element array of half-wave resonant dipoles, one a driver and the other a parasite. The currents on both are equal in amplitude and opposite in phase. (a) Array configuration. (b) H -plane pattern computed from simple array theory.

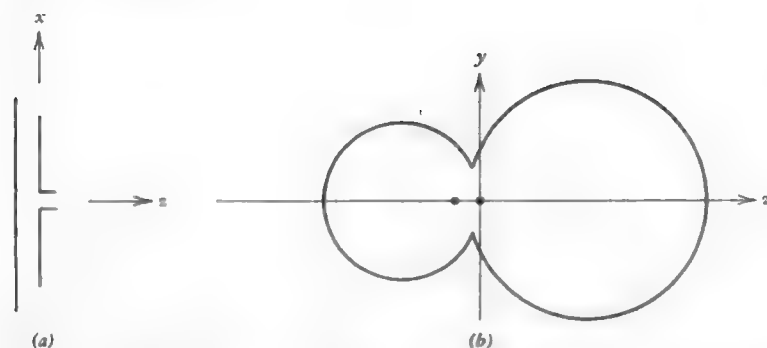


Figure 5-28 Two-element Yagi-Uda antenna consisting of a driver of length 0.4781λ and a reflector of length 0.49λ spaced 0.04λ away. The wire radius for both is 0.001λ . (a) Array configuration. (b) H -plane pattern computed from numerical methods.

If the parasite is shorter than the driver, but now placed on the other side of the driver, the pattern effect is similar to that when using a reflector in the sense that main beam enhancement is in the same direction. The parasite is then referred to as a *director* since it appears to direct radiation in the direction from the driver toward the director. The parasitic array in Fig. 5-29a consisting of a driver and a director has the pattern shown in Fig. 5-29b.

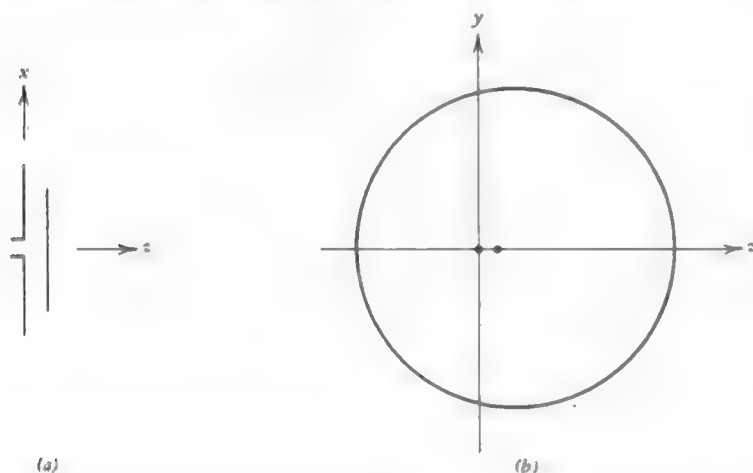


Figure 5-29 Two-element Yagi-Uda antenna consisting of a driver of length 0.4781λ and a director of length 0.45λ spaced 0.04λ away. The wire radius for both is 0.001λ . (a) Array configuration. (b) H -plane pattern computed from numerical methods.

The single endfire beam created by the use of a reflector or a director alone with a driver suggests that even further enhancement could be achieved with a reflector and a director on opposite sides of a driver. This is indeed the case. An example of a three-element Yagi is shown in Fig. 5-30a, which is a combination of the geometries of Figs. 5-28a and 5-29a. The pattern of Fig. 5-30b is improved over that of either two-element array. The E -plane pattern for the three-element Yagi is shown in Fig. 5-30c. It is essentially equal to the H -plane pattern multiplied by the element factor for the array, which is that of a half-wave dipole. Again these patterns were obtained by numerical solution.

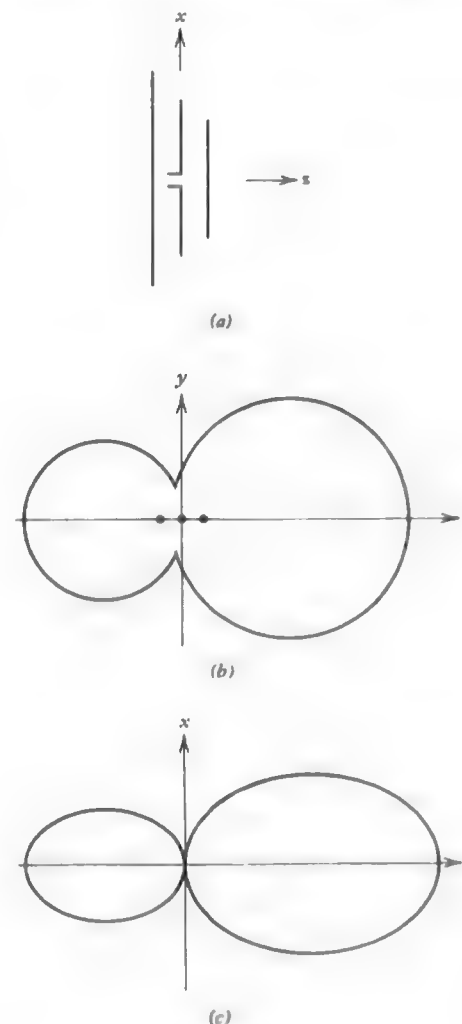


Figure 5-30 Three-element Yagi-Uda antenna consisting of a driver of length 0.4781λ , a reflector of 0.49λ , and a director of length 0.45λ , each spaced 0.04λ apart. The wire radius for each is 0.001λ . (a) Array configuration. (b) H -plane pattern computed from numerical methods. (c) E -plane pattern computed from numerical methods.

The maximum directivity obtainable from a three-element Yagi is about 9 dB [15]. The optimum spacings (for maximum directivity) are on the order of 0.15 to 0.25 wavelength between the reflector and driver and also between the driver and director. Typically the reflector is lengthened 5% or more and the director is shortened 5% or more from the length of the resonant length driver. The resonant length of the driver does not differ significantly from its resonant length when operated with no parasites present [16].

A considerable amount of experimental and theoretical work has been done on extending the Yagi array beyond the basic three element unit. It has been found that more than one reflector provides little improvement. On the other hand, the addition of more directors does increase the gain. The general Yagi array including several directors is shown in Fig. 5-31.

The Yagi is really an endfire traveling-wave antenna. A surface wave of the slow wave type, with a phase velocity less than that of a free space plane wave, propagates along the array. Since the array is parasitic the current on the director elements farther out from the driver have decreasing current amplitudes. If the amplitudes and phases of the currents on each element were known, array analysis could be used to determine the radiation pattern. Numerical techniques as found in Chapter 7 are required to determine the element currents. In the remainder of this section we will present the results of numerical analysis for Yagi antennas which can be used to design Yagis.

Because of the decreasing current amplitudes for the directors farther from the driver, there is a smaller gain increase for each director added to the end of the Yagi array. In fact, the addition of directors up to about five provides significant increase in gain. But further addition of directors gives little gain improvement, that is, there is a "point of diminishing returns." This is illustrated in Fig. 5-32 where gain is plotted versus the total number of elements in the array (including one reflector and one driver) [17]. The element spacing is fixed ($S_R = S_D = 0.15\lambda$) for this curve. Note that adding one director to increase N from 3 to 4 gives

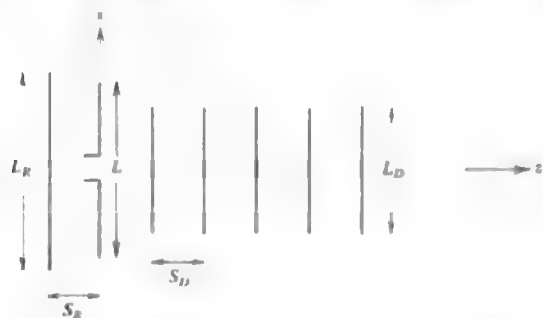


Figure 5-31 Configuration for a general Yagi-Uda antenna.

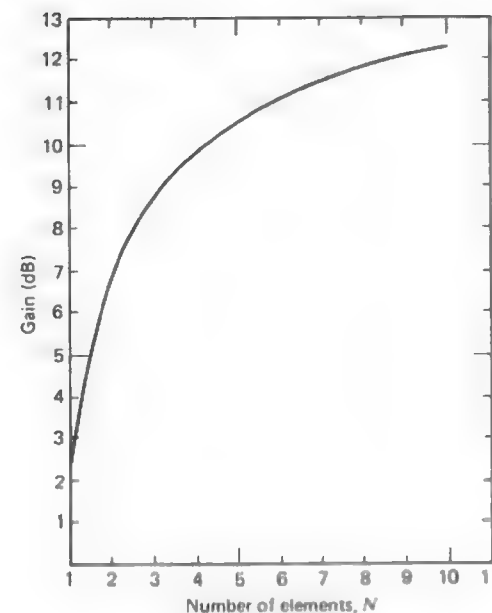


Figure 5-32 Gain of a typical Yagi-Uda antenna versus the total number of elements. The element spacings $S_R = S_D = 0.15\lambda$. The conductor diameters are 0.0025λ . (From Green [17].)

about 1-dB gain increase, whereas adding one director to increase N from 9 to 10 yields only about 0.2-dB gain increase.

The characteristics of a Yagi are affected by all of the geometric parameters of the array. Fortunately though, minor changes in the geometry likewise yield only minor changes in the Yagi performance. In Table 5-4 the characteristics of several Yagi antennas are listed. These data were obtained by the method of moments presented in Chapter 7. All array elements have a conductor diameter of 0.005λ , which corresponds to $L/2a \approx 100$. A popular construction material for Yagis is $\frac{1}{2}$ -in.-diameter tubular aluminum, which has a 0.005λ diameter at 118 MHz. However, the conductor diameter is not a critical parameter; Yagis can be constructed using the design data of Table 5-4 and commonly available materials without significantly affecting the electrical performance characteristics. The data in the table agrees well with experimental results; for example, see [18]. Details on precise design of Yagis are available in the literature [19].

In all cases given in Table 5-4 the half-power beamwidth in the E -plane (xz -plane) is smaller than in the H -plane (yz -plane). This is due to the element pattern of the array. In the E -plane the element pattern is approximately that of a half-wave dipole since all elements are about a half-wavelength long. However, in the H -plane the element pattern is isotropic because the elements are seen in end view giving nearly zero extent, which yields an isotropic element pattern.

Table 5-4 Characteristics of Equally Spaced Yagi-Uda Antennas

N, no. of elements	Element Lengths				Front to back ratio (dB)	Gain (dB)	H-Plane		E-Plane		
	Spacing (wavelengths)	Reflector, L_R (wavelengths)	Driver, L (wavelengths)	Directors, L_D (wavelengths)			Input impedance (ohms)	HP _H (degrees)	SLL _H (dB)	HP _E (degrees)	SLL _E (dB)
3	0.25	0.479	0.453	0.451	9.4	5.6	22.3 + j15.0	84	-11.0	66	-34.5
4	0.15	0.486	0.459	0.453	9.7	8.2	36.7 + j9.6	84	-11.6	66	-22.8
4	0.20	0.503	0.474	0.463	9.3	7.5	5.6 + j20.7	64	-5.2	54	-25.4
4	0.25	0.486	0.463	0.456	10.4	6.0	10.3 + j23.5	60	-5.8	52	-15.8
4	0.30	0.475	0.453	0.446	10.7	5.2	25.8 + j23.2	64	-7.3	56	-18.5
5	0.15	0.505	0.476	0.456	10.0	13.1	9.6 + j13.0	76	-8.9	62	-23.2
5	0.20	0.486	0.462	0.449	11.0	9.4	18.4 + j17.6	68	-8.4	58	-18.7
5	0.25	0.477	0.451	0.442	11.0	7.4	53.3 + j6.2	66	-8.1	58	-19.1
5	0.30	0.482	0.459	0.451	9.3	2.9	19.3 + j39.4	42	-3.3	40	-9.5
6	0.20	0.482	0.456	0.437	11.2	9.2	51.3 - j1.9	68	-9.0	58	-20.0
6	0.25	0.484	0.459	0.446	11.9	9.4	23.2 + j21.0	56	-7.1	50	-13.8
6	0.30	0.472	0.449	0.437	11.6	6.7	61.2 + j7.7	56	-7.4	52	-14.8
7	0.20	0.489	0.463	0.444	11.8	12.6	20.6 + j16.8	58	-7.4	52	-14.1
7	0.25	0.477	0.454	0.434	12.0	8.7	57.2 + j1.9	58	-8.1	52	-15.4
7	0.30	0.475	0.455	0.439	12.7	8.7	35.9 + j21.7	50	-7.3	46	-12.6

Conductor diameter = 0.005λ.

Example 5-1. A Six-Element Yagi for TV Channel 15

This example demonstrates how simple it is to design a Yagi antenna. Additionally, it is shown that liberties may be taken with the design values of Table 5-4 without significant performance degradation. The design has been tested by building the antenna according to the techniques detailed in Prob. 5.4-7 and it was found to operate very well. The midband frequency for TV Channel 15 from Appendix D.2 is 479 MHz, which corresponds to a wavelength of $\lambda = 62.63$ cm. Number 8 wire was used to construct the antenna elements. From Appendix E.2 No. 8 wire has a 0.3264-cm diameter which leads to $2a = 0.0052\lambda$. To test the sensitivity of Yagi performance to deviation from the lengths and spacings given in Table 5-4, the following geometry was used:

$$\begin{aligned}
 L_R &= 0.5\lambda = 31.3 \text{ cm} & S_R &= 0.25\lambda = 15.7 \text{ cm} \\
 L &= 0.47\lambda = 29.4 \text{ cm} & S_D &= 0.30\lambda = 18.8 \text{ cm} \\
 L_D &= 0.43\lambda = 26.9 \text{ cm}
 \end{aligned} \tag{5-46}$$

This six-element Yagi was evaluated using numerical methods with the following results: input impedance $Z_{in} = 59.5 + j47.5$ ohms, gain $G = 11.5$ dB, E -plane half-power beamwidth $HP_E = 56^\circ$, H -plane half-power beamwidth $HP_H = 62^\circ$, E -plane first side lobe $SLL_E = -16.6$ dB, H -plane first side lobe $SLL_H = -8.1$ dB, and a front-to-back ratio of 9.7 dB. These values are in general agreement with those of Table 5-4 for six-element Yagis. The computed radiation patterns for this antenna are plotted in Fig. 5-33.

In practice Yagi antennas are mounted on a mast that is usually constructed of tubular aluminum. It is not necessary to insulate the parasitic elements from the mast because very little current will be excited on it. Of course, the driven element must be insulated to avoid shorting the terminals. When using a metal mast it may be necessary to increase the element lengths slightly to achieve optimum performance. In most cases the driven element is a folded dipole. This serves two purposes. First, the input impedance of the driver is increased. This is desirable because the input resistance values of Table 5-4, which are computed for an ordinary resonant half-wave dipole feed, are relatively low and not well matched to common transmission lines. Second, the electrical performance of the antenna will remain stable over a wider bandwidth when a folded dipole feed is used. It is also quite common to employ multiple, series fed, folded dipole driven elements together with one reflector and several directors. Further gain can be obtained by arraying or "stacking" Yagi antennas. Maximum gain results for a stacking separation of almost one wavelength (see Fig. 3-20).

The Yagi is one of the most popular antennas in use today in the HF-VHF-UHF frequency range. It provides high gain while at the same time offering low weight and low cost. It has relatively narrow bandwidth, but if high gain is required the Yagi antenna may be the lowest cost antenna available over the stated frequency range.

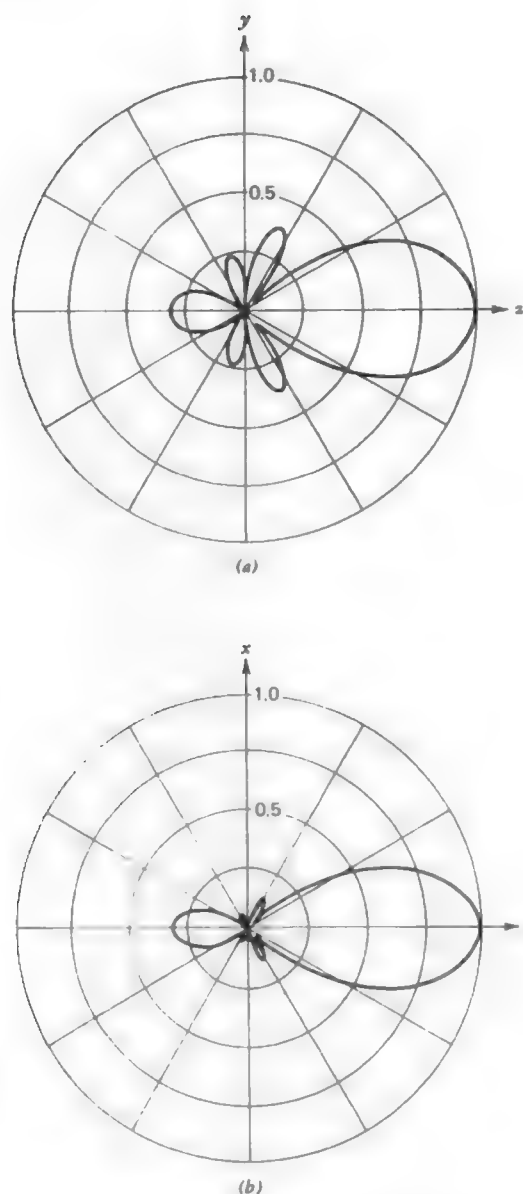


Figure 5-33 Six-element Yagi-Uda antenna for TV Channel 15 (Example 5-1). See Fig. 5-31 and (5-46) for the antenna geometry. (a) *H*-plane pattern. (b) *E*-plane pattern.

5.5 WIRE ANTENNAS ABOVE AN IMPERFECT GROUND PLANE

The operation of low-frequency (roughly VHF and below) antennas are affected significantly by the presence of typical environmental surroundings, such as the earth, buildings, and so forth. In Section 2.3 we discussed the principles for analyzing antennas above a perfect ground plane. A perfect ground plane in its ideal form is an infinite, plane, perfect conductor. It is well approximated in practice by a planar good conductor which is large relative to the antenna extent. Image theory from Section 2.3.1 reveals that an antenna above a perfect ground plane, or an approximation thereof, has an equivalent form that is an array. Array theory can then be used to obtain the radiation pattern above the ground plane.

In this section we consider ground planes which are not well approximated by a perfect ground plane. Since low-frequency antennas are most affected by their surroundings and low-frequency antennas are usually wire antennas, the illustrations will be for wire antennas above a ground plane. The general principles can, however, be applied to many antenna types.

A ground plane can take many forms, such as radial wires around a monopole, the roof of a car, or the real earth. In many situations the earth is well approximated as being infinite and planar, but it is a poor conductor. Good conductors have conductivities on the order of 10^7 mhos/m. Earth conductivity varies greatly, but is typically 10^{-1} to 10^{-3} mho/m with rich soil at the high end and rocky or sandy soil at the low end. With these low conductivities electric fields generated by a nearby antenna penetrate into the earth and excite currents which in turn give rise to $\sigma|E|^2$ ohmic losses. This loss appears as an increase in the input ohmic resistance and thus lowers the radiation efficiency of the antenna.

5.5.1 Pattern Effects of a Real Earth Ground Plane

The pattern of an antenna over a real earth is different from the pattern when the antenna is operated over a perfect ground plane. Approximate patterns can be obtained by using image theory. The same principles discussed in Section 2.3.1 for images in perfect ground planes apply, except that the strength of the image in a real ground will be reduced from that of the perfect ground plane case (equal amplitude, and equal phase for vertical elements and opposite phase for horizontal elements). The strength of the image can be approximated by weighting it with the plane wave reflection coefficient for the appropriate polarization of the field arriving at the ground plane. To illustrate, consider a short vertical dipole a distance h above a ground plane, shown in Fig. 5-34 together with its image. There is a direct and a reflected ray arriving in the far field. As can be

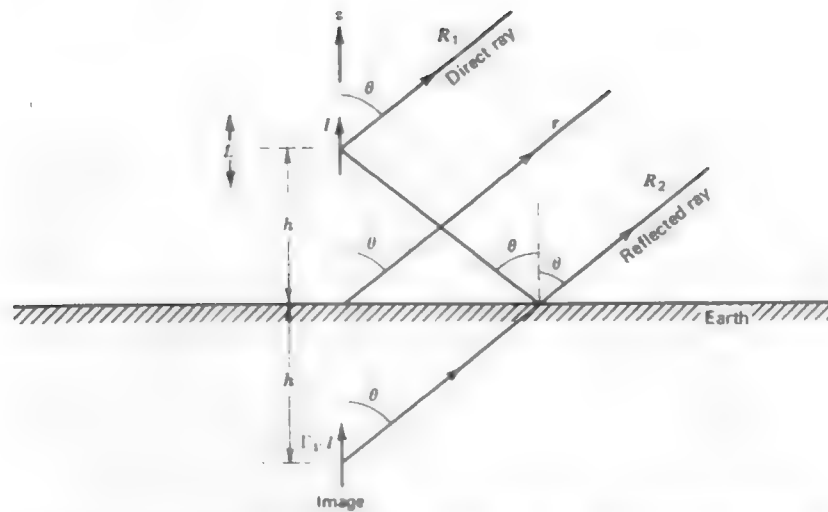


Figure 5-34 A short vertical dipole of current I above a real earth ground plane, together with its image of current $\Gamma_V I$.

seen, the reflected ray appears to be coming from the image antenna. The primary source and its image form an array. The electric field above the ground plane for this example, from (1-75) in (1-90), is

$$E_\theta = j\omega\mu \sin\theta \left(IL \frac{e^{-j\beta R_1}}{4\pi R_1} + \Gamma_V IL \frac{e^{-j\beta R_2}}{4\pi R_2} \right) \quad (5-47)$$

where L is the length of the short dipole and $\Gamma_V I$ is the current for the image dipole. Γ_V is the plane wave reflection coefficient for a planar earth and vertical incident polarization. Using parallel rays for far-field calculations gives the far-field distance expressions

$$R_1 = r - h \cos\theta \quad \text{and} \quad R_2 = r + h \cos\theta. \quad (5-48)$$

Then (5-47) reduces to

$$E_\theta = j\omega\mu \frac{IL e^{-j\beta r}}{4\pi r} \sin\theta (e^{j\beta h \cos\theta} + \Gamma_V e^{-j\beta h \cos\theta}) \quad (5-49)$$

where $R_1 \approx R_2 \approx r$ was used in the denominator. This expression is valid above the ground plane. It contains an element pattern $\sin\theta$ and an array factor, in the brackets, for a two-element array with elements spaced $2h$ apart.

Similarly for a horizontally oriented short dipole as shown in Fig. 5-35, we have (in the xz -plane)

$$E_\theta = j\omega\mu \frac{IL e^{-j\beta r}}{4\pi r} \cos\theta (e^{j\beta h \cos\theta} - \Gamma_V e^{-j\beta h \cos\theta}) \quad (5-50)$$

where the minus sign appears because the image current is in the opposite direction. This expression is valid only in the xz -plane. The field in the yz -plane is given by

$$E_\phi = j\omega\mu \frac{IL e^{-j\beta r}}{4\pi r} (e^{j\beta h \cos\theta} + \Gamma_H e^{-j\beta h \cos\theta}). \quad (5-51)$$

The element pattern is unity because a dipole has an omnidirectional pattern in the plane normal to the dipole axis. The horizontal reflection coefficient Γ_H is used in this case because the electric field from the primary antenna in the yz -plane is incident on the ground plane horizontally, that is, parallel to the plane.

There is no minus sign in the second term of (5-51) because of the definition of Γ_H , which is [20]

$$\Gamma_H = \frac{\cos\theta - \sqrt{\epsilon'_r - \sin^2\theta}}{\cos\theta + \sqrt{\epsilon'_r - \sin^2\theta}}. \quad (5-52)$$

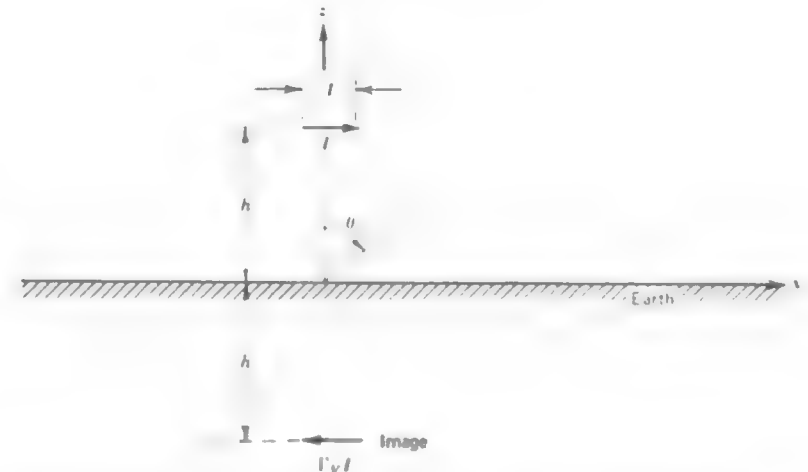


Figure 5-35 A short horizontal dipole of current I above a real earth ground plane together with its image of current $\Gamma_V I$ for the xz -plane. The image current in the yz -plane is $\Gamma_H I$.

This is the plane wave reflection coefficient for an incident electric field perpendicular to the plane of polarization (i.e., the plane formed by the surface normal and the direction of propagation). Further, for Γ_v we have [20]

$$\Gamma_v = \frac{\epsilon'_r \cos \theta - \sqrt{\epsilon'_r - \sin^2 \theta}}{\epsilon'_r \cos \theta + \sqrt{\epsilon'_r - \sin^2 \theta}} \quad (5-53)$$

This is the plane wave reflection coefficient for an incident electric field parallel to the plane of polarization. ϵ'_r is the relative complex effective dielectric constant (see Section 1.2) for the ground and is given by

$$\epsilon'_r = \frac{\epsilon'}{\epsilon_0} = \epsilon_r - j \frac{\sigma}{\omega \epsilon_0} \quad (5-54)$$

ϵ_r and σ are the relative dielectric constant and conductivity of the ground plane. The earth has an average value of $\epsilon_r = 15$. Ground conductivities across the United States vary from 10^{-3} to 3×10^{-2} mho/m [20]. A convenient parameter is the ratio of the imaginary part of ϵ'_r to the real part, ϵ_r , given by

$$n = \frac{\sigma}{\omega \epsilon_r \epsilon_0} \quad (5-55)$$

The value of n increases for decreasing frequency and increasing conductivity and is infinite for a perfect ground plane.

The reflection coefficients, Γ_H and Γ_v , both approach -1 for a real earth ground plane at angles of θ near 90° (grazing incidence). The reflection coefficient for vertical polarization has, in general, a rather complex behavior as a function of θ . On the other hand, Γ_H always has a phase of about 180° and a magnitude not too different from unity for all values of θ . In fact, for frequencies of 1 MHz or below and good earth conductivities the magnitude of Γ_H is very nearly unity for θ from 0 to 90° .

The use of plane wave reflection coefficients to obtain the image strength is only an approximation since antennas near a ground plane do not form plane waves incident on the ground plane. In addition to the radiation we have described above there is a surface wave that propagates along the ground plane surface. For HF and VHF frequencies the surface wave attenuates very rapidly. For grazing angles (θ near 90°) $\Gamma_v \approx -1$ and vertical antennas close to a real earth have zero radiation for $\theta = 90^\circ$; see (5-49). In this case the surface wave accounts for all propagation, as in daylight standard broadcast AM. The effect of neglecting the surface wave, and using the procedure given above, has been found not to be critical for vertical antennas [21]. For horizontal antennas the antenna should be at least 0.2λ above the earth for the plane wave reflection coefficient method to be valid [22].

The elevation pattern for a short vertical dipole at the surface of various

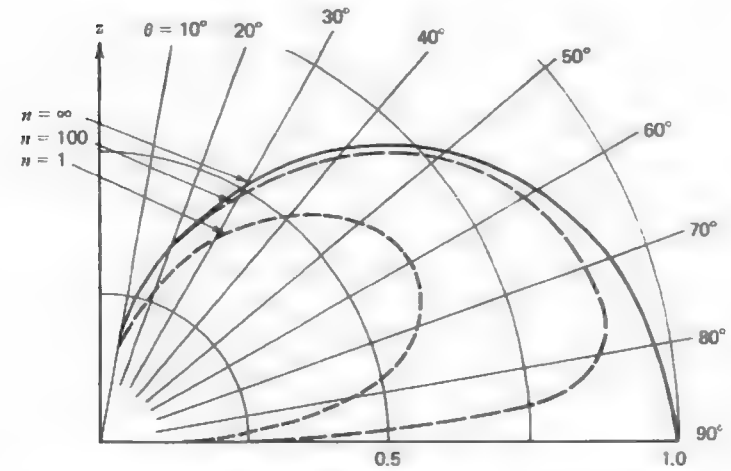


Figure 5-36 Elevation patterns of a vertical short dipole at the surface of the ground plane, for a perfect ground plane ($n = \infty$) and typical soils ($n = 1$ and 100) with $\epsilon_r = 15$. (After Jordan and Balmain [20]. Reprinted by permission of Prentice-Hall, Inc., Englewood Cliffs, NJ.)

ground planes is shown in Fig. 5-36. When the ground plane is perfect ($n = \infty$) the pattern above the ground plane is the same as that of a short dipole in free space, $\sin \theta$. Thus, in the perfect ground plane case radiation is maximum along the ground plane; whereas for a real earth ground plane the radiation maximum is tilted up away from the ground plane and is reduced in intensity, for the same input power, due to reduced efficiency. This is a general trend. The effect of a lossy earth on vertical antennas is to tilt the radiation pattern upward. A good radial ground system (to be discussed in Section 5.5.2) will make the pattern behave more nearly like that for a perfect ground plane, that is, increase the low angle radiation (along the ground plane). Low angle radiation is particularly important for long distance communication links that rely on ionospheric reflection (skip).

A short vertical dipole that is $\lambda/4$ above the ground plane forms a $\lambda/2$ spaced array with its image. For the perfect ground plane $\epsilon'_r = \infty$ and Γ_v from (5-53) is $+1$. The array is then a $\lambda/2$ spaced, equally excited, in-phase collinear array. The pattern for this is given in Fig. 3-17 and is also plotted in Fig. 5-37a ($n = \infty$). For a real earth ground plane $\Gamma_v \approx -1$ at grazing angles (θ near 90°). The array contributions thus cancel giving a null along the ground plane as shown in Fig. 5-37a. As the height h is increased to $\lambda/2$ the equivalent array of Fig. 5-34 has a λ spacing and multiple lobes appear in addition to the effects described for $h = \lambda/4$. The elevation patterns for $h = \lambda/2$ are plotted in Fig. 5-37b.

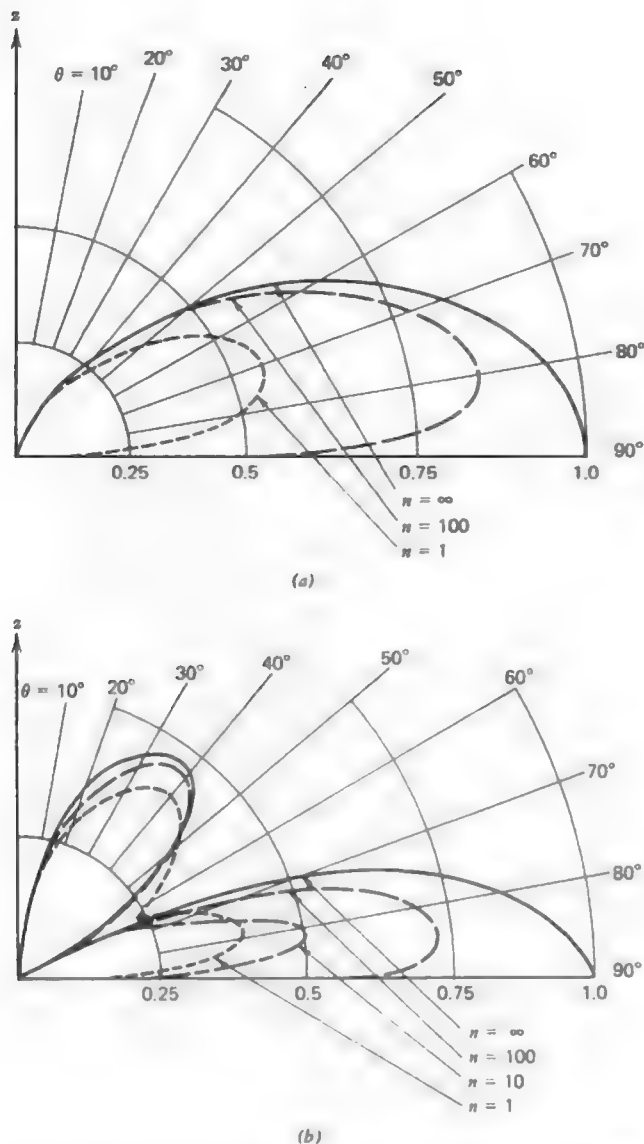


Figure 5-37 Elevation patterns (in the E -plane) of a vertical short dipole above various ground planes. $\epsilon_r = 15$ for real earth cases. (a) A quarter-wavelength above ground, $h = \lambda/4$. (b) A half-wavelength above ground, $h = \lambda/2$. (After Jordan and Balmain [20]. Reprinted by permission of Prentice-Hall, Inc., Englewood Cliffs, NJ.)

For a horizontal short dipole as shown in Fig. 5-35 the radiation is not the same for all planes through the z -axis, as for vertical antennas. In the yz -plane (perpendicular to the axis of the dipole) the radiation electric field is given by (5-51). The reflection coefficient Γ_H is exactly -1 for a perfect ground plane and approximately -1 for real earth ground planes at all angles θ . The element pattern is isotropic since the elements are seen in end view in the H -plane (yz -plane). Thus the array factor completely determines the pattern. The H -plane patterns for h equal to $\lambda/4$ and $\lambda/2$ are shown in Fig. 5-38 for various ground planes. Since the dipole and its image are nearly out-of-phase there will be a null along the ground plane. For $h = \lambda/4$ the half-wavelength spacing between the dipole and its image compensates for the near out-of-phase array condition giving a maximum for $\theta = 0^\circ$ in Fig. 5-38a (see Fig. 3-4 also). For $h = \lambda/2$ and a perfect ground plane, radiation from the dipole and its image are exactly out-of-phase in the $\theta = 0^\circ$ direction giving a null. For real earth ground planes the image is not exactly of equal amplitude and opposite phase so there is not a perfect null in the $\theta = 0^\circ$ direction but a low radiation value as seen in Fig. 5-38b. Notice that the effects of finite conductivity are much less pronounced for horizontal antennas than for vertical antennas.

The E -plane radiation from a horizontal short dipole can be found from (5-50).

The field expressions of (5-49) to (5-51) for short dipoles above a ground plane can be used for other antenna types by using the appropriate element pattern. In particular, $\sin \theta$ in (5-49) and $\cos \theta$ in (5-50) are replaced by the free-space pattern of the antenna considered.

5.5.2 Ground Plane Construction

An excellent ground plane can be constructed by using a metallic sheet that is much larger than the antenna extent. Such ground planes become impractical at low frequencies because of the size required. In this section various techniques are discussed for increasing the apparent conductivity of a real earth ground.

Consider a vertical monopole antenna with its base at ground level. (See Section 2.3.2 for a discussion of monopoles over a perfect ground plane.) Currents flowing up the antenna leave the antenna and form displacement currents in air. Upon entering the earth, conduction currents are formed which converge toward the base of the antenna. Losses in an earth ground can be reduced by providing a highly conductive return path. This is commonly achieved with a *radial ground system*. The size of the wires used is not critical and is determined by the mechanical strength required. Number 8 AWG wire is typical. They need not be buried, but it is usually convenient to do so. However, they should not be buried too deep in order to minimize the extent of earth through which the fields must pass. Sometimes the radial wires are linked together at the base of the

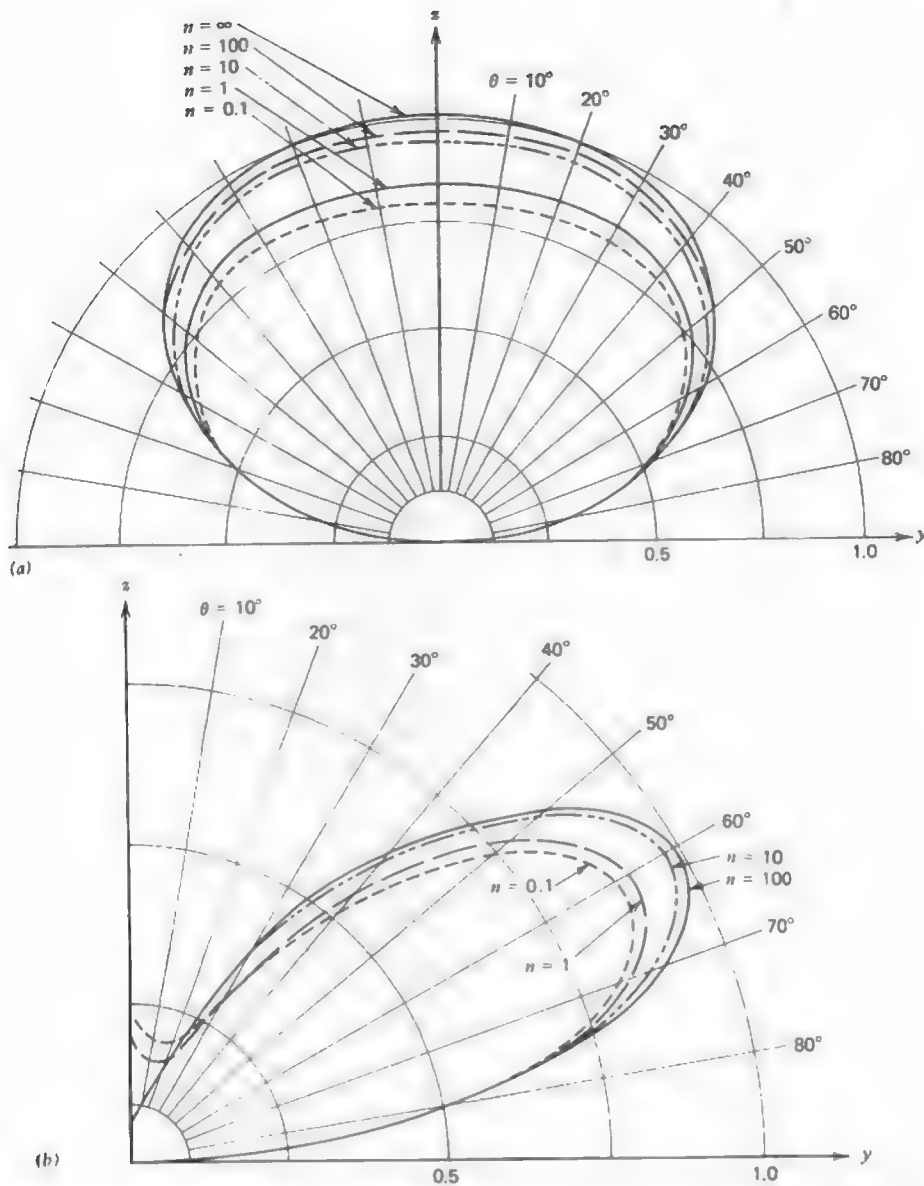


Figure 5-38 *H*-plane elevation radiation patterns for a horizontal short dipole above various ground planes. See Fig. 5-35. $\epsilon_r = 15$ for real earth cases. (a) A quarter-wavelength above ground, $h = \lambda/4$. (b) A half-wavelength above ground, $h = \lambda/2$. (After Jordan and Balmain [20]. Reprinted by permission of Prentice-Hall, Inc., Englewood Cliffs, NJ.)

monopole by a ring shaped ground strap. Occasionally one or more stakes are driven into the ground near the base of the monopole.

The ohmic resistance of the radial system and earth ground adds to the ohmic resistance of the monopole structure to determine the total ohmic resistance components of the input impedance. The efficiency of the antenna system depends on the proportion of radiation resistance and ohmic resistance; see (1-182). For high-power transmitting antennas it is important to have a well designed radial system to achieve high efficiency. On the other hand, for simple monopole structures, three equally spaced radial wires form the radial system.

The most sophisticated ground system such as used with a standard broadcast AM transmitting antenna is 120 radial wires spaced equally, 3° apart, around the tower out to a distance of about a quarter-wavelength from the tower. In general, the length of the radials is roughly equal to the height of the monopole antenna. The value of the total ohmic resistance of a ground system with 120 radials for typical soils is plotted in Fig. 5-39 for a few frequencies as a function of radial length [23]. Note that at 3 MHz a ground system with 120 radials that are about a quarter-wavelength long (25 m) gives a ground system resistance of 1 ohm. Since the surface resistance of the earth varies as the square root of frequency [see (1-185)] the ground system resistance will be constant for lower frequencies if the length of the radials is increased in proportion to the square root of wavelength. For frequencies above 3 MHz, the curve for radial length in Fig. 5-39 is only slightly to the right of the 3-MHz curve. This is because after the radials reach a length of about a quarter-wavelength most of the large current densities occur within the region of the radials and further length increase is of no major consequence.

The construction principles for a radial wire ground system on top of or in the earth can be summarized rather simply. The function of a radial system is to prevent the electromagnetic fields from the antenna from penetrating into the ground and exciting currents which in turn lead to $\sigma|E|^2$ ohmic loss. As can be seen from the above discussion, if 120 quarter-wavelength long radials are employed the ohmic resistance introduced by the ground system will be at most a few ohms and usually well under an ohm. In most applications it is impractical to install as many as 120 radials. Generally speaking, 50 radials about a quarter-wavelength long will reduce earth losses to a few ohms. When only a few radials are used the added resistance of the ground can be several ohms. Also if the radial lengths (almost independent of the number used) are reduced below a tenth of a wavelength the ground system resistance will increase significantly.¹ The radial wires can be laid on top of the ground or buried slightly (but never deeply buried). Wire selection is largely determined by mechanical considerations. As the number of radials is increased the less current each one will have to

¹ More details and references for ground system design are available in [24].

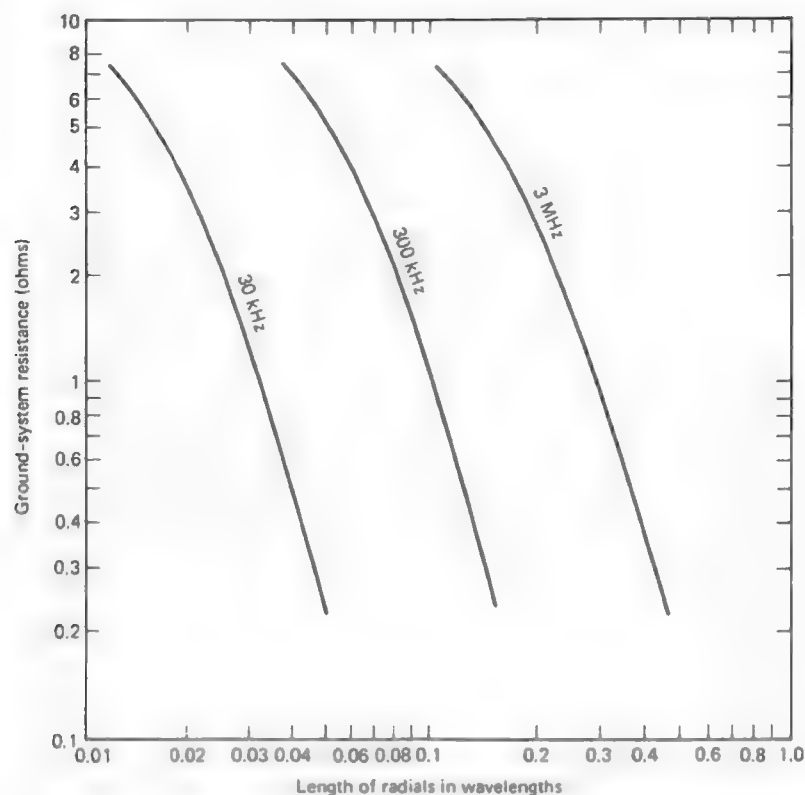


Figure 5-39 Typical resistance of radial ground systems using 120 radials in average soil. (From Griffith [23]. © 1962 McGraw-Hill. Used with permission of McGraw-Hill Book Company.)

carry and thus the smaller the wire diameter required. At the base of the antenna the radials should be connected together and to one or more ground stakes.

At high frequencies (VHF and above) antennas are often mounted over metallic (solid, mesh, or radial wire) ground planes of relatively small extent. Then the dimensions and shape of the ground plane are important. In general the radiation is greatest in the direction of the largest portion of the ground plane. For example, consider a monopole antenna mounted on an automobile. If it is placed on the right rear bumper a pattern maximum occurs off of the left front of the car. When the antenna is mounted in the center of the car roof there is some slight pattern enhancement in the forward and rear directions.

5.6 TRAVELING-WAVE WIRE ANTENNAS

The wire antennas we have discussed thus far have been resonant structures. The wave traveling outward from the feed point to the end of the wire is reflected, setting up a standing-wave type current distribution. This can be seen by examining the expression for the current in (5-1) for the top half of the dipole which can be written as

$$I_m \sin \left[\beta \left(\frac{L}{2} - z \right) \right] = \frac{I_m}{2j} e^{j\beta L/2} (e^{-j\beta z} - e^{j\beta z}). \quad (5-56)$$

The first term in brackets represents an outward traveling wave and the second term a reflected wave. The minus sign is the current reflection coefficient at an open circuit.

If the reflected wave is not present on an antenna it is referred to as a **traveling-wave antenna**. A traveling-wave antenna acts as a guiding structure for traveling waves whereas a resonant antenna supports standing waves. Traveling waves can be created by using matched loads at the ends to prevent reflections. Also, very long antennas will radiate most of the power, leading to small reflected waves by virtue of the fact that very little power is incident on the ends. In this section several wire forms of traveling-wave antennas will be discussed. Other traveling-wave antennas are discussed under the topic of broadband antennas in the next chapter. Some of the antennas in this section are essentially the traveling-wave counterparts of resonant wire antennas presented previously in this chapter. They tend to be broadband with bandwidths of as much as 2:1.

The simplest traveling-wave wire antenna is a straight wire carrying a pure traveling wave, referred to as the **traveling-wave long wire antenna**. A long wire is one that is greater than one-half wavelength long. The traveling-wave long wire is shown in Fig. 5-40 with a matched load R_L to prevent reflections from the wire end. Exact analysis of this structure, as well as others to be presented in this section, is formidable. We shall make several simplifying assumptions which permit pattern calculations that do not differ greatly from real performance. First, the ground plane effects will be ignored and we will assume the antenna

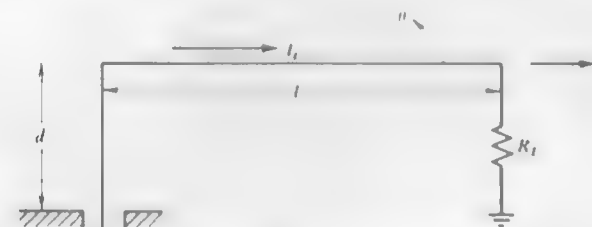


Figure 5-40 Traveling-wave long wire antenna

operates in free space. A traveling-wave long wire operated in the presence of a ground plane is called a **Beverage antenna**, or **wave antenna**. The ground plane can be accounted for using the techniques of the previous section. Second, the details of the feed are assumed to be unimportant. In Fig. 5-40 the long wire is shown being fed from a coaxial transmission line as one practical method. The vertical section of length d is assumed not to radiate, which is approximately true for $d \ll L$. Finally, we assume that the radiative and ohmic losses along the wire are small. When attenuation is neglected the current amplitude is constant and the phase velocity is that of free space [25]. We can then write

$$I_z(z) = I_m e^{-j\beta z} \quad (5-57)$$

which represents an unattenuated traveling wave propagating in the $+z$ -direction with the phase constant β of free space.

The current of (5-57) is that of a uniform line source with a linear phase constant of $\beta_o = -\beta$. From (4-6) $\beta_o = -\beta \cos \theta_o$, so the pattern factor maximum radiation angle (not including element factor effects) is $\theta_o = 0^\circ$, which implies an endfire pattern. The complete radiation pattern from (4-8) is

$$F(\theta) = K \sin \theta \frac{\sin[(\beta L/2)(1 - \cos \theta)]}{(\beta L/2)(1 - \cos \theta)} \quad (5-58)$$

where K is a normalization constant that depends on the length L . The polar pattern for $L = 6\lambda$ is shown in Fig. 5-41. The element factor $\sin \theta$ forces a null in

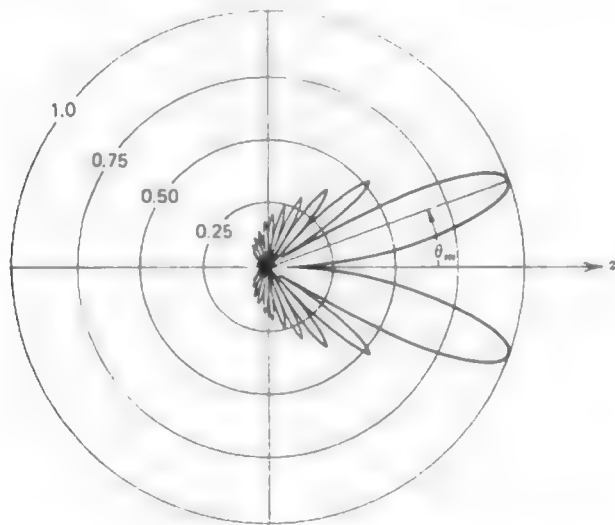


Figure 5-41 Pattern of a traveling-wave long wire antenna. $L = 6\lambda$ and $\theta_m = 20^\circ$.

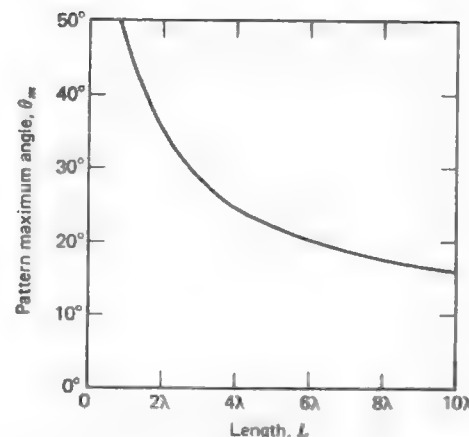


Figure 5-42 Pattern maximum angle for a traveling-wave long wire antenna of length L operating in free space. See (5-58).

the endfire direction. Hence, instead of having a single endfire lobe (which the pattern factor produces), the "main beam" is a rotational symmetric cone about the z -axis. The maximum radiation angle in this case is $\theta_m(L = 6\lambda) = 20.1^\circ$. In general it is a function of L . Solving (5-58) for θ_m as a function L produces the plot of Fig. 5-42. An approximate expression for the angle of maximum radiation is [26]

$$\theta_m = \cos^{-1} \left(1 - \frac{0.371}{L/\lambda} \right) \quad (5-59)$$

The beam direction values from Fig. 5-42 or (5-59) for a traveling-wave long wire of length L may be used to calculate an approximate beam direction for a standing-wave straight wire antenna (i.e., dipole). For example, θ_m for $L = 3\lambda/2$ from Fig. 5-42 is 40° and θ_m for the dipole of Fig. 5-4c is 42.6° . As L increases the traveling-wave and standing-wave antenna main beam maximum angles approach each other [27]. The standing-wave wire antenna is distinguished from its traveling-wave counterpart by the presence of a second major lobe in the reverse direction; see Fig. 5-4c. This can be seen by noting that the traveling-wave current of (5-57) corresponds to the first term of the standing-wave current of (5-56). The second term of (5-56), which is the reflected wave, produces a pattern similar in shape but oppositely directed. Thus a traveling-wave antenna has a beam with a maximum in the $\theta = \theta_m$ direction and a standing-wave antenna of the same length has an additional beam in the $\theta = 180^\circ - \theta_m$ direction.

The input impedance of a traveling-wave antenna is always predominantly real. This can be understood by recalling that the impedance of a pure traveling wave on a low-loss transmission line is equal to the (real) characteristic impedance of the transmission line. Antennas that support traveling waves operate in a similar manner. The radiation resistance of a traveling-wave long wire

antenna is 200 to 300 ohms (see Prob. 5.6-5). The termination resistance should equal the value of the radiation resistance.

The resonant vee antenna discussed in Section 5.1.2 can be made into a traveling-wave antenna by terminating the wire ends with matched loads. The **traveling-wave vee antenna** is shown in Fig. 5-43. The pattern due to each arm separately is expressed by (5-58), an example of which is shown in Fig. 5-41. From Fig. 5-43 it is seen that when $\alpha \approx \theta_m$, the beam maxima from each arm of the vee will line up in the forward direction. A more accurate analysis of vee (see Prob. 5.6-8) includes the spatial separation effects of the arms. Pattern calculations as a function of α reveal that a good vee pattern is obtained when

$$\alpha \approx 0.8\theta_m \quad (5-60)$$

where θ_m is found from Fig. 5-42 or (5-59). For $L = 6\lambda$, $\theta_m = 20^\circ$ from Fig. 5-42 and (5-60) yields $\alpha \approx 16^\circ$; the pattern for a vee with this geometry is shown in Fig. 5-43. The large side lobes arise from portions of the beams from each half of the vee which do not line up along axis. The pattern of the vee out of the plane of the vee is rather complicated due to the merging of the conical beams for each half of the vee. The traveling-wave vee provides relatively high gain for a bent wire structure.

By extending the ideas of a traveling-wave vee antenna we obtain a **rhombic antenna** as shown in Fig. 5-44. The operation of this antenna is visualized most easily by viewing it as a transmission line that has been spread apart and consequently the characteristic impedance is increased. The load resistor R_L is of such a value as to match the transmission line. The antenna carries outward

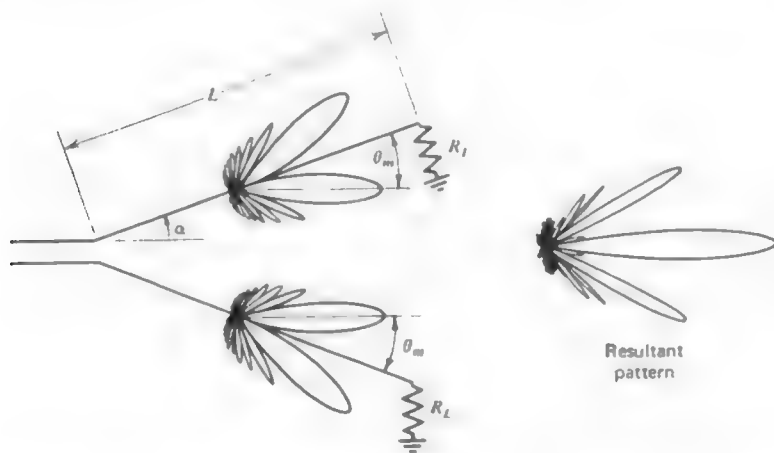


Figure 5-43 The traveling-wave vee antenna. In this case $L = 6\lambda$ and $\alpha = 0.8\theta_m = 16^\circ$.

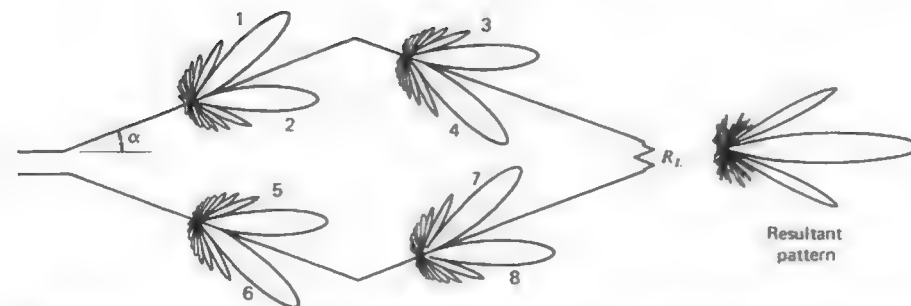


Figure 5-44 The rhombic antenna. Each side is of length L . Component beams 2 and 3, and 5 and 8 line up to form the main beam of the resultant pattern. In this case $L = 6\lambda$ and $\alpha = 16^\circ$.

traveling waves which are absorbed in the matched load. Since the separation between the lines is large relative to a wavelength, the structure will radiate. If designed properly a directive pattern with a single beam in the z -direction can be obtained.

A rhombic antenna operating in free space can be modeled as two traveling-wave vee antennas put together. Choosing $\alpha = 0.8\theta_m$ as for the vee, the beams of the rhombic in Fig. 5-44 numbered 2, 3, 5, and 8 will be aligned. Again θ_m follows from Fig. 5-42. Due to the spatial separation of the two vees the rhombic pattern will not be the same as that of a single vee [27]. (See Prob. 5.6-9.)

The effects of a rhombic operating above a real earth ground can be included by the techniques of the previous section. For a rhombic that is oriented horizontally the reflection coefficient $\Gamma_{||}$ is approximately -1 and the real earth may be modeled as a perfect conductor; Fig. 5-38 illustrates that this assumption has a minor effect for horizontal antennas. The array factor of a rhombic a distance h above a perfect ground plane produces a null along the ground plane. There are several designs for rhombics above a ground plane in the literature [26-29]. One such design is for alignment of the major lobe at a specific elevation angle. Then the rhombus angle α and the elevation angle of the main beam are equal, and the height above ground is given by

$$h = \frac{\lambda}{4 \sin \alpha} \quad (5-61)$$

and the length of each leg is

$$L = \frac{0.371\lambda}{\sin^2 \alpha} \quad (5-62)$$

For example, if $\alpha = 14.4^\circ$ then $L = 6\lambda$ and $h = 1\lambda$. Rhombic impedances are typically on the order of 600 to 800 ohms.

The efficiency of the rhombic antenna is decreased significantly because of the matched termination. The power that is not radiated is absorbed in the load R_L . However, this loss of power is essentially that which would have appeared in a large back lobe as a result of reflected current if the matched load were not present. The traveling wave feature not only improves the pattern but also produces wider bandwidth.

5.7 SQUARE LOOP ANTENNAS

Electrically small loop antennas with a perimeter that is much less than a wavelength were discussed in Section 2.4. It was found that the pattern and radiation resistance of a small loop are insensitive to the loop shape and depend only on the loop area. Also the radiation from a small loop is maximum in the plane of the loop and is zero along its axis. These facts follow directly as a consequence of the current amplitude and phase being constant over the loop, which in turn is due to the loop being electrically small. As the perimeter of a loop antenna becomes a sizable fraction of a wavelength, the current amplitude and phase will vary over the wire extent, much as we saw with dipole antennas. Therefore, loop antennas with a perimeter that is on the order of half-wavelength or larger will display performance variations with loop size and shape.

Discussions of large loop antennas are frequently approached by solving a loop antenna under the assumption of uniform current amplitude and phase (see Prob. 5.7-1). However, as we have mentioned, the current does not behave this way. Instead of assuming a uniform current, we will analyze the square loop antenna in a realistic fashion, thus yielding useful results. A square loop antenna with a perimeter of one wavelength will be analyzed in detail. Although the solution is rather involved, it provides an opportunity to show that the theoretical principles we have developed using a realistic current assumption will yield relatively accurate results. This is demonstrated by comparison to the more exact results from numerical solution methods.

The **one-wavelength square loop antenna** as shown in Fig. 5-45 has one-quarter wavelength sides. For a one-wavelength perimeter it is reasonable to assume that the current distribution is sinusoidal. Then the current distribution is continuous around the loop as shown in Fig. 5-45 (solid curve). With the feed point in the center of a side parallel to the x -axis this sinusoidal current is expressed as

$$\begin{aligned} I_1 = I_2 &= -\hat{x} I_0 \cos(\beta x') & |x'| \leq \frac{\lambda}{8} \\ I_4 = -I_3 &= \hat{y} I_0 \sin(\beta y') & |y'| \leq \frac{\lambda}{8} \end{aligned} \quad (5-63)$$

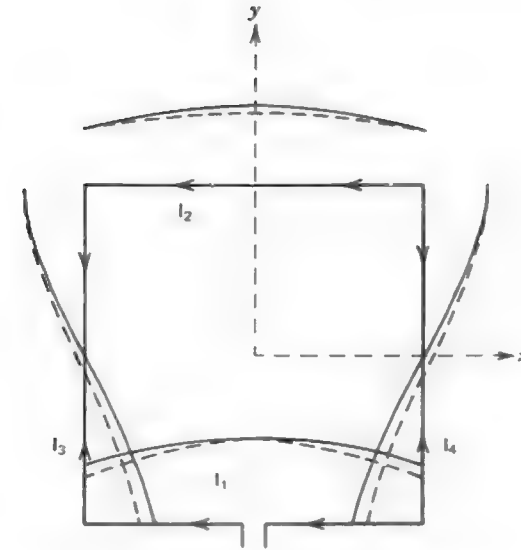


Figure 5-45 The one-wavelength square loop antenna. Each side is of length $\lambda/4$. The solid curve is the sinusoidal current distribution of (5-63). The dashed curve is the current magnitude obtained from more exact numerical methods.

Solution for the radiation properties proceeds in the usual manner. First the vector potential from (1-99) is

$$\mathbf{A} = \frac{e^{-j\beta r}}{4\pi r} \int_{\text{loop}} \mathbf{I} e^{j\beta \hat{\mathbf{r}} \cdot \mathbf{r}'} dl. \quad (5-64)$$

To find the phase function, the expressions for vectors from the origin to arbitrary positions on each side must be written. They are

$$\begin{aligned} \mathbf{r}'_1 &= x' \hat{\mathbf{x}} - \frac{\lambda}{8} \hat{\mathbf{y}} & \mathbf{r}'_2 &= x' \hat{\mathbf{x}} + \frac{\lambda}{8} \hat{\mathbf{y}} \\ \mathbf{r}'_3 &= -\frac{\lambda}{8} \hat{\mathbf{x}} + y' \hat{\mathbf{y}} & \mathbf{r}'_4 &= \frac{\lambda}{8} \hat{\mathbf{x}} + y' \hat{\mathbf{y}} \end{aligned} \quad (5-65)$$

where the numbered subscripts indicate the corresponding loop side. Using the expansion of \hat{r} from (A-4) and (5-65) in (5-64) with the loop integral broken into integrals over each side gives

$$\begin{aligned} \mathbf{A} &= \frac{e^{-j\beta r}}{4\pi r} I_o \left[-\hat{x} \int_{-\lambda/8}^{\lambda/8} \cos(\beta x') e^{j\beta x' \sin \theta \cos \phi} (e^{-j(\pi/4) \sin \theta \sin \phi} + e^{j(\pi/4) \sin \theta \sin \phi}) dx' \right. \\ &\quad \left. + \hat{y} \int_{-\lambda/8}^{\lambda/8} \sin(\beta y') e^{j\beta y' \sin \theta \sin \phi} (-e^{-j(\pi/4) \sin \theta \cos \phi} + e^{j(\pi/4) \sin \theta \cos \phi}) dy' \right] \\ &= \frac{e^{-j\beta r}}{4\pi r} I_o \left[-\hat{x} 2 \cos\left(\frac{\pi}{4} \sin \theta \sin \phi\right) \int_{-\lambda/8}^{\lambda/8} \cos(\beta x') e^{j\beta x' \sin \theta \cos \phi} dx' \right. \\ &\quad \left. + \hat{y} 2j \sin\left(\frac{\pi}{4} \sin \theta \cos \phi\right) \int_{-\lambda/8}^{\lambda/8} \sin(\beta y') e^{j\beta y' \sin \theta \sin \phi} dy' \right]. \quad (5-66) \end{aligned}$$

The first factors in each of the above two terms in brackets are the array factors for the pairs of sides 1, 2 and 3, 4, respectively. Evaluation of the integrals and subsequent simplification lead to

$$\begin{aligned} \mathbf{A} &= \frac{e^{-j\beta r}}{4\pi r} \frac{2\sqrt{2}I_o}{\beta} \left\{ \hat{x} \frac{\cos[(\pi/4)\cos \Omega]}{\sin^2 \gamma} \left[\cos \gamma \sin\left(\frac{\pi}{4} \cos \gamma\right) - \cos\left(\frac{\pi}{4} \cos \gamma\right) \right] \right. \\ &\quad \left. - \hat{y} \frac{\sin[(\pi/4)\cos \gamma]}{\sin^2 \Omega} \left[\cos \Omega \cos\left(\frac{\pi}{4} \cos \Omega\right) - \sin\left(\frac{\pi}{4} \cos \Omega\right) \right] \right\} \quad (5-67) \end{aligned}$$

where

$$\cos \gamma = \sin \theta \cos \phi \quad \text{and} \quad \cos \Omega = \sin \theta \sin \phi. \quad (5-68)$$

The angles γ and Ω have a geometrical interpretation; they are the spherical polar angles (similar to θ) for the x - and y -axes; see (A-4).

The far-zone electric field components are

$$\begin{aligned} E_\theta &= -j\omega\mu A_\theta = -j\omega\mu \mathbf{A} \cdot \hat{\theta} = -j\omega\mu (A_x \hat{x} \cdot \hat{\theta} + A_y \hat{y} \cdot \hat{\theta}) \\ &= -j\omega\mu (A_x \cos \theta \cos \phi + A_y \cos \theta \sin \phi). \quad (5-69a) \end{aligned}$$

$$E_\phi = -j\omega\mu \mathbf{A} \cdot \hat{\phi} = -j\omega\mu (-A_x \sin \phi + A_y \cos \phi). \quad (5-69b)$$

Substituting A_x and A_y from (5-67) gives

$$\begin{aligned} E_\theta &= \frac{jI_o \eta e^{-j\beta r}}{\sqrt{2\pi r}} \cos \theta \left\{ \frac{\sin \phi \sin[(\pi/4) \sin \theta \cos \phi]}{1 - \sin^2 \theta \sin^2 \phi} \right. \\ &\quad \cdot \left[\sin \theta \sin \phi \cos\left(\frac{\pi}{4} \sin \theta \sin \phi\right) - \sin\left(\frac{\pi}{4} \sin \theta \sin \phi\right) \right] \\ &\quad - \frac{\cos \phi \cos[(\pi/4) \sin \theta \sin \phi]}{1 - \sin^2 \theta \cos^2 \phi} \\ &\quad \cdot \left[\sin \theta \cos \phi \sin\left(\frac{\pi}{4} \sin \theta \cos \phi\right) - \cos\left(\frac{\pi}{4} \sin \theta \cos \phi\right) \right] \Big\} \quad (5-70a) \end{aligned}$$

$$\begin{aligned} E_\phi &= \frac{jI_o \eta e^{-j\beta r}}{\sqrt{2\pi r}} \left\{ \frac{\cos \phi \sin[(\pi/4) \sin \theta \cos \phi]}{1 - \sin^2 \theta \sin^2 \phi} \right. \\ &\quad \cdot \left[\sin \theta \sin \phi \cos\left(\frac{\pi}{4} \sin \theta \sin \phi\right) - \sin\left(\frac{\pi}{4} \sin \theta \sin \phi\right) \right] \\ &\quad + \frac{\sin \phi \cos[(\pi/4) \sin \theta \sin \phi]}{1 - \sin^2 \theta \cos^2 \phi} \\ &\quad \cdot \left[\sin \theta \cos \phi \sin\left(\frac{\pi}{4} \sin \theta \cos \phi\right) - \cos\left(\frac{\pi}{4} \sin \theta \cos \phi\right) \right] \Big\}. \quad (5-70b) \end{aligned}$$

These expressions are rather involved but were derived in a straightforward fashion using the principles set forth in Section 1.5.

The far-field expressions simplify somewhat in the principal planes. In the xy -plane, which is the plane of the loop (an E -plane), $\theta = 90^\circ$ and then (5-70) reduces to

$$E_\theta \left(\theta = \frac{\pi}{2} \right) = 0 \quad (5-71a)$$

$$\begin{aligned} E_\phi \left(\theta = \frac{\pi}{2} \right) &= \frac{jI_o \eta e^{-j\beta r}}{\sqrt{2\pi r}} \frac{\pi}{4} \left\{ \frac{\sin[(\pi/4) \cos \phi]}{(\pi/4) \cos \phi} \left[\sin \phi \cos\left(\frac{\pi}{4} \sin \phi\right) - \sin\left(\frac{\pi}{4} \sin \phi\right) \right] \right. \\ &\quad \left. + \frac{\cos[(\pi/4) \sin \phi]}{(\pi/4) \sin \phi} \left[\cos \phi \sin\left(\frac{\pi}{4} \cos \phi\right) - \cos\left(\frac{\pi}{4} \cos \phi\right) \right] \right\}. \quad (5-71b) \end{aligned}$$

The E_ϕ expression is plotted in Fig. 5-46a (solid curve) in normalized form. Along the x -axis ($\phi = 0^\circ$ and 180°) $E_\phi = 0$. This is true because the sides 3 and 4 alone each have patterns that are zero in the broadside direction since the

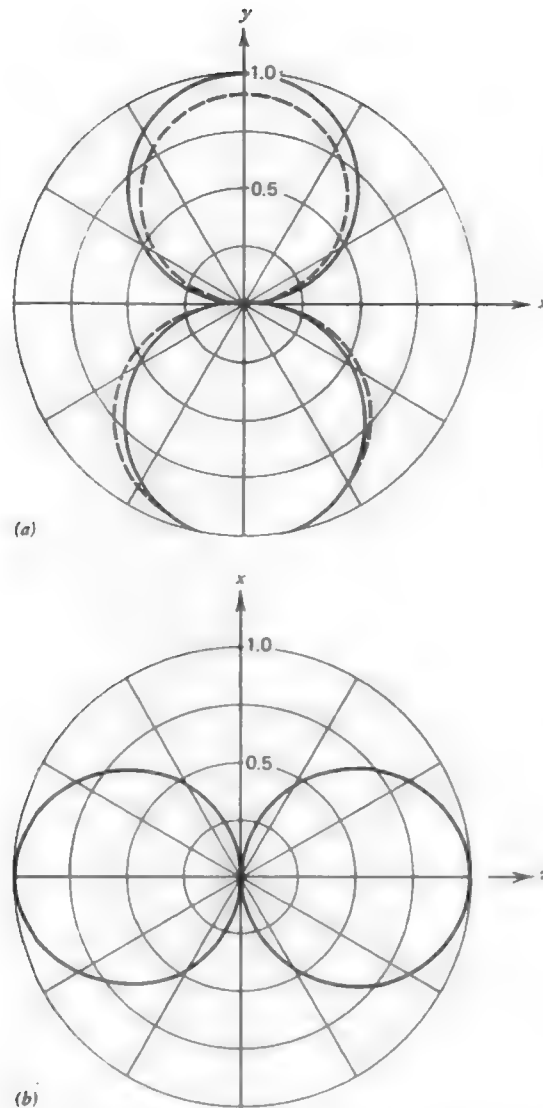


Figure 5-46 Principal plane patterns for one-wavelength square loop antenna. The solid curves are the patterns based on a sinusoidal current distribution of Fig. 5-45. The dashed curves are the patterns arising from the current distribution obtained by the more exact numerical methods. (a) The xy -plane normalized pattern plot of E_θ . In this plane $HP = 94^\circ$. (b) The xz -plane normalized pattern plot of E_θ . In this plane $HP = 85^\circ$. The patterns from the two methods coincide in this plane.

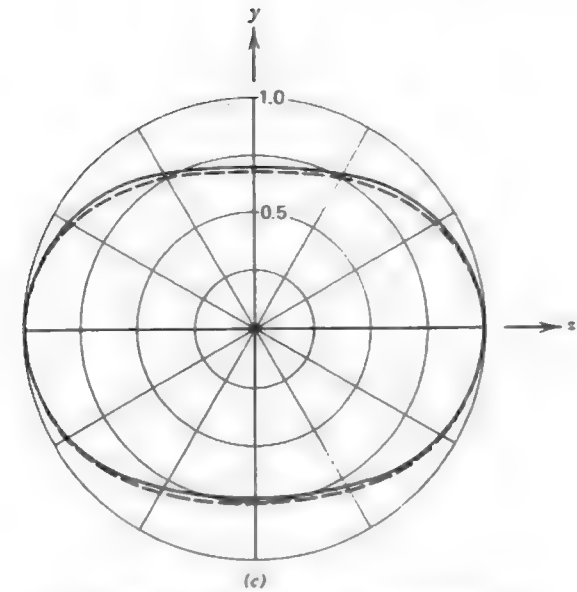


Figure 5-46 (c) The yz -plane pattern plot of E_θ .

current distributions on these sides are odd about their midpoints. Along the y -axis (5-71b) reduces to

$$E_\phi \left(\theta = \frac{\pi}{2}, \phi = \frac{\pi}{2} \right) = -\frac{jI_0 \eta e^{-j\beta r}}{\sqrt{2\pi r}} \frac{1}{\sqrt{2}} \quad (5-72)$$

In the xz -plane, which is an E -plane, (5-70) yields

$$E_\phi(\phi = 0) = 0 \quad (5-73a)$$

$$E_\theta(\phi = 0) = \frac{jI_0 \eta e^{-j\beta r} \sin \theta \sin[(\pi/4)\sin \theta] - \cos[(\pi/4)\sin \theta]}{\sqrt{2\pi r} \cos \theta} \quad (5-73b)$$

The normalized form of this E_θ expression is plotted in Fig. 5-46b (solid curve). It can be shown that (5-73b) goes to zero for $\theta = 90^\circ$, as it should by (5-71a).

In the yz -plane, which is the H -plane, (5-70) reduces to

$$E_\theta \left(\phi = \frac{\pi}{2} \right) = 0 \quad (5-74a)$$

$$E_\phi \left(\phi = \frac{\pi}{2} \right) = -\frac{jI_0 \eta e^{-j\beta r}}{\sqrt{2\pi r}} \cos \left(\frac{\pi}{4} \sin \theta \right). \quad (5-74b)$$

Figure 5-46c (solid curve) gives the plot of the normalized form of this E_ϕ expression. The $\cos[(\pi/4)\sin\theta]$ pattern is the array factor for two point sources at the midpoints of sides 1 and 2. Note that in the z -direction (5-73) and (5-74) give the same result (for $\theta = 0^\circ$): an electric field parallel to the x -axis given by

$$E_x = -\frac{jI_0 \eta e^{-j\beta r}}{\sqrt{2\pi r}} \quad (5-75)$$

which is a factor of $\sqrt{2}$ greater than E_x in the y -direction given in (5-72). This is also seen in Fig. 5-46c.

From the patterns in Fig. 5-46 we can make some general conclusions about the radiation properties of the one-wavelength square loop antenna. Radiation is maximum normal to the plane of the loop (along the z -axis) and in that direction is polarized parallel to the loop side containing the feed. In the plane of the loop there is a null in the direction parallel to the side containing the feed point (along the x -axis), and there is a lobe in a direction perpendicular to the side containing the feed (along the y -axis). These results are quite different from the small loop antenna which has a null on-axis and maximum (uniform) radiation in the plane of the loop.

The accuracy of our results can be investigated by solving the square loop problem without assuming the current distribution to be sinusoidal. The numerical methods of Chapter 7 applied to the one-wavelength loop antenna for a wire radius of 0.001λ renders the current magnitude shown in Fig. 5-45 (dashed curve). Note that the agreement is actually very good. The impact of the slight differences in these current distributions are revealed in Fig. 5-46. The dashed curves are the patterns corresponding to the exact current distribution and calculated by a radiation integral procedure similar to that detailed above for the assumed current. The agreement between the patterns arising from the simple current assumption and that of more exact methods is very good. In fact, in the xz -plane the agreement is nearly exact. This detailed comparison of the approximate antenna analysis methods employed thus far in the book to that of more exact (but more difficult) numerical methods serves to provide confidence that good engineering results can be obtained from reasonable assumptions about the operation of antennas.

The square loop antenna is most useful in practice for a one-wavelength perimeter because of the desirable input impedance properties. The impedance of a square loop antenna with a wire radius of 0.001λ is plotted in Fig. 5-47 as a function of the perimeter. Note that for a one-wavelength perimeter the input reactance is relatively small, and also note that resonance occurs for a 1.09λ perimeter. The input resistance for a one-wavelength perimeter is about 100 ohms. Other perimeter values give rather awkward input impedances.

The gain of the one-wavelength square loop is 3.09 dB, which is less than the 3.82 dB gain of a straight wire one-wavelength dipole. This is to be expected from the obviously less directive pattern of the loop in Fig. 5-46 compared to that of the one-wavelength dipole in Fig. 5-4b.

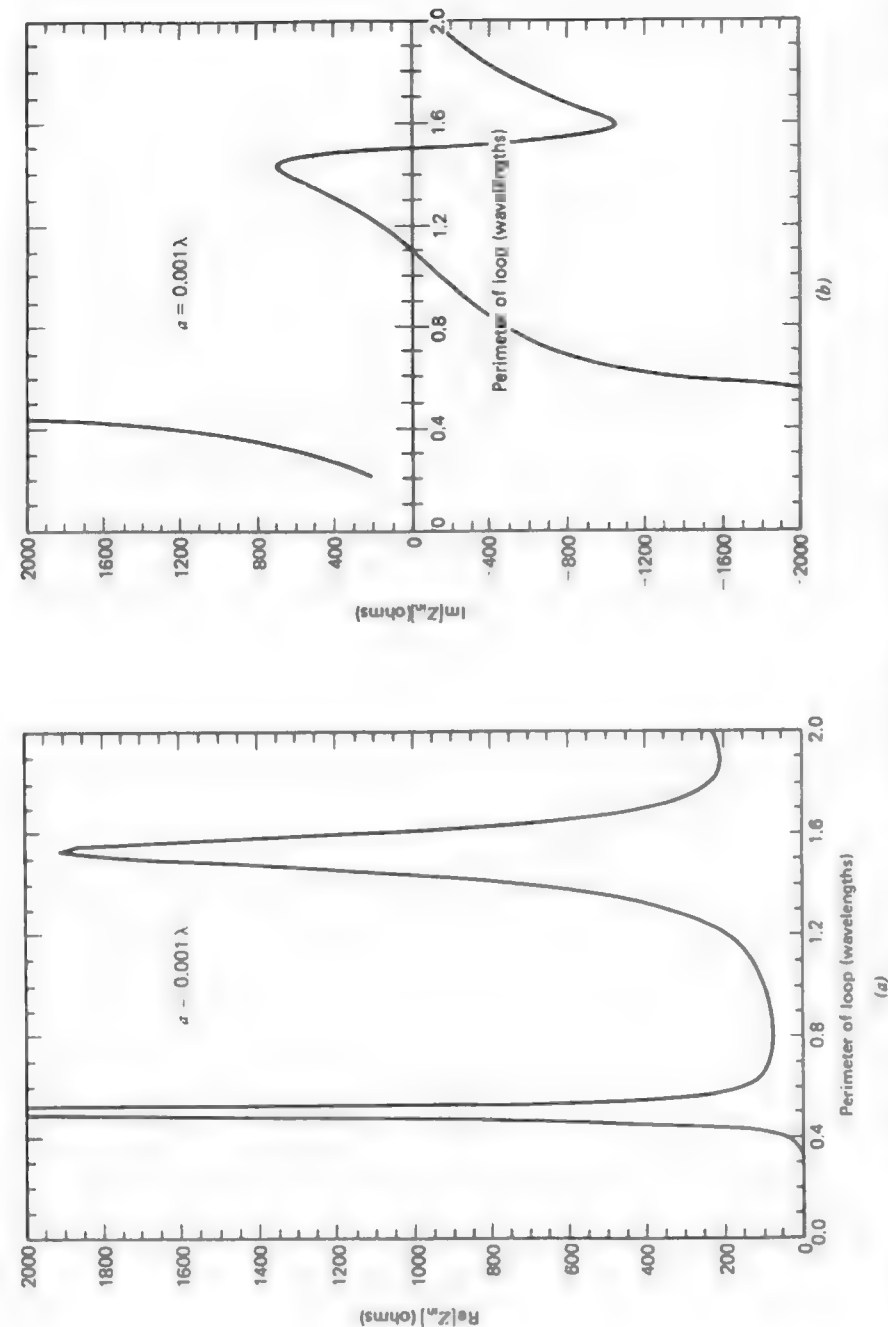


Figure 5-47 Input impedance of a square loop antenna as a function of the loop perimeter. The loop is fed in the center of one side and has a wire radius of $a = 0.001\lambda$. Numerical calculation methods were used. (a) Input resistance (b) Input reactance.

REFERENCES

1. R. W. P. King, "The linear antenna—eighty years of progress," *Proceedings of the IEEE*, vol. 55, pp. 2–16, Jan. 1967.
2. R. W. P. King, *The Theory of Linear Antennas*, Harvard University Press, Cambridge, Mass., 1956.
3. R. W. P. King, *Tables of Antenna Characteristics*, Plenum, New York, 1961.
4. J. D. Kraus, *Antennas*, McGraw-Hill, New York, 1950; p. 139.
5. R. W. P. King, H. R. Mimno and H. H. Wing, *Transmission Lines, Antennas, and Waveguides*, Dover, New York, 1965; p. 86.
6. M. Abramowitz and I. A. Stegun, *Handbook of Mathematical Functions*, NBS Applied Math. Series 55, U.S. Government Printing Office, Washington, D.C., 1964; Chapter 5.
7. E. Jordan and K. Balmain, *Electromagnetic Waves and Radiating Systems*, 2nd Edition, Prentice-Hall, Englewood Cliffs, N.J., 1968; Chapter 14.
8. R. F. Schwartz, "Input impedance of a dipole or monopole," *Microwave Journal*, vol. 15, p. 22, Dec. 1972.
9. "IEEE Standard definitions of terms for antennas," *IEEE Transactions on Antennas and Propagation*, vol. AP-22, Jan. 1974.
10. H. Jasik, Editor, *Antenna Engineering Handbook*, McGraw-Hill, New York, 1961; Section 3.3.
11. E. Wolff, *Antenna Analysis*, Wiley, New York, 1967; p. 67.
12. E. Jordan and K. Balmain, *Electromagnetic Waves and Radiating Systems*, Second Edition, Prentice-Hall, Englewood Cliffs, N.J., 1968; p. 402.
13. G. A. Thiele, "Analysis of Yagi-Uda type antennas," *IEEE Trans. on Ant. and Prop.*, vol. AP-17, pp. 24–31, Jan. 1969.
14. H. Yagi, "Beam transmission of ultra-short waves," *Proceedings of IRE*, vol. 16, p. 715, 1928.
15. S. Uda and Y. Mushiake, *Yagi-Uda Antenna*, Sasaki Printing and Publishing Company, Ltd., Sendai, Japan, 1954.
16. H. W. Ehrenspeck and H. Poehler, "A new method for obtaining maximum gain for Yagi antennas," *IRE Trans. on Antennas and Propagation*, vol. AP-7, pp. 379–386, Oct. 1959.
17. H. E. Green, "Design data for short and medium length Yagi-Uda arrays," *Institution of Engineers (Australia), Electrical Engineering Transactions*, pp. 1–8, March 1966.
18. G. A. Thiele, *Computer Techniques for Electromagnetics*, vol. 7, Edited by R. Mittra, Pergamon Press, Oxford, 1973; p. 47.
19. P. Viezbickie, "Yagi antenna design," *NBS Technical Note 688*, U.S. Government Printing Office, Dec. 1976.
20. E. C. Jordan and K. G. Balmain, *Electromagnetic Waves and Radiating Systems*, Second Edition, Prentice-Hall, Englewood Cliffs, N.J., 1968; Chapter 16.
21. E. K. Miller et al., "Analysis of wire antennas in the presence of a conducting half-space. Part I. The vertical antenna in free space," *Canadian J. Physics*, vol. 50, pp. 879–888, 1972.
22. E. K. Miller et al., "Analysis of wire antennas in the presence of a conducting

half-space. Part II. The horizontal antenna in free space," *Canadian J. Physics*, vol. 50, pp. 2614–2627, 1972.

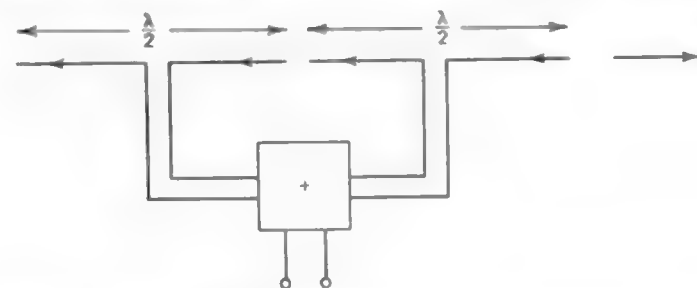
23. B. W. Griffith, *Radio-Electronic Transmission Fundamentals*, McGraw-Hill, New York, 1962; Chapter 43.
24. W. L. Weeks, *Antenna Engineering*, McGraw-Hill, New York, 1968; Section 2.6.
25. C. H. Walter, *Traveling Wave Antennas*, Dover, New York, 1965; Section 8-2.
26. E. A. Wolff, *Antenna Analysis*, Wiley, New York, 1966; Chapter 8.
27. H. Jasik, Editor, *Antenna Engineering Handbook*, McGraw-Hill, New York, 1961; Chapter 6.
28. S. A. Schelkunoff and H. T. Friis, *Antenna Theory and Practice*, Wiley, New York, 1952; Chapter 14.
29. J. D. Kraus, *Antennas*, McGraw-Hill, New York, 1950; Chapter 14.

PROBLEMS

5.1-1 Use the integral from (F-11) in (5-3) to prove (5-4).

5.1-2 Starting with (5-6) show that for $L \ll \lambda$, the radiation pattern of a dipole reduces to that of a short dipole, $\sin \theta$.

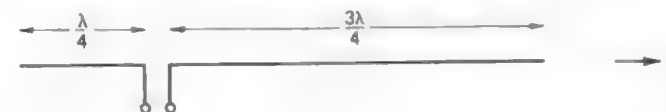
5.1-3 (a) The outputs from two collinear, closely spaced, half-wave dipoles are added together as indicated by a summing device in the figure below. The transmission lines from the antennas to the summer are of equal length. Write the pattern $F_\theta(\theta)$ of this antenna system using array techniques.



(b) Now consider a center-fed, full-wave dipole which is along the z -axis. Write its pattern expression $F_\theta(\theta)$.

(c) Now draw the current distributions $I_x(a)$ and $I_x(z)$ for both antennas. From these current distributions can you make a statement about the patterns from the two antennas? Return to the pattern expressions and prove your statement mathematically.

5.1-4 The center-fed, full-wave dipole is rarely used because it has a current minimum at the feed point. If it is instead fed as shown below, sketch the current distribution. Also, rough sketch how you think the pattern should look, and explain how you obtained it.



5.1-5 (a) The array of Prob. 5.1-3(a) is parallel fed, in-phase array. Show how the parallel wire transmission lines are connected to perform the summing function. Also put current arrows on each wire.

(b) Consider an array similar to that of part (a) except now the array elements (half-wave dipoles) are fed 180° out-of-phase. Show how the transmission lines are arranged to accomplish this subtraction function. Again show the currents on each wire.

5.1-6 Use the results of the cosine-tapered current distribution in Section 4.2 to derive the pattern of a half-wave dipole in (5-7).

5.1-7 Verify that the normalization constant in (5-9) is 0.7148 for the pattern of a $3\lambda/2$ dipole. What are the angles θ_0 in degrees for maximum radiation?

5.1-8 A resonant half-wave dipole is to be made for receiving TV Channel 7 of frequency 177 MHz. If $\frac{1}{2}$ -in. diameter tubular aluminum is used, how long (in centimeters) should the antenna be?

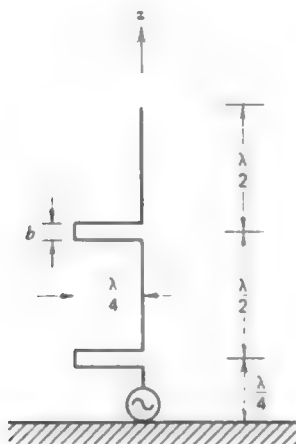
5.1-9 A four-element collinear array of half-wavelength spaced, half-wave dipoles are placed along the z -axis. All elements are fed with equal amplitude and phase.

(a) Determine the complete radiation pattern $F(\theta)$ for the array.

(b) Plot a sketch of the pattern in linear, polar form using array concepts.

5.1-10 Repeat Prob. 5.1-9 except now the half-wave dipole elements are parallel to each other and the x -axis, and are phased for ordinary endfire. The centers of the four elements are located on the z -axis and are spaced a half-wavelength apart.

5.1-11 The antenna shown is operated over a perfect ground plane. Its purpose is to enhance radiation in the xy -plane over that of a single quarter-wave monopole.



(a) Determine and sketch the current distribution. Assume $b \ll \lambda$.

(b) Use array concepts to obtain a linear, polar plot of the radiation pattern in a plane containing the z -axis.

5.1-12 (a) Show that the power radiated by a center-fed dipole of arbitrary length L with a sinusoidal current is

$$P_r = \frac{\eta I_m^2}{4\pi} \left\{ 0.5772 + \ln(\beta L) - \text{Ci}(\beta L) + \frac{1}{2} \sin(\beta L) [\text{Si}(2\beta L) - 2 \text{Si}(\beta L)] \right. \\ \left. + \frac{1}{2} \cos(\beta L) \left[0.5772 + \ln\left(\frac{\beta L}{2}\right) + \text{Ci}(2\beta L) - 2 \text{Ci}(\beta L) \right] \right\}$$

(b) Derive an expression for the directivity and then plot directivity as a function of dipole length for L from 0 to 3λ .

5.1-13 Use the length reduction procedure for half-wave resonance in Table 5-2 to calculate the resonant frequencies of the two dipoles in Fig. 5-7.

5.1-14 Design an optimum directivity vee dipole to have a directivity of 6 dB.

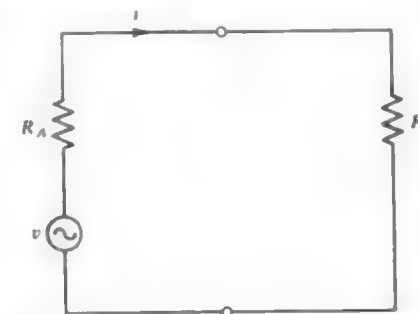
5.1-15 To show that the vee dipole results of (5-23) and (5-24) give roughly the correct results for a full-wave straight wire dipole; use $D = 2.41$ and determine γ .

5.2-1 (a) It is desired to have a simple formula for the length of a thin-wire half-wave folded dipole antenna. Show that it is $L(\text{cm}) = 14,250/f(\text{MHz})$.

(b) Determine the length in centimeters of half-wave folded dipoles for practical application as receiving antennas for each VHF TV channel and the FM broadcast band (100 MHz). Tabulate results.

5.2-2 Calculate the input impedance of a folded dipole of length $L = 0.4\lambda$, wire size $2a = 0.001\lambda$, and wire spacing $d = 12.5a$ using the transmission line model. Compare your results to values from Fig. 5-15.

5.3-1 A receiving antenna with a real impedance R_L attached to its terminals has the equivalent circuit shown. Prove that maximum power transfer to the load for a fixed real antenna impedance R_A occurs for $R_L = R_A$.



5.3-2 A transmitter with a real impedance of R_T is connected to a lossless transmission line of real characteristic impedance R_0 and then to an antenna of real input impedance R_0 .

(a) Derive an expression for the transmit efficiency, that is, power delivered to antenna/total power dissipated. Neglect any mismatch effects.

(b) Find the percent efficiency for $R_T = R_0$, $R_T = 0.5R_0$, and $R_T = 0.1R_0$.

5.4-1 Use array theory to analyze the array of Fig. 5-27a where the pattern of each element is that of a half-wave dipole.

- (a) Plot the H -plane pattern and compare to Fig. 5-27b.
 (b) Plot the E -plane pattern.

The program ARRPAT can be used.

5.4-2 Numerical methods reveal that the currents on the elements of the two-element parasitic array of Fig. 5-27a are nearly sinusoidal and the current amplitudes and phases at each element center are $1.0 \angle -88^\circ$ for the driver and $0.994 \angle 81.1^\circ$ for the parasite. Use simple array theory to obtain and plot the H -plane pattern in linear, polar form. The program ARRPAT can be used.

5.4-3 Phasor diagrams are often helpful in obtaining a rough idea about how arrays perform. To illustrate, use phasor diagrams to obtain the relative far-zone field values in the endfire directions of the two-element parasitic array of Prob. 5.4-2 (i.e., find the front to back ratio). To do this find the total phasor at each element location including the spatial phase delay due to the element separation. Assume the amplitudes of each element are unity and the phases are -88° for the driver and 81.1° for the parasite.

5.4-4 Design a three-element Yagi for FM broadcast reception at 100 MHz using the data of Table 5-4. Give dimensions in centimeters.

5.4-5 Design a seven-element Yagi for TV Channel 13. Space all elements 0.25 λ apart and use the values of Table 5-4. Give dimensions in centimeters.

5.4-6 Construction project—a ten cent Yagi. This project is designed to demonstrate how a high gain antenna can be built for under ten cents! Locate a channel on your (or a cooperating friend's) TV receiver which has marginal reception, such as a snowy picture when a modest antenna (like rabbit ears) is used. If it happens to be Channel 13 you can use the design values from Prob. 5.4-5. If not, repeat the calculations for the channel you have chosen. The construction phase proceeds as follows. Find a large rigid piece of corrugated cardboard and trim it so that it is several centimeters longer than the total array length and about 5 cm narrower than the director length. Now locate several thick coat hangers. Straighten them as much as possible and cut them to the lengths required for the reflector and directors. The feed element is a folded dipole constructed from a piece of twin-lead transmission line. Cut it to a length that is a little longer than the driver dimension. Strip the ends and solder the two wires at each end together such that the overall length is equal to the driver dimension. Next cut one wire of the driver at the center of the folded dipole and solder the ends to a long piece of twin-lead which serves as a transmission line for the antenna. Lay out all element positions on the cardboard by marking appropriately. Tape the folded dipole onto the cardboard at the driver location. The coat hanger parasitic elements are positioned by merely inserting them into the corrugations in the cardboard. Now connect the transmission line to the receiver. Rotate the antenna and note the effect on the reception. Large performance differences should be observed. Note that it may be necessary to elevate the antenna by placing it in the attic, for example. With this construction it is very easy to change the element spacings by placing the coat hanger elements into different corrugations. Very little difference will be observed for small distance changes. Normally the best performance is achieved for horizontal polarization, that is, elements parallel to the ground.

5.4-7 Construction project—a slightly more expensive Yagi. A fairly rugged Yagi antenna can be constructed using the following technique. Select a TV channel with marginal reception and design a Yagi for that frequency. The materials required for this project are a 1 by 2 in. board of length slightly greater than the overall length of the array and a few

meters of aluminum wire (usually No. 8 AWG). Trim and straighten wires for the reflector and directors. Drill holes in the wooden mast at the appropriate positions for the reflector and the directors. The holes should be just slightly greater than the wire diameter. Be sure all holes are along a straight line. The driver is a folded dipole oriented such that the plane of the dipole is perpendicular to the line of the array. Drill one hole in the mast about 2 cm above the array line. At the same distance below the array line drill in from each side of the mast about 0.5 cm. Cut a piece of wire more than twice the length of the driver. Push it through the top hole and center it. Bend the wire at the required length at each end and fold it back to the mast. Now carefully trim away any excess wire such that the wire ends can just be forced into the shallow holes and still form a symmetric folded dipole. Now wrap the bared ends of a twin-lead transmission line to the ends of the folded dipole close to the mast (at the feed point). Be sure to get a good mechanical contact. Also leave a tab of polyethylene where you stripped the twin lead. Small wire brads can be wedged between the wire ends at the feed point and the mast, and at the same time pinch the twin lead connection between the antenna wire and the brad. Solder the feed point connections. Tack the polyethylene tab to the bottom of the mast to provide strain relief. Insert the remaining elements into their holes, center them, and nail brads into the hole alongside the wires to secure their positions. The construction is now complete and you can connect the transmission line to the receiver and test the reception. Try several antenna locations and orientations.

5.5-1 A resonant, half-wave, thin, vertical dipole is operated a half-wavelength above a perfect ground plane. Calculate the input impedance. Use the results in Section 3.6.

5.5-2 Derive an expression for the directivity of an ideal (infinitesimal) dipole as a function of its height h above a perfect ground plane. The dipole is oriented perpendicular to the ground plane. Make use of the results in Sections 2.3 and 3.4.

5.5-3 A short dipole is a quarter-wavelength above a perfect ground plane. Use simple array theory for the dipole and its image to obtain polar plot sketches of the E - and H -plane patterns when the dipole is oriented (a) vertically, and (b) horizontally.

5.5-4 Repeat Prob. 5.5-3 for a short dipole a half-wavelength above a perfect ground plane.

5.5-5 A horizontal short dipole is a quarter-wavelength above a planar real earth and is operating at 1 MHz. The conductivity of the earth is $\sigma = 12 \times 10^{-3}$ mho/m and the relative dielectric constant is $\epsilon_r = 15$. For this frequency, σ , and ϵ_r , we can approximate $|\Gamma_H|$ by 0.9 and the phase of Γ_H by -190° for all θ .

(a) Calculate and plot the H -plane elevation pattern in polar form in the upper half-space.

(b) Compare the pattern with that of the short dipole over a perfectly conducting ground plane (i.e., the results of Prob. 5.5-3b).

5.5-6 A vertical short dipole is located a half-wavelength above the surface of the earth at 100 MHz. $\sigma = 12 \times 10^{-3}$ mho/m and $\epsilon_r = 15$. The reflection coefficient may be approximated as

$$\begin{aligned}\Gamma_V &= 0.5 \angle -0^\circ, & 0 < \theta &\leq 40^\circ \\ \Gamma_V &= 0.3 \angle -10^\circ, & 40^\circ < \theta &\leq 70^\circ \\ \Gamma_V &= 0.1 \angle -90^\circ, & 70^\circ < \theta &\leq 80^\circ \\ \Gamma_V &= 0.5 \angle -180^\circ, & 80^\circ < \theta &\leq 90^\circ\end{aligned}$$

- (a) Calculate and plot the elevation pattern in polar form.
 (b) Compare the pattern with that of the short dipole over a perfectly conducting ground plane [Prob. 5.5-4(a)].
- 5.5-7 A quarter-wave resonant monopole is to be used as a transmitting antenna at 1 MHz. A radial system of 120 radials is to be used. If 97% efficiency is to be achieved, how long must the radial wires be? Neglect any tower ohmic resistance.
- 5.6-1 Verify that the maximum of the radiation from a traveling-wave long wire antenna which is 6λ long occurs at an angle of 20.1° from the wire.
- 5.6-2 Compare the approximate beam maximum angle formula of (5-59) for a traveling-wave long wire with the values of Fig. 5-42 for $L/\lambda = 1, 3, 6, 10$.
- 5.6-3 Show that the power radiated from a traveling-wave long wire antenna is

$$P_r = 30I_m^2 \left[2.108 + \ln\left(\frac{L}{\lambda}\right) - \text{Ci}(2\beta L) + \frac{\sin(2\beta L)}{2\beta L} \right]$$

Use (4-8), (5-58), and (1-127).

- 5.6-4 Use the radiated power expression from Prob. 5.6-3 for a traveling-wave long wire to:

- (a) Derive the directivity expression

$$D = \frac{1.69 \cot^2 \left[\frac{1}{2} \cos^{-1} \left(1 - \frac{0.371}{L/\lambda} \right) \right]}{2.108 + \ln\left(\frac{L}{\lambda}\right) - \text{Ci}(2\beta L) + \frac{\sin(2\beta L)}{2\beta L}}$$

- (b) Evaluate the directivity for $L/\lambda = 2, 5, 10, 20$. $\text{Ci}(2\beta L)$ is approximately zero for these values of L .
- 5.6-5 Use the radiated power expression from Prob. 5.6-3 for a traveling-wave long wire to:
- (a) Find an expression for the radiation resistance.
 (b) Evaluate the radiation resistance for $L/\lambda = 2, 5, 10, 20$. $\text{Ci}(2\beta L)$ is approximately zero for these values of L .
- 5.6-6 Plot the linear, polar plot of a traveling-wave long wire antenna which is eight wavelengths long.
- 5.6-7 To be completely general, the traveling-wave long wire antenna has a current distribution given by

$$I_z(z) = I_m e^{-az} e^{-j\beta_0 z}$$

where a is the attenuation coefficient representing radiation and ohmic losses. β_0 is the phase constant and is related to the velocity factor $p = v/c$ as $\beta_0 = \beta/p$.

- (a) Derive the pattern function

$$F(\theta) = K \sin \theta \frac{\sinh \left[\frac{aL}{2} + j \frac{\beta L}{2} \left(\frac{1}{p} - \cos \theta \right) \right]}{\frac{aL}{2} + j \frac{\beta L}{2} \left(\frac{1}{p} - \cos \theta \right)}$$

- (b) Show that this reduces to (5-58) for $a = 0$ and $p = 1$.
 (c) Plot the polar pattern for $a = 0$ and $L = 6\lambda$, for $p = 1.0, 0.75, 0.5$.

5.6-8 *Traveling-wave vee antenna.*

- (a) Place the zero-phase reference point at the vertex of the vee antenna of Fig. 5-43, and derive the radiation pattern as

$$F_v(\theta) = K_v [F_1(\theta) - F_2(\theta)]$$

where

$$F_1(\theta) = e^{j\beta L/2 [1 - 1 + \cos(\theta - \alpha)]} \sin(\theta - \alpha) \frac{\sin[(\beta L/2)(1 - \cos(\theta - \alpha))]}{(\beta L/2)(1 - \cos(\theta - \alpha))}$$

and $F_2(\theta)$ is the same as $F_1(\theta)$ except $-\alpha$ is replaced by α . This pattern expression is valid only in the plane of the vee.

- (b) Plot the polar pattern in Fig. 5-43 for $L = 6\lambda$ and $\alpha = 16^\circ$.

5.6-9 *Rhombic antenna.*

- (a) Show that the pattern of the rhombic in Fig. 5-44 is

$$F_R(\theta) = K_R [F_1(\theta) - F_2(\theta) + e^{-j\beta L} \{F_3 - F_4\}]$$

where $F_3 = e^{j\beta L \cos(\theta - \alpha)} F_2$ and $F_4 = e^{j\beta L \cos(\theta + \alpha)} F_1$. F_1 and F_2 are given in Prob. 5.6-8. This expression is valid only in the plane of the rhombic.

- (b) Plot the polar pattern in Fig. 5-44 for $L = 6\lambda$ and $\alpha = 16^\circ$.

5.6-10 A rhombic antenna above ground is to be designed for a main beam maximum at an elevation angle of 20° . Determine the rhombic configuration required.

5.7-1 *The uniform circular loop antenna.* A circular loop in the xy -plane with its center at the origin and a radius b carries a uniform amplitude, uniform phase current given by

$$\mathbf{I} = I_0 \hat{\phi}$$

- (a) Due to symmetry the pattern will not be a function of ϕ and \mathbf{A} will have only a ϕ -component. Using these facts, show that

$$\mathbf{A} = \hat{\phi} \frac{e^{-j\beta r}}{4\pi r} I_0 b \int_0^{2\pi} \cos \phi' e^{j\beta b \sin \theta \cos \phi'} d\phi'$$

in the far field. Use symmetry to reason that $\phi = 0$ can be assumed and that only a ϕ -component exists.

- (b) Find an expression for E_ϕ . *Hint:* use (F-7).

- (c) Show that this result reduces to that for a small loop antenna in (2-53). *Hint:* $J_1(x) \approx x/2$ for $x \ll 1$.

5.7-2 Show that (5-66) yields (5-67). To perform the integrations decompose the functions $\cos(\beta x')$ and $\sin(\beta y')$ into sums of exponential functions using (C-6) and (C-7).

5.7-3 Compute the input reactance of a square loop antenna with a 0.2λ perimeter using small loop analysis and compare to the value from Fig. 5-47b.

6

BROADBAND ANTENNAS

In many applications an antenna must operate effectively over a wide range of frequencies. An antenna with wide bandwidth is referred to as a *broadband antenna*. The term "broadband" is a relative measure of bandwidth and varies with the circumstances. We shall be specific in our definition of broadband. Bandwidth is computed in one of two ways. Let f_U and f_L be the upper and lower frequencies of operation for which satisfactory performance is obtained. The center (or sometimes the design frequency) is denoted as f_C . Then bandwidth as a percent of the center frequency is

$$\frac{f_U - f_L}{f_C} \times 100. \quad (6-1)$$

Bandwidth is also defined as a ratio by

$$\frac{f_U}{f_L}. \quad (6-2)$$

The bandwidth of narrow band antennas is usually expressed as a percent using (6-1) whereas wide band antennas are quoted as a ratio using (6-2).

In the previous chapter we saw that resonant antennas have small bandwidths. For example, the half-wave dipoles in Fig. 5-7 have bandwidths of 8 and 16% (f_U and f_L were determined by the VSWR = 2.0 points). On the other hand,

antennas that have traveling waves on them rather than standing waves (as in resonant antennas) operate over wider frequency ranges. The definition of a broadband antenna is somewhat arbitrary and depends on the particular antenna, but we shall adopt a working definition. *If the impedance and the pattern of an antenna do not change significantly over about an octave ($f_U/f_L = 2$) or more, we will classify it as a broadband antenna.*

As we will see in this chapter, broadband antennas usually require structures that do not emphasize abrupt changes in the physical dimensions involved, but instead utilize materials with smooth boundaries. Smooth physical structures tend to produce patterns and input impedances that also change smoothly with frequency. This simple concept is very prominent in broadband antennas.

6.1 HELICAL ANTENNAS

If a conductor is wound into a helical shape and is fed properly it is referred to as a **helical antenna**, or simply as a **helix**.¹ The typical geometry for a helix is shown in Fig. 6-1. If one turn of the helix is uncoiled the relationships among the various helix parameters are revealed, as shown in Fig. 6-2. The symbols used to describe the helix are defined as follows:

D = diameter of helix (between centers of coil material)

C = circumference of helix = πD

S = spacing between turns = $C \tan \alpha$

α = pitch angle = $\tan^{-1} \frac{S}{C}$

L = length of one turn = $\sqrt{C^2 + S^2}$

N = number of turns

A = axial length = NS

d = diameter of helix conductor.

Note that when $S = 0$ ($\alpha = 0^\circ$) the helix reduces to a loop antenna and when $D = 0$ ($\alpha = 90^\circ$) it reduces to a linear antenna.

The helix can be operated in two modes, the normal mode and the axial mode. The normal mode yields radiation that is most intense normal to the axis of the helix. This occurs when the helix diameter is small compared to a wavelength. The axial mode provides a radiation maximum along the axis of the helix. When the helix circumference is on the order of a wavelength the axial mode will result.

¹ Most of the pioneering work on the helix was performed by J. D. Kraus. See [1] and [2].

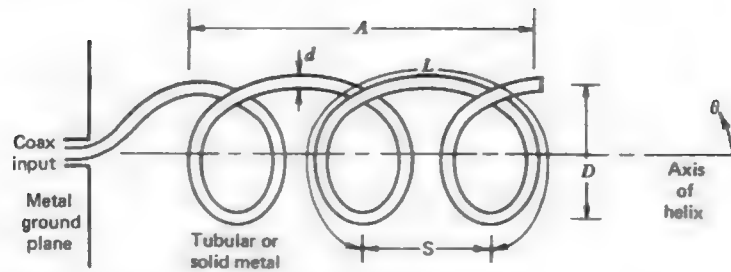


Figure 6-1 Geometry and dimensions of a helical antenna. This is a left-hand wound helix.

6.1.1 Normal Mode of Radiation

In the normal mode of operation the radiated field is maximum in a direction normal to the helix axis and for certain geometries, in theory, will emit circularly polarized waves. For normal mode operation the dimensions of the helix must be small compared to a wavelength, that is, $D \ll \lambda$. The normal mode helix is electrically small and thus its efficiency is low.

Since the helix is small, the current is assumed to be constant in magnitude and phase over its length. The far-field pattern is independent of the number of turns and may be obtained by examining one turn. One turn can be approximated as a small loop and ideal dipole as shown in Fig. 6-3. The far-zone electric field of the ideal dipole from (1-71) is

$$\mathbf{E}_D = j\omega\mu I S \frac{e^{-j\beta r}}{4\pi r} \sin\theta \hat{\theta} \quad (6-3)$$

where S , the spacing between helical turns, is the length of the ideal dipole in Fig. 6-3. The far-zone electric field of the small loop from (2-53) is

$$\mathbf{E}_L = \eta\beta^2 \frac{\pi}{4} D^2 I \frac{e^{-j\beta r}}{4\pi r} \sin\theta \hat{\phi} \quad (6-4)$$

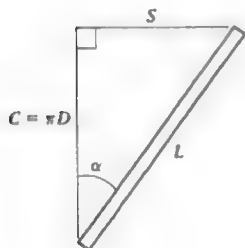


Figure 6-2 One uncoiled turn of a helix.

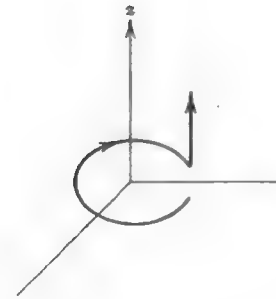


Figure 6-3 One turn of a normal mode helix approximated as a small loop and an ideal dipole.

where $\pi D^2/4$ is the area of the loop. The total radiation field for one turn, as modeled in Fig. 6-3, is the vector sum of the fields in (6-3) and (6-4). Note that both components have a $\sin\theta$ pattern (see Fig. 6-4) and they are 90° out-of-phase. The axial ratio of the polarization ellipse is found from the ratio of (6-3) and (6-4) as

$$|AR| = \frac{|E_\theta|}{|E_\phi|} = \frac{4\omega\mu S}{\sqrt{(\mu/\epsilon)}\omega\sqrt{\mu\epsilon}(2\pi/\lambda)\pi D^2} = \frac{2S\lambda}{\pi^2 D^2} \quad (6-5)$$

Since the (perpendicular) linear components are 90° out-of-phase, circular polarization is obtained if the axial ratio is unity. This occurs for

$$C = \pi D = \sqrt{2S\lambda} \quad (6-6)$$

which was found by setting (6-5) equal to one. This circular polarization is obtained in all directions, except of course where the pattern is zero (along the axis of the helix).

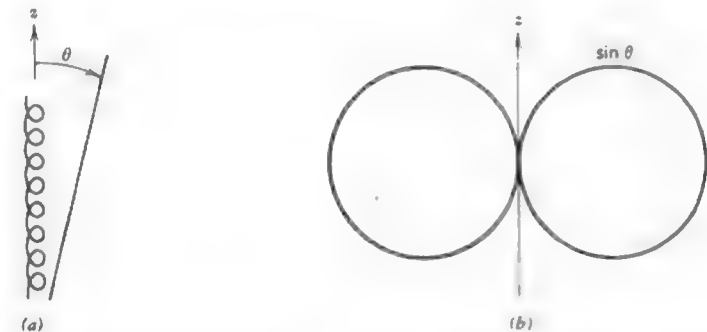


Figure 6-4 The normal mode helix and its radiation pattern. (a) Geometry used. (b) Radiation pattern of both $|E_\theta|$ and $|E_\phi|$.

From Fig. 6-2 it is seen that

$$L \sin \alpha = S \quad \text{or} \quad \alpha = \sin^{-1} \frac{S}{L} \quad (6-7)$$

and

$$C^2 + S^2 = L^2. \quad (6-8)$$

For circular polarization in the normal mode, the circumference of the helix given by (6-6) and used in (6-8) gives

$$S^2 + 2S\lambda - L^2 = 0. \quad (6-9)$$

This is a quadratic equation which may be solved for S as

$$S = \frac{-2\lambda \pm \sqrt{4\lambda^2 + 4L^2}}{2} = \lambda \left[-1 \pm \sqrt{1 + \left(\frac{L}{\lambda}\right)^2} \right]. \quad (6-10)$$

Choosing the plus sign to keep the physical length S positive and substituting into (6-7) yields the pitch angle required for circular polarization

$$\alpha_{CP} = \sin^{-1} \left[\frac{-1 + \sqrt{1 + (L/\lambda)^2}}{L/\lambda} \right]. \quad (6-11)$$

6.1.2 Axial Mode of Radiation

In the axial mode of radiation the helix radiates as an endfire antenna with a single maximum along the axis of the helix (+ z -direction in Fig. 6-1). The radiation is close to circular polarization near the axis. Further, the half-power beamwidth can be reduced by increasing the number of turns. The axial mode occurs when the helix circumference is on the order of one wavelength. In fact, the expressions presented in this section remain valid over at least a frequency range corresponding to

$$\frac{3}{4}\lambda < C < \frac{5}{4}\lambda. \quad (6-12)$$

If f_U is the upper and f_L the lower frequency over this band, the bandwidth ratio is

$$\frac{f_U}{f_L} = \frac{c/\lambda_U}{c/\lambda_L} = \frac{\frac{4}{3}}{\frac{4}{5}} = \frac{16}{9} = 1.78 \quad (6-13)$$

which is nearly the two-to-one bandwidth required to fit our definition of a broadband antenna.

The axial mode helix carries nearly a pure traveling wave outward from the feed. The electric field vector rotates around in a circular fashion as does the current on the helix. The polarization is thus close to circular on axis. At the end

of the helix there is very little reflection of the outward traveling wave. Therefore, there will be very weak fields incident back onto the ground plane (except for very short helices with $A < \lambda/2$), and the effect of the ground plane may be neglected. The ground plane size is also not very critical, but should be made wider than a half-wavelength. In addition, the conductor diameter d has little effect on the axial mode helix antenna properties. The helix is most conveniently fed using a coaxial transmission line with the center conductor attached to the helix and the outer conductor attached to the ground plane as suggested in Fig. 6-1. The ground plane can be either square or circular, made from either solid metal or wire mesh.

The normal mode helix supports a wave that corresponds to a current along the helix which is nearly uniform in amplitude and phase if the helix dimensions are small relative to a wavelength. However, the axial mode helix has a circumference of about a wavelength, so the transmission mode in this case leads to a current distribution that has opposite phase on opposite sides of a turn (since they are separated by about a half-wavelength of conductor). Also the helix coil acts to reverse the current direction for opposite points. Thus the current at opposite points of a turn are essentially in phase, leading to far-field reinforcement along the helix axis. The radiation pattern can be found by considering the helix to be an array of N identical elements (or turns). The element pattern for one turn is approximately that of a one-wavelength loop. An approximate expression for this is $\cos \theta$; see Fig. 5-46b. Assuming equal amplitude of excitation for each turn, the array factor is that of a uniformly excited, equally spaced array given in (3-33). The total pattern is then

$$F(\theta) = K \cos \theta \frac{\sin(N\psi/2)}{N \sin(\psi/2)} \quad (6-14)$$

where

$$\psi = \beta S \cos \theta + \alpha \quad (6-15)$$

and K is a normalization constant.

The traveling wave along the helix produces an endfire beam along the helix axis (z -axis). Suppose initially that the helix can be modeled as an ordinary endfire array. Then a main beam maximum occurs in the $\theta = 0$ direction for $\psi = 0$, which yields $\alpha = -\beta S$ from (6-15); also see (3-36). The $-\beta S$ phase is phase delay due to axial propagation corresponding to the distance S along the axis for one turn. However, the current wave follows the helix. This introduces another -2π of phase shift since the circumference is about a wavelength. Thus for ordinary endfire $\alpha = -\beta S - 2\pi$. Quite amazingly it turns out that the traveling-wave mode on the axial mode helix corresponds to nearly a naturally occurring Hansen-Woodyard increased directivity type endfire array. This effect

is accounted for with an additional $-\pi/N$ phase delay over the ordinary endfire case; see (3-49). Thus, the element-to-element phase shift is

$$\alpha = -\left(\beta S + 2\pi + \frac{\pi}{N}\right). \quad (6-16)$$

This phase shift leads to a value for the phase velocity of the traveling wave. To see this we write the phase shift of the wave in one transit around a turn of length L as

$$\alpha = -\beta_h L \quad (6-17)$$

where β_h is the phase constant associated with wave propagation along the helical conductor. Equating this to (6-16) gives

$$\beta_h = \frac{1}{L} \left(\beta S + 2\pi + \frac{\pi}{N} \right). \quad (6-18)$$

The velocity factor (phase velocity relative to the free-space velocity of light) is

$$p = \frac{v}{c} = \frac{\omega/c}{\omega/v} = \frac{\beta}{\beta_h} \quad (6-19)$$

where v is the phase velocity of the traveling wave along the helical conductor. Using (6-18) in (6-19) yields

$$p = \frac{L/\lambda}{S/\lambda + (2N + 1)/2N}. \quad (6-20)$$

A typical configuration is $C = \lambda$, $\alpha = 12^\circ$, and $N = 12$. Then $S = C \tan \alpha = 0.213\lambda$, $L = \sqrt{C^2 + S^2} = 1.022\lambda$, and $p = 0.815$. Therefore, the traveling wave has a phase velocity less than that if it were a plane wave in free space. Such a wave is referred to as a *slow wave*. Another remarkable feature of the helix is that as the helix parameters vary over rather large ranges ($5^\circ < \alpha < 20^\circ$ and $\frac{1}{2}\lambda < C < \frac{3}{2}\lambda$) the phase velocity adjusts automatically to maintain increased directivity.

Returning to the pattern calculation, the main beam maximum occurs for $\theta = 0$ and from (6-15) and (6-16), $\psi = -2\pi - \pi/N$. Then (6-14) is

$$F(\theta = 0) = K \frac{\sin(-N\pi - \pi/2)}{N \sin(-\pi - \pi/2N)} = \frac{K(-1)^{N+1}}{N \sin(\pi/2N)}. \quad (6-21)$$

Normalizing such that the maximum is unity yields $K = (-1)^{N+1} N \sin(\pi/2N)$, and the final pattern function is

$$F(\theta) = (-1)^{N+1} \sin \frac{\pi}{2N} \cos \theta \frac{\sin(N\psi/2)}{\sin(\psi/2)} \quad (6-22)$$

where

$$\psi = \beta S(\cos \theta - 1) - 2\pi - \frac{\pi}{N}. \quad (6-23)$$

This pattern expression applies to both E_θ and E_ϕ .

From a large number of measurements an empirical formula for the half-power beamwidth has been developed. It is

$$HP = \frac{52^\circ}{(C/\lambda)\sqrt{N(S/\lambda)}}. \quad (6-24)$$

This formula holds for $12^\circ < \alpha < 15^\circ$, $\frac{1}{2}\lambda < C < \frac{3}{2}\lambda$, and $N > 3$. Notice that as N increases the beamwidth decreases. Also this is the beamwidth in any plane containing the axis of the helix since the beam is circularly symmetric.

The directivity of the axial mode helix can be found from (8-80) as

$$D = \frac{4\pi}{\Omega_A} \approx \frac{41,253}{HP_E HP_H} \quad (6-25)$$

where HP_E and HP_H are the half-power beamwidths in the E - and H -planes in degrees. This expression follows from the fact that $4\pi \text{ sr} = 4\pi(180/\pi)^2 = 41,253$ square degrees and the beam solid angle $\Omega_A \approx HP_E HP_H$. Substituting (6-24) into (6-25) for both HP_E and HP_H , since the pattern is circularly symmetric, gives

$$D = 15 \left(\frac{C}{\lambda} \right)^2 \frac{NS}{\lambda}. \quad (6-26)$$

This directivity expression is a ratio (not decibels), and approximately equals the gain since the axial mode helix is nearly lossless.

We have been assuming E_θ and E_ϕ to be equal in magnitude. This is only approximately true. The infinite helix has perfect circular symmetry but a finite helix does not, so one would expect that the fields radiated from a finite helix to be slightly asymmetric. It has been found that the axial ratio is given by

$$|AR| = \frac{2N + 1}{2N} \quad (6-27)$$

in the main beam maximum direction. As N becomes large $|AR|$ approaches unity and the wave approaches perfect circular polarization, since the fields E_θ and E_ϕ are also in time-phase quadrature. The sense of the polarization is determined by the sense of the helix windings as shown in Fig. 6-5, that is, a right- (left-) hand wound helix is a right- (left-) hand sensed polarized antenna.

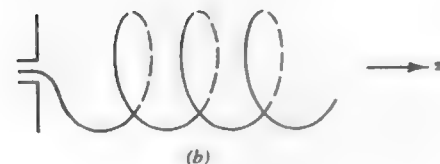
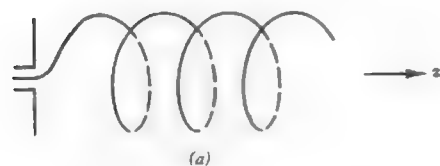


Figure 6-5 Left- and right-hand wound helices. For the axial mode helix the sense of the windings determines the sense of polarization of the antenna. (a) Left-hand sensed helix. (b) Right-hand sensed helix.

In general, the terminal impedance of a helical antenna operating in the axial mode is nearly purely resistive since it is essentially a traveling-wave antenna. An empirically derived formula for input resistance is

$$R_{in} = 140 \frac{C}{\lambda} \text{ ohms} \quad (6-28)$$

which is accurate to $\pm 20\%$ for $12^\circ < \alpha < 15^\circ$, $\frac{1}{4}\lambda < C < \frac{3}{4}\lambda$, and $N > 3$.

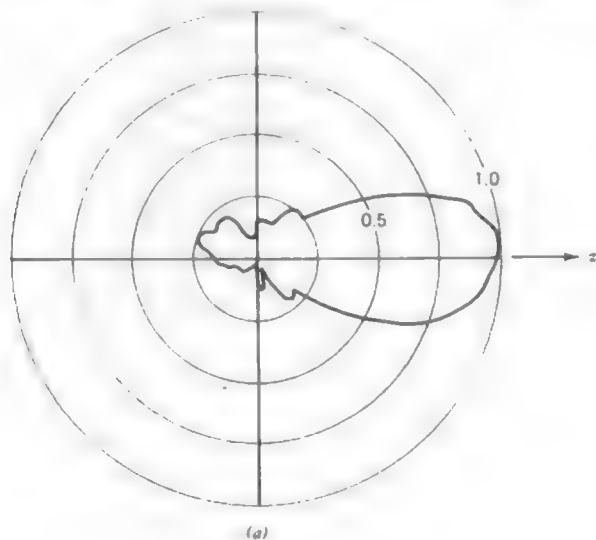


Figure 6-6

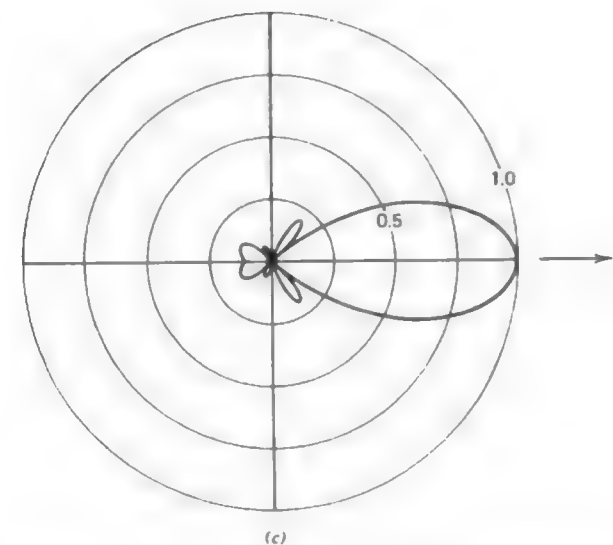
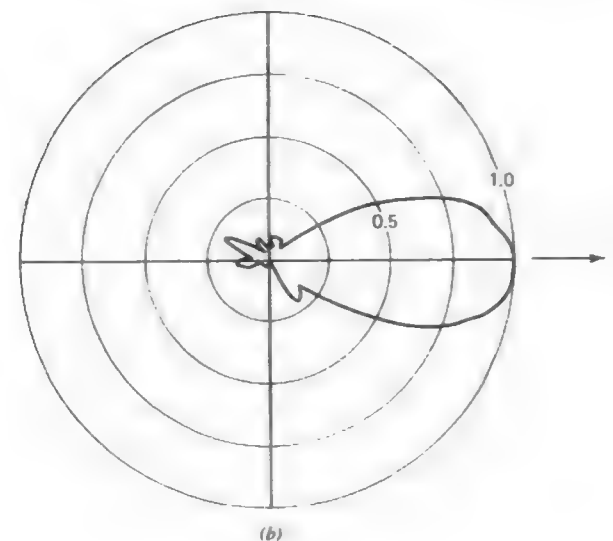


Figure 6-6 Radiation patterns of a 10-turn axial mode helix with $C = \lambda$ and $\alpha = 13^\circ$ (Example 6-1). (a) Measured E_θ pattern at 8 GHz [3]. (b) Measured E_θ pattern at 8 GHz [3]. (c) Pattern computed from (6-22).

Example 6-1. A 10-Turn Helix Antenna

The helix antenna is rather easy to construct and will perform approximately as predicted by the simple theory presented in this section, as will be demonstrated in this example. Calculations are compared to experimental results for a 10-turn helix constructed for a center frequency of 8 GHz ($\lambda = 3.75$ cm). At the center frequency the helix is designed to have a circumference of $C = 0.92\lambda$, or $C = 3.45$ cm. The helix was built with a pitch angle of $\alpha = 13^\circ$. The spacing between turns is then $S = C \tan \alpha = 3.45 \tan 13^\circ = 0.796$ cm. The measured radiation patterns for the two principal planes are shown in Figs. 6-6a and 6-6b [3]. Note that these patterns are nearly identical, as required for circular polarization. The theoretical pattern based on (6-22) is plotted in Fig. 6-6c. Note the good agreement with the measured patterns. The half-power beamwidth of the calculated pattern is 38.8° and the beamwidth of the measured patterns is 45° . The empirical formula of (6-24) with $C = 0.92\lambda$, $N = 10$, and $S = C \tan \alpha = \lambda \tan 13^\circ = 0.231\lambda$ gives

$$HP = \frac{52^\circ}{1/\sqrt{10(0.231)}} = 37.2^\circ \quad (6-29)$$

6.2 BICONICAL ANTENNAS

The bandwidth of a simple dipole antenna can be increased by using thicker wire. This concept can be extended to further increase bandwidth if the conductors are flared to form a biconical structure. Then the fixed wire diameter is replaced by a smoothly varying diameter and a fixed angle (of the conical surfaces). In this section the idealized biconical antenna is considered first, followed by two practical forms—the finite biconical antenna and the discone.

6.2.1 The Infinite Biconical Antenna

If the conducting halves of an antenna are two infinite conical conducting surfaces end-to-end, but with a finite gap at the feed point, the **infinite biconical antenna** of Fig. 6-7 results. Since the structure is infinite it can be analyzed as a transmission line. With a time-varying voltage applied across the gap, currents will flow radially out from the gap along the surface of the conductors. These currents in turn create an encircling magnetic field H_ϕ . Assuming a TEM transmission line mode (all fields transverse to direction of propagation), the electric field will be perpendicular to the magnetic field and be θ -directed. When the potential on the top cone is positive and the bottom cone is negative, the electric field lines extend from the top to the bottom cone as indicated in Fig. 6-7.

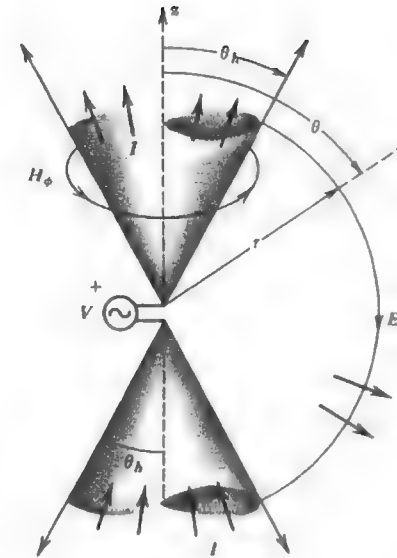


Figure 6-7 Infinite biconical antenna. The field components and current are shown.

In the region between the cones $\mathbf{J} = 0$, $\mathbf{H} = H_\phi \hat{\phi}$, and $\mathbf{E} = E_\theta \hat{\theta}$. Then Ampere's law, $\nabla \times \mathbf{H} = j\omega\epsilon\mathbf{E} + \mathbf{J}$, reduces to

$$\frac{1}{r \sin \theta} \frac{\partial}{\partial \theta} (\sin \theta H_\phi) = j\omega\epsilon E_\theta = 0 \quad (6-30)$$

for the r -component and

$$-\frac{1}{r} \frac{\partial}{\partial r} (r H_\phi) = j\omega\epsilon E_\theta \quad (6-31)$$

for the θ -component. From (6-30) we see that $\partial/\partial\theta (\sin \theta H_\phi) = 0$ so

$$H_\phi \propto \frac{1}{\sin \theta} \quad (6-32)$$

Since the structure acts as a guide for spherical waves we can write (6-32) as

$$H_\phi = H_0 \frac{e^{-j\beta r}}{4\pi r \sin \theta} \quad (6-33)$$

Then, substituting this into (6-31) we obtain

$$\begin{aligned} E_\theta &= \frac{-1}{j\omega\epsilon} \frac{1}{r} \frac{H_0}{4\pi \sin \theta} \frac{\partial}{\partial r} (e^{-j\beta r}) = \frac{\beta H_0}{\omega\epsilon} \frac{1}{r} \frac{e^{-j\beta r}}{4\pi \sin \theta} \\ &= \eta H_0 \frac{e^{-j\beta r}}{4\pi r \sin \theta} \end{aligned} \quad (6-34)$$

This equation is simply $E_\theta = \eta H_\phi$ which confirms our statement that the wave is TEM. The field components vary as $1/\sin \theta$, so the radiation pattern is

$$F(\theta) = \frac{\sin \theta_h}{\sin \theta} \quad \theta_h < \theta < \pi - \theta_h \quad (6-35)$$

which is normalized to unity at its maxima on the conductor surfaces. This pattern is plotted in Fig. 6-8.

In order to determine the input impedance we first find the terminal voltage and current. Referring to Fig. 6-7 we see the voltage is found by integrating along a constant radius r and it is

$$V(r) = \int_{\theta_h}^{\pi - \theta_h} E_\theta r d\theta. \quad (6-36)$$

This can be performed for any r since the cones are equipotential surfaces. Substituting (6-34) into the above equation yields

$$\begin{aligned} V(r) &= \frac{\eta H_o}{4\pi} e^{-j\beta r} \int_{\theta_h}^{\pi - \theta_h} \frac{d\theta}{\sin \theta} = \frac{\eta H_o}{4\pi} e^{-j\beta r} \left[\ln \left| \tan \frac{\theta}{2} \right| \right]_{\theta_h}^{\pi - \theta_h} \\ &= \frac{\eta H_o}{2\pi} e^{-j\beta r} \ln \left(\cot \frac{\theta_h}{2} \right). \end{aligned} \quad (6-37)$$

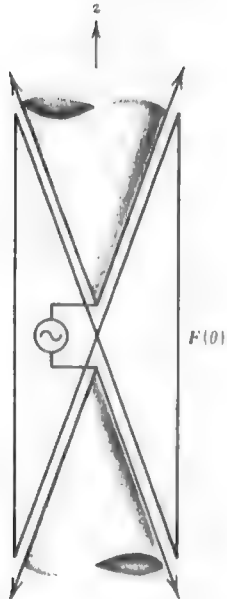


Figure 6-8 Radiation pattern of an infinite biconical antenna.

The boundary condition on H_ϕ at the conductor surface is $J_s = H_\phi$. The total current on one cone is found by integrating the current density J_s around the cone as shown in Fig. 6-7, so

$$I(r) = \int_0^{2\pi} H_\phi r \sin \theta d\phi = 2\pi r H_\phi \sin \theta. \quad (6-38)$$

Substituting (6-33) in the above gives

$$I(r) = \frac{H_o}{2} e^{-j\beta r}. \quad (6-39)$$

The characteristic impedance at any point r , from (6-37) and (6-39), is

$$Z_o = \frac{V(r)}{I(r)} = \frac{\eta}{\pi} \ln \left(\cot \frac{\theta_h}{2} \right). \quad (6-40)$$

Since this is not a function of r it must be also the impedance at the input ($r = 0$). Thus, using $\eta \approx 120\pi$ in (6-40) gives the input impedance

$$Z_{in} = Z_o = 120 \ln \left(\cot \frac{\theta_h}{2} \right) \text{ ohms.} \quad (6-41)$$

For θ_h less than 20°

$$Z_{in} = Z_o \approx 120 \ln \left(\frac{2}{\theta_h} \right) \text{ ohms} \quad (6-42)$$

where θ_h is in radians. The input impedance is real because there is only a pure traveling wave. Since the structure is infinite there are no discontinuities present to cause reflections setting up standing waves, which would show up as a reactive component in the impedance (except at a few resonance points). If $\theta_h = 1^\circ$, $Z_{in} = 568 + j0$ ohms. If $\theta_h = 50^\circ$, $Z_{in} = 91 + j0$ ohms.

If one cone is flared all the way out to form a perfect ground plane a single infinite cone above a ground plane results. This monopole version of the infinite bicone then has an input impedance which is half that of the infinite bicone.

6.2.2 The Finite Biconical Antenna

A practical biconical antenna is made by ending the two cones of the infinite bicone. This **finite biconical antenna** is shown in Fig. 6-9. Inside an imaginary sphere of radius h just enclosing the antenna, TEM waves exist together with higher order modes created at the ends of the cones. Outside this sphere only higher order modes exist. The ends of the cones cause reflections that set up standing waves that lead to a complex input impedance. For a given voltage

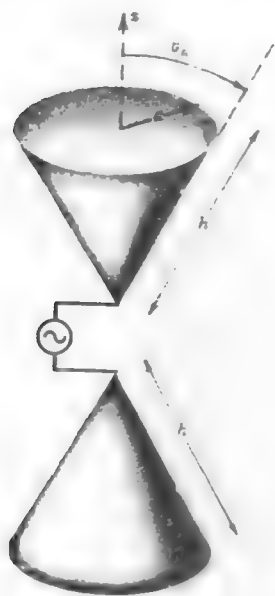


Figure 6-9 Finite biconical antenna.

excitation the resulting modes of H_ϕ can be obtained [4]. The boundary condition leads to the current as in (6-38) and then the impedance expression is found. The values of input impedance resulting from this procedure are plotted in Fig. 6-10 [5]. The capacitive effect of the ends has been neglected. To use these curves first compute the characteristic impedance Z_0 from (6-41) using the appropriate cone half-angle θ_h . Notice that the input resistance becomes very large and the input reactance very small for an overall antenna length $2h$ of slightly less than one-wavelength, just as with an ordinary dipole.

The pattern of the finite biconical antenna for small cone angles is very similar to that of an ordinary dipole of the same length.

6.2.3 The Discone Antenna

If one cone of the finite biconical antenna is replaced with a disk-shaped ground plane, the structure becomes a disk-cone, or **discone**, antenna (see Fig. 6-11). The discone antenna was developed by Kandoian [6] in 1945, followed several years later by experimental design studies [7, 8]. It is used (like a vertical dipole) for vertical polarization and nearly uniform azimuth coverage (i.e., an omnidirectional pattern). But the discone offers satisfactory operation over a wide frequency range (several octaves) while maintaining acceptable pattern and impedance properties.

The discone is constructed as shown in Fig. 6-11. The outer conductor of the coaxial transmission line is connected to the cone and the inner conductor is attached to the disk ground plane. The cone and disk can be either solid metal or radial wires. Ideally the pattern between the ground plane and the cone is that of the infinite bicone. This omnidirectional pattern is well suited to broadcast applications.

The discone antenna can be designed for broadband impedance performance (typically 50 ohms), while maintaining acceptable pattern behavior with frequency [8]. Typical center frequency dimensions are $H = 0.7\lambda$, $B = 0.6\lambda$, $D = 0.4\lambda$, $\theta_h = 25^\circ$, and $\delta \ll D$. For example, the discone with the patterns of Fig. 6-12 has a center frequency of 1 GHz ($\lambda = 30$ cm). So at 1 GHz,

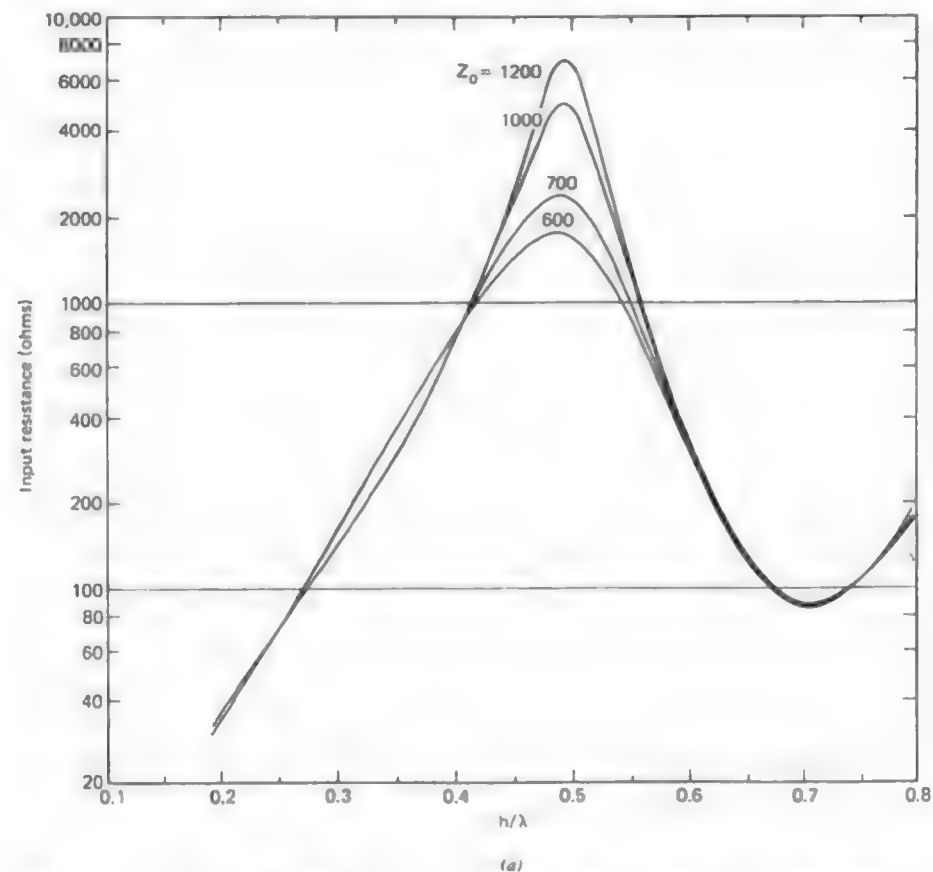


Figure 6-10 Input impedance of a finite biconical antenna of half-length h . $Z_0 = 120 \ln[\cot(\theta_h/2)]$. (Reproduced, by permission, from [5]. © 1952 John Wiley.) (a) Input resistance.

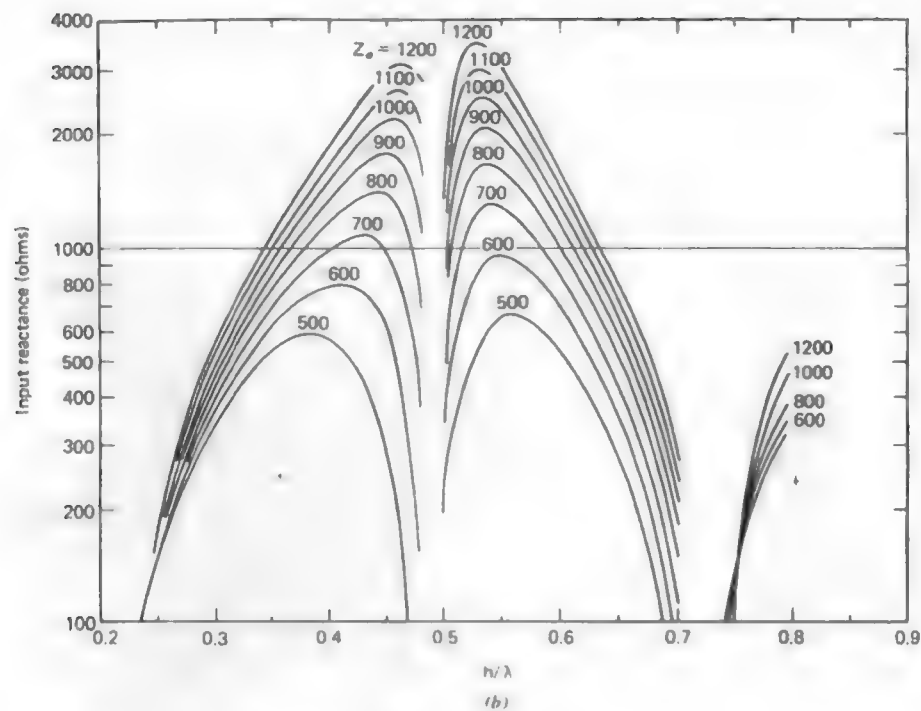
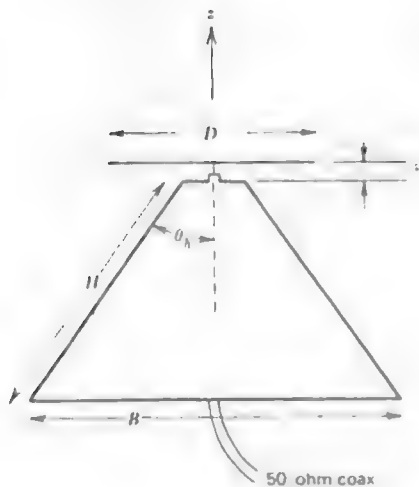
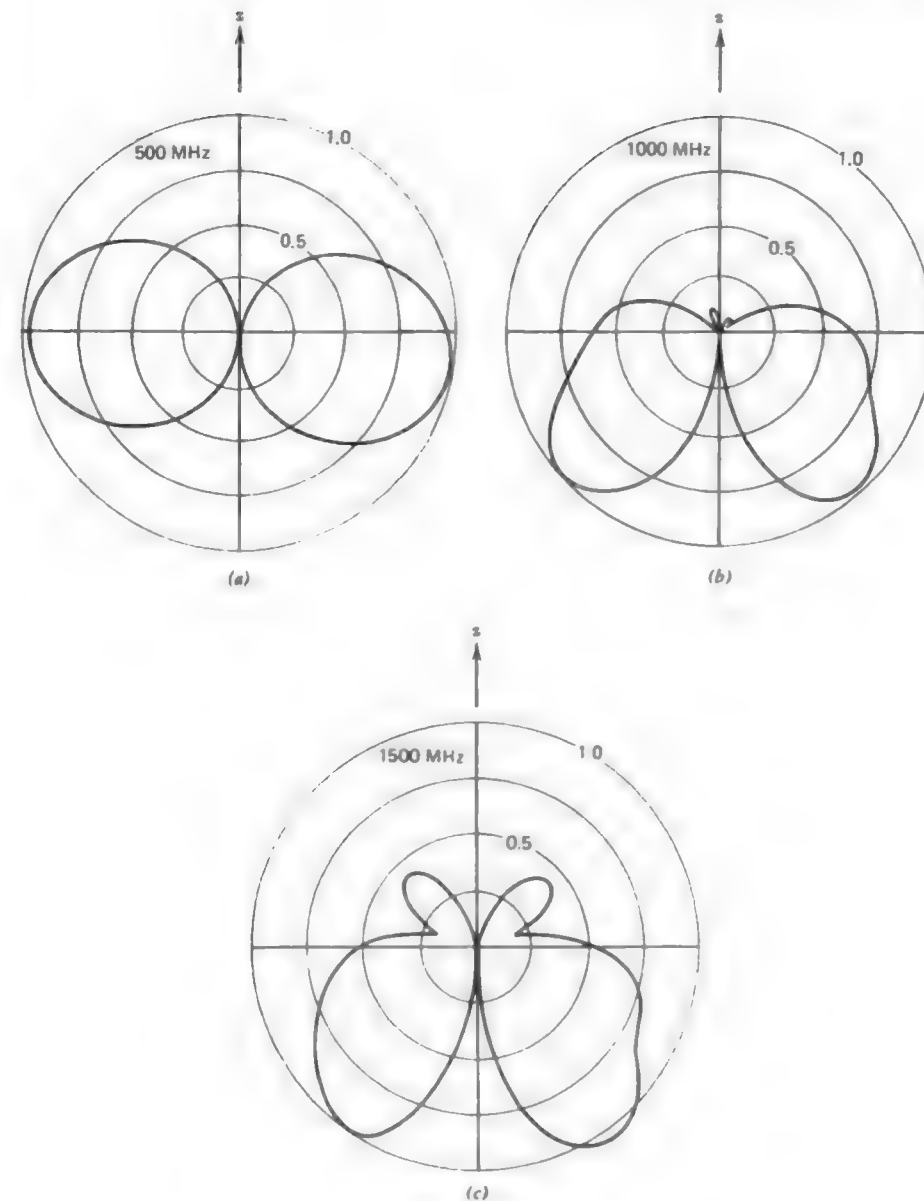


Figure 6-10 (b) Input reactance.

Figure 6-11 Discone antenna. Typical dimensions are $H \sim 0.7\lambda$, $B \sim 0.6\lambda$, $D \sim 0.4\lambda$, and $\delta \ll D$.Figure 6-12 Measured patterns of a discone antenna for $H = 21.3$ cm, $B = 19.3$ cm, and $\theta_h = 25^\circ$ [8]. (a) 500 MHz, (b) 1000 MHz, (c) 1500 MHz.

$H = 21.3 \text{ cm} = 0.71\lambda$, $B = 19.3 \text{ cm} = 0.64\lambda$, and $\theta_h \approx \sin^{-1}[(B/2)/H] = 27^\circ$. Nail [7] has given optimum design formulas of $D = 0.7B$ and $\delta = 0.3C$, independent of H and θ_h .

The pattern performance over a 3 to 1 bandwidth is revealed in Fig. 6-12. At low frequencies the structure is small relative to a wavelength, and the pattern is not too different from that of a short dipole (see Fig. 6-12a). As frequency increases the electrical size of the ground plane increases and the pattern is confined more to the lower half-space (see Fig. 6-12b). For further increases in frequency, the antenna behavior approaches that of an infinite structure. For example, at 1500 MHz, the pattern (of Fig. 6-12c) is very close to that of the monopole version of the infinite biconical antenna in Fig. 6-8. Measurements with several disk parameters, D , and spacings between the cone, δ , showed that the patterns are insensitive to these parameters [8].

6.3 SLEEVE ANTENNAS

In Section 5.1 we saw that the dipole antenna is very frequency sensitive and its bandwidth is much less than the octave bandwidth provided by the antennas studied previously in this chapter. However, the addition of a sleeve to a dipole or monopole can increase the bandwidth to more than an octave. In this section we will briefly examine a few forms of the **sleeve antenna**, which incorporates a tubular conductor sleeve around an internal radiating element. Emphasis will be placed on practical configurations.

6.3.1 Sleeve Monopoles

Three **sleeve monopole** configurations are shown in Fig. 6-13 fed from a coaxial transmission line. The sleeve exterior acts as a radiating element and the interior of the sleeve acts as the outer conductor of the feed coaxial transmission line. The length of the sleeve may be any portion of the total length of the monopole from zero (no sleeve) to that of Fig. 6-13b where the sleeve constitutes the entire radiating portion of the antenna. There is an endless number of sleeve antenna configurations. Frequently the sleeve is a large conducting structure or the center radiating element is conical. These are, however, complex structures and we will consider only the more common simple sleeve monopole of Fig. 6-13c. Its characteristics are a function of the dimensions shown as well as frequency. As for an ordinary monopole with no sleeve, the antenna dimensions affect the impedance more than the pattern.

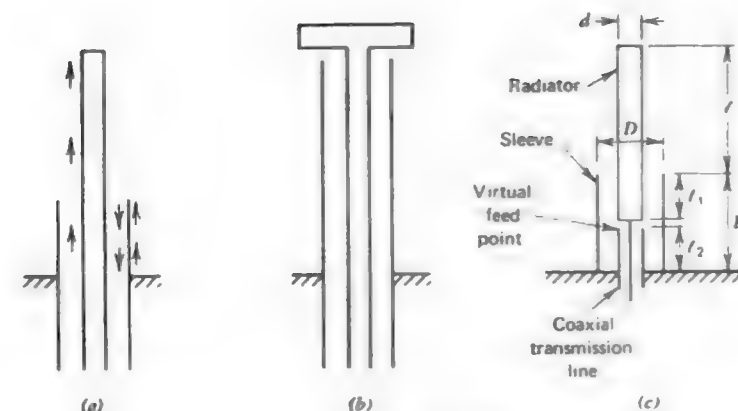


Figure 6-13 Sleeve monopole configurations. The arrows in (a) indicate polarity when $l + L \leq \lambda/2$.

The first sleeve monopole resonance, as might be expected, occurs at a frequency where the monopole length $l + L$ is approximately $\lambda/4$. Design proceeds by locating this first resonance near the lower end of the frequency band, thereby fixing the total physical length $l + L$. The remaining design variable is l/L . It has been found experimentally that a value of $l/L = 2.25$ yields optimum (nearly constant with frequency) radiation patterns over a 4:1 band [9]. The value of l/L has little effect for $l + L \leq \lambda/2$ since the current on the outside of the sleeve will have approximately the same phase as that on the top portion of the monopole itself, as suggested by the arrows of Fig. 6-13a. However, for longer electrical lengths the ratio l/L becomes very important and has a marked effect on the radiation pattern, since the current on the outside of the sleeve will not necessarily be in phase with that on the top portion of the monopole. Some typical specifications for optimum performance are given in Table 6-1. In some applications the VSWR may be too high, requiring a matching network.

Table 6-1 Specifications for Optimum Pattern Design of a Sleeve Monopole

Pattern bandwidth	4:1
$l + L$	$\lambda/4$ at low end of band
l/L	2.25
D/d	3.0
VSWR	less than 8:1

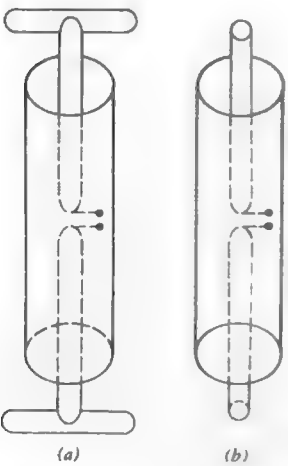


Figure 6-14 Sleeve dipole configurations.

6.3.2 Sleeve Dipoles

The sleeve monopole has a counterpart in the **sleeve dipole** antenna, two forms of which are shown in Fig. 6-14. The sleeve dipole of Fig. 6-14b can be approximated with an **open-sleeve dipole** in which the tubular sleeve is replaced by two conductors close to either side of the driven element as shown in Fig. 6-15. The length of the parasites (simulated sleeve) is approximately one-half that of the center-fed dipole. The open-sleeve dipole we will describe from an experimental viewpoint is operated in front of a flat reflector, or ground plane [10]. The results are also applicable to sleeve dipoles without a flat reflector present.

The antenna was designed for the 225–400 MHz frequency band. The dipole to reflector spacing S_d was chosen to be 0.29λ at 400 MHz to avoid the deterioration of the radiation pattern which occurs for larger spacings. All of the dimensions required for design of the open-sleeve dipole are given in Table 6-2. These

Table 6-2 Electrical Dimensions of an Open-Sleeve Dipole with a Reflector for Lowest VSWR

Parameter	Electrical dimension at lowest frequency (225 MHz)	Electrical dimension at highest frequency (400 MHz)
D	0.026λ	0.047λ
H	0.385λ	0.684λ
L	0.216λ	0.385λ
S	0.0381λ	0.0677λ
S_d	0.163λ	0.29λ

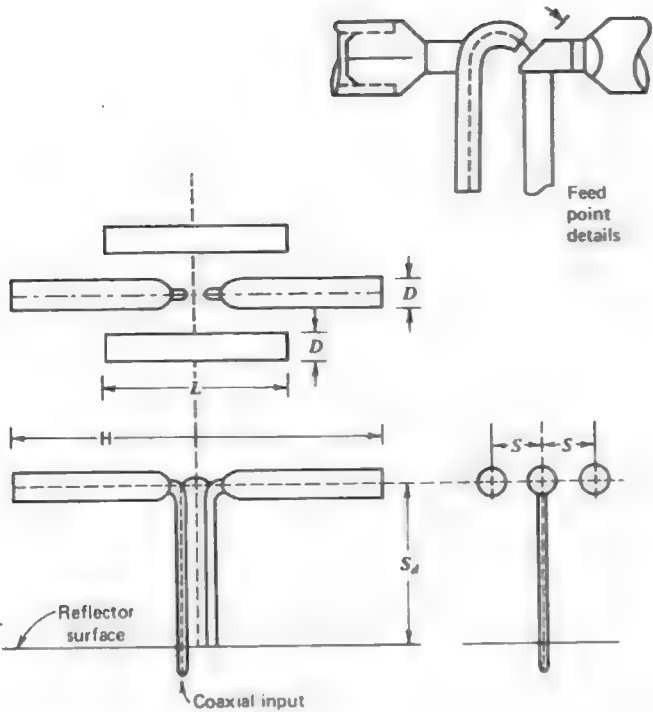


Figure 6-15 The open-sleeve dipole antenna with a flat reflector shown in front, top, and side views.

design values yield low VSWR over a wide bandwidth. This is illustrated in Fig. 6-16 by a comparison of the VSWR characteristics of a conventional (unsleeved) dipole and an open-sleeve dipole with a diameter D of 2.9 cm. While these results do not represent exhaustive design data for the open-sleeve dipole, they do serve as a starting point in the design of open-sleeve dipoles with or without a reflector present.

6.4 SPIRAL ANTENNAS

Frequently it is desirable to have the pattern and impedance of an antenna remain constant over a very wide range of frequencies (say 10 : 1 or higher). An antenna of this type is referred to as a **frequency independent antenna**. The biconical antenna forms the emergence of a frequency independent antenna. In Section 6.2 we found that the input impedance and pattern of the infinite biconical

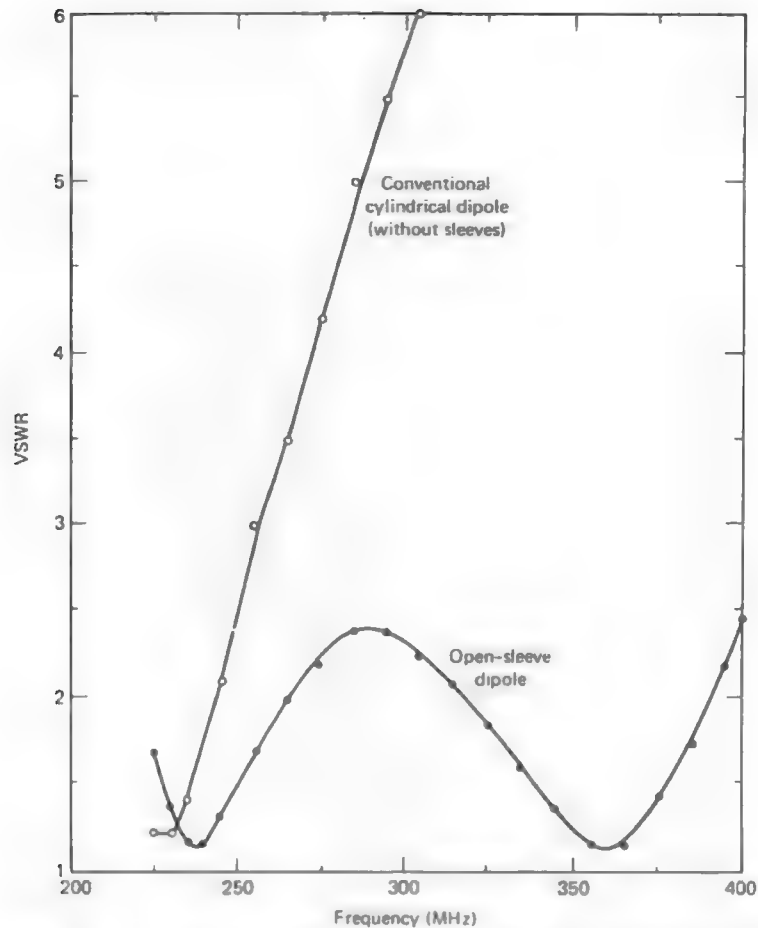


Figure 6-16 Comparison between the VSWR response of a conventional (unsleeved) cylindrical dipole and an open-sleeve dipole both with a diameter D of 2.9 cm [10].

antenna were independent of frequency. This is precisely the behavior we desire! What then is the most distinctive feature of this antenna? It is the emphasis on angles and complete removal of finite lengths. In fact, when the infinite biconical antenna is truncated forming a finite biconical antenna most of its broadband behavior disappears. The concept of angle emphasis has been exploited in recent years and has lead to a family of wide bandwidth antennas. These antennas can be divided into two types: frequency independent spiral antennas which we discuss in this section and log periodic antennas to be discussed in the following section.

If we are to completely remove finite lengths and replace them with angles, an infinite structure would always be required. Hence, in practice, *frequency independent antennas are designed to minimize finite lengths and maximize angular dependence.*

Before discussing specific antennas another feature of frequency independent antennas will be introduced. Consider a metal antenna with an input impedance Z_{metal} . A complementary structure can be formed which is an antenna with air replacing the metal and metal replacing the air (of the original metal antenna). Its impedance is Z_{air} . Complementary antennas are similar to a positive and negative in photography. An example would be a dipole made of ribbons of metal (instead of wire). Its complement is a slot in a sheet of metal. It can be shown (Babinet's principle) that the impedances of complementary antennas are related as follows.

$$Z_{\text{air}} Z_{\text{metal}} = \frac{\eta^2}{4} \quad (6-43)$$

If an antenna and its complement are actually the same, they are called *self-complementary*, and then

$$Z_{\text{air}} = Z_{\text{metal}} = \frac{\eta}{2} = 188.5 \text{ ohms.} \quad (6-44)$$

This relationship is frequency independent and is our second design principle for frequency independent antennas, that is, *self-complementary antennas tend to be frequency independent.* It turns out, however, that many frequency independent antennas are not self-complementary and still have relatively constant impedance.

Now we will examine a specific case of a self-complementary antenna. First consider an equiangular spiral curve as shown in Fig. 6-17. In cylindrical coordinates the distance of the curve from the origin is given by

$$r = r_0 e^{a\phi} \quad (6-45)$$

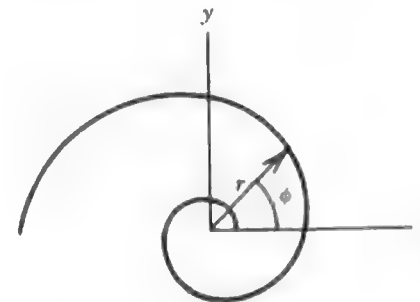


Figure 6-17 Equiangular spiral curve. $r = r_0 e^{a\phi}$ with $r_0 = 0.311$ cm and $a = 0.221$.

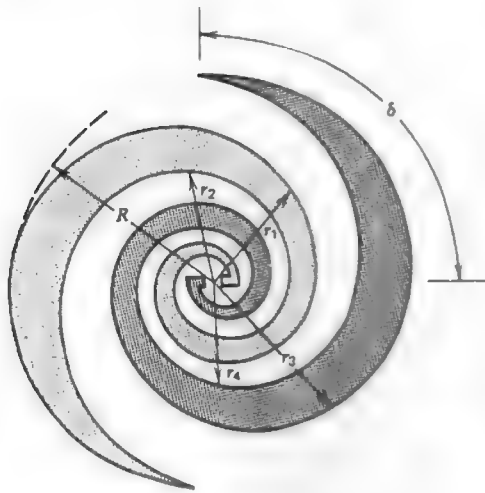


Figure 6-18 Planar equiangular spiral antenna. (Self-complementary case with $\delta = 90^\circ$.)

where r_0 is the radius for $\phi = 0$ and a is a constant giving the flare rate of the spiral. The spiral of Fig. 6-17 is right-handed; left-handed spirals can be generated using negative values of a . The equiangular spiral curve can be used to make the angular antenna shown in Fig. 6-18 which is referred to as a **planar equiangular spiral antenna**. The four edges of the metal (indicated by dots) each have an equation for their curves of the form in (6-45). In particular, edge no. 1 is that of Fig. 6-17, so $r_1 = r_0 e^{a\phi}$. Edge no. 2 has the same spiral curve but rotated through the angle δ , so $r_2 = r_0 e^{a(\phi - \delta)}$. The other half of the antenna has edges which make the structure symmetric, that is, by rotating one spiral arm one-half turn it would coincide with the other arm. So $r_3 = r_0 e^{a(\phi - \pi)}$ and $r_4 = r_0 e^{a(\phi - \pi - \delta)}$. The structure of Fig. 6-18 is self-complementary so $\delta = \pi/2$. It does not have to be constructed this way, but pattern symmetry is best for the self-complementary case.

The impedance, pattern, and polarization remain nearly constant over a wide range of frequencies. The feed point at the center, the overall radius, and the flare rate affect the performance. The flare rate a is more conveniently represented through the *expansion ratio*

$$\epsilon = \frac{r(\phi + 2\pi)}{r(\phi)} = \frac{r_0 e^{a(\phi + 2\pi)}}{r_0 e^{a\phi}} = e^{a2\pi} \quad (6-46)$$

which is the increase factor of the radius for one turn of the spiral. A typical value of ϵ is 4. Then from (6-46) $a = 0.221$. The high-frequency end of the

operating band is set by the feed structure: the minimum radius (r_0 for our right-hand wound spiral case) is about a quarter-wavelength for an expansion ratio ϵ of 4 [11]. Of course, the spiral terminates at this point and is connected to the feed transmission line. The low-frequency limit is set by overall radius R , roughly about a quarter-wavelength.

Spirals of from one-half to three turns have been found experimentally to be relatively insensitive to the parameters a and δ [12]. Around one and one-half turns appears to be optimum. For example, consider a one and one-half turn spiral with $a = 0.221$ as shown in Fig. 6-18. Each edge curve is of the form in (6-45), so the maximum radius is $R = r(\phi = 3\pi) = r_0 e^{0.221(3\pi)} = 8.03r_0$. This equals $\lambda_L/4$, where λ_L is the wavelength at the lower band edge frequency. At the feed point $r = r(\phi = 0) = r_0 e^0 = r_0$, and this equals $\lambda_U/4$ where λ_U is the wavelength at the upper frequency band edge. The bandwidth is then $f_U/f_L = \lambda_L/\lambda_U = (\lambda_L/4)/(\lambda_U/4) = 8.03r_0/r_0 = 8.03$. This 8:1 bandwidth is typical, however bandwidths of 20:1 can be obtained.

The self-complementary equiangular spiral, from (6-44), has a theoretical input impedance value of $188.5 + j0$ ohms. In practice the measured impedance values tend to be lower than this, as a result of the presence of the coaxial feed line which is wound along one arm toward the feed at the center [11]. In fact, an input impedance of about 164 ohms has been measured over a 6:1 frequency range from 500 MHz to 3 GHz [13].

The radiation from the self-complementary planar equiangular spiral antenna has been shown experimentally to be a bidirectional pattern with two wide beams broadside to the plane of the antenna. The field pattern is approximately $\cos \theta$ where the z -axis is normal to the plane of the antenna. The half-power beamwidth is, thus, approximately 90° . The polarization of the radiation is close to circular over wide angles, out to as far as 70° from broadside. The sense of the polarization is determined by the sense of the flare of the spiral. For example, the spiral of Fig. 6-18 radiates in the right-hand sense for directions out of the page and radiates in the left-hand sense for opposite propagation directions.

Another form of a planar spiral is the **Archimedean spiral antenna** shown in Fig. 6-19. This antenna, as are many spiral antennas, is easily constructed using printed circuit techniques. The equations of the two spirals in Fig. 6-19 are $r = r_0 \phi$ and $r_0(\phi - \pi)$. The properties of the Archimedean spiral antenna are similar to those of the equiangular planar spiral antenna. A single main beam can be obtained by placing a circularly cylindrical cavity on one side of the spiral, forming a **cavity-backed Archimedean spiral antenna**. Commercially available cavity-backed Archimedean spiral antennas have a 90° half-power beamwidth, 2:1 VSWR, and a 1.1 axial ratio of polarization on boresight, over a 10:1 bandwidth.

Nonplanar forms of spiral antennas can be employed to produce a single main beam. For example, the planar equiangular spiral antenna can be conformed

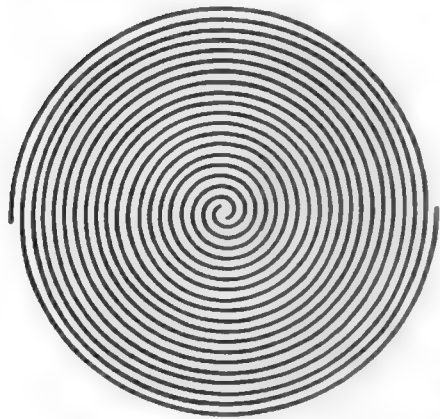


Figure 6-19 The Archimedean spiral antenna.

onto a conical surface, thus creating the **conical equiangular spiral antenna**. The equation for a conical equiangular spiral curve is

$$r = e^{(a \sin \theta_h) \phi} \quad (6-47)$$

The planar spiral is a special case with $\theta_h = 90^\circ$. The equations for the edges of one spiral of metal are that of (6-47) for r_1 , and $r_2 = e^{(a \sin \theta_h (\phi - \delta))}$; and $\delta = \pi/2$ for the self-complementary case. The other spiral arm is produced by a 180° rotation. The edges of the arms maintain a constant angle α with a radial line for any cone half-angle θ_h , and [11]

$$a = \cot \alpha. \quad (6-48)$$

The conical equiangular spiral antenna, unlike its planar counterpart, has a single main beam. In particular, there is more intense radiation off the cone tip ($-z$ -direction) than there is in the opposite direction. The self-complementary shape yields the best radiation patterns. Typical patterns for $\theta_h \leq 15^\circ$ and α about 70° have a broad main beam with a maximum in the $\theta = 180^\circ$ direction and a half-power beamwidth of about 80° . Since the structure is rotationally symmetric, the pattern is also nearly rotationally symmetric. The polarization of the radiated field is very close to circular in all directions, with the sense determined by the sense of the spirals. However, the ellipticity does increase with off-axis angle. The impedance [11] can be approximated by the relation

$$Z_o \approx 300 - 1.5\delta(\text{degrees}) \text{ ohms} \quad (6-49)$$

where $\delta(\text{degrees})$ is the angle δ of Fig. 6-20 in degrees. For the self-complementary case δ is 90° and from (6-49) $Z_o \approx 165$ ohms which is close to the 188.5 ohms theoretical value. The impedance is not affected significantly by θ_h or α .

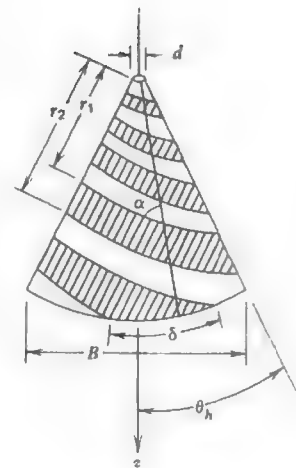


Figure 6-20 The conical equiangular spiral antenna.

Design of the conical equiangular spiral antenna is rather simple and proceeds as follows [14]. The upper frequency f_u of the operating band occurs when the truncated apex diameter is a quarter-wavelength, that is, $d = \lambda_u/4$. The lower band edge frequency f_l is determined by the base diameter B and occurs for $B = 3\lambda_l/8$. θ_h is usually less than 15° and α about 70° . For $\theta_h = 10^\circ$ and $\alpha = 73^\circ$ the front-to-back ratio is 15 dB and the axial ratio of the polarization is well below 2 on axis.

In spiral antennas most radiation comes from the region of the structure where the circumference is about one wavelength, often called the *active region*. Thus, as frequency is changed a different part of the spiral supports the majority of the current. This feature is responsible for the broadband performance. To see this recall that the current amplitude on an infinite biconical antenna is constant with distance from the feed. Therefore, it will be altered when the structure is terminated to form a finite biconical antenna. On the other hand, an antenna with a distinct active region in which the current farther out from the feed point is very small essentially appears as if it were infinite. This property is exploited further in the next section.

6.5 LOG-PERIODIC ANTENNAS

The spiral antennas of the previous section illustrate the principle that emphasis on angles will lead to a broadband antenna. Although spiral antennas are not complex structures, construction would be simplified if simple geometries, involving circular or straight edges, could be utilized. Antennas of this type are

discussed in this section. To see how the ideas develop, first consider the **bowtie antenna** (also called the **bifin antenna**) of Fig. 6-21. It is the planar version of the finite biconical antenna (see Fig. 6-9). It has a bidirectional pattern with broad main beams perpendicular to the plane of the antenna. It is also linearly polarized. The bowtie antenna is used as a receiving antenna for UHF TV channels, frequently with a wire grid ground plane behind it to reduce the back lobe. Since currents are abruptly terminated at the ends of the fins, the antenna has limited bandwidth. As we shall see shortly, by modifying the simple bowtie antenna as shown in Fig. 6-22, the currents will then die off more rapidly with distance from the feed point. The introduction of periodically positioned teeth distinguishes this antenna as one of a broad class of log-periodic antennas. A **log-periodic antenna** is an antenna having a structural geometry such that its impedance and radiation characteristics repeat periodically as the logarithm of frequency. In practice the variations over the frequency band of operation are minor, and log-periodic antennas are usually considered to be frequency independent antennas.

Most of the work on frequency independent antennas took place at the University of Illinois in the late 1950s and the 1960s [15]. A series of antennas were developed through many experiments. Several geometries were examined, and those that produced broadband behavior led to determination of the properties necessary for wide bandwidth. Frequency independent spiral antennas were discussed in the previous section. In this section we outline the development of the log-periodic antenna family. The metamorphosis of the log-periodic produced the log-periodic dipole antenna, which is made up of only straight wire segments.

One of the first log-periodic antennas was the **log-periodic toothed planar antenna** shown in Fig. 6-22. It is similar to the bowtie antenna except for the teeth. The teeth act to disturb the currents which would flow if the antenna were of bowtie-type construction. Currents flow out along the teeth and, except at the frequency limits, are not significant at the ends of the antenna. The rather unusual shape of this antenna is explained by examining the planar equiangular spiral

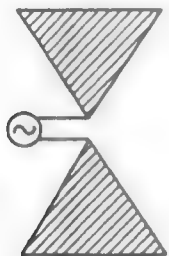


Figure 6-21 The bowtie antenna.

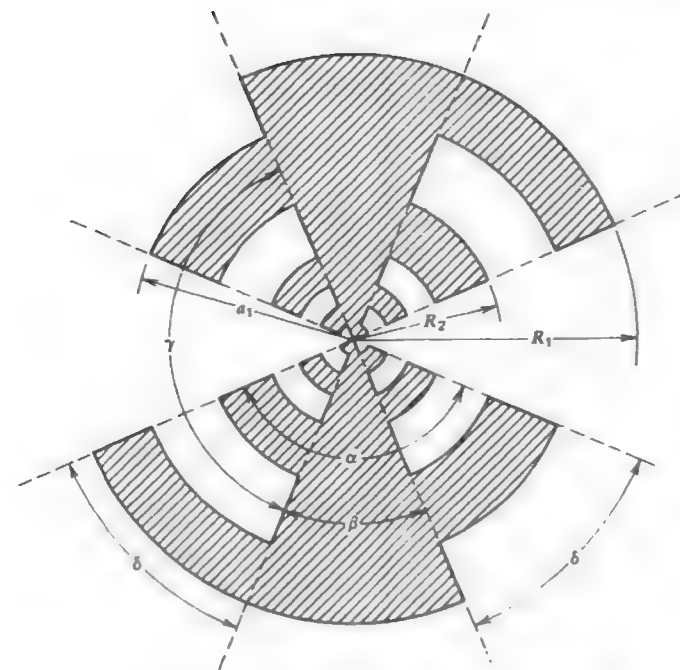


Figure 6-22 Log-periodic toothed planar antenna. (Self-complementary.)

antenna. Along a radial line from the center of the spiral, the positions of the far (or near) edges of a conductor from (6-45) are

$$r_n = r(\phi + n2\pi) = r_0 e^{j(\phi + n2\pi)}. \quad (6-50)$$

The ratio of the $n + 1$ th position to the n th position is

$$\frac{r_{n+1}}{r_n} = \frac{r_0 e^{j(\phi + (n+1)2\pi)}}{r_0 e^{j(\phi + n2\pi)}} = e^{j2\pi} = 1 \quad (6-51)$$

which is the expansion factor of (6-46). This is a constant, and thus the distances (or period) of the edges are of constant ratio for the planar spiral. For the structure of Fig. 6-22 the ratio of edge distances is also a constant, and is given by the following scale factor

$$\tau = \frac{R_{n+1}}{R_n} < 1. \quad (6-52)$$

The slot width is expressed by

$$\sigma = \frac{a_n}{R_n} < 1. \quad (6-53)$$

These relations are true for any n . The parameter τ gives the period of the structure. We would thus expect periodic pattern and impedance behavior with the same period. In other words, if frequencies f_{n+1} and f_n from adjacent periods lead to identical performance, then

$$\frac{f_n}{f_{n+1}} = \tau \quad f_n < f_{n+1}. \quad (6-54)$$

Forming $f_{n+1} = f_n/\tau$ from this equation and taking the logarithm of both sides, we have

$$\log f_{n+1} = \log f_n + \log(1/\tau). \quad (6-55)$$

Thus, the performance is periodic in a logarithmic fashion, and hence the name log-periodic antenna. All log-periodic antennas have this property.

If the teeth sizes of the log-periodic toothed planar antenna are adjusted properly, the structure can be made self-complementary. From Fig. 6-22 we see that in general (whether self-complementary or not)

$$\gamma + \beta = 180^\circ \quad \text{and} \quad \beta + 2\delta = \alpha. \quad (6-56)$$

If the structure is self-complementary (as shown)

$$\alpha = \gamma \quad \text{and} \quad \beta = \delta. \quad (6-57)$$

Substituting (6-57) into (6-56) yields $\alpha + \beta = 180^\circ$ and $\beta + 2\beta = \alpha$. Solving these two equations gives

$$\alpha = 135^\circ \quad \text{and} \quad \beta = 45^\circ \quad (6-58)$$

for a self-complementary log-periodic toothed planar antenna. As we saw in the previous section, an antenna that is self-complementary tends to be broadband and has an input impedance of 188.5 ohms.

If the widths of the teeth and gaps are equalized, $\sigma = a_n/R_n = R_{n+1}/a_n$. Using (6-52) and solving for σ gives

$$\sigma = \sqrt{\tau}. \quad (6-59)$$

This relationship and the self-complementary feature are popular in practice.

The properties of the log-periodic toothed planar antenna depend upon τ . It has been found experimentally that the half-power beamwidth increases with increasing values of τ [11] as shown in Fig. 6-23. The pattern has two lobes with maxima in each normal direction to the plane of the antenna. The radiation is

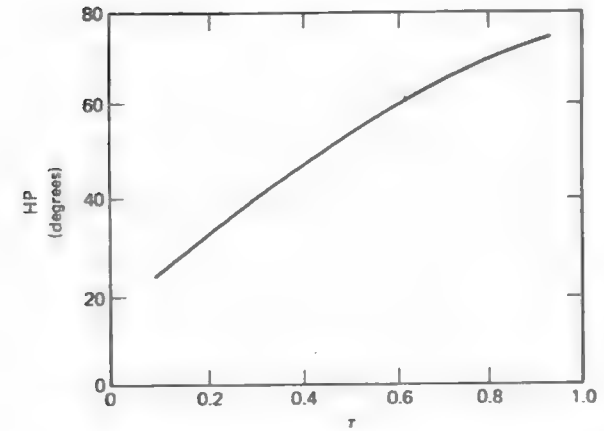


Figure 6-23 Half-power beamwidth of the self-complementary toothed planar antenna (for $\sigma = \sqrt{\tau}$) as a function of scale factor τ .

linearly polarized parallel to the teeth edges. This is perpendicular to what it would be if there were no teeth ($\delta = 0$), in which case the antenna would be a bowtie. The fact that transverse current flow dominates over radial current flow is significant. Most of the current appears on teeth that are about a quarter-wavelength long (the active region). This, we have seen, is key to achieving wide bandwidths. The frequency limits of operation are set by the frequencies where the largest and smallest teeth are a quarter-wavelength long.

The log-periodic toothed planar antenna should have a performance (impedance and pattern) that repeats periodically with frequency with period τ given by (6-52). The self-complementary version of the antenna, while not producing frequency independent operation, does lead to performance that does not vary greatly for frequencies between periods, that is, for $f_n < f < f_{n+1}$. In fact, measurements have produced nearly identical patterns over a 10:1 bandwidth [11].

The log-periodic toothed wedge antenna of Fig. 6-24 is a unidirectional pattern form of its planar version in Fig. 6-22, in which the included angle ψ is 180° . A single broad main beam exists in the $+z$ -direction. The patterns are nearly frequency independent for $30^\circ < \psi < 60^\circ$. The polarization is linear and y -directed for on-axis radiation, as indicated in Fig. 6-24. There is a small cross polarized component (x -directed) arising from the radial current mode, as found in a biconical antenna. Typically this cross-polarized component is 18 dB down from the copolarized (y -directed) component on-axis, indicating a strong excitation of the transverse current mode associated with frequency independent behavior. The bandwidth of the wedge version is similar to the sheet version but the

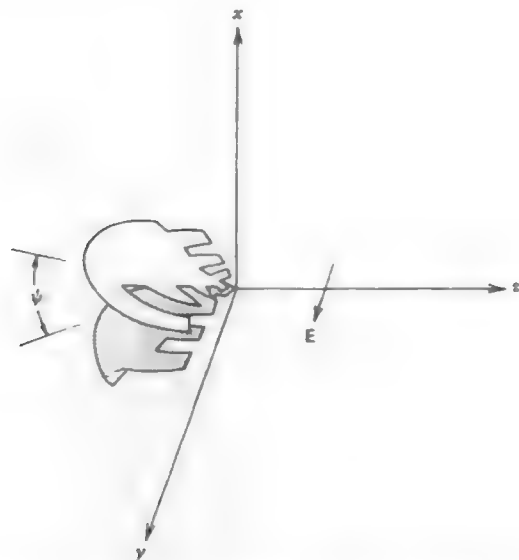


Figure 6-24 Log-periodic toothed wedge antenna.

input impedance is reduced for decreasing ψ . For the planar case ($\psi = 180^\circ$) the self-complementary antenna, which should have an impedance of 188.5 ohms, has an impedance of about 165 ohms, whereas the wedge form with $\psi = 30^\circ$ has a 70-ohm impedance. As ψ is decreased the impedance variation over a period of the structure (frequency ratio of τ) increases. For example, a 3:1 variation occurs for $\psi = 60^\circ$ relative to the geometric mean [11].

From a construction standpoint it would be desirable if the toothed antennas could be made with straight edges. This simplification of the structure turns out to be of little consequence in the performance of the antenna. This is another major step in the development of the log-periodic antenna. As an example, if the tooth edges of the log-periodic toothed planar antenna in Fig. 6-22 are replaced by straight edges the **log-periodic toothed trapezoid antenna** of Fig. 6-25 results. The performance of this antenna is similar to its curved edge version in Fig. 6-22. A **log-periodic toothed trapezoid wedge antenna** can be formed by bending the planar version into a wedge, creating an antenna similar to that of Fig. 6-24. In fact, the patterns of the two wedge forms (curved edge and trapezoid) are similar, but the trapezoid version has better impedance performance with only about a 1.6:1 variation over a period for $\psi = 60^\circ$ [11].

The solid metal (or sheet) antennas we have described are practical for short wavelengths, but for low frequencies the required structures can become rather

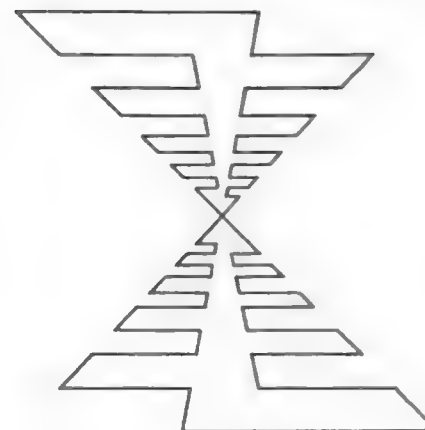


Figure 6-25 Log-periodic toothed trapezoid antenna.

impractical. It turns out that the sheet antennas can be replaced by a wire version in which thin wires are shaped to follow the edges of the sheet antenna. An example of this major structural simplification is that of Fig. 6-26, which is the wire version of Fig. 6-25. This **log-periodic trapezoid wire antenna** can also be bent at the apex to form a wedge that produces a unidirectional pattern. The **log-periodic trapezoid wedge wire antenna** has a performance similar to its sheet version. Measurements for a wedge angle $\psi = 45^\circ$ have yielded *E*- and *H*-plane half-power beamwidths of 66° , a gain of 9.2 dB, and a front-to-back ratio of 12.3 dB. The average input impedance has been measured as 110 ohms with a VSWR of 1.45 over a 10:1 band [16]. As with other wedge log-periodics, the

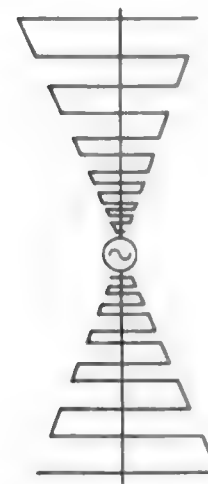


Figure 6-26 Log-periodic trapezoid wire antenna.



Figure 6-27 Log-periodic zig-zag wire antenna.

main beam maximum is straight off the apex and the radiation is linearly polarized.

Other even simpler log-periodic wire antennas exist in both planar and wedge shapes. The **log-periodic zig-zag wire antenna** of Fig. 6-27 is an example.

The final phase in this metamorphosis of log-periodic antennas is the use of only parallel wire segments. This is the **log-periodic dipole array** of Fig. 6-28 [17, 18]. The log-periodic dipole array (LPDA) is a series-fed array of parallel wire dipoles of successively increasing lengths outward from the feed point at the apex. Note that the interconnecting feed lines cross over between adjacent elements. This can be explained by noting that the LPDA of Fig. 6-28 resembles the toothed trapezoid of Fig. 6-25 when folded on itself, making a wedge with zero included angle. The two center fins of metal then form a parallel transmission line with the teeth coming out from them on alternate sides of the fins. This alternate arm geometry occurs for all wedge log-periodic antennas.

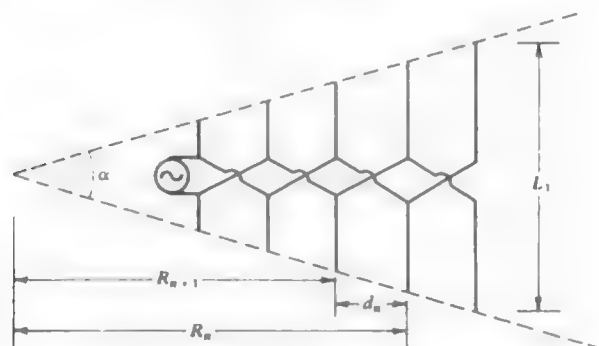


Figure 6-28 Log-periodic dipole array geometry.

A particularly successful method of constructing an LPDA is shown in Fig. 6-29. A coaxial transmission line is run through the inside of one of the feed conductors. The outer conductor of the coax is attached to that conductor and the inner conductor of the coax is connected to the other conductor of the LPDA transmission line.

As shown in Fig. 6-28, a wedge of enclosed angle α bounds the dipole lengths. The scale factor τ for the LPDA is

$$\tau = \frac{R_{n+1}}{R_n} < 1. \quad (6-60)$$

Right triangles of enclosed angle $\alpha/2$ reveal that

$$\tan \frac{\alpha}{2} = \frac{L_n/2}{R_n} = \frac{L_{n+1}/2}{R_{n+1}}. \quad (6-61)$$

Thus

$$\frac{L_1}{R_1} = \dots = \frac{L_n}{R_n} = \frac{L_{n+1}}{R_{n+1}} = \dots = \frac{L_N}{R_N}. \quad (6-62)$$

Using this result in (6-60) gives

$$\tau = \frac{R_{n+1}}{R_n} = \frac{L_{n+1}}{L_n}. \quad (6-63)$$

Thus, the ratio of successive element positions equals the ratio of successive dipole lengths.

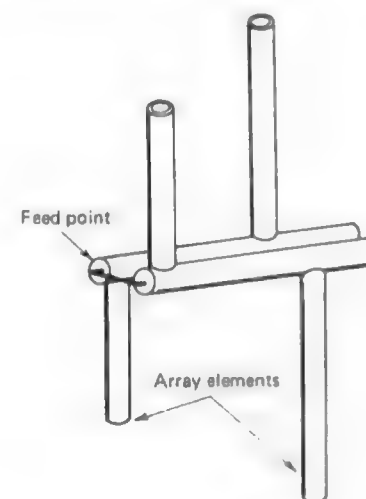


Figure 6-29 Construction details of the log-periodic dipole array.

The spacing factor for the LPDA is defined as

$$\sigma = \frac{d_n}{2L_n} \quad (6-64)$$

where the element spacings as shown in Fig. 6-28 are given by

$$d_n = R_n - R_{n+1}. \quad (6-65)$$

But $R_{n+1} = \tau R_n$, so

$$d_n = R_n - \tau R_n = (1 - \tau)R_n. \quad (6-66)$$

From (6-61) $R_n = L_n/2 \tan(\alpha/2)$. Using this in (6-66) yields

$$d_n = (1 - \tau) \frac{L_n}{2 \tan(\alpha/2)}. \quad (6-67)$$

Substituting this in (6-64) gives

$$\sigma = \frac{d_n}{2L_n} = \frac{1 - \tau}{4 \tan(\alpha/2)} \quad (6-68)$$

or,

$$\alpha = 2 \tan^{-1} \left(\frac{1 - \tau}{4\sigma} \right). \quad (6-69)$$

Combining (6-68) with (6-63), we note that all dimensions are scaled by

$$\tau = \frac{R_{n+1}}{R_n} = \frac{L_{n+1}}{L_n} = \frac{d_{n+1}}{d_n}. \quad (6-70)$$

As we have seen with other log-periodic antennas, there is also an active region for the LPDA, where the few dipoles near the one that is a half-wavelength long support much more current than do the other radiating elements. It is convenient to view the LPDA operation as being similar to that of a Yagi-Uda antenna. The longer dipole behind the most active dipole (with largest current) behaves as a reflector and the adjacent shorter dipole in front acts as a director. The radiation is then off of the apex. The wedge enclosing the antenna forms an arrow pointing in the direction of the main beam maximum.

As the operating frequency changes, the active region shifts to a different portion of the antenna. The frequency limits of the operational band are roughly determined by the frequencies at which the longest and shortest dipoles are half-wave resonant, that is,

$$L_1 \approx \frac{\lambda_L}{2} \quad \text{and} \quad L_N \approx \frac{\lambda_U}{2} \quad (6-71)$$

where λ_L and λ_U are the wavelengths corresponding to the lower and upper frequency limits. Since the active region is not confined completely to one dipole, often dipoles are added to each end of the array to ensure adequate performance over the band. The number of additional dipoles required is a function of τ and σ [19, 20]. But for noncritical applications (6-71) is sufficient.

The pattern, gain, and impedance of an LPDA depend upon the design parameters τ and σ . Since the LPDA is a very popular broadband antenna of simple construction, low cost, and light weight, we will give the design details and illustrate them by examples. Gain contours are plotted in Fig. 6-30 as a function of τ and σ [18]. Note that high gain requires a large value of τ , which means a very slow expansion, that is, a LPDA of large overall length. Gain is only slightly affected by the dipole thickness. It increases about 0.2 dB for a doubling of the thickness [11]. Optimum gain is indicated in Fig. 6-30, and it gives the smallest scale factor for a given gain value.

Further details on the design and calculations for the LPDA are available in the literature [19-23]. Also the LPDA can be constructed in a size reduced form or using printed circuit techniques [24-26].

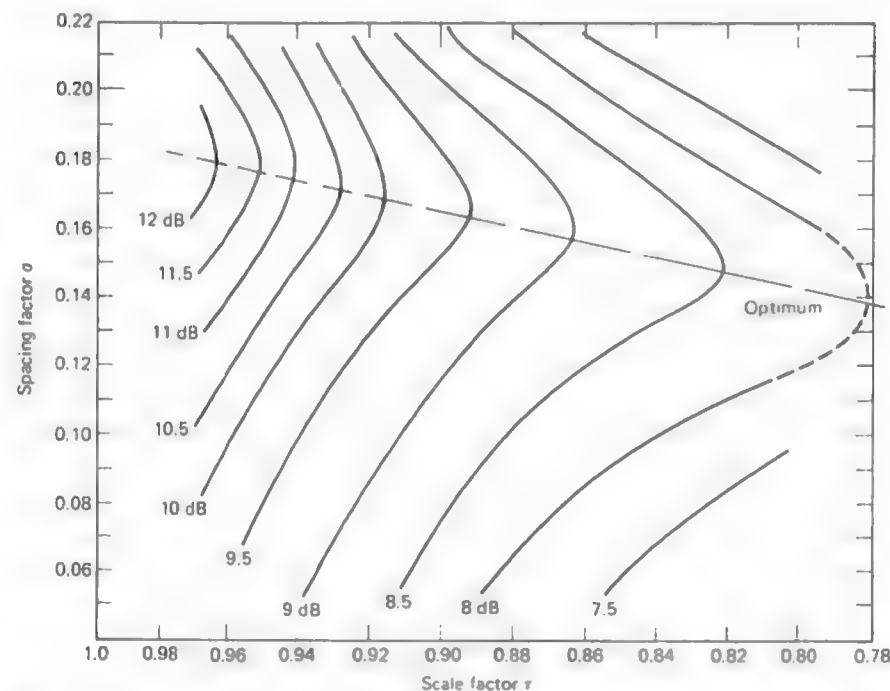


Figure 6-30 Gain of a log-periodic dipole array. (From Carrel [18]. © 1961 IRE (now IEEE). Reprinted with permission of IEEE.)

Example 6-2. Optimum Design of a 54–216 MHz Log-Periodic Dipole Antenna

It is desired to have an antenna that operates over the entire VHF-TV and FM broadcast bands, which span the 54 to 216 MHz frequency range for a 4:1 bandwidth. Suppose the design gain is chosen to be 8.5 dB. The corresponding values of τ and σ for optimum design from Fig. 6-30 are

$$\tau = 0.822 \quad \text{and} \quad \sigma = 0.149. \quad (6-72)$$

Then from (6-69) we have

$$\alpha = 2 \tan^{-1} \left[\frac{1 - 0.822}{4(0.149)} \right] = 33.3^\circ. \quad (6-73)$$

The length of the longest dipole is determined first. At the lowest frequency of operation, (54 MHz) the dipole length from (6-71) should be near a half-wavelength, so

$$L_1 = 0.5\lambda_L = 0.5(5.55) = 2.78 \text{ m}. \quad (6-74)$$

The shortest dipole length should be on the order of $L_U = 0.5\lambda_U = 0.694 \text{ m}$ at 216 MHz. The LPDA element lengths are computed until a length on the order of 0.694 m is reached. To be specific, element lengths are found from L_1 using $L_{n+1} = \tau L_n$. For example,

$$L_2 = \tau L_1 = (0.822)(2.78) = 2.28 \text{ m}$$

and

$$L_3 = \tau L_2 = (0.822)(2.28) = 1.88 \text{ m}.$$

Completing this process leads to

$$\begin{array}{llll} L_1 = 2.78 \text{ m}, & L_2 = 2.28 \text{ m}, & L_3 = 1.88 \text{ m}, & L_4 = 1.54 \text{ m}, \\ L_5 = 1.04 \text{ m}, & L_6 = 0.856 \text{ m}, & L_7 = 0.704 \text{ m}, & L_8 = 0.578 \text{ m}. \end{array} \quad (6-75)$$

The array was terminated with eight elements since $L_8 = 0.578 \text{ m}$ is less than the 0.694-m length for the highest operating frequency. Elements could be added to either end to improve performance at the band edges.

The element spacings for this example are found from (6-68) as

$$d_n = 2\sigma L_n = 2(0.149)L_n = 0.298L_n. \quad (6-76)$$

Using the element lengths of (6-75) gives

$$\begin{array}{llll} d_1 = 0.828 \text{ m}, & d_2 = 0.679 \text{ m}, & d_3 = 0.459 \text{ m}, & d_4 = 0.378 \text{ m}, \\ d_5 = 0.310 \text{ m}, & d_6 = 0.255 \text{ m}, & d_7 = 0.210 \text{ m}. \end{array} \quad (6-77)$$

These dipole lengths and spacings completely specify the LPDA, as shown in Fig. 6-28. The total length of the array is the sum of the spacings in (6-77), which gives 3.119 m. The outline of the antenna fits into an angular sector of angle $\alpha = 33.3^\circ$.

Example 6-3. Characteristics of a 200–600 MHz LPDA

In this example we examine the gain, pattern, impedance, and current distribution of a LPDA as a function of frequency. Suppose it is to be constructed for operation over the 200 to 600 MHz band. For optimum performance and a design goal of 10 dB gain, we see from Fig. 6-30 that $\tau = 0.917$ and $\sigma = 0.169$. The lowest frequency of operation (200 MHz) has a wavelength of $\lambda_L = 1.5 \text{ m}$, so the first element has a length of $L_1 = \lambda_L/2 = 0.75 \text{ m}$. The length of the shortest element should be on the order of a half-wavelength at 600 MHz, and $\lambda_U/2 = 0.500 \text{ m}/2 = 0.250 \text{ m}$. Using the design techniques illustrated in the previous example and four extra elements at the narrow end gives the 18 element LPDA shown in Fig. 6-31a. (The antenna geometry details are left as a problem.)

The LPDA of Fig. 6-31a was modeled using the computer techniques of Section 7.9. The resulting current distributions at the band edges and one midway frequency are

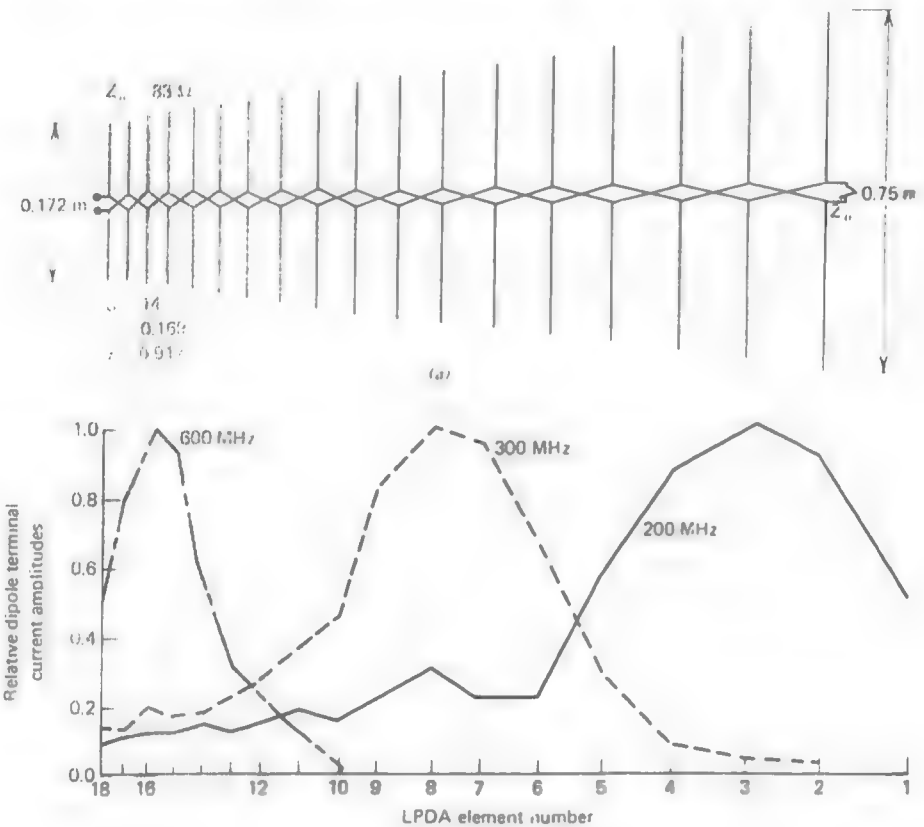


Figure 6-31 An optimum log-periodic dipole antenna for operation in the 200 to 600 MHz band (Example 6-3). (a) The geometry. (b) Current distributions.

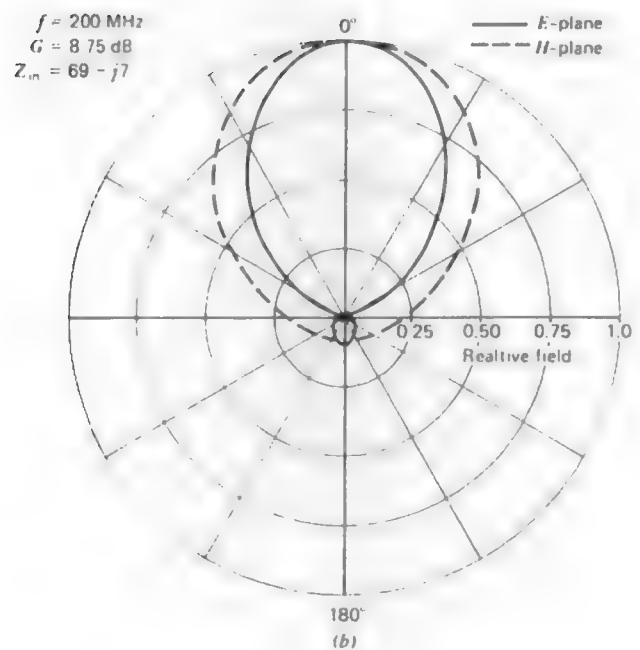
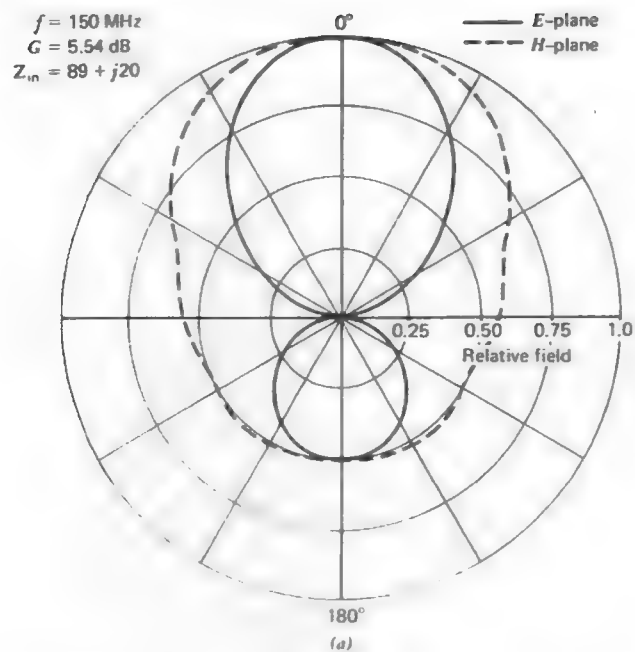


Figure 6-32

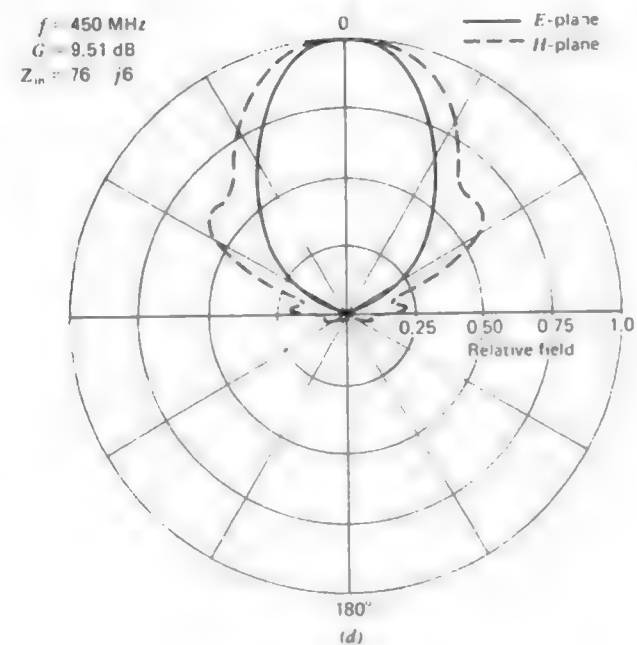
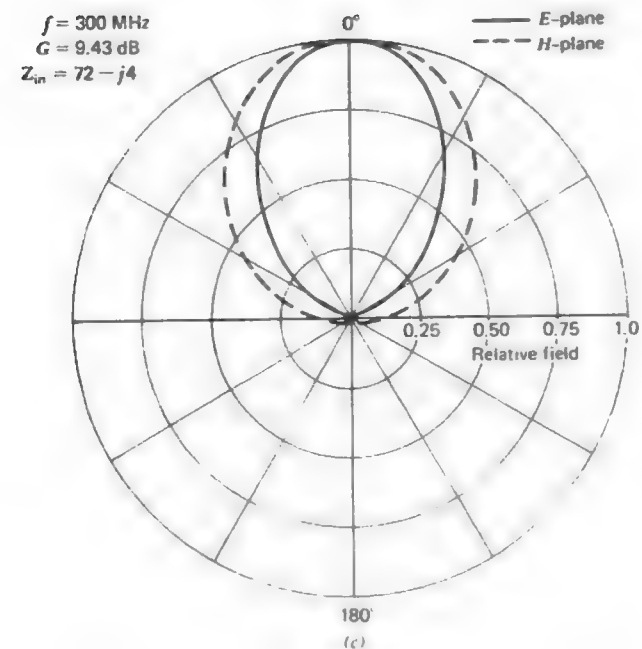


Figure 6-32

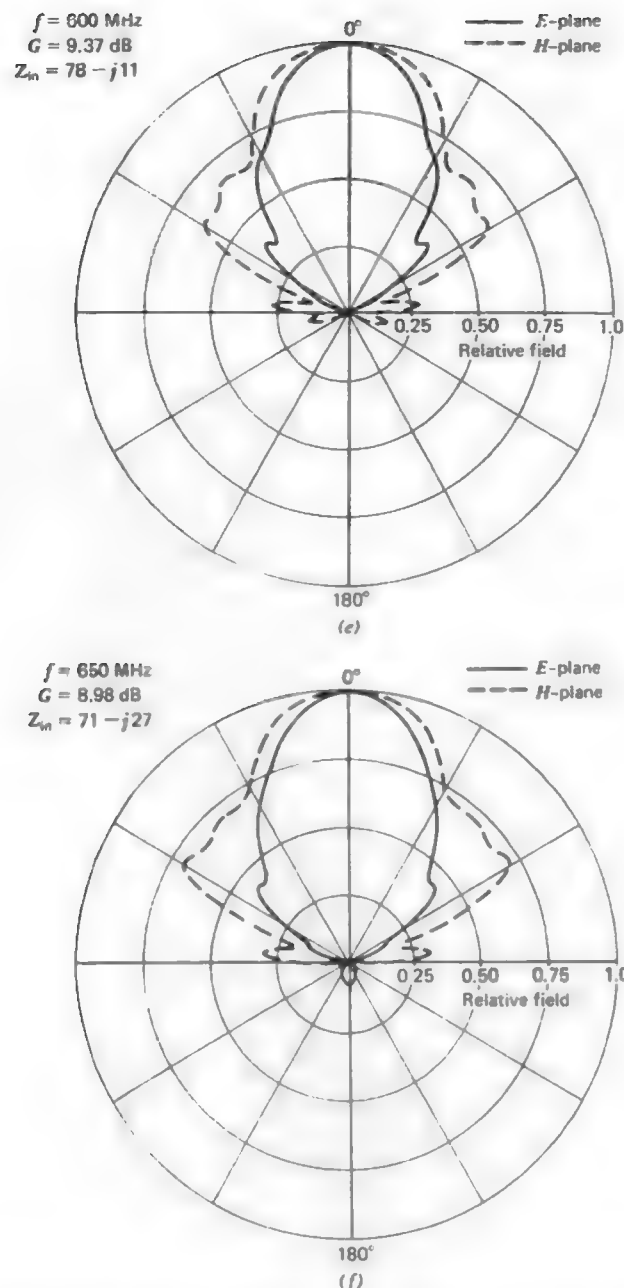


Figure 6-32 Radiation patterns at several frequencies for the log-periodic dipole antenna of Example 6-3. The gain and impedance values are also given. (a) 150 MHz. (b) 200 MHz. (c) 300 MHz. (d) 450 MHz. (e) 600 MHz. (f) 650 MHz.

shown in Fig. 6-31b. These currents illustrate the active region behavior we have mentioned several times. For example, at 200 MHz there are three dipoles with strong currents on them and a total of five with significant currents. This is also true for other frequencies in the operating band, with the active region shifted to some other portion of the antenna as seen in Fig. 6-31b. At the high-frequency limit element 14 is about a half-wavelength long and the extra four elements provide support for the active region at 600 MHz.

The gain, pattern, and impedance behavior as a function of frequency are shown in Fig. 6-32. At 150 MHz the gain is considerably less than the 10-dB design value due to the large back lobe. Also the input impedance has a substantial imaginary part. This inferior performance is, of course, caused by insufficient antenna length required for proper support of the active region at that frequency. At the lower band edge of 200 MHz, however, the pattern has little back radiation, the gain is approaching the design goal, and the input impedance has a small imaginary part. Similarly, at 650 MHz the performance is only slightly inferior to that at the upper band edge of 600 MHz because of the added elements. At intermediate frequencies between the band edges the gain, pattern, and impedance remain reasonably constant, indicating frequency independent behavior. Figures 6-32c and 6-32d are typical of intermediate frequencies. The fact that the gain never quite reaches the design goal of 10 dB is mostly due to the use of a characteristic impedance termination of the transmission line rather than a reactive termination (that is, open or short circuit). The use of a reactive termination can lead to unwanted resonances on the LPDA caused by energy being trapped between the termination and the stop region on the termination side of the active region. These high Q resonances can be eliminated by using a termination that is at least slightly resistive or by using a relatively high value for the LPDA transmission line impedance (e.g., $Z_0 \sim 150$ ohms) since this will cause the dipole elements to more heavily load the line. This makes the active region more efficient [27], with the result that there is relatively little energy left to propagate past the active region and cause a strong resonance effect on the radiation pattern.

REFERENCES

1. J. D. Kraus, *Antennas*, McGraw-Hill, New York, 1950; Chapter 7.
2. H. Jasik, Editor, *Antenna Engineering Handbook*, McGraw-Hill, New York, 1961; Chapter 7.
3. T. S. M. Maclean and R. G. Kouyoumjian, "Bandwidth of the uniform helical antenna," Ohio State University Research Foundation Technical Report 662-27, March, 31, 1959.
4. E. A. Wolff, *Antenna Analysis*, Wiley, New York, 1967; Section 3.10.
5. S. A. Schellkunoff and H. T. Friis, *Antennas: Theory and Practice*, Wiley, New York, 1952; Section 13.20.
6. A. G. Kandoian, "Three new antenna types and their applications," *Proc. IRE*, vol. 34, pp. 70W-75W, Feb. 1946.
7. J. J. Nail, "Designing discone antennas," *Electronics*, vol. 26, pp. 167-169, Aug. 1953.
8. T. H. Crowley and W. Marsh, "Discone type antennas," Ohio State Research Foundation Technical Report 510-13, June 30, 1954.

9. A. J. Poggio and P. E. Mayes, "Pattern bandwidth optimization of the sleeve monopole antenna," *IEEE Trans. on Antennas and Propagation*, vol. AP-14, pp. 643-645, Sept. 1966.
10. H. E. King and J. L. Wong, "An experimental study of a balun-fed, open-sleeve dipole in front of a metallic reflector," Aerospace Corp. Rept. No. TR-0172 (2158)-2, Feb. 1972.
11. V. Rumsey, *Frequency Independent Antennas*, Academic Press, New York, 1966.
12. J. D. Dyson, "The equiangular spiral antenna," *IRE Trans. on Antennas and Propagation*, vol. AP-7, pp. 181-187, 1959.
13. E. A. Wolff, *Antenna Analysis*, Wiley, New York, 1967; Chapter 9.
14. J. D. Dyson, "The unidirectional equiangular spiral antenna," *IRE Trans. on Antennas and Propagation*, vol. AP-7, pp. 329-334, Oct. 1959.
15. R. H. DuHammel and D. E. Isbell, "Broadband logarithmically periodic antenna structures," *IRE Intern. Conv. Record*, pp. 119-128, 1957.
16. R. S. Elliott, "A view of frequency independent antennas," *Microwave Journal*, vol. 5, pp. 61-68, Dec. 1962.
17. D. E. Isbell, "Log periodic dipole arrays," *IRE Trans. on Antennas and Propagation*, vol. AP-8, pp. 260-267, May 1960.
18. R. Carrel, "The design of log-periodic dipole antennas," *IRE International Convention Record*, part 1, pp. 61-75, 1961.
19. G. DeVito and G. B. Stracca, "Comments on the design of log-periodic dipole antennas," *IEEE Trans. on Antennas and Propagation*, vol. AP-21, pp. 303-308, May 1973.
20. Carl E. Smith, *Log Periodic Antenna Design Handbook*, Smith Electronics, Inc., Cleveland, Ohio, 1966.
21. G. DeVito and G. B. Stracca, "Further comments on the design of log-periodic dipole antennas," *IEEE Trans. on Antennas and Propagation*, vol. AP-22, pp. 714-718, Sept. 1974.
22. P. C. Butson and G. T. Thompson, "A note on the calculation of the gain of log-periodic dipole antennas," *IEEE Trans. on Antennas and Propagation*, vol. AP-14, pp. 105-106, Jan. 1976.
23. M. T. Ma, *Theory and Application of Antenna Arrays*, Wiley, New York, 1974; Chapter 5.
24. D. F. DiFonzo, "Reduced size log periodic antennas," *Microwave Journal*, vol. 7, pp. 37-42, Dec. 1964.
25. S. C. Kuo, "Size-reduced log-periodic dipole array antenna," *Microwave Journal*, vol. 15, pp. 27-33, Dec. 1972.
26. C. K. Campbell, et. al., "Design of a stripline log-periodic dipole antenna," *IEEE Trans. on Antennas and Propagation*, vol. AP-25, pp. 718-721, Sept. 1977.
27. C. C. Bantin and K. G. Balmain, "Study of compressed log-periodic dipole antennas," *IEEE Trans. on Antennas and Propagation*, vol. AP-18, pp. 195-203, March 1970.

PROBLEMS

6.1-1 An unfurled helix was built with an overall length of 78.7 cm, a diameter of 4.84 cm, and a pitch angle of 11.7° . The center frequency of operation is 1.7 GHz. Calcul-

late the number of turns, the directivity in decibels, the half-power beamwidth in degrees, and the axial ratio for the helix.

6.1-2 It is desired to achieve a right-hand circularly polarized wave with a pattern having a half-power beamwidth of 39° . One of the easiest ways to do this is with a helix antenna. It is to be built with a pitch angle of 12.5° , and the circumference of one turn is to be one wavelength at the center frequency of operation, which is 475 MHz.

- (a) Calculate the number of turns needed.
- (b) What is the directivity in decibels?
- (c) What is the axial ratio of the on-axis fields?
- (d) Over what range of frequencies will these parameters remain relatively constant?
- (e) Find the input impedance at the design frequency and at the ends of the band.

6.1-3 A commercially available axial mode helix antenna has six turns made of 0.95-cm aluminum tubing supported by fiberglass insulators attached to a 3.8-cm aluminum shaft. The band of operation is 300 to 520 MHz. The mechanical characteristics are: length of helix 118 cm, diameter of helix (center to center) 22.3 cm, ground screen diameter 89 cm.

- (a) Determine the pitch angle α .
- (b) Compute the gain in decibels at edges of the frequency band of operation.

6.1-4 A 12-turn axial mode helix has a circumference of 0.197 m, a pitch angle of 8.53° , and operates at 1525 MHz. Calculate and plot the radiation pattern in linear-polar form.

6.2-1 Calculate the input impedance for infinite biconical antennas of the following cone half angles: 0.1° , 1° , 10° , 20° , 50° .

6.2-2 A finite biconical antenna has cones that are each 0.3λ long and a half-angle 1° . Determine the input impedance using Fig. 6-10.

6.3-1 *Construction project.* Select a frequency for which you have laboratory equipment to measure impedance (probably in the VHF or UHF range). Construct both an optimum open-sleeve dipole and its ordinary dipole version. (Alternatively, monopoles may be constructed.) Measure the input impedance of both antennas over a 2:1 frequency range about the center frequency. (Alternatively, measure the VSWR.)

6.4-1 Design an equiangular spiral antenna for operation over the entire UHF TV broadcast band (use 450 to 900 MHz).

6.4-2 *Construction project.* Construct the equiangular spiral antenna of the previous problem using aluminum foil glued to cardboard. Test its performance with a receiver (perhaps a television).

6.5-1 Design a self-complementary log-periodic toothed planar antenna for operation from 400 MHz to 2 GHz with a half-power beamwidth of 70° .

6.5-2 A log-periodic dipole array is to be designed to cover the frequency range 84 to 200 MHz and have 9-dB gain. Give the required element lengths and spacings for optimal design.

6.5-3 Evaluate the dipole lengths and spacings for the LPDA of Example 6-3.

6.5-4 Design an LPDA to operate over the UHF TV broadcast band with 10-dB gain. Add one extra element to each end over that required by (6-71).

7

MOMENT METHODS

Thus far we have studied a variety of antenna configurations, but for the most part we have assumed either that the current distribution was uniform (e.g., the ideal dipole) or that it was sinusoidal. It was then a relatively straight-forward procedure to obtain the near-zone and far-zone fields created by the current.

In this chapter we wish to eliminate the need for assuming the form of the current distribution. Naturally, this greatly expands the number of antenna configurations which we can investigate. Indeed, we find that we are able to study, for example, wire antennas of almost arbitrary configuration. The methods we use to do this are, therefore, very general methods capable of yielding answers whose accuracy is within the limit of experimental error. The potential price we pay for such a powerful technique lies in the effort required to write the necessary computer software and the time required for computer execution. Fortunately, for many problems efficient computer software is readily available and it is not necessary to write software from "scratch."

The general method we employ in this chapter is the *method of moments*. The method of moments is a procedure for reducing an integral equation of the form

$$\int I(z')K(z, z') dz' = -E^i(z) \quad (7-1)$$

to a system of simultaneous linear algebraic equations in terms of the unknown current $I(z')$. Then, as we have seen in the previous chapters, once the current is known, it is a fairly straightforward procedure to determine the radiation pattern and impedance.

Electromagnetic radiation problems can always be expressed as an integral equation of the general form in (7-1) with an inhomogeneous source term on the right and the unknown within the integral. However, it was not until the availability of modern high-speed digital computers in the mid 1960s that it was feasible to solve most such equations. Since that time a large amount of effort has been expended toward the understanding of the various numerical procedures involved and the development of computer software [2-5].

In this chapter we will set forth the basic principles involved in solving integral equations via the method of moments and will demonstrate the procedure with several examples. The serious student is encouraged to write a simple computer program using the basic principles described herein, such as that suggested by Prob. 7.2-1.

7.1 POCKLINGTON'S INTEGRAL EQUATION

One of the common integral equations that arises in the treatment of wire antennas or wire scatterers is that derived by Pocklington in 1897 which enabled him to show that on thin wires the current distribution is approximately sinusoidal and propagates with nearly the velocity of light. To derive this equation let us consider the situation in Fig. 7-1 where we have a wire of conductivity σ surrounded by free space (μ_0, ϵ_0). Since the wire radius is taken to be much less

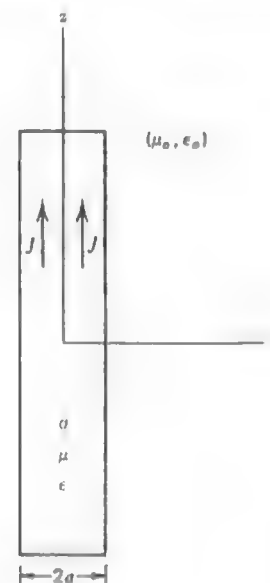


Figure 7-1 Wire of conductivity σ in free space.

than the wavelength, we may assume only z -directed currents are present. From the Lorentz gauge condition in (1-44) we may write

$$\frac{\partial A_z}{\partial z} = -j\omega\epsilon_0\Phi \quad (7-2)$$

where Φ is the scalar potential and A_z is the z -component of the magnetic vector potential. Using (1-39)

$$\mathbf{E} = -j\omega\mu_0\mathbf{A} - \nabla\Phi \quad (7-3)$$

we may write for the situation in Fig. 7-1 the scalar equation

$$E_z = -j\omega\mu_0 A_z - \frac{\partial\Phi}{\partial z} \quad (7-4)$$

Taking the derivative of (7-2) and substituting into (7-4) we obtain

$$E_z = \frac{1}{j\omega\epsilon_0} \left(\frac{\partial^2 A_z}{\partial z^2} + \beta^2 A_z \right) \quad (7-5)$$

If we consider a z -directed current element $J dv'$

$$dE_z = \frac{1}{j\omega\epsilon_0} \left[\frac{\partial^2 \psi(z, z')}{\partial z^2} + \beta^2 \psi(z, z') \right] J dv' \quad (7-6)$$

where $\psi(z, z')$ is the free space Green's function given in (1-54) as

$$\psi(z, z') = \frac{e^{-j\beta R}}{4\pi R} \quad (7-7)$$

where R is the distance between the observation point (x, y, z) and the source point (x', y', z') or

$$R = \sqrt{(x - x')^2 + (y - y')^2 + (z - z')^2} \quad (7-8)$$

The total contribution to the electric field is the integral over the wire volume

$$E_z = \frac{1}{j\omega\epsilon_0} \iiint \left[\frac{\partial^2 \psi(z, z')}{\partial z^2} + \beta^2 \psi(z, z') \right] J dv' \quad (7-9)$$

We only need consider a volume distribution of current density if the wire is not of sufficiently high conductivity. If we assume the conductivity to be infinite, then the current is confined to the wire surface and (7-9) reduces to

$$E_z = \frac{1}{j\omega\epsilon_0} \oint_c \int_{-L/2}^{L/2} \left[\frac{\partial^2 \psi(z, z')}{\partial z^2} + \beta^2 \psi(z, z') \right] J_s dz' d\phi' \quad (7-10)$$

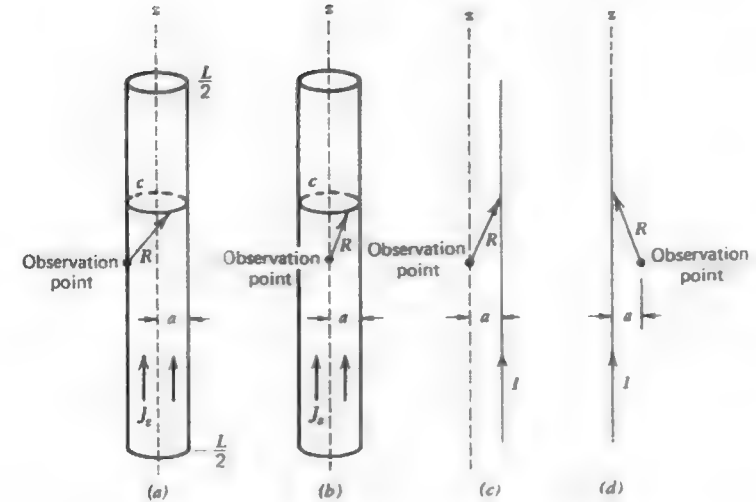


Figure 7-2 (a) Wire with surface current density J_s and observation point on the surface. (b) Wire with surface current density J_s and observation point on the wire axis. (c) Equivalent filamentary line source for the situation in (b). (d) Alternate representation of (c).

where c is the cross-sectional curve of the wire surface as shown in Fig. 7-2a. For wires of good conducting material the assumption of a surface current is approximately true and leads to no complications. If one observes the surface current distribution from a point on the wire axis as in Fig. 7-2b, then

$$R = \sqrt{(z - z')^2 + a^2} \quad (7-11)$$

Since $a \ll \lambda$ and we have assumed the current distribution to be uniform with respect to ϕ' , we may reduce (7-10) to a line integral of current. Thus,

$$E_z = \frac{1}{j\omega\epsilon_0} \int_{-L/2}^{L/2} \left[\frac{\partial^2 \psi(z, z')}{\partial z^2} + \beta^2 \psi(z, z') \right] I(z') dz' \quad (7-12)$$

We note that the equivalent filamentary line source is located a radial distance a from the observation point as in Fig. 7-2c and 7-2d and that we have not assumed the wire to be infinitely thin as was the case for dipoles studied in Chapters 2 and 5.

In accordance with the surface equivalence principle [6] of Section 8.1, we can denote the quantity E_z in (7-12) as the scattered field E_z^s . That is E_z^s is the field radiated in free space by the equivalent current $I(z')$. The other field present is the

incident or impressed field E_z^i . At the surface of the perfectly conducting wire and also interior to the wire, the sum of the scattered field and the incident field must be zero. Hence, $E_z^s = -E_z^i$, and we may write (7-12) as

$$\frac{1}{j\omega\epsilon_0} \int_{-L/2}^{L/2} I(z') \left[\frac{\partial^2 \psi(z, z')}{\partial z'^2} + \beta^2 \psi(z, z') \right] dz' = -E_z^i(z) \quad (7-13)$$

which is the type derived by Pocklington and is of the general form discussed at the beginning of this chapter in (7-1).

Equation (7-13) is known as an integral equation of the first kind because the unknown $I(z')$ appears only under the integral. In the following section we will illustrate how an integral equation such as this may be solved numerically and point out how the procedure is analogous to Kirchhoff's network equations as noted by Schelkunoff [1] many years ago.

7.2 INTEGRAL EQUATIONS AND KIRCHHOFF'S NETWORK EQUATIONS

One purpose of this section is to show the resemblance between integral equations of the type given in (7-13) and Kirchhoff's network equations

$$\sum_{n=1}^N Z_{mn} I_n = V_m, \quad m = 1, 2, 3, \dots, N. \quad (7-14)$$

Thus, we will solve the integral equation numerically by writing N equations in N unknowns just as we would do if we were solving an N mesh or N node circuit problem.

For convenience, let us write (7-13) in the form

$$\int_{-L/2}^{L/2} I(z') K(z, z') dz' = -E_z^i(z). \quad (7-15)$$

Let us assume that the current is approximated by a series of expansion functions F_n such that

$$I(z') = \sum_{n=1}^N I_n F_n(z') \quad (7-16)$$

where the I_n 's are complex expansion coefficients. To keep the discussion as simple as possible, we will assume the expansion functions are a set of orthogonal pulse functions given by

$$F_n(z') = \begin{cases} 1 & \text{for } z' \text{ in } \Delta z'_n \\ 0 & \text{otherwise} \end{cases} \quad (7-17)$$

The expansion in terms of pulse functions is a "staircase" approximation to the current distribution on the wire, where the wire is divided into N segments of length $\Delta z'_n$.

Substituting (7-16) into (7-15) we obtain

$$\int_{-L/2}^{L/2} \sum_{n=1}^N I_n F_n(z') K(z_m, z') dz' \approx -E_z^i(z_m) \quad (7-18)$$

where the subscript m on z_m indicates the integral equation is being enforced at segment m . Note that the left side is only approximately equal to the right side because we have approximated the actual current distribution with an approximate distribution. Using (7-17) in (7-18) enables us to write

$$\sum_{n=1}^N I_n \int_{\Delta z'_n} K(z_m, z') dz' \approx -E_z^i(z_m). \quad (7-19)$$

For convenience, we let

$$f(z_m, z'_n) = \int_{\Delta z'_n} K(z_m, z') dz'. \quad (7-20)$$

Then (7-16) and (7-17) in (7-15) yield

$$\begin{aligned} \int_{-L/2}^{L/2} I(z') K(z_m, z') dz' &\approx I_1 f(z_m, z'_1) \\ &+ I_2 f(z_m, z'_2) + \dots + I_n f(z_m, z'_n) + \dots \\ &+ I_N f(z_m, z'_N) \approx -E_z^i(z_m) \end{aligned} \quad (7-21)$$

as illustrated in Fig. 7-3. A physical interpretation of this equation is as follows. The wire has been divided up into N segments each of length $\Delta z'_n = \Delta z'$ with the current being an unknown constant over each segment. At the center of the m^{th}

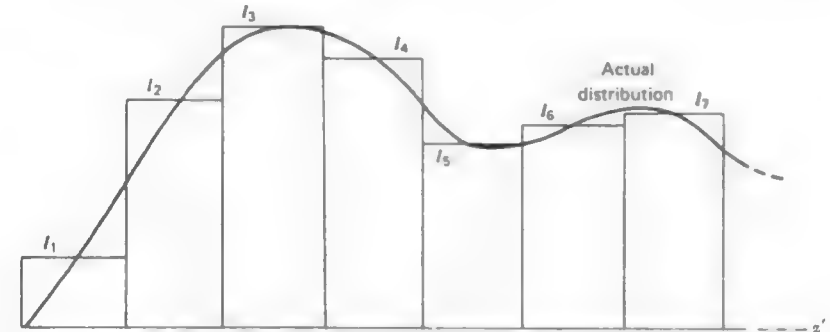


Figure 7-3 "Staircase" approximation to an actual current distribution.

segment, the sum of the scattered fields from all N segments is set equal to the negative of the incident field at the point z_m . The incident field is a known field arising from either a source located on the wire (transmitting case) or from a source located at a large distance (receiving case or radar scattering case). As we might surmise, if we need a more accurate representation of $I(z')$, then shorter segments (and a larger N) may be used. More will be said about this later.

Equation (7-21) leads to

$$\sum_{n=1}^N Z_{mn} I_n = V_m \quad (7-22)$$

where in this example situation

$$Z_{mn} = f(z_m, z'_n) \quad (7-23)$$

and

$$V_m = -E_z^i(z_m). \quad (7-24)$$

Note that we have achieved our goal of reducing the electromagnetic problem to (7-22) which is identical to the network formulation of (7-14). It should be mentioned, however, that in network problems we know Z_{mn} at the start, whereas in electromagnetic problems it is necessary to calculate Z_{mn} as we have shown in this elementary example.

So far we have only generated one equation in N unknowns. We need $N-1$ additional independent equations so that we can solve for the N unknowns. To obtain these additional equations, we choose a different z_m for each equation. That is, we enforce the integral equation at N points on the axis of the wire. The process of doing this is called *point-matching*. It is a special case of the more general method of moments.

Point-matching at N points results in the following system of equations

$$\begin{aligned} I_1 f(z_1, z'_1) + I_2 f(z_1, z'_2) + \cdots + I_N f(z_1, z'_N) &= -E_z^i(z_1) \\ I_1 f(z_2, z'_1) + I_2 f(z_2, z'_2) + \cdots + I_N f(z_2, z'_N) &= -E_z^i(z_2) \\ \vdots &\vdots \\ I_1 f(z_N, z'_1) + I_2 f(z_N, z'_2) + \cdots + I_N f(z_N, z'_N) &= -E_z^i(z_N) \end{aligned} \quad (7-25)$$

which can be written in matrix form as

$$\begin{bmatrix} f(z_1, z'_1) & f(z_1, z'_2) & \cdots & f(z_1, z'_N) \\ f(z_2, z'_1) & f(z_2, z'_2) & \cdots & f(z_2, z'_N) \\ \vdots & \vdots & \ddots & \vdots \\ f(z_N, z'_1) & f(z_N, z'_2) & \cdots & f(z_N, z'_N) \end{bmatrix} \begin{bmatrix} I_1 \\ I_2 \\ \vdots \\ I_N \end{bmatrix} = \begin{bmatrix} -E_z^i(z_1) \\ -E_z^i(z_2) \\ \vdots \\ -E_z^i(z_N) \end{bmatrix} \quad (7-26)$$

or in the compact notation as

$$[Z_{mn}][I_n] = [V_m] \quad (7-27)$$

where Z_{mn} and V_m are given by (7-23) and (7-24), respectively. We refer to the first index (m) as the match point index because it is associated with the observation point at which the m^{th} equation is valid. We refer to the second index as the source point index since it is associated with the field from the n^{th} segment or n^{th} source. Because of the analogy to the network equations, the matrices $[Z_{mn}]$, $[I_n]$, and $[V_m]$ are referred to as *generalized* impedance, current and voltage matrices, respectively. But this is only an analogy and thus the units of $[Z_{mn}]$, $[I_n]$, and $[V_m]$ need not necessarily be ohms, amperes, and volts, respectively. The analogy is not restricted to collinear segments as in the example treated here, but applies to arbitrary configurations of wires as well.

We can write the solution to (7-27) symbolically as

$$[I_n] = [Z_{mn}]^{-1} [V_m]. \quad (7-28)$$

In practice, we will usually not explicitly generate $[Z_{mn}]^{-1}$, but instead solve the system of equations by one of several fairly standard matrix algorithms. Once we have found $[I_n]$, we know the current distribution in discrete form and can then proceed to determine impedance and radiation patterns or the radar cross section.

Example 7-1. Point matching on a short dipole

Let us illustrate the application of (7-26) with a simple example. Suppose we wish to calculate the input impedance of a dipole that has a length of 0.1λ and a radius of 0.005λ . For convenience we choose $N = 5$. We then obtain for $[Z_{mn}]$

$$[Z_{mn}] = 10^2 \cdot \begin{bmatrix} 679.2 \angle -90.01^\circ & 292.4 \angle 90.03^\circ & 33.01 \angle 90.27^\circ & 9.74 \angle 90.01^\circ & 4.24 \angle 92.08^\circ \\ 292.4 \angle 90.03^\circ & 679.2 \angle -90.01^\circ & 292.4 \angle 90.03^\circ & 33.01 \angle 90.27^\circ & 9.74 \angle 90.91^\circ \\ 33.01 \angle 90.27^\circ & 292.4 \angle 90.03^\circ & 679.2 \angle -90.01^\circ & 292.4 \angle 90.03^\circ & 33.01 \angle 90.27^\circ \\ 9.74 \angle 90.91^\circ & 33.01 \angle 90.27^\circ & 292.4 \angle 90.03^\circ & 679.2 \angle -90.01^\circ & 292.4 \angle 90.03^\circ \\ 4.24 \angle 92.08^\circ & 9.74 \angle 90.91^\circ & 33.01 \angle 90.27^\circ & 292.4 \angle 90.03^\circ & 679.2 \angle -90.01^\circ \end{bmatrix}$$

For a 1-V excitation at the center of the short dipole, the following voltage matrix $[V_m]$ would be obtained using the frill source discussed in Section 7.7,

$$[V_m] = \begin{bmatrix} 0.502 \angle -179.69^\circ \\ 3.248 \angle -179.95^\circ \\ 70.55 \angle -179.99^\circ \\ 3.248 \angle -179.95^\circ \\ 0.502 \angle -179.69^\circ \end{bmatrix}$$

Solving (7-28) for $[I_n]$ yields

$$[I_n] = 10^{-3} \cdot \begin{bmatrix} 0.81 \angle 89.54^\circ \\ 1.54 \angle 89.64^\circ \\ 2.44 \angle 89.75^\circ \\ 1.54 \angle 89.64^\circ \\ 0.81 \angle 89.54^\circ \end{bmatrix}$$

We note that the current distribution decreases from the center toward the ends as expected. The input impedance may be found from $Z_{in} = V_{in}/I_{in} = 1.0/(2.44 \times 10^{-3} \angle 89.75^\circ) = 409.74 \angle -89.75^\circ = 1.788 - j409.74$ ohms. Comparing with the thinner dipole in Figs. 5-5 and 5-6, we see that the input impedance of a 0.1λ long dipole also has a very small real part and a large negative reactive part. Further, the real part of 1.788 ohms compares fairly well with the approximate formula $20\pi^2(L/\lambda)^2 = 1.974$ ohms even though only five segments were used here. These results can be verified with the computer program in Appendix G.7.

To summarize this section, we have obtained an elementary numerical solution to an integral equation of the form given in (7-15). This was done by successively enforcing the integral equation at N different points, as illustrated in (7-25). For mathematical convenience and simplicity, the locations of the points were chosen to be at the center of the N equal length segments into which the wire was divided. Strictly speaking, in order for the equations in (7-25) to be

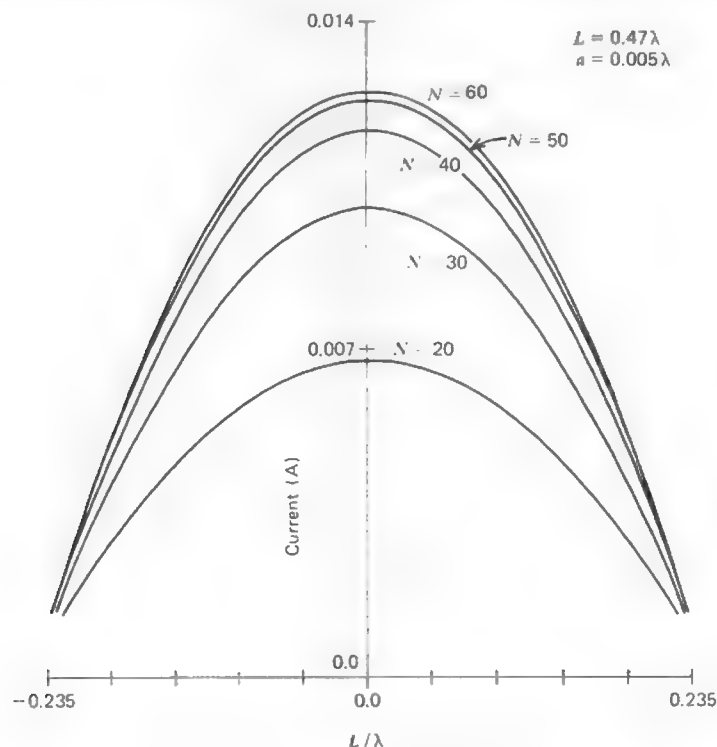


Figure 7-4 Current distributions on a half-wave dipole for various numbers of pulse expansion functions and a unit voltage excitation.

exact equalities, N must approach infinity. However, in practice we can obtain accurate solutions for the current distribution by allowing N to be sufficiently large. This is illustrated in Fig. 7-4 which shows the current distribution on a half-wave dipole for several values of N , and in Fig. 7-5 which shows the corresponding input impedance for various values of N . In both instances, it is apparent that for N sufficiently large, but finite, the solution has converged to a final or stable result. It should be emphasized that N cannot be made arbitrarily large without encountering a numerically unstable result in many instances. Thus, a curve such as those in Fig. 7-5 is well worth the effort since it clearly shows the convergence behavior of the solution. A comparison with experimental data is shown in Fig. 7-6.

As mentioned earlier, the point-matching procedure demonstrated in this section is a special case of the more general method of moments. In the next section we will develop a general moment method procedure.

7.3 WEIGHTED RESIDUALS AND THE MOMENT METHOD

Our objective in this section is to derive a moment method procedure more general than the point-matching method of the previous section. We will accomplish this by using an approach known as the method of weighted residuals [7].

Consider the straight wire example of the previous section. Let us define the residual R to be the sum of the tangential components of the scattered and incident fields

$$R = E_{tan}^s + E_{tan}^i. \quad (7-29)$$

Clearly we wish the residual to be zero and thereby satisfy the boundary condition. In our example with pulse expansion functions the residual is found from (7-19) to be

$$R(z) = \sum_{n=1}^N I_n f(z, z'_n) + E_z(z). \quad (7-30)$$

Stated in terms of the electric field boundary condition, the residual is the sum of the tangential components of the scattered and incident fields at the wire surface. Equation (7-30) when evaluated for $z = z_m$ gives the residual at the m th match point where, of course, the residual must be zero since the solution for the I_n 's was obtained subject to the electric field boundary condition at the N matching points. However, at points other than the match points, the total tangential electric field will not generally be zero as Fig. 7-7 indicates. Therefore the residual for $z \neq z_m$, $m = 1, 2, 3, \dots, N$, will not be zero either. Physically we can view the point-matching procedure as a relaxation of the boundary condition such that it is only satisfied at specified points. In between those points we can

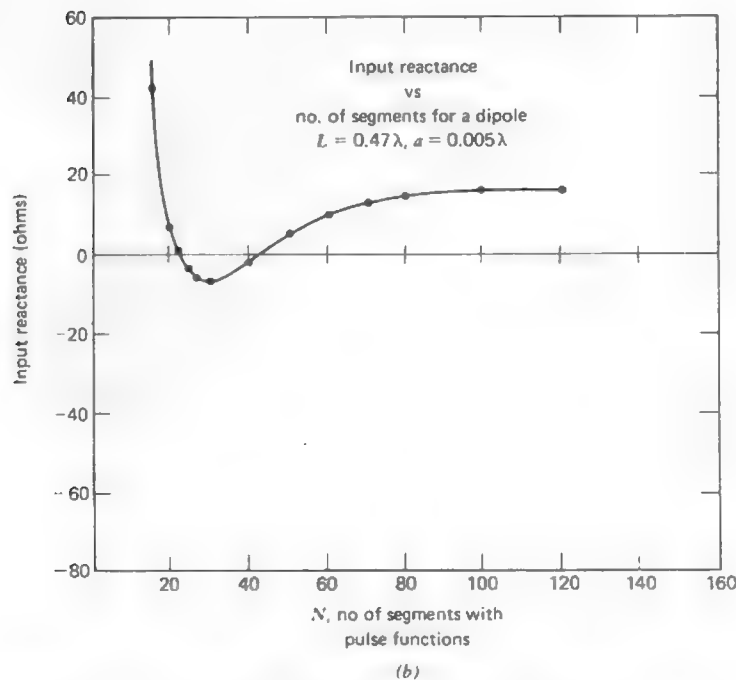
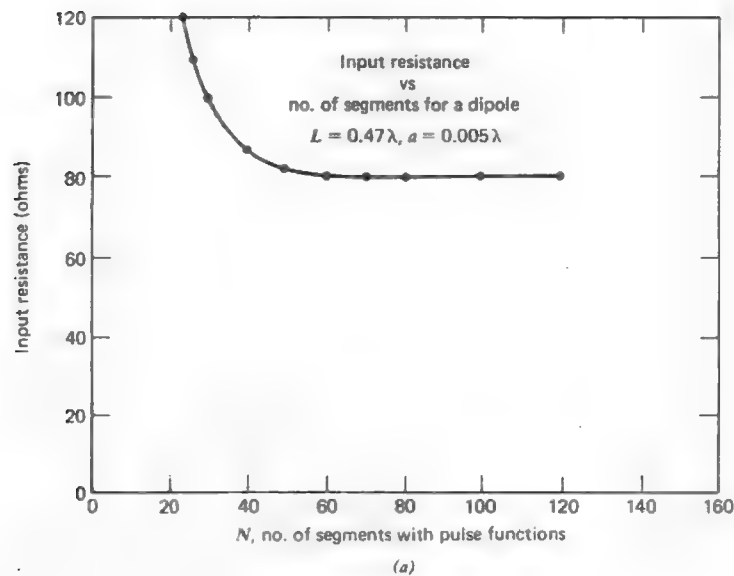


Figure 7-5 Curve showing convergence of input impedance as the number of pulse functions is increased. (a) Input resistance. (b) Input reactance.

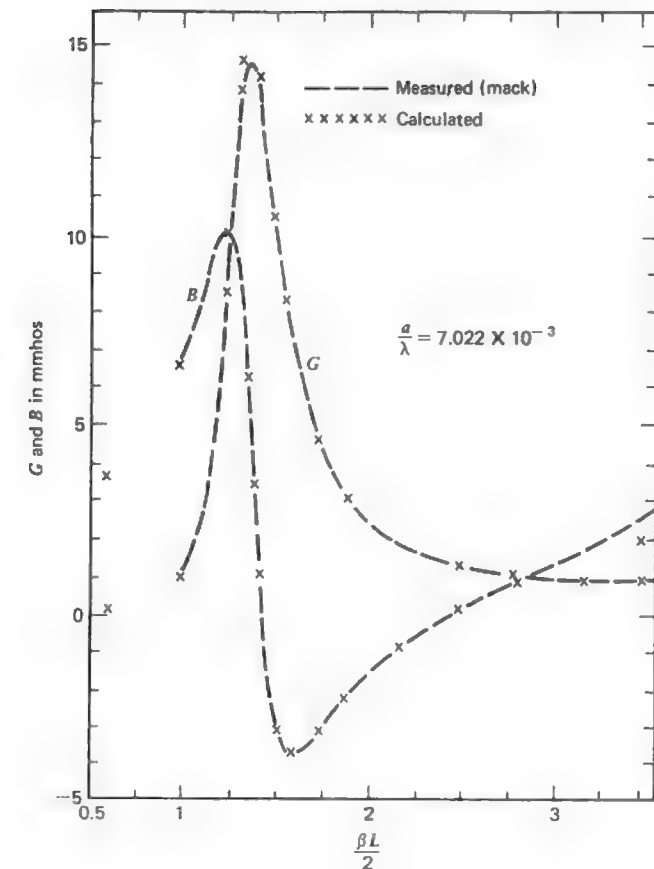


Figure 7-6 Comparison of measured dipole admittance with data calculated using pulse functions ($N = 100$).

only hope that the boundary condition is not so badly violated that the solution is rendered useless. Thus, it is not surprising that as N is increased (within limits) the solution tends to improve as we saw in Figs. 7-4 and 7-5.

In the method of weighted residuals the I_n 's are found such that the residual is forced to zero in an average sense. So, in the wire problem of Fig. 7-1 the weighted integrals of the residual are set to zero as follows.

$$\int W_m(z)R(z) dz = 0, \quad m = 1, 2, 3, \dots, N \quad (7-31)$$

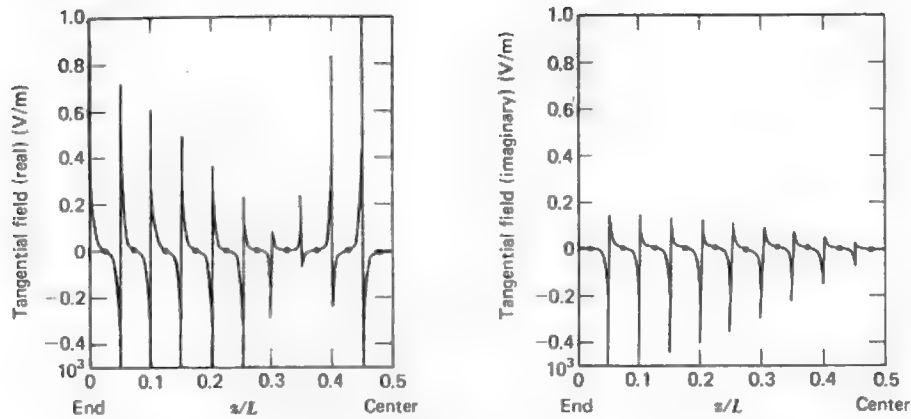


Figure 7-7 Normalized tangential electric field along one-half of a center-fed dipole with pulse expansion functions and delta weighting functions (courtesy of E. K. Miller). Dots indicate match point locations.

where $W_m(z)$ is called a *weighting* or *testing* function. Substituting (7-30) into (7-31) gives

$$\int_{-L/2}^{L/2} W_m(z) \sum_{n=1}^N I_n f(z, z'_n) dz + \int_{-L/2}^{L/2} W_m(z) E_z^i(z) dz = 0, \quad (7-32)$$

$$m = 1, 2, 3, \dots, N.$$

If the weighting functions are Dirac delta functions

$$W_m(z) = \delta(z - z_m) \quad (7-33)$$

then (7-32) reduces to (7-21). If the weighting functions are the pulse functions

$$W_m(z) = \begin{cases} 1 & \text{for } z \text{ in } \Delta z_m \\ 0 & \text{otherwise} \end{cases} \quad (7-34)$$

then (7-32) becomes

$$\sum_{n=1}^N I_n \int_{\Delta z_m} f(z, z'_n) dz + \int_{\Delta z_m} E_z^i(z) dz = 0, \quad (7-35)$$

$$m = 1, 2, 3, \dots, N.$$

The current obtained from solving (7-35) will not necessarily be such that the sum of the scattered and incident fields (i.e., the residual) is zero everywhere along the surface of the wire, but the average over the wire will tend to be zero, presumably giving a more accurate current distribution for a given N than when

the weight functions are delta functions. Actually this may or may not be the case depending on the particular choice of expansion functions for the current and weighting (or testing) functions.

The question of how one chooses the expansion functions and weighting functions is certainly a valid one. It is, however, a question without a concise answer. But, as rules of thumb, it is desirable to choose expansion functions that closely resemble the anticipated form of the current on the wire and to use the same functions for the weighting functions as used for the expansion functions. There are exceptions to these rules including the pulse point-matching solution of Section 7.2. When the expansion function and the weight function are the same, the procedure is often referred to as *Galerkin's method* which is closely related to variational methods [7].

Example 7-2. Galerkin's method on a short dipole

We now repeat Example 7-1 but instead use pulse functions for weight functions instead of delta functions. The impedance matrix for this pulse-pulse Galerkin solution based on (7-35) is

$$[Z_{mn}] = 10^2 \cdot \begin{bmatrix} 14.4 \angle -90.01^\circ & 6.14 \angle 90.03^\circ & 0.759 \angle 90.24^\circ & 0.206 \angle 90.86^\circ & 0.087 \angle 92.02^\circ \\ 6.14 \angle 90.03^\circ & 14.4 \angle -90.01^\circ & 6.14 \angle 90.03^\circ & 0.759 \angle 90.24^\circ & 0.206 \angle 90.86^\circ \\ 0.759 \angle 90.24^\circ & 6.14 \angle 90.03^\circ & 14.4 \angle -90.01^\circ & 6.14 \angle 90.03^\circ & 0.759 \angle 90.24^\circ \\ 0.206 \angle 90.86^\circ & 0.759 \angle 90.24^\circ & 6.14 \angle 90.03^\circ & 14.4 \angle -90.01^\circ & 6.14 \angle 90.03^\circ \\ 0.087 \angle 92.02^\circ & 0.206 \angle 90.86^\circ & 0.759 \angle 90.24^\circ & 6.14 \angle 90.03^\circ & 14.4 \angle -90.01^\circ \end{bmatrix}$$

The voltage matrix is

$$[V_m] = \begin{bmatrix} 0.010 \angle -179.72^\circ \\ 0.087 \angle -179.97^\circ \\ 0.795 \angle -179.99^\circ \\ 0.087 \angle -179.97^\circ \\ 0.010 \angle -179.72^\circ \end{bmatrix}$$

and the resulting solution for $[I_n]$ is

$$[I_n] = 10^{-3} \cdot \begin{bmatrix} 0.49 \angle 89.57^\circ \\ 0.91 \angle 89.66^\circ \\ 1.38 \angle 89.76^\circ \\ 0.91 \angle 89.66^\circ \\ 0.49 \angle 89.57^\circ \end{bmatrix}$$

We note that all of these three matrices are different from those in Example 7-1. Of course, we would expect $[Z_{mn}]$ and $[V_m]$ to be different because they are computed by a different process. The reason $[I_n]$ is different is solely attributable to the fact that N is only 5. As in Example 7-1, a larger value of N is required in order to obtain a converged result. The input impedance based on the above current is $Z_{in} = 3.08 - j723$ ohms, whereas the correct impedance is $Z_{in} = 2.35 - j556$ ohms based on $N = 25$.

Next, we wish to relate the quantities in the weighted residual integral to Kirchhoff's network equations, just as was done in Section 7.2. In doing so let us generalize somewhat and consider a wire as shown in Fig. 7-8. In this case the residual may be written

$$R(\ell) = E_{\text{tan}}^s(\ell) + E_{\text{tan}}^i(\ell) = \sum_{n=1}^N I_n E_n^i(\ell) + E_{\text{tan}}^i(\ell) \quad (7-36)$$

and the weighted residual as

$$\int_{\text{along wire}} W_m(\ell) \cdot R(\ell) d\ell = 0 \quad (7-37)$$

so that we have

$$\int_{-\ell_m/2}^{\ell_m/2} W_m(\ell) \cdot E^s(\ell) d\ell + \int_{-\ell_m/2}^{\ell_m/2} W_m(\ell) \cdot E^i(\ell) d\ell = 0, \quad (7-38)$$

$$m = 1, 2, 3, \dots, N.$$

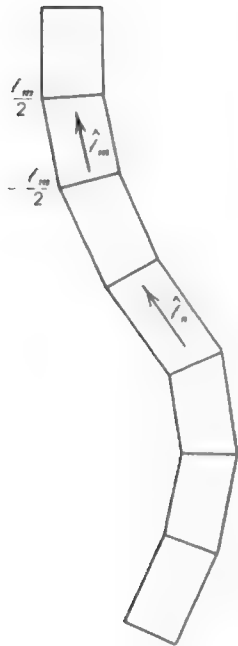


Figure 7-8 Segmented curved wire.

This equation can be viewed in the form of (7-14) and if we denote the scattered field from the n^{th} expansion function of the current by $E_n^s(\ell)$, then we may write for the general m^{th} element in the generalized impedance matrix

$$Z_{mn} = \int_{-\ell_m/2}^{\ell_m/2} W_m(\ell) \cdot E_n^s(\ell) d\ell \quad (7-39)$$

and for the m^{th} generalized voltage matrix element

$$V_m = - \int_{-\ell_m/2}^{\ell_m/2} W_m(\ell) \cdot E^i(\ell) d\ell \quad (7-40)$$

where $W_m(\ell)$ is the m^{th} testing function taken to be located interior to the wire as suggested in Fig. 7-8. Strictly speaking, the test function should be located at the wire surface (see Fig. 7-2a) in which case (7-39) and (7-40) would be double integrals over the surface. In placing the test function on the axis we are in a sense modifying the electric field boundary condition for the sake of mathematical simplification. In doing this, experience has shown that we are restricted to wires for which the radius is less than about 0.01λ . This is sufficient for most wire antenna or scattering problems. For thicker wires, a more exact formulation is available [8].

The process of expanding the unknown current $I(\ell')$ in a series of expansion functions and then generating N equations in N unknowns using the weighted residual integral of (7-37) is more commonly referred to in the electromagnetics literature as the method of moments [1, 3-5]. The method of moments is, as we have seen in this section, equivalent to the method of weighted residuals. If the testing or weighting functions are delta functions, then the specific moment method procedure is known as *point-matching* which is also known as *collocation*. This was the procedure used to obtain the system of equations in (7-25). If both the test function and the expansion function are the same, then the specific moment method procedure is known as *Galerkin's method*. A pulse-pulse Galerkin formulation was used in Example 7-2. There are functions other than the pulse function which have been shown to be useful. One of the most useful functions for wire geometries in empty space is the piecewise sinusoid. In Section 7.5 we will use the piecewise sinusoid in a Galerkin formulation for the wire. In the next section we wish to discuss the concept of reaction which is yet another way of physically interpreting the method of moments.

7.4 REACTION INTEGRAL EQUATION

In 1954 Rumsey introduced a physical observable (e.g., mass, length, charge, etc.) called *reaction* which permitted a general approach to boundary value problems in electromagnetic theory [9]. His approach resulted in the formulation of the

reaction integral equation. Equation (7-38) is really a special form of the reaction integral equation which applies to wire geometries. A rigorous derivation of the reaction integral equation may be done using only principles of electromagnetic theory. The derivation is somewhat difficult to follow and so we will obtain it by inductive reasoning here, having derived (7-38) in the previous section by the relatively straightforward weighted residual approach.

Reaction is basically "a measure of the coupling" between one source and another. Thus, if we view the test function (weight function) as a *test source*, then the impedance matrix elements given by (7-39) may be taken as a calculation of the coupling between the m^{th} test source and the scattered field from the n^{th} expansion function or *actual source*. Similarly, the m^{th} voltage matrix element in (7-40) may be interpreted as the coupling between the m^{th} test source and the incident field. In talking about (7-40) for instance, we might say that we are "reacting" the m^{th} test source with the incident field, or in the case of (7-39) that we are "reacting" the electric field from the n^{th} actual source with the current on the m^{th} test source.

We obtained (7-38) for a wire. The method of moments or the method of weighted residuals applies to geometries other than just wire geometries as indicated in Fig. 7-9. Consider the equivalent situation in Fig. 7-10. Let $(\mathbf{J}_m, \mathbf{M}_m)$ be the surface current densities of a test source and let $(\mathbf{E}_m, \mathbf{H}_m)$ be the fields from the test source. The currents on the conducting body are both replaced by equivalent surface currents $(\mathbf{J}^s, \mathbf{M}^s)$ radiating the fields $(\mathbf{E}^s, \mathbf{H}^s)$ in free space. The generalization of (7-38) then becomes

$$\iint_S (\mathbf{J}_m \cdot \mathbf{E}^s - \mathbf{M}_m \cdot \mathbf{H}^s) ds + \iint_S (\mathbf{J}_m \cdot \mathbf{E}^i - \mathbf{M}_m \cdot \mathbf{H}^i) ds = 0 \quad (7-41)$$

$$m = 1, 2, 3, \dots, N.$$

The minus sign associated with \mathbf{M}_m can be justified by referring to the reciprocity field theorems in Sections 1.7. The physical interpretation of (7-41) is that we wish to have zero reaction (i.e., zero coupling) between the test source and the sum of the incident and scattered fields. Clearly, this is equivalent to the condi-

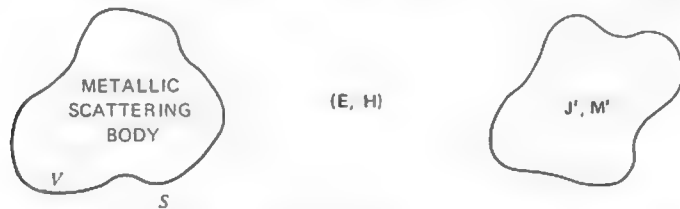


Figure 7-9 Source current densities \mathbf{J}' and \mathbf{M}' acting in the presence of a metallic scattering body bounded by surface S create fields (\mathbf{E}, \mathbf{H}) exterior to S .

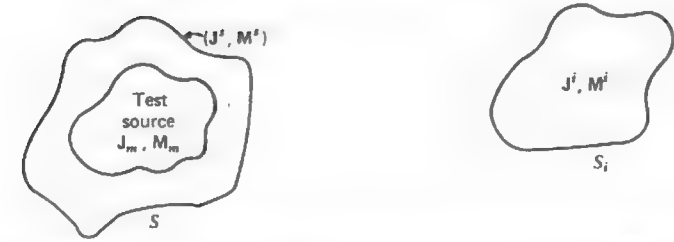


Figure 7-10 Test source interior to surface S with equivalent currents $(\mathbf{J}^s, \mathbf{M}^s)$ in free space.

tion stated by (7-31). Nevertheless, the alternative physical interpretation offered by (7-41) and the reaction concept is a useful one and the student will find it used in the literature.

If we denote the fields from the n^{th} expansion function of the actual current by $(\mathbf{E}_n^s, \mathbf{H}_n^s)$, the sum of the N fields being $(\mathbf{E}^s, \mathbf{H}^s)$, then we may write for the general mn^{th} element in the generalized impedance matrix

$$Z_{mn} = \iint_S (\mathbf{J}_m \cdot \mathbf{E}_n^s - \mathbf{M}_m \cdot \mathbf{H}_n^s) ds. \quad (7-42)$$

Similarly, we may write the general m^{th} element in the voltage matrix

$$V_m = - \iint_S (\mathbf{J}_m \cdot \mathbf{E}^i - \mathbf{M}_m \cdot \mathbf{H}^i) ds. \quad (7-43)$$

The incident field $(\mathbf{E}^i, \mathbf{H}^i)$, which originates from the impressed currents \mathbf{J}^i in Fig. 7-9, may be the field from a source located on S (antenna situation) or from a source located at a great distance from S (radar scattering situation).

The general relationships in (7-42) and (7-43) will be useful in later sections for both wire and nonwire geometries. In the next section we will need to only consider the specialized forms of (7-42) and (7-43) which appear in (7-39) and (7-40), respectively.

7.5 PIECEWISE SINUSOIDAL GALERKIN METHOD

One of the most useful functions in moment method solutions of thin wire problems is the piecewise sinusoid shown in Fig. 7-11a. It may be expressed mathematically for z -directed segments by

$$F_n(z) = \hat{z} \frac{\sin \beta(z - z_{n-1})}{\sin \beta(z_n - z_{n-1})} \quad z_{n-1} \leq z < z_n \quad (7-44a)$$

$$F_n(z) = \hat{z} \frac{\sin \beta(z_{n+1} - z)}{\sin \beta(z_{n+1} - z_n)} \quad z_n \leq z < z_{n+1}. \quad (7-44b)$$

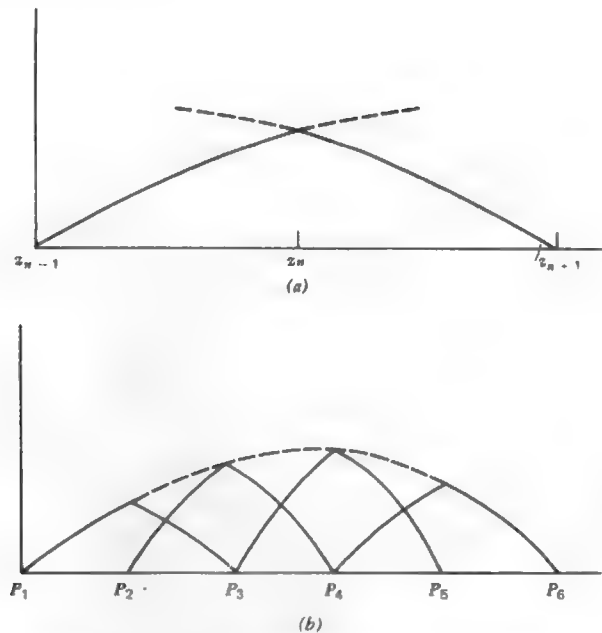


Figure 7-11 (a) Piecewise sinusoidal expansion function. (b) Set of overlapping piecewise sinusoidal expansion functions.

An example of a piecewise sinusoidal approximation to a current distribution is given in Fig. 7-11b. Note that each piecewise sinusoidal function spans two connected segments and that each segment contains two piecewise sinusoidal functions except those that have an unconnected end point (i.e., P_1 and P_6).

Experience has shown that the use of piecewise sinusoidal testing (weighting) functions with piecewise sinusoidal expansion functions leads to a procedure that is numerically efficient and highly accurate. Since both the expansion function and testing function are the same, it is a Galerkin method. It is possible to use the pulse function for both the testing function and the expansion function. However, experience has shown that the improvement of the pulse-pulse Galerkin formulation over the pulse point-matching procedure is usually rather small and not worth the added numerical computation involved. On the other hand, the computational efficiency of the piecewise sinusoidal Galerkin formulation over the pulse Galerkin method is very substantial. This is demonstrated in Fig. 7-12 which shows the rate of convergence for a dipole of this same dimension used in Fig. 7-5. We note that almost 10 times fewer segments are required

for the piecewise sinusoidal (PWS) expansion function as for the pulse expansion function. For thinner wires, the convergence of the piecewise sinusoid is even faster since the approximation of Fig. 7-2b is less significant [10].

7.5.1 Two-Segment Solution

To illustrate both the use of the reaction integral equation and the piecewise sinusoidal function, let us consider first the problem of a dipole divided into two segments. This means there will be only one piecewise sinusoidal function in the expansion of the surface current density J in Fig. 7-13a and only one test source which will also have a piecewise sinusoidal current $I_1(z)$ given by

$$I_1(z) = \frac{\sin \beta(h - |z|)}{\sin \beta h} \quad (7-45)$$

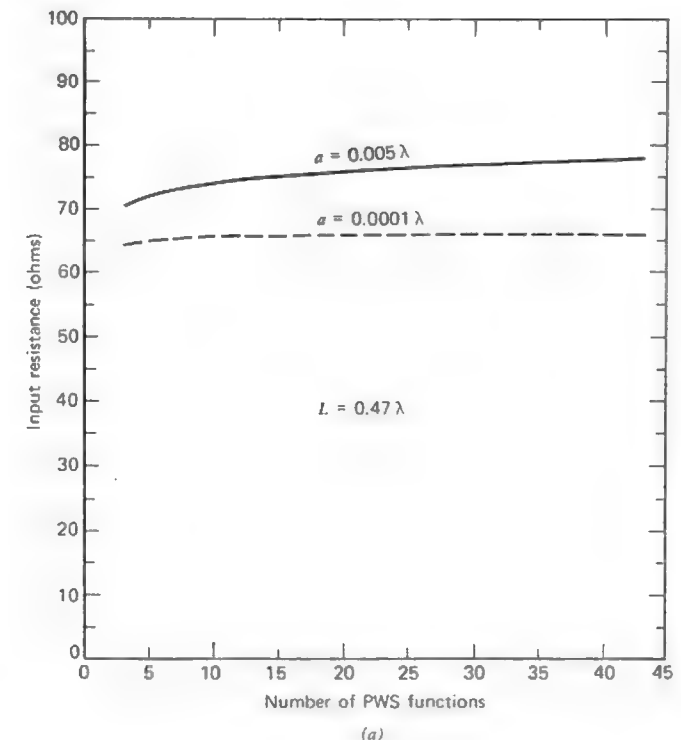


Figure 7-12 (a) Input resistance convergence rate for the piecewise sinusoid for two different wire radii.

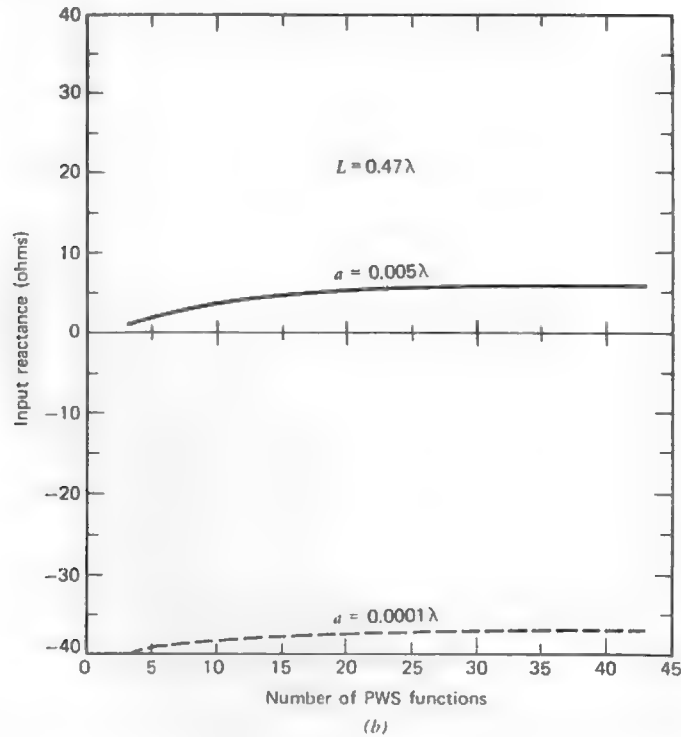


Figure 7-12 (b) Input reactance convergence rate for the piecewise sinusoid for two different wire radii.

where h is the dipole half-length and z is measured from the center. The current on the equivalent filamentary source in Fig. 7-13b is given by the classical formula

$$I(z) = I_1 \frac{\sin \beta(h - |z|)}{\sin \beta h} \quad (7-46)$$

What we wish to do is to determine the terminal current I_1 excited by a given voltage generator of voltage V_1 . To do this we employ (7-39) where \mathbf{E}_1 is the field from the expansion function $I(z)$. Thus, $ZI_1 = V_1$ where

$$Z = \int_{-h}^h \frac{\sin \beta(h - |z|)}{\sin \beta h} \hat{\mathbf{z}} \cdot \mathbf{E}_1^s dz \quad (7-47)$$

and the solution for I_1 follows. We note in passing that this two-segment solution coincides with the well-known induced emf theory.

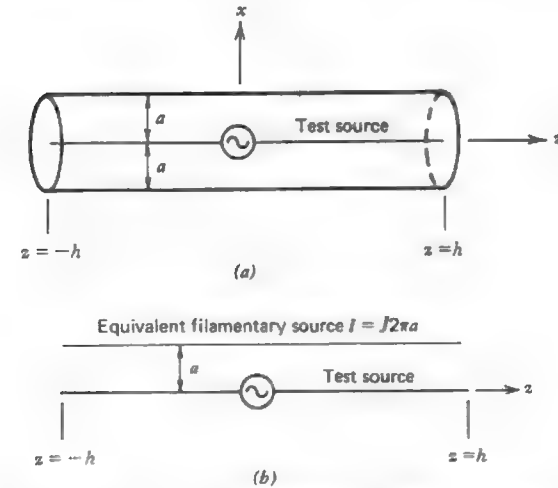


Figure 7-13 (a) Two-segment piecewise sinusoidal problem with the weighting function (test source) located on the wire axis. (b) Current on the wire surface replaced by equivalent filamentary source.

The two segment solution is obviously useful only for a limited range of antenna lengths. Therefore, let us consider next the four-segment solution for a single linear antenna. The extension to the N segment solution for a single antenna or for coupled antennas will then be obvious.

7.5.2 Four-Segment Solution

Consider the symmetrical dipole of Fig. 7-14a divided into four segments. The complex coefficients I_1 , I_2 , and I_3 represent samples of the current function $I(z)$ at the junctions of the various segments.

$$I_1 = I(0) \quad (7-48a)$$

$$I_2 = I\left(\frac{h}{2}\right) = I\left(-\frac{h}{2}\right) = I_3 \quad (7-48b)$$

The current is assumed to vanish at the ends of the antenna.

$$I(h) = 0 = I(-h). \quad (7-49)$$

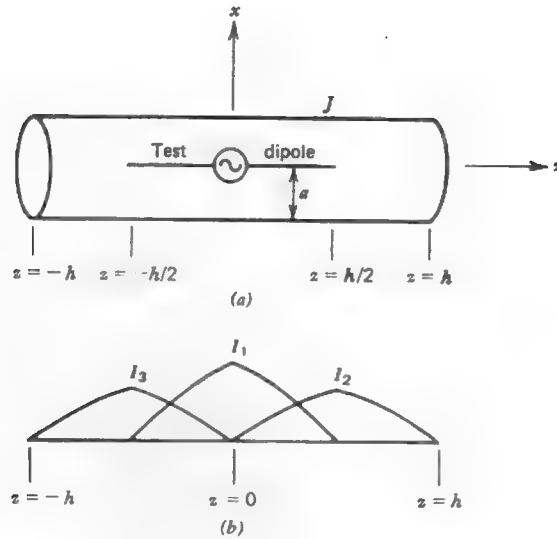


Figure 7-14 (a) Four-segment piecewise sinusoidal problem with weight function (test source) located on the wire axis. (b) Three overlapping piecewise sinusoids.

Thus, the current on the equivalent filamentary source is

$$I(z) = I_1 \frac{\sin \beta(h/2 - z)}{\sin(\beta h/2)} + I_2 \frac{\sin \beta z}{\sin(\beta h/2)}, \quad 0 \leq z \leq \frac{h}{2} \quad (7-50a)$$

$$I(z) = I_2 \frac{\sin \beta(h - z)}{\sin(\beta h/2)}, \quad \frac{h}{2} \leq z \leq h \quad (7-50b)$$

$$I(z) = I_1 \frac{\sin \beta(h/2 - |z|)}{\sin(\beta h/2)} + I_3 \frac{\sin \beta |z|}{\sin(\beta h/2)}, \quad -\frac{h}{2} \leq z \leq 0 \quad (7-50c)$$

$$I(z) = I_3 \frac{\sin \beta(h - |z|)}{\sin(\beta h/2)}, \quad -h \leq z \leq -\frac{h}{2} \quad (7-50d)$$

as illustrated in Fig. 7-14b. The objective is to determine I_1 , I_2 , and I_3 . This is accomplished by reacting each of the three test sources with the three filamentary sources in a manner similar to (7-47), the details of which are given in

Section 7.5.3. This results in three equations in three unknowns. Since $I_2 = I_3$, we need only solve for two unknowns, and thus

$$Z_{11}I_1 + (Z_{12} + Z_{13})I_2 = V_1 \quad (7-51a)$$

$$Z_{21}I_1 + (Z_{22} + Z_{23})I_2 = 0. \quad (7-51b)$$

Z_{11} and Z_{22} represent the mutual impedance between parallel filamentary dipoles with sideways displacement a and no stagger (with respect to the z -direction). To obtain Z_{12} and Z_{21} the dipoles are in echelon with displacement a and stagger $h/2$ whereas in obtaining Z_{13} and Z_{31} the stagger is h .

7.5.3 N -Segment Solution

Next let us consider the situation of an arbitrary number of equal length (Δz_n) segments which are either coincident with the z -axis or are parallel to it. Thus, we may consider, for example, a single dipole with N segments or an array of parallel dipoles. Using (7-44) we may write for the m th impedance matrix element as

$$Z_{mn} = \int_{z_{m-1}}^{z_m} \frac{\sin \beta(z - z_{m-1})}{\sin(\beta \Delta z_m)} \hat{z} \cdot \mathbf{E}_n^s dz + \int_{z_m}^{z_{m+1}} \frac{\sin \beta(z_{m+1} - z)}{\sin(\beta \Delta z_m)} \hat{z} \cdot \mathbf{E}_n^s dz. \quad (7-52)$$

We, of course, need an expression for the field \mathbf{E}_n from the n th actual source in order to evaluate (7-52). First we note that

$$\frac{\partial \psi(z, z')}{\partial z} = -\frac{\partial \psi(z, z')}{\partial z'} \quad (7-53)$$

and

$$\frac{\partial^2 \psi(z, z')}{\partial z^2} = \frac{\partial^2 \psi(z, z')}{\partial z'^2}. \quad (7-54)$$

Next integrate the first term of (7-12) by parts twice using (7-54), substitute the result into (7-12), and use (7-53) to obtain

$$E_z^1 = \frac{j}{\omega \epsilon_0} \left[\frac{dI(z')}{dz'} \psi(z, z') + I(z') \frac{\partial \psi(z, z')}{\partial z} \right]_{z'=z_1}^{z'=z_2} + \frac{1}{j\omega \epsilon_0} \int_{z_1}^{z_2} \left[\frac{d^2 I(z')}{dz'^2} + \beta^2 I(z') \right] \psi(z, z') dz' \quad (7-55)$$

where the limits of integration are only over one segment.

When the current on the segment is piecewise sinusoidal the bracketed expression in the integrand of (7-55) vanishes. Since we are using one-half of the piecewise sinusoidal function depicted in Fig. 7-11a, the z -component of the field from the unit current on the segment extending from z_1 to z_2 , $E_z^1(\rho, z)$, is [11]

$$E_z^1(\rho, z) = \frac{j}{4\pi\epsilon_0\omega} \left[\frac{\beta \cos \beta(z' - z_1)}{\sin \beta(z_2 - z_1)} + \frac{\sin \beta(z' - z_1)}{\sin \beta(z_2 - z_1)} \frac{\partial}{\partial z} \right] \frac{e^{-j\beta r}}{r} \Big|_{z'=z_1}^{z'=z_2} \quad (7-56)$$

where

$$r = \sqrt{\rho^2 + (z - z')^2}. \quad (7-57)$$

When we consider that portion of the source from z_2 to z_3 , we obtain $E_z^2(\rho, z)$. Then the total field from both halves of one piecewise sinusoid of unit amplitude is

$$E_z = E_z^1(\rho, z) + E_z^2(\rho, z). \quad (7-58)$$

We may generalize this result for the n^{th} and $(n+1)^{\text{st}}$ segments as

$$E_z = -j30 \left[\frac{e^{-j\beta R_{n-1}}}{R_{n-1} \sin \beta(z_n - z_{n-1})} - \frac{e^{-j\beta R_n} \sin \beta(z_{n+1} - z_{n-1})}{R_n \sin \beta(z_n - z_{n-1}) \sin \beta(z_{n+1} - z_n)} + \frac{e^{-j\beta R_{n+1}}}{R_{n+1} \sin \beta(z_{n+1} - z_n)} \right]. \quad (7-59)$$

The quantities R_{n-1} , R_n , and R_{n+1} are shown in Fig. 7-15 and defined below. A similar expression for E_ρ is obtainable but is not required here since all segments are z -directed [1].

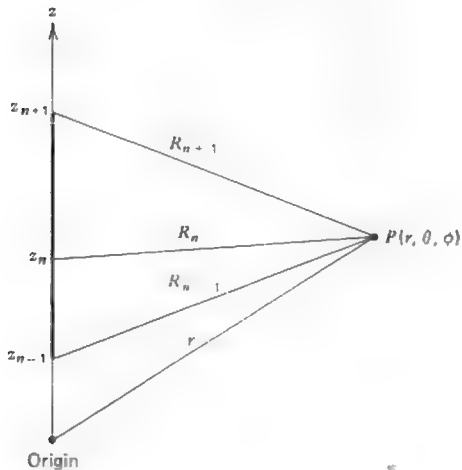


Figure 7-15 Wire segment along z -axis.

Finally, the elements of the generalized impedance matrix are given in general for z -directed segments by

$$Z_{mn} = \int_{z_m}^{z_{m+1}} \mathbf{I}_m \cdot \mathbf{E}_n^s dz = - \left[\int_{z_{m-1}}^{z_m} \frac{\sin \beta(z - z_{m-1})}{\sin(\beta \Delta z_m)} + \int_{z_m}^{z_{m+1}} \frac{\sin \beta(z_{m+1} - z)}{\sin(\beta \Delta z_m)} \right] \frac{j30}{\sin(\beta \Delta z_n)} \cdot \left[\frac{e^{-j\beta R_{n-1}}}{R_{n-1}} - 2 \cos(\beta \Delta z_n) \frac{e^{-j\beta R_n}}{R_n} + \frac{e^{-j\beta R_{n+1}}}{R_{n+1}} \right] dz \quad (7-60)$$

where

$$R_{n-1} = \sqrt{\rho^2 + (z - z_{n-1})^2}, \quad R_n = \sqrt{\rho^2 + (z - z_n)^2}, \quad (7-61)$$

$$R_{n+1} = \sqrt{\rho^2 + (z - z_{n+1})^2}$$

$$\Delta z_n = z_n - z_{n-1} = z_{n+1} - z_n, \quad \Delta z_m = z_m - z_{m-1} = z_{m+1} - z_m \quad (7-62)$$

Equation (7-60) may be evaluated without difficulty by numerical integration. However, when $\rho = a$ and a is quite small (i.e., wires of very small radius) it may be preferable to carry out the integration in the form of sine "Si" and cosine "Ci" integrals of (F-13) and (F-14). When this is done, the elements of Z_{mn} are given by $Z_{mn} = R_{mn} + jX_{mn}$ where

$$R_{mn} = \frac{15}{\sin(\beta \Delta z_m) \sin(\beta \Delta z_n)} \left[\cos \beta(z_{n-1} - z_{m-1}) \{ \text{Ci}(v_0) + \text{Ci}(u_0) - \text{Ci}(u_1) - \text{Ci}(v_1) \} + \sin \beta(z_{n-1} - z_{m-1}) \{ \text{Si}(v_0) - \text{Si}(u_0) + \text{Si}(u_1) - \text{Si}(v_1) \} + \cos \beta(z_{n+1} - z_{m-1}) \{ \text{Ci}(v_4) + \text{Ci}(u_4) - \text{Ci}(u_5) - \text{Ci}(v_5) \} + \sin \beta(z_{n+1} - z_{m-1}) \{ \text{Si}(v_4) - \text{Si}(u_4) + \text{Si}(u_5) - \text{Si}(v_5) \} - 2 \cos(\beta \Delta z_n) \cos \beta(z_n - z_{m-1}) \{ \text{Ci}(v_2) + \text{Ci}(u_2) - \text{Ci}(u_3) - \text{Ci}(v_3) \} - 2 \cos(\beta \Delta z_n) \sin \beta(z_n - z_{m-1}) \{ \text{Si}(v_2) - \text{Si}(u_2) + \text{Si}(u_3) - \text{Si}(v_3) \} + \cos \beta(z_{n-1} - z_{m+1}) \{ \text{Ci}(v_6) - \text{Ci}(v_1) + \text{Ci}(u_6) - \text{Ci}(u_1) \} + \sin \beta(z_{n-1} - z_{m+1}) \{ \text{Si}(v_6) - \text{Si}(u_6) + \text{Si}(u_1) - \text{Si}(v_1) \} + \cos \beta(z_{n+1} - z_{m+1}) \{ \text{Ci}(v_8) - \text{Ci}(v_5) - \text{Ci}(u_5) + \text{Ci}(u_8) \} + \sin \beta(z_{n+1} - z_{m+1}) \{ \text{Si}(v_8) - \text{Si}(u_8) + \text{Si}(u_5) - \text{Si}(v_5) \} - 2 \cos(\beta \Delta z_n) \cos \beta(z_n - z_{m+1}) \{ \text{Ci}(v_7) - \text{Ci}(v_3) - \text{Ci}(u_3) + \text{Ci}(u_7) \} - 2 \cos(\beta \Delta z_n) \sin \beta(z_n - z_{m+1}) \{ -\text{Si}(u_7) + \text{Si}(v_7) + \text{Si}(u_3) - \text{Si}(v_3) \} \right] \quad (7-63)$$

where

$$u_0 = \beta[\sqrt{\rho^2 + (z_{n-1} - z_{m-1})^2} + (L)(z_{m-1} - z_{n-1})] \quad (7-64a)$$

$$u_1 = \beta[\sqrt{\rho^2 + (z_{n-1} - z_m)^2} + (L)(z_m - z_{n-1})] \quad (7-64b)$$

$$u_2 = \beta[\sqrt{\rho^2 + (z_n - z_{m-1})^2} + (L)(z_{m-1} - z_n)] \quad (7-64c)$$

$$u_3 = \beta[\sqrt{\rho^2 + (z_n - z_m)^2} + (L)(z_m - z_n)] \quad (7-64d)$$

$$u_4 = \beta[\sqrt{\rho^2 + (z_{n+1} - z_{m-1})^2} + (L)(z_{m-1} - z_{n+1})] \quad (7-64e)$$

$$u_5 = \beta[\sqrt{\rho^2 + (z_{n+1} - z_m)^2} + (L)(z_m - z_{n+1})] \quad (7-64f)$$

$$u_6 = \beta[\sqrt{\rho^2 + (z_{n+1} - z_{m+1})^2} + (L)(z_{m+1} - z_{n+1})] \quad (7-64g)$$

$$u_7 = \beta[\sqrt{\rho^2 + (z_n - z_{m+1})^2} + (L)(z_{m+1} - z_n)] \quad (7-64h)$$

$$u_8 = \beta[\sqrt{\rho^2 + (z_{n+1} - z_{m+1})^2} + (L)(z_{m+1} - z_{n+1})] \quad (7-64i)$$

and $L = +1$. The v_i 's are found in similar manner as (7-64) with $L = -1$. X_{mn} can be obtained by replacing $Ci(x)$ by $-\text{Si}(x)$ and $\text{Si}(y)$ by $Ci(y)$ in the expression for R_{mn} .

The piecewise sinusoidal Galerkin method is treated in detail here because it is the best known moment method procedure for thin wire antenna and scattering problems in free space. While the mathematics of (7-63) and (7-64) may be a bit overwhelming to the student, the methods employed are those used to write general purpose computer programs given in the literature [12] and the one listed in Appendix G.8. Actually, an understanding of (7-60) is sufficient to appreciate the essential features of such programs.

The piecewise sinusoidal Galerkin method applies equally well to arbitrary configurations of wires. We have restricted our discussion here to z -directed wires for instructional convenience. The more general formulation appears in the literature [12].

7.6 CALCULATION OF ANTENNA AND SCATTERER CHARACTERISTICS

Thus far in our discussion of the method of moments we have been mainly concerned with acquiring a knowledge of some unknown current distribution. Let us now consider how we can obtain other information as well. But first, we should make one further remark about the currents derived from the solution of the matrix equation.

If pulse functions are used as the expansion functions in the point-matching technique, a knowledge of the current coefficients I_n means that the current

distribution at the match points is known "precisely," assuming, of course, that the solution has converged. In between the match points we do not know the current but, since the distance between the match points is small in terms of a wavelength, one can simply fit a curve through the current values at the match points to obtain a good approximation to the current distribution along the wire.

In the case of the piecewise-sinusoidal functions, a knowledge of the coefficients I_n again only means that the current is known at the junctions of the segments. Along the segments we can use the piecewise sinusoidal functions themselves to approximate the current distribution between segment junctions. This approximation is quite adequate except for some extremely unusual situations which need not concern us here.

Having determined the current distribution, the input or terminal current can be found by evaluating the current distribution at the antenna terminal location. In turn then the input impedance may be calculated by dividing the terminal voltage by the terminal current. The calculation of accurate impedance data is a task that is somewhat sensitive to the model used for the feed point. Two such models are discussed in the next section.

Distributive loading, which arises when a wire is not perfectly conducting, may affect the current distribution in certain situations [13]. For simplicity, consider a wire whose axis is parallel to the z -axis. When the wire has finite conductivity, we can relate the tangential electric field at the surface of the wire to the equivalent electric surface current density by the use of the surface impedance Z_s which is defined [14] as the ratio of the tangential electric field strength at the surface of a conductor to the current density which flows as a result of that tangential electric field. Thus,

$$\mathbf{E} = Z_s \mathbf{J}_s. \quad (7-65)$$

Using $\mathbf{M}_s = \mathbf{E} \times \hat{\mathbf{n}}$ and the relationship $\mathbf{J}_s = \hat{\mathbf{z}}I(z)/2\pi a$, we can write

$$\mathbf{M}_s = Z_s \mathbf{J}_s \times \hat{\mathbf{p}} = \frac{\hat{\phi} Z_s I(z)}{2\pi a} \quad (7-66)$$

Writing the reaction integral equation from (7-41) and reciprocity as

$$\iint_S (\mathbf{E}_m \cdot \mathbf{J}^s - \mathbf{H}_m \cdot \mathbf{M}^s) ds = V_m \quad (7-67)$$

and substituting (7-66) leads to

$$\int I(z) [\hat{\mathbf{z}} \cdot \mathbf{E}_m - Z_s \hat{\phi} \cdot \mathbf{H}_m] dz = V_m. \quad (7-68)$$

Note that if the wire is of perfect conductivity, the surface impedance goes to zero and (7-68) reduces to a form similar to (7-47). We can write for the generalized impedance matrix element Z'_{mn} , modified for finite conducting wires, as

$$Z'_{mn} = \int_{z_{n-1}}^{z_{n+1}} I_n(z) \hat{z} \cdot \mathbf{E}_m dz - Z_s \int_{z_{n-1}}^{z_{n+1}} I_n(z) \hat{\phi} \cdot \mathbf{H}_m dz. \quad (7-69)$$

From Ampere's law a suitable approximation for \mathbf{H}_m is

$$\hat{\phi} \cdot \mathbf{H}_m = \frac{I_m(z)}{2\pi a} \quad (7-70)$$

and thus (7-69) can be written as

$$Z'_{mn} = Z_{mn} - \frac{Z_s}{2\pi a} \int_{(m,n)} I_n(z) I_m(z) dz \quad (7-71)$$

where region (m, n) is the wire surface shared by testing function m and expansion function n . In the case of overlapping expansion functions such as the piecewise sinusoid, this region covers two intersecting segments if m and n are equal. When $m \neq n$, the shared region covers at most one wire segment. This means that distributive loading is accounted for by a modification of only the appropriate main diagonal elements and those elements adjacent to the modified main diagonal elements.

The effect of either lumped loading (considered in Section 7.9) or distributive loading is to alter the current distribution on the wire antenna or scatterer. Knowing the current distribution, the far field can be obtained by the classical methods used previously in this book. To illustrate, consider again z -directed segments with a piecewise sinusoidal expansion of the current. Let there be N expansion functions. Then, from (4-1), we have

$$E_\theta(\theta) = \frac{j\omega\mu}{4\pi r} e^{-j\beta r} \sin \theta \sum_{n=1}^N \frac{I_n}{\sin(\beta \Delta z_n)} \left[\int_{z_{n-1}}^{z_n} \sin \beta(z' - z_{n-1}) e^{j\beta z' \cos \theta} dz' + \int_{z_n}^{z_{n+1}} \sin \beta(z_{n+1} - z') e^{j\beta z' \cos \theta} dz' \right] \quad (7-72)$$

The numerical evaluation of this is most easily accomplished by changing the sine terms to exponentials, integrating the various exponentials, and then evaluating the result with the specified limits.

Once the far field is known in the direction of maximum radiation, the power gain may be determined from the general relationship

$$G(\theta, \phi) = \frac{[|E_\theta|^2 + |E_\phi|^2]r^2}{30|I_{in}|^2 R_{in}} \quad (7-73)$$

where R_{in} is the real part of the antenna input impedance. The directivity may be obtained by replacing R_{in} with R_{ri} , the radiation resistance.

The radar cross section may be found from (1-234) as

$$\sigma = \lim_{r \rightarrow \infty} 4\pi r^2 \frac{|E^s|^2}{|E^i|^2} \quad (7-74)$$

where E^s can be determined, for example, from (7-72). The radar cross section for a dipole scatterer is shown in Fig. 7-16.

The radiation efficiency is calculated using (1-184) as

$$e = \frac{R_{ri}}{R_{in}} = \frac{R_{ri}}{R_{ri} + R_{ohmic}} \quad (7-75)$$

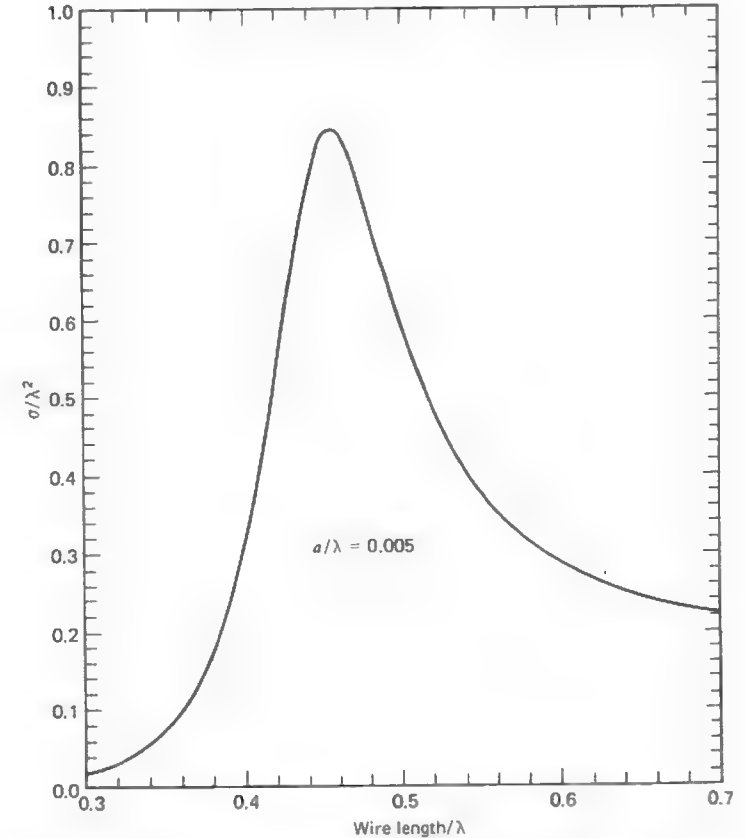


Figure 7-16 Monostatic radar cross section of a straight wire at normal incidence as a function of wire length.

$R_{r,i}$ is the radiation resistance referred to the input terminals and R_{ohmic} is the loss resistance due to dissipative loading, either distributed or lumped (see Section 7.9.1). Alternatively, we could determine the radiated power by integrating the power density in the far field as we did in Chapter 1. However, the above method (i.e. (7-75)) is computationally more efficient.

From the discussion in this section we can see, among other things, that such a refinement as the losses due to finite conductivity can be included into a moment method solution in a fairly straightforward manner. In the next section we will examine the lone remaining major aspect of modeling wire antennas or scatterers by the method of moments, namely the modeling of the source.

7.7 SOURCE MODELING

No doubt the most used generator model in wire antenna theory is the *delta gap model*, shown in Fig. 7-17a, which is often referred to as a *slice generator*. Although such sources do not exist in practice, they do permit surprisingly good calculations to be made. The source arises from the assumption that a voltage is placed across the gap giving rise to an impressed electric field $E^i = V/\delta$ confined entirely to the gap (i.e., no fringing).

Mathematically, the delta gap model enters into the method of moments in the following way. From (7-43) we note that one can write for the generalized voltage matrix element

$$V_m = - \iint_S (\mathbf{J}_m \cdot \mathbf{E}^i - \mathbf{M}_m \cdot \mathbf{H}^i) ds \quad (7-76)$$

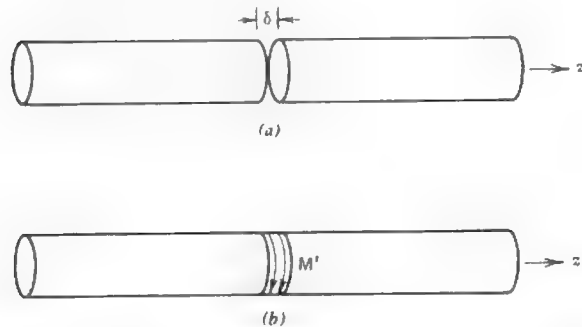


Figure 7-17 The delta gap source model. (a) Gap with impressed field $E^i = V/\delta$. (b) The equivalent magnetic current ring generator.

or by reciprocity (see Fig. 7-10)

$$V_m = - \iint_{V_i} (\mathbf{E}_m \cdot \mathbf{J}^i - \mathbf{H}_m \cdot \mathbf{M}^i) dv \quad (7-77)$$

If we replace the narrow gap region in Fig. 7-17a by the narrow strips of magnetic current ($\mathbf{M}^i = \mathbf{E}^i \times \hat{n}$) as in Fig. 7-17b, then, as the gap size tends toward zero (using the definition of the Dirac delta function)

$$V_m = \iint_S \mathbf{H}_m \cdot \mathbf{M}^i ds = \iint_S \frac{\delta(z)}{2\pi a} a d\phi dz = 1. \quad (7-78)$$

Consequently, only those positions in the generalized voltage matrix corresponding to segment junctions that contain generators will have nonzero values.

A second generator model, which has practical significance, is the so-called *frill generator*. Consider Fig. 7-18a which shows a coaxial line feeding a monopole on a ground plane. Assuming a purely dominant mode distribution (TEM) in the coaxial aperture and image theory, we can replace the ground plane and the coaxial aperture with a frill of magnetic current as shown in Fig. 7-18b. Since the assumed form of the electric field in the aperture is

$$E_\rho(\rho') = \frac{1}{2\rho' \ln(b/a)} \quad (7-79)$$

the corresponding magnetic current distribution is

$$M_\phi = \frac{-1}{\rho' \ln(b/a)} \quad (7-80)$$

from which it can be shown that the electric field on the axis of the monopole is [5, 14]

$$E_z(0, z) = \frac{1}{2 \ln(b/a)} \left(\frac{e^{-j\beta R_1}}{R_1} - \frac{e^{-j\beta R_2}}{R_2} \right) \quad (7-81)$$

where

$$R_1 = \sqrt{z^2 + a^2} \quad (7-82a)$$

$$R_2 = \sqrt{z^2 + b^2} \quad (7-82b)$$

if the frill center is at the coordinate origin. When this field is reacted with the test source current as required by (7-76), each entry in the generalized voltage matrix will have a nonzero entry. For segments not on the axis of the monopole, the form of E^i is more complicated than (7-81) and is available in the literature

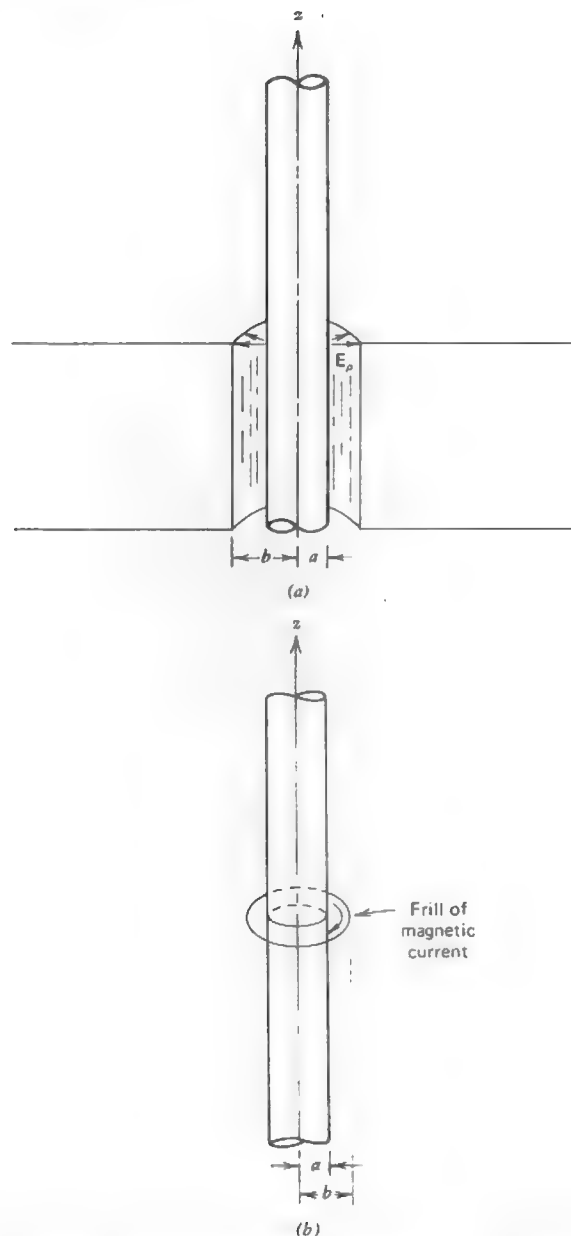


Figure 7-18 Magnetic frill generator. (a) Coaxial line feeding a monopole through a ground plane. (b) Mathematical model of Fig. 7-18a. (See Sec. 8.1).

Table 7-1 Voltage Matrix Values for a Frill Generator ($Z_0 = 50$ ohms) and Delta Function Testing Functions, ($L = 0.47\lambda$, $a = 0.005\lambda$, $b/a = 2.30$)

Segment no.	$ V_m $	$\angle V_m$
1	0.005	154.1°
2	0.007	159.5°
3	0.009	164.4°
4	0.013	168.8°
5	0.020	172.5°
6	0.034	175.5°
7	0.067	177.7°
8	0.170	179.1°
9	0.715	179.8°
10	10.948	180°
11	10.948	180°
12	0.715	179.8°
13	0.170	179.1°
14	0.067	177.7°
15	0.034	175.5°
16	0.020	172.5°
17	0.013	168.8°
18	0.009	164.4°
19	0.007	159.5°
20	0.005	154.1°

[5, 15]. Table 7-1 gives the values for $-E_z^i(0, z)$ and V_m when the testing function is a delta function. Note the rapid decrease in values with increasing distance from the generator compared with the numerical values of zero or one that exist when a delta gap generator is used.

7.8 SOME COMPUTATIONAL CONSIDERATIONS

There are essentially two limitations to the use of the moment method. These are: (1) the amount of computer storage necessary for the N^2 elements of the impedance matrix and, (2) the amount of time required to compute those N^2 elements and solve the resulting system of equations. In this section we first examine the time requirements of moment method techniques and then examine ways of using symmetry advantageously to reduce those time and storage requirements.

7.8.1 Computer Time Considerations

An impedance matrix of N^2 elements is said to be of order N . Let N_i be the number of different source or incident fields (i.e., radar cross section is a function of incidence angle) associated with a given impedance matrix and let N_a be the number of observation points at which the field is to be computed from the current solution; then the time t for execution will be approximately given by [8]

$$t \simeq AN^2 + B_3N^3 + CN^2N_i + DNN_iN_a \quad (7-83)$$

where the algorithm and computer dependent factors A , B , C , and D are:

A = time required to compute a typical impedance matrix element,

B_3 = time required to solve $[Z_{mn}][I_n] = [V_m]$ for $[I_n]$ by matrix inversion $[I_n] = [Z_{mn}]^{-1}[V_m]$ for a system of order N ,

C = time required to perform the operation $[Z_{mn}]^{-1}[V_m]$ or its equivalent for each new $[V_m]$,

D = time for computing far-field from $[I_n]$.

It is clear from (7-83) that the dominant factor in determining the required time lies in the second term which is associated with the solution of the system of equations. The dominant effect of this term can be reduced in a number of ways. If instead of actually finding the inverse $[Z_{mn}]^{-1}$, an algorithm such as Crout or Gauss-Jordan is used, then $B_3N^3 \rightarrow B_2N^2$ and we have

$$t \simeq AN^2 + B_2N^2 + CN^2N_i + DNN_iN_a \quad (7-84)$$

which is a significant reduction in the solution time required for a given N . If the impedance matrix is toeplitz (see Section 7.8.2), then $B_3N^3 \rightarrow B_1N^{5/3}$ and we have

$$t \simeq AN + B_1N^{5/3} + CN^2N_i + DNN_iN_a \quad (7-85)$$

for which there is a significant improvement in the first term as well as the second. Figure 7-19 shows curves of CPU time for various values of N . The curve labeled Crout follows from (7-84) and that labeled toeplitz follows from (7-85), which is a faster approach.

When the second term in (7-83) is on the order of N^2 or less, then usually the first term, which is associated with the time required to calculate the matrix elements, becomes the dominating factor. In the following subsections we examine briefly some ways for reducing the total time required for the operations associated with the first two terms in (7-83).

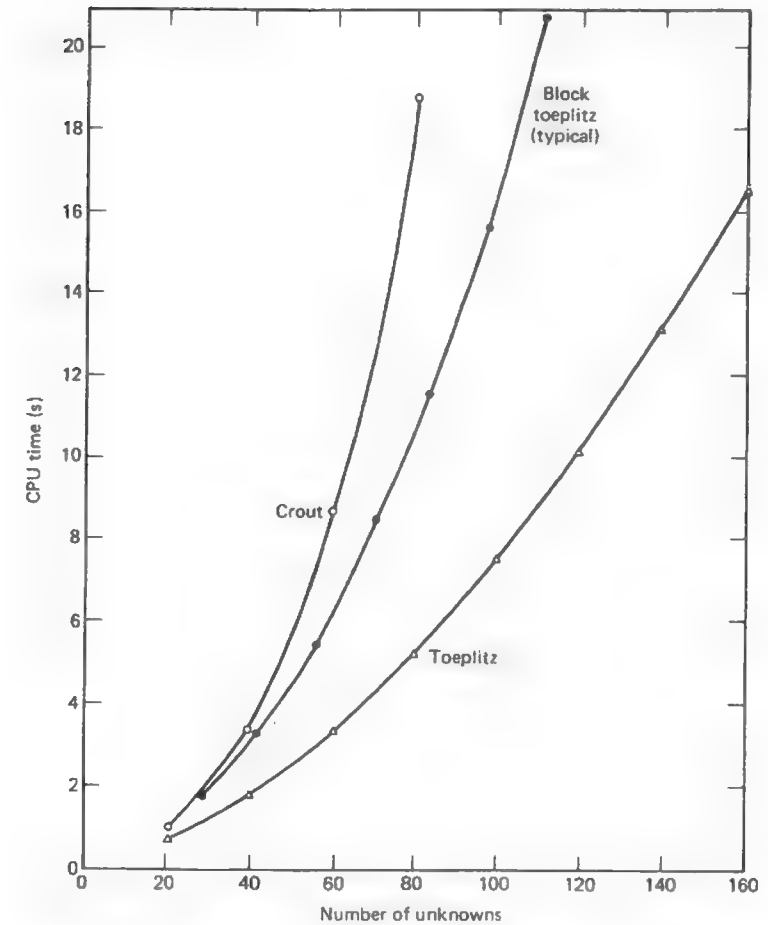


Figure 7-19 Typical CPU time for several types of matrix solutions.

7.8.2 Toeplitz Matrices

Certain types of problems produce impedance matrices wherein there is a systematic repetition in the matrix elements. Often this repetition can be used to decrease the impact of both the first and second terms in (7-83). Consider the straight wire in Fig. 7-1. If the segments are of equal length, all the values of the N^2 matrix elements are contained in any one row of $[Z_{mn}]$, say the first one. All other rows are merely a rearranged version of the first. The remaining elements can be obtained by the rearrangement algorithm

$$Z_{mn} = Z_{1, |m-n|+1} \quad m \geq 2, \quad n \geq 1. \quad (7-86)$$

Such a matrix is said to be a *toeplitz matrix*. Computer programs exist for solving toeplitz matrices that are considerably more efficient than ones for solving a non-toeplitz matrix. (See Appendix G.7.) For a toeplitz matrix the first two terms in (7-83) become AN and $BN^{5/3}$, respectively, and the execution time is approximately that given in (7-85).

Toeplitz matrices can arise in the treatment of certain wire geometries. These are the straight wire (see Examples 7-1 and 7-2), the circular loop, and the helix [16]. A toeplitz matrix can also arise in the treatment of geometries other than the wire, but these are outside the scope of this chapter.

7.8.3 Block Toeplitz Matrices

Consider the linear array in Fig. 7-20. The impedance matrix that characterizes the array will be toeplitz by blocks or by submatrices when the array elements are of the same length and are equally spaced. Thus, if the impedance matrix for the array $[Z]_{\text{array}}$ is written in terms of submatrices $[S]$ as

$$[Z]_{\text{array}} = \begin{bmatrix} [S]_{11} & [S]_{12} & \cdots & [S]_{1J} \\ [S]_{21} & [S]_{22} & \cdots & [S]_{2J} \\ \vdots & \vdots & \ddots & \vdots \\ [S]_{J1} & \cdots & \cdots & [S]_{JJ} \end{bmatrix} = \begin{bmatrix} [S]_{11} & [S]_{12} & \cdots & [S]_{1J} \\ [S]_{12} & [S]_{11} & \cdots & [S]_{1(J-1)} \\ \vdots & \vdots & \ddots & \vdots \\ [S]_{1J} & [S]_{1(J-1)} & \cdots & [S]_{11} \end{bmatrix} \quad (7-87)$$

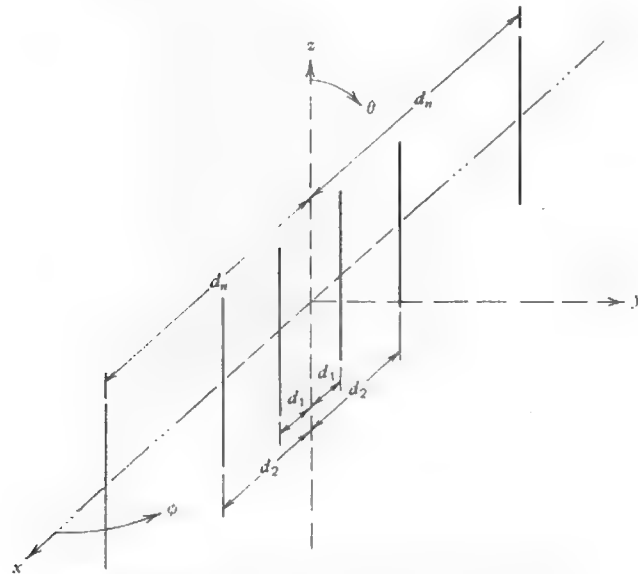


Figure 7-20 Linear array of parallel dipoles.

where $[S]_{ij} = [Z_{mn}]$, the entire impedance matrix is toeplitz by blocks. Thus, if one row of submatrices is known, the remaining submatrices may be filled by the algorithm

$$[S]_{ij} = [S]_{1, |i-j|+1} \quad i \geq 2, \quad j \geq 1. \quad (7-88)$$

Consequently the first term in (7-83) is of order N^2/J where J is the number of independent submatrices. The second term in (7-83) will be of order $N^{9/5}$.

If the submatrices are themselves toeplitz, as they would be if all segments are of identical length and radius, then the matrix fill time is reduced even further. Computer programs exist for solving block toeplitz matrices. (See Appendix G.8.) The potential savings in execution time for a problem that is block toeplitz over the same size nonblock toeplitz problem can be considerable (see Fig. 7-19).

7.8.4 Compressed Matrices

In certain problems there will be a repetition in the values within $[I_n]$ due to the symmetry of the problem. If this can be recognized in advance, it can be used to advantage to compress the matrix from order N to order N/L where L is the degree of symmetry.

Consider the following simple but very common example of symmetry suggested by Fig. 7-18a. Here the monopole and its image will have a symmetrical current about the feed point. Suppose $I_n = I_{n+N/2}$, then we can write

$$\sum_{n=1}^{N/2} (Z_{mn} + Z_{m, n+N/2}) I_n = V_m \quad m = 1, 2, 3, \dots, N/2 \quad (7-89)$$

Solution of this compressed system of $N/2$ equations will yield the $N/2$ independent I_n 's. From (7-84) we can see that the solution time for the system will be $B_2(N/2)^2$, or a reduction in time by a factor of 4 for this portion of the computing process. For higher degrees of symmetry the savings in time would be even more considerable. For some large problems it may be necessary to compress the matrix for another reason, namely storage requirements. It is possible that an impedance matrix may be so large that it cannot be stored in readily available core memory and that through symmetry it may be compressed to a reasonable size [5].

So it is the execution time and computer storage that tend to limit the electrical size of problems that may be reasonably treated by the moment method. In some of the remaining sections of this chapter we will approach certain situations in such a way that we tend to minimize the impact of these two limitations.

7.9 THE WIRE ANTENNA OR SCATTERER AS AN N -PORT NETWORK

In Section 7.2 we saw the resemblance between the simultaneous linear equation approximation of an integral equation and Kirchhoff's network equations. It follows that we may view the junction of two or more segments as a port in the usual circuit sense as indicated by Fig. 7-21a. At each port we may place either series or parallel elements which are either passive or active. Series connections are treated on an impedance basis while parallel connections are handled on an admittance basis. This section considers both types.

7.9.1 Series Connections

We already have used a single generator placed at the junction of two wire segments (e.g., Section 7.7). This generator was in series with the implied port terminals located at the ends of the two adjacent segments in question. We

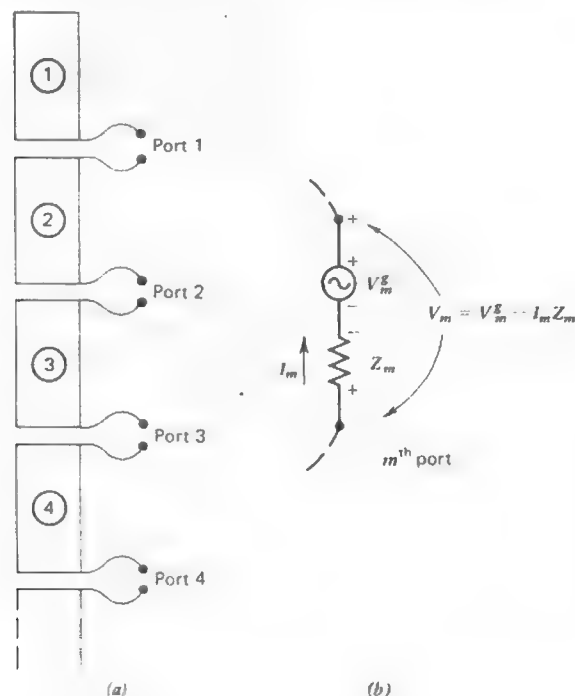


Figure 7-21 N segment wire (a) $N - 1$ port terminal pairs. (b) Equivalent circuit for the m th port.

could, of course, place as many generators on the wire as there are segment junctions. Thus, for an N -segment dipole there would be $N - 1$ ports. If there is no generator or passive element across the port, the port is understood to be short-circuited.

Previously in Section 7.6 we saw how distributed loading was accounted for in the moment method by modifying certain elements in the impedance matrix. Here, let us examine how lumped loading may be handled. If a load Z_m is inserted into a wire antenna at segment junction m having a current I_m , the total voltage acting at that point is

$$V_m = V_m^g - I_m Z_m \quad (7-90)$$

where V_m^g represents a voltage generator that may be located at point m in series with Z_m as indicated in Fig. 7-21b. In many cases V_m^g will be zero. Considering the m^{th} equation in a system of N linear equations, we can write

$$\sum_{n=1}^N Z_{mn} I_n = V_m^g - I_m Z_m \quad (7-91)$$

or

$$\sum_{n=1}^N Z'_{mn} I_n = V_m^g \quad (7-92)$$

where

$$Z'_{mn} = Z_{mn} + Z_m. \quad (7-93)$$

Except for the diagonal elements, the new impedance matrix is the same as the original, or $Z'_{mn} = Z_{mn}$, $m \neq n$. Thus, the effect of lumped loading may be accounted for by simply adding the load impedances Z_m to the corresponding diagonal elements in the impedance matrix. The effects of lumped loading can be substantial. For example, it can be used to achieve increased bandwidth, but at the expense of lower efficiency.

7.9.2 Parallel Connections

In the previous subsection we saw how circuit elements, when connected in series at a given port, resulted in modification of certain entries in the open-circuit moment method impedance $[Z_{mn}]$. If, however, we wish to connect one port in parallel with another as in a log-periodic antenna, then it is necessary to work with the short-circuit moment method admittance matrix $[Y_{mn}]$.

Consider Fig. 7-22 which shows a log-periodic dipole antenna (LPDA). The LPDA is viewed as the parallel connection of two N -port networks. One N -port represents the mutual coupling between N dipole antennas. The other represents

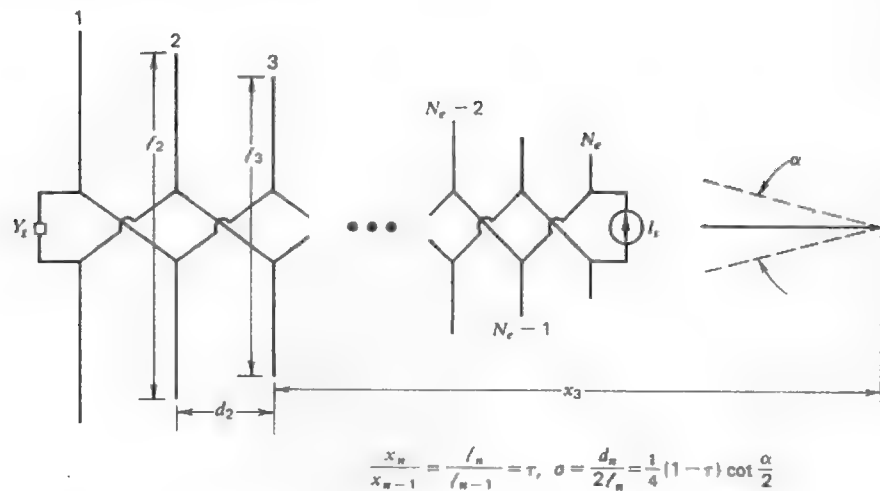


Figure 7-22 Single log-periodic dipole antenna.

the transmission line that interconnects the dipoles. Therefore, there is one *network* port for each of the dipoles in the system.

The approach is shown schematically in Fig. 7-23. The N -port labeled "antenna elements" includes the self- and mutual impedances between N unconnected dipole antennas located arbitrarily in space. The "transmission line" N -port represents the transmission line connecting the dipole antennas. Included in this network is the effect of reversing the polarity between successive dipoles. Note that there is a current source, I_s , on the LPDA. If there are N_e dipole elements on the antenna, this means that there are voltage sources applied on ports 1, 2, 3, ..., N_e . Also there is a terminating admittance on the LPDA antenna, Y_t , which exists at port 1. We do not know the numerical values of the applied voltage sources. Thus they must be found before we can solve for the currents on the LPDA.

Let $[Y_A]$ and $[Z_A]$ be the short-circuit admittance matrix and open-circuit impedance matrix, respectively, for the "antenna elements" network. Note that $[Z_A]$ is *not* the moment method impedance matrix. An element of $[Z_A]$, say $[Z_A]_{ij}$, represents the voltage induced on dipole i in the LPDA by a unit current on dipole j with all other dipoles open-circuited. Thus,

$$[Z_A]_{ij} = \frac{V_i}{I_j}. \quad (7-94)$$

Let $[Y_T]$ be the short-circuit admittance matrix for the "transmission line" network. Let $[I_A]$ and $[V_A]$ be the column matrices representing the voltage and

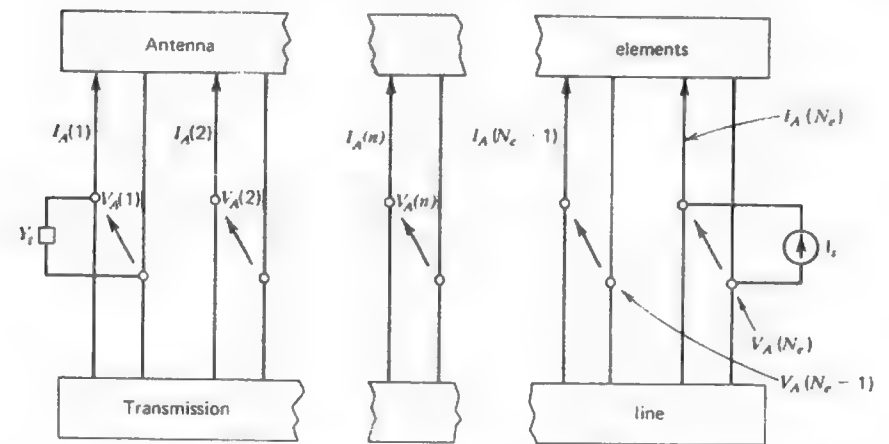


Figure 7-23 Schematic representation of the LPDA network.

current at each port of the "antenna elements" network. Since the two networks are in parallel, the total current can be written as

$$[I_s] = [[Y_A] + [Y_T]][V_A] \quad (7-95)$$

where $[I_s]$ represents the applied current sources. The $[I_s]$ matrix contains all zero elements, except at the port where there is a current source I_s . The current source, of course, represents the excitation of the LPDA antenna. Note in (7-95) that we know the entry in $[I_s]$ but not the entries in $[V_A]$. These must be found so that the moment method column matrix $[V_m]$ can be constructed and the usual equation $[I_n] = [Z_{mn}]^{-1}[V_m] = [Y_{mn}][V_m]$ solved for the current distributions in the antenna dipole elements. But, before we can solve (7-95) for $[V_A]$ and construct $[V_m]$, we must know $[Y_A]$ and $[Y_T]$.

To obtain the elements of $[Y_A]$ we proceed as follows. Consider an LPDA with N_e dipoles and M expansion functions on each dipole. The moment method impedance matrix will be of order $N_e \times M$. To obtain the moment method admittance matrix $[Y_{mn}]$ we note that $[Y_{mn}] = [Z_{mn}]^{-1}$ and

$$[I] = [Z_{mn}]^{-1}[V] = [Y_{mn}][V] \quad (7-96)$$

or

$$I_m = \sum_{n=1}^{M \times N_e} Y_{mn} V_n \quad m = 1, 2, \dots, M \times N_e. \quad (7-97)$$

To obtain $[Y_A]$ we note that most of the V_n 's will be zero since voltages are only applied by the transmission line on the center ports of each dipole in the LPDA. Suppose we rearrange the system of equations in (7-97) such that the first N_e

entries in $[V]$ correspond to the center ports of the dipoles in the LPDA. Then the currents at those ports containing a generator (i.e., antenna element ports) are related to the voltages at those ports by

$$I_j = \sum_{i=1}^{N_e} Y_{ji} V_i \quad j = 1, 2, \dots, N_e \quad (7-98)$$

or

$$[I_A] = [Y_A][V_A] \quad (7-99)$$

where all the V_i 's in $[V_A]$ will be nonzero. In finding $[Y_A]$ in this manner we have done so without making approximations other than those germane to the moment method itself. Indeed, all mutual couplings have been taken into account and we are not limited to LPDA's of less than 2:1 bandwidth as in the treatments by Carrel [17] and Kyle [18].

To obtain the transmission line admittance matrix $[Y_T]$ in (7-95) we first recognize that $[Y_T]$ is the transmission line admittance matrix for a simple terminated transmission line with a port at the position where each dipole is connected. Since $[Y_T]$ is the short-circuit admittance matrix, a given element $(Y_T)_{ji}$ represents the current induced across port j (which is shorted) by a unit voltage at port i , with all other ports shorted. Thus, $(Y_T)_{ji}$ is nonzero only for $i - 1 \leq j \leq i + 1$.

It is possible to write the transmission line admittance matrix $[Y_T]$ in a straightforward fashion [18]. For a single LPDA it is

$$[Y_T] = \begin{bmatrix} (Y_0 - jY_0 \cot \beta d_1) & -jY_0 \csc \beta d_1 & 0 & \dots & 0 \\ -jY_0 \csc \beta d_1 & -jY_0(\cot \beta d_1 + \cot \beta d_2) & -jY_0 \csc \beta d_2 & \dots & 0 \\ 0 & -jY_0 \csc \beta d_2 & -jY_0(\cot \beta d_2 + \cot \beta d_3) & \dots & 0 \\ \vdots & \vdots & \vdots & \ddots & \vdots \\ 0 & 0 & 0 & -jY_0 \csc \beta d_{N_e-1} & -jY_0 \cot \beta d_{N_e-1} \end{bmatrix} \quad (7-100)$$

where Y_0 is the transmission line characteristic admittance and β the propagation constant of the transmission line.

With the proper elements of both $[Y_A]$ and $[Y_T]$ in hand, we can obtain the voltages $[V_A]$ acting at the driven port of each dipole by

$$[V_A] = [(Y_A) + (Y_T)]^{-1} [I_s] \quad (7-101)$$

where $[I_s]$ has one nonzero entry. Having these voltages at each dipole, the moment method voltage matrix $[V_m]$ can be filled and the current distribution on each dipole in the LPDA obtained from

$$[I_n] = [Z_{mn}]^{-1} [V_m] \quad (7-102)$$

where the elements of $[V_A]$ are the nonzero elements of $[V_m]$ and the elements of $[I_n]$ are the complex coefficients associated with the expansion functions on the various dipole elements.

It is worthwhile to summarize the above procedure for analyzing the LPDA. First, the open circuit impedance matrix $[Z_{mn}]$ was formed in the usual manner. By taking the inverse of $[Z_{mn}]$, the short circuit admittance matrix was obtained. Next the antenna elements admittance matrix $[Y_A]$ was formed from $[Y_{mn}]$ as in (7-97) and (7-98). Then $[Y_A]$ was added to the transmission line admittance matrix $[Y_T]$. Then the current generator shown in Figs. 7-22 and 7-23 was used in (7-101) to obtain the voltage $[V_A]$ acting at each dipole port. These voltages were then used to obtain the moment method voltage matrix $[V_m]$. Solution for the currents $[I_n]$ on each dipole in the LPDA followed according to (7-102). Patterns obtained using this procedure are given in Fig. 6-32 and agree with those in [19].

7.10 ANTENNA ARRAYS

The use of moment methods in the analysis and design of arrays of wire antennas (or scatterers) has significant advantages over the more classical methods used in treating arrays in that mutual coupling between array elements is taken completely into account (e.g., see the LPDA treatment in Section 7.9.2). Furthermore, no unrealistic assumptions need be made regarding the current distributions on the wires, and the array elements can be excited at any point(s) or be loaded at any point(s) along their lengths. Thus, the type of wire element array problem that can be considered is rather general. In this section we examine several array configurations of parallel dipoles and illustrate some typical mutual coupling effects.

7.10.1 The Linear Array

Consider the linear array of parallel wire elements shown in Fig. 7-20. The elements need not be of the same length and radius or be equally spaced in order to be treated by the moment method. Clearly they could be quite arbitrarily configured and, in fact, need not even be parallel. However, in this subsection we wish to illustrate the effects of mutual coupling in a typical linear dipole array by comparing results obtained here by the moment method (using a voltage generator with an internal impedance of 72 ohms) with results suggested by the methods of Chapter 3 (i.e., current generator excitation). For this purpose, without loss of generality, we will consider a linear array of 12 equally spaced, parallel, center-fed, half-wave dipoles with $\lambda/2$ spacing. If we divide each dipole into six segments and place a 1-V generator in series with a 72-ohm resistance at

Table 7-2 Normalized Terminal Currents for a Linear Array of 12 Half-Wavelength Spaced, Parallel, Half-Wave Dipoles, $a = 0.0001\lambda$

Element number	Zero generator impedance		72-ohm generator impedance	
	$ I_{in} $	$ Z_{in} $	$ I_{in} $	$ Z_{in} $
1	0.689	107.1	0.746	183.9
2	0.698	105.9	0.760	180.6
3	0.728	101.5	0.799	171.6
4	0.753	98.2	0.829	165.5
5	0.768	96.3	0.847	161.9
6	0.777	95.2	0.856	160.2
7	0.781	94.7	0.854	160.6
8	0.775	95.4	0.837	163.8
9	0.753	98.2	0.806	170.1
10	0.713	103.7	0.777	176.4
11	0.689	107.3	0.802	170.8
12	1.000	74.0	1.000	137.1

the center port of each dipole, the piecewise sinusoidal current amplitudes obtained using (7-28) and the methods of Section 7.5 are given in Table 7-2. We note that neither the feed point currents nor the input impedances (see (3-96)) are identical. This is due to mutual coupling. Since the main beam is at $\phi_0 = 45^\circ$, there is no symmetry in the currents about the array center as there would be if the array were phased for broadside radiation.

The normalized patterns are shown in Figs. 7-24a and 7-24b along with the normalized pattern for uniform current excitation. In spite of the differences noted in Table 7-2, there is little difference seen in the three normalized patterns shown in Figs. 7-24a and 7-24b. There is, of course, some small difference in the directivity in the two cases. It is possible to synthesize (see Chapter 10) the excitation voltages such that maximum gain is achieved. If this were done, the resulting currents at the fed ports would be of unit magnitude while the voltages needed to establish these unit magnitude currents would generally be of nonunit magnitude.

7.10.2 The Circular Array

Consider the circular array in Fig. 7-25 which is also known as a ring array [20]. Such arrays have been used in radio direction finding, radar, sonar and in other systems applications. Usually circular arrays are composed of identical, equally spaced elements. We will assume the array of Fig. 7-25 to have these

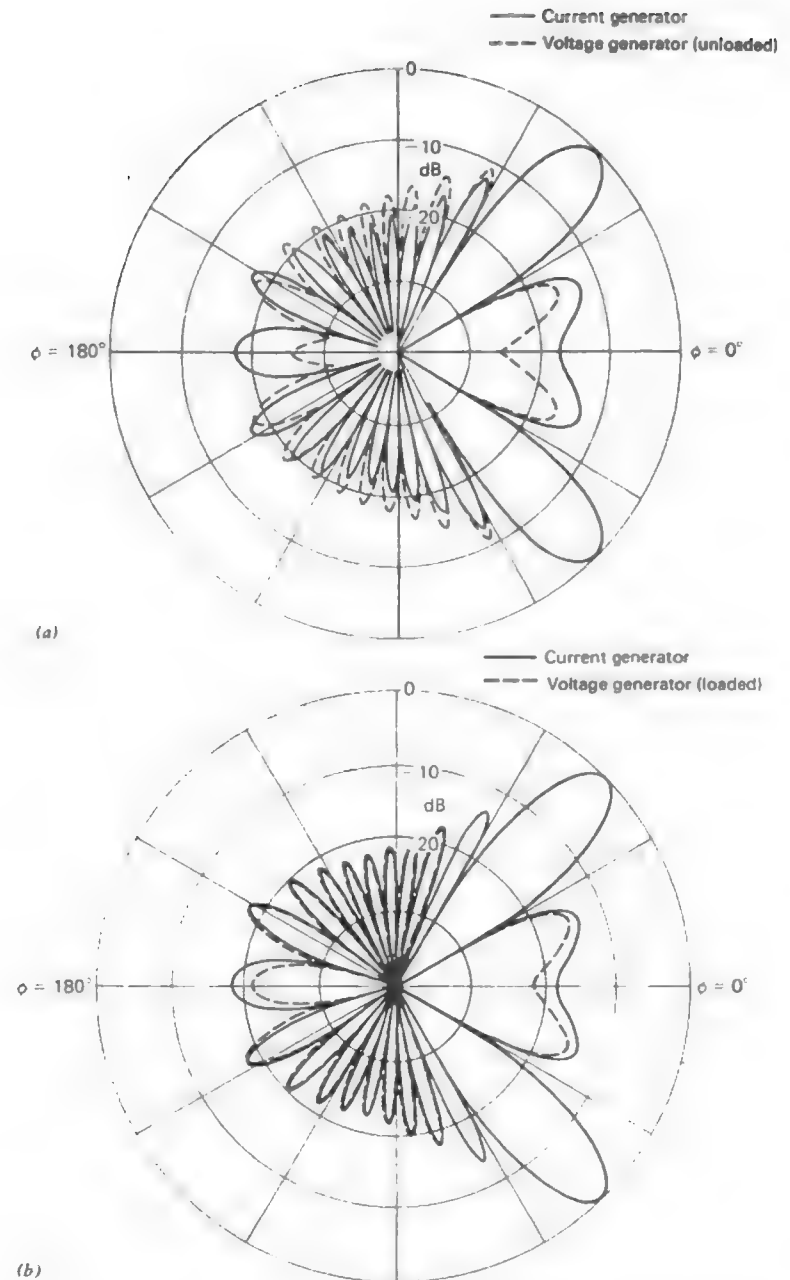


Figure 7-24 Linear array patterns with main beam steered to $\phi_0 = 45^\circ$ and ideal current generators (solid curve) compared to patterns from an array with voltage generators (see Table 7-2). (a) Linear array pattern for unloaded voltage generator excitations (dashed curve). (b) Linear array pattern for 72-ohm loaded voltage generator excitations (dashed curve).

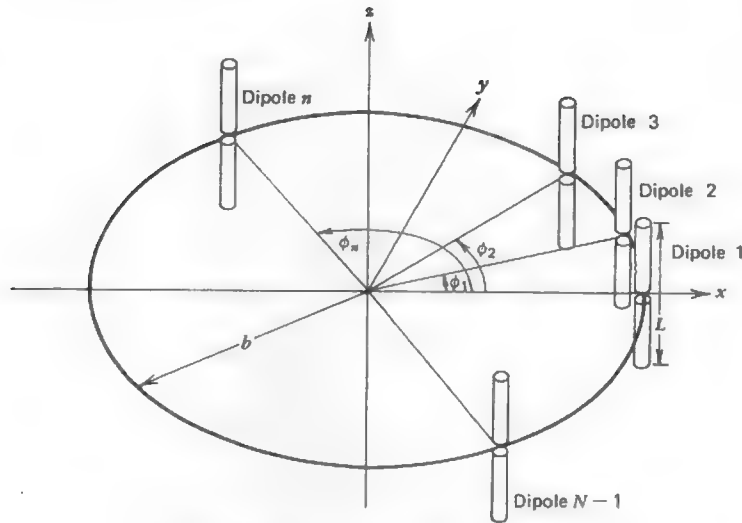


Figure 7-25 Circular array of dipoles.

characteristics and, further, that each dipole is excited at its center. If we temporarily replace each dipole with a point source at the excited dipole ports, we can write for the array factor (see Section 3.1)

$$AF(\theta, \phi) = \sum_{n=1}^N I_n e^{j\alpha_n} e^{j\beta \rho'_n \sin \theta \cos(\phi - \phi_n)} \quad (7-103)$$

where I_n is the current excitation of the n th element located at $\phi = \phi_n$, α_n is the associated phase excitation relative to the array center located at the coordinate origin, and ρ'_n is the radial distance of each element center from the origin (all of which equal b for the circular array case). For the usual case of cophasal excitation

$$\alpha_n = -\beta \rho'_n \sin \theta_0 \cos(\phi_0 - \phi_n) \quad (7-104)$$

where (θ_0, ϕ_0) is the desired position of the main beam maximum.

For the half-wave dipoles the element pattern is given approximately by (2-10). Thus, the complete pattern for the circular array of half-wave dipoles with an assumed sinusoidal current distribution can be written as

$$F(\theta, \phi) = \frac{\cos\left(\frac{\pi}{2} \cos \theta\right) \sum_{n=1}^N I_n e^{j\alpha_n} e^{j\beta \rho'_n \sin \theta \cos(\phi - \phi_n)}}{\sum_{n=1}^N I_n} \quad (7-105)$$

where the assumption is made that (3-109) applies rather than (3-108).

The analysis of the circular array in (7-103) to (7-105) is, of course, based on known currents on the array elements. In practice we usually apply voltages rather than currents to the array element ports. To determine the currents established by the voltages we can use the method of moments thereby including all mutual effects.

We will consider the circular array in Fig. 7-25 to be composed of identical, equally spaced dipoles. Thus, certain simplifications in the moment method formulation are possible. With the excitation at the centers of all dipoles, it is clear that the current distributions will have even symmetry about the $z = 0$ plane. This image symmetry can be used to compress the size of the impedance matrix $[Z_{mn}]$ of each dipole as discussed in Section 7.8.4. (This could also have been done for the linear array in the previous section.) In addition to this, the impedance matrix for the circular array will take the submatrix from

$$[Z]_{\text{array}} = \begin{bmatrix} [S]_{11} & [S]_{12} & \cdots & [S]_{1N} \\ [S]_{1N} & [S]_{11} & \cdots & [S]_{1(N-1)} \\ \vdots & \vdots & \ddots & \vdots \\ [S]_{12} & [S]_{13} & \cdots & [S]_{11} \end{bmatrix} \quad (7-106)$$

where $[S]_{ij} = [Z_{mn}]$, and each $[Z_{mn}]$ may be compressed as described in Section 7.8.4. The matrix in (7-106) is not only toeplitz but goes by the name "block circulant." It can be shown that the inverse of a block circulant matrix is also block circulant. Thus $[Y]_{\text{array}}$ would be block circulant.

Table 7-3 Normalized Terminal Currents for a Circular Array of 12 Half-Wavelength Spaced, Parallel Half-Wave Dipoles (72-ohm loaded voltage generators)

Element number	$ I_{in} $
1	0.735
2	0.566
3	0.628
4	0.517
5	0.547
6	0.791
7	1.000
8	0.791
9	0.547
10	0.517
11	0.628
12	0.566

With voltage generators of 1-V magnitude in series with a 72-ohm impedance at the center of each dipole in a 12-element circular array with $\lambda/2$ spacing, the currents given in Table 7-3 resulted. The almost 2 : 1 variation in current magnitude is the result of mutual coupling. The corresponding pattern in the azimuthal plane is shown in Fig. 7-26 where a simple extension of (7-72) was used. For purposes of comparison, also shown is the pattern for uniform (current) excitation calculated using (7-105). The difference between the two types of patterns is more noticeable here than in Fig. 7-24 for the linear array. Although the pattern with the voltage generator obtained using the moment method is the more realistic of the two, an advantage of the moment method is that it does yield the input impedance of the elements for any scan angle thereby providing information for the design of the feed network (see Section 3.7).

7.10.3 Two-Dimensional Planar Array of Dipoles

Consider a two-dimensional array of parallel dipoles located in the xz -plane as shown in Fig. 7-27. Our purpose here is to use the method of moments to show how the input impedance of a given element in the array can vary with scan angle.

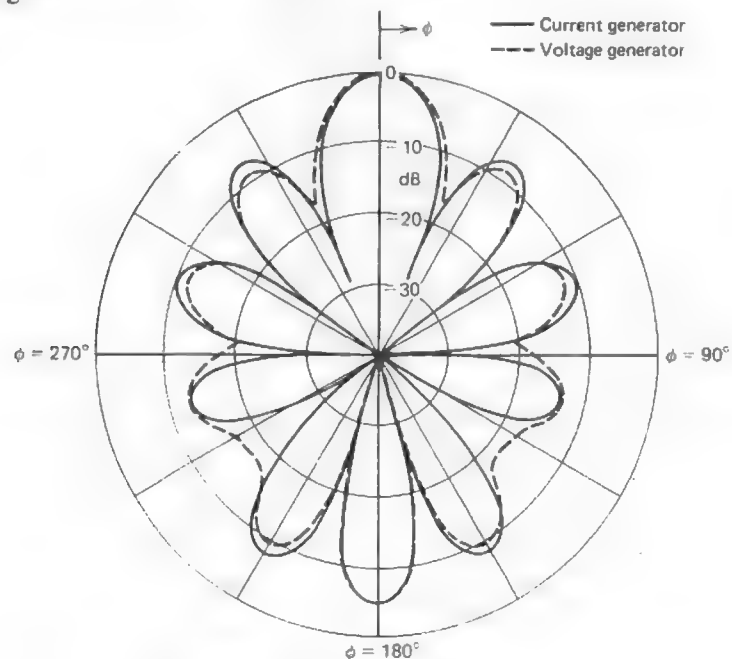


Figure 7-26 Patterns of the circular array of Fig. 7-25 with 12 elements for uniform current excitation (solid curve) and for 72-ohm loaded voltage generators with currents of Table 7-3 (dashed curve).

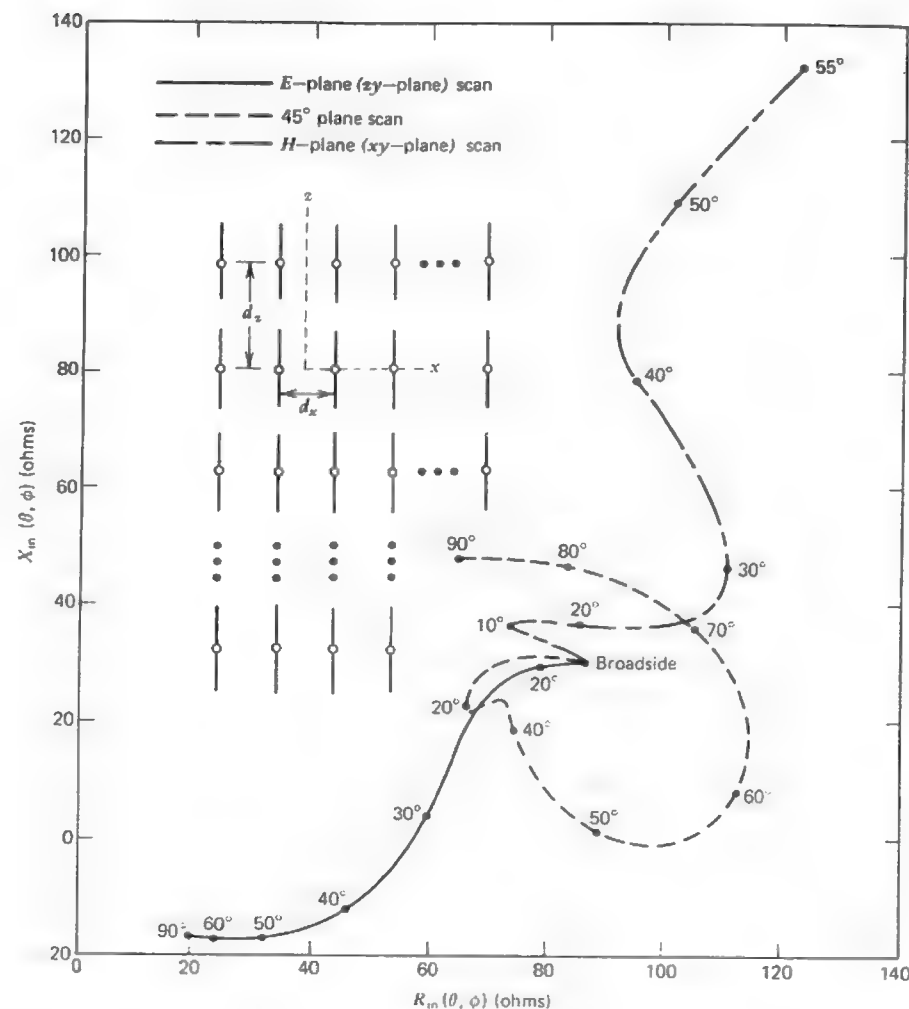


Figure 7-27 Input impedance variation of a central element in a 7 by 9 dipole array as a function of scan angle for three planes of scan ($d_x = d_z = 0.5\lambda$).

Figure 7-27 shows the input impedance variation of the center element in a 7 by 9 array (i.e., 7 collinear elements in an E -plane row by 9 parallel elements in an H -plane row). Three scanning conditions are illustrated: H -plane, E -plane, and the 45° plane between the E - and H -planes. It is clear from Fig. 7-27 that the input impedance does vary considerably with scan angle and that the variation is different for various planes of scan. Clearly this variation poses a challenging design problem for the engineer responsible for designing the feed and matching network for the array elements.

Note that as the array is scanned in the E -plane (zy -plane) to 90° (i.e., “endfire”), the real part of the input impedance is tending toward zero which in turn means the element is tending not to radiate! Indeed, although the other elements in the array will not have *exactly* the same behavior, most of them (except the edge elements) will behave similarly and the entire array will tend not to radiate! This phenomena is known as the *Wood's anomaly*, or blindspot phenomena, and it would seem inappropriate not to mention it in a book on antenna principles. The Wood's anomaly is more likely to occur in large arrays than in the relatively small one considered here. Fortunately the Wood's anomaly can be avoided in some arrays by suitable choices in the array design parameters as well as in the element design itself.

The moment method analysis of a two-dimensional array such as that in Fig. 7-27 is aided by the fact that such a problem is block toeplitz. Even so, the moment method of analysis of such an array is limited to arrays on the order of that analyzed here for the reasons mentioned in Section 7.8. For substantially larger arrays of either dipoles or slots, other methods of analysis may be used [21].

7.10.4 Summary

In this section we have illustrated, through the use of several examples, the application of the moment method to antenna arrays. The examples show us several things. First, the moment method takes into account all mutual couplings and makes it unnecessary to assume the current distribution on the elements in the array or to assume that each element has the same pattern. Second, the moment method directly provides accurate information concerning the input impedance of various elements under any scan condition. Third, the assumption of a sinusoidal current distribution on a thin half-wave dipole in an array environment is a pretty good one and therefore the classical methods of dipole array analysis based on this assumption are quite accurate. It is for elements other than the dipole that the moment method has an obvious additional advantage.

7.11 MODELING OF SOLID SURFACES

There are two principal ways in which the method of moments can be used to model either two-dimensional or three-dimensional bodies (e.g., infinite cylinder or finite cylinder, respectively). The simplest way to model a solid surface body is with a grid of wires, the so-called *wire-grid model*. Examples of this approach are illustrated in Fig. 7-28. The other common approach is to use a magnetic field integral equation (see Prob. 7.11-5) in which the surface is broken up into patches or cells each having a continuous metallic surface. In this section we take a brief look at both of these approaches.

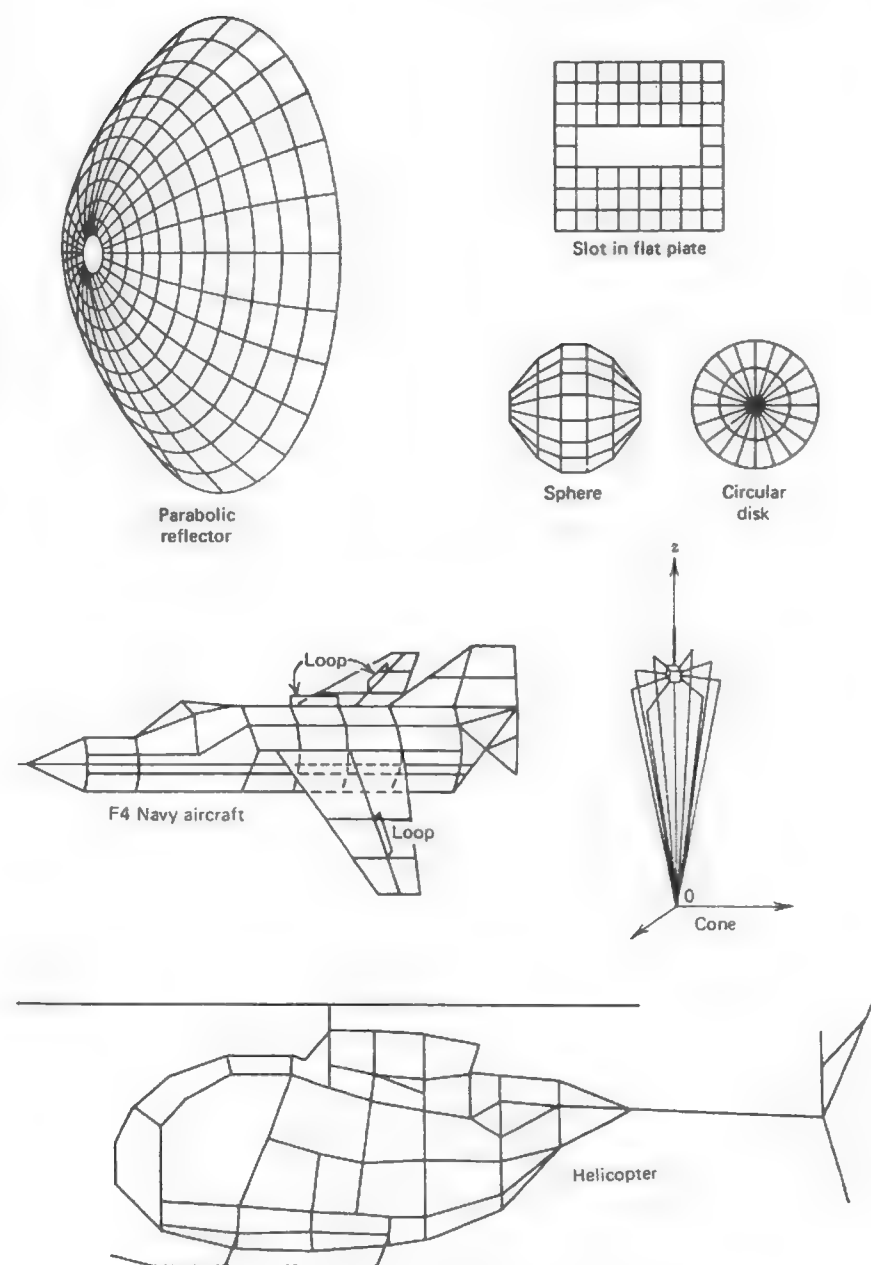


Figure 7-28 Examples of wire-grid modeling.

7.11.1 Wire-Grid Model

In this subsection we demonstrate the application of the wire segment procedure to model not just a wire antenna or wire scatterer, but also to model the metallic environment of the antenna. We can accomplish this by using a wire-grid or wire mesh to simulate an actual continuous metallic surface. The idea of using a wire mesh to simulate a continuous metallic surface precedes, of course, the time when the moment method came into widespread useage. There are many practical situations where the effect of a continuous metallic surface is required but the weight and/or wind resistance offered by a continuous surface is too large (e.g., a reflector surface).

The successful substitution of a wire-grid for a continuous metallic surface (in reality or in a model) depends upon the fact that as the grid size becomes smaller

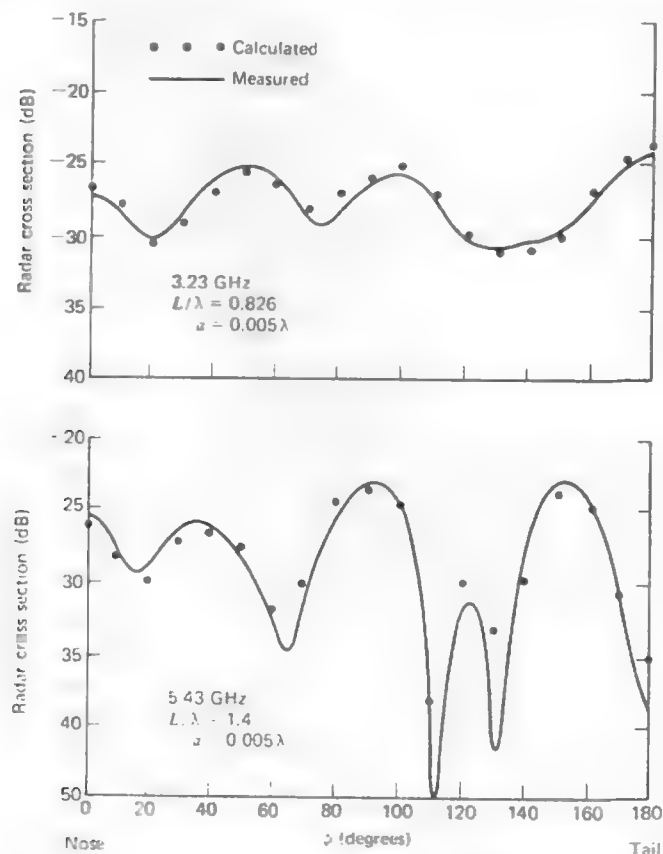


Figure 7-29 Radar cross section of a MIG 19 aircraft.
(L = fuselage length)

relative to the wavelength, the grid supports a current distribution which approximates that on the corresponding continuous surface. The current is only an approximation to the actual current, however, and as such it can be expected to reasonably predict the far fields but possibly not the near fields. This is due to the fact that the grid supports an evanescent reactive field on both sides of its surface [22]. An actual continuous conducting surface is not capable of supporting such a field.

The accuracy with which a wire-grid model simulates an actual surface depends on the computer code (i.e., expansion and weighting functions) used, the radius of the wire segments used, as well as the grid size. For example, with pulse expansion functions it has been found that a grid spacing of about 0.1λ to 0.2λ yields good results [23]. With the piecewise sinusoidal Galerkin method, it has been found that the grid size should not exceed $\lambda/4$ and that a suitable wire radius is $a = w/25$ where w denotes the width or length (whichever is greater) of the apertures [24]. A radar cross section result using the piecewise sinusoidal Galerkin method for a 70-segment aircraft model is shown in Fig. 7-29. The model is shown in Fig. 7-30 (1:200 scale).

Let us now consider the situation where a monopole is axially mounted on the base of a cone [5] as shown in Fig. 7-31. A wire-grid representation can be used in which the cone or frustum is represented by a number of "generating lines"

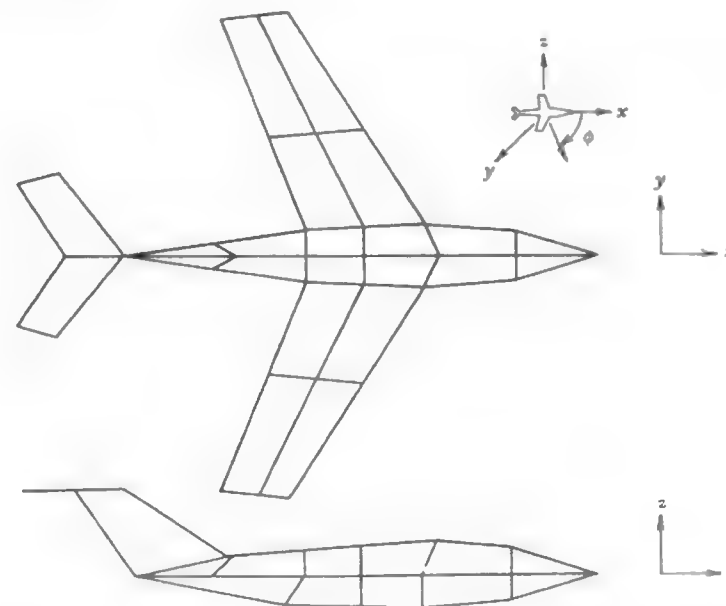


Figure 7-30 Wire-grid model for the MIG 19 with 70 segments.

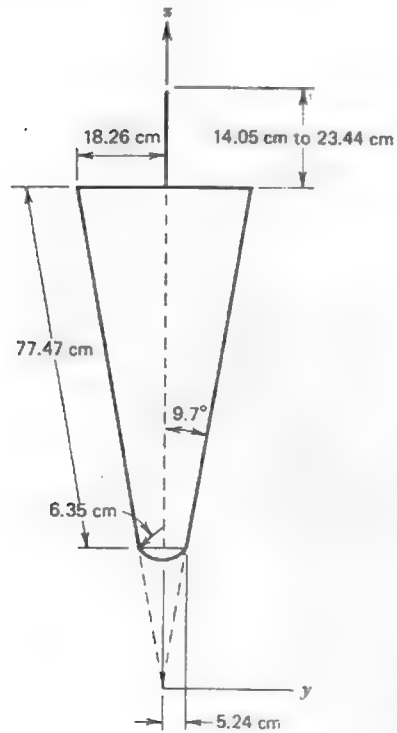


Figure 7-31 Dimensions of experimental cone model. The 18.75 cm monopole is a quarter-wavelength at 400 MHz.

consisting of a number of wires joined end to end, as shown in Fig. 7-32a. Except for the base, no wires need to be provided in planes normal to the z -axis because of symmetry. The length of the antenna and the dimensions for the cone, frustum, or frustum and spherical cap can be arbitrarily specified.

An interesting simplification (see Section 7.8.4) can be obtained from the symmetry of the configuration in the case where all generating lines have the same number of segments, each segment being identical (except for the orientation on the ϕ -coordinate) to the corresponding one on each other generating line. The currents on such corresponding segments should be equal in magnitude and phase, since $I(z)$ is independent of ϕ . Let the segments be numbered in a consecutive way, starting with the line at $\phi = 0$ and proceeding in a counter-clockwise direction along the other lines. Let M be the number of segments on each line, and L the number of generating lines. Thus, one can write

$$\sum_{j=1}^{L \cdot M} Z_{kj} I_j = -E_k^i, \quad k = 1, 2, \dots, L \cdot M. \quad (7-107)$$

Since the currents on corresponding segments are equal,

$$I_j = I_{(j+M)} = I_{(j+2M)} = I_{(j+(L-1)M)} \quad (7-108)$$

and (7-107) can be written as (see Sec. 7.8.4)

$$\sum_{j=1}^M I_j \left(\sum_{n=0}^{L-1} Z_{k(j+nM)} \right) = -E_k^i, \quad k = 1, 2, \dots, M. \quad (7-109)$$

The advantage of (7-109) is that it permits us to reduce the number of unknown currents to M , while the actual number of wire segments is $L \cdot M$, where L is arbitrary. As a result, there is no limitation other than computer running time to the number of generating lines (and thus to the total number of segments represented). The number of segments M in a generating line is, however, limited because of computer memory size. For the patterns calculated here L was chosen to be 10, M to be 170, and pulse basis functions were used.

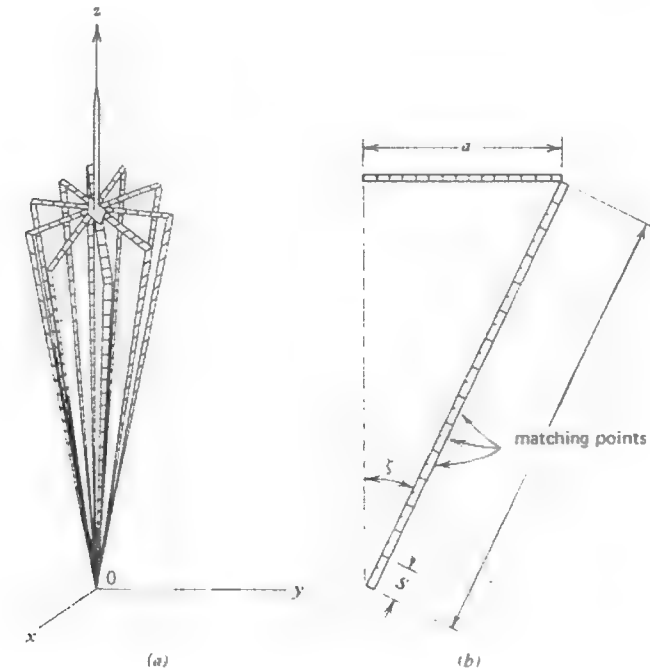


Figure 7-32 Wire grid model of cone in Fig. 7-33. (a) Model of monopole and cone. (b) Cone generating line showing distribution of segments and boundary matching points.

The left-hand side of (7-109) represents E^s for the cone problem under consideration here. It remains to determine E^i . For the monopole consider the geometry depicted in Fig. 7-33. Starting with the vector potential, the following expressions for the monopole configurations of Fig. 7-33 may be derived as

$$E_z^i = -j29.975 |I| \left[\frac{e^{-j\beta r_1}}{r_1} - \frac{e^{-j\beta r}}{r} \cos \beta H - j \frac{z}{r^2} e^{-j\beta r} \sin \beta H - \frac{z}{\beta r^3} e^{-j\beta r} \sin \beta H \right] \quad (7-110)$$

and

$$E_\rho^i = \frac{j29.975 |I|}{\rho} \left[(z-H) \frac{e^{-j\beta r_1}}{r_1} - \frac{z}{r} e^{-j\beta r} \cos \beta H - \frac{jz^2}{r^2} e^{-j\beta r} \sin \beta H + \frac{\rho^2}{\beta r^3} e^{-j\beta r} \sin \beta H \right] \quad (7-111)$$

Solving for the current on the cone makes it possible to calculate the far-field pattern of the cone-monopole structure by superimposing the fields of the cone and those of the monopole. A necessary but not sufficient check on the validity of the moment method solution in this problem requires that the currents at the junction of the monopole with the wire grid representation of the cone satisfy Kirchhoff's current law. For the formulation in (7-109) and (7-110) with $L = 10$,

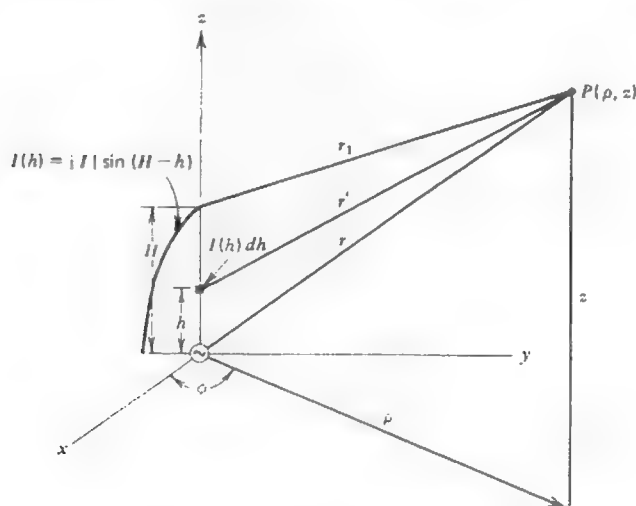


Figure 7-33 Configuration used for determining the near field of the monopole.

the current on each of the 10 wire grid lines was found to be 0.1 A when the monopole base current $|I| = 1.0$ A. That these 11 currents satisfy Kirchhoff's current law at their common junction is a direct consequence of Maxwell's equations since Kirchhoff's current law was not explicitly built into the system of equations [i.e., a constraining equation was not one of the equations in (7-109)].

To experimentally test the validity of the wire-grid representation of a metallic surface, an actual wire-grid cone was built around a styrofoam core in a configuration similar to that shown in Fig. 7-32a. A typical experimental comparison of the solid cone and its wire-grid counterpart is shown in Fig. 7-34a. Some representative results showing both the results calculated for the wire-grid cone and measurements for the solid surface cone are shown in Figs. 7-34b, 7-34c, and 7-34d. The results in all four cases are generally quite good. The difference between the two patterns in Fig. 7-34d for large angular values is due to the presence of the coaxial cable used on the experimental cone for measurement purposes.

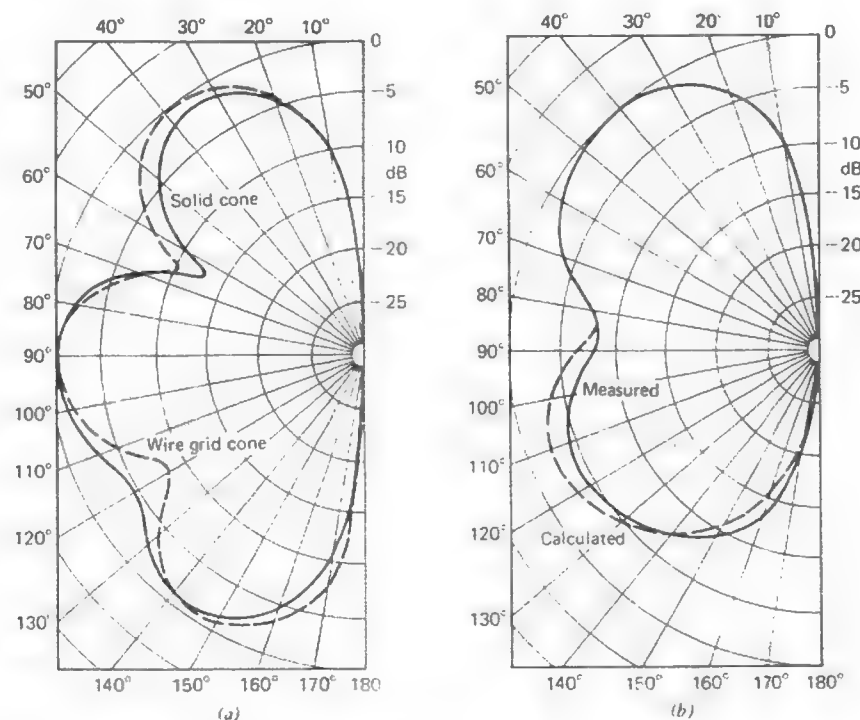


Figure 7-34 Cone patterns. (a) Experimental comparison at 400 MHz with a $\lambda/4$ monopole. (b) Patterns at 300 MHz using a $\lambda/4$ monopole.

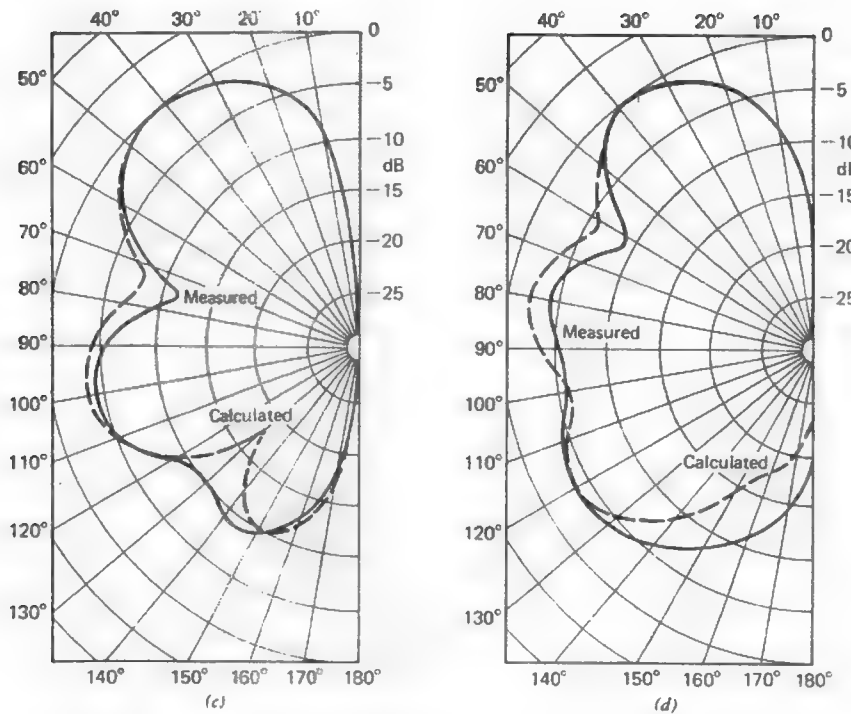


Figure 7-34 (c) Patterns at 350 MHz using a $\lambda/4$ monopole. (d) Patterns at 500 MHz using a 0.312λ monopole.

Other variations of the formulation given here are possible, of course. For example, instead of assuming the current distribution on the monopole, it may be treated as an unknown as are the currents on the metallic body. This could be done in a number of ways. The monopole terminal current value could be constrained to a particular value. This would take into account the interaction between the cone and monopole, but would not conveniently provide for the calculation of impedance. Alternatively one could use a voltage generator at the base of the monopole such as the magnetic frill current discussed previously. Calculation of the currents on the cone and monopole would account for the cone-monopole interaction and also yield directly the monopole impedance. Note that in either case the previously described symmetry for the cone due to the symmetrical excitation could still be used to advantage.

The accuracy of wire-grid models may be improved upon if the grid is reactively loaded with lumped loads [22]. The motivation for doing this is to eliminate the effects of the evanescent reactive field that is in proximity to the wire grid. Not only does this increase the accuracy of the model but it also permits larger

grid sizes to be used. Nevertheless, even without this loading, the wire-grid model is a convenient and relatively straightforward tool for engineering calculations.

7.11.2 Continuous Surface Model

The continuous surface model of a three-dimensional body is a complex problem which is beyond the scope of this text. The interested reader is referred to the literature for a discussion of this topic.

On the other hand, the continuous surface model of a two-dimensional body follows directly from the earlier sections in this chapter. We will consider two such examples here, that of a conducting cylinder with the incident electric field parallel to the axis of the cylinder (TM case) and that of a conducting cylinder with the incident magnetic field parallel to the axis of the cylinder (TE case).

In Section 1.3 we found the solution (Green's function) to the spherical wave equation. Here we need a solution to the cylindrical wave equation. For the TM case our equation is

$$\nabla^2 E_z + \beta^2 E_z = j\omega\mu J_z \quad (7-112)$$

where $E_z = E_z(x, y)$. A solution to this equation is

$$E_z = -\frac{\beta\eta}{4} I H_0^{(2)}(\beta|\rho - \rho'|) \quad (7-113)$$

where $H_0^{(2)}$ is the Hankel function of the second kind and zero order. It represents an outward cylindrical traveling wave just as does $e^{-j\beta r}$ for a spherical wave. The total scattered field is then the integral of (7-113) over the cross section of the cylinder or [4]

$$E_z(\rho) = -\frac{\beta\eta}{4} \iint J_z(\rho') H_0^{(2)}(\beta|\rho - \rho'|) ds' \quad (7-114)$$

where the integration is over the cross section of the cylinder of currents J_z as indicated in Fig. 7-35a.

A simple formulation is to require that (7-29) applies or (7-31) with delta weighting functions. Hence, the applicable integral equation is

$$E_z(\rho) = \frac{\beta\eta}{4} \int_c J_z(\rho') H_0^{(2)}(\beta|\rho - \rho'|) d\rho' \quad \rho \text{ on } c \quad (7-115)$$

where $E_z(\rho)$ is known and J_z is the unknown to be determined. Note that (7-115) has the same form as (7-1). If pulse expansion functions are used, the impedance matrix elements are

$$Z_{mn} = \frac{\beta\eta}{4} \int_{\Delta_n} H_0^{(2)}[\beta\sqrt{(x - x_m)^2 + (y - y_m)^2}] d\rho' \quad (7-116)$$

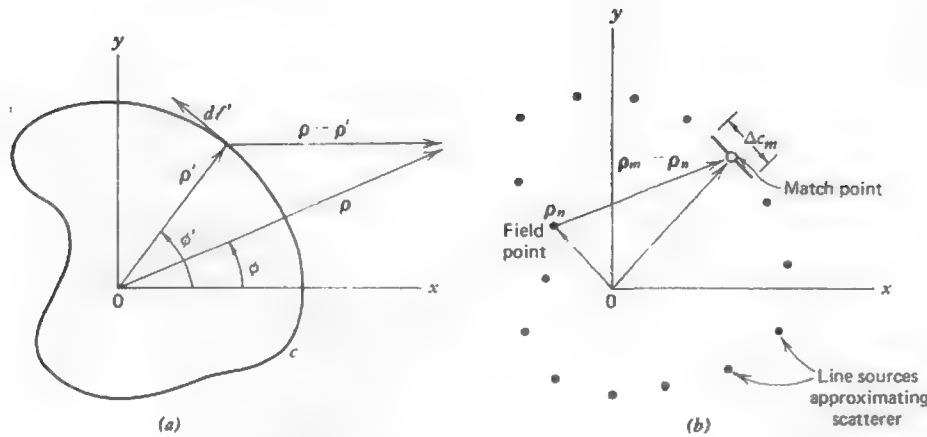


Figure 7-35 Cylinder of arbitrary cross section for scattering calculations. (a) Geometry for solid cylinder. (b) Line source approximation for the cylinder.

and the voltage matrix elements are

$$V_m = E_z^i(x_m, y_m). \quad (7-117)$$

In order to calculate the elements of the generalized impedance matrix, it is necessary to evaluate (7-116). Unfortunately there is no simple analytic expression for the integral, but it can be evaluated by one of several approximations. The simplest (and crudest) approximation is to view a current element $J_z \Delta c_n$ as a filament of current when the field point is not on Δc_n . Thus, when $m \neq n$

$$Z_{mn} \approx \frac{\eta}{4} \beta \Delta c_n H_0^{(2)}[\beta \sqrt{(x_n - x_m)^2 + (y_n - y_m)^2}]. \quad (7-118)$$

Note that although we are using a current filament approximation as shown in Fig. 7-35b, this is not a wire grid model and should not be confused with that approach.

To obtain Z_{nn} , we may recognize that the Hankel function has an integrable singularity and that the integral must be evaluated analytically. To do this, we note that the small argument formula for the Hankel function of argument $\beta\rho$ is

$$H_0^{(2)}(\beta\rho) \approx 1 - j\frac{2}{\pi} \log\left(\frac{\gamma\beta\rho}{2}\right) \quad (7-119)$$

where $\gamma = 0.5772 \dots$ is Euler's constant and obtain

$$Z_{nn} \approx \frac{\eta}{4} \beta \Delta c_n \left[1 - j\frac{2}{\pi} \log\left(\frac{\gamma\beta \Delta c_n}{4e}\right) \right] \quad (7-120)$$

where $e = 2.718$. Better formulations (e.g., faster convergence), although somewhat more complex, are possible with the use of other expansion functions and other weighting functions.

Results for the z -directed current on a cylinder are given in Fig. 7-36 for plane wave incidence where $E_z^i = e^{-j\beta x}$.

Next let us consider the TE case, where the incident magnetic field is parallel to the cylinder axis. We will, by choice, use a magnetic field integral equation (MFIE) which has the form

$$J_\phi(\rho) + \nabla \times \int J_\phi(\rho') \psi(\rho, \rho') d\rho' = H_z^i(\rho). \quad (7-121)$$

In contrast to the electric field integral equation (EFIE) in (7-1) where the unknown current only appears under the integral sign, here the unknown current appears both under and outside the integral sign. Thus, (7-121) is referred to as an integral equation of the second kind. Integral equations of the second kind are generally preferable for large smooth conducting bodies since the contribution by the integral part of the equation may be of second order importance. However, the electric field integral equation is also useful for large conducting bodies as we have seen in the treatment of the TM case. Magnetic field integral equations are not useful for treating thin wires due to the singularity in the integral. Recall that in Section 7.1 we avoided the singularity in the EFIE by using the approximation that the observation points lie on the axis of the wire rather than on the surface. That approach may not be employed for the MFIE.

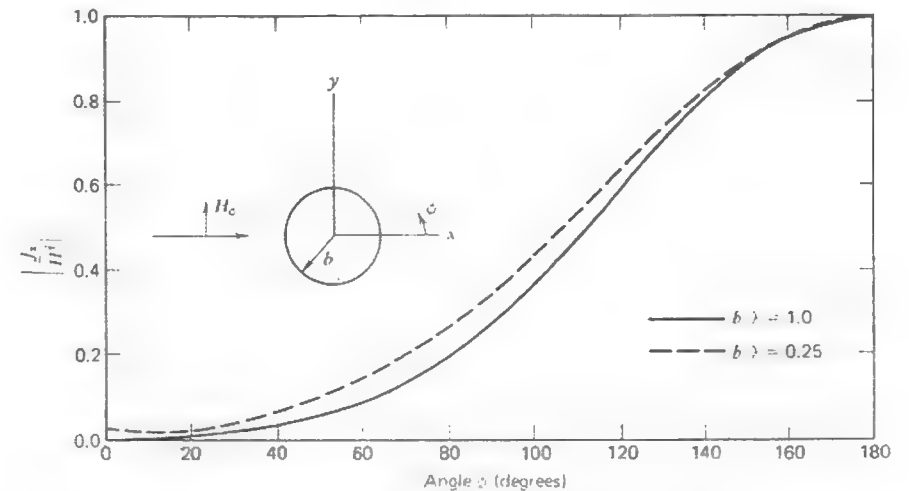


Figure 7-36 Normalized current on a conducting cylinder for TM polarization.

To derive the magnetic field integral equation for the two-dimensional problem of interest here, we note that there will only be a z -component of \mathbf{H} and a transverse component of \mathbf{J} , namely J_ϕ . The total magnetic field H_z at any point on or outside the surface of the conducting body is the sum of the impressed field H_z^i plus the scattered field H_z^s on the surface of the body. Thus,

$$H_z = H_z^i + H_z^s \quad (7-122)$$

Since $\mathbf{H} = \nabla \times \mathbf{A}$, we can write

$$H_z^s(\rho) = \hat{z} \cdot \nabla \times \int_c J_\phi(\rho) \psi(\rho, \rho') d\rho' \quad (7-123)$$

where ψ is the two-dimensional Green's function (used for the TM case) and $d\rho'$ specifies the reference direction of \mathbf{J} . The discontinuity in H_z at the conducting surface is equal to the current density J_ϕ . So,

$$J_\phi = -[H_z]_c \quad (7-124)$$

where c^+ indicates that H_z is evaluated just external to cross-sectional surface contour c . When (7-122) is applied to the contour c^+ , we may use (7-123) and (7-124) to write

$$J_\phi(\rho) = -[H_z^i(\rho) + \hat{z} \cdot \nabla \times \int_c J_\phi(\rho) \psi(\rho, \rho') d\rho']_{c^+} \quad (7-125)$$

This is the magnetic field integral equation for the two-dimensional problem of interest here. The current density J_ϕ is the unknown whereas the incident field H_z^i is known. The evaluation of the integral in (7-125) must be done with care since H_z is discontinuous at c and the Green's function is singular, precluding a simple interchange of differentiation and integration.

Rewriting (7-125) as

$$J_\phi(\rho) + [\hat{z} \cdot \nabla \times \int_c J_\phi(\rho) H_0^{(2)}(\beta|\rho - \rho'|) d\rho']_{c^+} = H_z^i|_{c^+} \quad (7-126)$$

and specifying pulse expansion functions and delta weighting functions enables us to write

$$Z_{mn} = \delta_{mn} + H_z(m, n) \quad (7-127)$$

where δ_{mn} is the Kronecker delta and $H_z(m, n)$ is the magnetic field at (x_m, y_m) on c^+ due to a unit current density on Δc_n at (x_n, y_n) , or

$$H_z(m, n) = [\hat{z} \cdot \nabla \times \int_{\Delta c_n} H_0^{(2)}[\beta\sqrt{(x - x_n)^2 + (y - y_n)^2} d\rho']_{c^+} \quad (7-128)$$

When the observation point and source segment coincide, $H_z(m, n)$ exhibits the singularity mentioned previously. However, Z_{mn} may be evaluated by noting that

$$H_z|_{c^+} = -H_z|_{c^-} = -\frac{1}{2} \quad (7-129)$$

since we are dealing with only a unit current. Thus,

$$Z_{mn} = 1 - \frac{1}{2} = \frac{1}{2} \quad (7-130)$$

To evaluate Z_{mn} for $m \neq n$ we can employ the approximation that when $\Delta c_n \ll \lambda$ and the field point at (x, y) is distant from the source Δc_n , the fields from the source appear to emanate from a magnetic line source located at the center of Δc_n . Thus,

$$H_z(m, n) = \frac{\Delta c_n}{4j} \frac{\partial}{\partial n} [H_0^{(2)}(\beta\rho)] \quad (7-131)$$

where the derivative is taken with respect to the normal to the surface and a local coordinate system is implied. If ϕ is the angle between $\hat{\rho}$ and \hat{n} , then

$$H_z(m, n) = \frac{j}{4} \beta \Delta c_n \cos \phi H_1^{(2)}(\beta\rho) \quad (7-132)$$

where $H_1^{(2)}$ is the Hankel function of the first order. It is necessary to translate this result from its local coordinate system to one with an arbitrary origin. This is accomplished by replacing ρ by $|\rho_m - \rho_n|$ and $\cos \phi$ by $\hat{n} \cdot \hat{R}$ where

$$\hat{R} = \frac{\rho_m - \rho_n}{|\rho_m - \rho_n|} \quad (7-133)$$

is a unit vector from the source point (x_n, y_n) to the field point (x_m, y_m) . Finally, for $m \neq n$, we have

$$Z_{mn} \approx \frac{j}{4} \beta \Delta c_n (\hat{n} \cdot \hat{R}) H_1^{(2)}(\beta|\rho_m - \rho_n|) \quad (7-134)$$

whereas for all m

$$V_m = -H_z^i(x_m, y_m) \quad (7-135)$$

Solution of the usual matrix equation $[Z_{mn}][I_n] = [V_m]$ yields the transverse currents on the conducting cylinder. A result for the current J_ϕ on a circular cylinder induced by a plane wave is shown in Fig. 7-37. The current is normalized with respect to the magnitude of the incident field.

We have not considered the subject of internal resonances here but it should be pointed out that it is possible to obtain erroneous currents on the cylinder at those precise frequencies where the interior dimensions of the cylinder correspond to the resonant frequency of a waveguide type mode [25]. Such erratic behavior may be avoided if a formulation is used which combines both the EFIE and the MFIE.

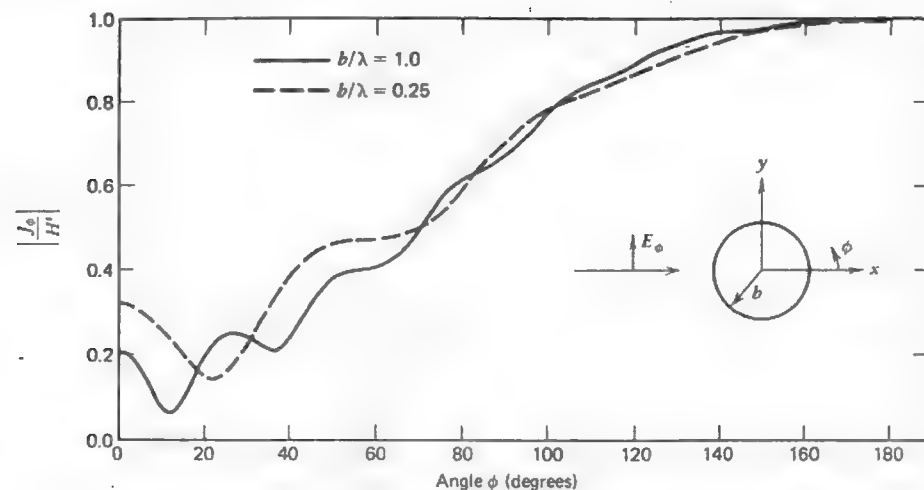


Figure 7-37 Normalized current on a conducting cylinder for TE polarization.

7.12 SUMMARY

In this chapter we have presented a very useful and powerful technique, the method of moments, for the analysis of certain types of antennas (e.g., wire antennas) and arrays of antennas (e.g., Sections 7.9 and 7.10). While the method has been applied primarily to z -directed wires, we have seen that it applies equally well to arbitrary configurations of wires, for example, Section 7.10, as well as to solid surfaces, for example, Section 7.11.2. Furthermore, the method of moments has been used to generate some of the data presented in Chapters 5 and 6.

The method of moments is often thought of as a low-frequency technique because it generally cannot be applied to bodies that are arbitrarily large in terms of the wavelength (e.g., Section 7.8). In contrast to this, in Chapter 9 we will study high-frequency techniques that apply best to bodies that are arbitrarily large in terms of the wavelength.

REFERENCES

1. S. A. Schelkunoff, *Advanced Antenna Theory*, Wiley, New York, 1952.
2. J. H. Richmond, "Digital computer solutions of the rigorous equations for scattering problems," *Proc. of the IEEE*, vol. 53, Aug. 1965.
3. R. F. Harrington, "Matrix methods for field problems," *Proc. of the IEEE*, vol. 55, Feb. 1967.

4. R. F. Harrington, *Field Computation by Moment Methods*, Macmillan, New York, 1968.
5. G. A. Thiele, "Wire Antennas," Chapter 2 in *Computer Techniques for Electromagnetics*, Pergamon Press, New York, 1973.
6. R. F. Harrington, *Time-Harmonic Electromagnetic Fields*, McGraw-Hill, New York, 1961.
7. B. A. Finlayson, *The Method of Weighted Residuals and Variational Principles*, Academic Press, New York, 1972.
8. E. K. Miller and F. J. Deadrick, "Some computational aspects of thin wire modeling," Chapter 4 in *Numerical and Asymptotic Techniques in Electromagnetics*, Springer-Verlag, New York, 1975.
9. V. H. Rumsey, "The reaction concept in electromagnetic theory," *Physical Review*, Ser. 2, vol. 94, June 1954.
10. W. A. Imbriale, "Applications of the method of moments to thin-wire elements and arrays," Chapter 2 in *Numerical and Asymptotic Techniques in Electromagnetics*, Springer-Verlag, New York, 1975.
11. S. A. Schelkunoff and H. T. Friis, *Antenna-Theory and Practice*, Wiley, New York, 1952.
12. J. H. Richmond, "Computer Program for Thin-Wire Structures in a Homogeneous Conducting Medium," National Technical Information Service, Springfield, VA 22151, NASA Contractor Report CR-2399, July 1973.
13. G. A. Thiele, "The maximum echo area of imperfectly conducting dipoles," *IEEE Trans. on Ant. and Prop.*, vol. AP-17, May 1969.
14. E. C. Jordan and K. G. Balmain, *Electromagnetic Waves and Radiating Systems*, Prentice-Hall, New Jersey, 1950, 1968.
15. L. L. Tsai, "A numerical solution for the near and far fields of an annular ring of magnetic current," *IEEE Trans. on Ant. and Prop.*, vol. AP-20, Sep. 1972.
16. G. A. Thiele, "Radar cross section of open circular loops," *IEEE Trans. on Ant. and Prop.*, vol. AP-16, May 1968.
17. R. Carrell, "Analysis and design of the log-periodic dipole antenna," Antenna Laboratory, University of Illinois Tech. Report, No. 52, April 1961.
18. R. H. Kyle, "Mutual coupling between log-periodic antennas," *IEEE Trans. on Ant. and Prop.*, vol. AP-18, Jan. 1970.
19. V. H. Rumsey, *Frequency Independent Antennas*, Academic Press, New York, 1966.
20. M. T. Ma, *Theory and Application of Antenna Arrays*, Wiley, New York, 1974.
21. N. Amitay, V. Galindo and C. P. Wu, *Theory and Analysis of Phased Array Antennas*, Wiley, New York, 1972.
22. K. S. H. Lee, L. Marin, and J. P. Castillo, "Limitations of wire-grid modeling of a closed surface," *IEEE Trans. on Electromagnetic Compatibility*, vol. EMC-18, Aug. 1976.
23. J. H. Richmond, "A wire-grid model for scattering by conducting bodies," *IEEE Trans. on Ant. and Prop.*, vol. AP-14, Nov. 1966.
24. Y. T. Lin and J. H. Richmond, "EM modeling of aircraft at low frequencies," *IEEE Trans. on Ant. and Prop.*, vol. AP-23, Jan. 1975.
25. M. G. Andreasen, "Comments on scattering by conducting rectangular cylinders," *IEEE Trans. on Ant. and Prop.*, pp. 235-236, vol. AP-12, March 1964.

PROBLEMS

7.1-1 Show that the left-hand side of (7-13) may be expressed as

$$E_z^i = \frac{1}{4\pi j\omega\epsilon_0} \int_{-L/2}^{L/2} I(z') \frac{e^{-j\beta R}}{R^3} [(1 + j\beta R)(2R^2 - 3a^2) + \beta^2 a^2 R^2] dz'$$

7.1-2 Through integration by parts, show that the left-hand side of (7-13) may be written

$$E_z^i = - \int_{-L/2}^{L/2} \left[j\omega\mu_0 I(z') - \frac{1}{j\omega\epsilon_0} \frac{\partial I(z')}{\partial z'} \frac{\partial}{\partial z} \right] \frac{e^{-j\beta R}}{4\pi R} dz'$$

This equation may be derived by using both the vector and scalar potentials [4].

7.1-3 Another equation for the treatment of wire antennas is Hallen's integral equation,

$$\int_{-L/2}^{L/2} I(z') \frac{e^{-j\beta R}}{4\pi R} dz' = -\frac{j}{\eta} (C_1 \cos \beta z + C_2 \sin \beta |z|)$$

where C_1 and C_2 are constants. The constant C_2 may be evaluated as $V_T/2$ where V_T is the terminal voltage of the antenna. Derive Hallen's equation for the dipole by writing a solution to the wave equation for A_z that is proportional to the right-hand side of the above equation and then equating this result to the integral form of the vector potential for A_z due to a perfectly conducting thin wire dipole.

7.2-1 In order to obtain some feeling for the method of moments, it is recommended that the student write a computer program to solve the following problem. Consider a straight dipole of length L (or monopole of length $L/2$) and radius a . Divide the dipole into N segments of equal length each containing a pulse expansion function.

(a) Use point-matching and the equation in Prob. 7.1-1 for the scattered field to compute the elements in the first row of the impedance matrix $[Z_{mn}]$ as given in (7-26) noting that these are the only independent matrix elements since the matrix is toeplitz (see Section 7.8.2). Note that the integrand tends toward singularity when $R = a$, but even so one may numerically integrate through this region if reasonable care is taken.

(b) Use (7-81) to compute the elements of $[V_m]$. Obtain $[I_n] = [Z_{mn}]^{-1} [V_m]$ and compare with the results in Fig. 7-5.

(c) Compute the far field pattern in the E -plane using (1-101) when $L = 0.47\lambda$.

(d) Having successfully completed (b) and (c) use the relationship

$$E_z^i(z_m) = e^{j\beta z} \cos \theta$$

to compute $[V_m]$ for $\theta = 90^\circ$ (i.e., the broadside case) and compute the radar cross section (see (7-74)) when $L = \lambda/2$. Compare your result with Fig. 7-16.

7.2-2 What are the units of the generalized voltage, current, and impedance matrix elements in (7-27)?

7.3-1 Expand the computer program in Prob. 7.2-1 to use pulse weighting functions in a fashion similar to that in (7-35).

7.4-1 Show that (7-42) and (7-43) follow from (7-39) and (7-40), respectively.

7.5-1 Derive (7-52) from (7-42).

7.5-2 Derive (7-55).

7.5-3 Derive (7-59) from (7-55) and (7-12).

7.5-4 Show that the radial components associated with the electric field in (7-59) is

$$E_r = \frac{-j\eta}{4\pi\rho \sin(\beta \Delta z_n)} \left[(z_{n-1} - z) \frac{e^{-j\beta R_{n-1}}}{R_{n-1}} - 2(z_n - z) \cos(\beta \Delta z_n) \frac{e^{-j\beta R_n}}{R_n} + (z_{n+1} - z) \frac{e^{-j\beta R_{n+1}}}{R_{n+1}} \right]$$

7.6-1 Derive (7-72) from the far-field relationship $\mathbf{E} = j\omega\mu A_z \sin \theta \hat{\theta}$, as in (1-90).

7.6-2 Derive (7-73) starting with the Poynting theorem.

7.7-1 Derive (7-78) from (7-43).

7.7-2 Starting with the electric vector potential and (7-80) derive (7-81).

7.8-1 Verify (7-87) using the algorithm in (7-88).

7.9-1 Extend the LPDA analysis in Section 7.9.2 to an array of M LPDA antennas as in [18].

7.9-2 In Section 7.9.2 we obtained a solution to the LPDA. One of the important points in that solution is the determination of $[Y_A]$ in the manner indicated in equations (7-96) to (7-99). Had we wished to then find $[Z_A]$, we could have obtained it from $[Z_A] = [Y_A]^{-1}$. Denote this method A. Suppose instead we find $[Z_A]$ by considering the two dipole mutual impedance problem as Carrel [17] and Kyle [18] did. For example, $[Z_A]_{mn}$ is obtained by temporarily removing all dipoles except m and n from the system and then calculating $[Z_A]_{mn}$. Denote this method B.

(a) Will $[Z_A]$ obtained by method A be the same as that obtained by method B? Why?

(b) The following question refers to the concepts implied by part (a). When we calculate a moment method impedance matrix $[Z_{mn}]$, in what way does that calculation process relate to method B above?

7.10-1 Show that (7-106) is valid.

7.11-1 Derive (7-109) from (7-107).

7.11-2 Sketch a wire-grid model for a square plate 1λ by 1λ . If pulse expansion functions are to be used, how many unknowns will your model have?

7.11-3 Sketch a wire-grid model for a quarter-wavelength monopole at the center of a circular ground plane of $\lambda/4$ radius. If pulse expansion functions are used, how many unknowns will your model have? If piecewise sinusoidal functions are used, how many unknowns will your model have?

7.11-4 Derive (7-115) from (7-112).

7.11-5 Derive (7-125) from (7-122).

7.11-6 Derive (7-134) from (7-125).

7.11-7 In Sections 7.3 and 7.11 we used pulse functions in the moment method. Expansion functions such as the pulse function (and piecewise sinusoidal function) are often called subdomain expansion functions because each expansion function is generally non-zero on only a relatively small part of the radiating body.

There is another type of expansion function called entire-domain expansion functions. In this case, the function is generally nonzero over the entire radiating body and the concept of segments is not used. For example, if one were to treat the dipole with an entire-domain expansion function (i.e., a Fourier series), one could write for the current

$$I(z') = \sum_{n=1}^N I_n F_n(z')$$

where

$$F_n(z') = \cos(2n-1) \frac{\pi z'}{L}, \quad -\frac{L}{2} \leq z' \leq \frac{L}{2}$$

(Note that each term in $F_n(z')$ goes to zero at the ends of the dipole.)

- (a) Sketch the first two terms in the series for $F_n(z')$.
- (b) If there are N terms and N match points (i.e., a point-matching solution), write an expression for Z_{mn} using the notation in Sections 7.2 and 7.3.
- (c) Give a physical interpretation of Z_{25} (i.e., complete a statement similar to the following: Z_{25} represents the field from _____ at _____).

8

APERTURE ANTENNAS

An antenna that has as part of its structure an aperture through which the electromagnetic fields pass is referred to as an **aperture antenna**. An obvious example of an aperture antenna is an open-ended waveguide. Slotted waveguides and horns are other examples. Although an effective aperture value can be calculated for any antenna (see Section 1.10), this chapter will deal with antennas that possess an obvious physical aperture. In the first section general principles will be developed for calculating the radiation patterns from any aperture antenna. Subsequent discussions will focus on rectangular and circular aperture shapes. The properties of specific antennas such as horns and circular parabolic reflectors then follow naturally. As in preceding chapters, the theoretical derivations lead to an accurate description of the antenna parameters, as well as to design techniques. Both rigorous and approximate methods of gain calculation are also presented in this chapter.

8.1 RADIATION FROM APERTURES AND HUYGENS' PRINCIPLE

Although aperture antennas were really not widely used until the World War II period, the basic concepts were available in 1690 when Huygens explained, in a simple way, the bending (or diffraction) of light waves around an object. This

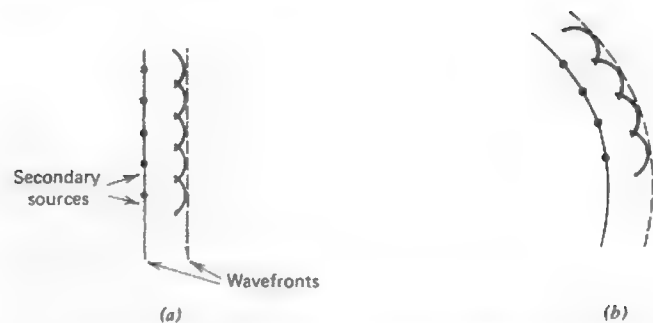


Figure 8-1 Secondary waves used to construct successive wavefronts. (a) Plane wave. (b) Spherical wave.

was accomplished by viewing each point of a wavefront as a secondary source of spherical waves. The next wavefront is the envelope of these secondary waves. Figure 8-1 shows how a plane wave and a spherical wave can be constructed from secondary waves. The envelope of secondary waves forms the new wavefront. Geometrical optics (ray-tracing) predicts that light shining through a slit in a screen will have a lit region and a completely dark shadow region with a sharp boundary between them. This is only approximately true, even for very large (relative to a wavelength) apertures. Using the secondary source concept beginning at the aperture, the secondary waves will lead to a spreading of the waves and a smooth blending of the lit and shadow regions. This diffraction effect is illustrated in Fig. 8-2 for a slit in an opaque screen with a plane wave incident on it.

This principle has been put on a theoretical foundation and is known as *Huygens' principle* or the *equivalence principle*. Let electromagnetic sources be contained in a volume V bounded by surface S with outward normal \hat{n} (see Fig. 8-3a).¹ The fields E and H exterior to S can be found by removing the sources in V and placing the following surface current densities on S (see Fig. 8-3b)

$$J_s = \hat{n} \times H(S) \quad \text{on } S \quad (8-1)$$

$$M_s = E(S) \times \hat{n} \quad \text{on } S \quad (8-2)$$

where $H(S)$ and $E(S)$ are the fields produced by the original sources and evaluated at the surface S . Thus, with a knowledge of the tangential fields over a surface due to the original sources, we can find the fields everywhere external to the surface through the use of equivalent surface current densities J_s and M_s (often referred to as the Huygens' source).

¹ In this chapter the upper case symbols V and S will be used to denote volume and surface

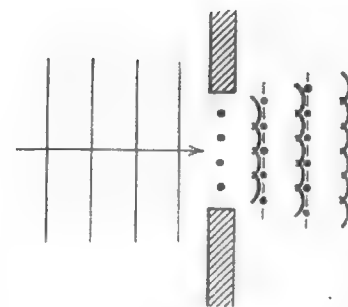


Figure 8-2 Plane wave incident on a slit in a screen. The edge diffraction leads to spreading of the radiation from the slit.

It is relatively easy to explain how this form of the equivalence theorem with zero fields inside (referred to as Love's equivalence principle) is obtained. This problem, as in any electromagnetic problem, is described by Maxwell's equations plus the boundary conditions. From differential equation theory we know that a solution that satisfies a differential equation and the boundary conditions is the solution. The solution to Maxwell's equations (including the sources) and the boundary conditions is unique. In the original problem of Fig. 8-3a, the fields which satisfy Maxwell's equations in the region exterior to volume V and which satisfy boundary conditions along S are unique. As long as the sources exterior to V and the boundary conditions along S are not changed, the solution E, H will not change. In the equivalent problem the sources exterior to V are not changed, since there are none. Also, the boundary conditions are not changed, as will now be explained. In the original problem the fields along the boundary are $E(S)$ and $H(S)$. In the equivalent problem the fields inside V are zero and the surface currents are given by (8-1) and (8-2). For the boundary conditions to be the same, the difference between the interior and exterior fields (tangential to and evaluated at S) must be the same as in the original problem. The boundary conditions (1-22) and (1-23) yield $\hat{n} \times (H(S) - 0) = J_s$ and $(E(S) - 0) \times \hat{n} = M_s$, which are identical to (8-1) and (8-2). Therefore, the boundary conditions are the same for the original and equivalent problems. Thus, the fields exterior to V are the same in the original and equivalent problems.

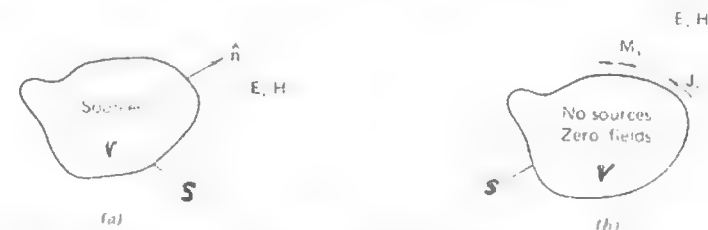


Figure 8-3 The equivalence principle. (a) Original problem (b) Equivalent problem.

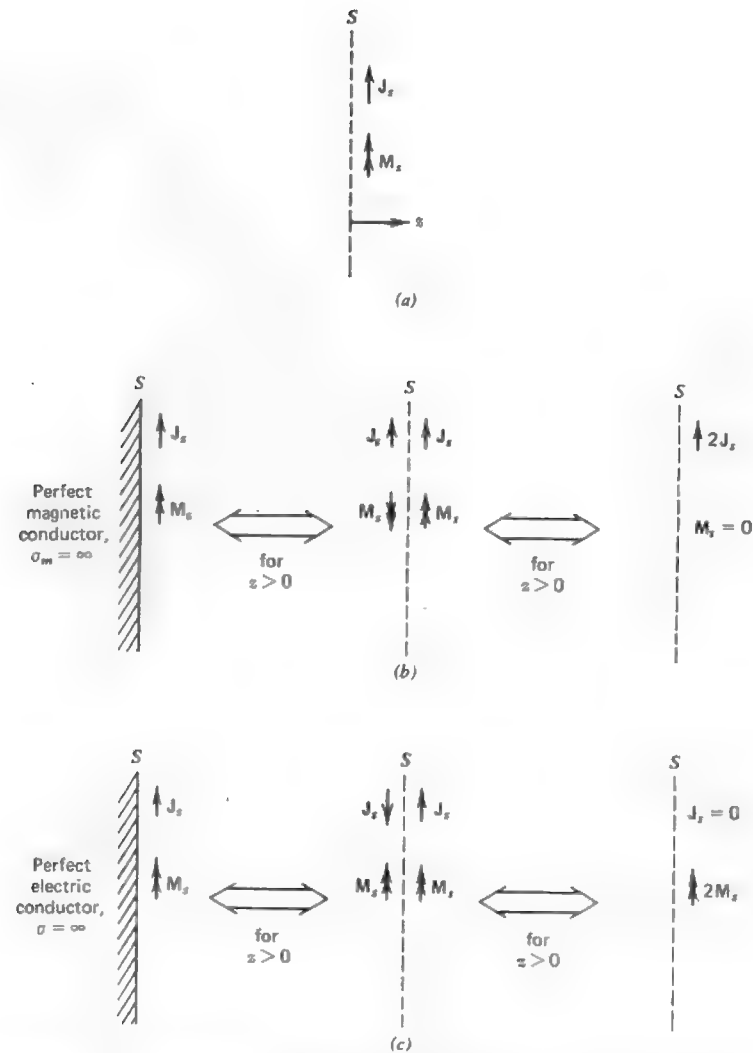


Figure 8-4 Equivalent current configurations for a planar aperture surface. (a) Both equivalent surface current densities acting in free space. (b) Equivalent electric current density alone. (c) Equivalent magnetic current density alone.

Since the fields inside S are zero in the equivalent problem, we may place a perfect conductor along part of this surface. M_z will vanish over that part because tangential E must be zero. Then J_z over this part of S equals the true electric surface current density induced on the perfect conductor and it radiates in the presence of the conductor. If there is an opening (or aperture) in the conductor, both currents J_z and M_z exist over the aperture portion.

In general it is difficult to calculate the radiation from sources over an arbitrary surface, which may have conducting portions. However, if the surface S is an infinite plane, the problem is simplified through the use of image theory. Many practical antennas, such as horns and parabolic reflectors, have a planar aperture, so this simplification is usually not restrictive. In any case, even though an antenna may not have a planar physical aperture, we can still define an equivalent planar aperture surface S ; this will be fruitful only if the tangential fields over S are known. We can find the fields in the half-space (say $z > 0$) which is exterior to the source half-space ($z < 0$) using the equivalent surface currents acting in free space. This equivalent system is shown in Fig. 8-4a.

The contribution to the radiation fields from the electric surface current density is found by evaluating the magnetic vector potential [see (1-99)]

$$\mathbf{A} = \frac{e^{-j\beta r}}{4\pi r} \iint_S \mathbf{J}_s(\mathbf{r}') e^{j\beta \hat{\mathbf{r}} \cdot \mathbf{r}'} dS' \quad (8-3)$$

The far-zone electric field from (1-102) is then found from the components of

$$\mathbf{E}_A = -j\omega\mu\mathbf{A} \quad (8-4)$$

which are transverse to $\hat{\mathbf{r}}$. The subscript A indicates that this field arises from the magnetic vector potential \mathbf{A} . By duality *electric vector potential* \mathbf{F} , which is associated with the magnetic current density, is found from²

$$\mathbf{F} = \frac{e^{-j\beta r}}{4\pi r} \iint_S \mathbf{M}_s(\mathbf{r}') e^{j\beta \hat{\mathbf{r}} \cdot \mathbf{r}'} dS' \quad (8-5)$$

The far-zone magnetic field arising from \mathbf{F} is the dual of (8-4), so

$$\mathbf{H}_F = -j\omega\epsilon\mathbf{F} \quad (8-6)$$

In both (8-4) and (8-6) we retain only those components that are transverse to $\hat{\mathbf{r}}$. The electric field associated with \mathbf{H}_F is found from the TEM relationship $\mathbf{E}_F = \eta\mathbf{H}_F \times \hat{\mathbf{r}}$. The total far-zone electric field of the equivalent current system of

² The symbol \mathbf{F} for magnetic vector potential should not be confused with the notation F for normalized radiation pattern.

Fig. 8-4a is then

$$\mathbf{E} = \mathbf{E}_A + \mathbf{E}_F = -j\omega\mu\mathbf{A} - j\omega\epsilon\eta\mathbf{F} \times \hat{\mathbf{r}} \quad (8-7)$$

where only transverse (θ and ϕ) components are retained.

The equivalent system of Fig. 8-4a involves both the electric and magnetic current densities. Computations would be reduced considerably if we had to deal with only one of the current densities. We will now show this is possible. Since the equivalent currents of Fig. 8-4a were obtained by using zero fields for $z < 0$, we can introduce materials in the left half-space without altering the fields there because they are zero. First we introduce a perfect magnetic planar conductor along surface S . The image currents shown in Fig. 8-4b are obtained by duality of images in a perfect electric ground plane; that is, a magnetic current parallel to the plane has an oppositely directed image and a parallel electric current has a similarly directed image. The fields for $z > 0$ are unchanged after removing the conducting plane and introducing the images, as shown in Fig. 8-4b. Since the currents and their images are adjacent to the plane S , we can add them vectorially to obtain the final equivalent system, which has a doubled electric surface current density and no magnetic surface current density. The radiation fields for $z > 0$ are then found as follows.

$$\mathbf{A} = \frac{e^{-j\beta r}}{4\pi r} \iint_S 2\mathbf{J}_s(\mathbf{r}') e^{j\beta \hat{\mathbf{r}} \cdot \mathbf{r}'} dS' \quad (8-8)$$

and

$$\mathbf{E} = -j\omega\mu A_\theta \hat{\theta} - j\omega\mu A_\phi \hat{\phi}. \quad (8-9)$$

In a similar fashion a perfect electric ground plane can be introduced along S as shown in the left most part of Fig. 8-4c. Image theory renders the images shown. These images acting together yield a zero total electric surface current density and a magnetic surface current density of $2\mathbf{M}_s$. Then radiation fields for $z > 0$ are found from

$$\mathbf{F} = \frac{e^{-j\beta r}}{4\pi r} \iint_S 2\mathbf{M}_s(\mathbf{r}') e^{j\beta \hat{\mathbf{r}} \cdot \mathbf{r}'} dS' \quad (8-10)$$

and

$$\mathbf{H} = -j\omega\epsilon F_\theta \hat{\theta} - j\omega\epsilon F_\phi \hat{\phi}. \quad (8-11)$$

The equivalence theorem in a form most suitable to radiation pattern calculations will now be summarized. A coordinate system is selected such that the real antenna is in the half-space for $z < 0$. If the antenna has a planar physical

aperture the xy -plane is often chosen to be tangent to it; in any event the aperture plane S is the xy -plane. Then the fields for $z > 0$ can be found by using one of three equivalent surface current configurations acting in free space:

(a) \mathbf{J}_s and \mathbf{M}_s on plane S

or

(b) $2\mathbf{J}_s$ on plane S

or

(c) $2\mathbf{M}_s$ on plane S

where \mathbf{J}_s and \mathbf{M}_s are given by (8-1) and (8-2). The radiation fields for each of these equivalent systems are obtained from the following:

(a) \mathbf{A} and \mathbf{F} from (8-3) and (8-5). \mathbf{E} from (8-7).

or

(b) \mathbf{A} from (8-8). \mathbf{E} from (8-9).

or

(c) \mathbf{F} from (8-10). \mathbf{H} from (8-11).

So far no approximations have been introduced. Indeed, if the exact fields $\mathbf{E}(S)$ and/or $\mathbf{H}(S)$ are used in any of the above three procedures, exact results (within the limits of usual far-field approximations) will be obtained in the half-space $z > 0$. However, such exact knowledge of the fields over the entire plane S is rarely available. Usually at best it is possible to obtain only an approximate knowledge of the fields over a finite portion of the infinite aperture plane. One such approach is the popular *physical optics approximation*, in which it is assumed that the aperture fields \mathbf{E}_a and \mathbf{H}_a are those of the incident wave. It is usually assumed that these fields exist over only some finite portion S_a of the infinite plane S and the fields elsewhere over S are zero. In most cases the aperture surface S_a coincides with the physical aperture of the antenna. These approximations improve as the dimensions of the aperture relative to a wavelength increase.

The three solution procedures will now be simplified. Suppose that aperture fields \mathbf{E}_a and \mathbf{H}_a , which exist over and are tangent to some portion S_a of the infinite plane S , are known, perhaps by employing the physical optics approximation. The equivalent surface current densities are then

$$\mathbf{J}_s = \hat{\mathbf{n}} \times \mathbf{H}_a \quad (8-12)$$

$$\mathbf{M}_s = \mathbf{E}_a \times \hat{\mathbf{n}} \quad (8-13)$$

on S_a and zero elsewhere. Using these in (8-3) and (8-5) gives

$$\mathbf{A} = \frac{e^{-j\beta r}}{4\pi r} \hat{\mathbf{n}} \times \iint_{S_a} \mathbf{H}_a e^{j\beta \hat{\mathbf{r}} \cdot \mathbf{r}'} dS' \quad (8-14)$$

$$\mathbf{F} = -\frac{e^{-j\beta r}}{4\pi r} \hat{\mathbf{n}} \times \iint_{S_a} \mathbf{E}_a e^{j\beta \hat{\mathbf{r}} \cdot \mathbf{r}'} dS' \quad (8-15)$$

The integral in each of the above two equations is a two-dimensional Fourier transform. The two-dimensional Fourier transform of an aperture field plays an important role in radiation calculations for aperture antennas, in a way similar to the Fourier transform of the current distribution for line sources (see Chapter 4). We therefore make the following definitions for the integrals

$$\mathbf{P} = \iint_{S_a} \mathbf{E}_a e^{j\beta \hat{\mathbf{r}} \cdot \mathbf{r}'} dS' \quad (8-16)$$

$$\mathbf{Q} = \iint_{S_a} \mathbf{H}_a e^{j\beta \hat{\mathbf{r}} \cdot \mathbf{r}'} dS' \quad (8-17)$$

The aperture surface S_a is in the xy -plane, so $\mathbf{r}' = x'\hat{\mathbf{x}} + y'\hat{\mathbf{y}}$. This with $\hat{\mathbf{r}}$ in spherical coordinates from (A-4) in (8-16) and (8-17) yields

$$P_x = \iint_{S_a} E_{ax}(x', y') e^{j\beta(x' \sin \theta \cos \phi + y' \sin \theta \sin \phi)} dx' dy' \quad (8-18a)$$

$$P_y = \iint_{S_a} E_{ay}(x', y') e^{j\beta(x' \sin \theta \cos \phi + y' \sin \theta \sin \phi)} dx' dy' \quad (8-18b)$$

$$Q_x = \iint_{S_a} H_{ax}(x', y') e^{j\beta(x' \sin \theta \cos \phi + y' \sin \theta \sin \phi)} dx' dy' \quad (8-19a)$$

$$Q_y = \iint_{S_a} H_{ay}(x', y') e^{j\beta(x' \sin \theta \cos \phi + y' \sin \theta \sin \phi)} dx' dy' \quad (8-19b)$$

Now, (8-14) and (8-15) together with $\hat{\mathbf{n}} = \hat{\mathbf{z}}$ reduce to

$$\mathbf{A} = \frac{e^{-j\beta r}}{4\pi r} (-Q_y \hat{\mathbf{x}} + Q_x \hat{\mathbf{y}}) \quad (8-20)$$

$$\mathbf{F} = -\frac{e^{-j\beta r}}{4\pi r} (-P_y \hat{\mathbf{x}} + P_x \hat{\mathbf{y}}) \quad (8-21)$$

Expressing $\hat{\mathbf{x}}$ and $\hat{\mathbf{y}}$ in spherical coordinates as in (A-1) and (A-2), and retaining only the θ - and ϕ -components gives

$$\mathbf{A} = \frac{e^{-j\beta r}}{4\pi r} [\hat{\theta} \cos \theta (Q_x \sin \phi - Q_y \cos \phi) + \hat{\phi} (Q_x \cos \phi + Q_y \sin \phi)] \quad (8-22)$$

$$\mathbf{F} = -\frac{e^{-j\beta r}}{4\pi r} [\hat{\theta} \cos \theta (P_x \sin \phi - P_y \cos \phi) + \hat{\phi} (P_x \cos \phi + P_y \sin \phi)] \quad (8-23)$$

Using these in (8-7) yield the final radiation field components

$$(a) E_\theta = j\beta \frac{e^{-j\beta r}}{4\pi r} [P_x \cos \phi + P_y \sin \phi + \eta \cos \theta (Q_y \cos \phi - Q_x \sin \phi)] \quad (8-24a)$$

$$E_\phi = j\beta \frac{e^{-j\beta r}}{4\pi r} [\cos \theta (P_y \cos \phi - P_x \sin \phi) - \eta (Q_y \sin \phi + Q_x \cos \phi)] \quad (8-24b)$$

In a similar fashion the other two equivalent systems reduce to

$$(b) E_\theta = j\beta \eta \frac{e^{-j\beta r}}{2\pi r} \cos \theta (Q_y \cos \phi - Q_x \sin \phi) \quad (8-25a)$$

$$E_\phi = -j\beta \eta \frac{e^{-j\beta r}}{2\pi r} (Q_y \sin \phi + Q_x \cos \phi) \quad (8-25b)$$

$$(c) E_\theta = j\beta \frac{e^{-j\beta r}}{2\pi r} (P_x \cos \phi + P_y \sin \phi) \quad (8-26a)$$

$$E_\phi = j\beta \frac{e^{-j\beta r}}{2\pi r} \cos \theta (P_y \cos \phi - P_x \sin \phi) \quad (8-26b)$$

If the exact aperture fields over the entire infinite aperture plane are used, the three formulations of (8-24), (8-25), and (8-26) each yield the same result. Use of the exact aperture fields leads to equal contributions arising from the electric and magnetic currents [1]. Therefore, the equivalent system using both current types, as in (8-24), gives zero total field for $z < 0$ because $\pi/2 \leq \theta \leq \pi$ renders $\cos \theta$ negative, and the contributions cancel as guaranteed by the equivalence theorem. However, the single current systems of (8-25) and (8-26) do not yield zero fields for $z < 0$. This is an expected result since image theory was involved in the development of these, and identical fields are obtained only in the region $z > 0$.

In practice only approximate information about the aperture fields is available, such as obtained from the physical optics approximation. Then the three formulations give different results. The accuracy of the three results depends on the accuracy of the aperture fields, but the differences are usually not significant. It is obvious that the equivalent system using both equivalent currents involves several more calculations than those using only one equivalent

current. Thus (8-25) or (8-26) are often used in preference to (8-24). Further, it is customary to work with the aperture electric field, so the formulation of (8-26) is very commonly used.

It can be shown (see Prob. 8.1-5) that the trigonometric functions appearing in (8-24) to (8-26) actually describe the projections of the aperture equivalent surface current densities onto the plane containing the far-field components (the $\theta\phi$ -plane). The element factor associated with the radiation fields from a line source is interpreted in a similar fashion. For aperture field expressions the trigonometric functions that multiply the radiation integrals are often referred to as obliquity factors.

Example 8-1. Slit in an Infinite Conducting Plane

The aperture antenna calculation procedures and the physical optics approximation can be illustrated rather simply for a plane wave normally incident on a slit in an infinite perfectly conducting plane as shown in Fig. 8-5. This is the same problem as in Fig. 4-6a, except for a coordinate system change. The physical optics approximation leads us to assume that the incident field $E_i = \hat{y}E_o e^{-j\beta z}$ associated with the plane wave propagating in the $+z$ -direction renders the field over the physical aperture, so

$$E_a = \begin{cases} \hat{y}E_o & |y| \leq \frac{L}{2}, \quad z = 0 \\ 0 & \text{elsewhere.} \end{cases} \quad (8-27)$$

The magnetic current formulation is appropriate in this case because the aperture electric field is zero over the perfectly conducting portion of the aperture surface. This is essentially a one-dimensional problem because the aperture field is uniform in the x -direction; and then the radiation fields will not change with position along the x -direction. We are thus concerned only with the yz -plane ($\phi = 90^\circ$), and since the aperture field is only y -directed, (8-18) reduces to

$$P = \hat{y}P_y = \hat{y} \int_{-L/2}^{L/2} E_o e^{j\beta y' \sin \theta} dy' = \hat{y}E_o L \frac{\sin[(\beta L/2)\sin \theta]}{(\beta L/2)\sin \theta}. \quad (8-28)$$

The total radiation electric field components are then found from (8-26) with $\phi = 90^\circ$ as

$$E_\theta = j\beta \frac{e^{-j\beta r}}{2\pi r} E_o L \frac{\sin[(\beta L/2)\sin \theta]}{(\beta L/2)\sin \theta}; \quad E_\phi = 0. \quad (8-29)$$

Notice that on the conducting plane ($\theta = 90^\circ$) E_θ is nonzero; but, this is acceptable because it is normal to the conductor. The normalized radiation pattern is

$$F(\theta) = \frac{\sin[(\beta L/2)\sin \theta]}{(\beta L/2)\sin \theta}. \quad (8-30)$$

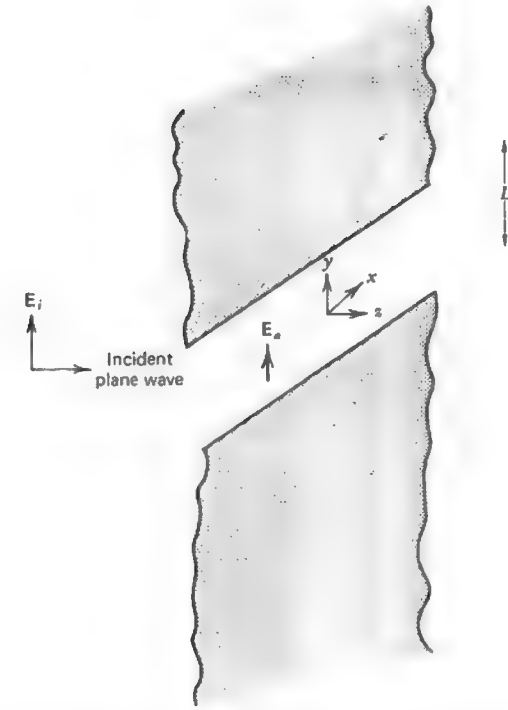


Figure 8-5 Plane wave incident on a slit in an infinite conducting plane. The slit is infinite in the x -direction and is L wide in the y -direction.

8.2 RECTANGULAR APERTURES

There are several antenna types which have a physical aperture that is rectangular in shape. For example, many horn antennas have rectangular apertures. Another example is a rectangular slot in a metallic source structure such as a waveguide. In this section we will present some general principles about rectangular apertures that have uniform and tapered excitations. In Section 8.4 these principles are applied to rectangular aperture horn antennas.

8.2.1 The Uniform Rectangular Aperture

A general rectangular aperture is shown in Fig. 8-6. It is excited in an idealized fashion such that the aperture fields are confined to the L_x by L_y region. If the aperture fields are uniform in phase and amplitude across the physical aperture,

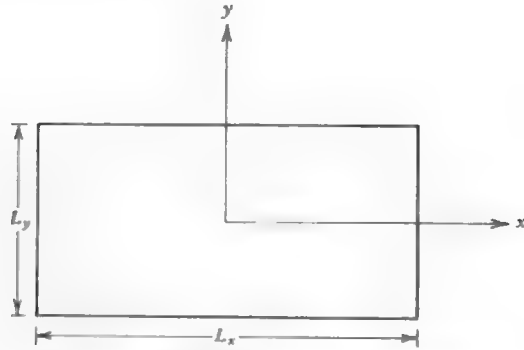


Figure 8-6 The rectangular aperture.

it is referred to as a *uniform rectangular aperture*. Suppose the aperture electric field is y-polarized, then the uniform rectangular aperture electric field is

$$\mathbf{E}_a = E_0 \hat{\mathbf{y}} \quad |x| \leq \frac{L_x}{2}, \quad |y| \leq \frac{L_y}{2}. \quad (8-31)$$

Then from (8-18b)

$$\begin{aligned} P_y &= E_0 \int_{-L_x/2}^{L_x/2} e^{j\beta x' \sin \theta \cos \phi} dx' \int_{-L_y/2}^{L_y/2} e^{j\beta y' \sin \theta \sin \phi} dy' \\ &= E_0 L_x L_y \frac{\sin[(\beta L_x/2)u]}{(\beta L_x/2)u} \frac{\sin[(\beta L_y/2)v]}{(\beta L_y/2)v} \end{aligned} \quad (8-32)$$

where we have introduced the pattern variables

$$u = \sin \theta \cos \phi, \quad v = \sin \theta \sin \phi. \quad (8-33)$$

The complete radiation fields are found from (8-26) as

$$E_\theta = j\beta \frac{e^{-j\beta r}}{2\pi r} E_0 L_x L_y \sin \phi \frac{\sin[(\beta L_x/2)u]}{(\beta L_x/2)u} \frac{\sin[(\beta L_y/2)v]}{(\beta L_y/2)v} \quad (8-34a)$$

$$E_\phi = j\beta \frac{e^{-j\beta r}}{2\pi r} E_0 L_x L_y \cos \theta \cos \phi \frac{\sin[(\beta L_x/2)u]}{(\beta L_x/2)u} \frac{\sin[(\beta L_y/2)v]}{(\beta L_y/2)v}. \quad (8-34b)$$

These fields are rather complicated functions of θ and ϕ , but fortunately they simplify in the principal planes. In the *E*-plane (*yz*-plane) $\phi = 90^\circ$, and (8-34) reduces to

$$E_\theta = j\beta \frac{e^{-j\beta r}}{2\pi r} E_0 L_x L_y \frac{\sin[(\beta L_y/2)\sin \theta]}{(\beta L_y/2)\sin \theta} \quad (\text{E-plane}). \quad (8-35)$$

In the *H*-plane (*xz*-plane) $\phi = 0^\circ$, and (8-34) becomes

$$E_\phi = j\beta \frac{e^{-j\beta r}}{2\pi r} E_0 L_x L_y \cos \theta \frac{\sin[(\beta L_x/2)\sin \theta]}{(\beta L_x/2)\sin \theta} \quad (\text{H-plane}). \quad (8-36)$$

The normalized forms of these principal plane patterns are

$$F_E(\theta) = \frac{\sin[(\beta L_y/2)\sin \theta]}{(\beta L_y/2)\sin \theta} \quad (8-37)$$

$$F_H(\theta) = \cos \theta \frac{\sin[(\beta L_x/2)\sin \theta]}{(\beta L_x/2)\sin \theta}. \quad (8-38)$$

For large apertures ($L_x, L_y \gg \lambda$) the main beam is narrow and the $\cos \theta$ factor is negligible, and the principal plane patterns are both of the form $\sin(x)/x$ which we have encountered several times before, as for example with the uniform line source. By neglecting the obliquity factors in (8-34) the normalized pattern factor for the uniform rectangular aperture is

$$f(u, v) = \frac{\sin[(\beta L_x/2)u]}{(\beta L_x/2)u} \frac{\sin[(\beta L_y/2)v]}{(\beta L_y/2)v} \quad (8-39)$$

which is the normalized version of P_y in (8-32).

The half-power beamwidths in the principal planes follow from the line source result in (4-14). In *xz*- and *yz*-planes the beamwidth expressions are

$$\text{HP}_x = 0.886 \frac{\lambda}{L_x}, \quad \text{HP}_y = 0.886 \frac{\lambda}{L_y}. \quad (8-40)$$

Example 8-2. A 20λ by 10λ Uniform Rectangular Aperture

The complete pattern for a uniform rectangular aperture which has $L_x = 20\lambda$ and $L_y = 10\lambda$ is from (8-39)

$$f(u, v) = \frac{\sin(20\pi u)}{20\pi u} \frac{\sin(10\pi v)}{10\pi v}. \quad (8-41)$$

The contour plot of this pattern is shown in Fig. 8-7. The principal plane patterns, which are profiles along the u and v axes of Fig. 8-7, are shown in Fig. 8-8. The aperture of Fig. 8-6 has a ratio $L_x/L_y = 2$ as in this example. Notice that the wide aperture dimension, L_x , leads to a narrow beamwidth in that direction (along the u -axis). The half-power beamwidth in the *xz*-plane from (8-40) is $\text{HP}_x = 0.0443 \text{ rad} = 2.54^\circ$, and in the *yz*-plane $\text{HP}_y = 0.0886 \text{ rad} = 5.08^\circ$.

The transformation from θ and ϕ to u and v given by (8-33) is essentially a collapsing of the spherical surface of unit radius described by θ and ϕ onto a planar surface through the equator, giving a circular disk of unit radius. There is

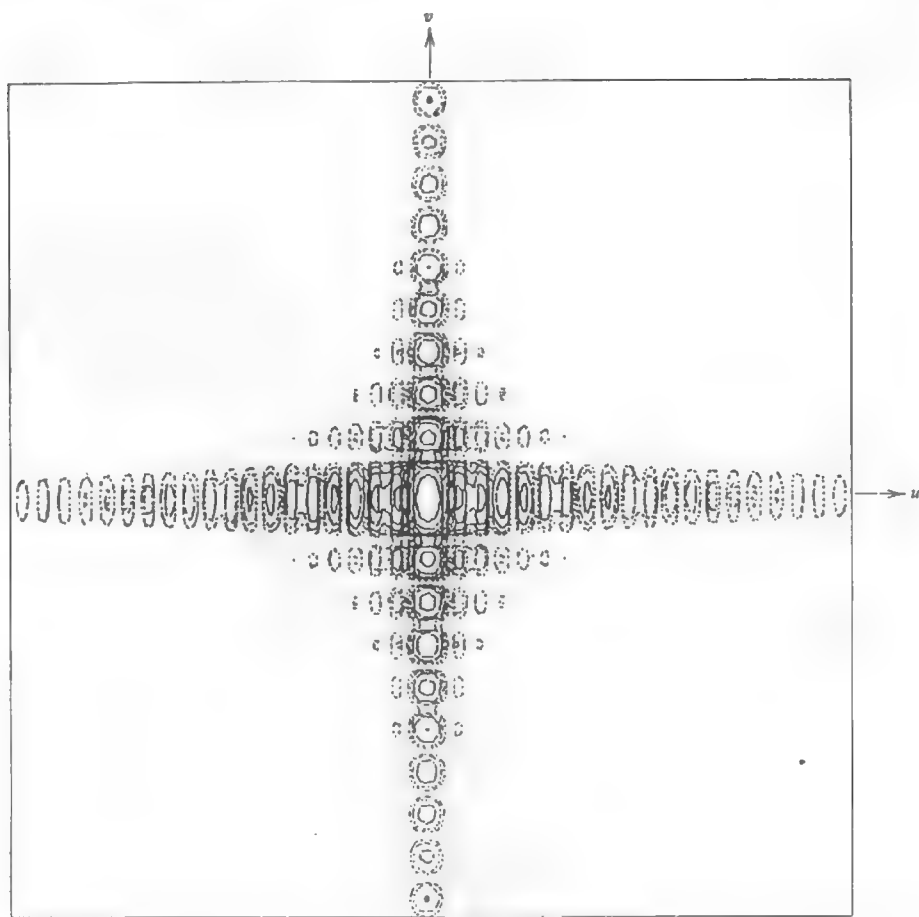


Figure 8-7 Contour plot of the pattern from a uniform amplitude, uniform phase rectangular aperture ($L_x = 20\lambda$, $L_y = 10\lambda$). The solid contour levels are 0, -5, -10, -15, -20, -25, -30 dB. The dashed contour levels are -35 and -40 dB. Principal plane profiles are shown in Fig. 8-8.

an ambiguity here because points on the upper hemisphere ($\theta < \pi/2$) project onto the top of the u, v disk, and points on the lower hemisphere map onto the bottom of the u, v disk. This is not a problem when using our equivalent current/image theory formulation, because the solution is valid only over the upper hemisphere ($z > 0$). The visible region in u and v corresponding to $\theta \leq \pi/2$ is

$$u^2 + v^2 = \sin^2 \theta \leq 1 \quad (8-42)$$

which follows from (8-33).

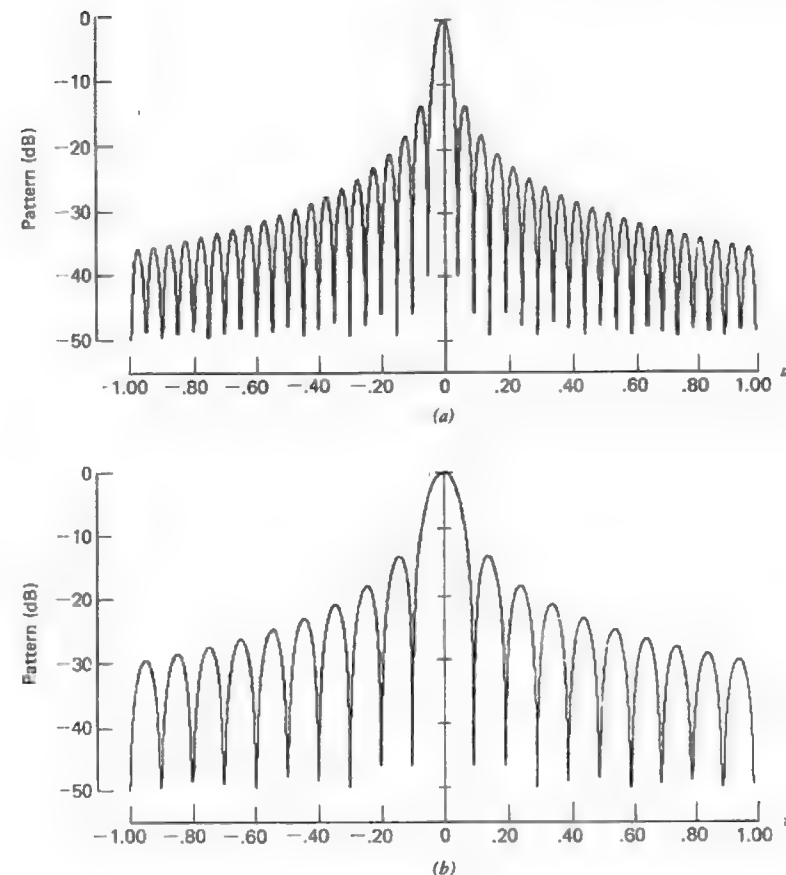


Figure 8-8 Principal plane patterns for a uniform amplitude, uniform phase rectangular aperture ($L_x = 20\lambda$, $L_y = 10\lambda$). The complete pattern is shown in Fig. 8-7. (a) The xz -plane pattern; $u = \sin \theta$. (b) The yz -plane pattern; $v = \sin \theta$.

Directivity calculations are greatly simplified when the u and v variables are used. The beam solid angle is

$$\Omega_A = \int_0^{2\pi} \int_0^{\pi/2} |F(\theta, \phi)|^2 d\Omega \quad (8-43)$$

where, as mentioned above, only radiation for $\theta \leq \pi/2$ is considered. The beam solid angle can be evaluated by integrating over the entire visible region in terms of u and v . First, consider the projection of $d\Omega$ onto the u, v plane; it is given by

$du dv = \cos \theta d\Omega$. From (8-42) it is seen that $\cos \theta = \sqrt{1 - u^2 - v^2}$. Therefore, $d\Omega = du dv / \sqrt{1 - u^2 - v^2}$ and (8-43) becomes

$$\Omega_A = \iint_{u^2 + v^2 \leq 1} |F(u, v)|^2 \frac{du dv}{\sqrt{1 - u^2 - v^2}}. \quad (8-44)$$

This is a general expression. For a large uniform phase aperture (L_x and $L_y \gg \lambda$) the radiation will be concentrated in a narrow region about $u = v = 0$ ($\theta = 0$). Then the square root in (8-44) is approximately one. Also, since the side lobes are very low we can extend the limits to infinity without appreciably affecting the value of the integral. Using these results and (8-39) for the uniform rectangular aperture in (8-44) yields

$$\Omega_A = \int_{-\infty}^{\infty} \frac{\sin^2[(\beta L_x/2)u]}{[(\beta L_x/2)u]^2} du \int_{-\infty}^{\infty} \frac{\sin^2[(\beta L_y/2)v]}{[(\beta L_y/2)v]^2} dv. \quad (8-45)$$

The following change of variables

$$u' = \frac{\beta L_x}{2} u = \frac{\beta L_x}{2} \sin \theta \cos \phi \quad (8-46a)$$

$$v' = \frac{\beta L_y}{2} v = \frac{\beta L_y}{2} \sin \theta \sin \phi \quad (8-46b)$$

leads to

$$\Omega_A = \frac{2}{\beta L_x} \frac{2}{\beta L_y} \int_{-\infty}^{\infty} \frac{\sin^2 u'}{(u')^2} du' \int_{-\infty}^{\infty} \frac{\sin^2 v'}{(v')^2} dv'. \quad (8-47)$$

Each integral above, see (F-12), equals π ; so

$$\Omega_A = \frac{4}{(2\pi/\lambda)^2 L_x L_y} \pi^2 = \frac{\lambda^2}{L_x L_y}. \quad (8-48)$$

The directivity of the rectangular aperture with uniform amplitude and phase is then

$$D = \frac{4\pi}{\Omega_A} = \frac{4\pi}{\lambda^2} L_x L_y. \quad (8-49)$$

From this expression the physical area of the aperture can be identified as $A_p = L_x L_y$. Comparing this to $D = 4\pi A_{em}/\lambda^2$ from (1-213) we see that the maximum effective aperture A_{em} equals the physical aperture A_p for the uniform rectangular aperture. This is true for any shape aperture with uniform excitation. Also note that for ideal apertures there are no ohmic losses (radiation efficiency $e = 1$), so gain equals directivity and $A_e = A_{em}$.

8.2.2 Tapered Rectangular Apertures

In the previous section we saw that the uniform rectangular aperture has an effective aperture equal to its physical aperture. In other words, uniform illumination leads to the most efficient use of the aperture area. It will be shown in Section 8.3 that uniform excitation amplitude for an aperture gives the highest directivity possible for all constant phase excitations of that aperture. In the antenna design problem high directivity is not the only parameter to be considered. Frequently low side lobes are very important. As we saw in Chapter 4, the side lobes can be reduced by tapering the excitation amplitude toward the edges of a line source. This is also true for two-dimensional apertures. In fact, many of the line source results can be directly applied to aperture problems.

To simplify our general discussion of rectangular aperture distributions, we shall omit the polarization of the aperture electric field, so that E_a can represent either the x - or y -component of the aperture field. Then (8-18) becomes

$$P = \iint_{S_a} E_a(x', y') e^{j\beta u x'} e^{j\beta v y'} dx' dy'. \quad (8-50)$$

Most practical aperture distributions are *separable* and can be expressed as a product of functions of each aperture variable alone:

$$E_a(x', y') = E_{a1}(x') E_{a2}(y'). \quad (8-51)$$

Then (8-50) reduces to

$$P = \int_{-L_x/2}^{L_x/2} E_{a1}(x') e^{j\beta u x'} dx' \int_{-L_y/2}^{L_y/2} E_{a2}(y') e^{j\beta v y'} dy'. \quad (8-52)$$

Each of these integrals is recognized as the pattern factor of a line source along the respective aperture directions. The normalized pattern factor for the rectangular aperture is then

$$f(u', v') = f_1(u') f_2(v') \quad (8-53)$$

where $f_1(u')$ and $f_2(v')$ arise from the first and second integrals in (8-52), which are essentially pattern factors of line source distributions along the x - and y -directions. Again here we have neglected any obliquity factors. The uniform rectangular aperture result corresponding to (8-53) is (8-39). It is obtained directly from $\sin(u)/u$ of (4-9) by using u' of (8-46a) in place of u for $f_1(u')$ and v' of (8-46b) in place of u for $f_2(v')$. Note the different definition of u in Chapter 4 and this chapter.

Thus, the pattern expression for a rectangular aperture distribution which is separable as in (8-51) is obtained by finding the patterns f_1 and f_2 corresponding to the distributions E_{a1} and E_{a2} , and then employing (8-53).

Example 8-3. The Open-Ended Rectangular Waveguide

Suppose the aperture electric field is cosine tapered in the x -direction, similar to (4-23), and is uniform in the y -direction. This particular example is similar to an open-ended rectangular waveguide operating in the dominant TE_{10} mode, which has a cosine distribution in the broad dimension and a uniform distribution in the narrow dimension [2]. f_1 is obtained from (4-27) by replacing u by u' and f_2 is obtained from $\sin(u)/u$ by replacing u by v' . Thus

$$f(u', v') = \frac{\cos u'}{1 - [(2/\pi)u']^2} \frac{\sin v'}{v'} \quad (8-54a)$$

or

$$f(u, v) = \frac{\cos[(\beta L_x/2)u]}{1 - [(2/\pi)(\beta L_x/2)u]^2} \frac{\sin[(\beta L_y/2)v]}{(\beta L_y/2)v}. \quad (8-54b)$$

The half-power beamwidths in the principal planes are controlled by the aperture distributions in the same planes, so from Table 4-2

$$HP_x = 1.19 \frac{\lambda}{L_x}, \quad HP_y = 0.886 \frac{\lambda}{L_y}. \quad (8-55)$$

The directivity (see Example 8-4 in Section 8.3) is 0.81 of a uniform aperture of the same size, or

$$D = 0.81 \frac{4\pi L_x L_y}{\lambda^2} = \frac{32 L_x L_y}{\pi \lambda^2}. \quad (8-56)$$

8.3 GAIN CALCULATIONS FOR APERTURE ANTENNAS

During the discussions of specific aperture antennas which follow, we shall have need for the gain calculation techniques presented in this section. The gain of aperture antennas can, in most cases, be estimated rather simply. Gain estimation methods will be presented after a discussion of more formal methods.

Maximum power gain (or simply gain) is found from directivity using (1-153) as

$$G = eD \quad (8-57)$$

where e is the radiation efficiency arising from ohmic losses on the antenna structure. Directivity from (1-143) is

$$D = \frac{4\pi U_m}{P_r} = \frac{4\pi}{\Omega_A} \quad (8-58)$$

where U_m is the maximum of the radiation intensity defined by

$$U(\theta, \phi) = \frac{1}{2\eta} [|E_\theta|^2 + |E_\phi|^2] r^2 = U_m |F(\theta, \phi)|^2. \quad (8-59)$$

Ω_A is the beam solid angle given by (8-43), and P_r is the total radiated power evaluated by integrating (8-59) over all radiation space.

If the tangential electric and magnetic aperture fields nearly form a plane wave, the radiation intensity expression simplifies. This assumption provides a good approximation if the aperture fields vary slowly relative to a wavelength and if the aperture phase is nearly uniform. The plane wave assumption for the aperture fields leads to

$$H_{ax} = -\frac{E_{ay}}{\eta} \quad \text{and} \quad H_{ay} = \frac{E_{ax}}{\eta}. \quad (8-60)$$

These applied to (8-18) and (8-19) yield

$$Q_x = -\frac{P_y}{\eta} \quad \text{and} \quad Q_y = \frac{P_x}{\eta}. \quad (8-61)$$

Using these and the general aperture radiation field expressions of (8-24) in (8-59) gives

$$U(\theta, \phi) = \frac{\beta^2}{32\pi^2\eta} (1 + \cos\theta)^2 [|P_x|^2 + |P_y|^2]. \quad (8-62)$$

The maximum value of this function, which corresponds to the main beam peak, for a uniform phase aperture occurs in the broadside direction ($\theta = 0$); so from (8-16)

$$U_m = \frac{\beta^2}{8\pi^2\eta} \left| \iint_{S_a} \mathbf{E}_a dS' \right|^2 \quad (8-63)$$

since $\hat{\mathbf{r}} \cdot \mathbf{r}' = 0$ in the broadside case, because $\hat{\mathbf{r}} = \hat{\mathbf{z}}$ and \mathbf{r}' is in the xy -plane.

Integration of (8-62) to obtain P_r is, in general, rather difficult. This can be avoided by observing that the total power reaching the far field must have passed through the aperture. Under the assumptions of (8-60) the power density in the aperture is $|\mathbf{E}_a|^2/2\eta$, and we can determine the radiated power from

$$P_r = \frac{1}{2\eta} \iint_{S_a} |\mathbf{E}_a|^2 dS'. \quad (8-64)$$

Substituting (8-63) and (8-64) in (8-58) gives a simplified, but powerful, directivity relationship

$$D = \frac{4\pi}{\lambda^2} \frac{\left| \iint_{S_a} \mathbf{E}_a dS' \right|^2}{\iint_{S_a} |\mathbf{E}_a|^2 dS'}. \quad (8-65)$$

Note the similarity of this result and that of (3-93) for a half-wavelength spaced linear array.

If the aperture distribution is of uniform amplitude ($E_a = E_o$), then (8-65) reduces to

$$D_u = \frac{4\pi}{\lambda^2} A_p \quad (8-66)$$

where A_p is the physical aperture area. This was shown to be true for the rectangular aperture by direct evaluation; see (8-49). Further, (8-66) is a general result. *The directivity of a uniform amplitude aperture is the highest obtainable from a uniform phase aperture.* This is true because the maximum of (8-65) occurs for a uniform illumination, which yields (8-66); see Prob. 8.3-2.

Example 8-4. The Open-Ended Rectangular Waveguide

To illustrate the aperture field integration method of determining directivity, we return to the open-ended waveguide operating in the TE_{10} mode as described in Example 8-3. The aperture field distribution is

$$E_a = \hat{y} E_o \cos \frac{\pi x'}{a} \quad -\frac{a}{2} \leq x' \leq \frac{a}{2} \quad (8-67)$$

where the waveguide (and, thus, the aperture) has wide and narrow dimensions of a and b ($L_x = a$ and $L_y = b$ in Fig. 8-6). Then

$$\left| \iint_{S_a} E_a dS' \right|^2 = \left(E_o \int_{-a/2}^{a/2} \cos \frac{\pi x'}{a} dx' \int_{-b/2}^{b/2} dy' \right)^2 = E_o^2 \left(\frac{2a}{\pi} \right)^2 b^2 \quad (8-68)$$

and

$$\iint_{S_a} |E_a|^2 dS' = E_o^2 \int_{-a/2}^{a/2} \cos^2 \frac{\pi x'}{a} dx' \int_{-b/2}^{b/2} dy' = E_o^2 \frac{a}{2} b. \quad (8-69)$$

Substituting these into (8-65) gives

$$D = \frac{4\pi}{\lambda^2} \left(\frac{8}{\pi^2} ab \right) = \frac{32 ab}{\pi \lambda^2}. \quad (8-70)$$

Gain is easily obtained from directivity using $G = eD$. For most aperture antennas the ohmic losses are very small, so

$$e \approx 1 \quad (8-71)$$

and therefore

$$G \approx D. \quad (8-72)$$

Many gain calculations, though, can be performed without first computing directivity by using (1-222)

$$G = \frac{4\pi}{\lambda^2} A_e \quad (8-73)$$

where A_e is the effective aperture. It is convenient for aperture antennas to relate effective aperture directly to the physical aperture area A_p of the antenna as

$$A_e = \epsilon_{ap} A_p \quad 0 \leq \epsilon_{ap} \leq 1 \quad (8-74)$$

where the *aperture efficiency* ϵ_{ap} is a measure of how efficiently the antenna physical area A_p is utilized. Once ϵ_{ap} is calculated or estimated, it is a simple matter to calculate gain from (8-73) and (8-74).

The aperture efficiency factor ϵ_{ap} represents many sources of efficiency reduction. In particular, it can be factored as

$$\epsilon_{ap} = e \epsilon_t \epsilon_1 \epsilon_2 \epsilon_3 \cdots \quad (8-75)$$

As mentioned above e is approximately unity. Exceptions to this are: if the antenna size is on the order of a wavelength or less, if a lossy transmission line is considered to be part of the antenna, and if lossy materials are an integral part of the antenna (such as in a dielectric lens antenna). The factor ϵ_t is the *aperture taper efficiency*, which represents intentional gain loss due strictly to the design aperture distribution. If an antenna is designed to have a directivity D_d , then ϵ_t gives the fractional loss in directivity, and gain, relative to the maximum attainable, that is, from the uniformly illuminated case; thus

$$\epsilon_t = \frac{D_d}{D_u}. \quad (8-76)$$

Values of ϵ_t were given in Section 4.2 for line sources.

The remaining factors $\epsilon_1 \epsilon_2 \epsilon_3 \cdots$ are referred to as *achievement factors*. They represent the fractional deviation from design directivity caused by the many changes from the design aperture illumination which occur when the antenna is constructed. They are a measure of how the directivity D of the actual antenna differs from the design directivity:

$$\epsilon_t \epsilon_1 \epsilon_2 \epsilon_3 \cdots = \frac{D}{D_u}. \quad (8-77)$$

Hence, the gain loss given by ϵ_{ap} in (8-75) is composed of an ohmic loss factor e and directivity loss factors $\epsilon_t, \epsilon_1, \epsilon_2, \epsilon_3, \dots$. For simple directly radiating antennas such as horns, slots, and so forth, the achievement factors are usually taken to be unity. Antennas involving more complex configurations usually have

achievement factor values less than unity. For example, reflector systems have several sources of gain loss, such as spillover, random surface errors, aperture blockage, and so forth. These will be discussed in Section 8.6.3.

Any of the efficiency factors in (8-75) can be expressed as a gain factor in decibels as

$$\epsilon_i(\text{dB}) = 10 \log \epsilon_i. \quad (8-78)$$

The gain "loss" would be the negative of this. For example, the aperture taper efficiency for Example 8-4 is $\epsilon_t = D_u/D_a = [(32/\pi)(ab/\lambda^2)]/[(4\pi/\lambda^2)ab] = 8/\pi^2 = 0.81$, so $\epsilon_t(\text{dB}) = -0.91$ dB. Gain in decibels is then computed as $G(\text{dB}) = 10 \log(4\pi A_p/\lambda^2) + e(\text{dB}) + \epsilon_t(\text{dB}) + \epsilon_i(\text{dB}) + \dots$. Recall that polarization mismatch factor p and impedance mismatch factor q are not included in aperture efficiency nor gain, but they play a role similar to the efficiency factors (as discussed in Section 1.11).

If the aperture efficiency is known, the gain can be calculated very simply, from (8-73) and (8-74), which give

$$G = \epsilon_{ap} \frac{4\pi}{\lambda^2} A_p = \epsilon_{ap} D_u. \quad (8-79)$$

The range of ϵ_{ap} for aperture antennas is about 30 to 90%. Horn antennas have values of ϵ_{ap} from about 40% to 80%. Optimum gain horn antennas typically have an aperture efficiency of 50%. The aperture efficiency of circular parabolic reflector antennas is about 55%.

The gain of an aperture antenna can be estimated very quickly using (8-79). If the aperture efficiency is unknown, a value of 50% is usually a good estimate. For a 20-dB gain antenna, if the aperture efficiency were really 60% instead of 50%, the error is only 0.8 dB.

Directivity, and thus gain, can also be estimated from a knowledge of the principal plane half-power beamwidths, HP_E and HP_H . If the main beam of the radiation pattern is relatively narrow and the side lobes are negligibly small, then all power in the main beam can be imagined to be redistributed such that it is uniform inside the half-power points and zero outside. Then the beam solid angle (see Fig. 1-13b) is approximated by a rectangular solid angle HP_E by HP_H , so $\Omega_A \approx \text{HP}_E \text{HP}_H$. The directivity is approximated as

$$D = \frac{4\pi}{\Omega_A} \approx \frac{4\pi}{\text{HP}_E \text{HP}_H} = \frac{41,253}{\text{HP}_E \text{HP}_H} \quad (8-80)$$

where HP_E and HP_H are the principal plane half-power beamwidths in degrees. Most pattern main beams have a smoothly varying cross section which is nearly elliptical, rather than rectangular. The area is then $(\pi/4)\text{HP}_E \text{HP}_H$ instead of $\text{HP}_E \text{HP}_H$, so

$$D \approx \frac{41,253}{(\pi/4)\text{HP}_E \text{HP}_H} = \frac{52,525}{\text{HP}_E \text{HP}_H}. \quad (8-81)$$

Actual antenna patterns will, of course, have side lobes which are not negligible. Comparisons with several horn and circular parabolic antennas in practice today reveal that the gain is fairly well approximated by 50% of the directivity in (8-81), so

$$G \approx \frac{26,000}{\text{HP}_E \text{HP}_H}. \quad (8-82)$$

This is an extremely simple yet very useful result.

Example 8-5. Pyramidal Horn Antenna

A pyramidal horn antenna (see Fig. 8-16a), with a rectangular aperture of width A and height B , designed for optimum gain has an aperture efficiency of 50%; so from (8-79)

$$G = 0.5 \frac{4\pi}{\lambda^2} AB. \quad (8-83)$$

As a specific example, a "standard gain horn" operating from 33 to 50 GHz has a measured gain of 24.7 dB ($G = 295.1$) at 40 GHz ($\lambda = 0.75$ cm). The aperture dimensions of this horn are $A = 5.54$ cm and $B = 4.55$ cm. Using these values of λ , A , and B in (8-83) gives $G = 281.6 = 24.5$ dB. The gain can also be estimated from the principal plane half-power beamwidths, measured at 40 GHz to be $\text{HP}_E = 9^\circ$ and $\text{HP}_H = 10^\circ$. Then (8-82) yields $G = 288.9 = 24.6$ dB. The gain values from both of these methods agree very well with the measured gain of 24.7 dB.

Example 8-6. Circular Parabolic Reflector Antenna

The aperture efficiency of a typical circular parabolic reflector antenna with diameter d is 55%, so (8-79) becomes

$$G = 0.55 \frac{4\pi}{\lambda^2} A_p = 0.55 \frac{4\pi}{\lambda^2} \left(\pi \frac{d^2}{4} \right) = 5.43 \frac{d^2}{\lambda^2}. \quad (8-84)$$

For a specific example, a 3.66-m (12-ft) circular reflector operating at 11.7 GHz ($\lambda = 2.564$ cm) has a measured value of $G = 50.4$ dB and $\text{HP}_E = \text{HP}_H = 0.5^\circ$. Again we will check our estimation formulas. First, (8-84) gives $G = 5.43(366/2.564)^2 = 110,644 = 50.4$ dB. Next, (8-82) yields $G = 26,000/(0.5)^2 = 104,000 = 50.2$ dB. Both of these estimates are in good agreement with the measured gain.

8.4 RECTANGULAR HORN ANTENNAS

Horn antennas are extremely popular antennas in the microwave region above about 1 GHz. Horns provide high gain, low VSWR, relatively wide bandwidth, low weight, and they are rather easy to construct. As an additional benefit the theoretical calculations for horn antennas are achieved very closely in practice.

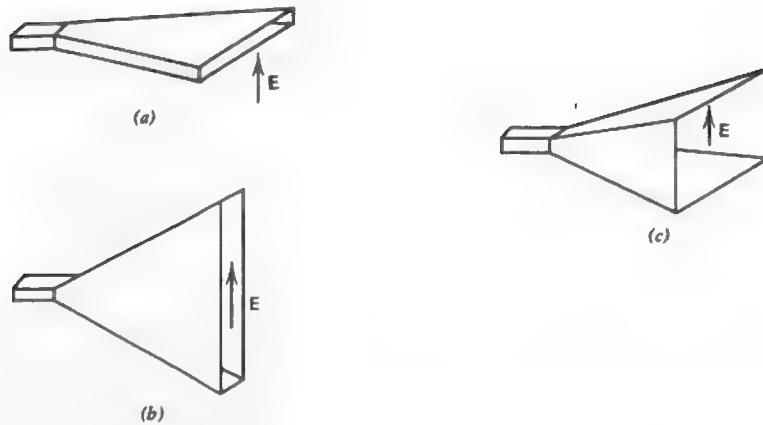


Figure 8-9 Rectangular horn antennas. (a) *H*-plane sectoral horn. (b) *E*-plane sectoral horn. (c) Pyramidal horn.

The three basic types of horn antennas which utilize rectangular geometry are illustrated in Fig. 8-9. These horns are fed by a rectangular waveguide which is oriented with its broad wall horizontal. For dominant waveguide mode excitation the *E*-plane is then vertical and the *H*-plane horizontal. If the horn serves to flare the broad wall dimension and leave the narrow wall of the waveguide unchanged, it is called an *H*-plane sectoral horn antenna as shown in Fig. 8-9a. On the other hand, if the horn serves to flare only the *E*-plane dimension it is called an *E*-plane sectoral horn antenna and is shown in Fig. 8-9b. When both waveguide dimensions are flared it is referred to as a pyramidal horn antenna, which is shown in Fig. 8-9c.

The operation of a horn antenna can be viewed as analogous to a megaphone, which is an acoustic horn radiator providing directivity for sound waves. The electromagnetic horn acts as a smooth transition from the waveguide mode to the free-space mode. This smooth transition reduces reflected waves and emphasizes the traveling waves. This traveling wave behavior, as we have seen with other antennas, leads to low VSWR and wide bandwidth.

Since the 1930s several horn antennas have been developed.³ In addition to rectangular horns discussed in this section, conical shaped horn antennas are used when connection to circular waveguide is required. Special purpose horns are those loaded with dielectric material or lined with metallic corrugations. Corrugated horn antennas, as well as other horn types, are very popular for feeds in reflector antenna systems.

³ See [3] for a collection of many papers on horn antennas.

8.4.1 The *H*-Plane Sectoral Horn Antenna

The *H*-plane sectoral horn of Fig. 8-10a is fed from a rectangular waveguide of interior dimensions a and b , with a the broadwall dimension. The aperture is of width A in the *H*-plane and height b in the *E*-plane. The *H*-plane cross section of Fig. 8-10b reveals the geometrical parameters we shall use. The following relationships for the geometry will be of use in subsequent analysis:

$$\ell_H^2 = R_1^2 + \left(\frac{A}{2}\right)^2 \quad (8-85a)$$

$$\alpha_H = \tan^{-1}\left(\frac{A}{2R_1}\right) \quad (8-85b)$$

$$R_H = (A - a)\sqrt{\left(\frac{\ell_H}{A}\right)^2 - \frac{1}{4}} \quad (8-86)$$

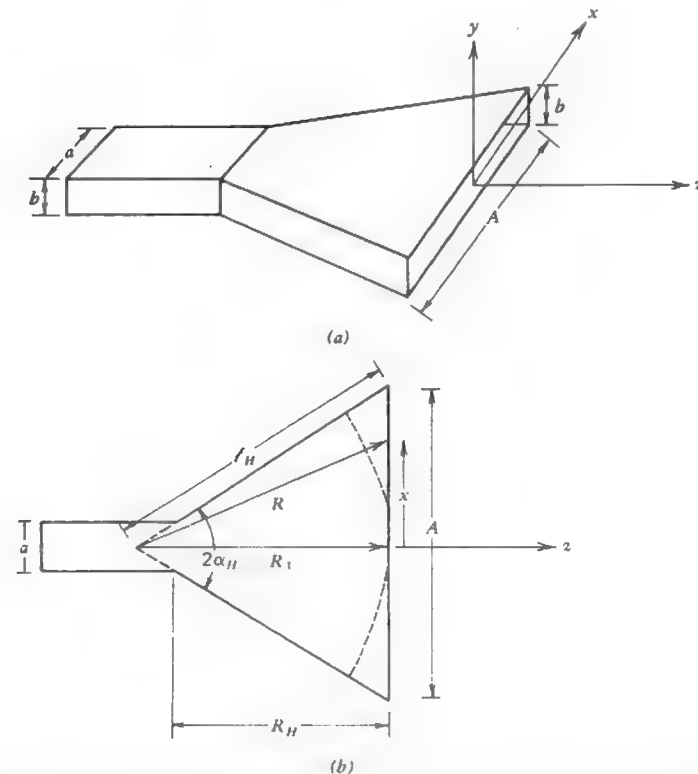


Figure 8-10 *H*-plane sectoral horn antenna. (a) Overall geometry. (b) Cross section through the *xz*-plane (*H*-plane).

It is an exercise to prove (8-86). The dimensions A and R_H (or ℓ_H or R_1) must be determined to allow construction of the horn. We shall investigate the principles of operation and then present design procedures for determining the horn dimensions.

The key to solving aperture antenna problems is to find the tangential fields over the aperture. The aperture plane for the H -plane sectoral horn shown in Fig. 8-10a will be taken to be the xy -plane. The aperture fields, of course, arise from the attached waveguide. As is usually the case in practice, we will assume that the waveguide carries the dominant TE_{10} rectangular waveguide mode. The transverse fields in the waveguide are then given by

$$E_y = E_o \cos \frac{\pi x}{a} e^{-j\beta_o z} \quad (8-87a)$$

$$H_x = -\frac{E_y}{Z_o} \quad (8-87b)$$

where $Z_o = \eta[1 - (\lambda/2a)^2]^{-1/2}$ is the waveguide characteristic impedance. The fields arriving at the aperture are essentially an expanded version of these waveguide fields. However, the waves arriving at different points in the aperture are not in phase because of the different path lengths. We will now determine this phase distribution.

The path length R from the (virtual) horn apex in the waveguide to the horn aperture increases toward the horn mouth edges. Thus waves arriving at aperture positions displaced from the aperture center lag in phase relative to those arriving at the center. The phase constant changes from that in the waveguide, β_o , to the free-space constant, β , as waves progress down the horn. But for relatively large horns the phase constant for waves in the vicinity of the aperture is approximately that of free space. The aperture phase variation in the x -direction is then given by

$$e^{-j\beta(R - R_1)} \quad (8-88)$$

The aperture phase is uniform in the y -direction. An approximate form for R using Fig. 8-10b is

$$\begin{aligned} R &= \sqrt{R_1^2 + x^2} = R_1 \left[1 + \left(\frac{x}{R_1} \right)^2 \right]^{1/2} \\ &\approx R_1 \left[1 + \frac{1}{2} \left(\frac{x}{R_1} \right)^2 \right] \end{aligned} \quad (8-89)$$

for $x \ll R_1$ which holds if $A/2 \ll R_1$. Then

$$R - R_1 \approx \frac{1}{2} \frac{x^2}{R_1} \quad (8-90)$$

The amplitude distribution is an expanded version of that in the waveguide, so it is a cosine taper in the x -direction. Using this fact and (8-90) in (8-88) leads to the aperture electric field distribution

$$E_{ay} = E_o \cos \frac{\pi x}{A} e^{-j\beta/2 R_1 x^2} \quad (8-91)$$

inside the aperture and zero elsewhere. The above phase distribution is often referred to as a quadratic phase error, since the deviation from a uniform phase condition varies as the square of the distance from the aperture center. This result can be derived more rigorously by representing the horn as a radial waveguide [4].

The quadratic phase error complicates the radiation integral, however the result is worth the effort. Substituting (8-91) into (8-18b) yields

$$P_y = E_o \int_{-A/2}^{A/2} \cos \frac{\pi x'}{A} e^{-j\beta/2 R_1 x'^2} e^{j\beta u x'} dx' \int_{-b/2}^{b/2} e^{j\beta v y'} dy' \quad (8-92)$$

After considerable work this reduces to

$$P_y = E_o \left[\frac{1}{2} \sqrt{\frac{\pi R_1}{\beta}} I(\theta, \phi) \right] \left[b \frac{\sin[(\beta b/2) \sin \theta \sin \phi]}{(\beta b/2) \sin \theta \sin \phi} \right] \quad (8-93)$$

where the factors in brackets correspond to each of the integrals in (8-92). The second factor is that for a uniform line source. The first involves the function

$$\begin{aligned} I(\theta, \phi) &= e^{j(R_1/2\beta)(\beta \sin \theta \cos \phi + \pi/A)^2} [C(s'_2) - jS(s'_2) - C(s'_1) + jS(s'_1)] \\ &\quad + e^{j(R_1/2\beta)(\beta \sin \theta \cos \phi - \pi/A)^2} [C(t'_2) - jS(t'_2) - C(t'_1) + jS(t'_1)] \end{aligned} \quad (8-94)$$

where

$$\begin{aligned} s'_1 &= \sqrt{\frac{1}{\pi \beta R_1}} \left(-\frac{\beta A}{2} - R_1 \beta u - \frac{\pi R_1}{A} \right) \\ s'_2 &= \sqrt{\frac{1}{\pi \beta R_1}} \left(\frac{\beta A}{2} - R_1 \beta u - \frac{\pi R_1}{A} \right) \\ t'_1 &= \sqrt{\frac{1}{\pi \beta R_1}} \left(-\frac{\beta A}{2} - R_1 \beta u + \frac{\pi R_1}{A} \right) \\ t'_2 &= \sqrt{\frac{1}{\pi \beta R_1}} \left(\frac{\beta A}{2} - R_1 \beta u + \frac{\pi R_1}{A} \right) \end{aligned} \quad (8-95)$$

and the functions $C(x)$ and $S(x)$ are Fresnel integrals defined in (F-17) and tabulated in [5].

The total radiation fields can now be obtained. Using (8-61) in (8-24) gives the far-zone electric field components

$$E_\theta = j\beta \frac{e^{-j\beta r}}{4\pi r} (1 + \cos \theta) \sin \phi P_y \quad (8-96a)$$

$$E_\phi = j\beta \frac{e^{-j\beta r}}{4\pi r} (1 + \cos \theta) \cos \phi P_y. \quad (8-96b)$$

These together with (8-93) give the complete radiated electric field

$$\mathbf{E} = j\beta E_0 b \sqrt{\frac{\pi R_1}{\beta}} \frac{e^{-j\beta r}}{4\pi r} \left(\frac{1 + \cos \theta}{2} \right) (\hat{\theta} \sin \phi + \hat{\phi} \cos \phi) \frac{\sin[(\beta b/2) \sin \theta \sin \phi]}{(\beta b/2) \sin \theta \sin \phi} I(\theta, \phi) \quad (8-97)$$

where $I(\theta, \phi)$ is still given by (8-94).

The complete radiation expression is rather cumbersome, so we will examine the principal plane patterns. In the E -plane $\phi = 90^\circ$, and the normalized form of (8-97) is

$$F_E(\theta) = \frac{1 + \cos \theta}{2} \frac{\sin[(\beta b/2) \sin \theta]}{(\beta b/2) \sin \theta} \quad (8-98)$$

The second factor is the pattern of a uniform line source of length b along the y -axis, as one would expect from the aperture distribution.

In the H -plane $\phi = 0^\circ$, and the normalized H -plane pattern is

$$F_H(\theta) = \frac{1 + \cos \theta}{2} \frac{I(\theta, \phi = 0^\circ)}{I(\theta = 0^\circ, \phi = 0^\circ)} \quad (8-99)$$

The H -plane pattern can be displayed rather simply using universal radiation pattern plots which are based on the maximum phase error across the aperture. The aperture distribution phase error as a function of position x is from (8-91)

$$\delta = \frac{\beta}{2R_1} x^2. \quad (8-100)$$

Since the maximum value of x is $A/2$ the maximum phase error is

$$\delta_{\max} = \frac{\beta}{2R_1} \left(\frac{A}{2} \right)^2 = 2\pi \frac{A^2}{8\lambda R_1} = 2\pi t \quad (8-101)$$

where t is defined to be

$$t = \frac{A^2}{8\lambda R_1} = \frac{1}{8} \left(\frac{A}{\lambda} \right)^2 \frac{1}{R_1/\lambda} \quad (8-102)$$

The function $I(\theta, \phi = 0^\circ)$ in (8-94) can be expressed in terms of t as

$$I(\theta, \phi = 0^\circ) = e^{j(\pi/8t)[(A/\lambda)\sin \theta + 1/2]^2} [C(s_2) - jS(s_2) - C(s_1) + jS(s_1)] + e^{j(\pi/8t)[(A/\lambda)\sin \theta - 1/2]^2} [C(t_2) - jS(t_2) - C(t_1) + jS(t_1)] \quad (8-103)$$

where

$$\begin{aligned} s_1 &= 2\sqrt{t} \left[-1 - \frac{1}{4t} \left(\frac{A}{\lambda} \sin \theta \right) - \frac{1}{8t} \right] \\ s_2 &= 2\sqrt{t} \left[1 - \frac{1}{4t} \left(\frac{A}{\lambda} \sin \theta \right) - \frac{1}{8t} \right] \\ t_1 &= 2\sqrt{t} \left[-1 - \frac{1}{4t} \left(\frac{A}{\lambda} \sin \theta \right) + \frac{1}{8t} \right] \\ t_2 &= 2\sqrt{t} \left[1 - \frac{1}{4t} \left(\frac{A}{\lambda} \sin \theta \right) + \frac{1}{8t} \right] \end{aligned} \quad (8-104)$$

This function is plotted in Fig. 8-11 for various values of t . It is normalized to the main beam peak for a zero phase error condition, which displays the directivity loss (reduction of the main beam peak) as the maximum phase error $2\pi t$ increases.

The curves in Fig. 8-11 are universal pattern plots from which antenna patterns can be derived for specific values of A , b , and λ . The H -plane plots (solid curves) are a function of $(A/\lambda)\sin \theta$. The E -plane plot (dashed curve) is the second factor of (8-98), and the abscissa for it is $(b/\lambda)\sin \theta$. The factor $(1 + \cos \theta)/2$ which appears in both pattern functions (8-98) and (8-99) is not included in Fig. 8-11. For most situations it has a small effect on the total pattern and may be neglected. Its effect, however, is easily included by adding $20 \log[(1 + \cos \theta)/2]$ to the corresponding pattern value for θ from the universal pattern. Note the E -plane plot of Fig. 8-11 has the -13.3 -dB side lobe level of a uniform line source pattern, and the H -plane constant phase ($t = 0$) plot has the -23 -dB side lobe level of a cosine-tapered line source pattern. As the phase error increases the H -plane pattern beamwidth and side lobes increase.

The directivity for an H -plane sectoral horn is obtained from the aperture integration method of (8-65) as

$$D_H = \frac{4\pi b R_1}{\lambda A} \{ [C(p_1) - C(p_2)]^2 + [S(p_1) - S(p_2)]^2 \} \quad (8-105a)$$

where

$$p_1 = \frac{1}{\sqrt{2}} \left[\frac{\sqrt{R_1/\lambda}}{A/\lambda} + \frac{A/\lambda}{\sqrt{R_1/\lambda}} \right], \quad p_2 = \frac{1}{\sqrt{2}} \left[\frac{\sqrt{R_1/\lambda}}{A/\lambda} - \frac{A/\lambda}{\sqrt{R_1/\lambda}} \right] \quad (8-105b)$$

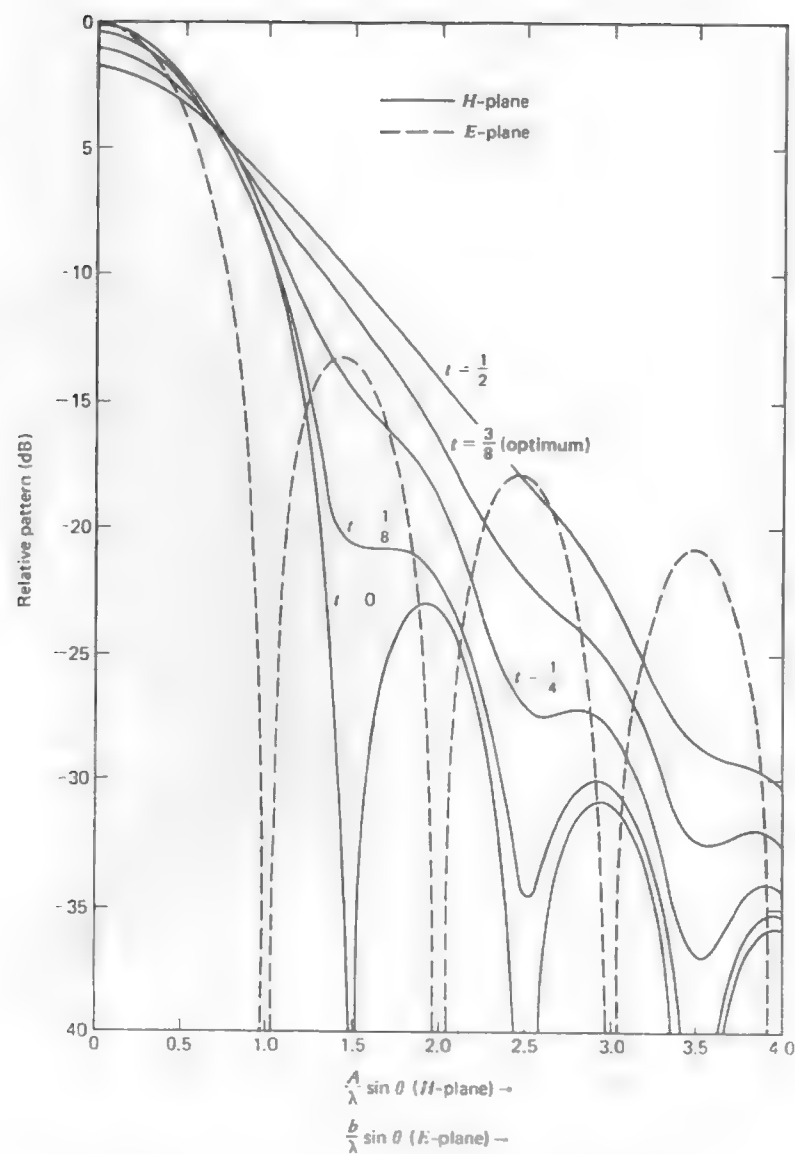


Figure 8-11 Universal radiation patterns for the principal planes of an H -plane sectoral horn as shown in Fig. 8-10. The factor $(1 + \cos \theta)/2$ is not included. (Reproduced, by permission, from [2]. © 1967 John Wiley.)

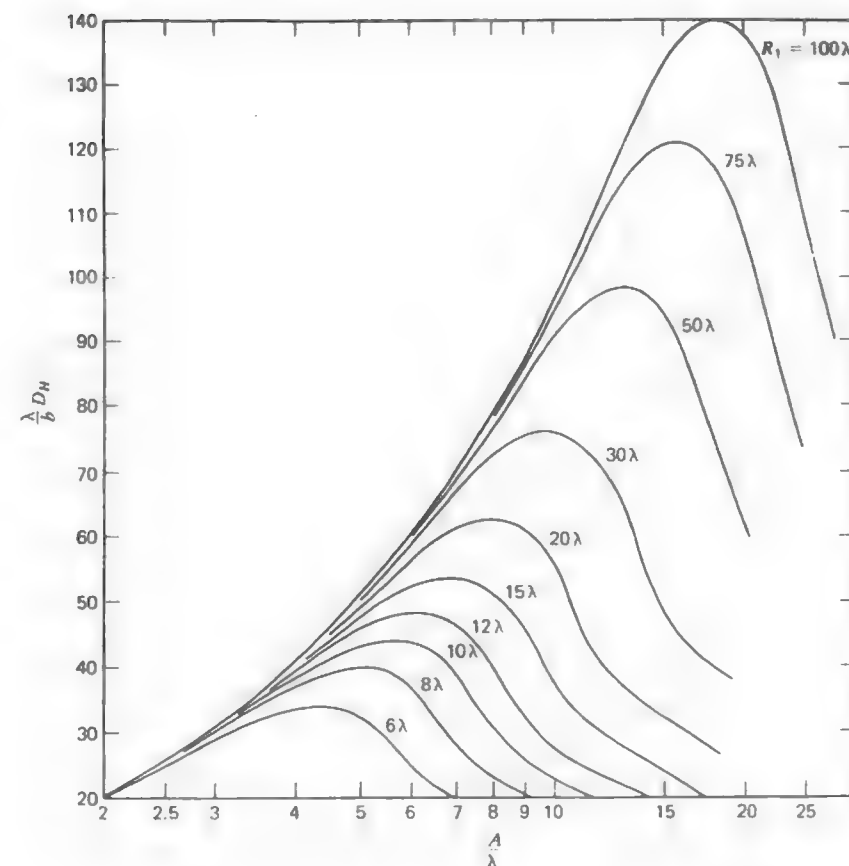


Figure 8-12 Universal directivity curves for an H -plane sectoral horn. For pyramidal horns the vertical axis values are $(\lambda/b)D_H$.

and $p_1 = -s_1' = t_2'$, $p_2 = s_2' = -t_1'$ in (8-95) for $u = 0$. A family of universal directivity curves is given in Fig. 8-12, where $\lambda D_H/b$ is plotted versus A/λ for various values of R_1/λ . Notice that for a given axial length R_1 , there is an optimum aperture width A corresponding to the peak of the appropriate curve. If values of A/λ corresponding to optimum operation are plotted versus R_1/λ , it is seen that a smooth curve with the equation $A/\lambda = \sqrt{3R_1/\lambda}$ passes through those points; so

$$A = \sqrt{3\lambda R_1} \quad (\text{optimum}). \quad (8-106)$$

For example, the value of A/λ for the peak of the $R_1/\lambda = 30$ curve of Fig. 8-12 is 9.5, and from (8-106) $A/\lambda = \sqrt{3R_1/\lambda} = \sqrt{3(30)} = 9.49$.

Equation (8-106) can be used to find the corresponding phase error parameter for optimum operation.

$$t_{\text{op}} = \frac{A^2}{8\lambda R_1} = \frac{3}{8} \quad (\text{optimum}). \quad (8-107)$$

The optimum behavior of the directivity curves can be explained rather simply. For a fixed axial length, as the aperture width A is increased from a small value the directivity increases by virtue of the increased aperture area. Optimum performance is reached when $t = t_{\text{op}} = \frac{3}{8}$, which corresponds to a phase lag at the aperture edges ($x = \pm A/2$) of $\delta_{\text{max}} = 2\pi t_{\text{op}} = 3\pi/4 = 135^\circ$. As A is increased beyond the optimum point, the phase deviations across the aperture lead to cancellations in the far-field and decreased directivity, as can be seen from the pattern plots of Fig. 8-11.

The half-power beamwidth relationship for optimum performance can be determined from the pattern plot of Fig. 8-11 for $t = \frac{3}{8}$. The 3-dB down point on the main beam occurs for $(A/\lambda)\sin\theta_H = 0.68$, so the H -plane beamwidth for an optimum H -plane sectoral horn is $2\theta_H = 2\sin^{-1}(0.68\lambda/A)$; and for $A \gg \lambda$

$$\text{HP}_H \approx 1.36 \frac{\lambda}{A} = 78 \frac{\lambda}{A}^\circ \quad (\text{optimum}). \quad (8-108)$$

8.4.2 The E -Plane Sectoral Horn Antenna

A rectangular horn antenna can also be formed by flaring the feed waveguide in the E -plane. The resulting horn is referred to as an E -plane sectoral horn antenna as shown in Fig. 8-13. The geometrical relationships for this horn are

$$r_E^2 = R_2^2 + \left(\frac{B}{2}\right)^2 \quad (8-109a)$$

$$\alpha_E = \tan^{-1}\left(\frac{B}{2R_2}\right) \quad (8-109b)$$

$$R_E = (B - b) \sqrt{\left(\frac{r_E}{B}\right)^2 - \frac{1}{4}}. \quad (8-110)$$

A similar line of reasoning as employed for the H -plane horn leads to the following aperture electric field distribution for the E -plane horn.

$$E_{av} = E_o \cos \frac{\pi x}{a} e^{-j\beta \frac{1}{2} R_2 y^2}. \quad (8-111)$$

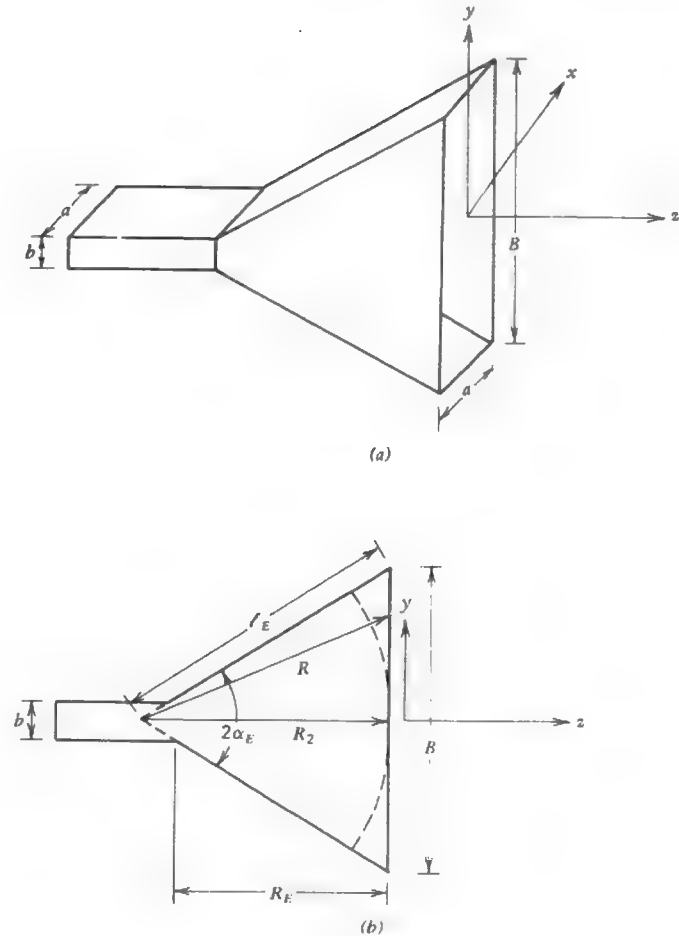


Figure 8-13 E -plane sectoral horn antenna. (a) Overall geometry. (b) Cross section through the y -plane (E -plane).

The same steps as used with the H -plane sectoral horn yields the radiation field

$$\mathbf{E} = j\beta E_o \sqrt{\frac{\pi R_2}{\beta}} \frac{4a}{\pi} \frac{e^{-j\beta r}}{4\pi r} e^{j\beta R_2 \frac{1}{2} y^2} (\hat{\theta} \sin \phi + \hat{\phi} \cos \phi) \cdot \frac{1 + \cos \theta}{2} \frac{\cos[(\beta a/2)u]}{1 - [(\beta a/\pi)u]^2} [C(r_2) - jS(r_2) - C(r_1) + jS(r_1)] \quad (8-112a)$$

where

$$r_1 = \sqrt{\frac{\beta}{\pi R_2}} \left(-\frac{B}{2} - R_2 v \right), \quad r_2 = \sqrt{\frac{\beta}{\pi R_2}} \left(\frac{B}{2} - R_2 v \right). \quad (8-112b)$$

The normalized H -plane pattern follows from (8-112) with $\phi = 0^\circ$ as

$$F_H(\theta) = \frac{1 + \cos \theta}{2} \frac{\cos[(\beta a/2) \sin \theta]}{1 - [(\beta a/\pi) \sin \theta]^2}. \quad (8-113)$$

The second factor in this expression is the pattern of a uniform phase, cosine amplitude tapered line source of length a .

The phase distribution in (8-111) is $\delta = (\beta/2R_2)y^2$. The maximum phase error occurs for $y = \pm B/2$, and there the phase error is $\delta_{\max} = (\beta/2R_2)(B/2)^2 = 2\pi(B^2/8\lambda R_2) = 2\pi s$, where we define the phase error parameter

$$s = \frac{B^2}{8\lambda R_2} = \frac{1}{8} \left(\frac{B}{\lambda} \right)^2 \frac{1}{R_2/\lambda}. \quad (8-114)$$

The E -plane pattern (magnitude) from (8-112) with $\phi = 90^\circ$ can be expressed in terms of s as

$$|F_E(\theta)| = \frac{1 + \cos \theta}{2} \frac{[C(r_4) - C(r_3)]^2 + [S(r_4) - S(r_3)]^2}{4[C^2(2\sqrt{s}) + S^2(2\sqrt{s})]}^{1/2}. \quad (8-115a)$$

where

$$r_3 = 2\sqrt{s} \left[-1 - \frac{1}{4s} \left(\frac{B}{\lambda} \sin \theta \right) \right], \quad r_4 = 2\sqrt{s} \left[1 - \frac{1}{4s} \left(\frac{B}{\lambda} \sin \theta \right) \right]. \quad (8-115b)$$

The universal patterns for the E -plane sectoral horn are plotted in Fig. 8-14. The E -plane patterns (solid curves) for various values of s are not normalized to 0 dB at the maximum point, but rather are given relative to the no phase error case (i.e., the $s = 0$ uniform line source pattern). The H -plane pattern (dashed curve) is that of a cosine tapered line source—the second factor of (8-113). The factor $(1 + \cos \theta)/2$ is not included in these plots.

The directivity of the E -plane sectoral horn is given by

$$D_L = \frac{32 a B C^2(q) + S^2(q)}{\pi \lambda^2 q^2} \quad (8-116)$$

where $q = B/\sqrt{2\lambda R_2}$. A family of universal directivity curves, $\lambda D_E/a$, for various values of R_2/λ is given in Fig. 8-15 as a function of B/λ . Again optimal performance is observed from these curves. A curve fit to pairs of values of A/λ and R_2/λ for optimum conditions yields

$$B = \sqrt{2\lambda R_2} \quad (\text{optimum}). \quad (8-117)$$

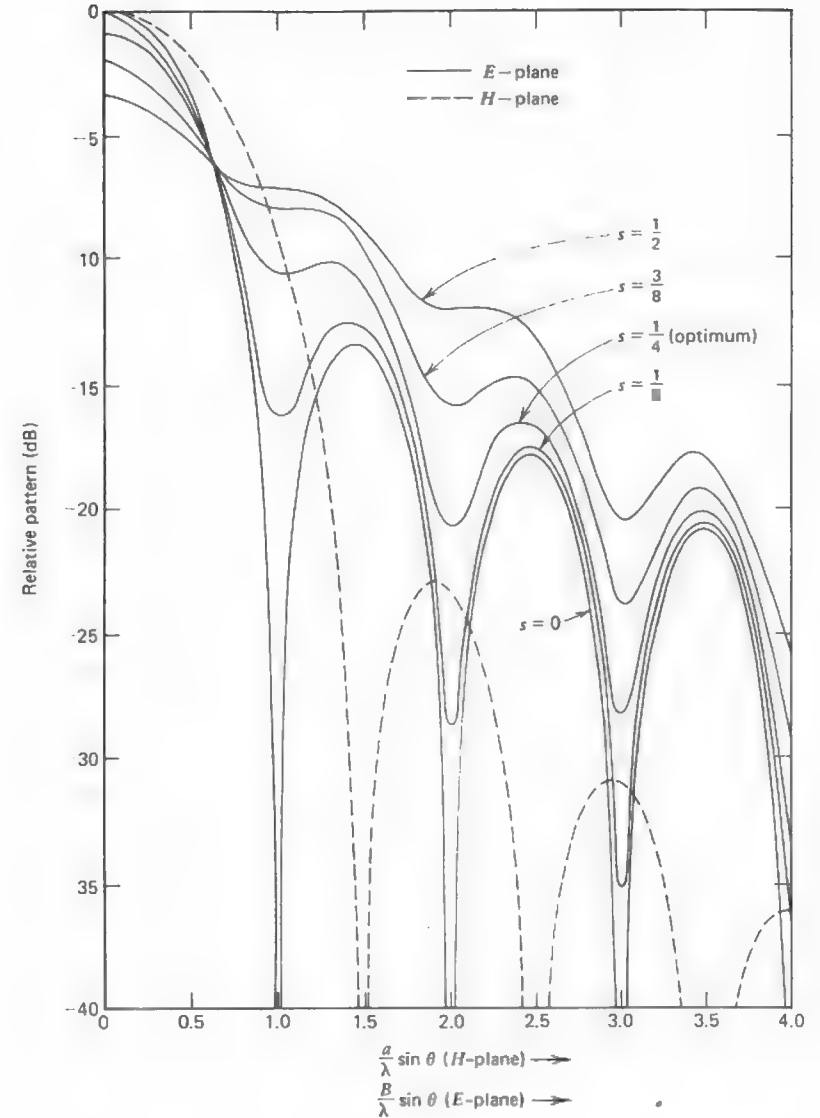


Figure 8-14 Universal radiation patterns for the principal planes of an E -plane sectoral horn antenna as shown in Fig. 8-13. The factor $(1 + \cos \theta)/2$ is not included. (Reproduced, by permission, from [2]. © 1967 John Wiley.)

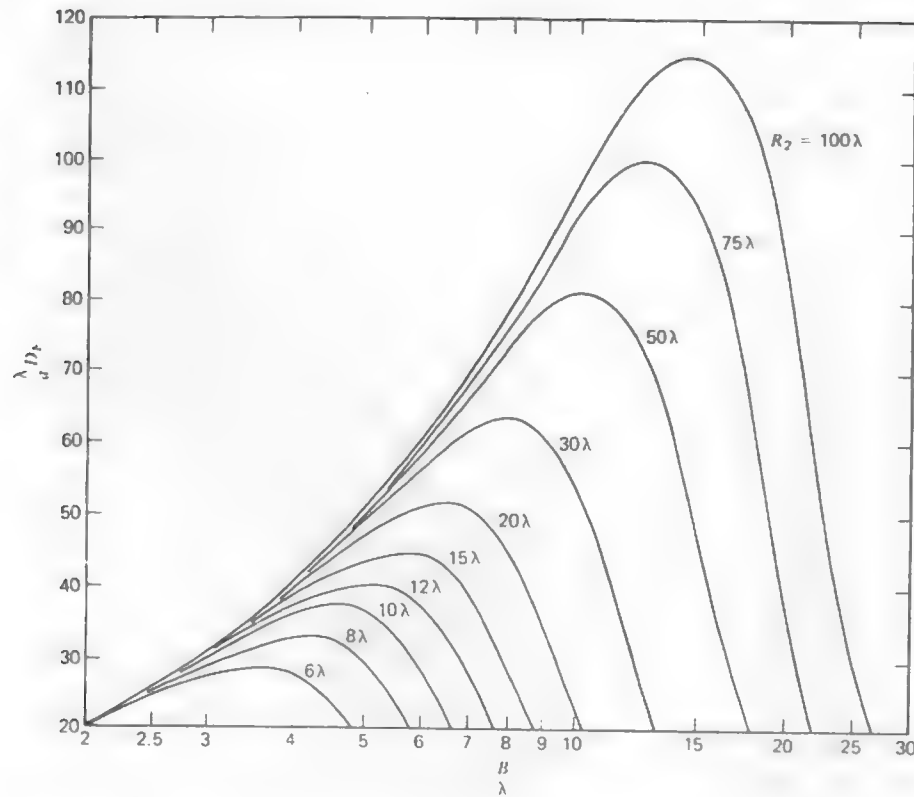


Figure 8-15 Universal directivity curves for an E -plane sectoral horn. For pyramidal horns the vertical axis values are $(\lambda/A)D_E$.

The corresponding value of s is

$$s_{\text{op}} = \frac{B^2}{8\lambda R_2} = \frac{1}{4} \quad (\text{optimum}). \quad (8-118)$$

The half-power beamwidth relationship follows from the $s = \frac{1}{4}$ plot in Fig. 8-14 and is

$$\text{HP}_E = 2 \sin^{-1} \frac{0.47}{B/\lambda} \approx 0.94 \frac{\lambda}{B} = 54 \frac{\lambda}{B}^\circ \quad (\text{optimum}). \quad (8-119)$$

Gain for horn antennas nearly equals directivity, so D_E (and D_H) are taken as G_E (and G_H). The gain of an E -plane sectoral horn has been shown to be more

accurately given by [6]

$$G_E = \frac{16aB}{\lambda^2(1 + \lambda_0/\lambda)} \frac{C^2(q_1) + S^2(q_1)}{q_1^2} e^{j\pi(\lambda/\lambda_0 - \lambda/\lambda_0)} \quad (8-120)$$

where $\lambda_0 = \lambda/\sqrt{1 - (\lambda/2a)^2}$ is the wavelength of the dominant mode in the waveguide feeding the antenna and $q_1 = B/\sqrt{Z\lambda g R_2}$. This expression yields values that agree quite well with experimental results. The values from (8-116) are about 20% or less under those of (8-120).

8.4.3 The Pyramidal Horn Antenna

Probably the most popular form of the rectangular horn antenna is the **pyramidal horn antenna**. As shown in Fig. 8-16, it is flared in both the E - and H -planes. This configuration will lead to narrow beamwidths in both principal planes, thus forming a pencil beam. The aperture electric field is obtained by combining the results for H - and E -plane sectoral horns from (8-91) and (8-111), giving

$$E_{ay} = E_0 \cos\left(\frac{\pi x}{A}\right) e^{-j\pi(2\lambda x^2/R_1 + y^2/R_2)}. \quad (8-121)$$

Following a procedure similar to that used for the sectoral horns will yield a general radiation field expression. It turns out, though, that the principal plane patterns are the same as those obtained from the sectoral horn calculations. To be precise, the E - and H -plane patterns of the pyramidal horn equal the E -plane pattern of the E -plane sectoral horn and the H -plane pattern of the H -plane sectoral horn. Therefore, the E -plane pattern of the pyramidal horn can be found from the universal pattern plots (solid curves) of Fig. 8-14, and the H -plane pattern can be found from the solid curves of Fig. 8-11.

The directivity of the pyramidal horn is found rather simply from

$$D_p = \frac{\pi}{32} \left(\frac{\lambda}{A} D_E \right) \left(\frac{\lambda}{B} D_H \right). \quad (8-122)$$

The terms in parentheses are obtained directly from the directivity curves for sectoral horns. To do this the ordinates of Figs. 8-12 and 8-15 are interpreted as $\lambda D_H/B$ and $\lambda D_E/A$, respectively. Gain values computed from (8-122) agree very well with experiment. It includes the geometrical optics fields and simply diffracted fields from the horn edges. Inclusion of multiple diffraction and diffraction at the edges arising from reflections from the horn interior leads to small oscillations in the gain about that predicted by (8-122) as a function of frequency, and even better agreement with experimental results is obtained [7].

A pyramidal horn must be designed such that when it is constructed it fits together with the feed waveguide. In order to have a realizable structure it is obvious from Fig. 8-16 that

$$R_E = R_H = R_p \quad (8-123)$$

Pyramidal horns are frequently designed for optimum gain. We shall now give a simple design procedure for optimum performance. Since the sectoral horn results apply, we can borrow them. For large horns where $R_1 \approx \ell_H$ and $R_2 \approx \ell_E$, (8-106) and (8-117) give

$$A = \sqrt{3\lambda R_1} \approx \sqrt{3\lambda \ell_H} \quad (8-124a)$$

$$B = \sqrt{2\lambda R_2} \approx \sqrt{2\lambda \ell_E} \quad (8-124b)$$

Typically a gain G is specified, and the problem is to determine A , B , and R_p . The effective aperture of an optimum horn is nearly 50% of its physical aperture area [8], so from (8-79)

$$G = \epsilon_{ap} \frac{4\pi}{\lambda^2} A_p = \frac{1}{2} \frac{4\pi}{\lambda^2} (AB) \quad (8-125)$$

which provides a relationship between gain and A and B . Combining this with (8-124) and enforcing the realizability condition $R_E = R_H$, through (8-86) and (8-110), gives the design equation

$$\left| \sqrt{2\sigma} - \frac{b}{\lambda} \right|^2 (2\sigma - 1) = \left(\frac{G}{2\sqrt{2\pi}} \frac{1}{\sqrt{\sigma}} - \frac{a}{\lambda} \right)^2 \left(\frac{G^2}{18\pi^2} \frac{1}{\sigma} - 1 \right) \quad (8-126)$$

where $\sigma = \ell_E/\lambda$. The waveguide dimensions a and b are known, as well as the gain G , so this equation can be solved by trial and error for σ to find ℓ_E . Then B follows from (8-124b), A from (8-125), ℓ_H from (8-124a), and $R_p = R_H = R_E$ from (8-86) or (8-110). As a first trial for the solution of (8-126) one should use

$$\sigma_1 = \frac{G}{2\pi\sqrt{6}} \quad (8-127)$$

A very simple horn design procedure available in the literature [9] claims 0.1-dB gain accuracy. The results from it are in good agreement with the above procedure.

Example 8-7. Design of an Optimum Gain Pyramidal Horn Antenna

A "standard gain" pyramidal horn antenna operates from 8.2 to 12.4 GHz (X-band). It is fed from WR90 waveguide with $a = 0.9$ in. = 2.286 cm and $b = 0.4$ in. = 1.016 cm, and is to have a gain of 22.1 dB at 9.3 GHz ($\lambda = 3.226$ cm). For optimum gain (8-126) must be

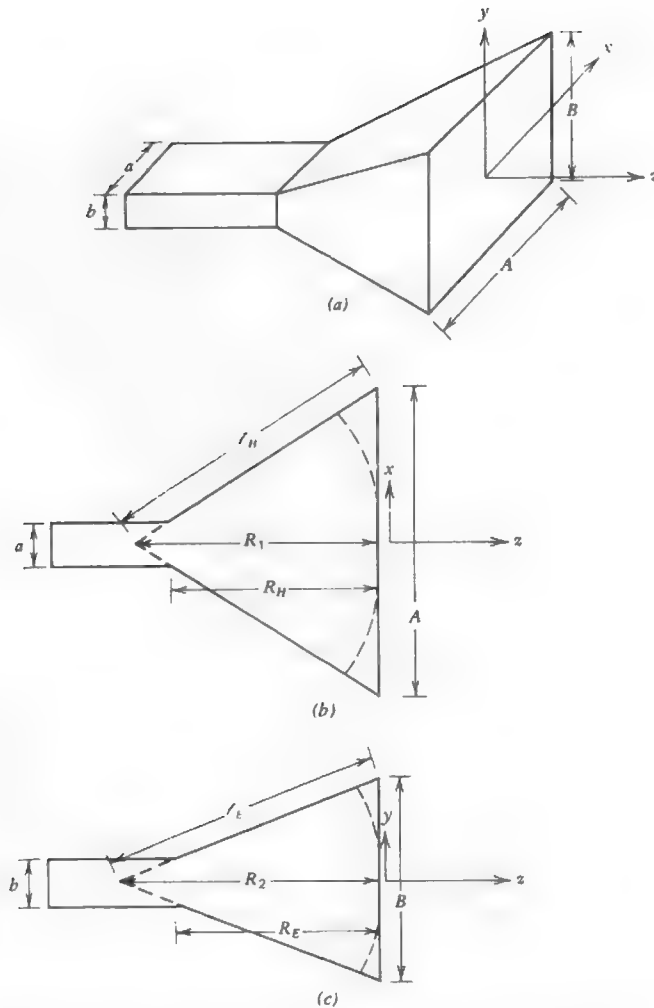


Figure 8-16 Pyramidal horn antenna. (a) Overall geometry. (b) Cross section through the xz -plane (H -plane). (c) Cross section through the yz -plane (E -plane).

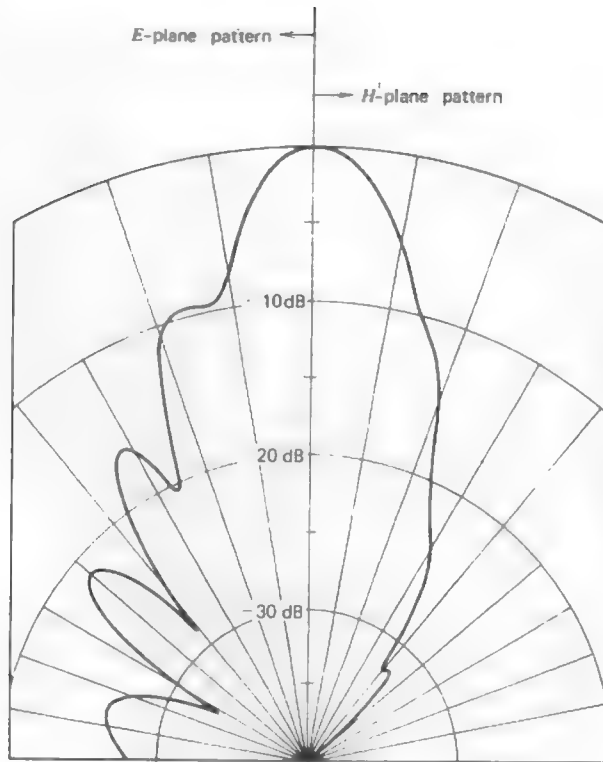


Figure 8-17 Principal plane patterns for the optimum pyramidal horn antenna of Example 8-7 at 9.3 GHz. The patterns include the $(1 + \cos \theta)/2$ factor. $HP_E = 12.0^\circ$ and $HP_H = 13.6^\circ$.

solved using known values of $G = 10^{2.21} = 162.18$, $a/\lambda = 0.7087$, and $b/\lambda = 0.315$. The first trial for $\sigma = \sigma_1 = 10.54$ from (8-127), followed by successive trials on σ leads to the solution $\sigma = f_e/\lambda = 10.17$. Then from (8-124b), (8-125), (8-124a), and (8-110) we find

$$\begin{aligned} A &= 18.46 \text{ cm}, & B &= 14.55 \text{ cm} \\ f_e &= 32.81 \text{ cm}, & f_H &= 35.21 \text{ cm} \\ R_E &= R_H = 29.75 \text{ cm}. \end{aligned} \quad (8-128)$$

As a check of our entire procedure we can locate the operating points on the gain curves. From (8-85a) and the computed data in (8-128) we find $R_1 = 33.98 \text{ cm}$. Then $R_1/\lambda = 10.53$ and $A/\lambda = 5.73$ locate a point on the directivity plot of Fig. 8-12 which falls in the optimum region. Similarly from (8-109a) we find $R_2 = 31.98 \text{ cm}$ and $R_2/\lambda = 9.91$. Using this and $B/\lambda = 4.51$ in Fig. 8-15 again reveals optimum behavior. Reading from these

curves gives $\lambda D_H/B = 44$ and $\lambda D_E/A = 37.5$, and from (8-122) $D_p = 162.0 = 22.1 \text{ dB}$, which is exactly the design gain value and is also the measured gain. The half-power beamwidths from (8-108) and (8-119) are $HP_H = 13.6^\circ$ and $HP_E = 12.0^\circ$, which are in good agreement with measured values of 13° and 12° . We can also check the gain estimation formula of (8-82) as $G \approx 26,000/(HP_E HP_H) = 26,000/(12.0 \cdot 13.6) = 159.3 = 22.0 \text{ dB}$, which is indeed a good result for such a simple formula.

The complete radiation patterns from (8-99) and (8-115) are plotted in Fig. 8-17. They include the $(1 + \cos \theta)/2$ factor. The half-power beamwidths are $HP_H = 13.6^\circ$ and $HP_E = 12.0^\circ$, which are exactly the same as obtained from (8-108) and (8-119) even though they do not include the effect of the $(1 + \cos \theta)/2$. So we see that for narrow beam patterns, (8-108) and (8-119) give very good results. The first side lobe of the H -plane pattern in Fig. 8-17 is located at $\theta = 42^\circ$ and has a value of -32.0 dB , and the E -plane pattern has a first side lobe at $\theta = 16^\circ$ with a value of -9.2 dB there. These compare to -31 and -9 dB from the patterns in Figs. 8-11 and 8-14, and we see that the $(1 + \cos \theta)/2$ factor has a minor effect on the first side lobe.

8.5 CIRCULAR APERTURES

An antenna that has a physical aperture opening with a circular shape is said to have a *circular aperture*. Various forms of circular aperture antennas are encountered in practice. In this section we will discuss ideal circular aperture distributions with uniform and tapered amplitudes. This is followed in the next section by a study of parabolic reflector antennas which are the most popular circular aperture antennas.

8.5.1 The Uniform Circular Aperture

A general circular aperture is shown in Fig. 8-18. If the aperture distribution amplitude is constant, it is referred to as a *uniform circular aperture*. This is approximated by a circular hole in a conducting sheet with a uniform plane wave incident from behind. Suppose the aperture electric field is x -directed, or

$$E_a = \hat{x} E_0 \quad r' \leq a. \quad (8-129)$$

Then (8-16) gives

$$P = \hat{x} E_0 \iint_{S_a} e^{j\beta \hat{r} \cdot \hat{r}'} dS'. \quad (8-130)$$

From Fig. 8-18 it is seen that

$$\hat{r}' = r' \cos \phi' \hat{x} + r' \sin \phi' \hat{y}. \quad (8-131)$$

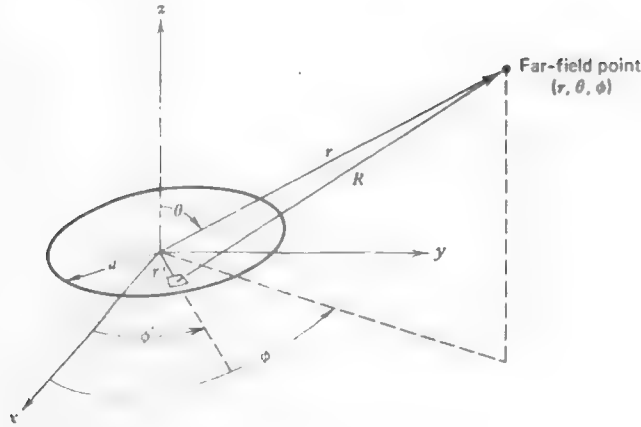


Figure 8-18 The circular aperture.

This with (A-4) yields

$$\begin{aligned}\hat{\mathbf{r}} \cdot \mathbf{r}' &= r' \sin \theta (\cos \phi \cos \phi' + \sin \phi \sin \phi') \\ &= r' \sin \theta \cos(\phi - \phi').\end{aligned}\quad (8-132)$$

Hence (8-130) becomes

$$\begin{aligned}\mathbf{P} &= \hat{\mathbf{x}} E_0 \int_0^a \left[\int_0^{2\pi} e^{j\beta r' \sin \theta \cos(\phi - \phi')} d\phi' \right] r' dr' \\ &= \hat{\mathbf{x}} E_0 2\pi \int_0^a r' J_0(\beta r' \sin \theta) dr'\end{aligned}\quad (8-133)$$

where (F-6) was used for the ϕ' integration. $J_0(x)$ is a Bessel function of the first kind and zero order, which is one at $x = 0$ and is a decaying oscillatory function for increasing x . The r' integration can be performed using

$$\int x J_0(x) dx = x J_1(x) \quad (8-134)$$

which follows from (F-9). $J_1(x)$ is a Bessel function of the first kind and first order, which is zero for $x = 0$ and is a decaying oscillatory function for increasing x . Transforming variables as $x = \beta r' \sin \theta$ and using (8-134) in (8-133) yields

$$\mathbf{P} = \hat{\mathbf{x}} E_0 2\pi \frac{a}{\beta \sin \theta} J_1(\beta a \sin \theta) = \hat{\mathbf{x}} P_x. \quad (8-135)$$

The equivalent magnetic current formulation of (8-26) renders the radiation field

$$\mathbf{E} = (\hat{\theta} \cos \phi - \hat{\phi} \sin \phi \cos \theta) j\beta \frac{e^{-j\beta r}}{2\pi r} P_x. \quad (8-136)$$

This together with (8-135) comprises the radiated electric field expression for a uniform circular aperture with an x -directed aperture electric field.

For large circular apertures the main beam will be narrow and for a uniform phase aperture (as we have assumed here) the main beam maximum will be in the $\theta = 0^\circ$ direction. Then $\cos \theta \approx 1$ near the z -axis ($\theta = 0^\circ$) and the polarization of radiation, from (8-136), will be $\hat{\mathbf{p}} = \hat{\theta} \cos \phi - \hat{\phi} \sin \phi$. Also the projection of $\hat{\mathbf{x}}$ onto a far-field sphere, from (A-1), is $\hat{\mathbf{x}} - \hat{\mathbf{r}} \sin \theta \cos \phi = \hat{\theta} \cos \theta \cos \phi - \hat{\phi} \sin \phi \approx \hat{\theta} \cos \phi - \hat{\phi} \sin \phi$ for θ small, which equals $\hat{\mathbf{p}}$. Therefore, the polarization of the radiated electric field equals that of the aperture electric field, or more accurately, the projection of it onto the far-field sphere.

The relative intensity of the radiation, from (8-135), is

$$f(\theta) = \frac{2J_1(\beta a \sin \theta)}{\beta a \sin \theta} \quad (8-137)$$

which is normalized for a maximum of unity when $\theta = 0^\circ$. This function is, of course, circularly symmetric since the aperture field amplitude is. It is plotted in Fig. 8-19 in the uv -plane for $a = 5\lambda$ out to the limit of the visible region ($\theta = 90^\circ$). A plot of the pattern through any plane passing through the center of Fig. 8-19 is shown in Fig. 8-20. Note the similarity of the $2J_1(u)/u$ function to the $\sin(u)/u$ function.

The half-power point of (8-137) occurs at $\beta a \sin \theta = 1.6$, so the half-power beamwidth is

$$\begin{aligned}\text{HP} &= 2\theta_{\text{HP}} = 2 \sin^{-1} \frac{1.6}{\beta a} \approx 2 \frac{1.6}{\pi} \frac{\lambda}{2a} \\ \text{HP} &= 1.02 \frac{\lambda}{2a} \text{ rad}\end{aligned}\quad (8-138)$$

for $a \gg \lambda$. For the 10λ diameter example $\text{HP} = 0.102 \text{ rad} = 5.84^\circ$. The side lobe level of any uniform circular aperture pattern is -17.6 dB . This can be seen in Fig. 8-20. Since the uniform circular aperture has uniform excitation amplitude, it has unity aperture efficiency and the directivity, from (8-66), is

$$D_u = \frac{4\pi}{\lambda^2} A_p = \frac{4\pi}{\lambda^2} (\pi a^2). \quad (8-139)$$

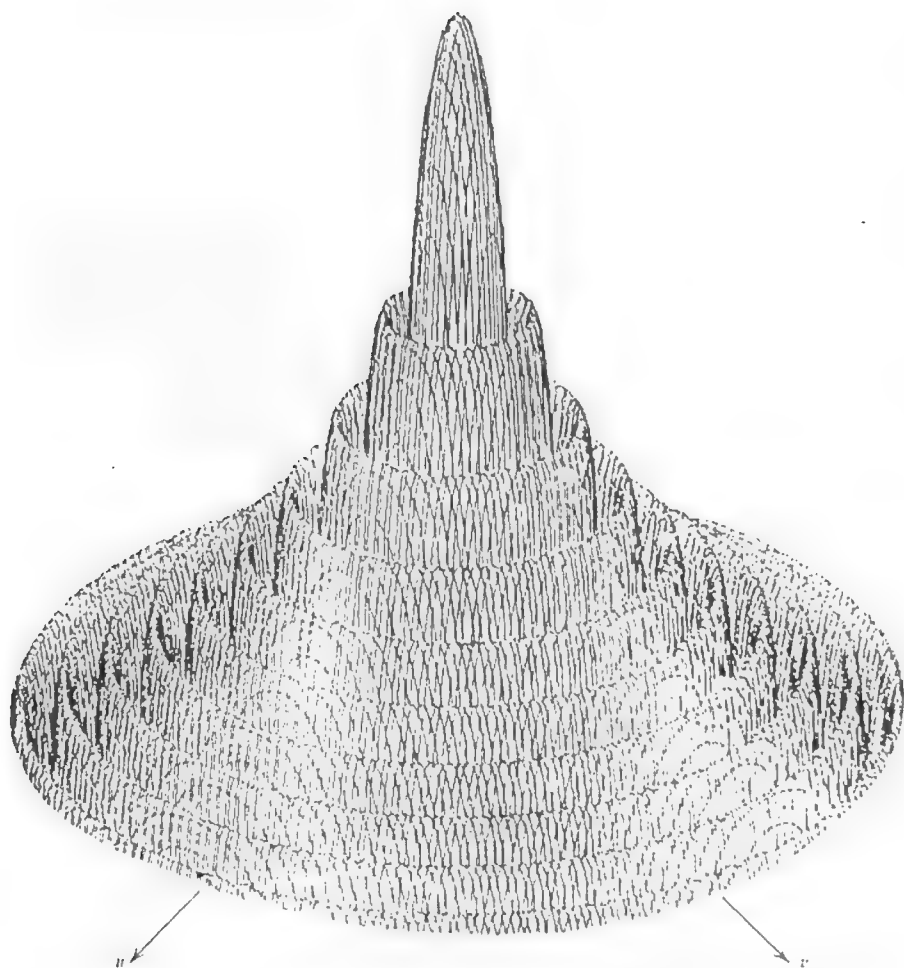


Figure 8-19 Radiation pattern of a uniform amplitude, uniform phase, 10-wavelength diameter circular aperture.

8.5.2 Tapered Circular Apertures

Many circular aperture antennas can be approximated as a circular aperture with an aperture field amplitude distribution which is tapered from the center of the aperture toward the edge. In practice many circular aperture distributions are close to radially symmetric; that is, not a function of ϕ' (see Fig. 8-18). We shall assume this is the case, and again we will confine our attention to a broadside circular aperture which is large in terms of a wavelength. Then the

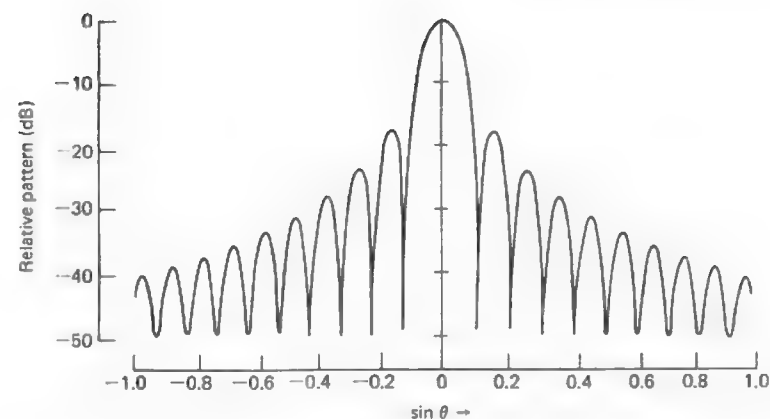


Figure 8-20 Pattern of a 10λ diameter uniform circular aperture. It equals the pattern in any plane passing through the center of Fig. 8-19.

pattern is well approximated by the unnormalized radiation integral

$$f_{un}(\theta) = \int_0^{2\pi} \int_0^a E_a(r') e^{j\beta r' \sin \theta \cos(\phi - \phi')} r' dr' d\phi'. \quad (8-140)$$

Performing the integration over ϕ' with the aid of (F-6) leads to

$$f_{un}(\theta) = 2\pi \int_0^a E_a(r') r' J_0(\beta r' \sin \theta) dr'. \quad (8-141)$$

This integral can be performed for various aperture tapers and normalized to obtain $f(\theta)$.

The results of several common circular aperture tapers are given in Table 8-1.⁴ This table is very similar to Table 4-2 for line sources. Note that the aperture taper efficiency ϵ_t is the directivity of the pattern relative to that of the same circular aperture uniformly illuminated (see Prob. 8.5-4). The parabolic taper ($n = 1$) is a smooth taper from the aperture center to zero at the aperture edge. The parabolic-squared taper ($n = 2$) gives an even more severe taper. Parabolic tapers on a pedestal provide for a nonzero edge illumination as might be encountered with a circular reflector antenna. The pedestal represents the fact that the reflector intercepts the feed illumination only out to the reflector rim. Notice that in all cases as the taper becomes more severe (n increases or C decreases) the beamwidth increases, the side lobe level decreases, and the directivity decreases.

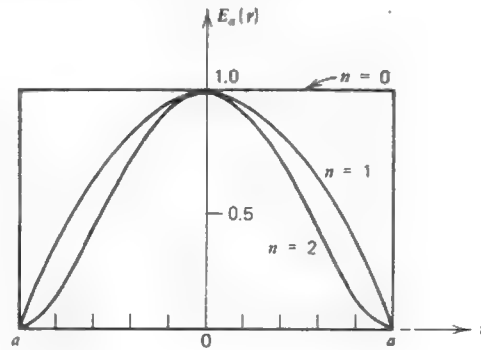
⁴ Extensive data are available in the literature for various aperture tapers [10, 11].

Table 8-1 Characteristics of Tapered Circular Aperture Distributions

(a) Parabolic taper

$$E_a(r) = \left| 1 - \left(\frac{r}{a} \right)^2 \right|^n$$

$$f(\theta, n) = \frac{2^{n+1}(n+1)!J_{n+1}(\beta a \sin \theta)}{(\beta a \sin \theta)^{n+1}}$$

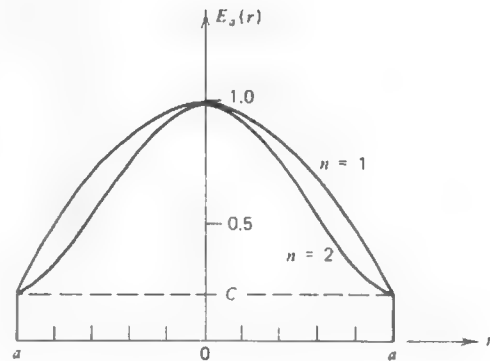


n	HP (rad)	Side lobe level (dB)	ϵ_t	Normalized pattern $f(\theta, n)$
0	$1.02 \frac{\lambda}{2a}$	-17.6	1.00	$\frac{2J_1(\beta a \sin \theta)}{\beta a \sin \theta}$
1	$1.27 \frac{\lambda}{2a}$	-24.6	0.75	$\frac{8J_2(\beta a \sin \theta)}{(\beta a \sin \theta)^2}$
2	$1.47 \frac{\lambda}{2a}$	-30.6	0.55	$\frac{48J_3(\beta a \sin \theta)}{(\beta a \sin \theta)^3}$

(b) Parabolic taper on a pedestal

$$E_a(r) = C + (1-C) \left| 1 - \left(\frac{r}{a} \right)^2 \right|^n$$

$$f(\theta, n, C) = \frac{C f(\theta, n=0) + \frac{1-C}{n+1} f(\theta, n)}{C + \frac{1-C}{n+1}}$$

**Table 8-1** (continued)

Edge illumination		$n = 1$			$n = 2$		
C(dB)	C	HP (rad)	Side lobe level (dB)	ϵ_t	HP (rad)	Side lobe level (dB)	ϵ_t
-8	0.398	$1.12 \frac{\lambda}{2a}$	-21.5	0.942	$1.14 \frac{\lambda}{2a}$	-24.7	0.918
-10	0.316	$1.14 \frac{\lambda}{2a}$	-22.3	0.917	$1.17 \frac{\lambda}{2a}$	-27.0	0.877
-12	0.251	$1.16 \frac{\lambda}{2a}$	-22.9	0.893	$1.20 \frac{\lambda}{2a}$	-29.5	0.834
-14	0.200	$1.17 \frac{\lambda}{2a}$	-23.4	0.871	$1.23 \frac{\lambda}{2a}$	-31.7	0.792
-16	0.158	$1.19 \frac{\lambda}{2a}$	-23.8	0.850	$1.26 \frac{\lambda}{2a}$	-33.5	0.754
-18	0.126	$1.20 \frac{\lambda}{2a}$	-24.1	0.833	$1.29 \frac{\lambda}{2a}$	-34.5	0.719
-20	0.100	$1.21 \frac{\lambda}{2a}$	-24.3	0.817	$1.32 \frac{\lambda}{2a}$	-34.7	0.690

To illustrate the circular aperture pattern computations consider the circular aperture with a parabolic taper. From (8-141) and the aperture field function in Table 8-1(a),

$$f_{un}(\theta) = 2\pi \int_0^a \left| 1 - \left(\frac{r'}{a} \right)^2 \right|^n r' J_0(\beta r' \sin \theta) dr'. \quad (8-142)$$

The integral can be evaluated using

$$\int_0^1 (1-x^2)^n x J_0(bx) dx = \frac{2^n n!}{b^{n+1}} J_{n+1}(b) \quad (8-143)$$

by letting $x = r'/a$ and $b = \beta a \sin \theta$. Then (8-142) reduces to

$$f_{un}(\theta) = \frac{\pi a^2}{n+1} f(\theta, n) \quad (8-144)$$

where

$$f(\theta, n) = \frac{2^{n+1}(n+1)!J_{n+1}(\beta a \sin \theta)}{(\beta a \sin \theta)^{n+1}} \quad (8-145)$$

is the normalized pattern function. The patterns given in Table 8-1(a) follow from (8-145).

8.6 REFLECTOR ANTENNAS

In long-distance radio communication and high-resolution radar applications, antennas with high gain are required. Reflector systems are perhaps the most widely used high gain antennas. Reflecting antennas routinely achieve gains far in excess of 30 dB in the microwave region. Such gains would be difficult to obtain with any single antenna we have discussed thus far. In this section we will consider a few of the more important forms of reflector antennas, with emphasis on those that have circular apertures.

8.6.1 Prime-Focus Parabolic Reflector Systems

The simplest reflector antenna consists of two components: a large (relative to a wavelength) reflecting surface and a much smaller feed antenna. The most prominent example is the **parabolic reflector antenna** as shown in Fig. 8-21a. The reflector (or "dish") has a paraboloid of revolution shape. The intersection with the reflector of any plane containing the reflector axis (z -axis) forms a curve of the parabolic type. The cross section in Fig. 8-21b is typical. The equation describing the parabolic reflector surface shape in the coordinates used is

$$(r')^2 = 4f(f - z') \quad r' \leq a \quad (8-146)$$

For a given displacement r' from the axis of the reflector the point P on the reflector surface is a distance ρ away from the focal point F . For example, at the apex of the dish $r' = 0$ and $z' = f$, and at the edge of the dish $r' = a$ and $z' = f - a^2/4f$. The parabolic curve can also be expressed in polar coordinate form as

$$\rho = \frac{2f}{1 + \cos \theta'} = f \sec^2 \frac{\theta'}{2} \quad (8-147)$$

or

$$r' = \rho \sin \theta' = \frac{2f \sin \theta'}{1 + \cos \theta'} = 2f \tan \frac{\theta'}{2} \quad (8-148)$$

At the apex ($\theta' = 0^\circ$), $\rho = f$, and $r' = 0$. At the reflector edge ($\theta' = \theta_o$), $\rho = 2f/(1 + \cos \theta_o)$.

The parabolic shaped reflector has a very unique feature: All path lengths from the focal point to the reflector and on to the aperture plane are the same. This can be shown using (8-147) as follows

$$\overline{FP} + \overline{PA} = \rho + \rho \cos \theta' = \rho(1 + \cos \theta') = 2f \quad (8-149)$$

The implications of this constant path length property will be examined by considering the reflector system to be a transmitting antenna. Suppose a feed

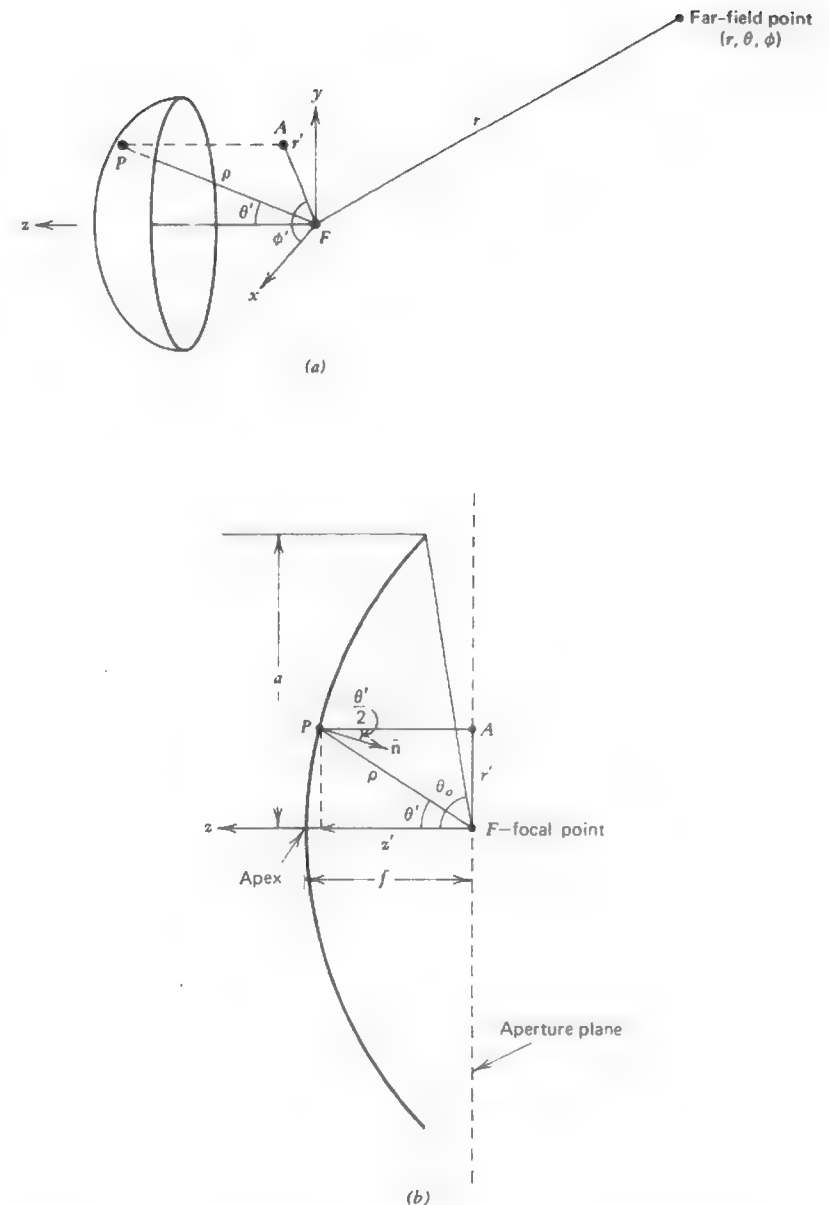


Figure 8-21 The parabolic reflector antenna. (a) Parabolic reflector and coordinate system. (b) Typical cross section.

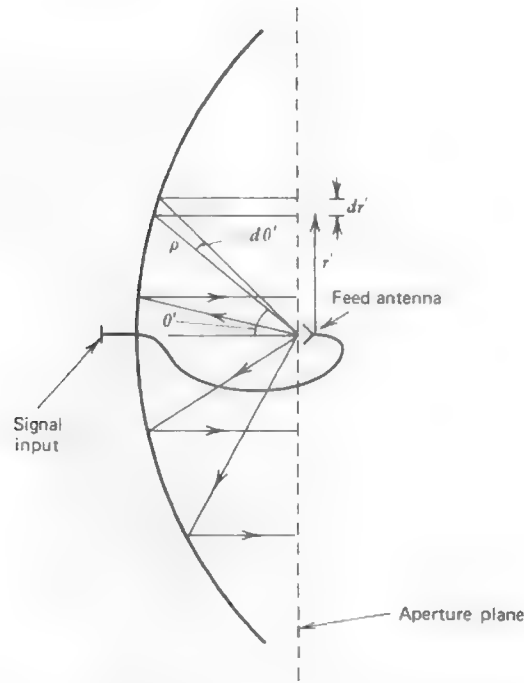


Figure 8-22 Prime-focus parabolic reflector antenna in cross section.

antenna is placed at the focal point; such a configuration is referred to as a *prime-focus* reflector antenna. For large reflectors ($a \gg \lambda$) geometrical optics principles can be applied and radiation from the feed antenna is analyzed by ray tracing as shown in Fig. 8-22. Since all rays from the feed travel the same physical distance to the aperture plane, the excitation is of uniform phase.

The field amplitude distribution over the aperture plane, of course, depends upon the radiation properties of the feed antenna. First assume the feed antenna is an isotropic point source at the focal point, so we can examine the effects of the reflector alone. The power density leaving the feed falls off as $1/\rho^2$ since the wave is spherical. After reflection there is no spreading loss since the wave is then planar. Hence, power density in the aperture varies as $1/\rho^2$, and the field intensity varies as $1/\rho$.

The power density variation in the aperture can also be determined using geometrical optics ideas (see Section 9.1), which apply to structures large relative to a wavelength. The assumption of geometrical optics is that power density in free space follows straight line paths. Applied to this case, the power in a conical

wedge of solid angle $d\Omega$ with cross-sectional angle $d\theta'$ (as shown in Fig. 8-22) will remain confined to that conical wedge as it progresses out from the feed. After reflection the power associated with the increment $d\theta'$ arrives at the aperture plane in a thin ring of thickness dr' and area dA . The power leaving the feed in this direction is proportional to $P_t d\Omega$ where P_t is the transmit power. This power is distributed over area dA in the aperture plane. Thus, the power density in the aperture plane varies as

$$S_a(r') \propto \frac{P_t d\Omega}{dA} \propto \frac{d\Omega}{dA} \quad (8-150)$$

since P_t is a constant. Now $d\Omega = 2\pi \sin \theta' d\theta'$ and $dA = 2\pi r' dr'$, so

$$S_a(r') \propto \frac{2\pi \sin \theta' d\theta'}{2\pi r' dr'} = \frac{\sin \theta' d\theta'}{r' dr'} \quad (8-151)$$

From (8-148)

$$\frac{dr'}{d\theta'} = \frac{d}{d\theta'} \left(2f \tan \frac{\theta'}{2} \right) = f \sec^2 \frac{\theta'}{2} = \rho \quad (8-152)$$

where (8-147) was used for the last equality. Then

$$\frac{d\theta'}{dr'} = \frac{1}{\rho} \quad (8-153)$$

Hence, (8-151) with (8-148) and (8-153) becomes

$$S_a \propto \frac{\sin \theta'}{\rho} \frac{1}{\sin \theta'} \frac{1}{\rho} = \frac{1}{\rho^2} \quad (8-154)$$

which we already noted from the spherical wave nature of the feed. The field variation then follows from $S_a = E_a^2/Z_0$.

$$E_a(\theta') \propto \frac{1}{\rho} \quad (8-155)$$

Thus, there is a natural amplitude taper in the aperture plane caused by the reflector.

If the primary (or feed) antenna is not isotropic the effect of its normalized radiation pattern $F_f(\theta', \phi')$, using the coordinate system of Fig. 8-21, can be included as

$$\mathbf{E}_a(\theta', \phi') = E_0 \frac{F_f(\theta', \phi')}{\rho} \hat{\mathbf{u}}_r \quad (8-156)$$

where $\hat{\mathbf{u}}_r$ is the unit vector of the aperture electric field. The coordinates r' and ϕ' are appropriate for describing the aperture electric field. Thus θ' and ρ must be

expressed in those coordinates. From (8-148)

$$\theta' = 2 \tan^{-1} \frac{r'}{2f} \quad (8-157)$$

and it may be shown from (8-147) and (8-148) that

$$\rho = \frac{4f^2 + r'^2}{4f} \quad (8-158)$$

Thus far we have derived the amplitude and phase of the aperture field distribution. It remains to determine the direction \hat{u}_r , which is the unit vector for \mathbf{E}_a in the aperture plane, after the feed radiation is reflected from the reflector. The reflection process for large reflectors is well approximated by Snell's law for planar reflection surfaces. Thus the angle of incidence and angle of reflection are equal; as shown in Fig. 8-21b this angle is $\theta'/2$ relative to the reflector surface unit normal \hat{n} . If \mathbf{E}_i and \mathbf{E}_r are the incident and reflected electric fields at the surface of the reflector, the tangential component of the total field $\mathbf{E}_i + \mathbf{E}_r$ must be zero to satisfy the boundary condition on a perfect conductor. Due to the symmetry about \hat{n} the normal components double. So $\mathbf{E}_i + \mathbf{E}_r = 2(\hat{n} \cdot \mathbf{E}_i)\hat{n}$, or

$$\mathbf{E}_r = 2(\hat{n} \cdot \mathbf{E}_i)\hat{n} - \mathbf{E}_i \quad (8-159)$$

Since the amplitude of the incident and reflected waves are equal, $|\mathbf{E}_r| = |\mathbf{E}_i|$, the above equation can be divided by this amplitude giving

$$\hat{u}_r = 2(\hat{n} \cdot \hat{u}_i)\hat{n} - \hat{u}_i \quad (8-160)$$

where $\hat{u}_r = \mathbf{E}_r / |\mathbf{E}_r|$ and $\hat{u}_i = \mathbf{E}_i / |\mathbf{E}_i|$.

The radiation pattern from the entire parabolic reflector antenna system, referred to as the *secondary pattern*, can now be calculated from the aperture field. We shall use the equivalent magnetic current formulation. From (8-16) and (8-132)

$$\mathbf{P} = E_o \int_0^{2\pi} \int_0^a \frac{F_f(\theta', \phi')}{\rho} \hat{u}_r e^{j k r' \sin \theta \cos(\phi - \phi')} r' dr' d\phi' \quad (8-161)$$

The complete radiation field is then obtained from (8-26).

The approach presented here for radiation pattern calculations is referred to as the "aperture method." The pattern could also be obtained by using the electric surface current excited on the reflector surface. The two methods are essentially equivalent. The aperture field is the projection of the surface current distribution onto the aperture plane. In both models it is usually assumed that the excitation does not extend beyond the reflector edge and that the direct feed radiation is small. We chose the aperture method to avoid integrating over the curved reflector surface.

As an example consider a short dipole at the focal point and oriented parallel to the y -axis. The radiation from the dipole has no ρ -component, and the electric field direction can be written from (A-2) as

$$\hat{u}_i = \frac{\hat{\theta}' \sin \phi' \cos \theta' + \hat{\phi}' \cos \phi'}{\sqrt{1 - \sin^2 \phi' \sin^2 \theta'}} \quad (8-162)$$

The reflector surface unit normal is

$$\hat{n} = -\hat{\rho} \cos \frac{\theta'}{2} + \hat{\theta}' \sin \frac{\theta'}{2} \quad (8-163)$$

Hence (8-160) leads to

$$\hat{u}_r = \frac{\hat{x} \sin \phi' \cos \phi' (1 - \cos \theta') - \hat{y} (\sin^2 \phi' \cos \theta' + \cos^2 \phi')}{\sqrt{1 - \sin^2 \phi' \sin^2 \theta'}} \quad (8-164)$$

The pattern of a short dipole along the z -axis is $\sin \theta$, and when along the y -axis it is

$$F_f(\theta', \phi') = \sqrt{1 - \sin^2 \phi' \sin^2 \theta'}. \quad (8-165)$$

Using (8-164) and (8-165) in (8-156) gives the aperture electric field

$$\mathbf{E}_a = E_o \frac{1}{\rho} [\hat{x} \sin \phi' \cos \phi' (1 - \cos \theta') - \hat{y} (\sin^2 \phi' \cos \theta' + \cos^2 \phi')]. \quad (8-166)$$

It is instructive to examine this aperture field. In the H -plane ($\phi' = 0^\circ$) the bracketed factor in (8-166) reduces to $-\hat{y}$ and in the E -plane ($\phi' = 90^\circ$) it reduces to $-\hat{y} \cos \theta'$. Thus in the principal planes the aperture field is polarized in the same fashion as the feed dipole; the radiation from the reflector will be also. For nonprincipal planes the radiation will contain field components orthogonal to that of the feed (x -components), that is, cross-polarized components. Figure 8-23 illustrates the orientation of the electric field vector over the aperture. The largest cross-polarized components introduced by the reflector occur along the 45° planes. As the focal length to diameter ($d = 2a$) ratio f/d increases, θ_o decreases and the cross-polarized component decreases.

The combination of the short electric dipole and a short magnetic dipole perpendicular to it along the x -axis at the feed point with the same phase and appropriate magnitude (called a *Huygen's source*) yields a purely linear polarized (y -directed) field over the aperture and thus a purely linear far field.

Since the radiation integral of (8-161) together with (8-157) and (8-158) is an involved analytical problem, it is rarely performed. To obtain the radiation pattern one of two approaches is commonly used: numerical evaluation of the radiation integral [12] or, if approximate results are satisfactory, the aperture

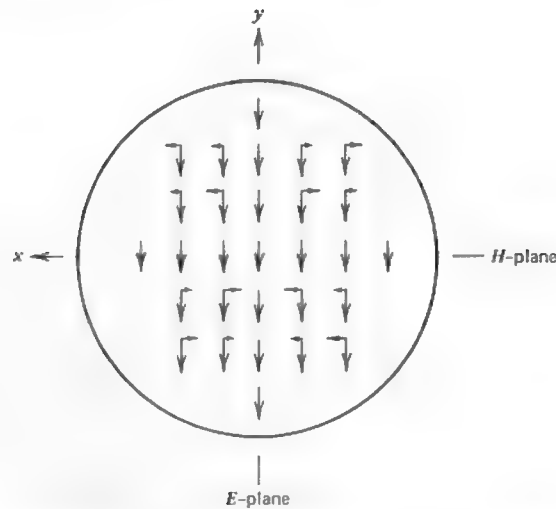


Figure 8-23 Electric field distribution in the aperture of a parabolic reflector for a y -polarized short dipole feed antenna. The electric field is decomposed into its x - and y -components. See (8-166).

distribution can be approximated and the techniques of Section 8.5.2 employed. We shall discuss the latter approach.

Most practical feed antennas have circularly symmetric patterns, that is, the feed pattern F_f is not a function of ϕ' (if it is not symmetric, the average of the E - and H -plane pattern values can be used). The aperture field in (8-156) consists of two factors, the primary (feed) pattern F_f and the $1/\rho$ spreading loss of an isotropic feed. Using (8-148) and (8-158) leads to the normalized aperture field distribution

$$E_a(r') = F_f \left(r' = 2f \tan \frac{\theta'}{2} \right) \left[1 + \left(\frac{r'}{2f} \right)^2 \right]^{-1}$$

$$= 20 \log |F_f| - 20 \log \left[1 + \left(\frac{r'}{2f} \right)^2 \right] \text{ dB.} \quad (8-167)$$

This could be used in (8-141) to obtain the pattern of the reflector system. However, the aperture distribution is often well approximated by a parabolic-squared taper (or sometimes a parabolic taper) on a pedestal. The edge illumination is found from (8-167) with $\theta' = \theta_o$ for the feed pattern and $r' = a = d/2$ for

the spreading loss term, giving

$$C(\text{dB}) = 20 \log |F_f(\theta_o)| - 20 \log \left[1 + \frac{1}{16} \left(\frac{d}{f} \right)^2 \right]. \quad (8-168)$$

The secondary pattern of the reflector is then obtained from Table 8-1(b). A simplified method for obtaining such patterns is available in the literature [11].

Example 8-8. A 28-GHz Parabolic Reflector Antenna

A prime focus parabolic reflector antenna is used at VPI&SU to receive a beacon signal from the COMSTAR series of satellites. The characteristics of this antenna are given in Table 8-2.⁵ The characteristics listed are measured values. The reflector is an epoxy fiberglass structure coated with metal. The feed antenna is a circular corrugated horn, positioned at the focal point and supported by four thin spars. The differences in the beamwidths and side lobe levels of the secondary radiation pattern are caused by the asymmetry of the feed radiation and the presence of the feed waveguide and support structure. We will give the details of the E -plane pattern calculations. From (8-157), at the reflector rim,

$$\theta_o = 2 \tan^{-1} \left(\frac{1}{4} \frac{d}{f} \right) = 2 \tan^{-1} \left(\frac{1}{4} \cdot 2 \right) = 53.1^\circ \quad (8-169)$$

Table 8-2 Characteristics of the 28 GHz Parabolic Reflector Antenna of Example 8-8

Frequency	28.56 GHz
Reflector characteristics:	
Diameter, d	1.219 m (4 ft)
Focal length/diameter, f/d	0.50
Surface tolerance (rms)	0.2 mm (0.008 in.)
Feed characteristics:	
E -plane HP	56°
E -plane 10-dB beamwidth	104°
H -plane HP	59°
H -plane 10-dB beamwidth	112°
System characteristics:	
E -plane HP	0.605°
E -plane side lobe level	-28.5 dB
H -plane HP	0.556°
H -plane side lobe level	-17.5 dB
Gain	47.6 dB

⁵ The antenna was manufactured by Alpha Industries, Inc., TRG Division.

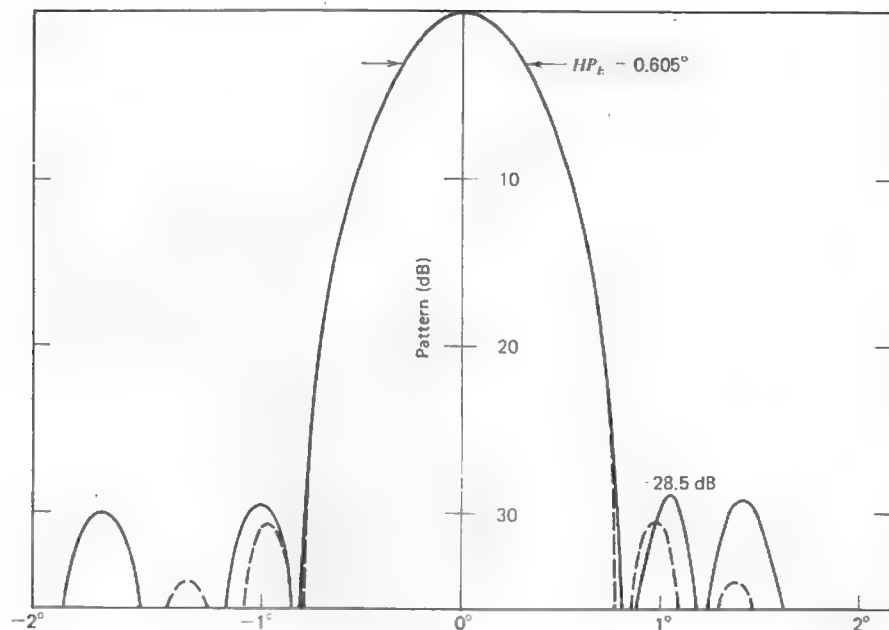


Figure 8-24 Measured (solid) and computed (dashed) E -plane patterns for the 1.22 m diameter prime-focus parabolic reflector antenna at 28.56 GHz (Example 8-8).

since $f/d = 0.5$. The feed radiation pattern is 10 dB down for $\theta' = 104^\circ/2 = 52^\circ$; thus, at the edge of the dish the illumination is slightly lower than -10 dB, or about -11 dB. The total edge illumination from (8-168) is then

$$C(\text{dB}) = -11 - 20 \log[1 + \frac{1}{16}(2)^2] = -12.9, \text{ or } C = 0.2265. \quad (8-170)$$

Using the pattern of a parabolic-squared taper on a pedestal in (8-145) and evaluating for $C = 0.2265$ gives

$$\text{HP}_E = 1.214 \frac{\lambda}{2a} = 0.01045 \text{ rad} = 0.599^\circ \quad (8-171)$$

since $\lambda = 0.0105$ m and $d = 2a = 1.22$ m. The computed side lobe level is -30.5 dB. These values agree very well with the measured values of $\text{HP}_E = 0.605^\circ$ and $\text{SLL}_E = -28.5$ dB. In fact, the computed radiation pattern agrees amazingly well with the measured pattern as shown in Fig. 8-24.

8.6.2 Cassegrain Reflector Systems

Another very popular form of the circular parabolic reflector is the **Cassegrain reflector antenna** shown in Fig. 8-25. It consists of a feed horn, a subreflector,

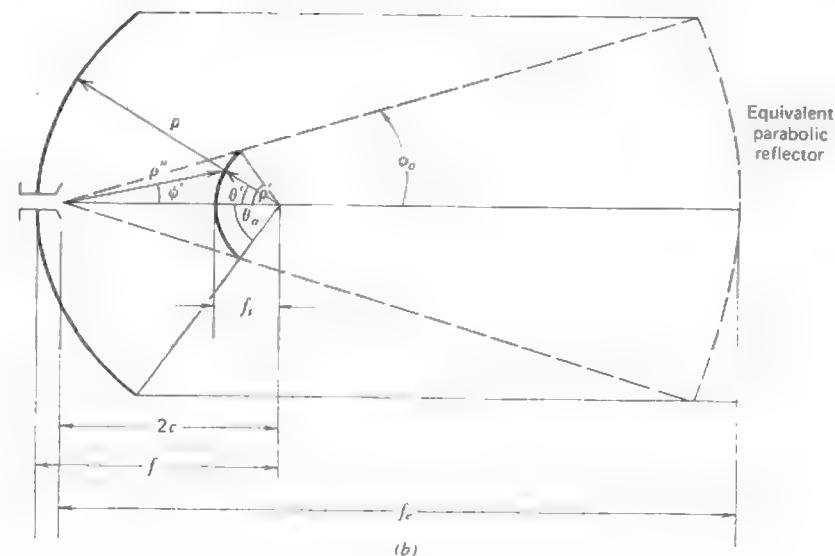
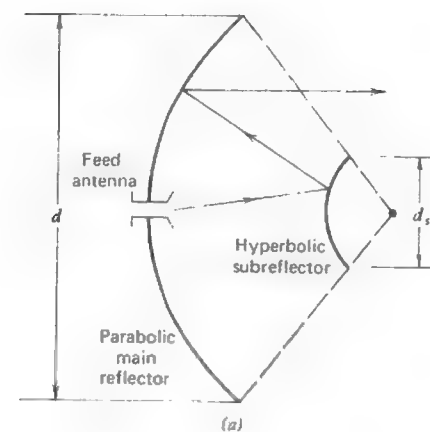


Figure 8-25 The Cassegrain reflector antenna. (a) The ray paths. (b) The parameters.

and a main reflector with rays from the feed experiencing reflections off of both the subreflector and main reflector. The antenna operates in fashion similar to the prime-focus parabolic reflector except for the extra reflection introduced by the subreflector. The subreflector is a hyperboloid of revolution. Its cross section as shown in Fig. 8-25 is a hyperbolic curve expressed by

$$\rho'' = \frac{-ep}{1 - e \cos \phi'} \quad (8-172)$$

where

$$p = c \left(1 - \frac{1}{e^2} \right) \quad (8-173)$$

and the eccentricity is

$$e = \frac{\sin[\frac{1}{2}(\theta_o + \phi_o)]}{\sin[\frac{1}{2}(\theta_o - \phi_o)]} \quad (8-174)$$

The parabola is still defined by (8-147). If

$$\frac{f}{d} = \frac{f_s}{d_s} \quad (8-175)$$

where f , f_s , d , and d_s are the focal lengths and diameters of the main and subreflectors, then the Cassegrain system is highly efficient.

There is an equivalent single prime-focus parabolic reflector which produces the same aperture distribution as the Cassegrain system (see Fig. 8-25b). The equivalent paraboloid has a focal length f_e , diameter d , and half-angle ϕ_o .

The Cassegrain system offers several advantages over a prime-focus parabolic reflector of the same main reflector size. First, the primary feed antenna is near the apex of the main reflector facilitating access and adjustments such as feed rotation. Also the feed waveguide length is reduced, thus reducing attendant loss and noise. For reflector systems there is always a portion of the feed antenna pattern which is not intercepted by the main reflector in the prime focus case and by the subreflector in the Cassegrain case. This is referred to as *spillover*. For receiving antennas this spillover contributes to noise pickup from the environment surrounding the antenna. For earth terminal receiving antennas the spillover from a Cassegrain antenna is directed toward the relatively low noise sky, whereas the prime-focus antenna spillover is directed toward the more noisy ground. Thus, the Cassegrain system inherently has lower noise. The Cassegrain antenna is also capable of providing a lower cross-polarization level. This can be seen by the fact that the equivalent parabola for the Cassegrain antenna is of long focal length and, as we saw earlier, cross polarization reduces as focal length increases for the simple focus-fed reflector.

On the other hand, the subreflector tends to be much larger than the feed horn for a prime-focus reflector. These structures in front of the main reflector block the final emergent rays leading to gain reduction. This *aperture blockage* is thus smaller for the prime-focus reflector. For this reason, the Cassegrain reflector configuration is usually only employed for situations requiring narrow half-power beamwidths (about a degree or less).

8.6.3 Gain Calculations for Reflector Antennas

In Section 8.3 gain calculations for aperture antennas were discussed. Since gain is perhaps the single most important parameter for a reflector antenna, we shall return to the topic of gain calculations for this purpose. Once we have determined the aperture efficiency ϵ_{ap} the gain is obtained from (8-79) as

$$G = \epsilon_{ap} \frac{4\pi}{\lambda^2} A_p = \epsilon_{ap} \left(\frac{\pi d}{\lambda} \right)^2 \quad (8-176)$$

where from (8-75)

$$\epsilon_{ap} = e\epsilon_t\epsilon_1\epsilon_2\epsilon_3 \cdots \quad (8-177)$$

The radiation efficiency e for reflector antennas represents the ohmic losses, which are usually very small, unless lossy devices are included as part of the feed system. Hence, usually we take $e \approx 1$.

The aperture taper efficiency ϵ_t is the gain loss due to an aperture illumination that is tapered relative to uniform illumination, which produces maximum gain. In Example 8-8 we saw that the parabolic-squared taper on a pedestal provided good pattern results. The aperture taper efficiency values from Table 8-1(b) are plotted in Fig. 8-26.

The remaining efficiency factors, referred to as achievement factors, represent many factors causing gain reduction by not achieving the aperture distribution assumed in the aperture efficiency factor. The most prominent of this is the *spillover (or feed) efficiency* ϵ_1 . In the aperture taper calculation it was assumed that the aperture fields were confined to the circular area represented by the reflector aperture. However, the feed antenna illumination does not drop to zero beyond the reflector rim in the prime focus case and the subreflector rim in the Cassegrain case. That portion of the feed radiation which is not intercepted by the reflector (spillover) leads to gain loss, since this power is not directed in the main beam maximum direction. We define ϵ_1 as that fraction of power radiated by the feed which is intercepted by the main reflector of prime focus systems and by the subreflector of Cassegrain systems. As the aperture taper increases, the spillover will decrease (and thus ϵ_1 increases) [13], while the aperture taper efficiency factor decreases. The tradeoff between ϵ_t and ϵ_1 has an optimum solution,

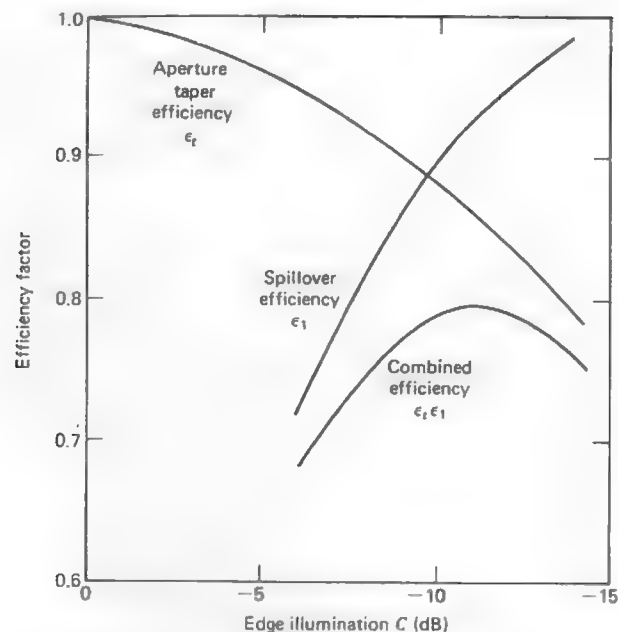


Figure 8-26 Aperture taper and spillover efficiencies as a function of edge illumination for a circular parabolic reflector antenna.

as indicated by the combined efficiency $\epsilon_t \epsilon_s$ in Fig. 8-26. The maximum of $\epsilon_t \epsilon_s$ occurs for an edge taper of about -11 dB and has a value of about 0.8. A value of -10 -dB edge taper is frequently quoted as being optimum.

The *random surface error factor* ϵ_2 is the efficiency factor associated with far-field cancellations arising from phase errors in the aperture field. For small phase errors $\epsilon_2 = e^{-(2\pi\delta/\lambda)^2}$ where δ is the rms phase front deviation from planar over the aperture. For reflector antennas δ is replaced by $2\delta'$ where δ' is the rms surface deviation from the true paraboloid. The factor of two comes from the two-way path, leading to a doubling of the phase error. Then

$$\epsilon_2 = e^{-(4\pi\delta'/\lambda)^2} \quad (8-178)$$

In many cases ϵ_2 is very nearly unity. Table 8-3 gives typical rms surface tolerances for various reflector construction methods. For example, the best spun aluminum reflector has $\delta' = (0.15/30)\lambda$ at 10 GHz ($\lambda = 30$ mm), and $\epsilon_2 = 0.996$. Equation (8-178) is based on flat reflectors ($f/d = \infty$) and ϵ_2 is increased somewhat as f/d is reduced; that is, it is a worst case value. The values in Table 8-3

Table 8-3 Typical Reflector Surface Tolerances

Reflector type	RMS surface tolerance, δ'
Spun aluminum—good	0.64 mm (0.025 in.)
Spun aluminum—best	0.15 mm (0.006 in.)
Metalized plastic	0.06 mm (0.0025 in.)
Machined aluminum	0.04 mm (0.0015 in.)

are primarily for small reflectors. A simple formula representing current state-of-the-art reflector surface accuracy as a function of reflector diameter is given by

$$\delta' = 3 \times 10^{-2} d \text{ mm} \quad (8-179)$$

where d is in meters. For example, a 1-m reflector has a surface error of 0.03 mm, whereas a 10-m diameter reflector has a 0.3-mm accuracy.

Structures placed in front of the aperture will block the emergent radiation, leading to a gain loss. The *aperture blockage efficiency* ϵ_3 is due to the presence of a feed antenna or a subreflector in the Cassegrain case. Also sometimes prime-focus reflector systems employ a metal structure behind the feed to house RF signal processing hardware, giving additional blockage. Values of ϵ_3 are given in Table 8-4 as a function of the ratio of the diameter of the blocking structure near the focal point d_f to the main reflector diameter d . Blockage can also arise from the spars (or struts) used to support the feed antenna or subreflector. The *spar blockage efficiency* ϵ_4 values are given in Table 8-4 for various main reflector sizes and numbers of half-wavelength thick spars.

If the feed antenna is not placed at the focal point of a reflector system (this is sometimes done intentionally when using multiple feed antennas) reduced efficiency results. The *squint factor* ϵ_5 represents lateral displacement (in the aperture plane), which squints, or shifts, the main beam maximum off axis. If the beam shifts off axis by one half-power beamwidth, $\epsilon_5 \approx 0.98$. The *astigmatism efficiency* ϵ_6 represents axial displacements of the feed. It is a function of frequency and f/d . For example, for a 0.1λ axial displacement ϵ_6 is 0.996, 0.98, and 0.93 for an f/d of $\frac{1}{2}$, $\frac{1}{3}$, and $\frac{1}{4}$, respectively.

Other efficiency factors are possible. If a reflector antenna employs mesh surface rather than continuous metal the *surface leakage efficiency* ϵ_7 is slightly less than unity; that is, $\epsilon_7 \approx 0.99$ for a mesh with several grid wires per wavelength. Also an effective gain loss arises from depolarization; that is, power generated in a polarization state orthogonal to that desired. The *depolarization efficiency* ϵ_8 is usually greater than 0.98.

To illustrate these efficiency factors, we return to Example 8-8. If the parabolic-squared taper on a -12.9 -dB pedestal used for the E -plane was valid

Table 8-4 Blockage Efficiencies for Reflector Antennas(a) Aperture blockage efficiency ϵ_3

d_f/d	0.05	0.10	0.20
ϵ_3	0.990	0.956	0.835

(b) Spar blockage efficiency ϵ_4

$N \backslash d$	10λ	100λ	200λ
3	0.946	0.995	0.999
4	0.935	0.994	0.998

 d_f = diameter of blocking structure near focal point d = diameter of main reflector N = number of support spars which are $\lambda/2$ thick

for the entire aperture, then ϵ_t would equal 0.81; see Prob. 8.5-4. As can be seen from Table 8-2, though, since the feed pattern is not symmetric, the aperture distribution will not be either. If an effective -10 -dB edge taper is assumed, the combined efficiency $\epsilon_t \epsilon_1$ from Fig. 8-26 is about 0.78. Now, for a 0.2-mm surface error and a 10.5-mm wavelength, (8-178) yields $\epsilon_2 = e^{-[4\pi(0.2)/10.5]^2} = 0.94$. The feed horn diameter is about 0.05 m so $d_f/d = 0.05/1.22 = 0.04 \sim 0.05$, and Table 8-4(a) yields $\epsilon_3 = 0.99$ for aperture blockage efficiency. The spar blockage efficiency follows from Table 8-4(b) as $\epsilon_4 = 0.994$, since $d = 1.22/0.01/\lambda \approx 100\lambda$ and $N = 4$. The remaining achievement factors are all near unity, so we have

$$\epsilon_{ap} = (1)(0.78)(0.94)(0.99)(0.994) = 0.72. \quad (8-180)$$

Typical efficiency values quoted for high efficiency feeds, such as in this case, are from 0.65 to 0.70. The efficiency of (8-180) would lead to a gain of

$$G = 0.72 \left(\frac{\pi 1.22}{0.0105} \right)^2 = 95,934 = 49.8 \text{ dB}. \quad (8-181)$$

However, the antenna system of Example 8-8 had several waveguide components behind the feed horn to provide for adjustable dual polarization. Thus, the measured gain of 47.6 dB indicates losses of $49.8 - 47.6 = 2.2$ dB. These feed losses are represented through the radiation efficiency, which is now $e = 0.60$. Then the overall aperture efficiency including these losses is $\epsilon_{ap} = 0.60(0.72) = 0.43$.

8.6.4 Other Reflector Antennas

The principles of reflecting surfaces for focusing have been employed in optical telescopes for several centuries. The reflector antenna, however, did not appear until 1888 when Hertz used a cylindrical parabolic mirror of zinc, fed with a dipole along the focal line connected to a spark-gap generator. He used a similar antenna for receiving, at a wavelength of 66 cm. Several other scientists investigated reflectors shortly after Hertz's work. But reflector antenna technology did not really emerge until shortly before World War II, when in 1937 Grote Reber constructed a 9.1-m-diameter prime-focus, reflector antenna for radio astronomy. More detailed history of reflector antennas can be found in [14] and [15].

The prime-focus and Cassegrain fed parabolic reflectors, as described so far in this chapter, were developed roughly from World War II through 1960. Since that period modifications to these basic reflector types have been introduced for the purpose of increasing the aperture efficiency or for special antenna pattern shaping applications to produce a pencil beam, a fan beam, a shaped main beam, low side lobes, or multiple main beams. There are several excellent reviews of the various reflector configurations, solution techniques, and feed design available in the literature [14–18]. We will give a brief accounting of a few of the prominent reflecting antennas in current use.

If a simple feed is used, a single-reflector antenna should be of paraboloidal shape (unless it is small in terms of a wavelength) to achieve a uniform phase over the aperture. The prime-focus parabolic reflector was discussed in Section 8.6.1. There are several variations of the paraboloidal reflectors as shown in Fig. 8-27. The *parabolic cylinder* is used for producing a narrow beamwidth in the plane of the axis of the reflector. The *parabolic torus* is, in a sense, a curved version of the parabolic cylinder and can be used for beam scanning with a rotating feed or for multiple beams with a cluster of feeds. The *spherical reflector* can be used in a similar fashion to produce a pencil beam, because, unlike the paraboloidal reflector, the focal region is diffuse. This allows feed displacement for beam scanning without severe gain loss. Reflectors do not always involve curved structures. The *corner reflector* of Fig. 8-27e is made of planar reflecting sheets joined together forming an angle α . It can be used in either an active or passive manner. In the passive case, the angle α is 90° and incoming plane waves will be reflected back in the same direction. Such an antenna is called *retro-directive*. The corner reflector can be used actively by placing a feed antenna between the reflecting sheets [19]. A rapidly advancing area of reflector technology is that of the *offset reflector*, an example of which is shown in Fig. 8-27f. Aperture blockage is reduced by off-setting the feed. However, the design is complicated by the need for determining the reflector shape.

Greater flexibility is often possible with *multiple-reflector systems*, some examples of which are shown in Fig. 8-28. The Cassegrain reflector antenna was

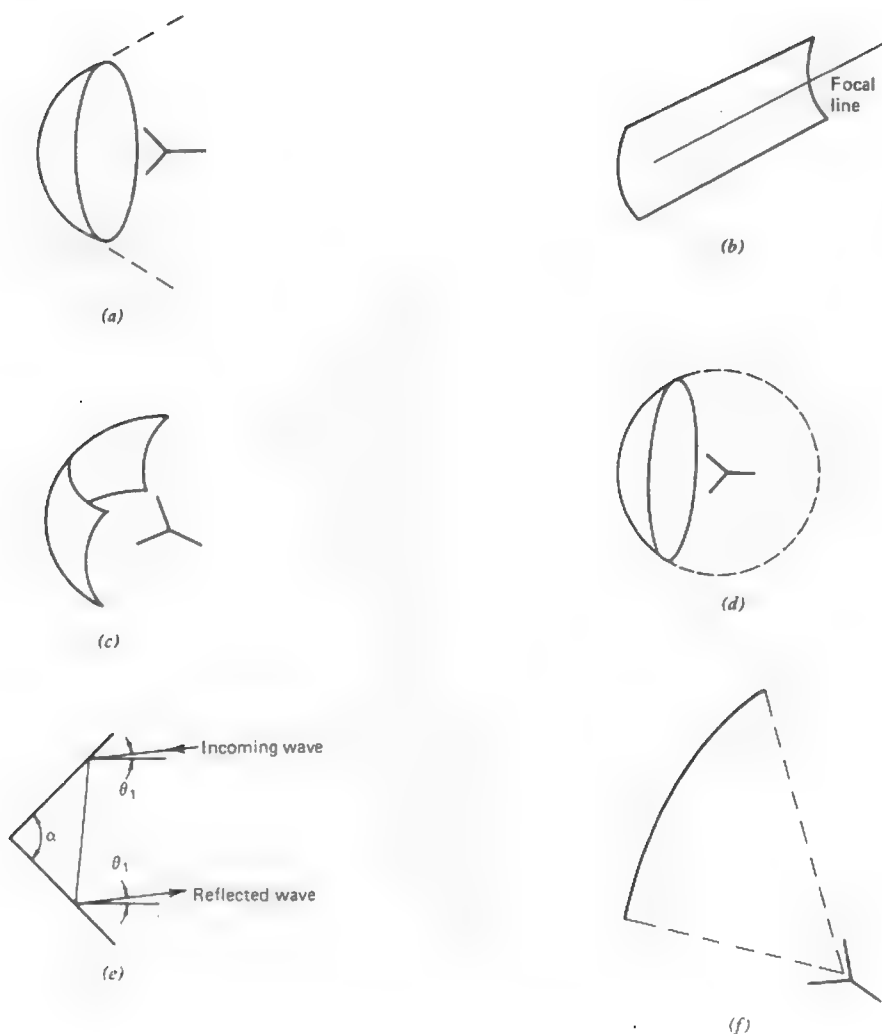


Figure 8-27 Some single-reflector antennas. (a) Paraboloid. (b) Parabolic cylinder. (c) Parabolic torus. (d) Spherical reflector. (e) Corner reflector ($\alpha = 90^\circ$). (f) Offset front-fed reflector.

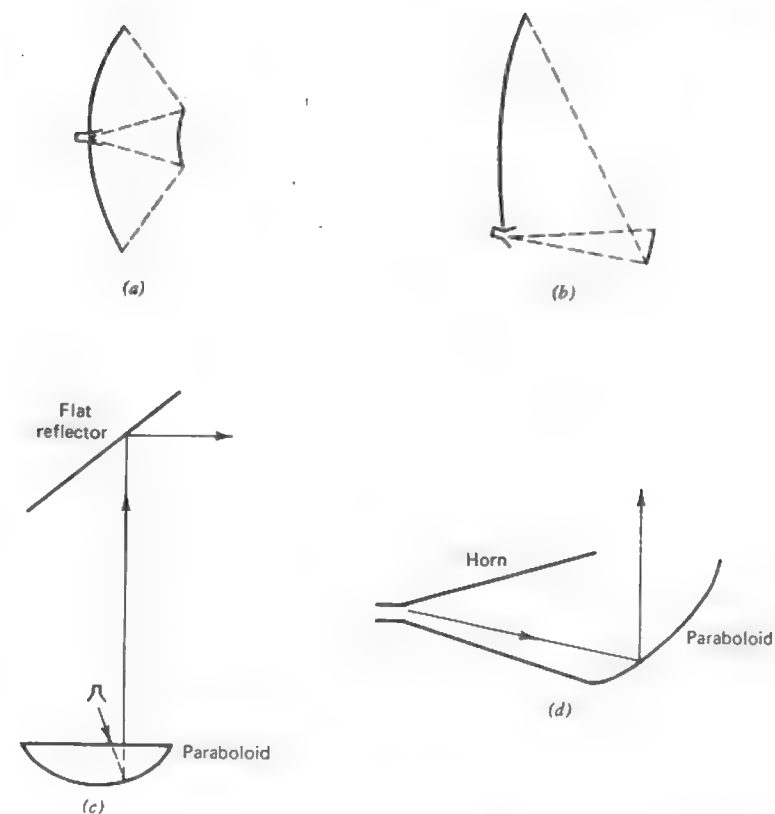


Figure 8-28 Multiple-reflector antenna systems. (a) Symmetrical dual reflector antenna. (b) Offset dual reflector antenna. (c) Periscope system. (d) Horn-reflector antenna.

discussed in Section 8.6.2. Increased pattern control is obtained by changing the paraboloidal main reflector and/or hyperboloidal subreflector shapes of the classical Cassegrain reflector system. Galindo [20] showed that it is possible to achieve arbitrary aperture phase and amplitude with the shaped dual reflector system of Fig. 8-28a. This can be done by starting with a conventional Cassegrain system and deforming the subreflector to obtain a nearly uniform amplitude aperture distribution. The phase errors introduced can then be corrected with minor changes to the main reflector shape without significantly altering the aperture amplitude. This approach provides dramatic improvement in the aperture efficiency [21]. The reflectors may also be shaped to produce low side lobes [22]. A reduced aperture blockage version of the dual reflector antenna is that

employing an offset subreflector, as shown in Fig. 8-28b. In this case the main reflector and subreflector shapes must be determined in the design process. A series of several small reflectors in the so-called *beam waveguide feed system* has several variations for special purpose feeds used with a single large reflector.

There are also several hybrid reflector systems involving different antenna types. The *periscope antenna* of Fig. 8-28c has been used extensively for microwave links. The paraboloidal antenna is located near the ground and the flat reflector on a tower redirects the radiation in the desired direction. Another hybrid antenna used very heavily in microwave links is the *horn-reflector antenna* of Fig. 8-28d. It combines a conical or pyramidal horn and a portion of a paraboloidal reflector. This is actually an offset feed configuration. It is excellent for low noise applications because of the low back lobes and far out side lobes, not afforded by open reflector systems. Horn-reflectors are well suited to side-by-side or back-to-back applications. The most notable horn-reflector antenna is the one in Andover, Maine used to track the Echo balloon in 1961. It is 15 m long and has a 6 by 6 m aperture.

Feeds for large reflector antennas have gradually evolved from dipoles to horns and finally to hybrid mode (combining both TE and TM modes) feeds, which are usually corrugated horns.

REFERENCES

1. R. E. Collin and F. J. Zucker, Editors, *Antenna Theory*, Part 1, McGraw-Hill, New York, 1969; p. 73.
2. E. A. Wolff, *Antenna Analysis*, Wiley, New York, 1967; Chapter 5.
3. A. W. Love, Editor, *Electromagnetic Horn Antennas*, IEEE Press, New York, 1976.
4. R. E. Collin and F. J. Zucker, Editors, *Antenna Theory*, Part 1, McGraw-Hill, New York, 1969; p. 636.
5. M. Abramowitz and I. Stegun, Editors, *Handbook of Mathematical Functions*, NBS Applied Mathematics Series 55, U.S. Printing Office, 1964; Chapter 7.
6. E. V. Jull and L. E. Allan, "Gain of an E-plane sectoral horn—A failure of the Kirchhoff theory and a new proposal," *IEEE Trans. on Ant. and Prop.*, vol. AP-22, pp. 221–226, March 1974.
7. E. V. Jull, "Errors in the predicted gain of pyramidal horns," *IEEE Trans. on Ant. and Prop.*, vol. AP-21, pp. 25–31, Jan. 1973.
8. H. Jasik, Editor, *Antenna Engineering Handbook*, McGraw-Hill, 1961; p. 10-8.
9. D. E. Cozzens, "Tables ease horn design," *Microwaves*, vol. 5, pp. 37–39, March 1966.
10. J. F. Ramsey, "Lambda functions describe antenna/diffraction patterns," *Microwaves*, vol. 6, pp. 69–104, June 1967.
11. A. F. Sciambi, "Instant antenna patterns," *Microwaves*, vol. 5, pp. 48–60, June 1966.
12. J. F. Kauffman, W. F. Croswell and L. J. Jowers, "Analysis of the radiation patterns of reflector antennas," *IEEE Trans. on Antennas and Prop.*, vol. AP-24, pp. 53–65, Jan. 1976.

13. K. E. McKee, A. G. Holtum and T. Charton, "Optimizing gain of parabolic antennas," *Microwaves*, vol. 6, pp. 34–39, March 1967.
14. R. C. Hansen, Editor, *Microwave Scanning Antennas, Vol. I—Apertures*, Academic Press, New York, 1964; Chapter 2.
15. A. W. Love, Editor, *Reflector Antennas*, IEEE Press, New York, 1978.
16. W. V. T. Rusch and P. D. Potter, *Analysis of Reflector Antennas*, Academic Press, New York, 1970.
17. P. J. B. Clarricoats and G. T. Poulton, "High-efficiency microwave reflector antennas—a review," *Proc. IEEE*, vol. 65, pp. 1470–1504, Oct. 1977.
18. P. J. B. Clarricoats, "Some recent advances in microwave reflector antennas," *Proc. IEE (London)*, vol. 126, pp. 9–25, Jan. 1979.
19. D. Proctor, "Graphs simplify corner reflector antenna design," *Microwaves*, vol. 14, pp. 48, 52, July 1975.
20. V. Galindo, "Design of dual-reflector antennas with arbitrary phase and amplitude distributions," *IEEE Trans. on Ant. and Prop.*, vol. AP-12, pp. 403–408, July 1964.
21. W. F. Williams, "High efficiency antenna reflector," *Microwave J.*, vol. 8, pp. 79–82, July 1965.
22. S. V. Parekh and J. H. Cook, "Reshaped subreflectors reduce antenna sidelobes," *Microwaves*, vol. 16, pp. 170–173, May 1977.

PROBLEMS

- 8.1-1 An ideal dipole with an infinitesimal current centered along the z-axis has only a θ -component of E . If this uniform current element is now rotated to line up with the x-axis, there will be both θ - and ϕ -components. Make the necessary changes to the far-zone E expression for the z-directed current case to obtain the far-zone E expression for the x-directed current case. Draw sketches in the xz- and yz-planes indicating the E and H field orientations for the x-directed ideal dipole.
- 8.1-2 Use the principle of duality to derive (8-5) and (8-6) from (8-3) and (8-4), respectively.
- 8.1-3 Show that (8-24) follows from (8-22) and (8-23).
- 8.1-4 Show that (8-26) follows from (8-11).
- 8.1-5 The trigonometric obliquity functions in the far-field expression of (8-24) actually represent projections of the aperture equivalent surface currents onto the plane containing the far-field components (i.e., the θ , ϕ -plane). Examine the relationships connecting the equivalent currents to the far-zone fields to show this for both the electric and magnetic currents. You need only examine the vector nature of the relationships.
- 8.1-6 If the incident field is x-polarized in Example 8-1, write radiation field E_ϕ and the pattern $F(\theta)$. Your answer will be that of (4-17) with a coordinate change. Is the appropriate boundary condition for E_ϕ satisfied on the conducting plane?
- 8.2-1 Derive (8-32).
- 8.2-2 Use geometric arguments to prove that $du\,dv = \cos\theta\,d\Omega$ where $d\Omega = \sin\theta\,d\theta\,d\phi$.
- 8.3-1 Prove (8-62).

8.3-2 Prove that the uniform amplitude aperture excitation yields the highest directivity of all uniform phase excitations. *Hint:* Use (8-65) and the Schwarz inequality

$$\left| \iint_S f g \, dS' \right|^2 \leq \iint_S f^2 \, dS' \iint_S g^2 \, dS'$$

for any functions f and g . Let $g = 1$ and f equal the aperture field.

8.3-3 Show that the aperture taper efficiency is $\frac{2}{3}$ for a rectangular aperture with a uniform amplitude distribution in one direction and a cosine squared distribution in the other.

8.3-4 A rectangular aperture (L_x by L_y) has a field distribution which is cosine tapered in both the x - and y -directions. Derive the directivity expression. What is the aperture taper efficiency?

8.3-5 Compute the directivity in decibels for a rectangular aperture with $L_x = 10\lambda$ and $L_y = 20\lambda$ for (a) a completely uniform aperture illumination and (b) a cosine amplitude taper in one direction and a uniform taper in the other aperture direction.

8.3-6 Evaluate the aperture taper efficiency for a triangular tapered aperture distribution where

$$E_a(x', y') = \left| 1 - \frac{2|x'|}{L_x} \right| \hat{x} \quad |x'| \leq \frac{L_x}{2}, \quad |y'| \leq \frac{L_y}{2}.$$

8.3-7 Is the uniform aperture distribution physically realizable? Why?

8.3-8 An antenna operating at 150 MHz has a physical aperture area of 100 m², a gain of 23 dB, and a directivity of 23.5 dB. Compute (a) effective aperture $A_{e\phi}$, (b) maximum effective aperture A_{em} , (c) aperture efficiency ϵ_{ap} , (d) radiation efficiency ϵ , and (e) D/D_0 .

8.3-9 Prove the last of (8-80).

8.3-10 The approximate directivity formula of (8-81) can be derived rather simply for the special case where $HP_E = HP_H = HP$ and HP is small. Assume all radiation is uniform and confined to a cone of half-angle $HP/2$. Then compute Ω_A by integration and utilize the fact that HP is small.

8.3-11 A horn antenna with a 185.5 by 137.4 cm rectangular aperture has the following measured parameter values at 0.44 GHz: $HP_E = 30^\circ$, $HP_H = 27^\circ$, and $G = 15.5$ dB.

(a) Compute the aperture efficiency.

(b) From the measured half-power beamwidths estimate the gain.

8.3-12 Repeat Prob. 8.3-11 for a horn with a 28.85 by 21.39 cm aperture and $HP_E = 12^\circ$, $HP_H = 13^\circ$, and $G = 22.1$ dB at 6.3 GHz.

8.3-13 A 3.66-m (12-ft) diameter circular parabolic reflector operates at 460 MHz. The measured parameters of this antenna are: $G = 22.2$ dB and $HP_E = HP_H = 12.5^\circ$. Estimate the gain using both (8-84) and (8-82).

8.3-14 Estimate the gain of a circular parabolic reflector operating at 28.56 GHz in two ways:

(a) Using only its size which is 1.22 m (4 ft) in diameter.

(b) Using only the measured half-power beamwidths which are $HP_E = 0.605^\circ$ and $HP_H = 0.556^\circ$.

8.4-1 Derive the expression for R_H in (8-86).

8.4-2 Derive the H -plane sectoral horn radiation field expression in (8-93) to (8-95).

8.4-3 In the H -plane pattern expression of (8-103) and (8-104) for an H -plane sectoral horn:

(a) Show that s_1 follows from s'_1 of (8-95).

(b) Show that the phase term $(\pi/8t)[(A/\lambda)\sin\theta + \frac{1}{2}]^2$ follows from the corresponding term in (8-94).

8.4-4 Derive the directivity formula (8-105) for an H -plane sectoral horn from (8-65). The numerator of (8-65) can be evaluated using (8-92) to (8-94).

8.4-5 Plot A/λ versus R_1/λ for an optimum H -plane sectoral horn using the approximate formula (8-106). Then indicate the points on this graph which correspond to optimum performance for each curve of the family of curves in Fig. 8-12.

8.4-6 The H -plane pattern for an H -plane sectoral horn arises from the first integral in (8-92).

(a) First evaluate this integral for a no phase error condition.

(b) Show that the on-axis value of the H -plane pattern relative to the on-axis value of the zero phase error case is given by

$$\frac{\pi}{16\sqrt{t}} I(\theta = 0^\circ, \phi = 0^\circ).$$

(c) Evaluate this for $t = \frac{1}{8}, \frac{1}{4}, \frac{3}{8},$ and $\frac{1}{2}$ and compare to the values from Fig. 8-11.

8.4-7 An H -plane sectoral horn antenna has an axial length of 5λ and a flare half-angle α_H of 12.6° .

(a) Plot the polar plot of the H -plane radiation pattern in decibels. Use Fig. 8-11.

(b) Compute the directivity function $\lambda D_H/h$ using (8-105) and compare to that obtained from Fig. 8-12.

(c) Since the aperture is not large relative to a wavelength, use the zero phase error directivity formula of (8-56) to compute $\lambda D_H/h$.

8.4-8 Design an optimum H -plane sectoral horn antenna with 12.15 dB gain at 10 GHz. It is fed with WR90 waveguide.

(a) Find the horn dimensions employing Fig. 8-12.

(b) Draw the H -plane horn geometry to scale.

(c) Use (8-105) to compute the directivity as a check.

8.4-9 Repeat Prob. 8.4-8(a) except use (8-106) in (8-105) instead of Fig. 8-12.

8.4-10 Derive the E -plane sectoral horn far-zone electric field expression of (8-112).

8.4-11 Show how the E -plane pattern magnitude expression for an E -plane sectoral horn of (8-115) follows from (8-112).

8.4-12 Find the physical length in wavelengths by which waves at the edges of a horn aperture trail those at the center. Do this for optimum operation and in both the H -plane and E -plane.

8.4-13 Use physical reasoning to explain why the phase error parameters for optimum E - and H -plane sectoral horns are different.

8.4-14 An optimum gain E -plane sectoral horn antenna is to have a half-power beamwidth of 11° in the E -plane at 10 GHz. It is to attach to a WR90 waveguide. Determine the horn dimensions to achieve the required beamwidth and 14.9 dB gain.

8.4-15 An E -plane sectoral horn antenna has an E -plane aperture height of 24.0 cm and a

half-flare angle of 16.5° . It is attached to a WR284 waveguide. Compute the gain at 3.75 GHz (a) using (8-116) and (b) using (8-120).

8.4-16 Explain why the E - and H -plane sectoral horn radiation fields do not go to zero for $\theta > \pi/2$ as we said they would in connection with (8-24).

8.4-17 Derive the optimum pyramidal horn antenna design equation of (8-126).

8.4-18 Start with the value of $\sigma = 10.17$ given in Example 8-7 and verify the horn dimensions of (8-128).

8.4-19 Design an optimum gain pyramidal horn antenna with 20 dB gain at 10 GHz. It is connected to a WR90 waveguide.

8.4-20 An "off-the-shelf" pyramidal horn antenna that operates from 18 to 26.5 GHz has a gain of 24.7 dB at 24 GHz. It is fed from WR42 waveguide.

(a) Use optimum design principles to determine the horn dimensions in centimeters necessary for construction of the antenna.

(b) Compute the principal plane half-power beamwidths in degrees.

(c) Use these beamwidth values to estimate the gain.

(d) Compute the half-power beamwidths that follow from line source theory with the same amplitude tapers in the principal planes as the horn. Compare to the values from (b) and explain any differences.

(e) Plot the E - and H -plane patterns in polar-dB form.

8.4-21 Derive the following relationship which must be satisfied for a physically realizable pyramidal horn antenna.

$$\frac{R_1}{\lambda} = \frac{1 - \frac{b/\lambda}{B/\lambda} \frac{R_2}{\lambda}}{1 - \frac{a/\lambda}{A/\lambda}}$$

8.4-22 A square main beam horn antenna. It is often desirable to have equal principal plane half-power beamwidths. This problem develops a design technique for a so-called square main beam pyramidal horn. If optimum design techniques under the condition of a square main beam are used, the resulting horn dimensions will render a horn that cannot be constructed. To avoid this problem we can design for a square main beam and aim for near optimum conditions. To do this we first determine the aperture dimensions that give the desired beamwidths and optimum operation. Then the axial lengths are adjusted to provide a physically realizable structure. This will probably not move the operating point too far from optimum. Follow this procedure to design a square main beam horn at 8 GHz with 12° beamwidths and fed by WR90 waveguide.

(a) Determine A/λ and B/λ .

(b) Use the results of Prob. 8.4-21 for adjusting the axial lengths. Do this to keep the fractional increase or decrease of both the same, that is, use

$$\frac{R_1}{\lambda} = \frac{R_{1\text{op}}}{\lambda} f \quad \text{and} \quad \frac{R_2}{\lambda} = \frac{R_{2\text{op}}}{\lambda} f$$

and solve for the constant f

(c) Evaluate the final phase error parameters t and s .

(d) Give the horn dimensions in centimeters.

(e) Evaluate the gain.

(f) Compute the aperture efficiency.

8.5-1 If the equivalent current formulation is used which includes both electric and magnetic surface current densities, write the radiated electric field expression analogous to (8-136).

8.5-2 Verify that the uniform circular aperture pattern of (8-137) is unity for $\theta = 0$.

8.5-3 Derive the pattern expression $f(\theta, n, C)$ in Table 8-1(b) for a parabolic taper on a pedestal.

8.5-4 The directivity of a circular aperture antenna can be found from (8-65).

(a) Show that for a parabolic taper ($n = 1$) on a pedestal that

$$e_t = \frac{D}{D_u} = \frac{1}{4} \frac{(1+C)^2}{C + \frac{1}{3}(1-C)^2}$$

(b) Show that for a parabolic taper squared ($n = 2$) on a pedestal that

$$e_t = \frac{D}{D_u} = \frac{1}{9} \frac{(1+2C)^2}{C^2 + \frac{2}{3}C(1-C) + \frac{1}{3}(1-C)^2}$$

(c) Evaluate e_t for $n = 1$ and 2 for a -10 -dB edge taper.

8.6-1 Derive (8-158).

8.6-2 Sketch to scale the cross section of parabolic reflectors for the f/d ratios of $\frac{1}{4}$, $\frac{1}{3}$, and $\frac{1}{2}$.

8.6-3 Plot the edge illumination (in decibels) of a circular parabolic reflector due to spreading loss only (i.e., for an isotropic feed) as a function of f/d from 0 to 1.

8.6-4 Compute the half-power beamwidth for the H -plane pattern of the parabolic reflector antenna of Example 8-8. Use the H -plane feed horn characteristics of Table 8-2. Interpolate between values given in Table 8-1 for a parabolic-squared on a pedestal taper.

8.6-5 A commercially available parabolic reflector antenna operating at 2.1 GHz has an aperture diameter of 1.83 m (6 ft). Compute the gain in decibels.

8.6-6 A commercially available parabolic reflector antenna operating at 11.2 GHz has an aperture diameter of 3.66 m (12 ft). Compute the gain in decibels.

9

HIGH-FREQUENCY METHODS

Optics is a well-understood area of physics which deals with the characteristics of light wave propagation. It was Maxwell who showed before 1873 that the propagation of light could be viewed as an electromagnetic phenomenon. Since the wavelength of light waves is usually small compared to objects with which it interacts, the analytical treatment of light wave propagation is much different than that employed to analyze lower frequency propagation where the size of a scattering surface is comparable to the wavelength.

A very useful and easily understood method for analyzing optical problems is the ray concept. The relationship between ray optics and wave propagation is apparent from the famous works of Huygens in 1690 and Fresnel in 1818, but was not formally shown until the works of Luneberg in 1944 and Kline in 1951 [1]. Since that time the well-known methods of optics have found increasing use in the treatment of many electromagnetic problems in the radio frequency portion of the spectrum for situations where the wavelength is small compared to the geometrical dimensions of the scatterer or antenna. In these cases asymptotic high-frequency methods must be employed since it is not practical to use moment methods (Chapter 7) or eigenfunction expansions. This is because the rate of convergence of both of these techniques is generally quite poor when dealing with an electrically large antenna or scatterer.

In this chapter we will first examine the principles of geometrical optics followed by a brief discussion of the more general concept of physical optics. We

will then see that in many situations geometrical optics is inadequate to completely describe the behavior of the electromagnetic field and that it is necessary to include another field called the diffracted field. The diffracted field, when added to the geometrical optics field, permits us to solve many practical radiation and scattering problems in a moderately straightforward manner that could not be solved any other way.

9.1 GEOMETRICAL OPTICS

Geometrical optics, or *ray optics* as it is often called, was originally developed to analyze the propagation of light where the frequency is sufficiently high that the wave nature of light need not be considered. Indeed, geometrical optics can be developed by simply considering the transport of energy from one point to another without any reference to whether the transport mechanism is particle or wave in nature.

Classical geometrical optics applies to isotropic lossless media which may or may not be homogeneous. In this chapter we will only consider homogeneous media where the index of refraction is assumed to be real and is given by

$$n = \frac{c}{v} \quad (9-1)$$

and is not a function of position within a given medium. Here c is approximately 3×10^8 m/s and v is the velocity of propagation in the medium. In a homogeneous medium energy moves along ray paths that are straight lines. Normal to these ray paths are a family of surfaces called the *eikonal* of the ray system. In applying geometrical optics it is only necessary that we know either the eikonal of the ray system or the ray paths, since the two are uniquely related.

For a plane wave in homogeneous media the eikonal surfaces are planes perpendicular to the ray paths as shown in Fig. 9-1a. For a spherical source, the eikonal surfaces are spherical surfaces perpendicular to the ray paths as shown in Fig. 9-1b.

The variation of the amplitude of the geometrical optics field within a ray tube is determined by the law of energy conservation since the rays are lines of energy flow. Consider two surfaces L_o and $L_o + \Delta L$ as shown in Fig. 9-2. Between the two surfaces we can construct a tube of constant energy flux by using the rays. Thus, the energy through cross section $d\sigma_o$ at P_o must equal the energy flux through cross section $d\sigma$ at P . If S is the rate of energy flow per unit area, the condition of constant energy flow through the flux tube is

$$S_o d\sigma_o = S d\sigma. \quad (9-2)$$

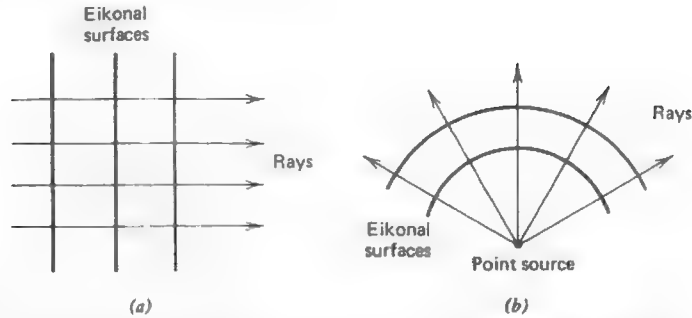


Figure 9-1 The relation of rays and eikonals for two types of sources. (a) Plane wave. (b) Spherical wave.

In the case of electromagnetic waves the quantity S is the real part of the complex Poynting vector and we can assume that

$$S = \frac{1}{2} \sqrt{\frac{\epsilon}{\mu}} |E|^2. \quad (9-3)$$

Substituting (9-3) into (9-2) yields

$$|E_o|^2 d\sigma_o = |E|^2 d\sigma. \quad (9-4)$$

Solving for $|E|$ we obtain

$$|E| = |E_o| \sqrt{\frac{d\sigma_o}{d\sigma}}. \quad (9-5)$$

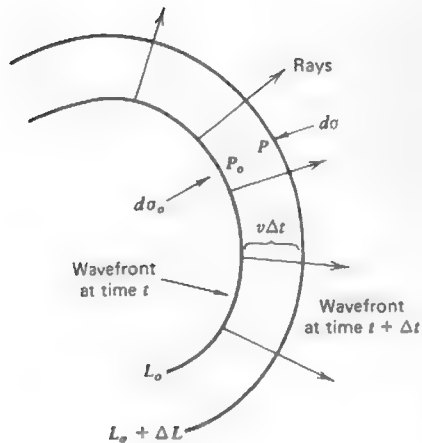


Figure 9-2 The relation of rays and wavefronts.

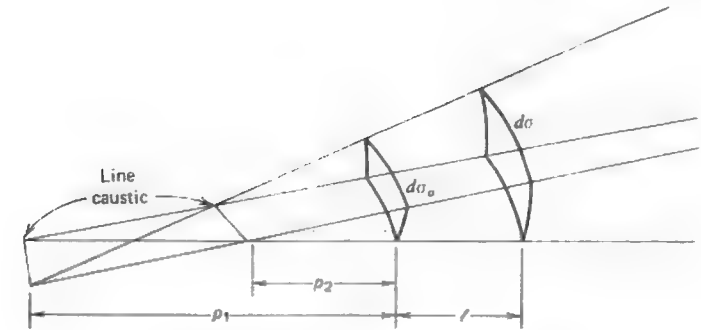


Figure 9-3 An astigmatic ray tube.

Therefore we have obtained a relationship between the amplitude of the geometrical optics field at one point in terms of the amplitude at another.

The relationship in (9-5) would be more useful if the radii of curvature of the wavefront surfaces $d\sigma$ and $d\sigma_o$ were used. Consider the astigmatic ray tube picture in Fig. 9-3. The principle radii of curvature of $d\sigma_o$ are ρ_1 and ρ_2 while the principle radii of curvature of $d\sigma$ are $(\rho_1 + l)$ and $(\rho_2 + l)$. We can write for the ratios

$$\frac{d\sigma_o}{\rho_1 \rho_2} = \frac{d\sigma}{(\rho_1 + l)(\rho_2 + l)} \quad (9-6)$$

and thus

$$\frac{d\sigma_o}{d\sigma} = \frac{\rho_1 \rho_2}{(\rho_1 + l)(\rho_2 + l)}. \quad (9-7)$$

From (9-5) we have

$$|E| = |E_o| \sqrt{\frac{\rho_1 \rho_2}{(\rho_1 + l)(\rho_2 + l)}}. \quad (9-8)$$

Note that the tube of rays converge to a line at $\rho_1 = 0$ and $\rho_2 = 0$ where the cross section of the ray tube goes to zero. Therefore the amplitude of the geometrical optics field description becomes infinite there although the actual field does not. The locus of points where the ray tube cross section exhibits such behavior is called a *caustic*. Caustics may be a point, a line, or a surface. For example, consider a point source as shown in Fig. 9-4. We can construct a ray tube from four rays and write

$$\frac{d\sigma_o}{\rho^2} = \frac{d\sigma}{(\rho + l)^2}. \quad (9-9)$$

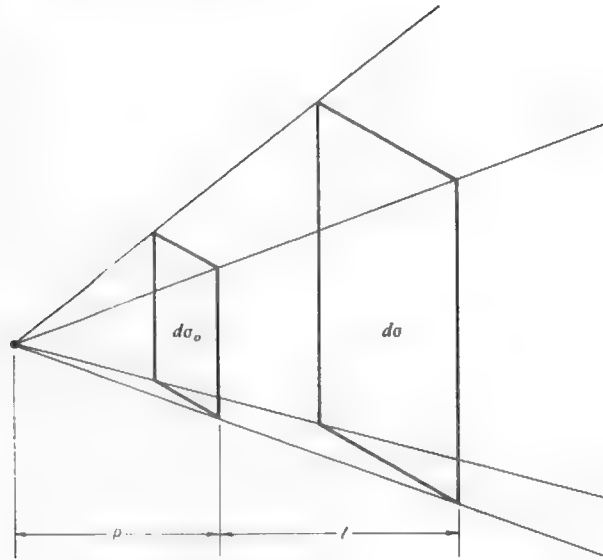


Figure 9-4 A tube of rays from a point source.

Thus

$$|E| = |E_0| \sqrt{\frac{\rho^2}{(\rho + \ell)^2}} = |E_0| \frac{\rho}{\rho + \ell}. \quad (9-10)$$

The caustic would be located at the point source in this case.

In both (9-8) and (9-10) we note that as ℓ becomes large we have the usual inverse distance type field dependence found in the far zone of a three-dimensional source. Often, however, one is concerned with two-dimensional problems where one of the radii of curvature, say ρ_2 , becomes infinite. In such problems

$$|E| = |E_0| \sqrt{\frac{\rho_1}{\rho_1 + \ell}}. \quad (9-11)$$

Here, the eikonal surfaces are cylindrical and, as $\ell \rightarrow \infty$, we have an amplitude dependence of the field at large distances of the form $1/\sqrt{\ell}$. Obviously, if both ρ_1 and ρ_2 are infinite the eikonal surfaces are planes and $|E|$ is a constant for all values of ℓ .

The results of (9-8), (9-10) and (9-11) are extremely important for they permit us to easily compute the amplitude of the geometrical optics field at one point in terms of its known value at another. In electromagnetic field problems, however, we must also include the phase. Phase can be introduced into (9-8) artificially.

First, we take our phase reference to coincide with the amplitude reference. Thus, the electrical phase of the ray tube is given by $e^{-j\beta\ell}$ and we may write for the amplitude and phase of the field in the ray tube of Fig. 9-3

$$E = E_0 e^{j\phi_0} \sqrt{\frac{\rho_1 \rho_2}{(\rho_1 + \ell)(\rho_2 + \ell)}} e^{-j\beta\ell} \quad (9-12)$$

or

$$E = E_0 e^{j\phi_0} A(\rho_1, \rho_2, \ell) e^{-j\beta\ell} \quad (9-13)$$

where E_0 is the reference amplitude at $\ell = 0$, ϕ_0 is the reference phase at $\ell = 0$, $A(\rho_1, \rho_2, \ell)$ is the general spatial attenuation factor, and $e^{-j\beta\ell}$ is the spatial phase delay factor.

Note that when ℓ becomes less than $-\rho_2$ the quantity under the radical sign in $A(\rho_1, \rho_2, \ell)$ becomes negative and a phase jump of $\pi/2$ occurs when the observer passes through the caustic. While we can neither predict the amplitude or the phase of the geometrical optics field at the caustic, we can determine the fields on either side of the caustic.

Equation (9-12) or (9-13) permits us to approximately express the field at a point (i.e., ℓ) in terms of the value at a known point (i.e., $\ell = 0$). Rigorously, the result is only approximate, becoming more accurate as the wavelength tends toward zero. In practice, however, we will find the geometrical optics expression to be highly accurate for engineering purposes where the assumptions of geometrical optics are valid.

To finish our initial discussion of geometrical optics, we illustrate its use by considering the problem of reflection at a curved surface and the subsequent calculation of the radar cross section of a sphere. From (9-12) it is apparent that we need an expression for the radii of curvature of the wavefront in terms of the geometrical radius of curvature of the surface. Consider Fig. 9-5 which depicts a line source parallel with the axis of a convex cylinder of arbitrary cross section. From Fig. 9-5a

$$\gamma_1 = \pi - \alpha - (\pi - \theta_0) = \theta_0 - \alpha. \quad (9-14)$$

The element of arc length in Fig. 9-5b is equal to $r_1^c \Delta\alpha$ and

$$r_1^c \Delta\alpha = \frac{\Delta\gamma_1 / \ell_0}{\cos \theta_0} = \frac{(\Delta\theta_0 - \Delta\alpha) / \ell_0}{\cos \theta_0}. \quad (9-15)$$

Since $\Delta\gamma_2 = \Delta\theta_0 + \Delta\alpha$ we have

$$r_1^c \Delta\alpha = \frac{\rho_1 \Delta\gamma_2}{\cos \theta_0} = \rho_1 \frac{\Delta\theta_0 + \Delta\alpha}{\cos \theta_0}. \quad (9-16)$$

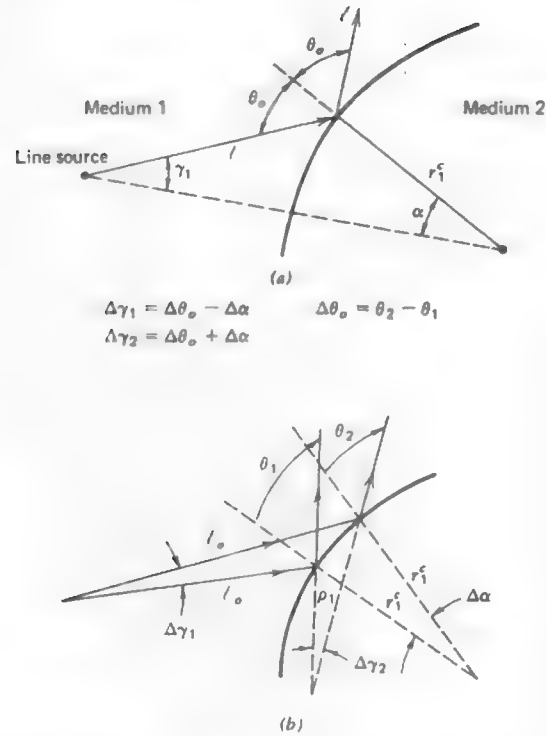


Figure 9-5 Ray geometry for reflection by a curved conducting surface.

Solving both (9-15) and (9-16) for $r_1^c \Delta\alpha \cos \theta_o$ we have, respectively,

$$r_1^c \Delta\alpha \cos \theta_o = l_o \Delta\theta_o - l_o \Delta\alpha \quad (9-17)$$

and

$$r_1^c \Delta\alpha \cos \theta_o = \rho_1 \Delta\theta_o + \rho_1 \Delta\alpha \quad (9-18)$$

Solving both of these equations for $\Delta\alpha$ and equating the two results yields

$$\frac{l_o \Delta\theta_o}{r_1^c \cos \theta_o + l_o} = \frac{\rho_1 \Delta\theta_o}{r_1^c \cos \theta_o - \rho_1} \quad (9-19)$$

which after some manipulation gives us the desired result

$$\frac{1}{\rho_1} = \frac{1}{l_o} + \frac{2}{r_1^c \cos \theta_o} \quad (9-20)$$

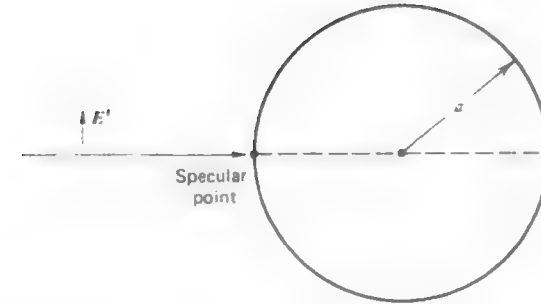


Figure 9-6 Geometrical optics scattering by a sphere.

This equation¹ relates the principal radii of curvature of the reflected wavefront to the geometrical radius of curvature of the surface at the point where the ray strikes the surface.

As a simple example of the application of (9-20), consider the situation shown in Fig. 9-6 wherein a plane wave is incident upon a sphere. We wish to find the field scattered back in the direction of the transmitter and from this *back-scattered field* find the radar cross section of the sphere. Thus, the only ray we need consider is that reflected from what is called the *specular point*. In this situation, then, $l_o = \infty$, $\theta_o = 0^\circ$, and $r_c = a$ in (9-20) and we have the result that

$$\rho_1 = \frac{a}{2} = \rho_2 \quad (9-21)$$

where ρ_2 is the radius of curvature of the reflected wavefront orthogonal to ρ_1 . (See Prob. 9.1-1 for an expression for ρ_2 .)

If the incident field has a value of E_o at the specular point, then in the backscattered direction,

$$E^s = -E_o \frac{\rho_1}{\rho_1 + l} e^{-j\beta l} \quad (9-22)$$

there being the same value for ρ_2 as for ρ_1 in this example. Therefore, using (1-234) the radar cross section is (at high frequencies)

$$\sigma = \lim_{l \rightarrow \infty} 4\pi l^2 \left| \frac{a/2}{a/2 + l} \right|^2 = \pi a^2. \quad (9-23)$$

¹ Even though this result is based on a two-dimensional configuration, the result is somewhat more general than this in that it holds true in the plane of incidence (see Section 9.4) whenever the plane of incidence coincides with the principal planes of the surface.

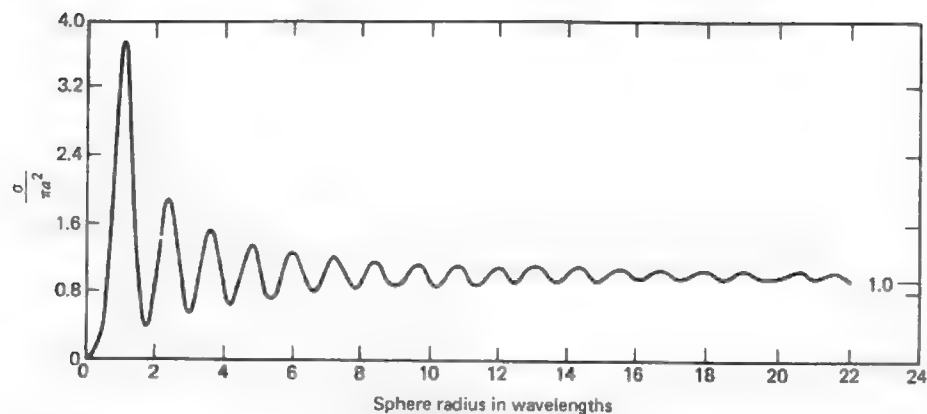


Figure 9-7 Radar cross section, σ , of a sphere versus the electrical radius of the sphere [2; 3, 4].

The exact value for $\sigma/\pi a^2$ is shown in Fig. 9-7. We note that as the radius of the sphere becomes larger, the more closely the geometric optics cross section approaches the exact result. That is what one would expect since geometrical optics assumes the wavelength is small when compared to the geometrical dimensions of the scattering surface. Furthermore, the result in (9-23) is frequency independent, which is typical of geometrical optics calculations.

9.2 PHYSICAL OPTICS

In the previous section we calculated the scattered field from the sphere by geometrical optics. Often we can calculate these same scattered fields by physical optics. The concept of *physical optics* can be considered to be somewhat more general than geometrical optics since the equations obtained from physical optics for the scattered field from a conducting body often reduce to the equations of geometrical optics in the high-frequency limit. In fact, it is assumed in physical optics that the field at the surface of the scattering body is the geometrical optics surface field. This implies that, at each point on the illuminated side of the scatterer, the scattering takes place as if there were an infinite tangent plane at that point while over the shadowed regions of the scatterer the field at the surface is zero.

For a perfectly conducting body the assumed physical optics surface current is

$$\mathbf{J}_{po} = \begin{cases} \hat{\mathbf{n}} \times \mathbf{H}_{total} & \text{in the illuminated region} \\ 0 & \text{in the shadowed region} \end{cases} \quad (9-24)$$

where $\hat{\mathbf{n}}$ is a unit normal vector outward from the surface of interest as shown in Fig. 9-8. Let us derive an expression for the scattered electric field from such a body. Starting with the vector potential, we have

$$\mathbf{A} = \iint_S \frac{\mathbf{J}_{po} e^{-j\beta R}}{4\pi R} ds \quad (9-25)$$

where R is the distance between the source point and observation point.

From image theory, the tangential components of \mathbf{H} at a perfect conductor are just twice those from the same source when the conducting scatterer is replaced by equivalent currents in free space. Thus the physical optics current is given by

$$\mathbf{J}_{po} = 2(\hat{\mathbf{n}} \times \mathbf{H}^i) \quad (9-26)$$

if we assume the incident field phase to be zero at the phase reference plane. Thus, making the customary far-field assumptions we can write

$$\mathbf{A} = \frac{e^{-j\beta r_o}}{4\pi r_o} \iint_S 2(\hat{\mathbf{n}} \times \mathbf{H}^i) e^{-j\beta r'} ds \quad (9-27)$$

from which the far-zone scattered field is given by $\mathbf{E}^s = -j\omega\mu\mathbf{A}$, or

$$\mathbf{E}^s = -\frac{j\omega\mu e^{-j\beta r_o}}{4\pi r_o} \iint_S 2(\hat{\mathbf{n}} \times \mathbf{H}^i) e^{-j\beta r'} ds \quad (9-28)$$

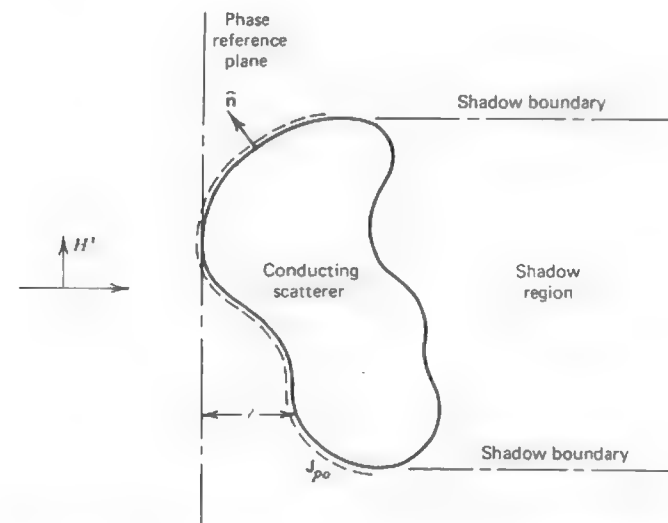


Figure 9-8 Physical optics current on a conducting scatterer.

where l is the distance from phase reference plane in Fig. 9-8 to the scatterer and l_o is the distance from the phase reference plane to the far-field observation point. It should be noted that this expression for the scattered field is frequency dependent in contrast to the geometrical optics expression which is frequency independent. It might, therefore, be intuitively inferred that physical optics provides a more accurate approximation to the scattered field. While this may be so in certain cases, a general conclusion cannot be reached since necessary and sufficient conditions for the valid application of physical optics are not known. It is fortunate for the engineer that physical optics works in many practical problems, even though in some of these problems prior justification of its application would be difficult to make.

Let us make a physical optics calculation of the radar cross section of the sphere, and then compare the result with that obtained via geometrical optics. From (9-28) we can write for the magnitude of E^s

$$|E^s| = \frac{\eta}{2\lambda l_o} \left| \iint_S 2(\hat{n} \times \mathbf{H}^i) e^{-j\beta l} ds \right|. \quad (9-29)$$

Using the definition of the radar cross section (RCS) we obtain

$$\sigma = \frac{4\pi}{\lambda^2} \left| \frac{1}{H^i} \iint_S (\hat{n} \times \mathbf{H}^i) e^{-j\beta l} ds \right|^2. \quad (9-30)$$

For the case of the sphere shown in Fig. 9-9, we note that the only component of current that will have a net contribution to the backscattered field is given by

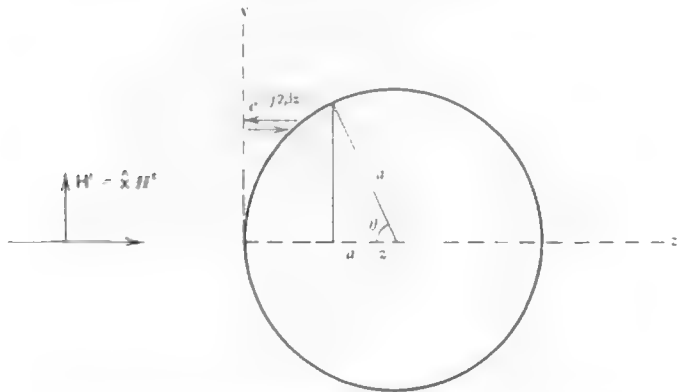


Figure 9-9 Physical optics scattering by a sphere.

$2\hat{z} \times (\hat{n} \times \hat{x})H^i$. Using the vector identity (A-7), this reduces to $-(\hat{z} \cdot \hat{n})\hat{x}H^i$. Thus,

$$\sigma = \frac{4\pi}{\lambda^2} \left| \iint_S -(\hat{z} \cdot \hat{n}) e^{-j2\beta z} ds \right|^2 \quad (9-31)$$

since $l = 2z$ due to the reference plane being the $z = 0$ plane. From Fig. 9-9 we note that

$$\hat{z} \cdot \hat{n} = \cos \theta = \frac{a - z}{a} \quad (9-32)$$

and that an element of surface area is $ds = a^2 \sin \theta d\theta d\phi$. Since $a - z = a \cos \theta$, $dz = a \sin \theta d\theta$ and we have

$$\sigma = \frac{4\pi}{\lambda^2} \left| \int_0^{2\pi} \int_0^\pi e^{-j2\beta z} \left(\frac{a - z}{a} \right) a dz d\phi \right|^2. \quad (9-33)$$

Performing the integration we have

$$\sigma = \frac{4\pi}{\lambda^2} \left| 2\pi \frac{1}{j2\beta} \left(a - \frac{1 - e^{-j2\beta a}}{j2\beta} \right) \right|^2. \quad (9-34)$$

The exponential term arises from the artificially imposed discontinuity in the current at the $\theta = \pi/2$ location on the sphere. Since this discontinuity is nonphysical, so too is the exponential term in (9-34) and we must disregard it. Thus,

$$\sigma = \pi a^2 \left| \frac{1}{j} \left(1 - \frac{1}{2j\beta a} \right) \right|^2 \xrightarrow{\beta a \rightarrow \infty} \pi a^2. \quad (9-35)$$

We see then that the radar cross section of the sphere obtained via physical optics reduces to the geometrical optics result in the high-frequency limit.

The fact that we have had to eliminate the third term in (9-34) is not a peculiarity of the sphere, but is common to any problem employing physical optics wherein a nonphysical discontinuity will give rise to an erroneous contribution to the scattered field that can be numerically significant when compared to the geometrical optics contribution.

The second term in (9-35) may be taken to be the second term in a high-frequency asymptotic expansion of the scattered field. Such an expansion is in inverse powers of the frequency and is known as a Luneburg-Kline expansion [1]. The Luneburg-Kline expansion satisfies the wave equation and is a formal way of showing the correspondence between optics and electromagnetics in the high-frequency limit. The leading term in the Luneburg-Kline expansion is, in fact, the geometrical optics term which is also the first term in (9-35).

Physical optics is more useful to us than just finding radar cross sections. For example, if we wish to find the far-field pattern of a parabolic reflector antenna, physical optics is one way of doing so. In fact, it is probably the easiest way of finding the radiated field on the forward axis of the reflector antenna. In directions other than on the forward axis of the reflector antenna, physical optics provides us with a nonzero estimate of the radiation pattern. This should be contrasted with geometrical optics which can only provide information in a specular direction, but does so in a straight-forward manner.

In summary, physical optics is an approximate method of considerable usefulness that can be expected to provide an accurate representation of the scattered field arising from a surface where the postulated physical optics current is reasonably close to the true current distribution. We recall from the discussion at the beginning of this section that the physical optics current will be a reasonable representation of the true current if the field at the scatterer surface is correctly given by the geometrical optics surface field. Thus, we can view physical optics as an extension of geometrical optics and as such it is a high-frequency method.

9.3 WEDGE DIFFRACTION THEORY

In the previous two sections we introduced the ray-optical concept of geometrical optics and the somewhat more general concept of physical optics. Both theories were applied to the calculation of the backscattered field from a sphere, but no attempt was made to determine the field in the forward scattering direction, in particular the shadowed region in Figs. 9-6 or 9-8. Since physical optics postulates a current only on the lit side and zero current on the shadowed side, the physical optics current alone is incapable of correctly predicting a nonzero field in the shadow region even though an actual measurement would generally indicate the presence of a field there. By simple ray tracing it is quite apparent that geometrical optics is also incapable of correctly predicting a nonzero field in the shadow region. However, geometrical optics may be extended to include a class of rays, called *diffracted rays* [5, 6], which permit the calculation of fields in the shadow region of a scatterer. Diffracted rays are produced, for example, when a ray strikes an edge, a vertex, or is incident tangentially to a curved surface as illustrated in Fig. 9-10. It is these rays that account for a nonzero field in the shadow region. In addition, they also modify the geometrical optics field in the illuminated region. It is the purpose of this section to examine in some detail one type of diffracted ray, the wedge diffracted ray of Fig. 9-10a.

Consider the wedge diffraction situation shown in Fig. 9-10a. Geometrical optics would predict a sharp discontinuity in the field at a *shadow boundary* as

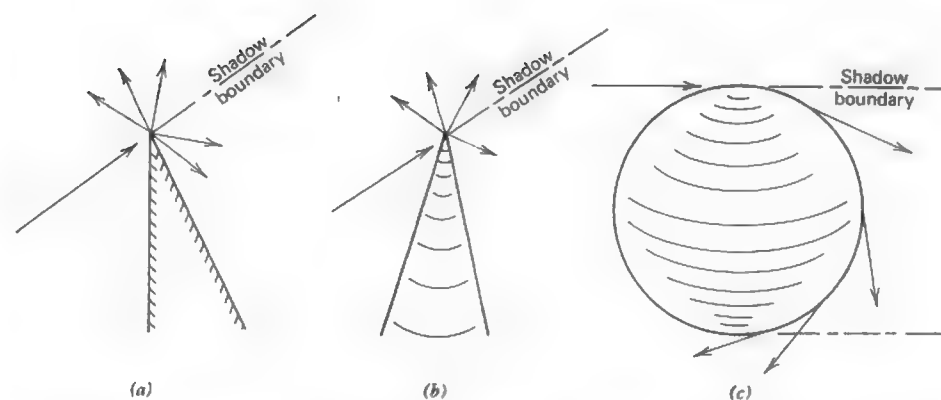


Figure 9-10 Examples of diffraction: (a) wedge diffraction, (b) tip diffraction, (c) curved surface diffraction.

shown in Fig. 9-11. Since physical phenomena in nature are not perfectly discontinuous, it is apparent that geometrical optics by itself constitutes an incomplete treatment of problems such as those in Fig. 9-10. It will be shown that the wedge diffracted rays will make the total electric field continuous across the shadow boundary in Fig. 9-10a.

Because diffraction is a local phenomena at high frequencies, the value of the field of a diffracted ray is proportional to the field value of the incident ray at the point of diffraction multiplied by a coefficient called the *diffraction coefficient*. That is, the diffraction coefficient is determined largely by the local properties of the field and the boundary in the immediate neighborhood of the point of diffraction. Since it is only the local conditions near the point of diffraction that are important, the diffracted ray amplitude may be determined from the solution

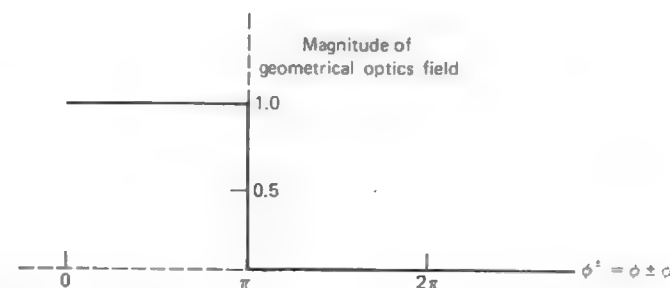


Figure 9-11 Magnitude of the geometrical optics field near either a reflected field shadow boundary ($\phi + \phi' = \pi$) or an incident field shadow boundary ($\phi - \phi' = \pi$).

of the appropriate boundary value problem having these local properties. Such a problem is called a canonical problem and wedge diffraction is one such canonical problem. Wedge diffraction is perhaps the most important canonical problem in the extension of geometrical optics as originally proposed by Joseph Keller in 1953. Keller's theory is known as the *geometrical theory of diffraction*, or GTD [5, 6, 7].

Through the use of geometrical optics and the solution to a number of canonical problems, such as those in Fig. 9-10, we can construct solutions to more complex problems via the principle of superposition. Let us now consider the canonical problem of wedge diffraction. To start, we will consider scalar diffraction by an infinitely conducting and infinitesimally thin half-plane sheet as shown in Fig. 9-12. The half-plane is a wedge of zero included angle. To calculate the field in the region $z > 0$, we will use Huygens principle in two dimensions. Thus, each point on the primary wavefront along $z = 0$ is considered to be a new source for a secondary cylindrical wave, the envelope of these secondary cylindrical waves being the secondary wavefront. Thus,

$$E(P) = \int_{x=a}^{x=\infty} dE \quad (9-36)$$

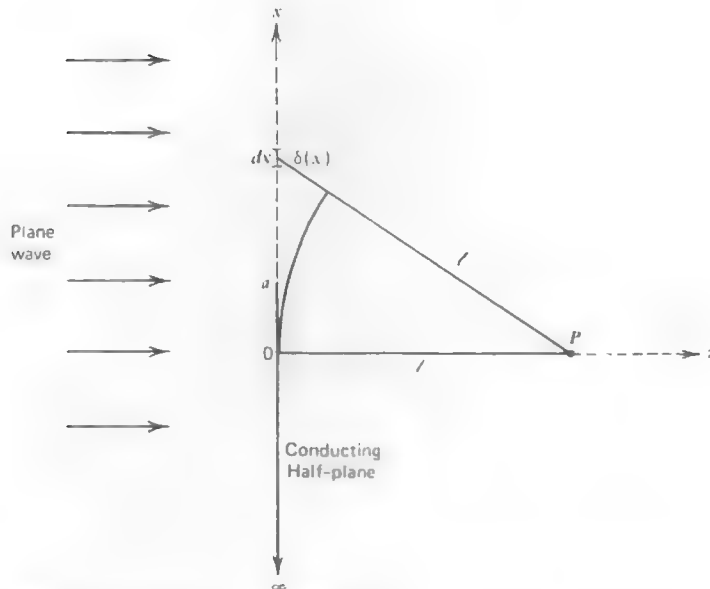


Figure 9-12 Plane wave diffraction by a conducting half-plane.

where dE is the electric field at P due to a magnetic line source parallel to the y -axis in the $z = 0$ plane, or

$$dE = \frac{C_1}{\sqrt{l + \delta(x)}} e^{-j\beta(l + \delta(x))} dx \quad (9-37)$$

where C_1 is a constant. If $(l + \delta) \gg \lambda$ and $l \gg \delta$, we may write for the contribution to $E(P)$ from those two-dimensional Huygens sources between $x = a$ and $x = x_0$

$$E(P) = \frac{C_1}{\sqrt{l}} e^{-j\beta l} \int_a^{x_0} e^{-j\beta\delta(x)} dx \quad (9-38)$$

We will consider the contribution from x_0 to ∞ later. When $\delta \ll l$, we can follow the same reasoning as in (1-81) to show that $l + \delta \approx l + x^2/2l$. Making the substitutions $\gamma^2 = 2/\lambda l$ and $u = \gamma x$ gives

$$E(P) = C_1 \sqrt{\lambda/2} e^{-j\beta l} \int_{\gamma a}^{\gamma x_0} e^{-j\beta\pi/2 u^2} du \quad (9-39)$$

If the upper limit in (9-39) is allowed to go to infinity, the integral will be in the standard form of a Fresnel integral [7, 8]. The Fresnel integral may be easily evaluated on a digital computer or from a graph known as Cornu's spiral, which is shown in Fig. 9-13a. A vector drawn from the origin to any point on the curve represents the magnitude of a Fresnel integral with lower limit zero and upper limit u_0 . As u_0 approaches infinity the tip of the vector will circle the point $(\frac{1}{2}, \frac{1}{2})$ an infinite number of times which suggests that the contribution to the value of the integral comes primarily between the limits zero and u_0 provided $u_0 > 1.26$. For this reason, we can argue that allowing $\gamma x_0 \rightarrow \infty$ in (9-39) has little effect on the value of the integral. Thus,

$$E(P) \approx C_1 \sqrt{\lambda/2} e^{-j\beta l} \int_{\gamma a}^{\infty} e^{-j\beta\pi/2 u^2} du \quad (9-40)$$

The value of the integral in (9-40) can be represented by a vector drawn from any point on the Cornu spiral to the point $(\frac{1}{2}, \frac{1}{2})$ (e.g., see Prob. 9.3-2).

If the lower limit in (9-40) is allowed to go to minus infinity $E(P)$ will equal the field strength without the half-plane present [8]. Thus,

$$E(P)|_{a=-\infty} = C_1 \sqrt{\lambda/2} (1 - j) e^{-j\beta l} = E_0 e^{-j\beta l} \quad (9-41)$$

Solving for C_1 and substituting into (9-40) gives the value of $E(P)$ in terms of the free space field E_0 ,

$$E(P) \approx \frac{E_0 e^{+j\pi/4}}{\sqrt{2}} e^{-j\beta l} \int_{\gamma a}^{\infty} e^{-j\beta\pi/2 u^2} du \quad (9-42)$$

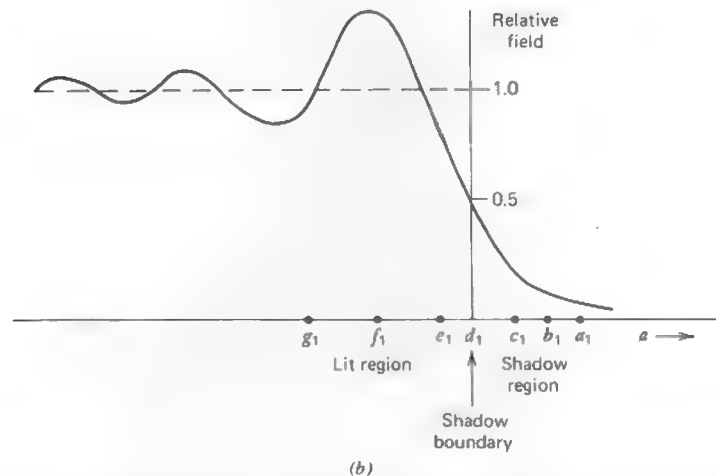
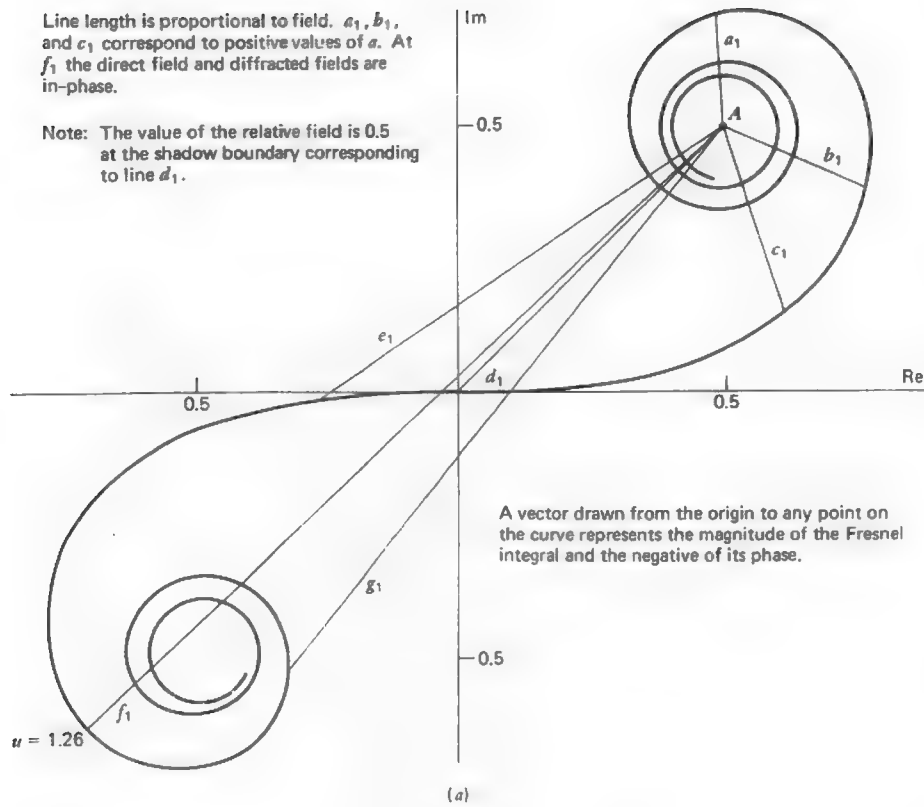


Figure 9-13 (a) Use of the Cornu spiral in evaluating the Fresnel integral as a function of the parameter a . (b) Relative magnitude of the diffracted field in the vicinity of a shadow boundary. Refer to Fig. 9-12 for values of a .

where for this approximate analysis to hold it is necessary that $\ell \gg \lambda$ and that the point $x = a$ not be far removed from the z -axis so that the assumption $\ell \gg \delta$ holds. A more exact (and complicated) analysis of this problem is possible but it has not been presented here for we wish simply to show how the Fresnel integral arises naturally in the study of wedge diffraction.

Equation (9-42) and the Cornu spiral make it possible to visualize the variation of the electric field as the point a moves along the x -axis causing the observation point to change from the lit region to the shadow region. The corresponding plot of the relative electric field in the vicinity of the shadow boundary is shown in Fig. 9-13b. We note that on the shadow boundary the value of the relative field is $\frac{1}{2}$ and that in the lit region the value of the field oscillates about the value of unity. This oscillation can be interpreted as being caused by interference between the diffracted field and the direct field. Since there is no direct field in the shadow region, we observe that no such oscillation occurs. Unfortunately it is not convenient to explicitly distinguish between the direct and diffracted field in (9-42). In many applications of the geometrical theory of diffraction it is essential that we be able to mathematically distinguish between the direct and diffracted fields, as well as the reflected field which we have yet to consider.

Referring to Fig. 9-14, we can identify two shadow boundaries, the incident or direct field shadow boundary and the reflected field shadow boundary. These two shadow boundaries serve to divide space into three regions wherein region I contains direct and diffracted rays as well as reflected rays; region II contains direct and diffracted rays but no reflected rays; region III contains only diffracted rays.

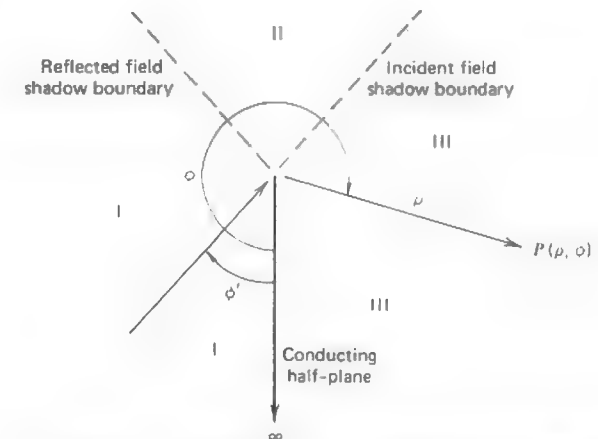


Figure 9-14 Diffraction by a conducting half-plane showing the location of shadow boundaries.

For a field in any one of the three regions let us write $E(\rho, \phi)$ as consisting of a reflected field $v^r(\rho, \phi + \phi')$ and an incident field $v^i(\rho, \phi - \phi')$. Thus,

$$E(\rho, \phi) = \pm v^r(\rho, \phi + \phi') + v^i(\rho, \phi - \phi'). \quad (9-43)$$

The choice of sign depends on the polarization of the incident field. If the electric field is perpendicular (parallel) to the diffracting edge, the plus (minus) sign is used. The field E at the point P must be a solution to the scalar wave equation with the appropriate boundary conditions. The boundary value problem depicted in Fig. 9-14 was first solved by Sommerfeld in 1896. We will first consider his solution. To do so we must examine (9-43) more fully.

The first term in (9-43) gives the reflected fields while the term $v^i(r, \phi - \phi')$ represents the incident field. If the ground plane were infinite in extent, the reflected field term would simply be the geometrical optics reflected field. However, in the case of the half-plane in Fig. 9-14, the reflected field will consist of two parts, namely a geometrical optics reflected field and a diffracted field. Both parts of the reflected field will appear to originate from an image source behind the half-plane. Similarly, the incident field can be thought to consist of two parts, a geometrical optics incident field and a diffracted field. Thus, for the reflected field

$$\pm v^r(\rho, \phi + \phi') = \pm [v_{*}^r(\rho, \phi + \phi') + v_B^r(\rho, \phi + \phi')] \quad (9-44)$$

and for the incident field

$$v^i(\rho, \phi - \phi') = v_{*}^i(\rho, \phi - \phi') + v_B^i(\rho, \phi - \phi') \quad (9-45)$$

where v_{*} denotes the geometrical optics field and v_B denotes the diffracted field. Thus, (9-43) may be thought of as being composed of four parts. Each of the terms on the right-hand side of (9-44) and (9-45) satisfies the wave equation individually except at the reflected field and incident field shadow boundaries, respectively. However, the sum of v_{*}^r and v_B^r makes v^r continuous across the reflected field shadow boundary and thus v^r satisfies the wave equation there. (Similar comments apply to v^i .) But, neither v^r nor v^i alone satisfy the boundary conditions at the wedge. However, the sum of v^r and v^i in (9-43) does satisfy the boundary conditions as well as the wave equation.

From simple geometrical considerations we can see that for reflected geometrical optics rays, all points on a constant phase wavefront are given by

$$v_{*}^r(\rho, \phi + \phi') = e^{j\beta\rho \cos(\phi + \phi')}, \quad 0 < \phi < \pi - \phi' \text{ in region I} \quad (9-46)$$

wherein the phase reference is taken to be at the edge of the half-plane in Fig. 9-15 since we are using a cylindrical coordinate system whose origin is on

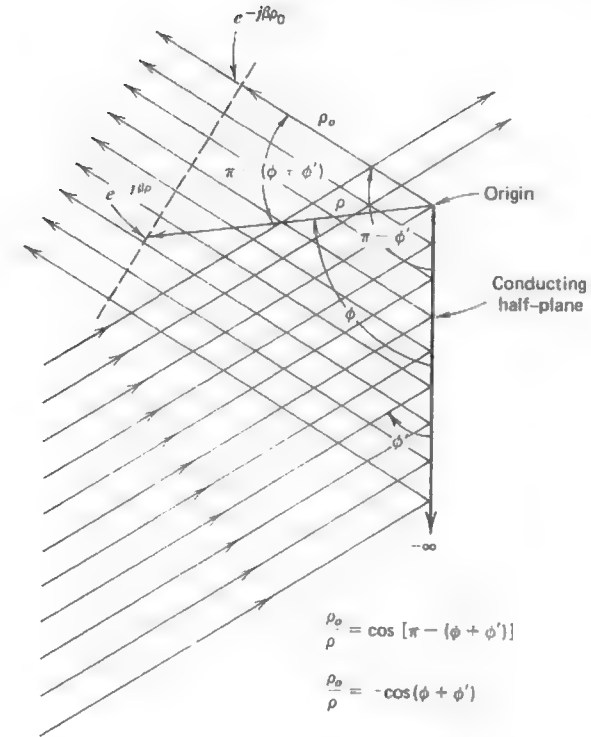


Figure 9-15 Geometry for the reflected field wavefront from a conducting half-plane.

the edge of the wedge. By similar considerations for direct incident rays, points on a constant phase wavefront are given by

$$v_{*}^i(\rho, \phi - \phi') = e^{j\beta\rho \cos(\phi - \phi')}, \quad 0 < \phi < \pi + \phi' \text{ in regions I and II.} \quad (9-47)$$

For other values of ϕ

$$v_{*}^i = 0 = v_{*}^r. \quad (9-48)$$

In other words, v_{*} is zero in regions II and III for reflected rays and is zero in region III for direct or incident rays. It is the diffracted field that compensates for this discontinuity in the geometrical optics field as shown in Fig. 9-16. We see in Fig. 9-16 that for $\phi > 255^\circ$ the total field is just the diffracted field and that the total field is continuous across the incident field shadow boundary at $\phi = 255^\circ$ where the value of the diffracted field is 0.5. For $105^\circ < \phi < 255^\circ$, the total field oscillates due to the interference between the incident field and the diffracted field. At $\phi = 105^\circ$ the diffracted field again rises to 0.5 and the total field

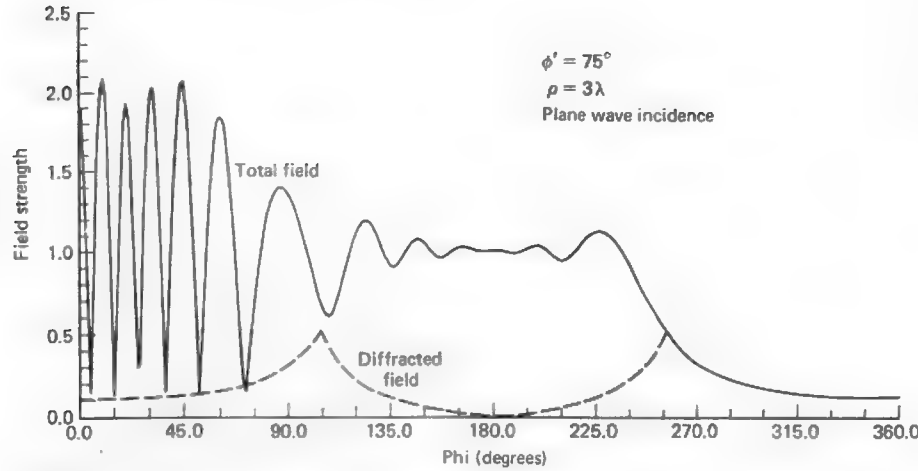


Figure 9-16 Diffraction by a half-plane showing the total electric field and the total diffracted field separately. The incident field is polarized perpendicular to the edge of the half-plane.

is continuous across the reflected field shadow boundary. For $\phi < 105^\circ$, the total field oscillates almost between zero and two due mainly to the standing wave produced in region I by the incident and reflected fields and the fact that the field is observed at a constant distance ($\rho = 3\lambda$) from the edge of the half-plane requiring the observation point to sweep through the standing wave field. The field is normal to the half-plane at $\phi = 0$ and is nonzero there.

Mathematical expressions for the diffracted field v_B have been a subject of considerable research in the past several decades in an effort to improve upon the early classical work of Sommerfeld [9]. For the half-plane problem of Fig. 9-14, Sommerfeld obtained an expression for the diffracted field due to an incident plane wave in terms of the Fresnel integral. This expression is²

$$v_B(\rho, \phi^\pm) = -e^{j(\pi/4)} \sqrt{\frac{2}{\pi x}} \cdot e^{j\beta\rho \cos \phi^\pm} \cos \frac{\phi^\pm}{2} \int_{\sqrt{2\beta\rho}}^{\infty} e^{j\tau^2} d\tau \quad (9-49)$$

² Note that in (9-49) we are really writing two equations, one for $v_B^+(r, \phi^+)$ and the other for $v_B^-(r, \phi^-)$. The use of the notation ϕ^\pm is for convenience and the reader should keep in mind that wherever it appears there are two separate equations implied, one associated with the reflected field and one associated with the incident field.

where

$$\phi^\pm = \phi \pm \phi' \quad (9-50)$$

and

$$\alpha = 1 + \cos \phi^\pm. \quad (9-51)$$

We note that this solution is in a form somewhat similar to that of (9-42). The mathematical details of deriving the above are beyond the scope of this text.

Sommerfeld's work was more general than that of just a half-plane. He also considered the more general case of a plane wave illuminating a conducting wedge of interior angle $(2 - n)\pi$ where $0 < n \leq 2$.³ For this case he obtained an asymptotic evaluation of a contour integral representation for the diffracted field which is given by

$$v_B(\rho, \phi^\pm) = \frac{e^{-j(\beta\rho + \pi/4)}}{\sqrt{2\pi\beta\rho}} \frac{(1/n)\sin(\pi/n)}{\cos(\pi/n) - \cos(\phi^\pm/n)}. \quad (9-52)$$

Unfortunately, this asymptotic form yields infinite fields in the immediate vicinity of the shadow boundary [10]. The region near a shadow boundary is usually referred to as a *transition region*. Equation (9-52) is only valid outside a transition region where the condition

$$\beta\rho \left(\cos \frac{\pi}{n} - \cos \frac{\phi^\pm}{n} \right)^2 \gg 1 \quad (9-53)$$

is satisfied. This condition is always met if the quantity $\beta\rho(1 + \cos \phi^\pm)$ is large, which means that the observation point at $P(\rho, \phi, z)$ must be at a large electrical distance from the diffracting edge. Nevertheless, (9-52) is a useful one if the observation point is not near a shadow boundary and the above conditions are met.

In 1938 Pauli [11] improved upon the work of Sommerfeld by obtaining a series form for Sommerfeld's contour integral solution. Pauli's result is given by

$$v_B(\rho, \phi^\pm) = \frac{2e^{j(\pi/4)}}{n\sqrt{\pi}} \frac{\sin(\pi/n)}{\cos(\pi/n) - \cos(\phi^\pm/n)} \left| \cos \frac{\phi^\pm}{2} \right| \cdot e^{j\beta\rho \cos \phi^\pm} \int_{\sqrt{2\beta\rho}}^{\infty} e^{-\tau^2} d\tau + [\text{higher order terms}]. \quad (9-54)$$

This expression is far more accurate, particularly near the shadow boundaries, than (9-52) while being only slightly more difficult to evaluate. It is valid for $0 < n \leq 2$. In the case of the half-plane ($n = 2$), the higher order terms are

³ Refer forward to Fig. 9-17.

identically zero and Pauli's result in (9-54) reduces to that of Sommerfeld in (9-49). Pauli's expression was the first practical formulation of Sommerfeld's original solution which included a finite observation distance.

Example 9-1. Sample wedge diffraction calculations

The use of equations (9-49), (9-52), and (9-54) is best illustrated by an example. Let us calculate the diffracted field in Fig. 9-16 for $\phi = 250^\circ$. Using (9-49) we obtain

$$\begin{aligned} r_B(3, \phi^-) &= (-9.146 - j9.146)(0.0436) \\ &\quad \cdot (0.997 + j0.0717)(0.359 - j0.620) \\ &= -0.397 + j0.0760 \\ r_B(3, \phi^+) &= (-0.418 - j0.418)(-0.954) \\ &\quad \cdot (-0.964 + j0.264)(-0.0237 + j0.0820) \\ &= 0.0345 - j0.0335 \end{aligned}$$

Thus the exact Sommerfeld solution gives for the diffracted field magnitude $|-0.3625 + j0.0435| = 0.365$ which agrees with Fig. 9-16. Using (9-54) we should obtain the same result for the half-plane case since Pauli's equation reduces to Sommerfeld's. Thus,

$$\begin{aligned} r_B(3, \phi^-) &= (0.798 + j0.798)(-11.46)(0.0436) \\ &\quad \cdot (0.997 + j0.0717)(0.359 - j0.620) \\ &= -0.397 + j0.0760 \\ r_B(3, \phi^+) &= (0.798 + j0.798)(0.524) \\ &\quad \cdot (0.954)(-0.964 + j0.264) \\ &\quad \cdot (-0.0237 + j0.0820) \\ &= 0.0345 - j0.0335 \end{aligned}$$

and the diffracted field magnitude is once again 0.365. We note that since $\phi = 250^\circ$ is near the incident field shadow boundary, $r_B(3, \phi^-)$ is the major contributor to the diffracted field and $r_B(3, \phi^+)$, which is associated with the reflected field shadow boundary, makes only a minor contribution. Both (9-49) and (9-54) would go to infinity precisely at the shadow boundary $\phi = 255^\circ$ (or $\phi = 105^\circ$). For this reason we have elected to use $\phi = 250^\circ$ in this example. Finally, let us use the asymptotic form in (9-52). Thus

$$\begin{aligned} r_B(3, \phi^-) &= (0.065 - j0.065)(-11.46) \\ &= -0.745 + j0.745 \\ r_B(3, \phi^+) &= (0.065 - j0.065)(0.524) \\ &= 0.034 - j0.034 \end{aligned}$$

and the magnitude of the diffracted field alone exceeds unity or that of the incident field. This result is in error because the condition in (9-53) has been violated. The result would be only 10% in error at $\rho = 10\lambda$ if $\phi = 255^\circ \pm 12^\circ$, at 20λ if $\phi = 255^\circ \pm 5^\circ$ at 30λ if $\phi = 255^\circ \pm 4^\circ$, and at 100λ if $\phi = 255^\circ \pm 3^\circ$. However, no matter how large ρ is, the asymptotic form will be singular right at the shadow boundary.

Starting in 1953 it was Keller [5, 6] who systematically developed the geometrical theory of diffraction, or GTD as it is often referred to. In his work, he has called the quantities $D(\phi^+)$ and $D(\phi^-)$ diffraction coefficients where

$$[v_B^i(\rho, \phi^-) \mp v_B^r(\rho, \phi^+)] = [D(\phi^-) \mp D(\phi^+)] \frac{e^{-j\beta\rho}}{\sqrt{\rho}} \quad (9-55)$$

and used the asymptotic expression of Sommerfeld in (9-52) to calculate the diffracted field due to plane wave incidence. The postulates of Keller's theory are

1. The diffracted field propagates along ray paths that include points on the boundary surface. These ray paths obey the principle of Fermat, known also as the principle of shortest optical path.
2. Diffraction, like reflection and transmission, is a local phenomenon at high frequencies. That is, it depends only on the nature of the boundary surface and the incident field in the immediate neighborhood of the point of diffraction.
3. A diffracted wave propagates along its ray path so that
 - (a) power is conserved in a tube of rays, and
 - (b) phase delay equals the wave number times the distance along the ray path.

A consequence of the second postulate is that the diffracted fields caused by the edge of the infinite wedge in Fig. 9-15, for example, appear to be cylindrical wave fields that originate at the wedge edge. This is consistent with the $(\rho)^{-1/2}$ dependence in (9-55).

The simple ray formulation of Keller's geometrical theory of diffraction is restricted to the calculation of fields in regions of space that exclude transition regions adjacent to shadow boundaries, caustics, and focal points. To calculate the field at such points, additions and modifications to the geometrical theory of diffraction are required. Further, if the incident field is not a plane wave, but a cylindrical or spherical wave, GTD must be modified to accept these incident fields as well. These various modifications will be considered in later sections.

9.4 THE RAY-FIXED COORDINATE SYSTEM

In the previous section we considered the scalar diffracted field due to a plane wave normally incident (i.e., traveling in the negative ρ -direction) upon a perfectly conducting infinite wedge whose edge was along the z -axis. Such a coordinate system is said to be an edge-fixed coordinate system. On the other hand, the obliquely incident and obliquely diffracted rays associated with the point Q

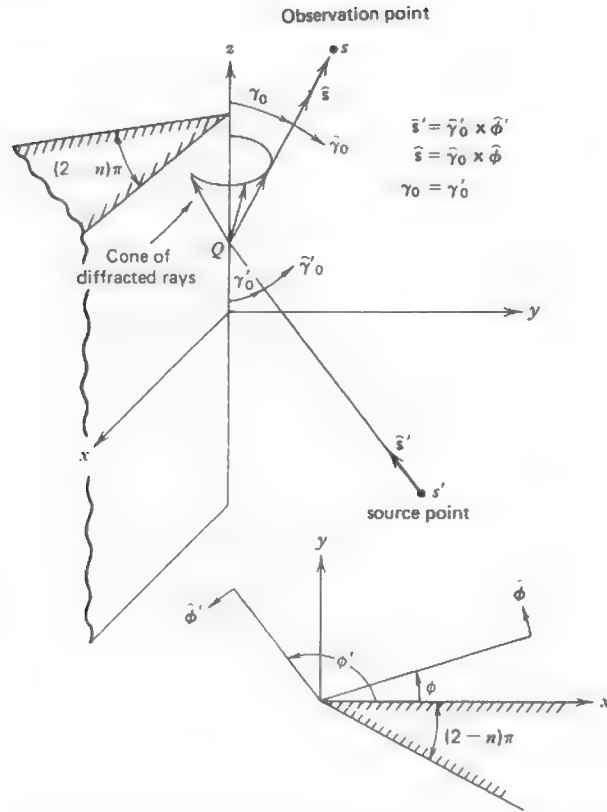


Figure 9-17 Geometry for three-dimensional diffraction problem.

in Fig. 9-17 are more conveniently described in terms of spherical coordinates centered at Q . Such a coordinate system is said to be ray-fixed [1]. Let the position of the source of the incident ray be defined by the spherical coordinates (s', γ_0', ϕ') , and the observation point by the coordinates (s, γ_0, ϕ) as indicated in Fig. 9-17. Note that the point Q is a unique point on the edge for a given source location and a given observation point.

The plane containing the incident ray and the edge of the wedge will be referred to as the plane of incidence, while that plane containing the diffracted ray and the edge of the wedge will be referred to as the plane of diffraction. The unit vector \hat{s}' is in the direction of incidence and the unit vector \hat{s} is in the direction of diffraction. It is then apparent that the unit vectors $\hat{\gamma}_0'$ and $\hat{\phi}'$ are parallel and perpendicular, respectively, to the plane of incidence, and that the

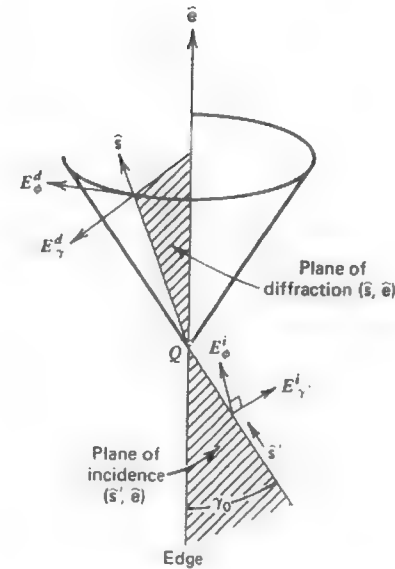


Figure 9-18 Ray-fixed coordinate system.

unit vectors $\hat{\gamma}_0$ and $\hat{\phi}$ are parallel and perpendicular, respectively, to the plane of diffraction as shown in Fig. 9-18. γ_0' and γ_0 are angles less than $\pi/2$ measured from the edge to the incident and diffracted rays, respectively, while $\hat{\gamma}_0'$ and $\hat{\gamma}_0$ are the implied unit vectors. Further, ϕ' and ϕ are angles measured from one face of the wedge to the plane of incidence and diffraction, respectively, while $\hat{\phi}'$ and $\hat{\phi}$ are the implied unit vectors. Note that ϕ' and ϕ are measured from the same face of the wedge.

Let us write a symbolic expression for the diffracted field in matrix form as

$$[E^d] = [D][E^i]A(\rho)e^{-j\beta\rho} \quad (9-56)$$

where $[E^d]$ and $[E^i]$ are column matrices consisting of the scalar components of the diffracted and incident fields respectively. $[D]$ is a square matrix of the appropriate scalar diffraction coefficients, and ρ is the distance from the wedge edge to the observation point and $A(\rho)$ is a spreading factor. Now if the edge-fixed coordinate system is used, it is clear that $[E^d]$ will have in general three scalar components E_ρ^d , E_ϕ^d , and E_z^d and that $[D]$ will be a three by three matrix. It can be shown that in such a situation seven of the nine terms in $[D]$ are nonvanishing. However, when the ray-fixed coordinate system is used, there is no component of the diffracted field in the direction of the diffracted ray tube since the incident field is not allowed to have a component in the direction of the incident ray tube. It follows that there are then only two possible components of the diffracted field, E_γ^d and E_ϕ^d , and only two components of the incident field, E_γ^i

and E_ϕ^i . Clearly $[D]$ is a two by two matrix. In this case $[D]$ has nonvanishing terms on the main diagonal. Thus, for plane wave incidence in the ray-fixed system (9-56) can be written as

$$\begin{bmatrix} E_\gamma^d(s) \\ E_\phi^d(s) \end{bmatrix} = \begin{bmatrix} -D_\parallel & 0 \\ 0 & -D_\perp \end{bmatrix} \begin{bmatrix} E_\gamma^i(Q) \\ E_\phi^i(Q) \end{bmatrix} A(s)e^{-j\beta s} \quad (9-57)$$

where the scalar diffraction coefficients D_\parallel and D_\perp are momentarily undefined and will be given in the following section.

It is apparent that the use of the ray-fixed coordinate system instead of the edge-fixed system reduces the diffraction matrix from a three by three matrix with seven nonvanishing terms to a two by two matrix with but two nonvanishing terms. Thus, the ray-fixed system is the natural coordinate system to be used for wedge diffraction and the importance of using it can hardly be overemphasized.

We have chosen to use the notation D_\parallel in association with $E_\gamma^i(Q)$ and D_\perp in association with $E_\phi^i(Q)$ not because E_γ^i and E_ϕ^i are parallel and perpendicular, respectively, to the diffracting edge (which they are at normal incidence when $\gamma_0 = 90^\circ$), but because E_γ^i and E_ϕ^i are parallel and perpendicular, respectively, to the plane of incidence as shown in Fig. 9-18.

Since E_γ^i and E_ϕ^i are parallel and perpendicular, respectively, to the plane of incidence we will let E_γ^i be written as E_\parallel^i and let E_ϕ^i be written as E_\perp^i . Similarly, $E_\gamma^d(s)$ and $E_\phi^d(s)$ are parallel and perpendicular respectively to the plane of diffraction as shown in Fig. 9-18. Thus, we will let E_γ^d be written as E_\parallel^d and let E_ϕ^d be written as E_\perp^d . With these notational changes, (9-57) may be rewritten as

$$\begin{bmatrix} E_\parallel^d(s) \\ E_\perp^d(s) \end{bmatrix} = \begin{bmatrix} -D_\parallel & 0 \\ 0 & -D_\perp \end{bmatrix} \begin{bmatrix} E_\parallel^i(Q) \\ E_\perp^i(Q) \end{bmatrix} A(s)e^{-j\beta s} \quad (9-58)$$

We will use this notation throughout the remainder of the chapter keeping in mind that when the \parallel and \perp symbols are primed, reference to the plane of incidence is implied. When the \parallel and \perp symbols are unprimed, reference to the plane of diffraction is implied.

9.5 A UNIFORM THEORY OF WEDGE DIFFRACTION

The modern version of GTD can be divided into the two basic canonical problems of wedge diffraction and curved surface diffraction plus the lesser but more complex problems of vertex diffraction and tip diffraction. In the application of wedge diffraction to antenna problems, the important features of antennas are

modeled by perfectly conducting wedges. For example, the pyramidal horn antenna can be modeled by two half-planes as shown in Fig. 9-20 for the purpose of analyzing the E -plane pattern [10]. In such a problem, however, it is necessary to use cylindrical wave diffraction coefficients instead of plane wave diffraction coefficients as in Section 9.3. The first use of cylindrical wave diffraction in the treatment of antenna problems such as in Section 9.6 was by Rudduck [10] who used Pauli's formulation together with the principle of reciprocity to calculate the necessary cylindrical wave diffraction. Problems involving spherical wave diffraction are also common.

In Section 9.3 some early developments in the study of diffraction by a conducting wedge were presented. We saw that although some of the formulas presented are certainly useful for some engineering calculations, they are limited in their accuracy in a transition (shadow boundary) region [e.g., (9-52)], or when the observation point is near ($r < \lambda$) the diffracting edge [e.g., (9-54)]. It would obviously be useful and convenient if there were available to us a theory of wedge diffraction having the property that it could accurately predict the diffracted field in such places as the transition regions or near the diffracting edge without the necessity for considering each type of incident field separately. Such a theory is available and is known as a *uniform theory* of wedge diffraction because it applies in all situations consistent with the postulates of the geometrical theory of diffraction given in Section 9.3. It is the purpose of this section to present the important results in this theory, known as the UTD, which is based on the numerous works of Kouyoumjian and Pathak [12, 13, 14].

In 1967 Kouyoumjian and co-workers obtained a generalized version of Pauli's result [i.e., (9-54)] with the resultant diffraction function v_B expressed as $v_B(L, \phi^\pm)$ where L is a distance parameter more general than just the distance ρ used in Section 9.3 while ϕ^\pm retains the meaning used previously. In their work the distance parameter L is given by

$$L = \begin{cases} s \sin^2 \gamma_0 & \text{for plane waves} \\ \frac{\rho' \rho}{\rho + \rho'} & \text{for cylindrical waves} \\ \frac{s's \sin^2 \gamma_0}{s + s'} & \text{for conical and spherical waves.} \end{cases} \quad (9-59)$$

We note immediately that L is dependent upon the type of incident wave and the angle of incidence γ_0 (which equals the angle of reflection γ_0) as well as the distances involved. The distance parameter L in (9-59) can be found by imposing the condition that the total field, which is the sum of the geometrical-optics field and the diffracted field, be continuous at shadow or reflection boundaries.

When the work of Kouyoumjian and co-workers is expressed in terms of the scalar diffraction coefficients D_{\parallel} and D_{\perp} where

$$D_{\parallel}(L, \phi, \phi') = [v_B(L, \phi^-) - v_B(L, \phi^+)] \frac{\sqrt{L} e^{j\beta L}}{\sin \gamma_0} \quad (9-60)$$

$$D_{\perp}(L, \phi, \phi') = [v_B(L, \phi^-) + v_B(L, \phi^+)] \frac{\sqrt{L} e^{j\beta L}}{\sin \gamma_0} \quad (9-61)$$

we have (without proof) [12, 14]

$$D_{\perp}(L, \phi, \phi') = \frac{-e^{-j\pi/4}}{2n\sqrt{2\pi\beta} \sin \gamma_0} \times \left[\cot\left(\frac{\pi + (\phi - \phi')}{2n}\right) F[\beta La^+(\phi - \phi')] + \cot\left(\frac{\pi - (\phi - \phi')}{2n}\right) F[\beta La^-(\phi - \phi')] \mp \cot\left(\frac{\pi + (\phi + \phi')}{2n}\right) F[\beta La^+(\phi + \phi')] + \cot\left(\frac{\pi - (\phi + \phi')}{2n}\right) F[\beta La^-(\phi + \phi')] \right] \quad (9-62)$$

where, if the argument of F is represented by X ,

$$F(X) = 2j|\sqrt{X}| e^{jX} \int_{|\sqrt{X}|}^{\infty} e^{-j\tau^2} d\tau. \quad (9-63)$$

Again we see that a Fresnel integral appears in the expression for the diffraction coefficient. The factor $F(X)$ may be regarded as a correction factor to be used in the transition regions of the shadow and reflection boundaries. Outside of the transition regions where the argument of F exceeds about 3, the magnitude of F is approximately equal to one as Fig. 9-19 shows. Even within a given transition region, usually only one of the four terms in (9-62) is significantly different from unity.

The argument of the transition function, which is $X = \beta La^{\pm}(\phi \pm \phi')$, may be calculated for a known value of βL if a^{\pm} as a function of $(\phi \pm \phi')$ is known. To determine $a^+(\phi \pm \phi')$ and $a^-(\phi \pm \phi')$ we use

$$a^{\pm}(\phi \pm \phi') = 2 \cos^2 \left| \frac{2n\pi N^{\pm} - (\phi \pm \phi')}{2} \right| \quad (9-64)$$

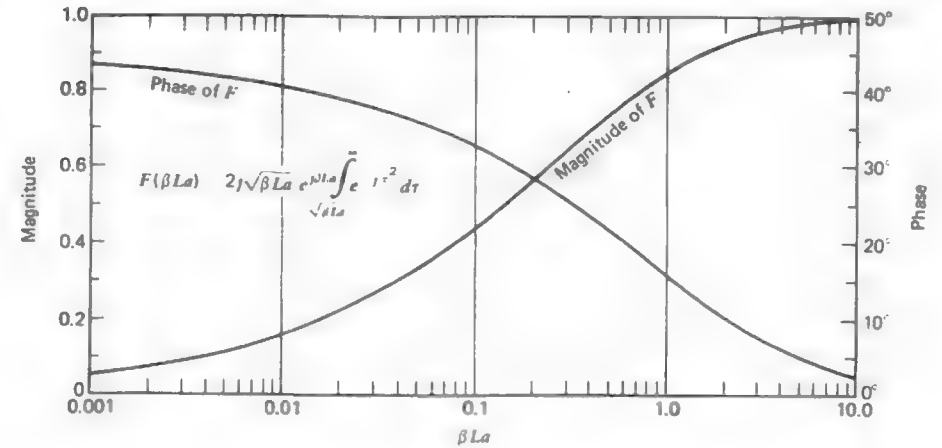


Figure 9-19 Magnitude and phase of the transition function $F(\beta La)$ where $a = a^+$ or a^- .

in which N^{\pm} are the integers which most nearly satisfy the four equations

$$2n\pi N^+ - (\phi \pm \phi') = \pi \quad (9-65)$$

and

$$2n\pi N^- - (\phi \pm \phi') = -\pi. \quad (9-66)$$

We note that N^+ and N^- may each have two separate values in a given problem. For exterior wedge diffraction where $1 < n \leq 2$, $N^+ = 0$ or 1 but $N^- = -1$, 0 or 1. The factor $a^{\pm}(\phi \pm \phi')$ may be interpreted physically as a measure of the angular separation between the field point and a shadow or reflection boundary.

Now that we have all the necessary relationships to calculate D and D_{\perp} , we repeat (9-57) in the format of UTD as

$$\begin{bmatrix} E_{\parallel}^d(s) \\ E_{\perp}^d(s) \end{bmatrix} = \begin{bmatrix} -D_{\parallel} & 0 \\ 0 & -D_{\perp} \end{bmatrix} \begin{bmatrix} E_{\parallel}^i(Q) \\ E_{\perp}^i(Q) \end{bmatrix} A(s) e^{-j\beta s} \quad (9-67)$$

where the spatial attenuation factor $A(s)$ is defined as

$$A(s) = \begin{cases} \frac{1}{\sqrt{s}} & \text{for plane, cylindrical, and conical wave incidence} \\ \left| \frac{s'}{s(s' + s)} \right|^{1/2} & \text{for spherical wave incidence.} \end{cases} \quad (9-68)$$

It should also be mentioned that, since diffraction concepts apply to acoustical problems, the diffraction coefficients D_{\parallel} and D_{\perp} in (9-67) are sometimes written D_s and D_h , respectively, which correspond to the acoustic soft and hard boundary conditions [14]. Equation (9-67) for the UTD is programmed in Appendix G.9.

Example 9-2 Sample UTD Calculation

The use of equations (9-59) to (9-68) is best illustrated by an example. Suppose we wish to calculate the diffracted field in Fig. 9-16 when $\phi = 250^\circ$. We have in this case: $\phi + \phi' = 325^\circ$; $\phi - \phi' = 175^\circ$; $L = 3\lambda$; $\beta L = 6\pi$; $n = 2$. Thus, from (9-64) to (9-66)

$$\begin{aligned} a^+(\phi + \phi') &= 2 \cos^2(197.5^\circ), & \text{where } N^+ &= 1 \\ a^+(\phi - \phi') &= 2 \cos^2(87.5^\circ), & \text{where } N^+ &= 0 \\ a^-(\phi + \phi') &= 2 \cos^2(162.5^\circ), & \text{where } N^- &= 0 \\ a^-(\phi - \phi') &= 2 \cos^2(87.5^\circ), & \text{where } N^- &= 0. \end{aligned}$$

From Fig. 9-19, using the respective values of a^+ and a^- above, we obtain

$$\begin{aligned} F(6\pi \cdot 1.819) &= 0.999 + j0.0146 \\ F(6\pi \cdot 0.0038) &= 0.318 + j0.216 \\ F(6\pi \cdot 1.819) &= 0.999 + j0.0146 \\ F(6\pi \cdot 0.0038) &= 0.318 + j0.216. \end{aligned}$$

Using (9-62) and (9-68)

$$\begin{aligned} D_1(L, \phi, \phi') &= -0.628 + j0.0735 \\ A(s)e^{-j\beta s} &= 0.577. \end{aligned}$$

From (9-67)

$$E_1^d(s) = -0.363 + j0.0424$$

or

$$|E_1^d(s)| = 0.365$$

which agrees with Fig. 9-16. It is worth noting that when the four correction factors F above are multiplied by their associated cotangent factor, it is the fourth term above which is much larger than the others. As mentioned earlier, usually just one of the terms in (9-62) turns out to be large, even close to a shadow boundary. Equation (9-62) will not exhibit a singular behavior at a shadow boundary as was the case in Section 9.3 with (9-49) and (9-54).

If the field point is not close to a shadow or reflection boundary and $\phi' \neq 0$ or $n\pi$ (grazing incidence), the scalar diffraction coefficients D_{\parallel} and D_{\perp} reduce to Keller's diffraction coefficients [see (9-52) and (9-53)] which may be written as

$$D_{\parallel}(\phi, \phi'; \gamma'_0) = \frac{e^{-j\pi/4} \sin(\pi/n)}{n\sqrt{2\pi\beta} \sin \gamma'_0} \cdot \left[\frac{1}{\cos \frac{\pi}{n} - \cos \frac{\phi - \phi'}{n}} \mp \frac{1}{\cos \frac{\pi}{n} - \cos \frac{\phi + \phi'}{n}} \right]. \quad (9-69)$$

This expression is valid for all four types of incident waves given in (9-59), which is important because the diffraction coefficient should be independent of the edge illumination away from shadow and reflection boundaries. However, from Section 9.3 we know that (9-69) will become singular as a shadow or reflection boundary is approached.

Grazing incidence, where $\phi' = 0$ or $n\pi$, is a special case which must be considered separately. In this case $D_{\parallel} \approx 0$, and the expression for E_1^d must be multiplied by a factor of $\frac{1}{2}$. If we consider grazing incidence to be the limit of oblique incidence, we can see how the need for the factor of $\frac{1}{2}$ arises, because at grazing incidence the incident and reflected fields merge. When they merge, one-half of the total field propagating along the face of the wedge toward the edge is the incident field and the other half is the reflected field. The merged field is then regarded as being the "incident" field but it is too large by a factor of 2 and the factor of $\frac{1}{2}$ becomes necessary. That is, (9-67) requires the use of the free space incident field and not the merged field.

The uniform theory of wedge diffraction described in this section (which is programmed in Appendix G.9) permits us to consider diffraction problems where in both the source and observation points are quite close to the diffracting edge (i.e., a wavelength or even less). It also permits us to consider any type of TEM incident field. A more general expression for L , valid for an arbitrary wavefront incident on the straight edge of a wedge, appears in the literature [13, 14].

Unlike the edge diffraction formulas presented in Section 9.3, (9-62) is valid in the transition regions of the incident field shadow boundary and the reflected field shadow boundary. Equation (9-62) cannot be used to calculate the field at a caustic of the diffracted ray. This does not conflict with the concept of a uniform theory of wedge diffraction because geometrical optics itself is incapable of determining the field at a caustic. The field at a caustic may, however, be found through use of a supplementary solution in the form of an integral representation of the field. The equivalent sources in the integral representation are determined from a suitable high-frequency approximation such as a geometrical optics or the geometrical theory of diffraction. The calculation of the field at a caustic by such methods will be considered in Section 9.10.

9.6 E-PLANE ANALYSIS OF HORN ANTENNAS

To illustrate the application of the uniform theory of diffraction presented in the previous section, consider the E -plane horn antenna shown in Fig. 9-20a. In this section we use the model shown in Fig. 9-20b to compute the complete E -plane pattern of the horn antenna. The model is simple and therefore particularly well-suited to use as a first example of the application of the UTD. The model has only three sources of radiation and is two-dimensional in nature (i.e., infinite in the $\pm x$ -directions) which in the E -plane well-represents a three-dimensional horn antenna.

The equations applicable to the analysis are as follows. Note that the angle ζ ($0 \leq \zeta \leq 2\pi$) is used instead of θ ($0 \leq \theta \leq \pi$) so that positions in the yz -plane may be defined unambiguously. In the far field we have (in the yz -plane)

$$r_1 = r - a \sin \zeta \quad (9-70)$$

$$r_2 = r + a \sin \zeta \quad (9-71)$$

$$r_3 = r + \rho_E \cos \zeta \cos \zeta_E \quad (9-72)$$

where r_1 and r_2 are distances to the far-field observation point $P(r, \zeta, \phi = \pi/2)$ from diffracting edges 1 and 2 respectively, and r_3 is the distance from the line source to the far-field observation point as shown in Fig. 9-20b. Thus, the incident field along the direct ray can be expressed by

$$E^i(P) = \frac{e^{-j\beta r_3}}{\sqrt{r_3}} \approx \frac{e^{-j\beta r}}{\sqrt{r}} e^{-j\beta \rho_E \cos \zeta \cos \zeta_E}, \quad -\zeta_E \leq \zeta \leq \zeta_E \quad (9-73)$$

and

$$E^i(P) = 0, \quad \zeta_E < \zeta < 2\pi - \zeta_E. \quad (9-74)$$

Note that in applying the UTD we do not replace the conducting surfaces with equivalent currents radiating in free space as in the preceding chapters of this book. Instead, the conducting surfaces are retained. As a consequence, for example, $E^i(P) = 0$ when $\zeta > \zeta_E$.

The edge diffracted field at $P(r, \zeta, \phi = \pi/2)$ from a diffraction point Q_1 on the "top" edge may be written

$$E_1^d(P) = \frac{1}{2} E_1^i(Q_1) D_1(L, \phi, \phi') \frac{e^{-j\beta r_1}}{\sqrt{r_1}} = \frac{1}{2} E_1^i D_1(L, \phi, \phi') \frac{e^{-j\beta r}}{\sqrt{r}} e^{j\beta a \sin \zeta}, \quad -\frac{\pi}{2} \leq \zeta \leq \pi + \zeta_E \quad (9-75)$$

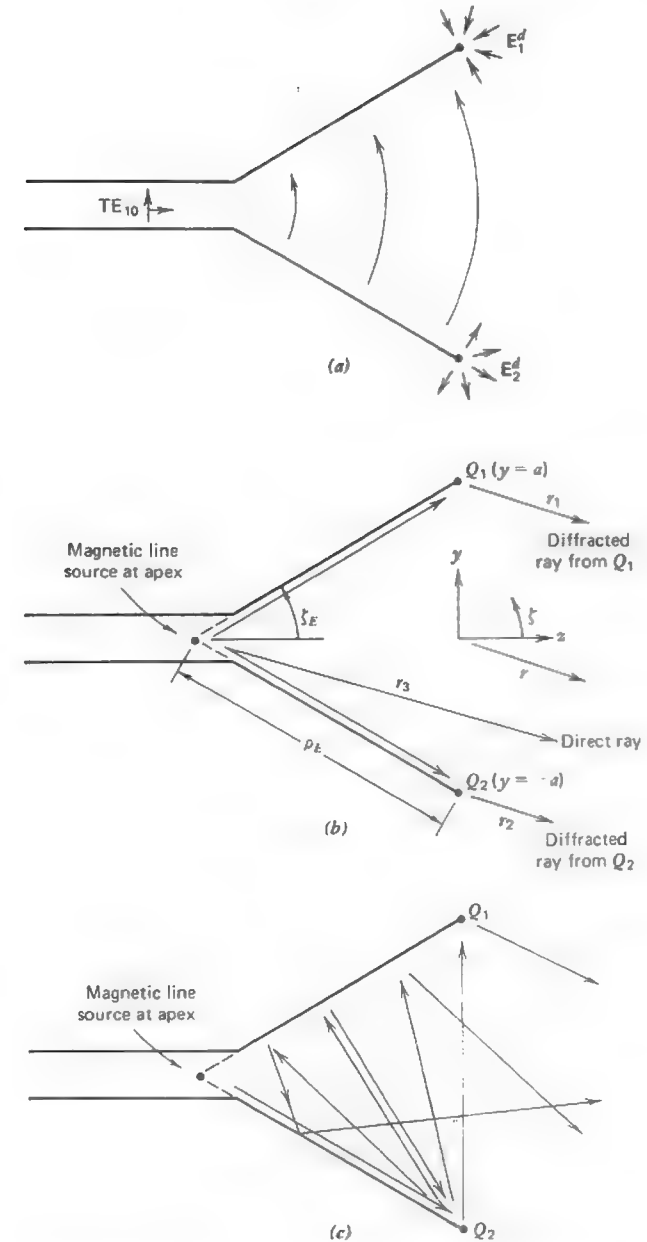


Figure 9-20 (a) E -plane sectoral horn. (b) Model of E -plane sectoral horn. (c) Neglected rays.

and

$$E_1^d(P) = 0, \quad \pi + \zeta_E < \zeta < \frac{3\pi}{2}. \quad (9-76)$$

Similarly, the diffracted field at $P(r, \zeta, \phi = \pi/2)$ from a diffraction point Q_2 on the "bottom" edge may be written

$$E_2^d(P) = \frac{1}{2} E_1^i(Q_2) D_1(L, \phi, \phi') \frac{e^{-j\beta r_2}}{\sqrt{r_2}} = \frac{1}{2} E_1^i D_1(L, \phi, \phi') \frac{e^{-j\beta r}}{\sqrt{r}} e^{-j\beta a \sin \zeta},$$

$$-\pi - \zeta_E \leq \zeta \leq \frac{\pi}{2} \quad (9-77)$$

and

$$E_2^d(P) = 0, \quad \frac{\pi}{2} < \zeta < \pi - \zeta_E \quad (9-78)$$

where

$$E_1^i(Q_1) = E_1^i(Q_2) = \frac{e^{-j\beta \rho_E}}{\sqrt{\rho_E}}. \quad (9-79)$$

Thus, the total field at an observation point $P(r, \zeta, \phi = \pi/2)$ may be written as the scalar sum

$$E(P) = E^i(P) + E_1^d(P) + E_2^d(P). \quad (9-80)$$

In the above equations scalar D_\perp denotes the diffraction coefficient at the point of diffraction Q_m for the case where the incident electric field is normal to the edge. The diffraction coefficient at Q_m depends on the geometry of the incident and diffracted rays at Q_m and is most accurately given by (9-59) and (9-62). Here, of course, we consider the incident field to be cylindrical and use the cylindrical wave form for the distance parameter L . $E^i(Q_m)$ is the incident field that is both perpendicular to the edge and to the incident ray.

At first glance the factor of one-half in (9-75) and (9-77) might appear to be incorrect. However, in this problem the rays from the line source are incident at a grazing angle with the surface of the horn walls and therefore deserve special consideration. Grazing incidence, where $\phi' = 0$ or π , requires that D_\perp in (9-67) be multiplied by a factor of $\frac{1}{2}$ as discussed in the preceding section.

Figure 9-21 shows results calculated with the model shown in Fig. 9-20b and also experimental data. The agreement between the calculated results without using double diffractions (dashed curve) and the experimental results is seen to be very good. Note that there is a discontinuity in the calculated results when $\zeta = 90^\circ$ (or 270°). This discontinuity may be removed simply by including rays which diffract from Q_2 (or Q_1) and travel across the horn aperture to Q_1 (or Q_2) and are diffracted a second time as indicated in Fig. 9-20c.

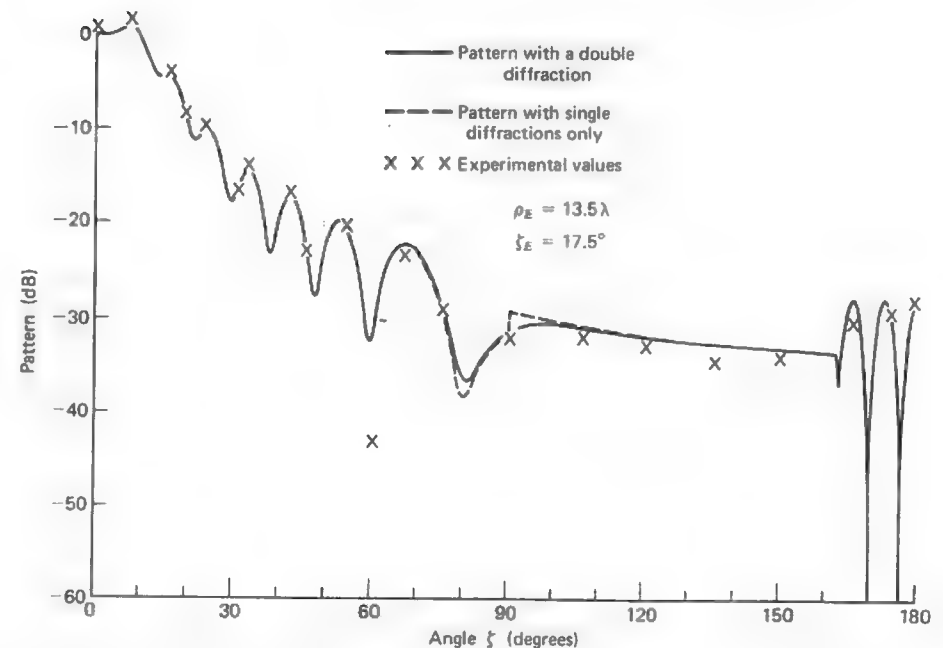


Figure 9-21 Calculated and experimental E -plane patterns of an E -plane sectoral horn.

Also shown in Fig. 9-20c are several other rays which have not been included in the calculated results because in this problem they provide a relatively weak numerical contribution. Strictly speaking, those rays shown in Fig. 9-20c which do not involve double diffractions should be included in the analysis. These are the two rays that experience a reflection after undergoing diffraction at Q_2 (or Q_1 , which are not shown). Of the two doubly diffracted rays shown, here only the one from Q_2 to Q_1 is important because it compensates for the shadowing of Q_2 when $\zeta > 90^\circ$. There is no similar compensation needed in the case of the other doubly diffracted ray which goes from Q_2 to the "top" wall and back to Q_2 .

In conclusion, we have used a simple model (i.e., Fig. 9-20b) to calculate the E -plane pattern of horn antennas with good results. Strictly speaking, we should have included some of the rays in Fig. 9-20c but did not do so for the sake of simplicity without a loss of accuracy. It is a fundamental fact that in applying the UTD (or GTD), one must be careful to identify and to include all rays that arise in the problem. In the horn problem here we were able to omit some of the rays only because they were not in or near a transition region.

9.7 CYLINDRICAL PARABOLIC ANTENNA

As a second example of the application of the UTD, we consider the cylindrical parabolic antenna shown in Fig. 9-22. We use the aperture integration procedure given in Chapter 8 to obtain the pattern in and near the main beam, but use the UTD to compute the pattern everywhere else. As in the study of the horn antenna in the previous section, the model here is two-dimensional. We consider only the diffractions that occur at the edges of the parabolic surface and ignore any higher order rays associated with the curved surface (e.g., see Section 9.12).

First let us consider the equation for obtaining the main beam and first few side lobes. From Section 8.1 we may write for the far field E^A obtained by aperture integration

$$E^A(P) = j\beta \frac{e^{-j\beta r}}{2\pi\sqrt{r}} \int_{-a}^a \frac{F_f(\theta_s)}{\sqrt{\rho}} e^{j\beta y' \sin \zeta} dy' \quad (9-81)$$

where $F_f(\theta_s)$ is the pattern of the electric line source current I^e which serves as the feed for the cylindrical parabolic reflector antenna. (If the line source pattern is

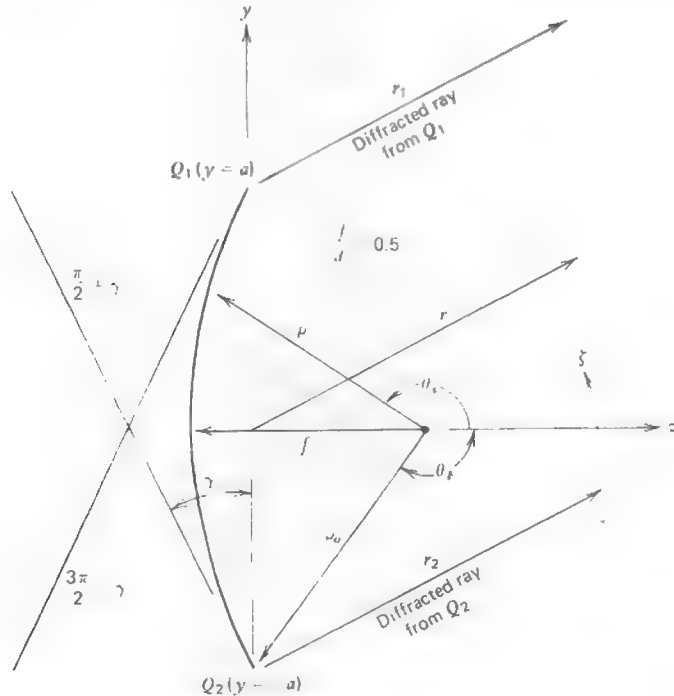


Figure 9-22 Cylindrical parabolic antenna geometry.

isotropic, $F_f(\theta_s) = 1$.) Equation (9-81) is a two-dimensional specialization of the equations in Section 8.1.

Equation (9-81) can, of course, give us the pattern for $90^\circ \geq \zeta \geq -90^\circ$. However, since we must perform the aperture integration anew for each value of ζ , it is more efficient in the computational sense to use (9-81) for $\zeta_o \geq \zeta \geq -\zeta_o$ where ζ_o is the angular extent of the main beam and the first side lobe or two and then to use the UTD for the remainder of the pattern. Clearly, we do not use aperture integration and the UTD simultaneously in the same angular sector.

For the UTD model of the antenna the following equations apply. For the singly diffracted field from Q_1 we have at the far-field observation point $P(r, \zeta, \phi = \pi/2)$

$$E_1^d(P) = 0, \quad \frac{3\pi}{2} - \gamma \leq \zeta \leq \frac{3\pi}{2} \quad (9-82)$$

and elsewhere

$$\begin{aligned} E_1^d(P) &= E_{||}^i(Q_1) D_{||}(L, \phi, \phi') \frac{e^{-j\beta r_1}}{\sqrt{r_1}} \\ &\approx E_{||}^i(Q_1) D_{||}(L, \phi, \phi') \frac{e^{-j\beta r}}{\sqrt{r}} e^{j\beta a \sin \zeta} \end{aligned} \quad (9-83)$$

where (9-70) has been used in (9-83). Similarly the diffracted field at $P(r, \zeta, \phi = \pi/2)$ from Q_2 may be written

$$E_2^d(P) = 0, \quad \frac{\pi}{2} \leq \zeta \leq \frac{\pi}{2} + \gamma \quad (9-84)$$

and elsewhere

$$\begin{aligned} E_2^d(P) &= E_{||}^i(Q_2) D_{||}(L, \phi, \phi') \frac{e^{-j\beta r_2}}{\sqrt{r_2}} \\ &\approx E_{||}^i(Q_2) D_{||}(L, \phi, \phi') \frac{e^{-j\beta r}}{\sqrt{r}} e^{-j\beta a \sin \zeta} \end{aligned} \quad (9-85)$$

where (9-71) has been used in (9-85). In both (9-83) and (9-85)

$$E_{||}^i(Q_1) = E_{||}^i(Q_2) = \frac{e^{-j\beta \rho_o}}{\sqrt{\rho_o}} F_f(\theta_s). \quad (9-86)$$

The total field at an observation point $P(r, \zeta, \phi = \pi/2)$ may be written as either

$$E(P) = E^i(P) + E^A(P) \quad (9-87)$$

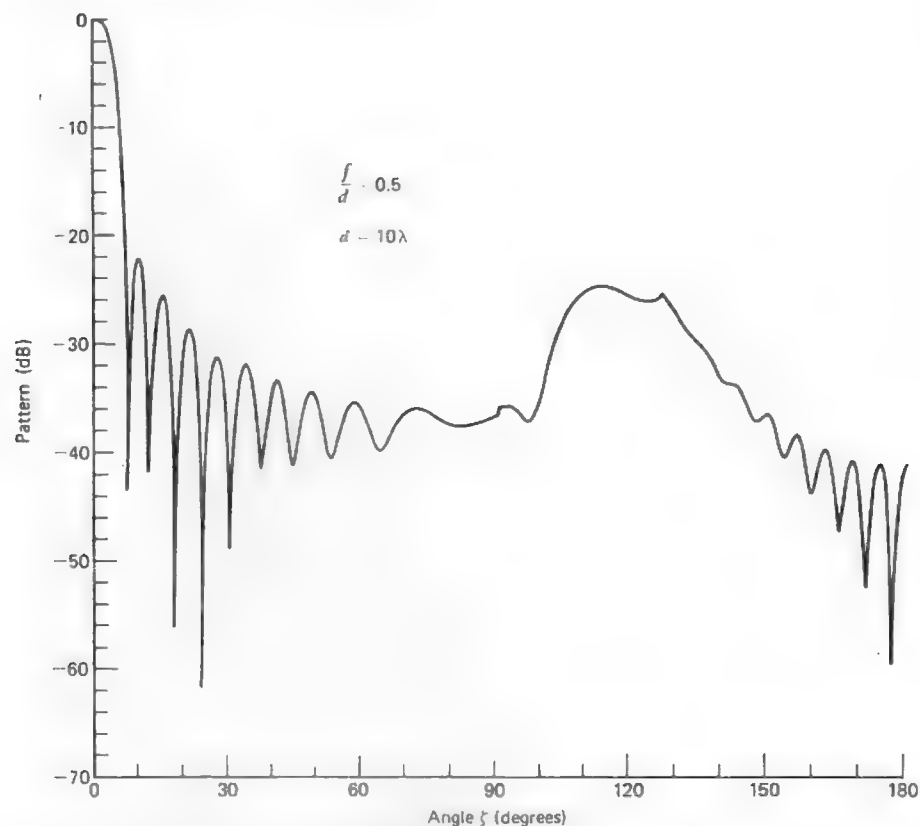


Figure 9-23 Calculated H -plane pattern of a cylindrical parabolic reflector 10λ across having a focal-length-to-diameter ratio of 0.5.

or

$$E(P) = E^i(P) + E_1^d(P) + E_2^d(P) \quad (9-88)$$

depending on the angle ζ as mentioned earlier.

Figure 9-23 shows a calculated pattern for a cylindrical parabolic reflector having a 10λ aperture (i.e., $2a = 10\lambda$) and a focal length to diameter ratio of 0.5. The electric line source that models the feed has a pattern of $F_f(\theta_s) = \cos^2 \theta_s$ for $\theta_s \geq 90^\circ$ and $F_f(\theta_s) = 0$ in the forward half-space where $\theta_s < 90^\circ$. We note that the pattern has a small discontinuity at $\zeta = 90^\circ$ (and 270°) and that this discontinuity can be removed by including double diffracted rays between Q_1 and Q_2 as was done for the horn in the previous section. We also note that there is a small discontinuity at about $\zeta = 127^\circ$ (and 233°) which is a result of the shadowing of

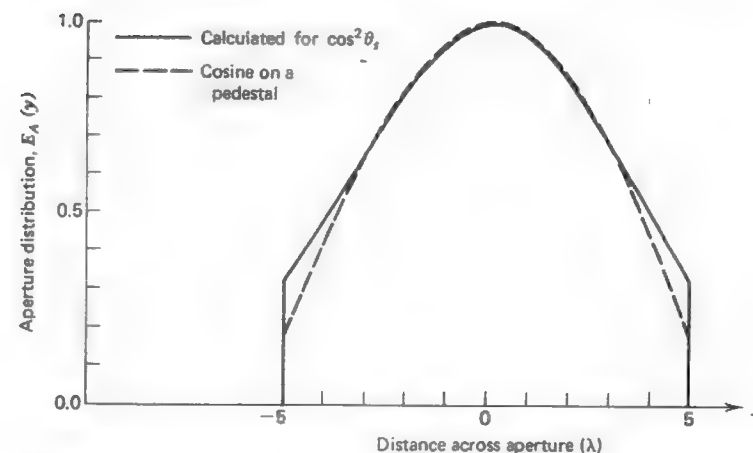


Figure 9-24 Aperture distribution for the parabola of Fig. 9-23 with a feed pattern of $\cos^2 \theta_s$.

Q_2 (or Q_1 when $\zeta \approx 233^\circ$). The relatively high level of the pattern in the vicinity of $\zeta = 120^\circ$ is due to the spillover caused by the feed pattern.

It is interesting to note that for the chosen feed pattern of $\cos^2 \theta_s$, the aperture electric field distribution is almost that of a cosine on a pedestal with a -15 -dB edge illumination as shown in Fig. 9-24. Referring to Table 4-2, we see that such a distribution should produce a pattern with a side lobe level of -22 dB. Examination of the pattern in Fig. 9-23 shows that indeed the side lobe level is -22 dB. Thus, the pattern in the forward half-space could be well-represented by a line source, as discussed in Chapter 4, once the aperture field distribution is known.

In this section we have examined the H -plane pattern of a cylindrical parabolic antenna (i.e., an electric line source was used to model the feed). We could also analyze the E -plane pattern when a magnetic line source is used to model the feed. This is left as an exercise for the student.

9.8 RADIATION BY A SLOT ON A FINITE GROUND PLANE

To illustrate further the application of the uniform theory of diffraction, consider the situation in Fig. 9-25 wherein a radiating slot is asymmetrically located along the x -axis of the rectangular plate. We desire pattern information in both principal planes to determine the amount of ripple in the pattern caused by edge diffraction. In general the edges denoted Q_1 and Q_2 will be illuminated unequally unless $d_1 = d_2$ and thus the pattern in the xz -plane will not be symmetrical about the z -axis.

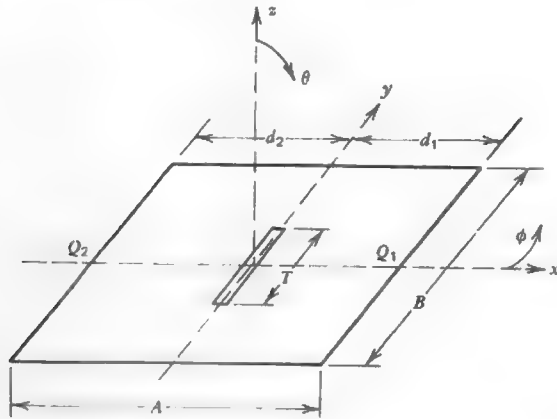


Figure 9-25 Geometry of a slot on a rectangular plate.

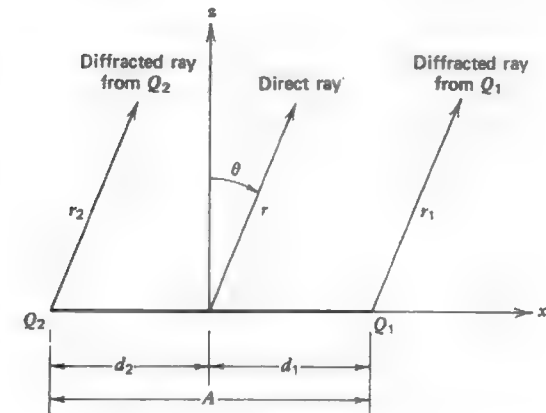
The geometry of the problem to be investigated, as depicted in Fig. 9-25, is a narrow aperture (or slot) with length T on a finite ground plane of dimensions A and B . The narrow slot has an electric field polarized in the x -direction and has a cosine-distribution in the y -direction. The length of the slot is taken to be one-half wavelength at the operating frequency.

For radiation in the xz -plane above the ground plane the problem is represented, to a first degree approximation, by an infinitely long slot. According to UTD there exists two edge-diffracted rays originating from edge points Q_1 and Q_2 due to the finiteness of the ground plane. Therefore, for a far-field observation point $P(r, \theta, \phi = 0)$ in the region of interest, the total field is the sum of the contributions from the direct ray and two edge-diffracted rays as shown in Fig. 9-26. Doubly diffracted rays exist but are small compared to the singly diffracted rays shown in Fig. 9-26 and are not included in the present analysis.

For radiation in the yz -plane above the ground plane, a sampling of $N + 1$ ideal dipole sources with cosine distribution is performed. There exists no first-order edge-diffracted rays because the incident ray is zero in the yz -plane. A geometry of five samplings ($N = 4$) is shown in Fig. 9-27. The end dipole sources are of zero amplitude since tangential E is zero at the ends of the slot.

First let us consider the radiation pattern in the xz -plane. The direct ray from the narrow slot at an observation point $P(r, \theta, \phi = 0)$ is

$$E_1^i(P) = \hat{\theta} E_0 \frac{e^{-j\beta r}}{\sqrt{r}} \quad (9-89)$$

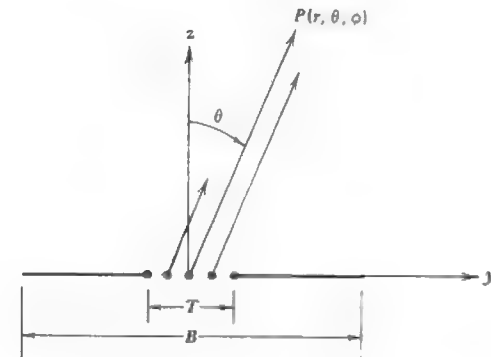
Figure 9-26 Direct and diffracted rays contributing to the xz -plane pattern.

The edge-diffracted ray from Q_1 at $P(r, \theta, \phi = 0)$ becomes

$$E_1^d(P) = \hat{\theta} \frac{1}{2} E_1^i(Q_1) D_1(L, \phi, \phi') \frac{e^{-j\beta r_1}}{\sqrt{r_1}} \quad (9-90)$$

with

$$E_1^i(Q_1) = \hat{z} E_0 \frac{e^{-j\beta d_1}}{\sqrt{d_1}} = \hat{z} E_1^i(Q_1) \quad (9-91)$$

Figure 9-27 Direct rays from the dipoles representing the slot contributing to the yz -plane pattern.

The edge-diffracted ray from Q_2 at $P(r, \theta, \phi = 0)$ yields

$$E_2^d(P) = \hat{\theta} \frac{1}{2} E_1^i(Q_2) D_\perp(L, \phi, \phi') \frac{e^{-j\beta r_2}}{\sqrt{r_2}} \quad (9-92)$$

with

$$E_1^i(Q_2) = \hat{z} E_o \frac{e^{j\beta d_2}}{\sqrt{d_2}} = \hat{z} E_1^i(Q_2). \quad (9-93)$$

The total field at an observation point $P(r, \theta, \phi = 0)$ then becomes (in the symmetrical case)

$$E(P) = E^i(P) + E_1^d(P) + E_2^d(P). \quad (9-94)$$

The parameters r , r_1 , d_1 , r_2 , and d_2 are shown in Fig. 9-26. The parameter E_o represents the magnitude of the electric field at the narrow slot in the xz -plane. $E_1^i(Q_m)$ is that component of the incident field which is both perpendicular to the edge and to the incident ray. To first order D_\parallel is zero. However, there is a small amount of diffraction that does take place and this is called slope diffraction (see Prob. 9.8-1). The addition of slope diffraction to the diffracted field ensures that not only is the total field continuous across a shadow boundary, but also that the derivative of the total field is continuous.

For the slot problem of Fig. 9-25, the radiation in the yz -plane may be analyzed in the region above the ground plane to a first degree approximation, by an array of dipole sources with a cosine distributed amplitude across the array. Let the total number of dipoles in the array be $N + 1$, then the separation between dipoles is

$$s = \frac{T}{N}. \quad (9-95)$$

The total field at an observation point $P(r, \theta, \phi = \pi/2)$ then becomes

$$E(P) = \hat{\theta} E_o \sin(90^\circ - \theta) \sum_{n=-N/2}^{N/2} \cos\left(\frac{n\pi}{T}\right) e^{jn\beta s \sin \theta} \quad (9-96)$$

In Fig. 9-27 the geometry of yz -plane with five dipoles ($N = 4$) in the array is shown.

Figure 9-28 shows the far-field pattern results in the xz - and yz -planes at both 1 GHz and 3 GHz. The ground plane is 61 by 61 cm but the slot is taken to be one-half wavelength at each frequency and diffraction in the yz -plane has been assumed to be negligible, and under this assumption the pattern in the yz -plane is the same at each frequency as indicated in Fig. 9-28. However, due to diffraction the two patterns in the xz -plane are different, the "ripple" in the patterns being the result of the diffracted energy. Since the slot is located symmetrically on the

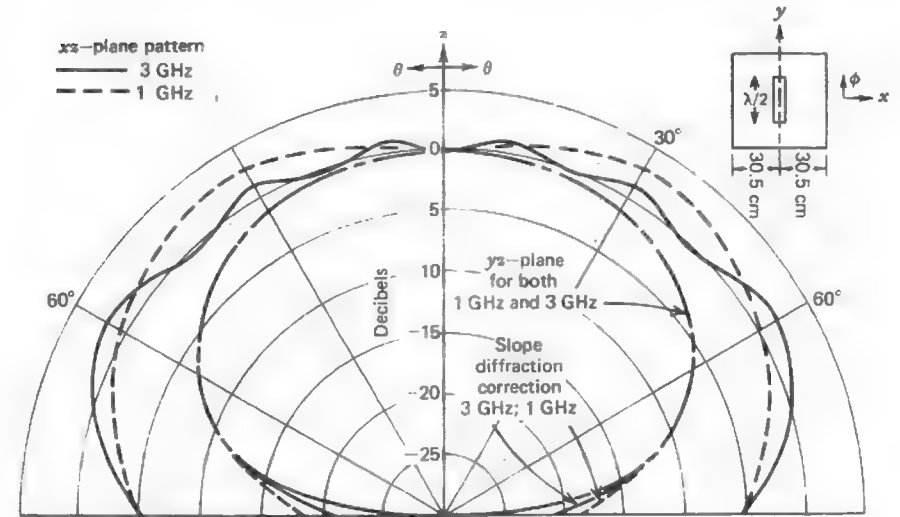


Figure 9-28 Far-field patterns in both principal planes at 1 GHz and 3 GHz.

ground plane, we see that the pattern is symmetric about the z -axis. For completeness the slope diffraction contribution to the yz -plane pattern at 1 GHz and 3 GHz is also shown.

While an experimental comparison is not shown here, such comparisons have been made with excellent results [14] even though diffraction from the four corners or vertices of the ground plane has been neglected. Although a formal solution for vertex diffraction does not yet exist, we know from experimental measurements that vertex diffraction is generally much weaker than wedge diffraction. Thus, the total far field is given to a good approximation by (9-94). In the problem considered here, vertex diffraction is weak in the $\phi = 45^\circ$ and $\phi = 135^\circ$ planes.

9.9 RADIATION BY A MONOPOLE ON A FINITE GROUND PLANE

As another application of the uniform theory of diffraction and also as an example of a problem with a caustic in it, let us consider the two situations depicted in Fig. 9-29. First, consider the situation in Fig. 9-29a of a $\lambda/4$ monopole on a square plate and suppose we wish to obtain the pattern in the xz -plane. For purposes of far-field calculation and conceptual simplicity, a suitable approximation to the $\lambda/4$ monopole is the ideal dipole of Chapter 1. We will

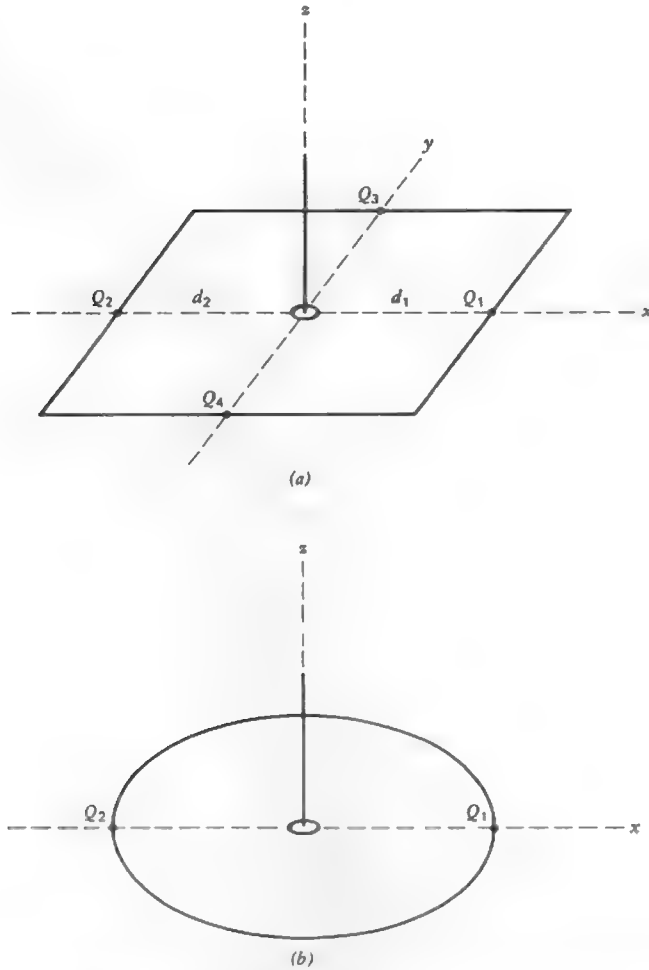


Figure 9-29 Monopole on a finite ground plane: (a) square ground plane, (b) circular ground plane.

consider the ideal dipole to be resting on the surface of the ground plane. Thus, following the development of the previous section for the slot, we have for the direct ray from the ideal dipole at $P(r, \theta, \phi = 0)$

$$E^i(P) = \hat{\theta} E_o \frac{e^{-j\beta r}}{r} \sin \theta \quad (9-97)$$

which now must obviously be considered to be a spherical wave. The edge-

diffracted ray from Q_1 at $P(r, \theta, \phi = 0)$ appears to emanate from a single point and is therefore

$$E_1^d(P) = \hat{\theta} \frac{1}{2} E^i(Q_1) D_{\perp}(L, \phi, \phi') \sqrt{d_1} \frac{e^{-j\beta r_1}}{r_1} \quad (9-98)$$

with

$$E^i(Q_1) = \hat{z} E_o \frac{e^{-j\beta d_1}}{d_1} = \hat{z} E_1^i(Q_1) \quad (9-99)$$

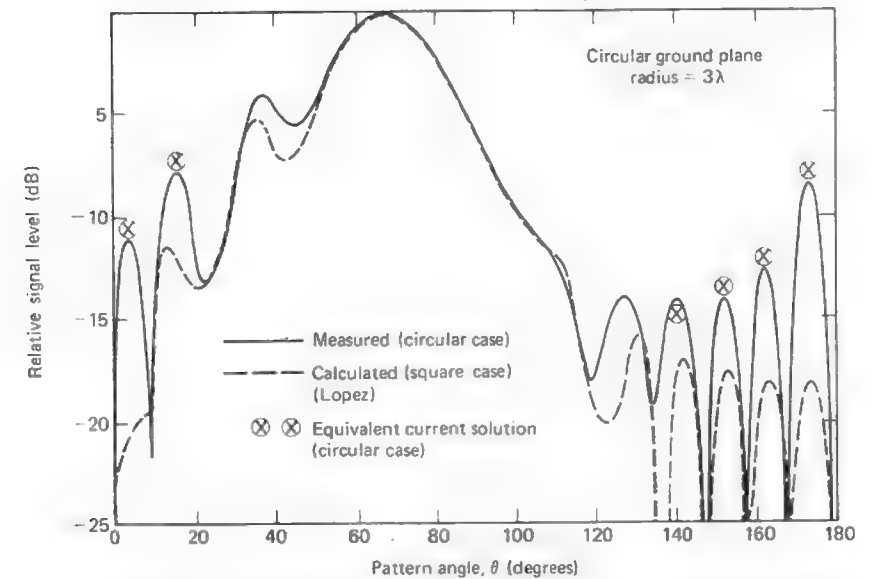
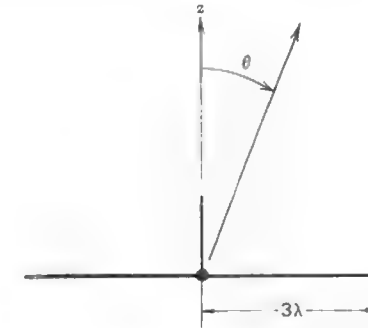


Figure 9-30 Radiation pattern of a short monopole on a circular ground plane 6λ in diameter. The calculated curve by Lopez [15] is for a $6\lambda \times 6\lambda$ square ground plane.

Similarly, the edge-diffracted ray from Q_2 at $P(r, \theta, \phi = 0)$ is

$$E_2^d(P) = \hat{\theta} \frac{1}{2} E_{\perp}^i(Q_2) D_{\perp}(L, \phi, \phi') \sqrt{d_2} \frac{e^{-j\beta r_2}}{r_2} \quad (9-100)$$

with $E_{\perp}^i(Q_2)$ given by (9-99) since the source is located at the center of the ground plane. Diffraction from the sides containing Q_3 and Q_4 does not contribute to the far field in the xz -plane since the monopole is positioned at the center of the ground plane and the diffracted fields from these two sides will cancel one another. As in the case of the slot of the previous section, we neglect diffraction from the four corners or vertices of the ground plane. The corresponding pattern for a 6λ square ground plane is given in Fig. 9-30 (dashed curve).

If we now consider the geometry of Fig. 9-29b, we note that in the xz -plane the diffracted radiation will also appear (due to Fermat's principle) to come from two points which are called stationary points. We note too that the z -axis is a caustic in this problem because all rays from the circular edge of the ground plane intersect along the z -axis. Therefore, while we can expect to use the two stationary points to calculate the diffracted field contribution to the pattern in regions not near the caustic [15], we can likewise expect the "two-point approximation" to be increasingly in error as the observation point P moves nearer the caustic. Figure 9-30 shows that indeed this is the case since the measured and two-point calculated patterns diverge both as $\theta \rightarrow 0$ and $\theta \rightarrow \pi$, which is also a caustic. The apparent difficulty in the vicinity of the caustic can be overcome, as suggested in Fig. 9-30, by the use of a fictitious equivalent edge current. As will be seen in the next section, the so-called equivalent current is not a physical current at all, but rather a mathematical artifice for predicting the correct diffracted field at or near a caustic.

9.10 EQUIVALENT CURRENT CONCEPTS

In the previous section we saw that, in the treatment of the circular ground plane, we could obtain the diffracted field using ordinary wedge diffraction theory if the point of observation was not near a caustic. In essence, we were treating the problem as a two-dimensional one with the diffraction being taken as that from an infinite two-dimensional wedge, whereas in fact we had a finite edge that was not straight, but curved.

To properly treat the diffraction by a curved edge or a finite wedge (i.e., finite length of the edge), it is necessary to consider the concept of equivalent currents [16]. As we shall see, the strengths (i.e., amplitude and phase) of these so-called equivalent currents will be determined by the canonical problem of wedge diffraction.

Consider the wedge of Fig. 9-17 to be of finite extent, $-\ell/2 \leq z(Q) \leq \ell/2$. To start, we assume the currents are the same as those on an infinite wedge. Let us determine the current flowing on the edge of the infinite wedge which would produce the scattered field predicted by wedge diffraction analysis. Thus, we specify an infinite line source whose current is determined by the diffraction coefficient. If the z -directed line source is an electric current, it can be shown in a manner similar to that used in Sections 1.3 and 7.11, that the solution to the scalar wave equation is [17]

$$\psi = \frac{I^e}{4j} H_0^{(2)}(\beta\rho) \quad (9-101)$$

and therefore that the z -component of the electric field is

$$E_z = \frac{-\beta^2 I^e}{4\omega\epsilon} H_0^{(2)}(\beta\rho) \quad (9-102)$$

where I^e denotes an electric current. If the argument of the Hankel function $H_0^{(2)}(\beta\rho)$ is large, then using the asymptotic representation of the Hankel function, we obtain

$$E_z = \eta\beta I^e \frac{e^{j(\pi/4)}}{2\sqrt{2\pi\beta\rho}} e^{-j\beta\rho} \quad (9-103)$$

We note that (9-103) represents an outward traveling wave in the cylindrical coordinate system with the proper $\sqrt{\rho}$ dependence for a two-dimensional problem. If instead the line source is a magnetic current I^m , then we have

$$H_z = -\frac{\beta}{\eta} I^m \frac{e^{j(\pi/4)}}{2\sqrt{2\pi\beta\rho}} e^{-j\beta\rho} \quad (9-104)$$

Since we are at present considering a strictly two-dimensional problem, we can also apply wedge diffraction theory to obtain the diffracted field from the edge for the two orthogonal polarizations. Thus,

$$E_z = D_{\perp}(L, \phi, \phi') E_z^i \frac{e^{-j\beta\rho}}{\sqrt{\rho}} \quad (9-105)$$

and

$$H_z = D_{\parallel}(L, \phi, \phi') H_z^i \frac{e^{-j\beta\rho}}{\sqrt{\rho}} \quad (9-106)$$

where D_{\perp} and D_{\parallel} are given in Section 9.5. Usually, however, we find that the use of equivalent currents involves the calculation of diffracted fields in regions away from an incident field or a reflected field shadow boundary or their associated transition regions. Thus, the asymptotic form in (9-69) for arbitrary incidence angle γ_0 is usually sufficient.

From (9-103) with (9-105) and also (9-104) with (9-106) we can solve for the electric and magnetic currents of an infinite line source which will produce the same far fields predicted using the diffraction coefficients. Thus,⁴

$$I^e = \frac{-2j}{\eta\beta} E_z^i D_\perp \left(\phi, \phi'; \frac{\pi}{2} \right) \sqrt{2\pi\beta} e^{j(\pi/4)} \quad (9-107)$$

and

$$I^m = \frac{2j\eta}{\beta} H_z^i D_\perp \left(\phi, \phi'; \frac{\pi}{2} \right) \sqrt{2\pi\beta} e^{j(\pi/4)} \quad (9-108)$$

We note that (9-107) and (9-108) give us the equivalent currents I^e and I^m but that they are numerically different for each value of ϕ and ϕ' . The fact that these currents are different for different observation points (i.e., values of ϕ) serves to emphasize the fact that these equivalent currents are not true currents, but fictitious currents that simply aid us in calculating diffracted fields.

Considering Fig. 9-17 with the ray incident normally on the edge ($\gamma_0' = \pi/2$), we have, respectively, for the far-zone diffracted fields

$$E_\theta^e = \frac{j\omega\mu \sin \theta}{4\pi r} e^{-j\beta r} \int_{-\rho/2}^{\rho/2} I_z^e(z') e^{j\beta z' \cos \theta} dz' \quad (9-109)$$

and

$$H_\theta^m = \frac{j\omega\mu \sin \theta}{4\pi r} e^{-j\beta r} \int_{-\rho/2}^{\rho/2} I_z^m(z') e^{j\beta z' \cos \theta} dz' \quad (9-110)$$

As in Chapter 4, we see that since the currents are constant with respect to z' , (9-109) and (9-110) reduce to results in the general form of $\sin(x)/x$ with respect to the θ -coordinate.

For the case of non-normal incidence (i.e., $\gamma_0' \neq \pi/2$), we can proceed in the same manner and show that

$$I^e = \frac{-2j}{\eta\beta} E_z^i D_\perp(\phi, \phi'; \gamma_0) \sqrt{2\pi\beta} e^{j(\pi/4)} e^{j\beta \rho' \cos \gamma_0} \quad (9-111)$$

and

$$I^m = \frac{2j\eta}{\beta} H_z^i D_\perp(\phi, \phi'; \gamma_0) \sqrt{2\pi\beta} e^{j(\pi/4)} e^{j\beta \rho' \cos \gamma_0} \quad (9-112)$$

which includes the phase term to account for the traveling wave type current due to the non-normal angle of incidence. In obtaining (9-111) and (9-112) we have neglected the effects of the terminations at $z = \pm \rho/2$. If the effect of the termination could be specified, an alternative equivalent current could be composed of

⁴ Note that we denote the diffraction coefficient to be a function of L , ϕ , and ϕ' to imply the Fresnel integral form of the uniform theory in (9-62) and use ϕ , ϕ' , and γ_0 when the asymptotic form in (9-69) is intended.

the currents given above plus a reflected current due to the termination. These reflection effects would be expected to be of most concern in the backscatter direction, rather than in the direction of the bistatic scattered field. Even so, as the edge becomes long in terms of the wavelength, termination effects diminish. In addition, usually the above currents find their application in the angular region near the plane normal to the edge, further diminishing any possible termination effects.

When we obtain equivalent currents, we invoke the postulate of diffraction theory that diffraction is a local phenomena. For curved edges, we stretch this postulate even further than for the straight edge. That is, we assume that each point on a curved edge acts as an incremental section of an infinite straight edge and thereby determine the equivalent current. Thus, for example, the equivalent current that would enable us to calculate the diffracted field at the caustic of the problem in Fig. 9-29b, would be [14]

$$I^m = -(\hat{\phi} \times \hat{s}') \cdot \mathbf{E}^i D_\perp \left(\phi, \phi'; \frac{\pi}{2} \right) \sqrt{\frac{8\pi}{\beta}} e^{-j(\pi/4)} \quad (9-113)$$

where we have used the result of (9-108) and the fact that $(\hat{\phi} \times \hat{s}')$ gives us the unit vector perpendicular to the ray from the sources to the edge. The use of (9-113) gives the calculated results in Fig. 9-30 which agree with experimental measurements in the caustic region.

If, on the other hand, the source in Fig. 9-29 were a magnetic dipole, then the required equivalent current would be [14]

$$I^e = -\frac{\hat{\phi} \cdot \mathbf{E}^i}{\eta} D_\parallel \left(\phi, \phi'; \frac{\pi}{2} \right) \sqrt{\frac{8\pi}{\beta}} e^{-j(\pi/4)} \quad (9-114)$$

For an arbitrary polarization of the incident wave, both electric and magnetic currents are necessary to obtain the total diffracted field. Such a situation would occur, for example, in the calculation of the fields at or near the rear axis of a circular parabolic reflector antenna which is a caustic region. At the rim of the parabolic dish, the polarization of the field incident from the feed is generally neither perpendicular nor parallel to the edge. Thus, both electric and magnetic equivalent currents at the rim would be required to obtain the total diffracted field in the rear axial region.

9.11 A MULTIPLE DIFFRACTION FORMULATION

In the previous two sections we considered radiating elements on infinitely thin ground planes (i.e., $n = 2$). If, instead, the ground plane were "thick" such that one side could be represented by two 90° wedges as shown in Fig. 9-31, then it

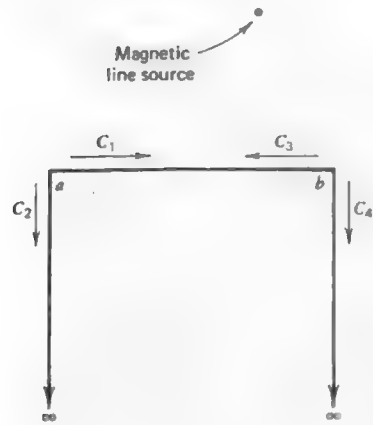


Figure 9-31 Magnetic line source exciting surface rays on a half-plane of finite thickness.

would have been necessary to consider the multiple diffractions that occur between the two closely spaced edges. In such a situation, some of the energy diffracted by one edge is in turn diffracted by the other giving rise to second order diffraction or to double diffracted rays. Clearly, some of these double diffracted rays give rise to still higher order multiple diffractions.

If, to reasonably approximate the total diffracted energy, it is necessary to include doubly diffracted rays, then it is usually simplest to include them in the same manner used to account for the first order diffraction in the previous two sections. On the other hand, if it is necessary to account for diffractions higher than second order, it is advantageous to use a procedure known as the *method of self-consistency*.

Briefly, the method of self-consistency incorporates all the diffracted rays (i.e., single as well as all higher order multiple ones) into a *total* (or net) diffracted field from each diffracting edge. Thus, each of these total edge diffracted fields is excited by a surface ray. Between the two diffracting edges there are, therefore, two surface rays traveling in opposite directions. The amplitudes and phases of these two surface rays are treated as unknowns. To solve for the two unknowns, two equations are generated by applying single diffraction conditions at each of the two diffracting edges.

To illustrate, consider Fig. 9-31. The coefficients C_1 and C_3 are the unknown amplitudes (i.e., magnitude and phase) of the two surface rays on the surface ab . The coefficients C_2 and C_4 are known once C_1 and C_3 are known. Thus, we may write the following equations. At edge a ,

$$C_1 = C_3 R_{ba} + V_1 \quad (9-115)$$

and at edge b ,

$$C_3 = C_1 R_{ab} + V_3 \quad (9-116)$$

and knowing C_1 and C_3 we have

$$C_2 = T_{ba} C_3 + V_2 \quad (9-117)$$

$$C_4 = T_{ab} C_1 + V_4 \quad (9-118)$$

where R and T are reflection and transmission coefficients, respectively, and V is the direct source contribution to the corresponding surface ray.

Equations (9-115) and (9-116) may be written in matrix form as

$$\begin{bmatrix} 1 & -R_{ba} \\ -R_{ab} & 1 \end{bmatrix} \begin{bmatrix} C_1 \\ C_3 \end{bmatrix} = \begin{bmatrix} V_1 \\ V_3 \end{bmatrix} \quad (9-119)$$

or compactly as

$$[Z][C] = [V] \quad (9-120)$$

where $[Z]$ is taken to be a coupling matrix and $[V]$ is the excitation matrix. The elements of the coupling matrix specify the interactions between the two surface rays. In general, two surface rays may couple only if they travel on the same or adjacent faces of a polygon as shown in Fig. 9-32. This, in general, leads to a sparse $[Z]$ matrix.

For the situation in Fig. 9-31, the reflection and transmission coefficients are

$$R_{ab} = \frac{e^{-j\beta\rho_{ab}}}{\sqrt{\rho_{ab}}} \frac{1}{2} D_1(L, \phi, \phi') \quad (9-121)$$

where $\phi^+ = \phi^- = 0$ and $\gamma_o = 90^\circ$, and

$$T_{ab} = \frac{e^{-j\beta\rho_{ab}}}{\sqrt{\rho_{ab}}} \frac{1}{2} D_1(L, \phi, \phi') \quad (9-122)$$

where $\phi^+ = 2\pi - \pi/2$, $\phi^- = 0$, and $\gamma_o = 90^\circ$. For T_{ab} , ϕ^+ is 2π less the interior wedge angle of $\pi/2$. In both cases the distance parameter L used is that for cylindrical waves. For the special situation depicted in Fig. 9-31, $R_{ab} = R_{ba}$ and

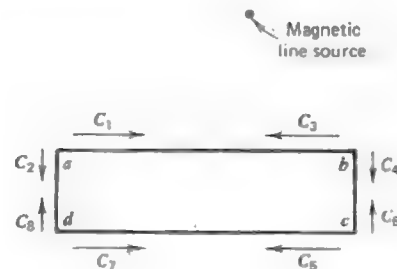


Figure 9-32 Magnetic line source exciting surface rays on an infinite four-sided polygon cylinder.



Figure 9-33 Polygon approximation of a curved surface cylinder. (a) Curved surface. (b) Polygon approximation.

$T_{ab} = T_{ba}$. This is not true in general. For example, it would not be true for the situation depicted in Fig. 9-33.

For the two excitation matrix elements we have

$$V_1 = \frac{e^{-j\beta\rho_{sa}}}{\sqrt{\rho_{sa}}} D_{\perp}(L, \phi, \phi') \quad (9-123)$$

$$V_3 = \frac{e^{-j\beta\rho_{sb}}}{\sqrt{\rho_{sb}}} D_{\perp}(L, \phi, \phi') \quad (9-124)$$

where ρ_{sa} is the distance from the line source to edge a and ρ_{sb} is the distance from the line source to edge b . If the line source did not directly illuminate, say, edge b , then V_3 would be zero. Here we have considered only the TE case. A consideration of the TM case requires a knowledge of slope diffraction (see Section 9.8).

As stated earlier, it may be sufficient in many problems to only take into account second order diffraction thereby neglecting all higher order multiply diffracted rays. An example of a situation where the method of self-consistency greatly simplifies the amount of work required for solution is suggested by Fig. 9-33. It is possible and practical to approximate the curved surface of Fig. 9-33a with a polygon such as that in Fig. 9-33b. For an accurate approximation to the curved surfaces, the edges in Fig. 9-33b may be sufficiently close together that higher order multiple diffractions should be taken into account. The easiest way of doing that is via the method of self-consistency. However, the self-consistent field method only works well provided an edge is not in the transition region of a diffraction from another edge. This is a possibility if adjacent edges of the polygon are closely aligned and this limits the degree to which the curved surface may be approximated.

9.12 DIFFRACTION BY CURVED SURFACES

In previous sections we have seen how a perfectly-conducting wedge diffracts energy into the shadow region. Curved surfaces may also diffract energy [14, 19]. That is, when an incident ray strikes a smooth, curved perfectly-conducting

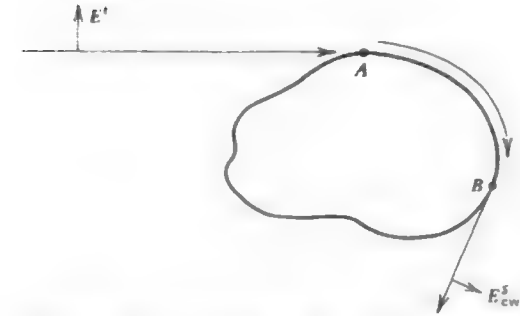


Figure 9-34 Creeping wave concept of diffraction by a curved surface.

surface at grazing incidence, a part of its energy is diffracted into the shadow region as illustrated by Fig. 9-34.

In Fig. 9-34, the incident plane wave undergoes reflection from the illuminated portion of the scatter and undergoes diffraction at the shadow boundary at point A which is a point of tangency for the incident ray. At this point a portion of the energy is trapped resulting in a wave which propagates on the surface of the scatterer, shedding energy by radiation as it progresses in directions tangent to the surface (e.g., point B).

This wave that propagates along the surface is known as a *creeping wave*. The creeping wave can be described by a launching coefficient at the point of capture, by a diffraction coefficient at the point of radiation, by an attenuation factor to account for the rate of radiation, and by a description of the path on the scatterer traversed by the creeping wave. Thus, we could write for the creeping wave contribution to the scattered field, E_{cw}^s , in the case of a two-dimensional problem

$$E_{cw}^s = E_A^i L_A D_B G(s) \frac{e^{-j\beta r}}{\sqrt{r}} e^{-\int_A^B \gamma(s) ds} \quad (9-125)$$

where

E_{cw}^s = creeping wave scattered field

L_A = the launching coefficient at point A

D_B = the curved surface diffraction coefficient at point B

$\gamma(s) = \alpha(s) + j\beta(s)$ = creeping wave propagation factor

s = arc length along the creeping wave path

$G(s)$ = the ray divergence factor determined by the geometry of the ray.

The concept of a creeping wave is valuable in that it helps one visualize the physical process involved in diffraction by curved surfaces. For example, the RCS of a sphere as a function of the sphere radius is presented in Fig. 9-7. We can interpret the oscillatory feature of the curve as being caused by two creeping waves traveling around the sphere in opposite directions. Depending upon the electrical size of the sphere, these two creeping waves tend to either constructively or destructively interfere with each other causing the RCS to oscillate about the value contributed by the specular scattering in (9-23). As the sphere becomes larger, the amount of oscillation decreases which may be attributed to the decreasing amplitudes of the two creeping waves due mostly to the factor $\alpha(s)$ in (9-125).

Diffraction by curved surfaces is mathematically more complex than that for the canonical problem of the wedge, so we will not pursue it further here. For many engineering purposes, the student can adequately approximate a curved surface by the method of the previous section.

9.13 EXTENSION OF MOMENT METHODS USING THE GTD

In Chapter 7 we saw how the method of moments could be applied to many antenna and scattering problems wherein the antenna or scatterer was not excessively large in terms of the wavelength. In this chapter we have seen how geometrical optics and the GTD can be applied to problems that are large in terms of the wavelength. The purpose of this section is to show how the class of problems solvable by moment methods can be enlarged by incorporating the GTD into the moment method solution [20]. In studying this section, the student will have an opportunity to test his or her understanding of the fundamental concepts developed in Chapter 7 and in the previous sections of this chapter.

Recall from (7-42) the elements of the generalized impedance matrix which may be given in inner product notation as

$$Z_{mn} = \langle \mathbf{J}_m, \mathbf{E}_n \rangle \quad (9-126)$$

This states that the Z_{mn} th element of the impedance matrix is found by reacting the m th test function with the electric field from the n th basis function. Similarly, the m th element in the generalized voltage matrix is found by reacting the m th test function with the incident field.

Now in a strictly moment method formulation of a given problem all material bodies are removed and replaced with equivalent currents radiating in free space. Thus, when one reacts the m th test function with the field from the n th basis function, it is only that field which directly arrives at the m th test function via the

shortest free space path which one needs to consider since it is the only possible field. However, suppose there exists in a given situation a portion of the structure which is not represented by equivalent currents (i.e., a material body remains as shown in Fig. 9-35). In this case, the calculation of the impedance matrix elements is more complex but not unduly so. Let these new impedance matrix elements be denoted Z'_{mn} . In terms of (9-126), the reaction of \mathbf{J}_m with \mathbf{E}_n may be interpreted to mean the reaction of the test source with not only the field from the true source arriving at the test source directly, but in addition the reaction of the test source with fields from the true source that arrive by other means as suggested by Fig. 9-35. Therefore, one can write

$$Z'_{mn} = \langle \mathbf{J}_m, a\mathbf{E}_n + b\mathbf{E}_n \rangle \quad (9-127)$$

where a may be set to unity and $b = b(m, n)$ is different for each m and n . The quantity $b\mathbf{E}_n$ also represents the field due to \mathbf{J}_n , but arriving at the m th observation point or region due to a physical process, such as a geometrical optics or a diffraction mechanism, which is not accounted for in that portion of the problem formulated by the moment method. Thus,

$$Z'_{mn} = \langle \mathbf{J}_m, \mathbf{E}_n \rangle + \langle \mathbf{J}_m, b\mathbf{E}_n \rangle \quad (9-128)$$

or

$$Z'_{mn} = Z_{mn} + Z_{mn}^g, \quad (9-129)$$

where the superscript g denotes that Z_{mn}^g is an additional term added to, in general, each impedance matrix element due to a physical process g that redirects energy from the n th basis current function to the location of the m th test source.

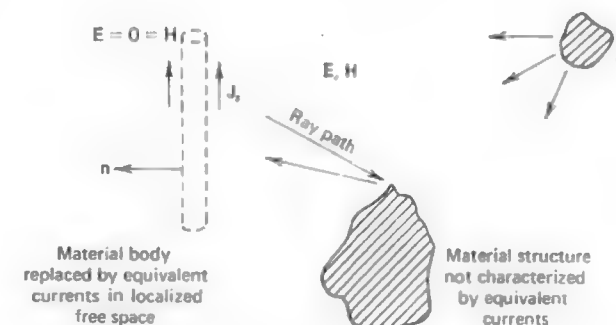


Figure 9-35 A source radiating in free space with one scatterer replaced by an equivalent current and the other remaining as a material body.

As implied by Fig. 9-35, there is also a modification of the usual generalized voltage matrix terms. That is,

$$V'_m = \langle \mathbf{J}_m, \mathbf{E}_i + c\mathbf{E}_i \rangle, \quad (9-130)$$

where \mathbf{E}_i is the incident field arriving directly at region m and $c\mathbf{E}_i$ is that field from the source redirected to region m by a physical process g . We note that $c = c(m)$ is different for each m .

$$V'_m = \langle \mathbf{J}_m, \mathbf{E}_i \rangle + \langle \mathbf{J}_m, c\mathbf{E}_i \rangle, \quad (9-131)$$

or

$$V'_m = V_m + V_m^g. \quad (9-132)$$

As a direct consequence of the foregoing discussion, we have

$$[Z'] [I'] = [V'] \quad (9-133)$$

and its solution as

$$[I'] = [Z']^{-1} [V'] \quad (9-134)$$

where $[I']$ is the current on, for example, an antenna operating in the presence of scattering mechanisms that may be accounted for by either geometrical optics techniques or GTD.

Initially, to combine the method of moments and GTD into a hybrid technique, consider the problem of a monopole near a perfectly conducting wedge as shown in Fig. 9-36. If we describe the monopole on an infinite ground plane strictly by the moment method matrix representation given in (7-42), then for the monopole near the conducting wedge we utilize (9-133) where in (9-129) the term Z_{mn}^g is obtained by considering that energy radiated by the n th basis

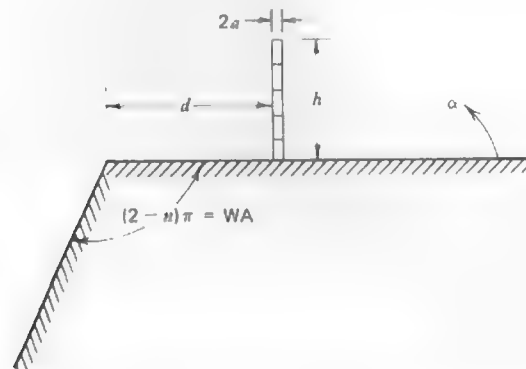


Figure 9-36 Monopole on a conducting wedge.

function on the monopole that is diffracted by the wedge to the m th observation point or region. In the work here we employ pulse basis functions and point-matching wherein the testing functions are delta functions. However, the choice of basis and testing functions is not restricted to these functions.

To calculate Z_{mn}^g we compute the electric field from the n th pulse basis function incident upon the edge of the wedge at the stationary point. Taking that component of the electric field perpendicular to the edge and to the direction of propagation of the incident field, we then compute the energy diffracted to the observation point at the center of the m th segment on the monopole. The component of this field tangential to segment m is the term Z_{mn}^g of (9-129) since we are employing delta weighting functions. To compute the diffracted field, we use the formulation in Section 9.5 for the case of spherical wave incidence.

Shown in Fig. 9-37a is a calculated curve for the input resistance of a quarter-wavelength monopole a distance d from the edge of a perfectly conducting wedge (see Fig. 9-36). We note that the resistance oscillates about the value for a quarter-wavelength monopole on an infinite ground plane and also that the amount of variation is relatively small being only a few ohms. A similar curve is shown in Fig. 9-37b for the input reactance. Data for both curves was obtained directly from (9-134) without the need for any *a priori* knowledge of the current distribution or the terminal current value.

Thus far the discussion has centered upon the calculation of input impedance. Obviously, if one can accurately compute the input impedance, then quite accurate far-field information can readily be obtained too. For example, in the case of a monopole near a single wedge, as in Fig. 9-36, there may be as many as three contributors to the far field. First, there is direct source radiation except in the shadow region. Second, there is the reflected field, which is most conveniently accounted for by using the image in the horizontal surface. Third, there is the diffracted field that contributes in all regions and, of course, is the only source of radiation in the shadow region. A typical far-field pattern is shown in Fig. 9-38. Note that for $\alpha = 90^\circ$ the field does not go to zero as would be the case if the ground plane was infinite in extent.

If we wish to investigate a circular ground plane as in Fig. 9-39, we must use the equivalent edge currents described in Section 9.10. Thus, we replace the edge of the disk with an equivalent magnetic current M given by

$$M = -2E_0 e^{-j\pi/4} D_\perp(L, \phi, \phi') \sqrt{\lambda}. \quad (9-135)$$

This equivalent magnetic current is used to calculate the field at the segment at s due to the current at s' as indicated in Fig. 9-39. Note that an equivalent magnetic ring current must be calculated for each choice of s and s' .

It is useful for us to break up the equivalent magnetic ring current of Fig. 9-39 into differential elements $d\ell$ so that the observation point is in the far field of each element even though it may be in the near field of the total ring current.

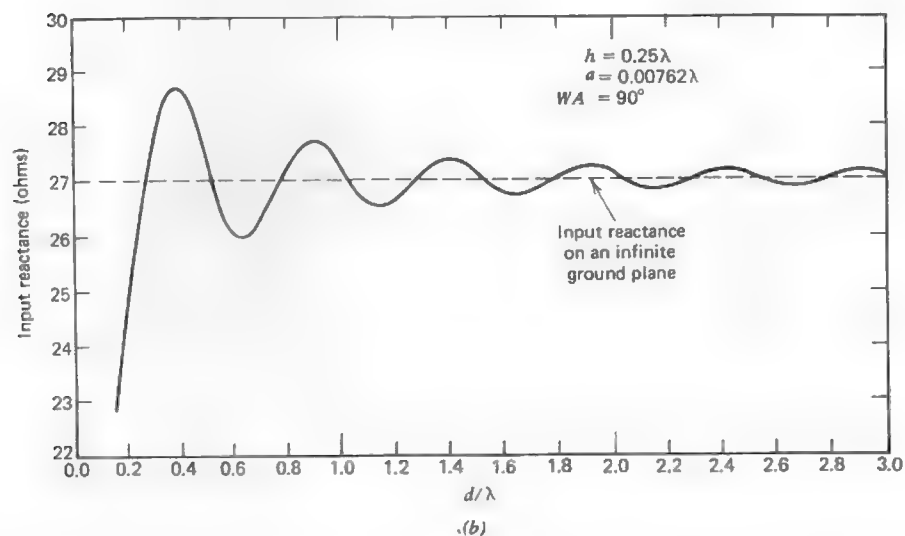
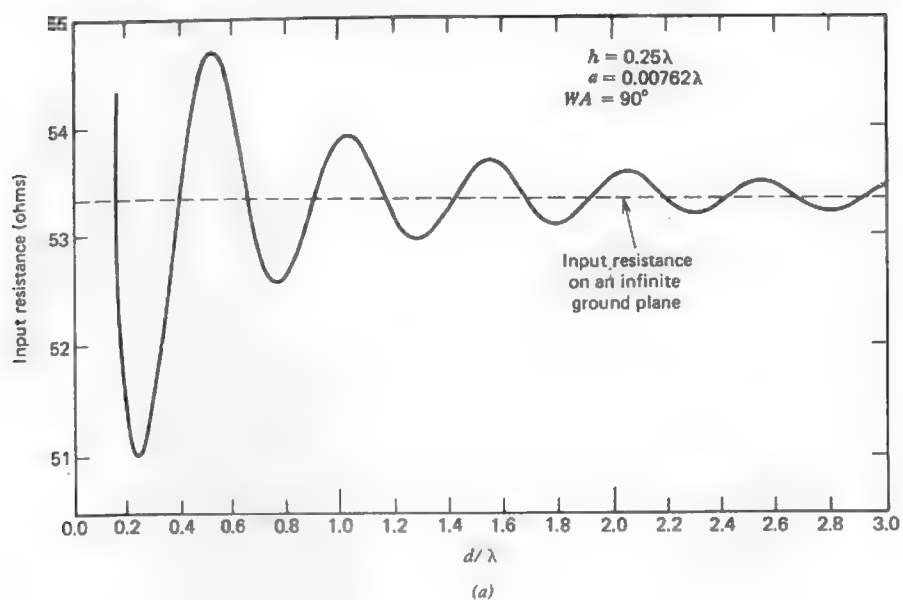


Figure 9-37 Input impedance of a monopole on a conducting wedge as a function of the distance d from the edge as shown in Fig. 9-36. (a) Input resistance. (b) Input reactance.

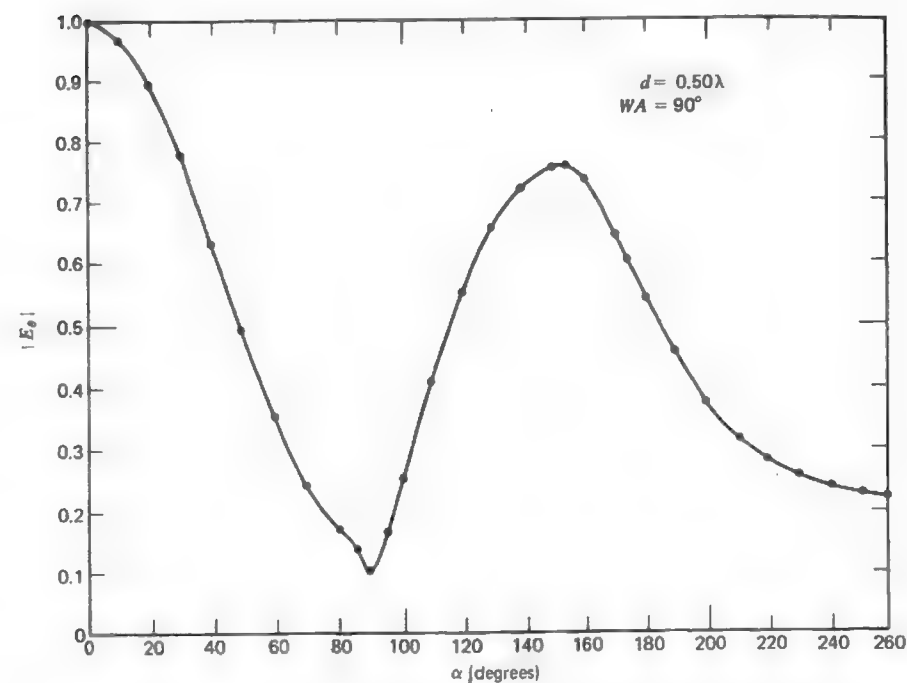


Figure 9-38 Normalized far-field pattern of a quarter-wave monopole on a conducting wedge.

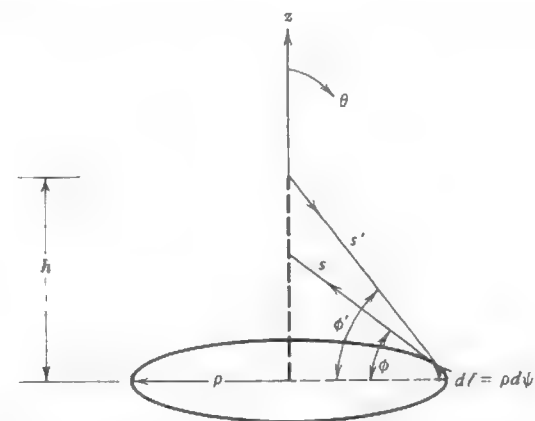


Figure 9-39 Segmented monopole encircled by a magnetic ring current for analysis of a monopole on a circular ground plane.

The electric field in a plane perpendicular to an element $d\ell$ is given by

$$dE_z = \frac{M d\ell}{4\pi} \left(\frac{j\omega}{cr} + \frac{1}{r^2} \right) e^{-j\beta r} \quad (9-136)$$

where $r = (\rho^2 + z^2)^{1/2}$. Letting $d\ell = \rho d\psi$ where ψ is the azimuth angle, taking only the z -component at the monopole, and integrating over the range $\psi = 0$ to $\psi = 2\pi$ yields

$$E_z = \frac{M\rho^2}{2r} \left(\frac{j\beta}{r} + \frac{1}{r^2} \right) e^{-j\beta r}. \quad (9-137)$$

The value for E_z is the term Z_{mn}^g that is added to the impedance element obtained for a monopole on an infinite ground plane. This process gives the modified impedance element needed Z'_{mn} to calculate the modified currents (and hence input impedance) of a monopole on the finite circular ground plane.

Figures 9-40a and 9-40b show a comparison between calculations made with the equivalent magnetic ring current and measurements for a monopole of length 0.224λ and radius 0.003λ on a circular ground plane for varying radius. It is apparent that the correct variation is accurately predicted for both the real and imaginary parts of the input impedance. For the input resistance the agreement between the measurements and the theory is excellent. For the input reactance the agreement is very good but there is a slight shift in the calculated curve when compared to the measurements. The amount of this shift is sufficiently small that it can be attributed to the usual problems associated with modeling the region in proximity to the driving point.

Next, consider the situation shown in Fig. 9-41 where a monopole of height h is a distance d_1 away from a vertical conducting step. To properly determine the Z_{mn}^g term in (9-129), it is necessary to determine all the various combinations of reflections that can occur for rays emanating from the monopole and reflecting back to it as well as the diffraction from the top edge of the step. Since the vertical wall is at a right angle to the lower horizontal surface, there will be no diffraction from the interior wedge and all the reflections can most conveniently be accounted for by imaging the monopole into the horizontal ground plane and then imaging the resulting dipole into the plane of the vertical wall.

Shown in Fig. 9-41 are two example situations that depict the utilization of the images. Considering the uppermost segment of the monopole to be the source segment, one set of rays shows the use of the image in the horizontal surface to calculate reflected-diffracted energy reaching the segments of the monopole. The other set of rays shows the use of the image in the vertical wall to calculate singly reflected energy. In the calculated results that follow, all combinations of singly reflected, doubly reflected, diffracted, diffracted-reflected, reflected-diffracted, and reflected-diffracted-reflected rays are taken into account.

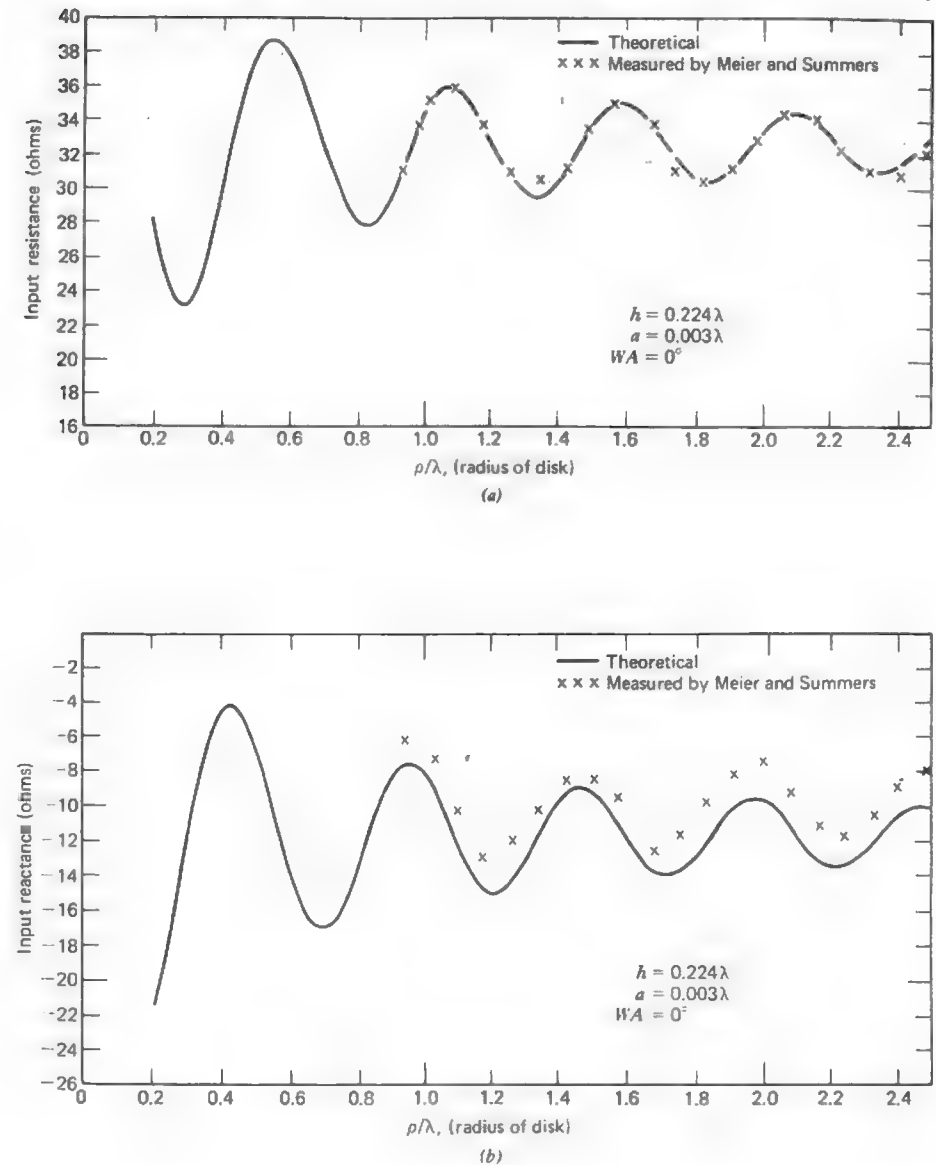


Figure 9-40 Theoretical and experimental input impedance of a monopole of radius 0.003λ at the center of a circular disk as shown in Fig. 9-39. (a) Input resistance. (b) Input reactance.

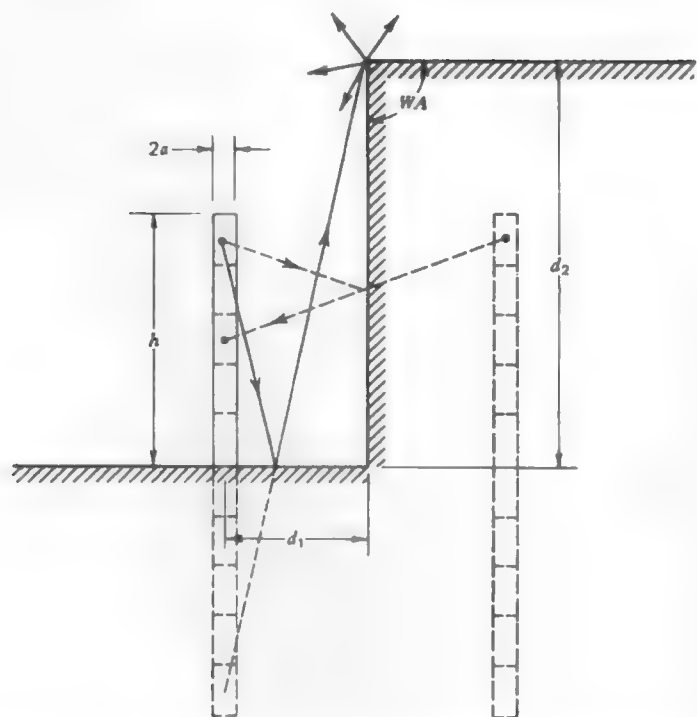


Figure 9-41 Monopole near a conducting step showing the partial use of images.

All rays that involve combinations of double (or higher order) diffractions are negligible.

Figure 9-42 shows the calculated input impedance for a quarter-wavelength monopole a quarter-wavelength away from a vertical wall whose height is $d_2 > 0.25\lambda$. As d_2 increases the impedance oscillates about the value for the case where $d_2 = \infty$. The results of Fig. 9-42a and 9-42b show that as the diffracting edge recedes from the vicinity of the monopole, its effect upon the input impedance rapidly diminishes. Although we have not shown results for the case where the step height is less than the height of the monopole the same method could be used to investigate such situations.

In combining moment methods with GTD we have proceeded from the philosophical viewpoint of extending the method of moments via GTD. In so doing we have shown that modifying the impedance matrix to account for diffraction effects (or geometrical optics effects) enables one to accurately treat a larger class of problems than could be treated by moment methods alone. An alternative interpretation of the hybrid method is also possible. That is, the procedure

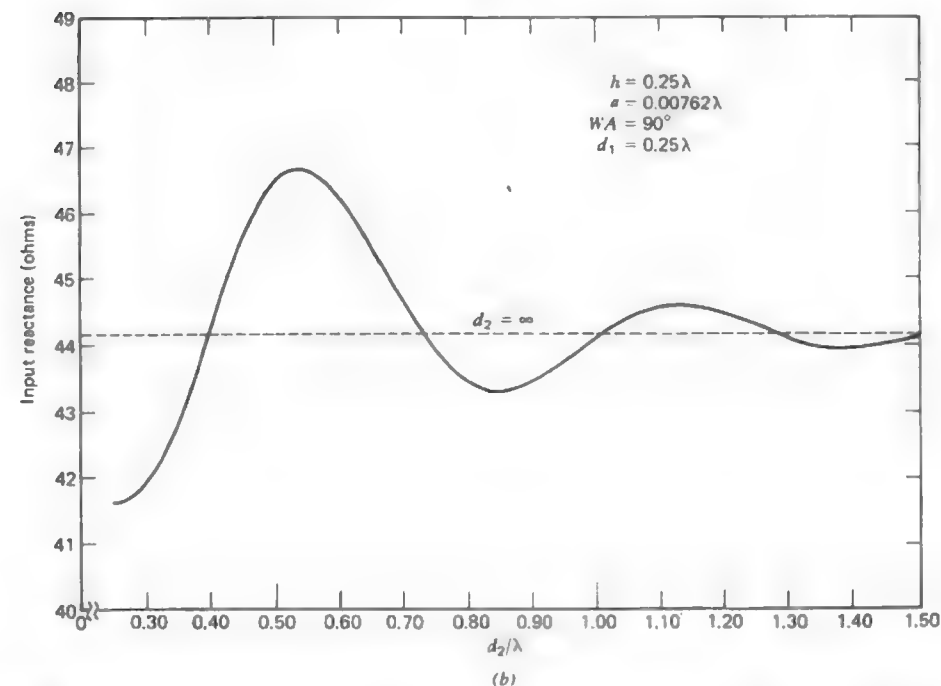
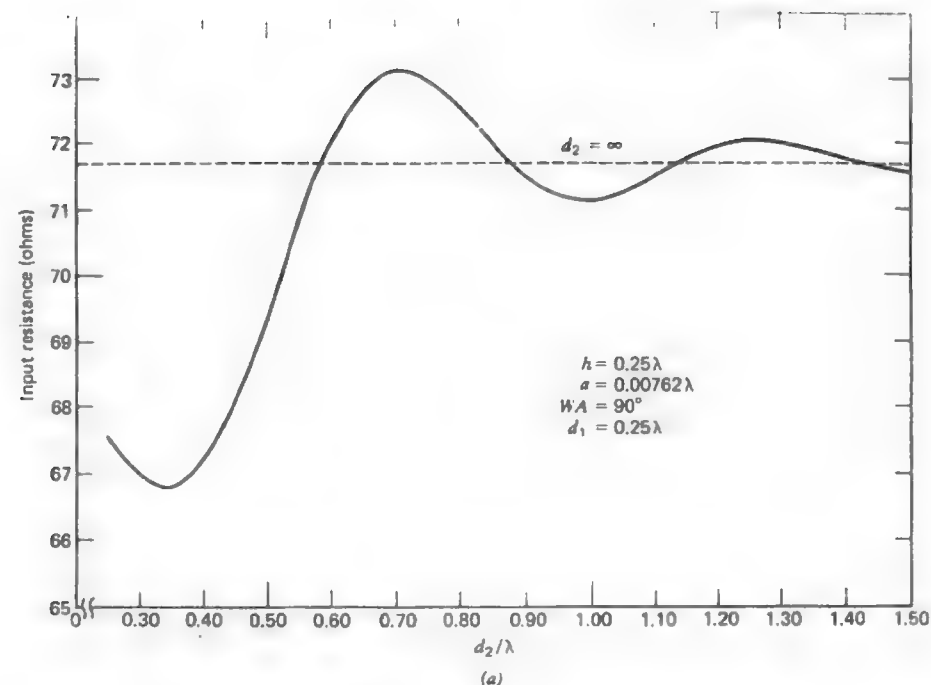


Figure 9-42 Input impedance of a quarter-wave monopole as a function of step height for the geometry of Fig. 9-41. (a) Input resistance. (b) Input reactance.

employed can be viewed as using GTD to obtain an approximation to the exact Green's function needed.

While the hybrid method possesses many of the advantages inherent in both moment method (MM) and GTD, it also has some of the limitations peculiar to each. For example, as in the usual MM problem, one can treat arbitrary configurations of wire antennas (or slot antennas) taking into account lumped loading, finite conductivity, and so forth, and obtain accurate impedance data and current distributions. Naturally, one still must take the usual precaution of using a sufficient number of basis functions to assure convergence. On the other hand, as in the usual GTD problem, one must take care that the antenna is not too close to a source of diffraction (e.g., $d > 0.2\lambda$).

9.14 SUMMARY

In this chapter on high-frequency methods we have presented a variety of techniques for predicting both the near- and far-zone fields from perfectly conducting bodies whose dimensions are large in terms of the wavelength. Particularly valuable for computational purposes is the uniform theory for wedge diffraction presented in Section 9.5 which can also be used to approximate curved surfaces as in Section 9.11.

The importance of the GTD method in antenna and scattering problems stems from the significant advantages to be gained from its use, namely: (a) it is simple to use, and yields accurate results; (b) it provides some physical insight into the radiation and scattering mechanisms involved; (c) it can be used to treat problems for which exact analytical solutions are not available. The GTD is also used in acoustic problems such as SONAR and in problems involving inhomogeneous media or anisotropic media [21].

The methods of this chapter tend to complement the low-frequency moment method techniques presented in Chapter 7. And, as we have seen in Section 9.13, the two techniques may be formally combined into a hybrid technique which extends the class of problems to which we can apply moment methods. We can do so not only because both the method of moments and the GTD are highly practical techniques, but also because they are inherently flexible in their application to analysis and design problems.

REFERENCES

1. M. Born and E. Wolf, *Principles of Optics*, Pergamon Press, New York, 1959.
2. G. T. Ruck, Editor, *Radar Cross Section Handbook*, Plenum Press, New York and London, 1970.

3. J. J. Bowman, T. B. A. Senior, and P. L. E. Uslenghi, Editors, *Electromagnetic and Acoustic Scattering by Simple Shapes*, North-Holland Publishing Co., Amsterdam, 1969.
4. J. W. Crispin and K. M. Siegel, Editors, *Methods of Radar Cross-Section Analysis*, Academic Press, New York and London, 1968.
5. J. B. Keller, "Geometrical theory of diffraction," *J. Opt. Soc. of Am.*, Vol. 52, pp. 116-130, 1962.
6. L. M. Graves, Editor, "A geometrical theory of diffraction," in *Calculus of Variations and its Applications*, McGraw Hill, 1958; pp. 27-52.
7. G. L. James, *Geometrical Theory of Diffraction*, Peter Peregrinus Ltd., England, 1976.
8. E. C. Jordan and K. G. Balmain, *Electromagnetic Waves and Radiating Systems*, Prentice Hall, Englewood Cliffs, N.J., 1968.
9. A. Sommerfeld, *Optics*, Academic Press, New York, 1954.
10. P. M. Russo, R. C. Rudduck, and L. Peters, Jr., "A method for computing E-plane patterns of horn antennas," *IEEE Trans. Ant. and Prop.*, Vol. AP-13, pp. 219-224, 1965.
11. W. Pauli, "On asymptotic series for functions in the theory of diffraction of light," *Phys. Rev.*, Vol. 54, pp. 924-931, 1938.
12. R. G. Kouyoumjian and P. H. Pathak, "A uniform geometrical theory of diffraction for an edge in a perfectly conducting surface," *Proc. IEEE*, Vol. 62, pp. 1448-1461, 1974.
13. R. G. Kouyoumjian, "Asymptotic high frequency methods," *Proc. IEEE*, Vol. 53, pp. 864-876, 1965.
14. R. G. Kouyoumjian, "The geometrical theory of diffraction and its application," in *Numerical and Asymptotic Techniques in Electromagnetics*, Springer-Verlag, New York, 1975.
15. A. R. Lopez, "The geometrical theory of diffraction applied to antenna and impedance calculations," *IEEE Trans. Ant. and Prop.*, Vol. 14, pp. 40-45, 1966.
16. C. E. Ryan, Jr. and L. Peters, Jr., "Evaluation of Edge Diffracted Fields Including Equivalent Currents for the Caustic Regions," *IEEE Trans. Ant. and Prop.*, Vol. AP-17, pp. 292-299, 1969. (See also correction in Vol. AP-18, pp. 275, 1970.)
17. R. F. Harrington, *Time-Harmonic Electromagnetic Fields*, McGraw-Hill, New York, 1961.
18. N. Wang, "Self-consistent GTD formulation for conducting cylinders with arbitrary convex cross section," *IEEE Trans. Ant. and Prop.*, Vol. AP-24, pp. 463-468, 1976.
19. P. H. Pathak and R. G. Kouyoumjian, "An analysis of the radiation from apertures in curved surfaces by the geometrical theory of diffraction," *Proc. IEEE*, Vol. 62, pp. 1438-1447, 1974.
20. G. A. Thiele and T. H. Newhouse, "A hybrid technique for combining moment methods with the geometrical theory of diffraction," *IEEE Trans. Ant. and Prop.*, Vol. AP-23, pp. 62-69, 1975.
21. L. B. Felsen and N. Marcuvitz, *Radiation and Scattering of Waves*, Prentice-Hall, Englewood Cliffs, N.J., 1973.

PROBLEMS

9.1-1 It can be shown [12] that the principal radii of curvature of the geometrical optics reflected wavefront are given by

$$\frac{1}{\rho_1} = \frac{1}{2} \left(\frac{1}{\rho_1^i} + \frac{1}{\rho_2^i} \right) + \frac{1}{f_1} \quad \text{and} \quad \frac{1}{\rho_2} = \frac{1}{2} \left(\frac{1}{\rho_1^i} + \frac{1}{\rho_2^i} \right) + \frac{1}{f_2}$$

where ρ_1^i and ρ_2^i are the principal radii of curvature of the incident wavefront and ρ_1 and ρ_2 are the principal radii of curvature of the reflected wavefront. General expressions for f_1 and f_2 are given in the literature [12]. However, for an incident spherical wave,

$$\frac{1}{f_{1,2}} = \frac{1}{\cos \theta_i} \left(\frac{\sin^2 \theta_2}{r_1^i} + \frac{\sin^2 \theta_1}{r_2^i} \right) \pm \sqrt{\frac{1}{\cos^2 \theta_i} \left(\frac{\sin^2 \theta_2}{r_1^i} + \frac{\sin^2 \theta_1}{r_2^i} \right)^2 - \frac{4}{r_1^i r_2^i}}$$

where θ_1 and θ_2 are the angles between the incident ray and the principal directions (i.e., tangent unit vectors) associated with the principal radii of curvature of the surface r_1^i and r_2^i , respectively.

(a) Show that for $\theta_1 = \theta_0$ and $\theta_2 = 90^\circ$, the first equation reduces to (9-20) and the second to

$$\frac{1}{\rho_2} = \frac{1}{f_0} + \frac{2 \cos \theta_0}{r_2^i}$$

(b) Without using (9-20) or the expression for ρ_2 immediately above, show that in the case of plane wave illumination

$$\sqrt{\rho_1 \rho_2} = \frac{1}{2} \sqrt{r_1^i r_2^i}$$

9.1-2 An infinite elliptical paraboloid is described by the equation

$$\frac{x^2}{2r_1^i} + \frac{y^2}{2r_2^i} = -z$$

where r_1 and r_2 are the principle radii of curvature at the specular point. Using geometrical optics, show that the radar cross section for axial incidence is

$$\sigma = \pi r_1^i r_2^i$$

Actually, this result applies to any surface expressible in terms of a second-degree polynomial where r_1^i and r_2^i are the principle radii of curvature at the reflection point [2, 3]. Is the above result valid for a cylindrical surface or flat plate? Why not?

9.1-3 A plane wave is incident on a smooth three-dimensional conducting convex body. The two principal radii of curvature of the body at the specular point are $r_1^i = 5\lambda$ and $r_2^i = 10\lambda$. Write expressions for the electric and magnetic backscattered fields if the incident plane wave fields are

$$\mathbf{E}^i = \hat{\mathbf{y}} e^{-j\beta x} \quad \text{and} \quad \mathbf{H}^i = \hat{\mathbf{z}} \frac{e^{-j\beta x}}{\eta}$$

9.2-1 Using physical optics show that the radar cross section of a flat rectangular plate at normal incidence is

$$\sigma = 4\pi \frac{A^2}{\lambda^2}$$

where A is the area of the plate.

9.2-2 Equation (9-31) can be converted to a different and often useful form by noting that $(\hat{\mathbf{z}} \cdot \hat{\mathbf{n}}) ds$ is the projection of the element of surface area ds onto the xy -plane. Thus,

$$(\hat{\mathbf{z}} \cdot \hat{\mathbf{n}}) ds = ds_z = \left(\frac{ds_z}{d\ell} \right) d\ell$$

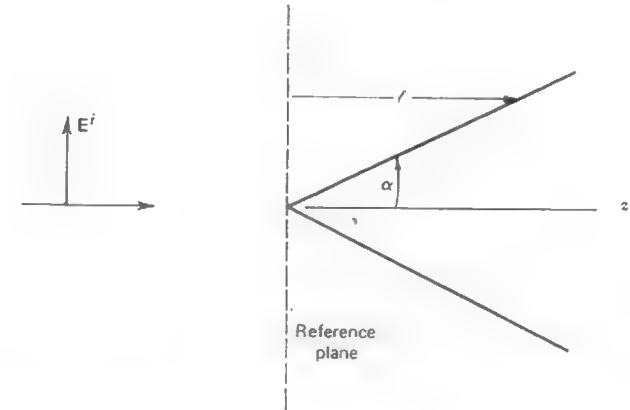
where ds_z is the projection of ds onto the xy -plane. Then (9-31) becomes

$$\sigma = \frac{4\pi}{\lambda^2} \left(\int_0^L e^{-j2\beta\ell} \frac{ds_z}{d\ell} d\ell \right)$$

where ℓ is the distance from the reference plane to the surface. Use the above expression for the radar cross section to derive the physical optics expression for the RCS of the sphere.

9.2-3 Show that the RCS of an infinite cone (as shown) is

$$\sigma = \frac{\lambda^2 \tan^4 \alpha}{16\pi}$$



9.2-4 Show that the RCS of a square flat plate with edges parallel to the x - and y -axes, and the direction of incidence in the xz -plane, is

$$\sigma = \frac{4\pi a^4}{\lambda^2} \left[\frac{\sin(\beta a \sin \theta)}{\beta a \sin \theta} \right]^2 \cos^2 \theta$$

where a is the length of one side. Compare the angular variation of this result with that of the uniformly illuminated line source in Chapter 4.

9.2-5 Show that the RCS of a circular flat plate, or disk, in the xy -plane is

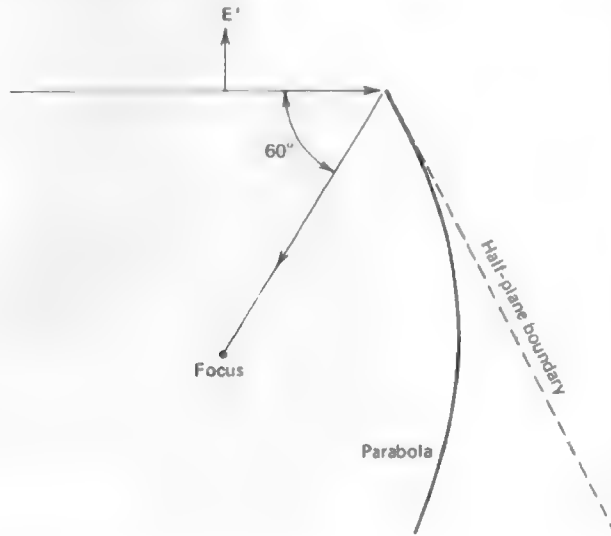
$$\sigma = \frac{\pi a^2}{\tan^2 \theta} \left[J_1 \left(\frac{4\pi a \sin \theta}{\lambda} \right) \right]^2$$

where a is the radius of the disk and $J_1(x)$ is the Bessel function of order one. Also show that at $\theta = 0^\circ$ the above expression reduces to

$$\sigma = \frac{4\pi}{\lambda^2} A^2$$

where A is the area of the disk [4].

9.3-1 A plane wave is incident upon a cylindrical parabolic reflector as shown. To obtain the diffracted field from the top edge (only) at any point in space, the edge may be analyzed as if a half-plane were tangent to the upper most portion of the parabolic surface. Divide the space around the top edge into three separate regions and write general expressions (with numerical values for ϕ') for the total electric field from the top edge in those three regions of space. In which of the three regions is the total geometrical optics field zero?



9.3-2 Evaluate the following Fresnel integrals:

(a) $\int_0^\infty e^{-j\tau^2} d\tau.$

(b) $\int_0^5 e^{-j\tau^2} d\tau.$

(c) $\int_5^\infty e^{-j\tau^2} d\tau.$

9.3-3 Find $v_B(\rho, \phi^\pm)$ using both (9-52) and (9-54) for a 90° interior angle wedge when:

(a) $\phi' = 45^\circ, \rho = 10\lambda, \phi = 220^\circ.$

(b) $\phi' = 45^\circ, \rho = 10\lambda, \phi = 230^\circ.$

Compare your results in (a) and (b) and explain any differences. What is v_ϕ in parts (a) and (b)?

9.3-4 Find $v_B(\rho, \phi^\pm)$ for a 90° interior wedge angle (both polarizations) when:

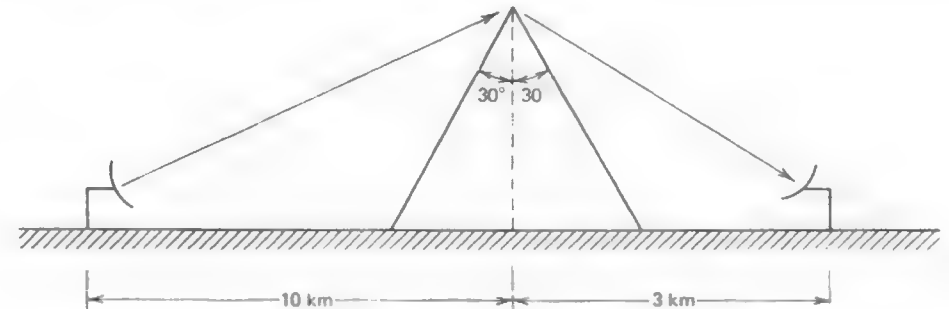
(a) $\phi' = 45^\circ, \rho = 10\lambda, \phi = 90^\circ.$

(b) $\phi' = 45^\circ, \rho = 10\lambda, \phi = 138^\circ.$

(c) $\phi' = 45^\circ, \rho = 10\lambda, \phi = 180^\circ.$

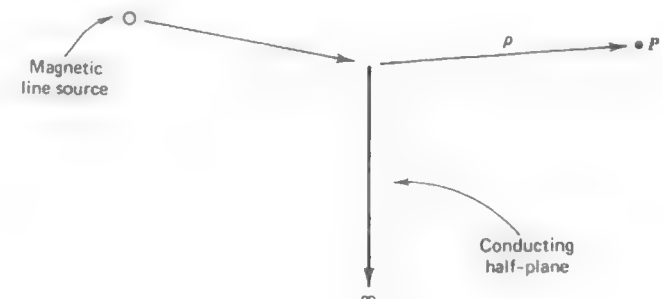
Comment on your results and justify the formulas you used to evaluate the diffracted field in each case.

9.3-5 A vertically polarized TV antenna transmits 10 kW at 600 MHz. A receiving antenna is shadowed by a 1-km high ridge normal to a line drawn between the two antennas as shown. How much power is available at the terminals of the receiving antenna if the gain of the receiving antenna in the direction of the ridge is 8 dB and that of the transmitting antenna is 10 dB toward the ridge? As a rough approximation, assume the ridge is perfectly conducting.



9.3-6 Substitute (9-44) and (9-45) into (9-43) and explain the physical significance of each of the four terms you obtain.

9.4-1 Consider a magnetic line source parallel to the edge of a half-plane as shown. In this situation the diffracted field appears to originate from a magnetic line source located



at the edge. Using the flux tube concept of Fig. 9-3, show that the diffracted field may be written as

$$E_{\perp}^d(\rho) = -D_{\perp} E_{\perp}^i(Q) \frac{e^{-j\beta\rho}}{\sqrt{\rho}}$$

where $E_{\perp}^i(Q)$ is the value of the incident field at the edge.

9.4-2 Repeat Prob. 9.4-1 when the magnetic line source is replaced by an electric line source and show that

$$E_{\parallel}^d(\rho) = -D_{\parallel} E_{\parallel}^i(Q) \frac{e^{-j\beta\rho}}{\sqrt{\rho}}$$

9.4-3 Consider the situation where a point source illuminates the edge of a half-plane at normal incidence. Unlike the previous two problems, in this case there will be spreading in both principal planes. Using the flux tube concept of Fig. 9-3, show that the diffracted field may be written as either

$$E_{\parallel}^d(s) = -D_{\parallel} E_{\parallel}^i(Q) \sqrt{\frac{s'}{s' + s}} \frac{e^{-j\beta s}}{\sqrt{s}}$$

or

$$E_{\perp}^d(s) = -D_{\perp} E_{\perp}^i(Q) \sqrt{\frac{s'}{s' + s}} \frac{e^{-j\beta s}}{\sqrt{s}}$$

9.4-4 Show that the diffraction coefficient matrix $[D]$ in (9-56) will generally have seven nonvanishing coefficients if an edge-fixed coordinate system is used rather than a ray-fixed system.

9.5-1 Derive (9-69) from (9-62) and show that (9-69) is the same as (9-52).

9.5-2 Consider the case where a half-plane is illuminated by a plane wave and the observation point is near the edge of the wedge.

(a) Show that the UTD reduces to the Sommerfeld/Pauli result in (9-54) and hence that the UTD is exact.

(b) Is the UTD an exact solution if the source is near the wedge edge and the observation point is at a very large distance? Why?

(c) If both the source and observation points are near the wedge edge, the UTD solution will not be exact. Why? (Although the solution may not be exact, the results may still be useful—see Section 9.13.)

9.5-3 Show that an alternative to (9-65) would be to define N^+ as the value of $[(\phi \pm \phi') + \pi]/2\pi n$ rounded to the nearest integer. Define a similar alternative to (9-66).

9.5-4 Consider a wedge illuminated by either an electric or magnetic line source parallel to the edge and at some distance from it ($\rho' \gg \lambda$).

(a) At the reflection boundary (or incident boundary) show that the diffraction coefficient must have a discontinuity of magnitude $\sqrt{\rho'\rho/(\rho + \rho')}$.

(b) Show that at the reflection boundary (or incident boundary) the UTD diffraction

coefficient is discontinuous by an amount $\pm\sqrt{L}$. What determines the sign of the discontinuity? The following approximation is useful:

$$F(X) \simeq \left[\sqrt{\pi X} - 2X e^{j(\pi/4)} - \frac{2}{3} X^2 e^{-j(\pi/4)} \right] e^{j(\pi/4 + \pi)}$$

which is valid when X is small.

(c) From the results of (a) and (b) show that the total field is continuous across the reflection (or incident) shadow boundary.

9.5-5 A plane wave is incident at an angle of $\gamma'_0 = 45^\circ$, $\phi' = 30^\circ$ on the edge of a 90° ($n = \frac{3}{2}$) conducting wedge.

(a) Use (9-62) and Fig. 9-19 to calculate E_{\perp}^d at a distance $s = 2\lambda$ when $\phi = 120^\circ, 132^\circ, 138^\circ, 180^\circ, 222^\circ, 228^\circ$, and 260° when $E_{\perp}^i = 1$ V/m.

(b) Repeat (a) for E_{\parallel}^d when $E_{\parallel}^i = 1$ V/m.

9.6-1 Use the E -plane model in Fig. 9-20b and the computer program in the Appendix G.9 to verify the curves in Fig. 8-14 which were obtained by aperture integration.

9.6-2 Show why the rays in Fig. 9-20c make a negligible contribution to the radiation pattern except when $\zeta \approx 90^\circ$.

9.6-3 Show that the doubly diffracted field from Q_1 in Fig. 9-20c can be written as

$$E_{1,2}^d(P) = \frac{1}{2} \frac{e^{-j\beta\rho_E}}{\sqrt{\rho_E}} D_{1,2}(L, \phi, \phi') D_{1,1}(L, \phi, \phi') \frac{e^{-j\beta 2a}}{\sqrt{2a}} \frac{e^{-j\beta r}}{\sqrt{r}} e^{j\beta a \sin \zeta}$$

9.7-1 Use the computer program in Appendix G.9 to calculate the total diffracted field for $0 \leq \zeta \leq 2\pi$ for the antenna of Fig. 9-22. Compare your results with Fig. 9-23. Why is there a difference?

9.7-2 Draw a sketch of the "creeping wave" rays (see Section 9.12) on the back side of the parabolic reflector of Fig. 9-22. Now draw rays which originate at Q_1 or Q_2 and reflect several times along the inside surface parabolic reflector. These rays are called whispering gallery rays.

9.7-3 Show that the doubly diffracted ray from Q_1 in Fig. 9-22 can be written as

$$E_{1,2}^d(P) = \frac{e^{-j\beta\rho_o}}{\sqrt{\rho_o}} f(\theta_E) D_{1,2}(L, \phi, \phi') D_{1,1}(L, \phi, \phi') \frac{e^{-j\beta 2a}}{\sqrt{2a}} \frac{e^{-j\beta r}}{\sqrt{r}} e^{j\beta a \sin \zeta}$$

9.7-4 Derive (9-81).

9.7-5 If the line source in Fig. 9-22 is a magnetic line source, calculate the far-field pattern. Your result will be similar to that in Fig. 9-23, except that the discontinuity at $\zeta = 90^\circ$ will be greater and the back lobes will be about 8 dB higher. Why?

9.7-6 Use the UTD to calculate the H -plane pattern of a 90° corner reflector antenna with a dipole feed. The dipole feed is 0.5λ from the apex of the reflector, the reflector sides are 1.0λ long and the aperture of the corner reflector is 1.414λ across.

9.8-1 The diffracted field that is neglected in (9-96) may be written generally as [14]

$$E_{SD}^d(P) = \frac{1}{2j\beta} \frac{\partial E^i(Q)}{\partial n} \frac{\partial}{\partial \phi} D_{||} \Big|_{\phi'=0} \sqrt{\frac{\rho}{s(\rho+s)}} e^{-j\beta s}.$$

Compare the value of this slope diffracted field with the direct field in (9-96) when $\theta = 90^\circ$.

9.8-2 (a) Using (9-46) and (9-47) in (9-43) show how a factor of two arises in $E(\rho, \phi)$ for the perpendicular polarization in the infinite ground plane case ($r_B = 0$) when the plane wave has grazing incidence to the ground plane ($\phi' = 0$).

(b) Then verify in general that at grazing incidence the diffracted field must be multiplied by $\frac{1}{2}$, as in (9-90) and (9-92), to obtain the correct value of the diffracted field. To do this use either the asymptotic form in (9-52) or (9-69) to show that $D_{||} \rightarrow 0$ and that a factor of 2 naturally arises in $D_{||}$.

9.9-1 A short monopole (stub antenna) is mounted at the center of a circular ground plane 6λ in diameter as shown in Fig. 9-29b.

(a) Using the two point approximation show that the relative diffracted field in the region $90^\circ < \theta \leq 180^\circ$ can be expressed by

$$E^d = -\frac{e^{-j\beta\rho(1+\pi/4)}}{\sqrt{2\rho\beta r}} \left[\frac{1}{\cos(\phi/2)} - \frac{e^{-j6\beta \cos \phi}}{\cos(\phi/2)} \right]$$

where $\phi = 3\pi/2 - \theta$.

(b) Why must the diffracted field be zero when $\theta = 180^\circ$ for this problem? Use a sketch and physical reasoning to explain why.

(c) Calculate and plot a graph of the diffracted field for $90^\circ < \theta \leq 180^\circ$. Compare your results with Fig. 9-30.

9.10-1 Derive (9-107) and (9-108).

9.10-2 Derive (9-111) and (9-112).

9.10-3 A short monopole (stub antenna) is mounted at the center of a circular ground plane 6λ in diameter as shown in Fig. 9-29b.

(a) Using the equivalent concept, show that the relative diffracted field in the region $90^\circ \leq \theta \leq 180^\circ$ can be expressed by

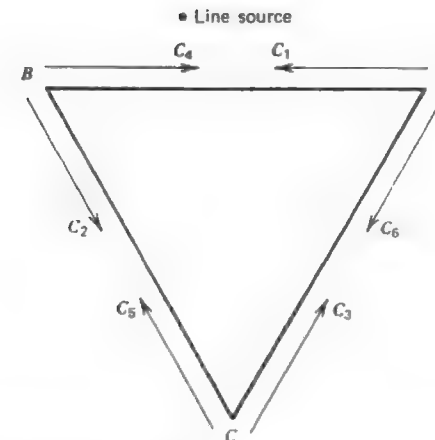
$$E^d = -\frac{e^{-j\beta\rho(1+\pi/4)}}{\sqrt{2\pi\beta\rho}} \frac{1}{\cos(\phi/2)} 2\pi j J_1(6\pi \sin \theta)$$

where J_1 is the first order Bessel function. Note that

$$\int_0^{2\pi} \cos(\xi - \xi') e^{jx \cos(\xi - \xi')} d\xi' = 2\pi J_1(x).$$

(b) Calculate the diffracted field and compare with that calculated in Prob. 9.9-1.

9.11-1 A triangular cylinder is illuminated by a line source as shown. Apply the self-consistent method to this problem by setting up (9-120) in a form similar to (9-119). Note that some of the matrix elements will be zero. Check your solution with that in [18].



9.13-1 Consider a monopole at the center of a square ground plane whose sides are $\lambda/2$ long. The monopole is to be represented using pulse basis functions and delta weighting functions. The four sides of the ground plane are to be accounted for using wedge diffraction. Diffraction by the four corners is to be ignored. Derive the necessary equations that would enable you to calculate Z_{mn}^g in (9-133).

9.13-2 Derive (9-135).

9.13-3 For the problem in Fig. 9-41, show all possible ray paths that do not involve double (or higher order) diffractions.

9.13-4 A dipole of length l is located a distance d from the surface of an infinitely long circular cylinder of radius a . The dipole is parallel to the axis of the cylinder. Show how you would account for the presence of the cylinder if only the dipole is represented by the method of moments.

10

ANTENNA SYNTHESIS

Thus far in this book attention has been focused on antenna analysis and design. The analysis problem is one of determining the radiation pattern and impedance of a given antenna structure. Antenna design is the determination of the hardware characteristics (lengths, angles, etc.) for a specific antenna to produce a desired pattern and/or impedance. Antenna synthesis is similar to antenna design and, in fact, the terms are frequently used interchangeably. However, antenna synthesis, in its broadest sense, is one of first specifying the desired radiation pattern and then using a systematic method or combination of methods to arrive at an antenna configuration which produces a pattern that acceptably approximates the desired pattern, as well as satisfying other system constraints. Hence, antenna synthesis, in general, does not depend on an *a priori* selection of the antenna type. Unfortunately, there is no single synthesis method that yields the "optimum" antenna for the given system specifications. There are, however, several synthesis methods for different classes of antenna types. In this chapter we shall discuss the more useful synthesis methods in current use. The discussion serves as an introduction to the topic of synthesis and should provide a foundation for studying more advanced treatments [1].

10.1 THE SYNTHESIS PROBLEM

We will pose the antenna synthesis problem as one of determining the excitation of a given antenna type that leads to a radiation pattern which suitably approximates a desired pattern. The desired pattern can vary widely depending on the

application. Several radiation pattern variables are listed in Table 10-1. To illustrate, consider a communication satellite in synchronous orbit which is required to generate separate antenna beams for the western United States and for Alaska. Two main beams are required, both shaped for nearly uniform illumination of each region. Also low side lobes may be specified to minimize interference over other regions of the earth, but higher side lobes could be permitted for directions not toward the earth. This type of pattern has multiple shaped main beams and a shaped side lobe envelope.

The antenna itself can take many forms as indicated by the antenna variables listed in Table 10-1. The antenna type is composed of the continuity, shape, and size. There are many other antenna specifications, or boundary conditions, that are often included in the synthesis problem. A few follow: frequency of operation, bandwidth, impedance, power handling capacity, polarization properties, efficiency, weight, and reliability. These specifications together with the desired pattern form the complete synthesis problem. A general solution procedure would provide the antenna type and excitation that give the best approximation to the pattern while satisfying all other specifications. Since no single method exists for such a solution, the synthesis methods are categorized by antenna type. Before discussing these methods a few preparatory remarks are required.

If the radiation electric field components E_θ and E_ϕ are specified in the synthesis problem, a secondary synthesis problem can be formulated in terms of antenna aperture field transform components. For example, the aperture magnetic equivalent surface current solution of (8-26) can be solved giving

$$\begin{bmatrix} P_x \\ P_y \end{bmatrix} = \left(j\beta \frac{e^{-j\beta r}}{4\pi r} \right)^{-1} \begin{bmatrix} \cos \phi & \sin \phi \\ -\cos \theta \sin \phi & \cos \theta \cos \phi \end{bmatrix}^{-1} \begin{bmatrix} E_\theta \\ E_\phi \end{bmatrix}. \quad (10-1)$$

This can be used to obtain P_x and P_y from specified functions E_θ and E_ϕ . The problem is then of synthesizing desired functions P_x and P_y , which are Fourier

Table 10-1 Antenna Synthesis Variables

Antenna variables	Radiation pattern variables
Continuity	Main beam region
Continuous	Narrow main beam
Discrete—array	Single beam
Shape	Multiple beams
Linear	Shaped beam
Planar	Side lobe region
Conformal	Nominal side lobes
Three-dimensional	Low side lobes
Size	Shaped side lobes

transforms of the aperture electric field components; see (8-18). The process is similar for each of P_x and P_y . Therefore we shall let $f(\theta, \phi)$ be the normalized pattern factor for either and frame our discussions using $f(\theta, \phi)$. As another example, consider a line source along the z -axis. If $F_d(\theta)$ is the normalized desired radiation pattern (from E_θ), then

$$f_d(\theta) = \frac{F_d(\theta)}{\sin \theta} \quad (10-2)$$

is the desired pattern factor.

Throughout this chapter we will discuss the synthesis of f , which can represent several antenna types; for example, either P_x or P_y of an aperture antenna. Also f can be used for one principal plane pattern of a separable aperture distribution function (see Section 8.2.2). The total pattern is then the product of the principal plane patterns which can be synthesized separately.

Our discussion of antenna synthesis will be limited to linear antennas, that is, either line sources or linear arrays. Many of the results, though, can be applied to two-dimensional antennas. Synthesis methods can be separated by antenna type or by pattern type. Only a few methods exist which can be applied to a variety of antenna and pattern types [2]. Usually synthesis methods for shaped beam patterns are completely different from those for low side lobe, narrow beam patterns, so we will separate the methods by pattern type. Line source and linear array synthesis principles with applications to shaped beam patterns are detailed in Sections 10.2 and 10.3. Low side lobe, narrow main beam methods are presented in Section 10.4.

10.2 LINE SOURCE METHODS

The radiation electric field from a line source of current (actual or equivalent) along the z -axis and of length L is given by (4-1). For synthesis problems we are only interested in the relative pattern variations. Furthermore, the element factor $g(\theta) = \sin \theta$ is accounted for separately; for narrow-beam, broadside line sources it is, in fact, negligible. The normalized pattern factor of a line source follows from (4-1) as¹

$$f(\theta) = \frac{1}{L} \int_{-L/2}^{L/2} i(z) e^{j\beta z \cos \theta} dz \quad (10-3)$$

where $i(z)$ is the normalized form of the current function $I(z)$, and it is usually normalized such that (10-3) produces a pattern $f(\theta)$ which is unity at its maxi-

¹ Frequently the z -axis is selected to be normal to the line source, in which case $\cos \theta$ in (10-3) becomes $\sin \theta$.

mum. The linear phase shift which scans the main beam is contained in $i(z)$, for example, see (4-3). For convenience we define²

$$w = \cos \theta \quad \text{and} \quad s = \frac{z}{\lambda} \quad (10-4)$$

Then (10-3) becomes

$$f(w) = \int_{-L/2\lambda}^{L/2\lambda} i(s) e^{j2\pi w s} ds \quad (10-5)$$

This equation forms the relationship between the relative current distribution $i(s)$ and the normalized pattern factor $f(w)$.

10.2.1 The Fourier Transform Method

Since the current distribution $i(z)$ extends only over the length L , [that is, $i(s)$ is zero for $|s| > L/2\lambda$], the limits of the integral in (10-5) can be extended to infinity giving

$$f(w) = \int_{-\infty}^{\infty} i(s) e^{j2\pi w s} ds \quad (10-6)$$

This is recognized as a Fourier transform. The corresponding inverse Fourier transform is

$$i(s) = \int_{-\infty}^{\infty} f(w) e^{-j2\pi w s} dw \quad (10-7)$$

(See Prob. 10.2-1). This immediately suggests a synthesis procedure. If $f_d(w)$ is the *desired pattern*, the corresponding current distribution $i_d(s)$ is found rather easily from (10-7) as

$$i_d(s) = \int_{-\infty}^{\infty} f_d(w) e^{-j2\pi w s} dw \quad (10-8)$$

This is very direct, but unfortunately the resulting $i_d(s)$ will *not*, in general, be confined to $|s| \leq L/2\lambda$ as required; it will usually be, in fact, of infinite extent. An approximate solution can be obtained by truncating $i_d(s)$ giving the synthesized current distribution as follows

$$i(s) = \begin{cases} i_d(s) & |s| \leq \frac{L}{2\lambda} \\ 0 & |s| > \frac{L}{2\lambda} \end{cases} \quad (10-9)$$

² Note that w is related to u of Chapter 4 by $u = (\beta L/2)w$.

The current $i(s)$ produces an approximate pattern $f(w)$ from (10-6). The current $i_d(s)$ extending over all s produces the pattern $f_d(w)$ exactly.

The Fourier transform synthesized pattern yields the least mean squared error (MSE), or least mean squared deviation from the desired pattern, over the entire w -axis. The mean squared error

$$\text{MSE} = \int_{-\infty}^{\infty} |f(w) - f_d(w)|^2 dw, \quad (10-10)$$

with $f(w)$ corresponding to $i(s)$ in (10-9), is the smallest of all patterns arising from line sources of length L . The Fourier transform synthesized pattern, however, does not provide minimum mean squared deviation in the visible region.

Example 10-1. Fourier Transform Synthesis of a Sector Pattern

A *sector pattern* is a shaped beam pattern which, ideally, has uniform radiation over the main beam (a sector of space) and zero side lobes. Such patterns are popular for search applications where vehicles are located by establishing communications or by a radar echo in the sector of space occupied by the antenna pattern main beam. As a specific example, let the desired pattern be

$$f_d(\theta) = \begin{cases} 1 & \cos^{-1}c \leq \theta \leq \cos^{-1}(-c) \\ 0 & \text{elsewhere} \end{cases} \quad (10-11a)$$

or, equivalently,

$$f_d(w) = \begin{cases} 1 & |w| \leq c \\ 0 & \text{elsewhere} \end{cases} \quad (10-11b)$$

$f_d(w)$ is shown in Fig. 10-1a by the dashed curve. Using (10-11b) in (10-8) and (10-9) gives

$$i(s) = 2c \frac{\sin(2\pi cs)}{2\pi cs} \quad |s| \leq \frac{L}{2\lambda} \quad (10-12)$$

If this $\sin(x)/x$ function were not truncated, its Fourier transform (its pattern) would be exactly the sector pattern of (10-11). The actual pattern from (10-6) using (10-12) is

$$f(w) = \frac{1}{\pi} \left| \text{Si} \left[\frac{L}{\lambda} \pi(w+c) \right] - \text{Si} \left[\frac{L}{\lambda} \pi(w-c) \right] \right| \quad (10-13)$$

where Si is the sine integral of (F-13). This synthesized sector pattern is plotted in Fig. 10-1a for $c = 0.5$ and $L = 10\lambda$.³ The pattern is plotted in linear form, rather than in decibels, to emphasize the details of the main beam. Note the oscillations about the desired pattern on the main beam, called *ripple*, and the nonzero side lobes. This appearance of main beam ripple and finite side lobes is typical of any synthesized pattern. The current distribution of (10-12) is plotted in Fig. 10-1b.

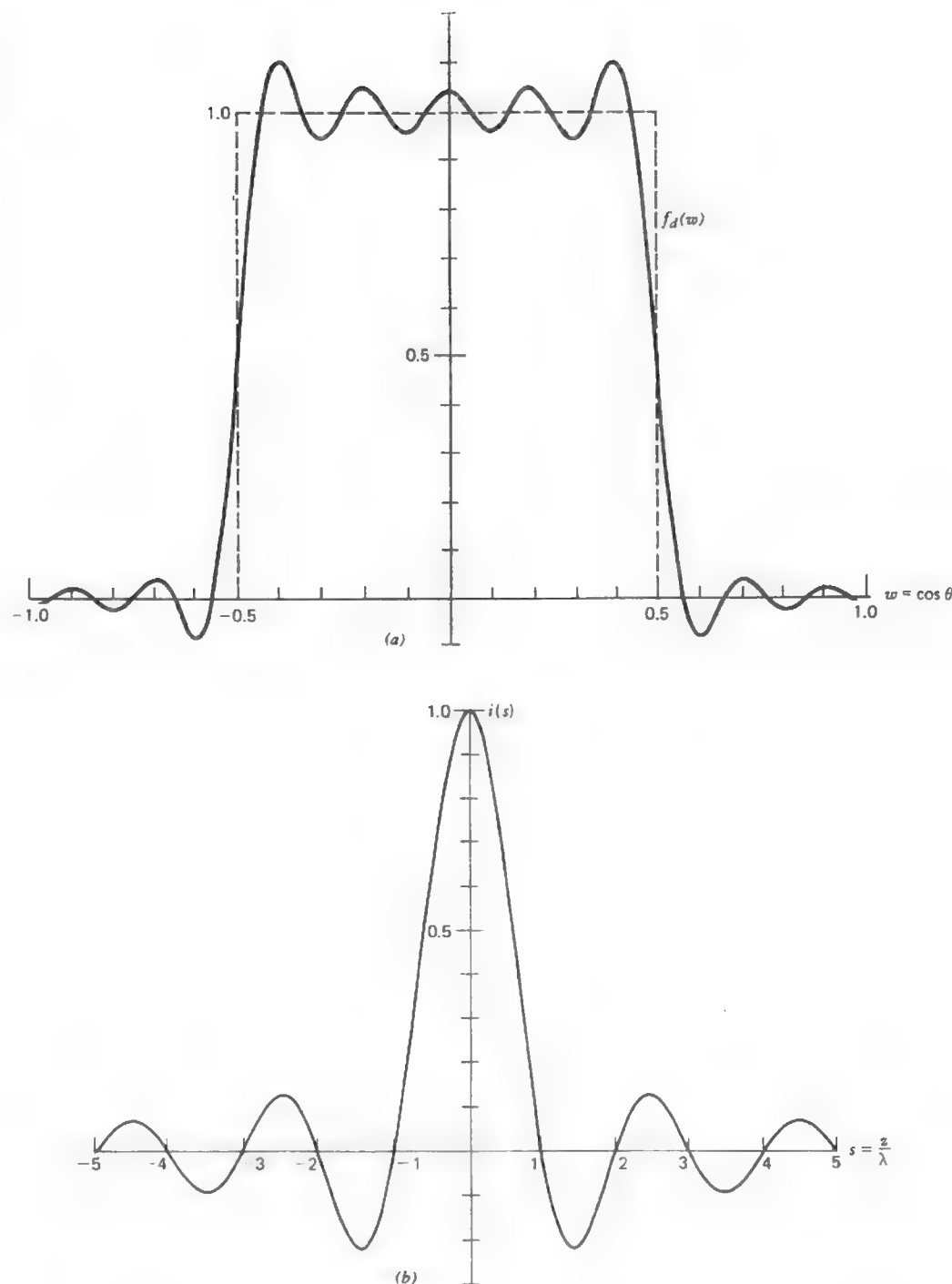


Figure 10-1 Fourier transform synthesis of a sector pattern using a 10λ line source (Example 10-1). (a) The synthesized pattern (solid curve) and the desired sector pattern (dashed curve). (b) The current distribution.

10.2.2 The Woodward-Lawson Sampling Method

A particularly convenient way to synthesize a radiation pattern is to specify values of the pattern at various points, that is, to sample the pattern. The Woodward-Lawson method is the most popular of the sampling methods [3, 4]. It is based on decomposition of the source current distribution into a sum of uniform amplitude, linear phase sources:

$$i_n(s) = \frac{a_n}{L/\lambda} e^{-j2\pi w_n s} \quad |s| \leq \frac{L}{2\lambda} \quad (10-14)$$

The pattern corresponding to this component current, from (10-6), is

$$f_n(w) = a_n \text{Sa} \left[\pi \frac{L}{\lambda} (w - w_n) \right] \quad (10-15)$$

where the sampling function $\text{Sa}(x)$ is defined as $\text{Sa}(x) = \sin(x)/x$. This component pattern has a maximum of a_n centered at $w = w_n$. The current component phase coefficient w_n in (10-14) controls the location of the component pattern maximum, and the current component amplitude coefficient a_n controls the component pattern amplitude.

In the Woodward-Lawson method the total current excitation is composed of a sum of $2M + 1$ component currents as

$$i(s) = \sum_{n=-M}^M i_n(s) = \frac{1}{L/\lambda} \sum_{n=-M}^M a_n e^{-j2\pi w_n s} \quad (10-16a)$$

where

$$w_n = \frac{n}{L/\lambda} \quad |n| \leq M, \quad |w_n| \leq 1.0. \quad (10-16b)$$

The pattern corresponding to this current is

$$\begin{aligned} f(w) &= \sum_{n=-M}^M f_n(w) = \sum_{n=-M}^M a_n \text{Sa} \left[\pi \frac{L}{\lambda} (w - w_n) \right] \\ &= \sum_{n=-M}^M a_n \text{Sa} \left[\pi \left(\frac{L}{\lambda} w - n \right) \right]. \end{aligned} \quad (10-17)$$

At pattern points $w = w_n = n\lambda/L$, we have $f(w = w_n) = a_n$. Thus, the pattern can be made to have specified values a_n , called pattern *sample values*, at the pattern locations w_n of (10-16b), called *sample points*. The pattern sample values are chosen to equal the values of the desired pattern at the sample points.

$$a_n = f_d(w = w_n). \quad (10-18)$$

The Woodward-Lawson synthesis procedure is very easy to visualize. The current distribution required to produce a pattern with values a_n at locations w_n is that of (10-16).

The Woodward-Lawson sampling method can be made more flexible by noting that as long as adjacent samples are separated by the sampling interval $\Delta w = \lambda/L$, the pattern values at the sample points are still uncorrelated, that is, (10-18) holds. The total number of samples is chosen such that the visible region is just covered; samples located outside the visible region could lead to superdirective results. Since the visible region is of extent 2 and $\Delta w = \lambda/L$, the number of samples $2M + 1$ is on the order of $2/(\lambda/L)$, or M is on the order of L/λ .

Example 10-2. Woodward-Lawson Line Source Synthesis of a Sector Pattern

The sector pattern of (10-11) is now to be synthesized with a 10 wavelength long line source using the Woodward-Lawson method. Sampling this pattern according to $a_n = f_d(w = w_n)$ with sample locations $w_n = n\lambda/L = 0.1n$ gives the values in Table 10-2. The sample value at the discontinuity ($w = 0.5$) could be selected as 1, 0.5, or 0 according to the specific application. Using $a_{\pm 5} = 1$ gives the widest main beam, whereas $a_{\pm 5} = 0$ gives the narrowest. In this case we choose $a_{\pm 5} = 0.5$ as a compromise. The synthesized pattern, from (10-18) with the values from Table 10-2, is plotted in Figure 10-2a. The sample points are indicated by dots. The SPAP computer program was used to generate the pattern; SPAP will produce any pattern that can be expressed in the Woodward-Lawson form of (10-17); see Appendix G.6.

Table 10-2 Sample Locations and Sample Values for a 10λ Woodward-Lawson Sector Pattern (Example 10-2)

n	Sample location, w_n	Pattern sample value, a_n
0	0	1
± 1	± 0.1	1
± 2	± 0.2	1
± 3	± 0.3	1
± 4	± 0.4	1
± 5	± 0.5	0.5
± 6	± 0.6	0
± 7	± 0.7	0
± 8	± 0.8	0
± 9	± 0.9	0
± 10	± 1.0	0

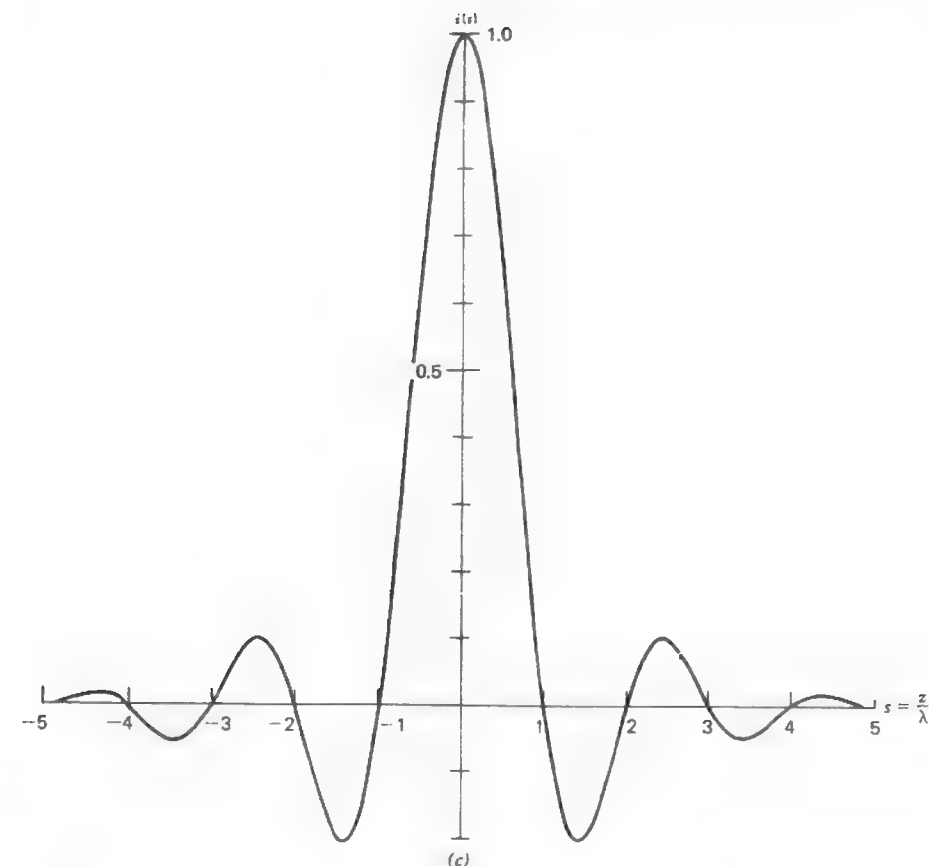
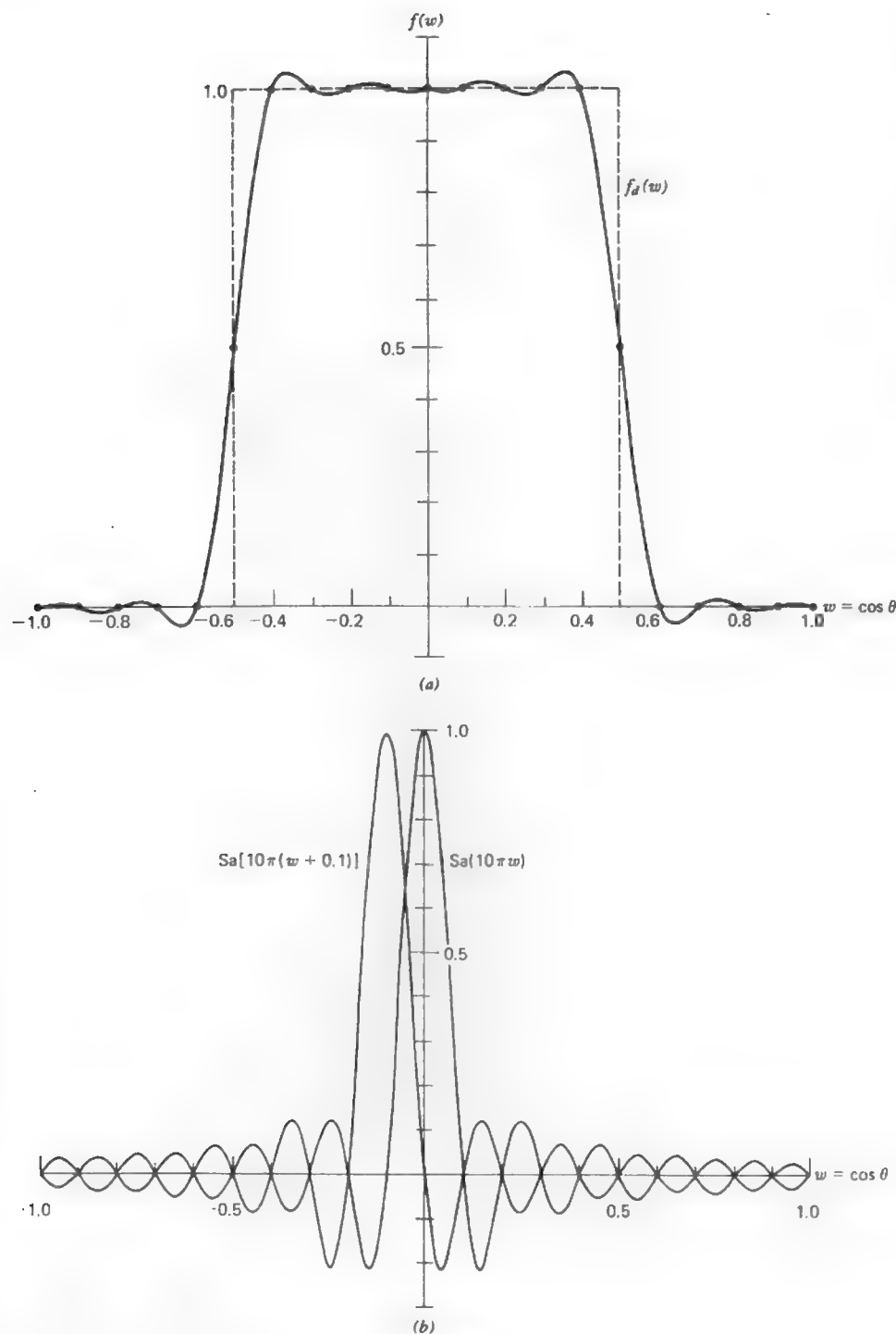


Figure 10-2 Woodward-Lawson synthesis of a sector pattern using a 10λ line source (Example 10-2). (a) The synthesized pattern (solid curve) and the desired pattern (dashed curve). The dots indicate the sample values and locations. (b) Two component patterns at sample locations $w_{-1} = -0.1$ and $w_0 = 0$. (c) The current distribution corresponding to the synthesized pattern.

To illustrate the sampling nature of the Woodward-Lawson method, two sampling functions from the sum in (10-17) are shown in Fig. 10-2b for sample locations $w_{-1} = -0.1$ and $w_0 = 0$. Note that when one sampling function is maximum the other is zero, thus making the samples independent. Further, each sampling function is zero at all sample locations $w_n = n\lambda/L$, except at its maximum. When all samples are included, the value of the total synthesized pattern at locations w_n is completely determined by the Sa function centered at that location. This is the beauty of the Woodward-Lawson sampling method.

Note that the Woodward-Lawson pattern of Fig. 10-2a is a better approximation to the

desired pattern (in the visible region) than is that of the Fourier transform method in Fig. 10-1a, both generated from a 10-wavelength line source. Detailed comparisons of all the sector pattern examples presented are found in Section 10.3.3.

The current distribution corresponding to the sector pattern of this example is plotted in Fig. 10-2c. It was obtained from (10-16) using the SPAP program. Note the similarity to the current distribution in Fig. 10-1b for the Fourier transform method. This occurs because the Fourier transform of any pattern is the antenna current distribution. Since the patterns in Examples 10-1 and 10-2 are both close to a sector pattern, their Fourier transforms (currents) must be close to that of an ideal sector pattern, which is $\sin(\pi s)/\pi s$ in these examples.

10.3 LINEAR ARRAY METHODS

In this section the Fourier series and Woodward-Lawson methods for equally spaced linear arrays are discussed. These two important pattern synthesis methods are the array counterparts of the Fourier transform and Woodward-Lawson methods of the previous section. Before presenting these methods we shall model the array configuration for use with any synthesis method.

Consider an equally spaced linear array along the z -axis with interelement spacings d . For simplicity the physical center of the array is located at the origin. The total number of elements in the array P can be either even (then let $P = 2N$) or odd (then let $P = 2N + 1$). For an odd element number, the element locations are given by

$$z_m = md \quad |m| \leq N \quad (10-19)$$

and $P = 2N + 1$. The corresponding array factor is

$$f(w) = \sum_{m=-N}^N i_m e^{j2\pi m(d/\lambda)w} \quad (10-20)$$

where i_m are the element currents and again $w = \cos \theta$. This expression is similar to (3-54).

For an even number of elements the element positions are

$$\begin{aligned} z_m &= \frac{2m-1}{2} d & 1 \leq m \leq N \\ z_{-m} &= -\frac{2m-1}{2} d & -N \leq -m \leq -1 \end{aligned} \quad (10-21)$$

and $P = 2N$. The corresponding array factor is

$$f(w) = \sum_{m=1}^N (i_{-m} e^{-j\pi(2m-1)(d/\lambda)w} + i_m e^{j\pi(2m-1)(d/\lambda)w}) \quad (10-22)$$

for P even.

For comparison to a line source the total array length is defined as

$$L = Pd. \quad (10-23)$$

This definition applies to both the even and odd element cases, and it includes a distance $d/2$ beyond each end element.

10.3.1 The Fourier Series Method

The array factor resulting from an array of identical discrete radiators (elements) is, of course, the sum over the currents for each element weighted by the spatial phase delay from each element to the far-field point. This array factor summation can be made to be of a form which is very similar to a Fourier series, just as the radiation integral for a continuous source resembles a Fourier transform (see Section 10.2.1). To see how this correspondence comes about, we first observe that a function $f_d(w)$, the desired pattern function, can be expanded into a Fourier series in the interval $-\lambda/2d < w < \lambda/2d$ as

$$f_d(w) = \sum_{m=-\infty}^{\infty} b_m e^{j2\pi m(d/\lambda)w} \quad (10-24)$$

where

$$b_m = \frac{d}{\lambda} \int_{-\lambda/2d}^{\lambda/2d} f_d(w) e^{-j2\pi m(d/\lambda)w} dw. \quad (10-25)$$

If we identify d as the spacing between elements of an equally spaced linear array and $w = \cos \theta$ where θ is the angle from the line of the array, the sum in (10-24) is recognized as the array factor of an array with an infinite number of elements with currents b_m .

An infinite array is, of course, not practical, but truncating the series (10-24) to a finite number of terms produces the following approximation to $f_d(w)$,

$$f(w) = \sum_{m=-N}^N b_m e^{j2\pi m(d/\lambda)w} \quad (10-26)$$

If we let the currents of each element in the array equal the Fourier series coefficients, that is,

$$i_m = b_m \quad |m| \leq N \quad (10-27)$$

then (10-26) is identical to (10-20), the array factor for an array with an odd number of elements.

The Fourier series synthesis procedure is, then, to use element excitations i_m equal to the Fourier series coefficients b_m calculated from the desired pattern f_d , as in (10-25). The array factor f arising from these element currents is an approximation to the desired pattern. This Fourier series synthesized pattern provides the least mean squared error [see (10-10)] over the region $-2d/\lambda < w < 2d/\lambda$. If the elements are half-wavelength spaced ($d = \lambda/2$), this region is exactly the visible region ($-1 < w < 1$, or $0 < \theta < \pi$).

A similar line of reasoning leads to the results for an even number of elements. In this case the Fourier series coefficient currents are

$$i_m = b_m = \frac{d}{\lambda} \int_{-\lambda/2d}^{\lambda/2d} f_d(w) e^{-j\pi(2m-1)(d/\lambda)w} dw \quad m \geq 1$$
$$i_{-m} = b_{-m} = \frac{d}{\lambda} \int_{-\lambda/2d}^{\lambda/2d} f_d(w) e^{j\pi(2m-1)(d/\lambda)w} dw \quad -m \leq -1 \quad (10-28)$$

for P even. The synthesized pattern is given by (10-22). Note that if N is infinite, (10-22) together with (10-28) is the Fourier series expansion of f_d , that is, $f(w) = f_d(w)$.

Example 10-3. Fourier Series Synthesis of a Sector Pattern

For an equally spaced linear array with an even number of elements and $c < \lambda/2d$, the sector pattern of (10-11) in (10-28) yields excitation currents

$$i_m = i_{-m} = 2 \frac{d}{\lambda} c \text{Sa} \left[\pi(2m-1) \frac{d}{\lambda} c \right] \quad 1 \leq m \leq N. \quad (10-29)$$

Since these currents are symmetric, the array factor of (10-22) reduces to

$$f(w) = 2 \sum_{m=1}^N i_m \cos \left[\pi(2m-1) \frac{d}{\lambda} w \right] \quad (10-30)$$

which is a real function. In general, the synthesized currents or current distribution will be real and symmetric if the desired pattern is real and symmetric, that is, if $f_d(-w) = f_d(w)$; and, in turn, the synthesized pattern will be real and symmetric.

The specific case of $c = 0.5$, $d/\lambda = 0.5$, and 20 elements ($N = 10$) has an array length $L = Pd = 10\lambda$ and excitation currents from (10-29) given by

$$i_m = i_{-m} = \frac{1}{2} \text{Sa} \left[\frac{\pi}{4} (2m-1) \right] \quad 1 \leq m \leq 10. \quad (10-31)$$

These excitation values are listed in Table 10-3, together with the element positions from (10-21). When these are used in the pattern expression (10-30) the pattern shown in Fig. 10-3 is produced. The NEESLAP computer program of Appendix G.5 can be used for these pattern calculations.

Table 10-3 Array Positions and Currents for a Fourier Series Synthesized Linear Array of 20 Half-Wavelength Spaced Elements for a Sector Pattern (Example 10-3)

Element number, m	Element position, z_m	Excitation current, i_m
± 1	$\pm 0.25\lambda$	0.4502
± 2	$\pm 0.75\lambda$	0.1501
± 3	$\pm 1.25\lambda$	-0.0900
± 4	$\pm 1.75\lambda$	-0.0643
± 5	$\pm 2.25\lambda$	0.0500
± 6	$\pm 2.75\lambda$	0.0409
± 7	$\pm 3.25\lambda$	-0.0346
± 8	$\pm 3.75\lambda$	-0.0300
± 9	$\pm 4.25\lambda$	0.0265
± 10	$\pm 4.75\lambda$	0.0237

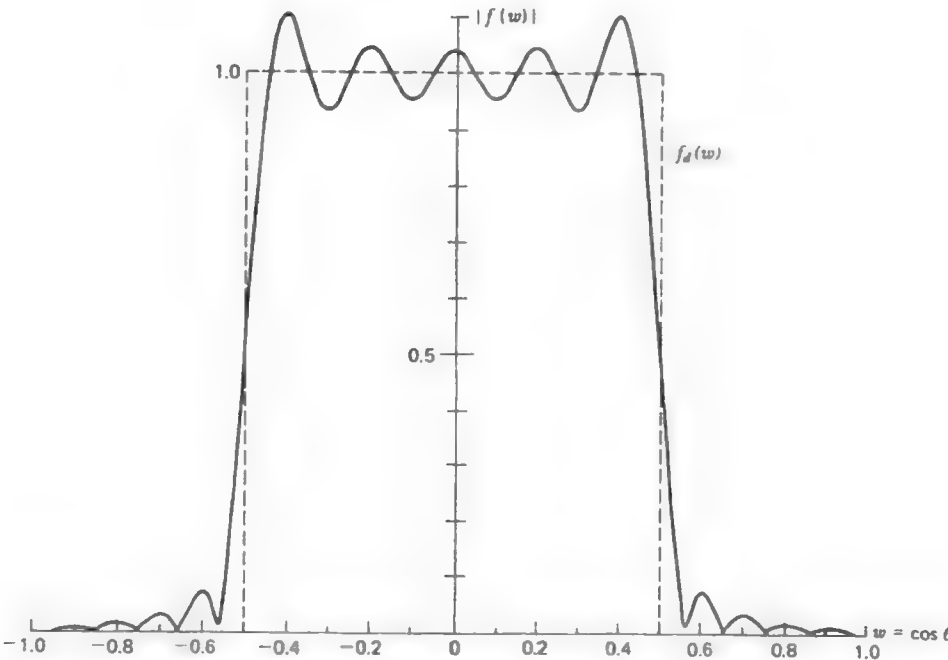


Figure 10-3 Fourier series synthesized array factor for a 20-element, $\lambda/2$ spaced linear array (Example 10-3). The desired pattern (dashed curve) is a sector pattern.

10.3.2 The Woodward-Lawson Sampling Method

The Woodward-Lawson sampling method for linear arrays is analogous to the Woodward-Lawson sampling method for line sources (see Section 10.2.2). In the array case the synthesized array factor is the superposition of array factors from uniform amplitude, linear phase arrays,

$$f(w) = \sum_{n=-M}^M a_n \frac{\sin[(P/2)(w - w_n)(2\pi/\lambda)d]}{P \sin[\frac{1}{2}(w - w_n)(2\pi/\lambda)d]} \quad (10-32)$$

where the sample values are

$$a_n = f_d(w = w_n) \quad (10-33)$$

and the sample points are

$$w_n = n \frac{\lambda}{Pd} = \frac{n}{L/\lambda} \quad |n| \leq M, \quad |w_n| \leq 1.0. \quad (10-34)$$

The element currents required to give this pattern are given by

$$i_m = \frac{1}{P} \sum_{n=-M}^M a_n e^{-j2\pi(z_m/\lambda)w_n}. \quad (10-35)$$

These results hold for arrays with either an even or odd number of elements.

Example 10-4. Woodward-Lawson Array Synthesis of a Sector Pattern

Again the sector pattern of (10-11) with $c = 0.5$ is to be synthesized, this time with a 20-element, half-wavelength spaced linear array using the Woodward-Lawson method.

Table 10-4 Element Currents and Positions Synthesized from the Woodward-Lawson Method for a Sector Pattern (Example 10-4)

Element number, m	Element position, z_m	Excitation current, i_m
± 1	$\pm 0.25\lambda$	0.44923
± 2	$\pm 0.75\lambda$	0.14727
± 3	$\pm 1.25\lambda$	-0.08536
± 4	$\pm 1.75\lambda$	-0.05770
± 5	$\pm 2.25\lambda$	0.04140
± 6	$\pm 2.75\lambda$	0.03020
± 7	$\pm 3.25\lambda$	-0.02167
± 8	$\pm 3.75\lambda$	-0.01464
± 9	$\pm 4.25\lambda$	0.00849
± 10	$\pm 4.75\lambda$	0.00278

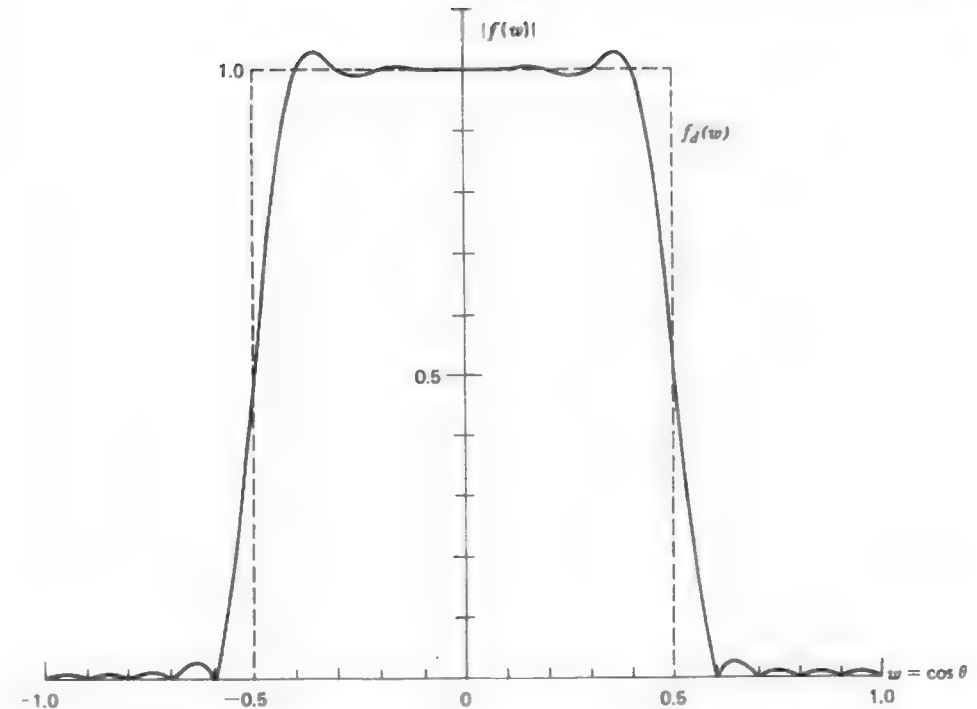


Figure 10-4 Woodward-Lawson synthesized array factor for a 20-element, $\lambda/2$ spaced linear array (Example 10-4). The desired pattern (dashed curve) is a sector pattern.

The sample locations from (10-34) are $w_n = 0.1n$. Thus the sample locations and values are the same as for Example 10-2 and are given in Table 10-2. Using these and element positions z_m from (10-21) in (10-35) yields the array currents of Table 10-4. The pattern can be generated from either the Woodward-Lawson pattern expression of (10-32), or by direct array computation using (10-30), which is the version of (10-22) for the symmetric case, and the array parameters of Table 10-4. The pattern is plotted in Fig. 10-4.

10.3.3 Comparison of Shaped Beam Synthesis Methods

Most shaped beam antenna patterns have three distinct types of pattern regions. The side lobe region is easily recognized, and the *side lobe level*, SLL, is defined from

$$\text{SLL} = 20 \log \left| \frac{\text{value of the highest side lobe peak}}{\text{maximum of desired pattern}} \right| \quad (10-36)$$

over the side lobe region. The quality of fit to the desired pattern $f_d(w)$ by the synthesized pattern $f(w)$ over the main beam is measured by the *ripple*, R , which is defined as

$$R = 20 \left| \log \left\{ \text{maximum} \left| \frac{f(u)}{f_d(u)} \right| \right\} \right| \text{ dB} \quad (10-37)$$

over the main beam. Also of interest is the region between the main beam and side lobe region, referred to as the transition region. In many applications, such as direction finding, it is desirable to have the main beam fall off very sharply into the side lobe region. To quantify this, *transition width* T is introduced and defined as

$$T = |w_{f=0.9} - w_{f=0.1}| \quad (10-38)$$

where $w_{f=0.9}$ and $w_{f=0.1}$ are the values of w where the synthesized pattern f equals 90% and 10% of the local discontinuity in the desired pattern. For unsymmetrical, single beam patterns there are two transition regions with different transition widths. Transition width is analogous to rise time in time-signal analysis.

The shaped beam synthesis methods we have discussed in this and the previous section can be compared rather easily using SLL, R , and T . The sector pattern results of Examples 10-1 to 10-4 are presented in Table 10-5. A few general trends can be extracted from the table. The Woodward-Lawson methods (for both line sources and arrays) tend to produce low side lobes and low main beam ripple at some sacrifice in transition width. On the other hand, Fourier methods yield somewhat inferior side lobe levels and ripples. The Fourier series synthesized pattern gives very sharp rolloff from the main beam to the side lobe region, that is, small transition width.

Table 10-5 Comparison of Synthesized Sector Patterns ($c = 0.5$, $L = 10\lambda$)

Method	Type	Example number	Figure number	Side level level, SLL (dB)	Ripple, R (dB)	Transition width, T
Fourier transform	10λ line source	10-1	10-1a	-21.9	0.83	0.0893
Woodward-Lawson	10λ line source	10-2	10-2a	-29.8	0.27	0.1303
Fourier series	20-element, $\lambda/2$ spaced array	10-3	10-3	-22.6	0.87	0.0941
Woodward-Lawson	20-element $\lambda/2$ spaced array	10-4	10-4	-29.6	0.27	0.1343

10.4 LOW SIDE LOBE, NARROW MAIN BEAM METHODS

The synthesis methods presented in the previous two sections are most useful for shaping the main beam of an antenna pattern. Another major class of pattern synthesis methods is that for achieving a narrow main beam accompanied by low side lobes. Patterns of this type have many applications, such as in point-to-point communications and direction finding. In this section we will discuss the two most important narrow main beam, low side lobe methods: the Dolph-Chebyshev method for linear arrays and the Taylor line source method. These two methods are closely related and the Dolph-Chebyshev method is presented first to simplify the development.

10.4.1 The Dolph-Chebyshev Linear Array Method

In Section 3.5 several excitations of equally spaced, linear arrays were examined. It was found that as the current amplitude taper from the center to the edges of the array increased the side lobe level decreased, but with an accompanying increase in width of the main beam. In most applications it is desirable to have both a narrow main beam as well as low side lobes. It would, therefore, be useful to have a pattern with an optimum compromise between beamwidth and side lobe level. In other words, for a specified beamwidth the side lobe level would be as low as possible; or vice versa, for a specified side lobe level the beamwidth would be as narrow as possible. In this section a method for achieving this is presented for broadside, linear arrays with equal spacings that are equal to or greater than a half-wavelength.

As might be expected the optimum beamwidth-side lobe level performance occurs when there are as many side lobes in the visible region as possible and when they have the same level. Dolph [5] recognized that Chebyshev polynomials possess this property, and he applied them to the synthesis problem. It is important to be familiar with Chebyshev polynomials, so we shall give a brief treatment of them before proceeding to synthesis.

The Chebyshev (sometimes spelled "Tchebyscheff") polynomials are defined by

$$T_n(x) = \begin{cases} (-1)^n \cosh(n \cosh^{-1} |x|) & x < -1 \\ \cos(n \cos^{-1} x) & -1 < x < 1 \\ \cosh(n \cosh^{-1} x) & x > 1. \end{cases} \quad (10-39)$$

A few of the lower order polynomials are

$$\begin{aligned} T_0(x) &= 1 \\ T_1(x) &= x \\ T_2(x) &= 2x^2 - 1 \\ T_3(x) &= 4x^3 - 3x \\ T_4(x) &= 8x^4 - 8x^2 + 1 \end{aligned} \quad (10-40)$$

Higher order polynomials can be generated from the recursive formula

$$T_{n+1}(x) = 2xT_n(x) - T_{n-1}(x) \quad (10-41)$$

or by letting $\delta = \cos^{-1} x$ and expanding $\cos m\delta$ in powers of $\cos \delta$. For example, $T_3(x) = \cos(3 \cos^{-1} x) = \cos 3\delta = 4 \cos^3 \delta - 3 \cos \delta$ from (B-13). Hence $T_3(x) = 4x^3 - 3x$. A few polynomials are plotted in Fig. 10-5.

Some important general properties of Chebyshev polynomials follow from (10-39) or Fig. 10-5. The even ordered polynomials are even, that is, $T_n(-x) = T_n(x)$ for n even, and the odd ordered ones are odd, that is, $T_n(-x) = -T_n(x)$ for n odd. All polynomials pass through the point (1, 1). In the range $-1 \leq x \leq 1$

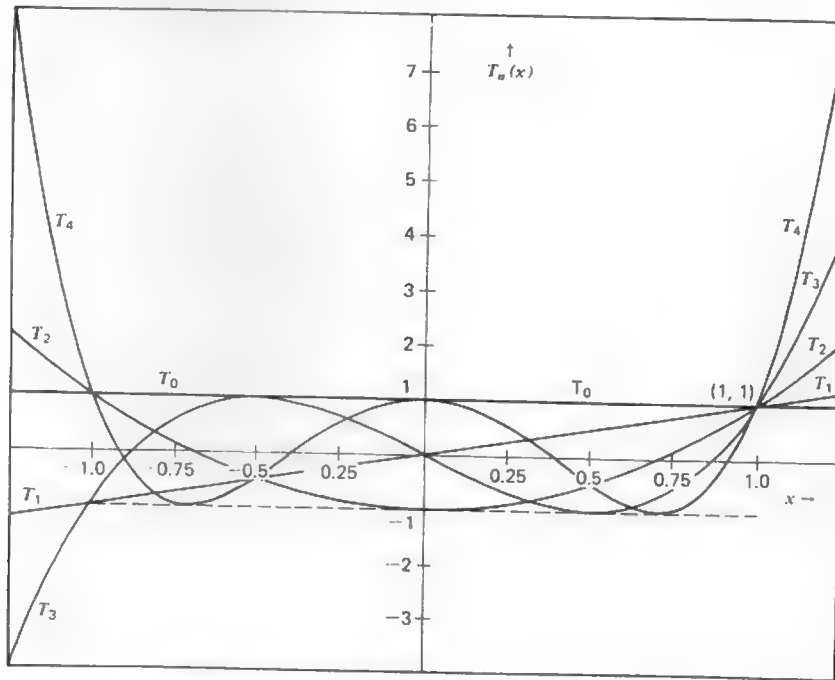


Figure 10-5 Chebyshev polynomials $T_0(x)$, $T_1(x)$, $T_2(x)$, $T_3(x)$, and $T_4(x)$.

the polynomial values lie between -1 and 1 , and the maximum magnitude is always unity there. All zeros (roots) of the polynomials also lie in $-1 \leq x \leq 1$.

The equal amplitude oscillations of Chebyshev polynomials in the region $|x| \leq 1$ is the desired property for equal side lobes. Also the polynomial nature of the functions makes them suitable for array factors since an array factor can be written as a polynomial. The connection between arrays and Chebyshev polynomials is established by considering a symmetrically excited, broadside array for which

$$i_{-m} = i_m \quad (10-42)$$

Symmetrical excitation leads to a real-valued array factor which, from (10-20) and (10-22), is given by

$$f(\psi) = \begin{cases} i_0 + 2 \sum_{m=1}^N i_m \cos m\psi & P \text{ odd} \\ 2 \sum_{m=1}^N i_m \cos \left[(2m-1) \frac{\psi}{2} \right] & P \text{ even} \end{cases} \quad (10-43)$$

where $\psi = 2\pi(d/\lambda)\sin\theta$. This array factor (for either odd or even P) is a sum of $\cos(m\psi/2)$ terms for m up to $P-1$. But each term containing $\cos(m\psi/2)$ can be written as a sum of terms with powers of $\cos(\psi/2)$ up to m , through the use of trigonometric identities. Therefore, the array factor is expressible as a sum of terms with powers of $\cos(\psi/2)$ up to $P-1$.

By choosing an appropriate transformation between x and ψ the array factor and Chebyshev polynomial will be identical. The transformation

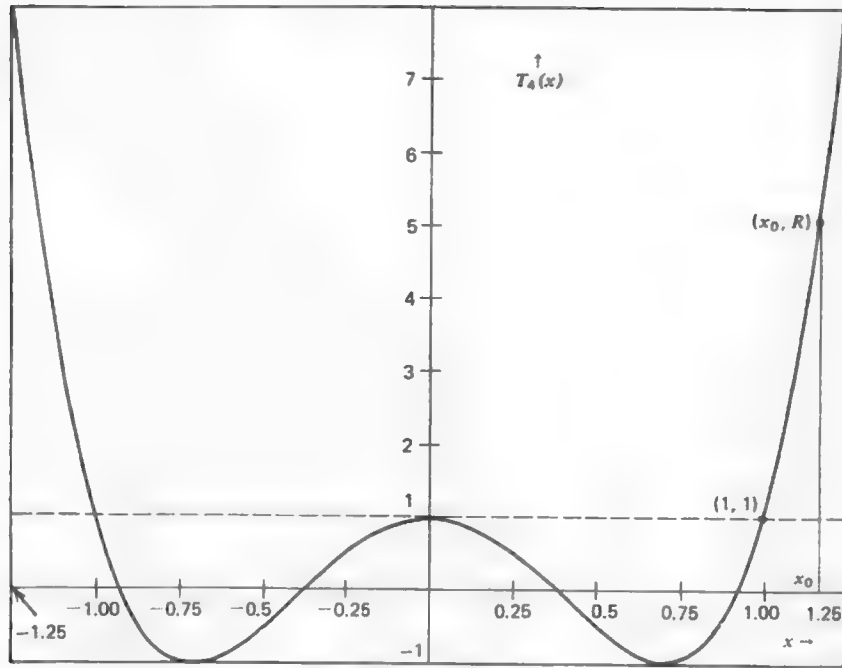
$$x = x_0 \cos \frac{\psi}{2} \quad (10-44)$$

and the correspondence

$$f(\psi) = T_{P-1} \left(x_0 \cos \frac{\psi}{2} \right) \quad (10-45)$$

will yield a polynomial in powers of $\cos(\psi/2)$ matching that of the array factor. The main beam maximum value of R occurs for $\theta = 90^\circ$, or $\psi = 0$, for a broadside array.⁴ Then (10-44) indicates that $x = x_0$ at the main beam maximum. The visible region extends from $\theta = 0^\circ$ to 180° , or $\psi = 2\pi(d/\lambda)$ to $-2\pi(d/\lambda)$. These limits correspond to $x = x_0 \cos(\pi d/\lambda)$; for half-wavelength spacing the limits are $x = 0$. Thus, for $d = \lambda/2$ the visible region begins at $x = 0$, or $\theta = 0^\circ$, and x increases as θ does until x_0 (the main beam maximum point) is reached and retraces back to $x = 0$, or $\theta = 180^\circ$ (see Fig. 10-6).

⁴ The symbol f is usually reserved for a pattern normalized to a maximum value of unity, but for the Dolph-Chebyshev array it is more convenient to normalize the array factor f to a maximum value of R .

Figure 10-6 Chebyshev polynomial $T_4(x)$.

The main beam-to-side lobe ratio, R , is the value of the array factor at the main beam maximum, since the side lobe level magnitude is unity (see Fig. 10-6). The side lobe level is thus $1/R$, or

$$\text{SLL} = -20 \log R \quad \text{dB.} \quad (10-46)$$

Evaluating (10-45) at the main beam maximum gives

$$R = T_{P-1}(x_0) = \cosh[(P-1)\cosh^{-1} x_0] \quad (10-47)$$

from (10-39). Or, solving for x_0 ,

$$x_0 = \cosh\left(\frac{1}{P-1} \cosh^{-1} R\right). \quad (10-48)$$

The design procedure can be summarized. For a given side lobe level, R can be determined from (10-46) leading to x_0 from (10-48). The array factor is then given by (10-45), or it can be computed from (10-43) directly from the current values. The excitation currents are found by comparison between the array factor of (10-43) and the Chebyshev polynomial of (10-45). This synthesis procedure will be illustrated by the following example.

Example 10-5. A Five-Element, Broadside, -20 -dB Side Lobe, Half-Wavelength Spaced Dolph-Chebyshev Array

For a five-element array ($P = 5$, $N = 2$) the array factor from (10-43) is

$$f(\psi) = i_0 + 2i_1 \cos \psi + 2i_2 \cos 2\psi \quad (10-49)$$

where $\psi = 2\pi(d/\lambda)\cos \theta = \pi \cos \theta$ for $d = \lambda/2$. Using $\cos(2\psi/2) = 2\cos^2(\psi/2) - 1$ from (B-12) and $\cos(4\psi/2) = 8\cos^4(\psi/2) - 8\cos^2(\psi/2) + 1$ from (B-14), the array factor can be written as

$$f(\psi) = (i_0 - 2i_1 + 2i_2) + (4i_1 - 16i_2)\cos^2 \frac{\psi}{2} + 16i_2 \cos^4 \frac{\psi}{2}. \quad (10-50)$$

And from (10-40)

$$\begin{aligned} T_4(x) &= 1 - 8x^2 + 8x^4 \\ &= 1 - 8x_0^2 \cos^2 \frac{\psi}{2} + 8x_0^4 \cos^4 \frac{\psi}{2} \end{aligned} \quad (10-51)$$

where (10-44) was used in the second step. Now the currents are found by successively equating coefficients of like terms of (10-50) and (10-51). From the $\cos^4(\psi/2)$ term

$$i_2 = \frac{1}{8}x_0^4. \quad (10-52)$$

The $\cos^2(\psi/2)$ term yields

$$i_1 = 4i_2 - 2x_0^2 = 2x_0^4 - 2x_0^2 \quad (10-53)$$

using (10-52). The final term gives

$$i_0 = -2i_2 + 2i_1 + 1 = 3x_0^4 - 4x_0^2 + 1 \quad (10-54)$$

using (10-52) and (10-53). The current values will be completely determined when x_0 is evaluated. This is accomplished by first finding the main beam-to-side lobe ratio from (10-46) using the specified -20 -dB side lobe level;

$$R = 10^{-\text{SLL}/20} = 10. \quad (10-55)$$

Then from (10-48) with $P = 5$ and $R = 10$,

$$x_0 = 1.293. \quad (10-56)$$

The element currents from (10-52) to (10-54) with (10-56) are

$$i_2 = i_{-2} = 1.3975, \quad i_1 = i_{-1} = 2.2465, \quad i_0 = 2.6978. \quad (10-57)$$

These currents yield a main beam maximum of $R = 10$ and unity side lobes. Normalizing these to unity edge currents gives a $1 : 1.61 : 1.93 : 1.61 : 1$ current distribution. The currents of (10-57) in (10-49), or in the NEESLAP program, lead to the pattern in Fig. 10-7, which was normalized to 0 dB on the main beam maximum. This same pattern was

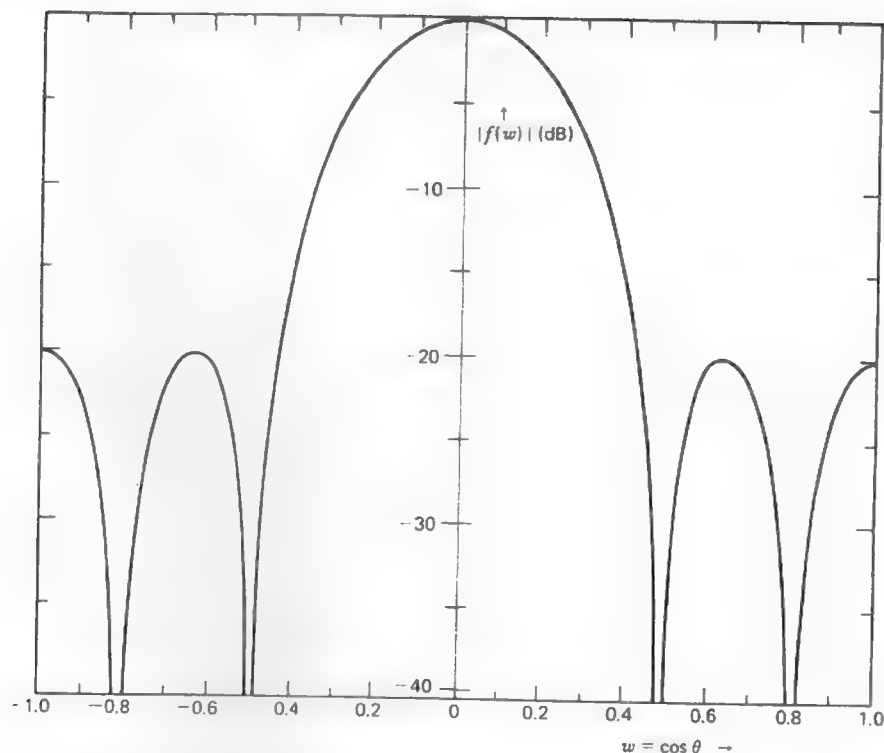


Figure 10-7 Dolph-Chebyshev synthesized array factor for a five-element, $\lambda/2$ spaced, broadside array with -20 -dB side lobes (Example 10-5).

plotted in Fig. 3-23d in polar form. The directivity for equiphased, half-wavelength spaced arrays can be obtained from (3-93). For this example the directivity is

$$D = \frac{\left| \sum_{m=-2}^2 i_m \right|^2}{\sum_{m=-2}^2 i_m^2} = 4.69. \quad (10-58)$$

If $d < \lambda/2$ the Dolph-Chebyshev broadside array is not optimum. Also if $x_0 \cos(\beta d/2) < -1$, additional main beams begin to appear. However, the Dolph-Chebyshev method can be extended to linear arrays with arbitrary spacings and to endfire applications [6, 7].

An approximate solution to the optimum (low side lobe, narrow main beam) linear array is obtained by setting the element currents equal to that of the Taylor line source at the appropriate locations; the Taylor line source is discussed in the next section. Also see Prob. 10.4-10.

10.4.2 The Taylor Line Source Method

The optimum narrow beam pattern from a line source antenna occurs when all side lobes are of equal level, just as in the array case. The required functional form, as we have seen, is that of the Chebyshev polynomial. The Chebyshev polynomial $T_N(x)$ has $N - 1$ equal level "side lobes" in the region $-1 < x < 1$, and for $|x| > 1$ its magnitude increases monotonically. A change of variables will transform the Chebyshev polynomial into the desired pattern form; that is with a zero slope main beam maximum at $x = 0$ and equal level side lobes. The new function resulting from the variable change is

$$P_{2N}(x) = T_N(x_0 - a^2 x^2) \quad (10-59)$$

where a is a constant and

$$x = \frac{L}{\lambda} \cos \theta = \frac{L}{\lambda} w. \quad (10-60)$$

At the pattern maximum

$$P_{2N}(w = 0) = T_N(x_0) = R \quad (10-61)$$

which is the main beam-to-side lobe ratio. A plot of (10-59) for $N = 4$ is shown in Fig. 10-8; it is the transformed version of Fig. 10-6.

From (10-39) we have in the side lobe region

$$P_{2N}(x) = \cos[N \cos^{-1}(x_0 - a^2 x^2)] \quad |x_0 - a^2 x^2| < 1. \quad (10-62)$$

The zeros of this function occur when cosine argument equals $(2n - 1)\pi/2$, or when the values of x are as follows,

$$x_n = \pm \frac{1}{a} \sqrt{x_0 - \cos \frac{(2n - 1)\pi}{2N}} \quad |n| \geq 1 \quad (10-63)$$

where the plus sign is used for zero locations on the positive x -axis and $x_{-n} = -x_n$. In the main beam region, from (10-39),

$$P_{2N}(x) = \cosh[N \cosh^{-1}(x_0 - a^2 x^2)] \quad |x_0 - a^2 x^2| > 1. \quad (10-64)$$

The main beam maximum value of P_{2N} is R and occurs for $x = 0$; see (10-60) and (10-61). Solving (10-64) for x_0 at the main beam maximum yields

$$x_0 = \cosh\left(\frac{1}{N} \cosh^{-1} R\right). \quad (10-65)$$

It is convenient to introduce A such that

$$A = \frac{1}{\pi} \cosh^{-1} R \quad (10-66)$$

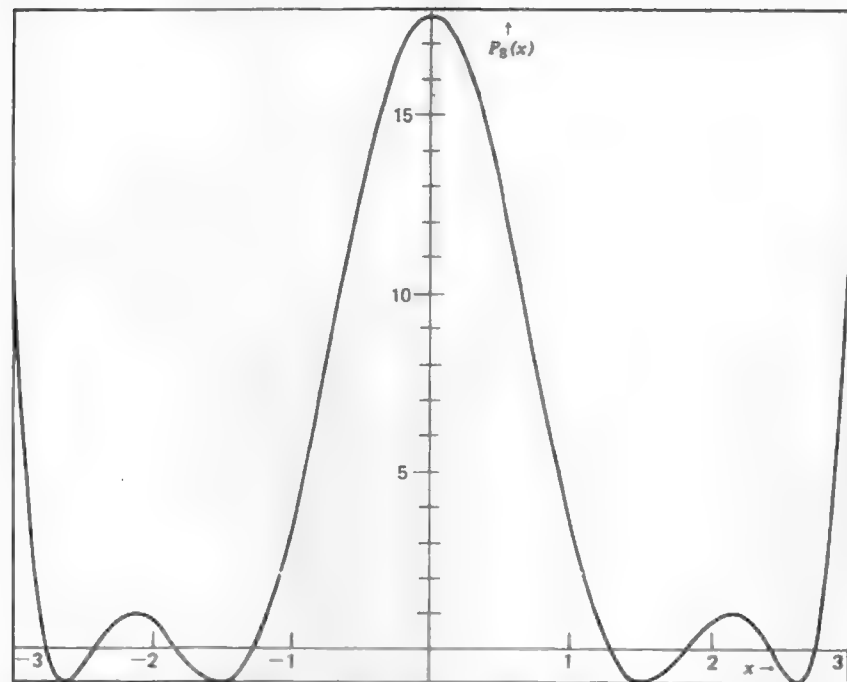


Figure 10-8 Transformed Chebyshev polynomial $P_8(x) = T_8(x_0 - a^2 x^2)$. Values of $a = 0.55536$ and $x_0 = 1.42553$ corresponding to Example 10-6 were used.

so then

$$x_0 = \cosh \frac{\pi A}{N}. \quad (10-67)$$

In order to have all side lobe levels equal we let N approach infinity, but simultaneously the argument of P_{2N} is changed to keep the first nulls stationary, thus leaving the beamwidth unchanged. For N large $x_0 = \cosh(\pi A/N) \approx 1 + \frac{1}{2}(\pi A/N)^2$ and

$$\cos \frac{(2n-1)\pi}{2N} \approx 1 - \frac{1}{2} \left[\frac{(2n-1)\pi}{2N} \right]^2,$$

and using these in (10-63) gives

$$x_n = \pm \frac{1}{a} \frac{\pi}{\sqrt{2N}} \sqrt{A^2 + (n - \frac{1}{2})^2} \quad N \rightarrow \infty. \quad (10-68)$$

By letting

$$a = \frac{\pi}{\sqrt{2N}} \quad (10-69)$$

the first zero location remains fixed as N increases. Then

$$x_n = \pm \sqrt{A^2 + (n - \frac{1}{2})^2}. \quad (10-70)$$

The pattern factor is a polynomial in x with an infinite number of roots x_n , and can be expressed as a product of factors $(x - x_n)$ for n from $-\infty$ to $+\infty$. And since $x_{-n} = -x_n$ the pattern is

$$\prod_{n=1}^{\infty} (x^2 - x_n^2) = \prod_{n=1}^{\infty} [x^2 - A^2 - (n - \frac{1}{2})^2]. \quad (10-71)$$

Normalizing this to unity at $x = 0$, gives

$$f(x) = \frac{\prod_{n=1}^{\infty} \left| 1 - \frac{x^2 - A^2}{(n - \frac{1}{2})^2} \right|}{\prod_{n=1}^{\infty} \left| 1 + \frac{A^2}{(n - \frac{1}{2})^2} \right|} = \frac{\cos(\pi \sqrt{x^2 - A^2})}{\cosh \pi A}. \quad (10-72)$$

The last step above utilizes the closed form expression for the infinite products. Using (10-60) and (10-66) in (10-72) gives the pattern in w as

$$f(w) = \frac{\cos[\pi \sqrt{[(L/\lambda)w]^2 - A^2}]}{R}. \quad (10-73)$$

Note that this is normalized to unity at the maximum ($w = 0$) and oscillates between $-1/R$ and $1/R$ in the side lobe region. For large w the argument of the cosine function in (10-73) is approximately $\pi w L/\lambda$, so the zero locations of the pattern are $w_n \approx \pm \lambda(n - \frac{1}{2})/L$ or $x_n \approx \pm (n - \frac{1}{2})$, and thus they are regularly spaced. Also note that for $w < \lambda A/L$ the cosine argument of (10-73) is imaginary and since $\cos(j\theta) = \cosh \theta$, (10-73) is more conveniently expressed as

$$f(w) = \frac{\cosh[\pi \sqrt{A^2 - [(L/\lambda)w]^2}]}{\cosh \pi A} \quad w < \frac{\lambda A}{L}. \quad (10-74)$$

This pattern is that of the *ideal Taylor line source* [8]. It is a function of A which is found from the side lobe level; see (10-46) and (10-66). The line source is "ideal" in the sense that equilevel side lobes extend to infinity in pattern space, thus leading to infinite power. The required source excitation, in turn, must possess infinite power and, in fact, will have singularities at each end of the line source.

An approximate realization of the ideal Taylor line source, referred to as the *Taylor line source*, renders the first few side lobes of a nearly equal level and

decreasing far-out side lobes [8]. The decaying side lobe envelope removes the infinite power difficulty encountered with the ideal Taylor line source. The Taylor line source pattern is again a polynomial in x , but with zero locations given by

$$x_n = \begin{cases} \pm \sigma \sqrt{A^2 + (n - \frac{1}{2})^2} & 1 \leq n < \bar{n} \\ \pm n & \bar{n} \leq n < \infty \end{cases} \tag{10-75}$$

The zeros for $n < \bar{n}$ are those of the ideal line source in (10-70) scaled by the factor σ . The far-out side lobes for $n \geq \bar{n}$ are located at the integer x positions. The zero arrangement for a $\sin(\pi x)/\pi x$ pattern is $x = \pm n$ for $n \geq 1$ so the Taylor pattern far-out side lobes are those of the $\sin(\pi x)/\pi x$ pattern. The scaling parameter σ is determined by making the zero location expressions in (10-75) identical for $n = \bar{n}$, which yields

$$\sigma = \frac{\bar{n}}{\sqrt{A^2 + (\bar{n} - \frac{1}{2})^2}} \tag{10-76}$$

From the zero locations of (10-75) we may write the approximate Taylor line source pattern as

$$f(x, A, \bar{n}) = \frac{\sin \pi x}{\pi x} \prod_{n=1}^{\bar{n}-1} \frac{1 - (x/x_n)^2}{1 - (x/n)^2} \tag{10-77}$$

The side lobes are nearly constant at the value $1/R$ out to $x = \bar{n}$ and decay as $1/x$ beyond $x = \bar{n}$. The pattern in terms of $w = \cos \theta$ is

$$f(w, A, \bar{n}) = \frac{\sin(\pi L w/\lambda)}{\pi L w/\lambda} \prod_{n=1}^{\bar{n}-1} \frac{1 - (w/w_n)^2}{1 - (Lw/\lambda n)^2} \tag{10-78}$$

where the pattern zero locations on the w -axis are

$$w_n = \begin{cases} \pm \frac{\lambda}{L} \sigma \sqrt{A^2 + (n - \frac{1}{2})^2} & 1 \leq n < \bar{n} \\ \pm \frac{\lambda}{L} n & \bar{n} \leq n < \infty \end{cases} \tag{10-79}$$

with σ given by (10-76).

The Taylor line source is actually a pattern of the Woodward-Lawson family. We shall show how this comes about and also determine the sample values and locations. First assume that the required source excitation can be expanded in a Fourier series as

$$i(s) = \frac{\lambda}{L} \sum_{n=-\infty}^{\infty} a_n e^{-j2\pi(\lambda/L)ns} \quad |s| \leq \frac{L}{2\lambda} \tag{10-80}$$

The corresponding pattern from (10-18) is

$$f(w) = \sum_{n=-\infty}^{\infty} a_n \text{Sa} \left[\left(w - \frac{\lambda}{L} n \right) \frac{L}{\lambda} \pi \right] \tag{10-81}$$

where the sample locations are identified as

$$w_n^* = \frac{\lambda}{L} n \tag{10-82}$$

The infinite expansion of (10-81) gives the exact pattern if the sample values are (see Prob. 10.4-6)

$$a_n = f(w = w_n^*) = f(n, A, \bar{n}) \tag{10-83}$$

But the pattern zeros correspond to the sample locations of (10-82) for $|n| \geq \bar{n}$ since $x_n = n$, or $w_n = (\lambda/L)n$ for $|n| \geq \bar{n}$ from (10-75). Thus

$$a_n = 0 \quad \text{for} \quad |n| \geq \bar{n} \tag{10-84}$$

Using (10-83) and (10-84) in (10-81) gives the pattern expression

$$f(w) = \sum_{n=-\bar{n}+1}^{\bar{n}-1} f(n, A, \bar{n}) \text{Sa} \left[\left(w - w_n^* \right) \frac{L}{\lambda} \pi \right] \tag{10-85}$$

The required current distribution from (10-80) is

$$i(s) = \frac{\lambda}{L} \left[1 + 2 \sum_{n=1}^{\bar{n}-1} f(n, A, \bar{n}) \cos \left(2\pi \frac{\lambda}{L} ns \right) \right] \tag{10-86}$$

The coefficients $f(n, A, \bar{n})$ are the samples of Taylor line source pattern for $x = n$ and $n < \bar{n}$. They are found from

$$f(n, A, \bar{n}) = \begin{cases} \frac{[(\bar{n} - 1)!]^2}{(\bar{n} - 1 + n)!(\bar{n} - 1 - n)!} \prod_{m=1}^{\bar{n}-1} \left(1 - \frac{n^2}{x_m^2} \right) & |n| < \bar{n} \\ 0 & |n| \geq \bar{n} \end{cases} \tag{10-87}$$

and $f(-n, A, \bar{n}) = f(n, A, \bar{n})$. Tables of the coefficient values are also available [9]. These coefficients together with (10-85) and (10-86) determine the Taylor line source pattern and current.

The half-power beamwidth expression is obtained rather easily for the ideal pattern. Evaluating (10-74) at the half-power points yields

$$\frac{1}{\sqrt{2}} = \frac{1}{R} \cosh \left[\pi \sqrt{A^2 - \left(\frac{L}{\lambda} w_{\text{HP}} \right)^2} \right] \tag{10-88}$$

Solving this gives the two solutions

w_{HP} = \pm \frac{\lambda}{L\pi} \left[(\cosh^{-1} R)^2 - \left(\cosh^{-1} \frac{R}{\sqrt{2}} \right)^2 \right]^{1/2} \tag{10-89}

The half-power beamwidth in w is then

HP_{w_i} = 2 |w_{HP}| = \frac{\lambda 2}{L\pi} \left[(\cosh^{-1} R)^2 - \left(\cosh^{-1} \frac{R}{\sqrt{2}} \right)^2 \right]^{1/2} \tag{10-90}

The angle from broadside is \gamma = \theta - 90^\circ, so w = \cos \theta = \cos(\gamma + 90^\circ) = -\sin \gamma and \gamma = -\sin^{-1} w. The half-power beamwidth based on the ideal Taylor line source is

HP_i = |\theta_{HP_{left}} - \theta_{HP_{right}}| = |\gamma_{HP_{left}} - \gamma_{HP_{right}}| = |\sin^{-1} w_{HP+} - \sin^{-1} w_{HP-}| = 2 |\sin^{-1} w_{HP}| = 2 \sin^{-1} \left\{ \frac{\lambda}{L\pi} \left[(\cosh^{-1} R)^2 - \left(\cosh^{-1} \frac{R}{\sqrt{2}} \right)^2 \right]^{1/2} \right\} \tag{10-91}

where w_{HP+} and w_{HP-} are the two solutions of (10-89). The beamwidth for the approximate Taylor line source is given approximately by [10]

HP_w \approx \sigma HP_{w_i} \tag{10-92}

and in \theta by

HP \approx 2 \sin^{-1} \left\{ \frac{\lambda \sigma}{L\pi} \left[(\cosh^{-1} R)^2 - \left(\cosh^{-1} \frac{R}{\sqrt{2}} \right)^2 \right]^{1/2} \right\} \tag{10-93}

Example 10-6. A 10-Wavelength Taylor Line Source With -25-dB Side Lobes and \bar{n} = 5

The main beam-to-side lobe level ratio, since SLL = -25 dB, is

R = 10^{-SLL/20} = 10^{1.25} = 17.7828. \tag{10-94}

From (10-66)

A = \frac{1}{\pi} \cosh^{-1} R = 1.13655. \tag{10-95}

Then from (10-76)

\sigma = \frac{\bar{n}}{\sqrt{A^2 + (\bar{n} - \frac{1}{2})^2}} = 1.07728. \tag{10-96}

Using these values of A and \sigma, the zero locations x_n can be calculated from (10-75), and then the sample coefficients follow from (10-87) as given in Table 10-6. The sample

Table 10-6 Sample Values and Locations for the Taylor Line Source of Example 10-6 (L = 10\lambda, \bar{n} = 5)

n	a_n = f(n, A, \bar{n}) = f(n, 1.13655, 5)	w_n^*
0	1.000000	0
\pm 1	0.221477	\pm 0.1
\pm 2	-0.005370	\pm 0.2
\pm 3	-0.006621	\pm 0.3
\pm 4	0.004917	\pm 0.4

locations from (10-82) are also tabulated. The pattern and current distribution can now be computed from (10-85) and (10-86) with the sample values and locations of Table 10-6. The resulting pattern and current distribution are plotted in Fig. 10-9; the SPAP program

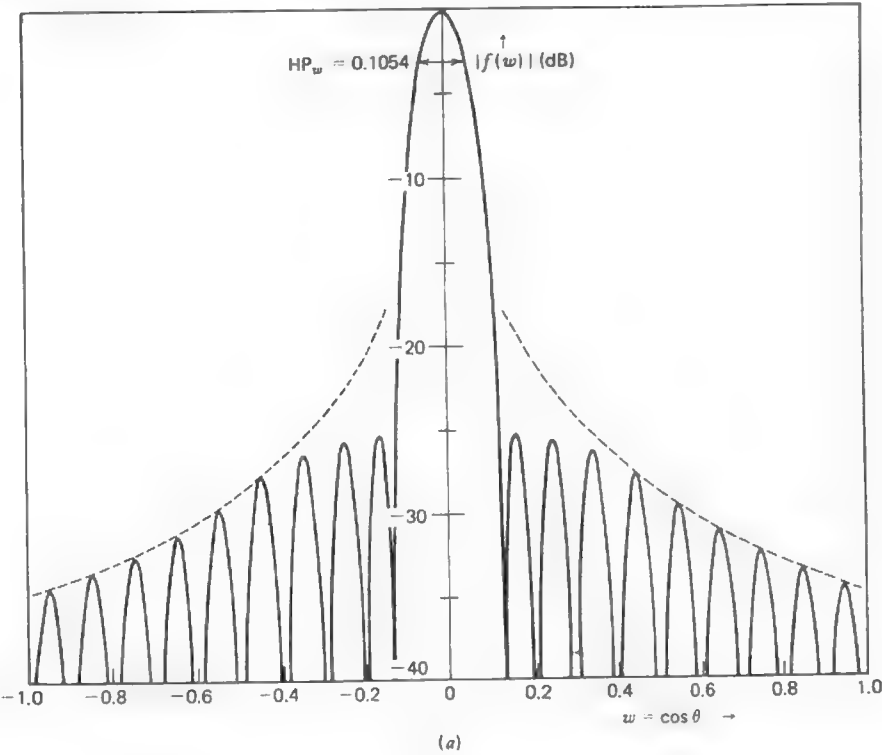


Figure 10-9 A 10\lambda Taylor line source with -25-dB side lobes and \bar{n} = 5 (Example 10-6). (a) The synthesized pattern.

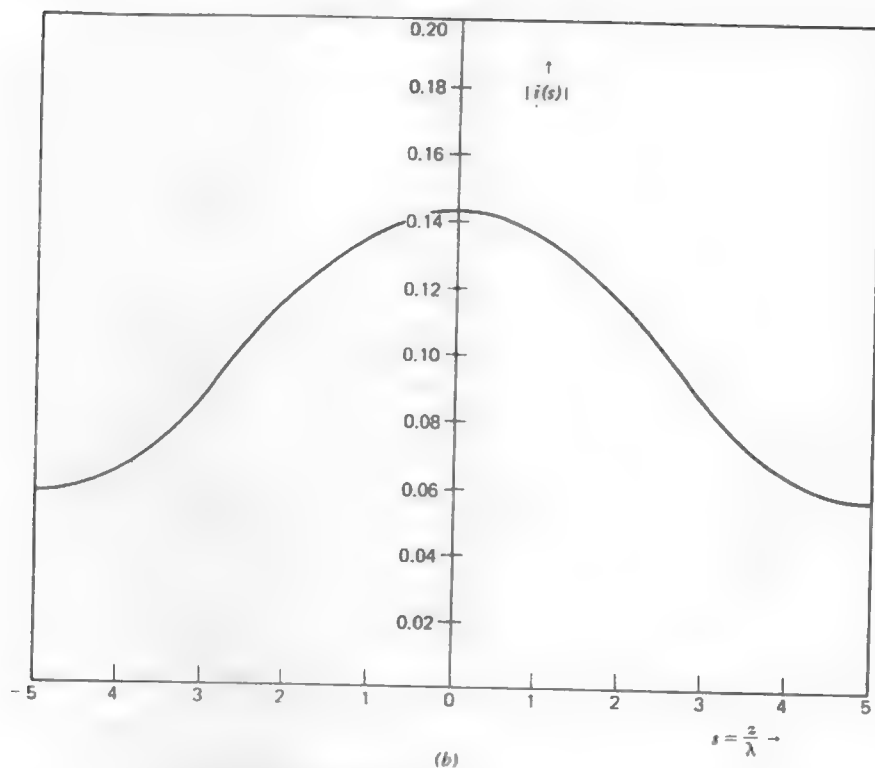


Figure 10-9 (continued) (b) The current distribution.

may be used to generate these. The side lobe decay envelope for the far-out side lobes of the pattern is shown in Fig. 10-9a. The half-power beamwidths from (10-90) to (10-93) are

$$\text{HP}_w = 0.0978 \quad \text{HP}_t = 5.606^\circ \quad (10-97)$$

and

$$\text{HP}_w \approx 0.1054 \quad \text{HP} \approx 6.039^\circ \quad (10-98)$$

In this case the ideal Taylor line source beamwidth is very close to that of the approximate Taylor line source. The half-power beamwidth HP_w is indicated in Fig. 10-9a.

REFERENCES

1. R. E. Collin and F. J. Zucker, Editors, *Antenna Theory*, Part 1, McGraw-Hill, New York, 1969; Chapter 7.
2. W. L. Stutzman and E. L. Coffey, "Radiation pattern synthesis of planar antennas using the iterative sampling method," *IEEE Trans. on Ant. and Prop.*, vol. AP-23, pp. 764-769, July 1975.

3. P. M. Woodward, "A method for calculating the field over a plane aperture required to produce a given polar diagram," *J. IEE*, vol. 93, Part III A, pp. 1554-1558, 1946.
4. P. M. Woodward and J. D. Lawson, "The theoretical precision with which an arbitrary radiation-pattern may be obtained from a source of finite extent," *J. IEE*, vol. 95, Part II, pp. 363-370, Sept. 1948.
5. C. L. Dolph, "A current distribution for broadside arrays which optimizes the relationship between beam width and side-lobe level," *Proc. IRE*, vol. 34, pp. 335-348, June 1946.
6. W. L. Weeks, *Antenna Engineering*, McGraw-Hill, New York, 1968; pp. 101-115.
7. R. E. Collin and F. J. Zucker, Editors, *Antenna Theory*, Part 1, McGraw-Hill, New York, 1969; pp. 186-194.
8. T. T. Taylor, "Design of line-source antennas for narrow beamwidth and low sidelobes," *IRE Trans. on Ant. and Prop.*, vol. AP-3, pp. 16-28, Jan. 1955.
9. R. C. Hansen, Editor, *Microwave Scanning Antennas*, Volume I, Academic Press, New York, 1964; Appendix I.
10. R. C. Hansen, Editor, *Microwave Scanning Antennas*, Volume I, Academic Press, New York, 1964; p. 56.

PROBLEMS

10.2-1 If $g(t)$ and $G(\omega)$ are a Fourier transform pair, then

$$G(\omega) = \int_{-\infty}^{\infty} g(t) e^{-j\omega t} dt$$

and

$$g(t) = \frac{1}{2\pi} \int_{-\infty}^{\infty} G(\omega) e^{j\omega t} d\omega.$$

If g , t , G , and ω are replaced by f , u , i , and $2\pi s$, respectively, show that (10-6) and (10-7) follow from the above equations.

10.2-2 Use (10-6) to find the pattern from a uniform amplitude, zero phase line source of length L centered on the z -axis.

10.2-3 Find the current distribution $i_x(s)$ required to exactly produce the sector pattern of (10-11b).

10.2-4 (a) Derive the Fourier transform synthesis pattern of (10-13) for a sector pattern. (b) Plot this pattern, thus verifying Fig. 10-1a. Numerical integration of the Fourier transform via computer may be easier than using (10-13).

10.2-5 Derive (10-15).

10.2-6 Repeat the Woodward-Lawson synthesis of the sector pattern of Example 10-2, but this time for a five-wavelength line source.

- (a) Plot the pattern in linear, rectangular form as a function of w .
- (b) Plot the current distribution.

10.2-7 A cosecant pattern (see Prob. 1.6-7 for a discussion of the cosecant pattern) is given by

$$f_d(w) = \begin{cases} 1 & 0 \leq w \leq 0.1 \\ \frac{0.1}{w} & 0.1 \leq w \leq 0.5 \\ 0 & \text{elsewhere} \end{cases}$$

Use the Woodward-Lawson method to synthesize an approximation to this pattern for a 10λ line source.

(a) Plot the pattern in linear, rectangular form together with the desired pattern as a function of w .

(b) Plot the required current amplitude and phase.

10.3-1 Discuss the conditions under which the $f_d(w)$ can be represented by the Fourier series in (10-24).

10.3-2 Derive the Fourier series coefficient expression in (10-25).

10.3-3 Derive the element current expression (10-29) for the Fourier series synthesis of a sector pattern.

10.3-4 Synthesize a sector pattern with $c = 0.5$ using the Fourier series method as in Example 10-3 for an array of 20 elements which are spaced 0.6λ apart.

(a) Determine the element locations and current values.

(b) Plot the radiation pattern in linear, rectangular form as a function of w .

10.3-5 Repeat Prob. 10.3-4 for an array of 10 elements and half-wavelength spacings.

10.3-6 Use the Fourier series synthesis method to synthesize a sector pattern with $c = 0.5$ for an array of 21 half-wavelength spaced elements. Derive the general element current expression and evaluate for each element. Plot the pattern. Compare to the 20-element array result of Example 10-3.

10.3-7 Repeat the cosecant pattern synthesis as in Prob. 10.2-7 using the Fourier series method for a 20-element, half-wavelength spaced array.

10.3-8 Show that the Woodward-Lawson sampling method pattern of (10-32) arises from the array factor with the currents of (10-35) for:

(a) An odd number of elements. *Hint:* use (10-19) and (10-20).

(b) An even number of elements. *Hint:* use (10-21) and (10-22).

10.3-9 Verify the array element positions and currents of Table 10-4 for the Woodward-Lawson synthesized sector pattern of Example 10-4.

10.3-10 Repeat the Woodward-Lawson synthesis as in Example 10-4 for a 10-element, half-wavelength spaced array.

10.3-11 A collinear array of 18 half-wave dipole antennas is to be used to synthesize a sector pattern with a main beam sector over the region $70^\circ \leq \theta \leq 110^\circ$, that is, $F_d(\theta) = 1$ over this region and zero elsewhere.

(a) For 0.65λ spacings determine the input currents required for Woodward-Lawson synthesis of the complete pattern. Account for the element factor.

(b) Plot the total array pattern in linear, polar form as a function of θ .

10.3-12 Repeat Prob. 10.3-11 for a cosecant desired pattern where $F_d(\theta)$ is 1 for $80^\circ \leq \theta \leq 90^\circ$, $\cos 80^\circ / \cos \theta$ for $0^\circ \leq \theta \leq 80^\circ$, and zero elsewhere.

10.4-1 For the five-element, broadside, -20 -dB side lobe, half-wavelength spaced Dolph-Chebyshev array of Example 10-5:

(a) Obtain the pattern plot in logarithmic, rectangular form as a function of w . The NEESLAP program may be used.

(b) Verify the side lobe level and beamwidth (see Fig. 3-23d) from your pattern calculations.

10.4-2 Design a Dolph-Chebyshev broadside array of five, half-wavelength spaced elements for -30 -dB side lobes.

(a) Verify the current distribution as given in Fig. 3-23e.

(b) Compute the directivity.

10.4-3 Design a broadside Dolph-Chebyshev array with six, 0.6λ spaced elements for -25 -dB side lobes.

(a) Obtain the element currents.

(b) Plot the pattern in logarithmic, rectangular form.

10.4-4 Derive the ideal Taylor line source pattern results of (10-71) and (10-72).

10.4-5 Show how the approximate Taylor line source pattern of (10-77) follows from the zero locations.

10.4-6 The sampling theorem from time-signal analysis states that a signal $g(t)$ is exactly reconstructed from the time samples $g(m/2B)$ as

$$g(t) = \sum_{m=-\infty}^{\infty} g\left(\frac{m}{2B}\right) \text{Sa}\left[2\pi B\left(t - \frac{m}{2B}\right)\right]$$

where B is the highest frequency component of the signal. Draw the appropriate analogies to antenna theory to obtain the sampled data pattern expression of (10-81).

10.4-7 Verify (10-89).

10.4-8 Compute the sample values a_n of Table 10-6 for the Taylor line source of Example 10-6.

10.4-9 Compute the half-power beamwidth values for the Taylor line source of Example 10-6. Compare your answers to those of (10-97) and (10-98).

10.4-10 An array antenna can be designed by choosing the element current excitations at the corresponding points of the continuous current from a line source synthesized for the

Array Excitations for Problem 10.4-10

m	z_m	i_m
± 1	± 0.25	0.14234
± 2	± 0.75	0.13833
± 3	± 1.25	0.13127
± 4	± 1.75	0.12175
± 5	± 2.25	0.10935
± 6	± 2.75	0.09429
± 7	± 3.25	0.07891
± 8	± 3.75	0.06676
± 9	± 4.25	0.05980
± 10	± 4.75	0.05720

desired pattern. This is illustrated in this problem with a narrow main beam, low side lobe pattern. The Taylor line source of Example 10-6 has current values appropriate for a 20-element array given in the table.

(a) Use these current values to obtain the array factor of the corresponding linear array.

(b) Compare the half-power beamwidths and side lobe levels of the array and line source patterns.

10.4-11 Design an eight-wavelength Taylor line source ($\bar{n} = 7$) with -30 -dB side lobes.

(a) Obtain and tabulate the sample values and locations.

(b) Plot the pattern in rectangular-logarithmic form as a function of w .

10.4-12 Evaluate σ for several values of \bar{n} for the case of a -25 -dB side lobe level. Using $HP_w \approx \sigma HP_{w_1}$, explain the half-power beamwidth behavior as a function of \bar{n} .

APPENDIX A

VECTORS

A.1 UNIT VECTOR REPRESENTATIONS

$$\hat{x} = \hat{r} \sin \theta \cos \phi + \hat{\theta} \cos \theta \cos \phi - \hat{\phi} \sin \phi \quad (\text{A-1})$$

$$\hat{y} = \hat{r} \sin \theta \sin \phi + \hat{\theta} \cos \theta \sin \phi + \hat{\phi} \cos \phi \quad (\text{A-2})$$

$$\hat{z} = \hat{r} \cos \theta - \hat{\theta} \sin \theta \quad (\text{A-3})$$

$$\hat{r} = \hat{x} \sin \theta \cos \phi + \hat{y} \sin \theta \sin \phi + \hat{z} \cos \theta \quad (\text{A-4})$$

$$\hat{\theta} = \hat{x} \cos \theta \cos \phi + \hat{y} \cos \theta \sin \phi - \hat{z} \sin \theta \quad (\text{A-5})$$

$$\hat{\phi} = -\hat{x} \sin \phi + \hat{y} \cos \phi \quad (\text{A-6})$$

A.2 VECTOR IDENTITIES

$$\mathbf{A} \times (\mathbf{B} \times \mathbf{C}) = (\mathbf{A} \cdot \mathbf{C})\mathbf{B} - (\mathbf{A} \cdot \mathbf{B})\mathbf{C} \quad (\text{A-7})$$

$$(\mathbf{A} \times \mathbf{B}) \times \mathbf{C} = (\mathbf{C} \cdot \mathbf{A})\mathbf{B} - (\mathbf{C} \cdot \mathbf{B})\mathbf{A} \quad (\text{A-8})$$

$$\nabla \cdot (\nabla \times \mathbf{G}) = 0 \quad (\text{A-9})$$

$$\nabla \times \nabla g = 0 \quad (\text{A-10})$$

$$\nabla \cdot \nabla g = \nabla^2 g \quad (\text{A-11})$$

$$\nabla(f + g) = \nabla f + \nabla g \quad (\text{A-12})$$

$$\nabla \cdot (\mathbf{F} + \mathbf{G}) = \nabla \cdot \mathbf{F} + \nabla \cdot \mathbf{G} \quad (\text{A-13})$$

$$\nabla(fg) = g\nabla f + f\nabla g \quad (\text{A-14})$$

$$\nabla \cdot (f\mathbf{G}) = \mathbf{G} \cdot (\nabla f) + f(\nabla \cdot \mathbf{G}) \quad (\text{A-15})$$

$$\nabla \times (f\mathbf{G}) = (\nabla f) \times \mathbf{G} + f(\nabla \times \mathbf{G}) \quad (\text{A-16})$$

$$\nabla \times (\nabla \times \mathbf{G}) = \nabla(\nabla \cdot \mathbf{G}) - \nabla^2 \mathbf{G} \quad (\text{A-17})$$

$$\nabla^2 \mathbf{G} = \hat{x}\nabla^2 G_x + \hat{y}\nabla^2 G_y + \hat{z}\nabla^2 G_z \quad (\text{A-18})$$

$$\nabla \cdot (\mathbf{F} \times \mathbf{G}) = \mathbf{G} \cdot (\nabla \times \mathbf{F}) - \mathbf{F} \cdot (\nabla \times \mathbf{G}) \quad (\text{A-19})$$

$$\mathbf{F} \cdot (\mathbf{G} \times \mathbf{H}) = \mathbf{G} \cdot (\mathbf{H} \times \mathbf{F}) = \mathbf{H} \cdot (\mathbf{F} \times \mathbf{G}) \quad (\text{A-20})$$

$$\nabla \times (\mathbf{F} \times \mathbf{G}) = \mathbf{F}(\nabla \cdot \mathbf{G}) - \mathbf{G}(\nabla \cdot \mathbf{F}) + (\mathbf{G} \cdot \nabla)\mathbf{F} - (\mathbf{F} \cdot \nabla)\mathbf{G} \quad (\text{A-21})$$

$$\nabla(\mathbf{F} \cdot \mathbf{G}) = (\mathbf{F} \cdot \nabla)\mathbf{G} + (\mathbf{G} \cdot \nabla)\mathbf{F} + \mathbf{F} \times (\nabla \times \mathbf{G}) + \mathbf{G} \times (\nabla \times \mathbf{F}) \quad (\text{A-22})$$

$$\iiint_V \nabla \cdot \mathbf{G} \, dv = \iint_S \mathbf{G} \cdot d\mathbf{s} \quad \text{divergence theorem} \quad (\text{A-23})$$

$$\iint_S (\nabla \times \mathbf{G}) \cdot d\mathbf{s} = \oint_l \mathbf{G} \cdot d\mathbf{l} \quad \text{Stokes' theorem} \quad (\text{A-24})$$

A.3 VECTOR DIFFERENTIAL OPERATORS

Rectangular Coordinates

$$\nabla g = \hat{x} \frac{\partial g}{\partial x} + \hat{y} \frac{\partial g}{\partial y} + \hat{z} \frac{\partial g}{\partial z} \quad (\text{A-25})$$

$$\nabla \cdot \mathbf{G} = \frac{\partial G_x}{\partial x} + \frac{\partial G_y}{\partial y} + \frac{\partial G_z}{\partial z} \quad (\text{A-26})$$

$$\nabla \times \mathbf{G} = \hat{x} \left(\frac{\partial G_z}{\partial y} - \frac{\partial G_y}{\partial z} \right) + \hat{y} \left(\frac{\partial G_x}{\partial z} - \frac{\partial G_z}{\partial x} \right) + \hat{z} \left(\frac{\partial G_y}{\partial x} - \frac{\partial G_x}{\partial y} \right) \quad (\text{A-27})$$

$$\nabla^2 g = \frac{\partial^2 g}{\partial x^2} + \frac{\partial^2 g}{\partial y^2} + \frac{\partial^2 g}{\partial z^2} \quad (\text{A-28})$$

Cylindrical Coordinates

$$\nabla g = \hat{r} \frac{\partial g}{\partial r} + \hat{\phi} \frac{1}{r} \frac{\partial g}{\partial \phi} + \hat{z} \frac{\partial g}{\partial z} \quad (\text{A-29})$$

$$\nabla \cdot \mathbf{G} = \frac{1}{r} \frac{\partial}{\partial r} (rG_r) + \frac{1}{r} \frac{\partial G_\phi}{\partial \phi} + \frac{\partial G_z}{\partial z} \quad (\text{A-30})$$

$$\nabla \times \mathbf{G} = \hat{r} \left(\frac{1}{r} \frac{\partial G_z}{\partial \phi} - \frac{\partial G_\phi}{\partial z} \right) + \hat{\phi} \left(\frac{\partial G_r}{\partial z} - \frac{\partial G_z}{\partial r} \right) + \hat{z} \frac{1}{r} \left[\frac{\partial}{\partial r} (rG_\phi) - \frac{\partial G_r}{\partial \phi} \right] \quad (\text{A-31})$$

$$\nabla^2 g = \frac{1}{r} \frac{\partial}{\partial r} \left(r \frac{\partial g}{\partial r} \right) + \frac{1}{r^2} \frac{\partial^2 g}{\partial \phi^2} + \frac{\partial^2 g}{\partial z^2} \quad (\text{A-32})$$

Spherical Coordinates

$$\nabla g = \hat{r} \frac{\partial g}{\partial r} + \hat{\theta} \frac{1}{r} \frac{\partial g}{\partial \theta} + \hat{\phi} \frac{1}{r \sin \theta} \frac{\partial g}{\partial \phi} \quad (\text{A-33})$$

$$\nabla \cdot \mathbf{G} = \frac{1}{r^2} \frac{\partial}{\partial r} (r^2 G_r) + \frac{1}{r \sin \theta} \frac{\partial}{\partial \theta} (G_\theta \sin \theta) + \frac{1}{r \sin \theta} \frac{\partial G_\phi}{\partial \phi} \quad (\text{A-34})$$

$$\begin{aligned} \nabla \times \mathbf{G} = & \hat{r} \frac{1}{r \sin \theta} \left[\frac{\partial}{\partial \theta} (G_\phi \sin \theta) - \frac{\partial G_\theta}{\partial \phi} \right] \\ & + \hat{\theta} \frac{1}{r} \left[\frac{1}{\sin \theta} \frac{\partial G_r}{\partial \phi} - \frac{\partial}{\partial r} (rG_\phi) \right] \\ & + \hat{\phi} \frac{1}{r} \left[\frac{\partial}{\partial r} (rG_\theta) - \frac{\partial G_r}{\partial \theta} \right] \end{aligned} \quad (\text{A-35})$$

$$\nabla^2 g = \frac{1}{r^2} \frac{\partial}{\partial r} \left(r^2 \frac{\partial g}{\partial r} \right) + \frac{1}{r^2 \sin \theta} \frac{\partial}{\partial \theta} \left(\sin \theta \frac{\partial g}{\partial \theta} \right) + \frac{1}{r^2 \sin^2 \theta} \frac{\partial^2 g}{\partial \phi^2} \quad (\text{A-36})$$

APPENDIX B

TRIGONOMETRIC RELATIONS

$$\sin(\alpha \pm \beta) = \sin \alpha \cos \beta \pm \cos \alpha \sin \beta \quad (\text{B-1})$$

$$\cos(\alpha \pm \beta) = \cos \alpha \cos \beta \mp \sin \alpha \sin \beta \quad (\text{B-2})$$

$$\sin\left(\frac{\pi}{2} \pm \alpha\right) = \cos \alpha \quad (\text{B-3})$$

$$\cos\left(\frac{\pi}{2} \pm \alpha\right) = \mp \sin \alpha \quad (\text{B-4})$$

$$\sin \alpha \cos \beta = \frac{1}{2}[\sin(\alpha + \beta) + \sin(\alpha - \beta)] \quad (\text{B-5})$$

$$\cos \alpha \sin \beta = \frac{1}{2}[\sin(\alpha + \beta) - \sin(\alpha - \beta)] \quad (\text{B-6})$$

$$\cos \alpha \cos \beta = \frac{1}{2}[\cos(\alpha + \beta) + \cos(\alpha - \beta)] \quad (\text{B-7})$$

$$\sin \alpha \sin \beta = -\frac{1}{2}[\cos(\alpha + \beta) - \cos(\alpha - \beta)] \quad (\text{B-8})$$

$$\sin \alpha = 2 \sin \frac{\alpha}{2} \cos \frac{\alpha}{2} \quad (\text{B-9})$$

$$\sin 2\alpha = 2 \sin \alpha \cos \alpha \quad (\text{B-10})$$

$$\cos \alpha = 2 \cos^2 \frac{\alpha}{2} - 1 = 1 - 2 \sin^2 \frac{\alpha}{2} \quad (\text{B-11})$$

$$\cos 2\alpha = 2 \cos^2 \alpha - 1 = \cos^2 \alpha - \sin^2 \alpha = 1 - 2 \sin^2 \alpha \quad (\text{B-12})$$

$$\cos 3\alpha = 4 \cos^3 \alpha - 3 \cos \alpha \quad (\text{B-13})$$

$$\cos 4\alpha = 8 \cos^4 \alpha - 8 \cos^2 \alpha + 1 \quad (\text{B-14})$$

$$\begin{aligned} \cos m\alpha = \cos m\alpha &= 2^{m-1} \cos^m \alpha - \frac{m}{1!} 2^{m-3} \cos^{m-2} \alpha \\ &+ \frac{m(m-3)}{2!} 2^{m-5} \cos^{m-4} \alpha + \dots \end{aligned} \quad (\text{B-15})$$

$$1 = \sin^2 \alpha + \cos^2 \alpha \quad (\text{B-16})$$

$$\sin \alpha = \alpha - \frac{\alpha^3}{3!} + \frac{\alpha^5}{5!} - \frac{\alpha^7}{7!} + \dots \quad (\text{B-17})$$

$$\cos \alpha = 1 - \frac{\alpha^2}{2!} + \frac{\alpha^4}{4!} - \frac{\alpha^6}{6!} + \dots \quad (\text{B-18})$$

$$e^{\pm j\alpha} = \cos \alpha \pm j \sin \alpha \quad (\text{B-19})$$

APPENDIX C

HYPERBOLIC RELATIONS

$$\sinh \alpha = \frac{e^{\alpha} - e^{-\alpha}}{2} = \alpha + \frac{\alpha^3}{3!} + \frac{\alpha^5}{5!} + \frac{\alpha^7}{7!} + \dots \quad (C-1)$$

$$\cosh \alpha = \frac{e^{\alpha} + e^{-\alpha}}{2} = 1 + \frac{\alpha^2}{2!} + \frac{\alpha^4}{4!} + \frac{\alpha^6}{6!} + \dots \quad (C-2)$$

$$\tanh \alpha = \frac{\sinh \alpha}{\cosh \alpha} = \frac{1}{\coth \alpha} \quad (C-3)$$

$$\sinh(\alpha \pm j\beta) = \sinh \alpha \cos \beta \pm j \cosh \alpha \sin \beta \quad (C-4)$$

$$\cosh(\alpha \pm j\beta) = \cosh \alpha \cos \beta \pm j \sinh \alpha \sin \beta \quad (C-5)$$

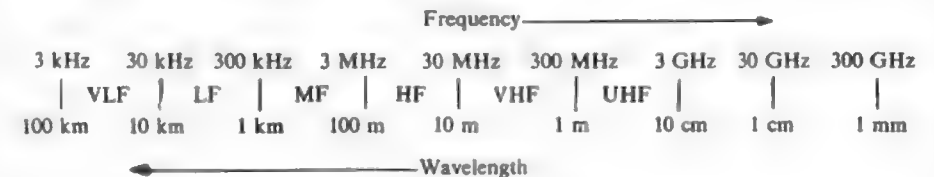
$$\sinh(j\alpha) = j \sin \alpha = \frac{e^{j\alpha} - e^{-j\alpha}}{2} \quad (C-6)$$

$$\cosh(j\alpha) = \cos \alpha = \frac{e^{j\alpha} + e^{-j\alpha}}{2} \quad (C-7)$$

APPENDIX D

TABLES OF COMMONLY USED FREQUENCIES

D.1 RADIO FREQUENCY BANDS



D.2 TELEVISION CHANNEL FREQUENCIES

VHF

Channel no.	Frequency range (MHz)	Channel no.	Frequency range (MHz)
2	54-60	8	180-186
3	60-66	9	186-192
4	66-72	10	192-198
5	76-82	11	198-204
6	82-88	12	204-210
7	174-180	13	210-216

UHF

Channel no.	Frequency range (MHz)	Channel no.	Frequency range (MHz)	Channel no.	Frequency range (MHz)
14	470-476	30	566-572	46	662-668
15	476-482	31	572-578	47	668-674
16	482-488	32	578-584	48	674-680
17	488-494	33	584-590	49	680-686
18	494-500	34	590-596	50	686-692
19	500-506	35	596-602	51	692-698
20	506-512	36	602-608	52	698-704
21	512-518	37	608-614	53	704-710
22	518-524	38	614-620	54	710-716
23	524-530	39	620-626	55	716-722
24	530-536	40	626-632	56	722-728
25	536-542	41	632-638	57	728-734
26	542-548	42	638-644	58	734-740
27	548-554	43	644-650	59	740-746
28	554-560	44	650-656	...	
29	560-566	45	656-662	83	884-890

Note: The carrier frequency for the video portion is the lower frequency plus 1.25 MHz. The audio carrier frequency is the upper frequency minus 0.25 MHz. All channels have a 6-MHz bandwidth. For example, Channel 2 video carrier is at 55.25 MHz and the audio carrier is at 59.75 MHz.

D.3 RADAR BANDS

World War II band designations		New IEEE band designations	
		hf	3-30 MHz
		vlf	30-300 MHz
		uhf	300-1000 MHz
L	390-1550 MHz	L-band	1-2 GHz
S	1550-3900 MHz	S-band	2-4 GHz
C	3.9-6.2 GHz	C-band	4-8 GHz
X	6.2-12.9 GHz	X-band	8-12 GHz
Ku	12.9-18 GHz	K _u -band	12-18 GHz
K	18-26.5 GHz	K-band	18-27 GHz
Ka	26.5-40 GHz	K _a -band	27-40 GHz
		Millimeter	40-300 GHz

APPENDIX E

CONDUCTOR DATA

E.1 CONDUCTIVITIES OF GOOD CONDUCTORS

Conductor	Conductivity (mhos/m)
Silicon steel	2×10^6
Brass	1.1×10^7
Aluminum	3.5×10^7
Gold	4.1×10^7
Copper	5.7×10^7
Silver	6.1×10^7

E.2 WIRE DATA

Wire size AWG	Diameter in mm (in.)	Single copper wire continuous duty current capacity (A)	Copper wire dc resistance per unit length (ohms/100 m)
8	3.264 (0.1285)	73	0.1952
9	2.906 (0.1144)		0.2462
10	2.588 (0.1019)	55	0.3103
11	2.305 (0.0907)		0.3914
12	2.053 (0.0808)	41	0.4935
13	1.828 (0.0720)	—	0.6224
14	1.628 (0.0641)	32	0.7849
16	1.291 (0.0508)	22	1.248
18	1.024 (0.0403)	16	1.984
20	0.812 (0.0320)	11	3.155
22	0.644 (0.0253)		5.017

APPENDIX
F

SOME USEFUL
MATHEMATICAL RELATIONS

F.1 DIRAC DELTA FUNCTION

The Dirac delta function (or impulse function) is zero everywhere except when the argument is zero

$$\delta(x - x_0) = 0 \quad \text{for } x \neq x_0. \tag{F-1}$$

For the zero argument case the function is singular but in a special way: the area is unity, that is,

$$\int_{-\infty}^{\infty} \delta(x - x_0) \, dx = 1. \tag{F-2}$$

Another useful property of the Dirac delta function follows,

$$\int_{-\infty}^{\infty} g(x) \delta(x - x_0) \, dx = g(x_0). \tag{F-3}$$

F.2 BINOMIAL THEOREM

$$(a+b)^n = a^n + na^{n-1}b + \frac{n(n-1)}{2!}a^{n-2}b^2 + \frac{n(n-1)(n-2)}{3!}a^{n-3}b^3 + \dots \quad (\text{F-4})$$

$$(1 \pm x)^n \approx 1 \pm nx \quad \text{for } x \ll 1 \quad (\text{F-5})$$

F.3 BESSEL FUNCTIONS

$$J_0(x) = \frac{1}{2\pi} \int_0^{2\pi} e^{jx \cos \alpha} d\alpha \quad (\text{F-6})$$

$$J_n(x) = \frac{j^{-n}}{2\pi} \int_0^{2\pi} e^{jx \cos \alpha} \cos(n\alpha) d\alpha \quad (\text{F-7})$$

$$= \sum_{m=0}^{\infty} \frac{(-1)^m x^{2m+n}}{m!(m+n)! 2^{2m+n}}$$

$$J_n(x) = \frac{2(n-1)}{x} J_{n-1}(x) - J_{n-2}(x) \quad (\text{F-8})$$

$$\int x^{n+1} J_0(x) dx = x^{n+1} J_{n+1}(x) \quad (\text{F-9})$$

$$\int_0^1 (1-x^2)^n x J_0(bx) dx = \frac{2^n n!}{b^{n+1}} J_{n+1}(b) \quad (\text{F-10})$$

F.4 SOME USEFUL INTEGRALS

$$\int \sin(ax+bx)e^{cx} dx = \frac{e^{cx}}{b^2+c^2} [c \sin(ax+bx) - b \cos(ax+bx)] \quad (\text{F-11})$$

$$\int_{-\infty}^{\infty} \frac{\sin^2 x}{x^2} dx = \pi \quad (\text{F-12})$$

$$\text{Si}(x) = \int_0^x \frac{\sin \tau}{\tau} d\tau \quad \text{sine integral} \quad (\text{F-13})$$

$$\text{Ci}(x) = -\int_x^{\infty} \frac{\cos \tau}{\tau} d\tau \quad \text{cosine integral} \quad (\text{F-14})$$

$$\text{Cin}(x) = \int_0^x \frac{1 - \cos \tau}{\tau} d\tau \quad (\text{F-15})$$

$$\text{Cin}(x) = 0.5772 + \ln(x) - \text{Ci}(x) \quad (\text{F-16})$$

$$C(x) = \int_0^x \cos\left(\frac{\pi}{2}\tau^2\right) d\tau; \quad C(-x) = -C(x) \quad (\text{F-17a})$$

$$S(x) = \int_0^x \sin\left(\frac{\pi}{2}\tau^2\right) d\tau; \quad S(-x) = -S(x) \quad (\text{F-17b})$$

Fresnel integrals

APPENDIX G

COMPUTER PROGRAMS

In this appendix FORTRAN statement listings of several computer programs are presented. Many are useful throughout the text. For example, the subprograms PLOT or PROFIL can be used to display data (generated by a main program) in a polar or rectangular form using the line printer of a computer. The program ARRFAC generates the array factor pattern of an equally spaced, uniformly excited linear array. The ARRPAT program is a general array program useful for any array geometry, excitations, or element type. The program NEESLAP is a general linear array factor program especially suited to the synthesis techniques of Chapter 10. The SPAP program is intended for use with the line source synthesis methods in Chapter 10 which are of the Woodward-Lawson or Taylor line source type.

G.1 LINE PRINTER POLAR PLOT SUBROUTINE—PLOT

Subroutine PLOT provides a polar plot, such as of an antenna pattern, on the line printer of a computer. It is used in conjunction with a program which generates the pattern values of a radiation pattern at 1° intervals and loads them in the data array DATA. For example DATA(1) is the pattern value at a polar angle of 1°, DATA(2) is the pattern value at angle 2°, and so on up to 360°. The

pattern does not have to be normalized to a maximum value of unity because this subroutine will automatically normalize it. In addition to the polar plot, the pattern values for all angles are tabulated. The locations and values of the pattern maxima and minima are printed out separately.

```

0001      SUBROUTINE PLOT(DATA)
0002      INTEGER LINE(131),LINE(360)
0003      REAL DATA(360)
0004      INTEGER BLANK/' ',STAR/'*',DASH/'-',VDASH/'|',ORIGIN/'C'
0005      DELTA1=1.E-07
0006      DELTA2=1.E-06
0007      AMAX=DATA(1)
0008      AMIN=DATA(1)
0009      DO 20 I=2,360
0010      IF (DATA(I)-LT.AMIN) AMIN=DATA(I)
0011      IF (DATA(I)-GT.AMAX) AMAX=DATA(I)
0012      IF ((AMAX-AMIN).GT.1.E-06) GO TO 23
0013      WRITE(6,4) AMAX
0014      4 FORMAT(1H0,7X,'NO PLOT PLOT GENERATED - - ALL VALUES EQUAL')
0015      RETURN
0016      23 CONTINUE
0017      WRITE(6,21)
0018      21 FORMAT(11,'SOX, TABLE OF DATA PLOTTED',//)
0019      WRITE(6,22)
0020      22 FORMAT(11,'S1'ANGLE',2X,'VALUE OF R',2X,'ANGLE',2X,'VALUE OF R')
0021      DO 8 I=1,60
0022      J=1+60
0023      K=J+60
0024      L=K+60
0025      M=L+60
0026      N=M+60
0027      8 WRITE(6,16) I,DATA(I),J,DATA(J),K,DATA(K),L,DATA(L),M,DATA(M),
0028      *N,DATA(N)
0029      16 FORMAT(11,'S(13,1X,E14.7,2X),13,1X,E14.7)
0030      2 FORMAT(11,'S1'ANGLE',2X,'VALUE OF R',2X,'ANGLE',2X,'VALUE OF R')
0031      1G14.7,///
0032      AMIN=AMIN/ABS(AMAX)
0033      DO 10 I=1,360
0034      DATA(I)=DATA(I)/ABS(AMAX)
0035      IF (DATA(I)-LE-1-DELTA1) WRITE(6,61) I
0036      IF (DATA(I)-GE-1-DELTA2) WRITE(6,62) I
0037      61 FORMAT(11,'MINIMUM VALUE OCCURS AT ANGLE=',14)
0038      62 FORMAT(11,'MAXIMUM VALUE OCCURS AT ANGLE=',14)
0039      10 CONTINUE
0040      WRITE(6,1)
0041      1 FORMAT(11,'S1'ANGLE',2X,'VALUE OF R',2X,'ANGLE',2X,'VALUE OF R')
0042      CONV=3.14159265/180.
0043      DO 30 I=1,360
0044      Y=ABS(DATA(I))*SIN(I*CONV)
0045      30 LINE(I)=39.5-Y*38.
0046      33 LINE(11)=BLANK
0047      LINE(66)=VDASH
0048      DO 40 J=1,77
0049      IF (J.NE.39) GO TO 60
0050      DO 100 NN=1,131
0051      LINE(NN)=DASH
0052      60 CONTINUE
0053      DO 50 I=1,360
0054      IF (LINE(I).NE.J) GO TO 50
0055      X=ABS(DATA(I))*COS(I*CONV)
0056      K=66.5+X*38.
0057      LINE(K)=STAR
0058      50 CONTINUE
0059      IF (J.EQ.39) LINE(66)=ORIGIN
0060      WRITE(6,3)(LINE(I),I=1,131)
0061      3 FORMAT(11,'S131A1)
0062      DO 120 L=1,131
0063      LINE(L)=BLANK
0064      LINE(166)=VDASH
0065      40 CONTINUE
0066      RETURN
0067      END

```

G.2 LINE PRINTER RECTANGULAR PLOT SUBROUTINE—PROFIL

Subroutine PROFIL provides a rectangular plot on the line printer of a computer. It is used for plotting patterns either as a function of angle or of a parameter such as $w = \cos \theta$. Current magnitudes and phases can also be plotted

The data values will be scaled automatically and the scale factor used will be printed. The independent variable runs down the output page and the dependent variable runs across. The exact dependent variable values in linear and decibel form are printed for each point plotted.

```

0001      SUBROUTINE PROFIL(DATA,NPT)
C THIS SUBROUTINE PRODUCES A LINE PRINTER PLOT OF THE DATA ARRAY "DATA"
C DATA(J,1) IS THE INDEPENDENT VARIABLE
C DATA(J,2) IS THE DEPENDENT VARIABLE
C NPT= NUMBER OF POINTS TO BE PLOTTED
C NO NORMALIZATION IS PERFORMED OTHER THAN 10**SF TO FIT DATA ONTO PLOT

0002      INTEGER SF
0003      INTEGER OUTPUT (101)
0004      INTEGER BLANK,PLUS,SLASH,STAR
0005      REAL DATA(401,2),BOUND(101)
0006      DATA BLANK,PLUS,SLASH,STAR/' ','+',',','*','/'

C
C      FIND THE RANGE OF DEPENDENT DATA AND SCALE IF NECESSARY

0007      IF(NPT.GT.401) GO TO 999
0008      BIG=-1.E10
0009      SMALL=1.E10
0010      DO 1 J=1,NPT
0011      IF(DATA(J,2).LT.SMALL) SMALL=DATA(J,2)
0012      IF(DATA(J,2).GT.BIG) BIG=DATA(J,2)
0013      1 CONTINUE
0014      DIFF=ABS(BIG-SMALL)
0015      SF=0
0016      IF(DIFF.GT.1.E-06) GO TO 8
0017      WRITE(6,101) DATA(1,1)
0018      101 FORMAT(1H0,7X,'NO PROFIL PLCT GENERATED -- ALL VALUES EQUAL'
C
C      1 F10.5)
0019      RETURN
0020      8 CONTINUE
0021      IF(DIFF.LT.0.1) GO TO 10
0022      IF(DIFF.E-10.) GO TO 21
0023      DO 2 J=1,10
0024      IF(DIFF*10.**(-J).GT.10.) GO TO 2
0025      SF=J
0026      GO TO 20
0027      2 CONTINUE
0028      400 WRITE(6,100)
0029      100 FORMAT('O YOUR DATA IS TOO LARGE FOR THIS PROGRAM')
0030      RETURN
0031      10 DO 3 J=1,6
0032      K=-J
0033      IF(DIFF*10**K.GT.10.) GO TO 3
0034      SF=K
0035      GO TO 20
0036      3 CONTINUE
0037      WRITE(6,102)
0038      102 FORMAT('O YOUR DATA IS TOO SMALL FOR THIS PROGRAM')
0039      20 DO 4 J=1,NPT
0040      4 DATA(J,2)=DATA(J,2)*10.**(-SF)
C
C      CALCULATE BOUNDS
0041      21 SCALE=DIFF/100.
0042      DO 5 J=1,101
0043      K=J-1
0044      5 BOUND(J)=(BIG-K*SCALE)*10.**(-SF)
C
C      PLOT PROFILE

0045      WRITE(6,4004) SF
0046      4004 FORMAT(1H1,53X,'SCALE FACTOR IS 10**',I2/)
0047      200 WRITE(6,6501)(BOUND(J),J=1,101,20)
0048      6501 FORMAT(4X,5(F7.3,13X),F7.3,2X,'REAL',4X,'DB°)
0049      DO 6 J=1,NPT
0050      6 J=1
0051      DO 50 K=1,101
0052      50 OUTPUT(K)=BLANK
0053      IF((J-1)/10*(10-(J-1)) 62,61,62

```

```

0054      61 DO 60 K=1,101,10
0055      60 OUTPUT(K)=PLUS
0056      GO TO 87
0057      62 OUTPUT(1)=SLASH
0058      OUTPUT(101)=SLASH
0059      87 DO 7 K=1,100
0060      IF (DATA(J,2)-GT-BOUNDI(K)) GO TO 7
0061      IF (DATA(J,2)-LE-BOUNDI(K+1)) GO TO 7
0062      OUTPUT(K)=STAR
0063      GO TO 69
0064      7 CONTINUE
0065      OUTPUT(101)=STAR
0066      69 IF (DATA(J,2)-EQ-0.) DATA(J,2)=1,E-6
0067      DATADB=20,1,ALG101(ABS(DATA(J,2)))
0068      IF ((J-1)/10*10-(J-1)) 140,141,140
0069      141 WRITE(6,4000) DATA(J,1),OUTPUT(K),K=1,101,DATA(J,2),DATADB
0070      4000 FORMAT(1X,F6.2,1X,101,1X,F7.3,1X,F6.2)
0071      GO TO 6
0072      140 WRITE(6,4001) OUTPUT(K),K=1,101,DATA(J,2),DATADB
0073      4001 FORMAT(1X,101,1X,F7.3,1X,F6.2)
0074      6 CONTINUE
0075      WRITE(6,650) (BOUND(J),J=1,101,20)
0076      650 RETURN
0077

```

G.3 EQUALLY SPACED, UNIFORMLY EXCITED ARRAY FACTOR PROGRAM—ARRFAC

The ARRFAC program computes the array factor values of a linear array of N equally spaced, uniformly excited elements. The main beam maximum can be steered to any specified direction θ_0 . It has been coded to use with the PLOT line printer plotting subroutine described in Section G.1.

```

C * * * * * ARRFACT * * * * *
C THIS PROGRAM COMPUTES AND PLOTS THE ARRAY FACTOR FOR AN EQUALLY
C SPACED UNIFORMLY EXCITED LINEAR ARRAY OF N ELEMENTS SPACED 0
C WAVELENGTHS APART WITH ALPHA INTERELEMNT PHASING
C THE SUBROUTINE PLOT IS REQUIRED TO GENERATE THE PATTERN PLOT
0001 REAL*8 PSI,FN
0002 DIMENSION DATA(360)
0003 CONTINUE
0004 1 READ(5,70,END=99) N,D,THETA0
0005 70 FORMAT(15,2F10.0)
C N=NUMBER OF ELEMENTS
C D=INTERELEMNT SPACING(WAVELENGTHS)
C THETA0=ANGLE OF MAIN BEAM MAXIMUM RELATIVE TO THE LINE
C OF THE ARRAY (IN DEGREES)
C
0006 PI=3.14159265
0007 DTR=PI/180.
0008 ALPHA=-2.*PI*1D*COS(THETA0*DTR)
C ALPHA=INTERELEMNT PHASE SHIFT
C
C ARRAY FACTOR OF AN EQUALLY SPACED ARRAY
C FN=N
C DC 10 I=1,360
C THETA=I*DTR
C PSI=2.*PI*D*COS(THETA)+ALPHA
C DATA(I)=1.
C IF(PSI.EQ.0.) DATA(I)=DSIN(FN*PSI/2.)/(FN*DSIN(PSI/2.))
C CONTINUE
C CALL PLOT(DATA)
C ALPHA=ALPHA/DTR
C NTEST=ALPHA/360.
C IF(NTTEST.GE.1 .OR. NTEST.LE.-1) ALPHA=ALPHA-NTEST*360.
C IF(ABS(ALPHA).LT.1.E-03) ALPHA=0.
C WRITE(6,80) N,D,THETA0,ALPHA
C 80 FORMAT(10X,'THE NUMBER OF ELEMENTS=N=',15/10X,'THE SPACINGS=D=',
C 1 F10.4,' WAVELENGTHS' /10X,'THE DESIRED MAIN BEAM MAXIMUM DIRECTI
C 2ON=THETA0=',F10.4,' DEGREES' /10X,'THE REQUIRED PHASE SHIFT BETWEEN
C 3N ELEMENTS=ALPHA=',F10.4,' DEGREES')
C GO TO 1
C 99 END
0023
0024
0025

```

The array information is inputted on one card (or card image) with an (I5, 2F10.0) format. First the number of elements N is given as an integer. Next the interelement spacing D in wavelengths is specified as a real number. And finally, the angle THETA θ relative to the line of the array is entered as a real number and is in degrees. Several arrays can be computed with a single computer run by stacking data cards, one card for each array.

The output from ARRFAC is the polar pattern generated by PLOT. Also, all input information is printed, as well as the interelement phase shift required to steer the main beam to the desired angle.

G.4 COMPLETE PATTERN PROGRAM FOR AN ARBITRARY ARRAY—ARRPAT

The program ARRPAT is used to compute and display the complete radiation pattern of an arbitrary antenna array. The array factor is computed in the subroutine ARFACT. The subroutine ELPAT performs the element pattern computations. It contains five element pattern types: isotropic (NETYPE=0), half-wave dipoles parallel to the z-axis (NETYPE=1) or x-axis (NETYPE=2), and short dipoles parallel to the z-axis (NETYPE=3) or x-axis (NETYPE=4). Other element types can be handled by adding the appropriate coding within ELPAT.

The input to the program begins with one card image with the integers N, NETYPE, and NPOINT using a 3I2 format. N is the number of elements in the array. NETYPE is the element type number as described above. NPOINT is set to zero unless it is desired to have the program adjust the element excitation phases to steer the main beam maximum to the (θ_0, ϕ_0) direction, in which case NPOINT is set to unity. If NPOINT=1 the next card image read in contains THETA0 and PHI0 in degrees using a floating point format with a field length of 10. The remaining card images are N in number, one for each element. Each of these card images contains five numbers in an 8F10.4 field. The first three are the x, y, and z coordinates for the element center location in wavelengths. The remaining two numbers are the current amplitude and phase (in degrees) for that element. There are no restrictions on the element locations and excitations.

The program outputs all element location and excitation data. If the beam is to be steered to (θ_0, ϕ_0) the phase is adjusted from that inputted to the program such that the desired beam pointing is accomplished. Next the pattern information is displayed for the xz, yz, and xy planes. In each plane both polar and rectangular plots are given.

The subroutines PLOT and PROFIL in Sections G.1 and G.2 must be added to the source listing below.

```

C ***** ARRPAT *****
C THE ARRPAT PROGRAM PRODUCES PATTERN PLOTS IN THE 3 PRINCIPAL
C PLANES FOR ANY 3-DIMENSIONAL ARRAY ANTENNA CONFIGURATION.
C THE ELEMENT POSITIONS, AMPLITUDES, AND PHASES ARE INPUTS.
C THE MAIN BEAM CAN BE STEERED TO POINTING ANGLE THETA0 IF
C DESIRED.
C ELEMENT PATTERNS ARE IN SUBPROGRAM ELPAT.
C
0001 REAL DATA(401,2)
0002 REAL DATA(360)
0003 DIMENS(CN,X(20),Y(20),Z(20),A(20),ALPHA(20)
0004 COMMON/BLOC1/ X,Y,Z,A,ALPHA
0005 COMMON/BLOC2/ N
C
0006 PI=3.14159265
0007 DTR=PI/180.
C
0008 1 CONTINUE
0009 READ(5,95,END=95) N,NETYPE,NPOINT
0010 FORMAT(3I2)
C
C *****
C 95 N=NUMBER OF ELEMENTS
C THETA0,PHI0= MAIN BEAM POINTING ANGLES IN DEGREES
C NETYPE= ELEMENT TYPE NUMBER
C 0: ISOTROPIC ELEMENTS
C 1: COLLINEAR HALF WAVE DIPOLES PARALLEL TO THE Z-AXIS
C 2: PARALLEL HALF WAVE DIPOLES PARALLEL TO THE X-AXIS
C 3: COLLINEAR SHORT DIPOLES PARALLEL TO THE Z-AXIS
C 4: PARALLEL SHORT DIPOLES PARALLEL TO THE X-AXIS
C
C NPOINT= 1 IF ELEMENT PHASES ARE TO BE ADJUSTED FOR STEERING
C THE MAIN BEAM IN THE (THETA0,PHI0) DIRECTION
C 0 IF NOT
C
0011 WRITE(6,86)
0012 FORMAT(1H1,40X,'ARRPAT'////)
0013 IF(NETYPE.EQ.0) WRITE(6,87)
0014 FORMAT(/' THE ELEMENTS ARE ISOTROPIC')
0015 IF(NETYPE.EQ.1) WRITE(6,88)
0016 FORMAT(/' THE ELEMENTS ARE COLLINEAR HALF-WAVE DIPOLES PARALLEL TO
0017 1 THE Z-AXIS')
0018 IF(NETYPE.EQ.2) WRITE(6,89)
0019 FORMAT(/' THE ELEMENTS ARE PARALLEL HALF-WAVE DIPOLES PARALLEL TO'
0020 1 ' THE X-AXIS')
0021 IF(NETYPE.EQ.3) WRITE(6,180)
0022 FORMAT(/' THE ELEMENTS ARE COLLINEAR SHORT DIPOLES PARALLEL TO THE
0023 1 Z-AXIS')
0024 IF(NETYPE.EQ.4) WRITE(6,181)
0025 FORMAT(/' THE ELEMENTS ARE SHORT DIPOLES PARALLEL TO THE X-AXIS')
C
0026 IF(APOINT.EQ.0) GO TO 42
0027 READ(5,201) THETA0,PHI0
0028 FORMAT(2F10.4)
C
0029 THETA0,PHI0= MAIN BEAM POINTING ANGLES IN DEGREES
0030 WRITE(6,96) THETA0,PHI0
0031 FORMAT(' THE BEAM IS TO BE STEERED TO THETA0=°,F10.5,
0032 1 ° DEGREES AND PHI0=°,F10.5, ° DEGREES')
0033 42 CONTINUE
C
0034 DO 45 I=1,N
0035 READ(5,90) X(I),Y(I),Z(I),A(I),ALPHA(I)
0036 ALPHA(I)=ALPHA(I)*DTR
0037 45 CONTINUE
0038 IF(NPOINT.EQ.0) GO TO 41
0039 THETA0=THETA0*DTR
0040 PHI0=PHI0*DTR
0041 DO 40 I=1,N
0042 ALPHA(I)=2.*PI*(X(I)*SIN(THETA0)*COS(PHI0)+Y(I)*SIN(THETA0)*SIN(P
0043 1 HI0)+Z(I)*COS(THETA0))+ALPHA(I)
0044 CONTINUE
0045 WRITE(6,83)
0046 FORMAT(1H0,///13X,'ELEMENT LOCATIONS, CURRENTS AND PHASES'
0047 1//5X,'1,5X,'X(I)',6X,'Y(I)',6X,'Z(I)',6X,'A(I)',4X,'ALPHA(I)')
0048 DO 43 I=1,N
0049 ALPDEG=ALPHA(I)*DTR
0050 WRITE(6,85) I,X(I),Y(I),Z(I),A(I),ALPDEG
0051 FORMAT(1H ,15,5F10.4)
0052 43 CONTINUE
C
C AZ-PLANE PATTERN
C
0053 PHI=0.
0054 DATA(1,1)=0.
0055 DATA(1,2)=ELPAT(0.,PHI,NETYPE)*ARFACT(0.,PHI)
0056 ENAX=DATA(1,2)
0057 DO 10 I=2,361
0058 J=I-1
0059 THETA=J*DTR
0060 DATA(J)=ELPAT(THETA,PHI,NETYPE)*ARFACT(THETA,PHI)
0061 IF(DATA(J).GT.ENAX) ENAX=DATA(J)
0062 IF(I.GT.181) GO TO 10
0063 DATA(1,1)=J
0064 DATA(1,2)=ELPAT(THETA,PHI,NETYPE)*ARFACT(THETA,PHI)
0065 10 CONTINUE
0066 IF(ENAX.EQ.0.) GO TO 12
0067 DATA(1,2)=DATA(1,2)/ENAX
0068 DO 11 I=2,361
0069 J=I-1
0070 DATA(I)=DATA(J)/ENAX
0071 IF(I.LE.181) DATA(1,2)=DATA(1,2)/ENAX
0072 11 CONTINUE
0073 12 CONTINUE
0074 WRITE(6,81)
0075 FORMAT(1H1,'XZ-PLANE PATTERN PLOT'///3X,'X-AXIS IS VERTICAL AND Z-A
0076 1 XIS IS HORIZONTAL'//23X,'ANGLE IS THETA')
0077 WRITE(6,111) ENAX

```

```

CALL PPLDT(DATA)
CALL PROFIL(DATA1,181)

C YZ-PLANE PATTERN
PHI=90.*DTR
DATA1(1,1)=0
DATA1(1,2)=ELPAT(0.,PHI,NETYPE)*ARFACT(0.,PHI)
EMAX=DATA1(1,2)
DO 20 I=2,361
  J=I-1
  THETA=J*DTR
  DATA(J)=ELPAT(THETA,PHI,NETYPE)*ARFACT(THETA,PHI)
  IF(CAT(J).GT.EMAX) EMAX=DATA(J)
  IF(I.GT.181) GO TO 20
  DATA1(1,1)=J
  DATA1(1,2)=ELPAT(THETA,PHI,NETYPE)*ARFACT(THETA,PHI)
20  CONTINUE
  IF(EMAX.EQ.0.) GO TO 22
  DATA1(1,2)=DATA1(1,2)/EMAX
  DO 21 I=2,361
    J=I-1
    DATA(J)=DATA(J)/EMAX
    IF(I.LE.181) DATA1(1,2)=DATA1(1,2)/EMAX
  21  CONTINUE
22  CONTINUE
WRITE(6,82)
82  FORMAT(1H,'YZ-PLANE PATTERN PLOT',//3X,'Y-AXIS IS VERTICAL AND Z-A
  X IS IS HORIZONTAL',//3X,'ANGLE IS THETA')
WRITE(6,111) EMAX
CALL PPLDT(DATA)
CALL PROFIL(DATA1,181)

C XY-PLANE PATTERN
THETA=90.*DTR
DATA1(1,1)=0
DATA1(1,2)=ELPAT(THETA,0.,NETYPE)*ARFACT(THETA,0.)
EMAX=DATA1(1,2)
DO 30 I=2,361
  J=I-1
  PHI=J*DTR
  DATA1(1,1)=J
  DATA1(1,2)=ELPAT(THETA,PHI,NETYPE)*ARFACT(THETA,PHI)
  DATA1(1,2)=DATA(J)
  IF(DATA(J).GT.EMAX) EMAX=DATA(J)
30  CONTINUE
  IF(EMAX.EQ.0.) GO TO 32
  DATA1(1,2)=DATA1(1,2)/EMAX
  DO 31 I=2,361
    J=I-1
    DATA(J)=DATA(J)/EMAX
    DATA1(1,2)=DATA1(1,2)/EMAX
  31  CONTINUE
32  CONTINUE
WRITE(6,110)
110 FORMAT(1H,'XY-PLANE PATTERN PLOT',//3X,'Y-AXIS IS VERTICAL AND X-
  AXIS IS HORIZONTAL',//3X,'ANGLE IS PHI')
WRITE(6,111) EMAX
111 FORMAT(1H,'THE PATTERN HAS BEEN DIVIDED BY EMAX=',F10.6)
CALL PPLDT(DATA)
CALL PROFIL(DATA1,361)
GO TO 1
99  STOP
END

```

J001

```

FUNCTION ARFACT(THETA,PHI)
C THIS SUBPROGRAM RETURNS THE ARRAY FACTOR VALUE OF A GENERAL ARRAY
  AT THE ANGLE (THETA,PHI)
C THE ARRAY FACTOR IS UNNORMALIZED
  COMPLEX TEMP,CEXP,IMAG,CABS
  DIMENSION X(20),Y(20),Z(20),A(20),ALPHA(20)
  COMMON/BLOC1/ X,Y,Z,A,ALPHA
  COMMON/BLOC2/ N
C PI=3.14159265
  IMAG=(0.,1.)
  TEMP=(0.,0.)
  DO 10 I=1,N
    TEMP=TEMP+A(I)*CEXP(IMAG*2.*PI*(X(I)*SIN(THETA)*COS(PHI)
  1  +Y(I)*SIN(THETA)*SIN(PHI)+Z(I)*COS(THETA))+IMAG*ALPHA(I))
  10  CONTINUE
  ARFACT=CABS(TEMP)
  IF(ARFACT.LT.1.E-06) ARFACT=0.
  RETURN
END

```

J001

```

FUNCTION ELPAT(THETA,PHI,NETYPE)
C THIS SUBPROGRAM RETURNS THE ELEMENT PATTERN VALUE FOR THE
  ANGLE (THETA,PHI)
C NETYPE IS A PARAMETER FOR THE VARIOUS ELEMENT TYPES
C PI=3.14159265
  ELPAT=1.0
C TYPE 1: NETYPE=1
  COLLINER HALF-WAVE DIPOLES PARALLEL TO THE Z-AXIS
  IF(NETYPE.NE.1) GO TO 10
  ELPAT=0.0
  ST=SIN(THETA)
  IF(ABS(ST).GT.1.E-5) ELPAT=COS(PI*COS(THETA)/2.)/ST
  10  CONTINUE
C TYPE 2: NETYPE=2
  PARALLEL HALF-WAVE DIPOLES PARALLEL TO THE X-AXIS
  IF(NETYPE.NE.2) GO TO 20
  T1=SIN(THETA)*COS(PHI)

```

```

0011 T2=SQRT(1.-T1*T1)
0012 IF(T2.EQ.0.) ELPAT=0.
0013 IF(T2.NE.0.) ELPAT=COS(PI*T1/2.)/T2
0014 CONTINUE
20 TYPE 3: NETYPE=3
  SHORT DIPOLES PARALLEL TO THE Z-AXIS
  IF(NETYPE.NE.3) GO TO 30
  ELPAT=SIN(THETA)
  CONTINUE
30 TYPE 4: NETYPE=4
  SHORT DIPOLES PARALLEL TO X-AXIS
  IF(NETYPE.NE.4) GO TO 40
  T1=SIN(THETA)*COS(PHI)
  ELPAT=SQRT(1.-T1*T1)
40 CONTINUE
  RETURN
  END
0018
0019
0020
0021
0022
0023

```

G.5 NONUNIFORMLY EXCITED, (UN)EQUALLY SPACED LINEAR ARRAY PROGRAM—NEESLAP

The NEESLAP program is used to plot the array factor of a linear array, either equally or unequally spaced. The plot is given as a function of $w = \cos \theta$ as employed in Chapter 10.

The first card image inputted to the program is to contain the number of elements NP in an I5 format. This is followed by NP number of card images, one for each element. Each of these contains the position (in wavelengths), the current amplitude, and the current phase (in degrees) in a 3F10.5 format.

All input data is printed out, followed by the pattern plot of the array factor. The subroutine PROFIL of Section G.2 is to be added to the statement listing below.

```

C ***** NEESLAP *****
C NONUNIFORMLY EXCITED, (UN)EQUALLY SPACED LINEAR ARRAY PROGRAM
C THIS PROGRAM PLOTS THE ARRAY FACTOR MAGNITUDE FOR A NONUNIFORMLY
  EXCITED EQUALLY (OR UNEQUALLY) SPACED LINEAR ARRAY
C
  COMPLEX IMAG,TEMP
  REAL DATA(401,2)
  REAL S(25),A(25),PHASE(25)
C
  PI=3.14159265
  DTR=PI/180.
  IMAG=(0.,1.)
C
  READ(5,80) NP
  FORMAT(15)
  DO 10 I=1,NP
    READ(5,81) S(I),A(I),PHASE(I)
    FORMAT(3F10.5)
  10  CONTINUE
C NP= NUMBER OF ELEMENTS
C I= ELEMENT NUMBER
C S(I)= POSITION OF ITH ELEMENT/WAVELENGTH
C A(I),PHASE(I)= AMPLITUDE AND PHASE OF CURRENT OF ITH ELEMENT
  WRITE(6,90)
90  FORMAT(1H,42X,'***** NEESLAP *****')
  WRITE(6,91) NP
91  FORMAT(1H,15X,'THE NUMBER OF ARRAY ELEMENTS =',I5)
  WRITE(6,92)
92  FORMAT(1H,75X,'I',4X,'S(I)',4X,'A(I)',4X,'PHASE(I)')
  WRITE(6,93) (I,S(I),A(I),PHASE(I),I=1,NP)
93  FORMAT(1H,15,F10.4,F10.6,F10.4)
C
  PATTERN COMPUTATION
C
  W=-1.0
  DO 30 J=1,401
    TEMP=(0.,0.)
    DO 20 I=1,NP
      TEMP=TEMP+A(I)*CEXP(IMAG*2.*PI*S(I)+IMAG*PHASE(I)*DTR)
    20  CONTINUE
    DATA1(J,1)=W
    DATA1(J,2)=CABS(TEMP)
    W=W+0.005
  30  CONTINUE
C PRINT OUT RESULTS
  WRITE(6,94)
94  FORMAT(1H,50X,'THE PATTERN MAGNITUDE PROFILE')
  CALL PROFIL(DATA1,401)
  STOP
  END
0001
0002
0003
0004
0005
0006
0007
0008
0009
0010
0011
0012
0013
0014
0015
0016
0017
0018
0019
0020
0021
0022
0023
0024
0025
0026
0027
0028
0029
0030
0031
0032
0033
0034
0035

```

G.6 SAMPLING PATTERN ANTENNA PROGRAM—SPAP

The SPAP program computes and displays the pattern, current amplitude distribution, and current phase distribution for a line source antenna whose pattern can be described by a sum of sampling functions. This pattern class includes the Woodward-Lawson and Taylor line sources described in Chapter 10.

The first card image required for input contains the number of Sa functions NP and the length of the line source LEN in wavelengths in an (I10, F10.5) format. The following input card images (NP in number) each contain the sample locations in the pattern variable w and the pattern sample values in an 8F10.6 format.

The output begins with a printing of all input data. Next the pattern is plotted as a function of $w = \cos \theta$. This is followed by plots of the current amplitude and phase as a function of position along the line source in wavelengths.

The subroutine PROFIL of Section G.2 must be added to the following statement listing.

```

C ***** SAMPLING PATTERN ANTENNA PROGRAM (SPAP) *****
C THIS PROGRAM COMPUTES AND PLOTS ANY PATTERN EXPRESSIBLE AS A SUM
C OF SAMPLING FUNCTIONS --
C SUCH AS WOODWARD-LAWSON AND TAYLOR LINE SOURCES
C THE CURRENT MAGNITUDE AND PHASE ARE ALSO PLOTTED
C
C REAL LEN
C REAL WN(25),A(25)
C COMPLEX CTMP,CURREN
C COMMON/BLOC1/TYPE,PI
C COMMON/BLOC1/LEN,NP,WN,A
C
C PI=3.14159265
C DTR=PI/180.
C
C WRITE(6,70)
C 70 FORMAT(1H1,5X,'SPAP - SAMPLING PATTERN ANTENNA PROGRAM')
C 71 FORMAT(1H1,10X,LEN,NP)
C 71 FORMAT(1H1,10.5)
C NP= NUMBER OF SAMPLING FUNCTIONS
C LEN= APERTURE LENGTH IN WAVELENGTHS
C DO 15 I=1,NP
C READ(5,72) WN(I),A(I)
C 72 FORMAT(1H1,10.6)
C 15 CONTINUE
C WRITE(6,80)
C 80 FORMAT(1H0,'THIS PATTERN IS EXPRESSIBLE AS A SUM OF SA FUNCTION')
C WRITE(6,81) LEN,NP
C 81 FORMAT(1H0,'APERTURE LENGTH= LEN=',F8.4,
C 1 ' WAVELENGTHS'//1H,'NUMBER OF SAMPLE POINTS= NP=',15)
C WRITE(6,82)
C 82 FORMAT(1H0,4X,'1',4X,'WN(I)',4X,'A(I)')
C 83 FORMAT(1H0,15,2F10.6)
C PATTERN PLOT IN VARIABLE W
C WRITE(6,85)
C 85 FORMAT(1H1,'W-PROFILE PLOT OF PATTERN')
C W=-1.0
C DO 20 I=1,401
C DATA(1,1)=W
C DATA(1,2)=PAT(W)
C W=W+0.005
C 20 CONTINUE
C CALL PROFIL(DATA1,401)
C
C CURRENT MAGNITUDE PLOT IN VARIABLE S
C S= APERTURE POSITION/WAVELENGTH
C
C WRITE(6,86)
C 86 FORMAT(1H1,'CURRENT MAGNITUDE PLOT AS A FUNCTION OF S')
C DELTA=LEN/200.
C S=LEN/2
C DO 30 I=1,201

```

```

0039 DATA(1,1)=S
0040 DATA(1,2)= CABS(CURREN(S))
0041 S=S+DELTA
0042 CONTINUE
0043 CALL PROFIL(DATA1,201)
C
C CURRENT PHASE PLOT
C WRITE(6,87)
C 87 FORMAT(1H1,'CURRENT PHASE PLOT AS A FUNCTION OF S')
C S=LEN/2
C DELTA=LEN/200.
C DO 40 I=1,201
C DATA(1,1)=S
C CTMP=CURREN(S)
C CR=REAL(CTMP)
C CI=AIMAG(CTMP)
C IF (ABS(CI).LT. 1.E-5 .AND. ABS(CR).LT.1.E-5) GO TO 41
C IF (ABS(CI).LT. (ABS(CR)*1.E-5)) CI=0.
C DATA(1,2)= ATAN2(CI,CR)/DTR
C GO TO 42
C 41 DATA(1,2)=0.
C 42 CONTINUE
C S=S+DELTA
C 40 CONTINUE
C CALL PROFIL(DATA1,201)
C STOP
C END
C
C FUNCTION PAT(W)
C THIS SUBPROGRAM GENERATES PATTERN VALUES FOR AN INPUT VALUE OF W
C REAL LEN
C REAL WN(25),A(25)
C COMMON/BLOC1/TYPE,PI
C COMMON/BLOC1/LEN,NP,WN,A
C
C PAT=0.
C DO 25 I=1,NP
C IF (W.EQ.WN(I)) GO TO 26
C PAT=PAT+A(I)*SIN((W-WN(I))*LEN*PI)/((W-WN(I))*LEN*PI)
C 25 CONTINUE
C 26 PAT=PAT+A(I)
C 26 CONTINUE
C 26 RETURN
C 26 END
C
C FUNCTION CURREN(S)
C THIS SUBPROGRAM GENERATES CURRENT VALUES CORRESPONDING TO THE
C PATTERN IN PAT
C REAL LEN
C REAL WN(25),A(25)
C COMPLEX CURREN,IMAG,CEXP,CABS
C COMMON/BLOC1/TYPE,PI
C COMMON/BLOC1/LEN,NP,WN,A
C
C IMAG=(0.,1.)
C
C CURREN=(0.,0.)
C DO 20 I=1,NP
C CURREN=CURREN+A(I)*CEXP(-IMAG*2.*PI*WN(I)*S)/LEN
C 20 CONTINUE
C GO TO 99
C 99 RETURN
C 99 END

```

G.7 MOMENT METHOD PROGRAM FOR A CENTER-FED DIPOLE

The computer program in this appendix uses pulse expansion functions and point-matching to analyze a center-fed linear dipole. A general subroutine for solving a toeplitz matrix is included.

The variables in the main program are

- A = wire radius in wavelengths
- N = number of segments
- L = length of the dipole in wavelengths

The main program ends just after statement 40. The first subroutine, which follows the main program, uses Simpson's rule to numerically integrate Pocklington's integral equation, the kernel of which is numerically evaluated in the second subroutine. The third subroutine evaluates the generalized voltage matrix using (7-81). The fourth subroutine solves a system of equations with toeplitz properties as discussed in Section 7-8. The parameters necessary to use this subroutine are described in the subroutine listing. Sample output from the first row of the generalized impedance matrix and the corresponding solution for the current matrix are listed at the end of the program.

C MOMENT METHOD (POINT MATCHING) PROGRAM FOR A CENTER FED DIPOLE
C OF LENGTH L AND RADIUS A WITH MAGNETIC FRILL GENERATOR

```
REAL L,LL,LLP
COMPLEX I(201),V(201),J,ZZ(201),AM(201),AM1(201)
COMPLEX INGRK,EINC,KERNEL
COMMON/CNSTNS/A,A2,B,B2,J
A=.005
N=100
L=.47
DELZ=L/N
PI=3.141592624
J=(0.,1.)
B=2.*PI
B2=B*B
A2=A*A
LL=-.5*L
LLP=LL
DELZO2=DELZ*.5
Z=LL+DELZO2
```

C FILL VOLTAGE MATRIX AND FIRST ROW OF IMPEDANCE MATRIX

```
DO 100 II=1,N
UL=LL+DELZ
ZM=LL+DELZO2
NINT=INT(80.0001-II*(60./N))
ZZ(II)=-4.7724*J*INGRKL(NINT,LL,UL,Z)
V(II)=-EINC(ZM)
```

100 LL=UL

C WRITE OUT INPUT PARAMETERS AND FIRST ROW OF IMPEDANCE MATRIX

```
WRITE(6,10) N,L,A
10 FORMAT(1H,30X,'INPUT PARAMETERS'//1H,27X,'N=' ,I5
2,' SEGMENTS'//1H,27X,'L=' ,F8.5,' WAVELENGTHS'//1H,27X
3,'A=' ,F8.5,' WAVELENGTHS'//1H,20X,'FIRST ROW OF'
4,' IMPEDANCE MATRIX Z(1,N)'//1H,19X,'N',12X,'REAL',14X
5,'IMAGINARY'//
DO 200 K=1,N,5
```

200 WRITE(6,20) K,ZZ(K)

20 FORMAT(1H,18X,I3,2(1PE20.7))

C CALL TOEPLITZ MATRIX SOLVING SUBROUTINE

CALL TPLZ(ZZ,AM,AM1,N,V,I,1,XNORM,IER)

C WRITE OUT CURRENT VECTOR

```
WRITE(6,30)
30 FORMAT(1H//1H,29X,'CURRENT VECTOR I(N)'//1H,19X,'N'
2,12X,'REAL',14X,'IMAGINARY'//
DO 300 KK=1,N,5
300 WRITE(6,40) KK,I(KK)
40 FORMAT(1H,18X,I3,2(1PE20.7))
CALL EXIT
END
```

C THIS SUBPROGRAM USES SIMPSON'S RULE TO NUMERICALLY INTEGRATE
C POCKLINGTON'S EQUATION

```
COMPLEX FUNCTION INGRKL(NINT,LL,UL,Z)
REAL LL
COMPLEX KERNEL,S,HALF
H=(UL-LL)/NINT
HOVER2=.5*H
S=(0.,0.)
HALF=KERNEL(Z,LL+HOVER2)
NINTM1=NINT-1
DO 100 I=1,NINTM1
ZP=LL+I*H
S=S+KERNEL(Z,ZP)
100 HALF=HALF+KERNEL(Z,ZP+HOVER2)
INGRKL=(H/6.)*(KERNEL(Z,LL)+KERNEL(Z,UL)+4.*HALF+2.*S)
RETURN
END
```

C THIS SUBPROGRAM COMPUTES VALUES OF THE INTEGRAND IN
C POCKLINGTON'S EQUATION

```
COMPLEX FUNCTION KERNEL(Z,ZP)
COMPLEX J
COMMON/CNSTNS/A,A2,B,B2,J
R=SQRT(Z*Z-2.*Z*ZP+ZP*ZP+A2)
R2=R*R
R5=R2*R2*R
KERNEL=CEXP(-J*B*R)*((1.+J*B*R)*(2.*R2-3.*A2)+B2*A2*R2)/R5
RETURN
END
```

C THIS SUBPROGRAM COMPUTES THE INCIDENT FIELD FROM A MAGNETIC
C FRILL GENERATOR

```
COMPLEX FUNCTION EINC(Z)
COMPLEX J
COMMON/CNSTNS/A,A2,B,B2,J
R1=SQRT(Z*Z+A2)
R2=SQRT(Z*Z+4.9729*A2)
EINC=.62344*((CEXP(-J*B*R1)/R1)-(CEXP(-J*B*R2)/R2))
RETURN
END
```

C SUBROUTINE TPLZ

SUBROUTINE TPLZ(TAU,A,A1,NZ,VIN,VOUT,MM,XNORM,IER)

PURPOSE

TO SOLVE A SYSTEM INVOLVING A TOEPLITZ MATRIX. TPLZ REQUIRES
ONLY 5N STORAGE LOCATIONS FOR AN N BY N MATRIX.
REMARKS

A TOEPLITZ MATRIX HAS THE FIRST ROW EQUAL TO THE FIRST COLUMN.
ALL ELEMENTS ALONG THE MAIN DIAGONAL ARE EQUAL. ANY DIAGONAL OFF
THE MAIN DIAGONAL WILL HAVE THIS SAME PROPERTY.

DESCRIPTION OF PARAMETERS

```
NZ -ORDER OF MATRIX.
TAU -FIRST ROW OR COLUMN OF THE TOEPLITZ MATRIX (VECTOR
LENGTH NZ).
A,A1 -ARE VECTORS OF LENGTH NZ NEEDED FOR SCRATCH AREA.
VIN -FOR THE MATRIX EQUATION (Z)(I)=(V), VIN IS V. (Z,I,
-AND V MAY BE THOUGHT OF AS GENERALIZED IMPEDANCES,
CURRENTS, AND VOLTAGES, RESPECTIVELY). V IS A NZ BY
MM MATRIX.
MM -NUMBER OF COLUMN VECTORS ON RIGHT SIDE OF MATRIX
EQUATION (Z)(I)=(V) (USUALLY 1).
VOUT -SOLUTION I, OF MATRIX EQUATION (Z)(I)=(V). SOLUTION I
WILL BE AN NZ BY MM MATRIX.
XNORM -UPON RETURN THIS IS INFINITE MATRIX NORM OF INVERSE.
IER -ERROR CODE WHICH IS 0 IF NO TROUBLE.
COMPLEX TAU1,ALMDA,ALPHA,COEF,FAC,C1,C2,V,V1,V2
COMPLEX TAU(NZ),A(1),A1(1),VIN(1),VOUT(1),ONE,ZERO
DATA ONE/(100,000),ZERO/(000,000)/
```

```

DATA ONNE/1D0/,ZRR0/0D0/
N=NZ-1
IER=0
C NORMALIZE INPUT MATRIX
TAU1=TAU(1)
DO 2000 II=1,N
2000 TAU(II)=TAU(II+1)/TAU1
C THE FOLLOWING CALCULATES THE ITERATIVE VARIABLES TO OBTAIN
C A(N) AND ALMDA
C NOTE--VECTOR A(I) HAS 1 ELEMENTS AND IS STORED AS A(I,J),J=1,N
ALMDA=ONE-TAU(1)*TAU(1)
A(1)=-TAU(1)
I=2
1 KK=I-1
ALPHA=ZERO
DO 2 M=1,KK
LL=I-M
2 ALPHA=ALPHA+A(M)*TAU(LL)
ALPHA=-(ALPHA+TAU(I))
IF(CABS(ALPHA).EQ.0.00)GO TO 15
COEF=ALPHA/ALMDA
ALMDA=ALMDA-COEF*ALPHA
DO 3 J=1,KK
L=I-J
3 A1(J)=A(J)+COEF*A(L)
DO 7 J=1,KK
7 A(J)=A1(J)
A(I)=COEF
IF(I.GE.N)GO TO 5
I=I+1
GO TO 1
C THE FOLLOWING COMPUTES THE VALUES OF EACH ELEMENT OF THE INVERSE
5 NH=(NZ+1)/2
FAC=ALMDA*TAU1
XNORM=ZRR0
NP=NZ+1
DO 51 I=1,NH
XNM=ZRR0
IF(I.NE.1)GO TO 52
A1(1)=ONE/FAC
XNM=CABS(A1(1))
DO 53 J=2,NZ
A1(J)=A(J-1)/FAC
53 XNM=CABS(A1(J))+XNM
GO TO 54
52 XNM=ZRR0
JH=I-1
C1=A(JH)
NNPI=NP-I
C2=A(NNPI)
DO 55 JJ=1,N
J=NP-JJ
INPJ=NP-J
JL=J-1
A1(J)=A1(JL)+(C1*A(JL)-C2*A(INPJ))/FAC
55 XNM=CABS(A1(J))+XNM
A1(1)=A(I-1)/FAC
XNM=XNM+CABS(A1(1))
54 IF(XNM.GT.XNORM)XNORM=XNM
C MATRIX MULTIPLY
DO 56 II=1,NH
ID=(II-1)*NZ
V=ZERO
V1=ZERO
DO 57 J=1,NZ

```

```

NIDJ=ID+J
V2=VIN(NIDJ)
V=V+V2*A1(J)
KNPJ=NP-J
57 V1=V1+V2*A1(KNPJ)
NIDI=ID+I
VOUT(NIDI)=V
KIDNPI=ID+NP-I
56 VOUT(KIDNPI)=V1
51 CONTINUE
RETURN
15 WRITE(6,700)

```

```

700 FORMAT('ERROR HAS OCCURED. MATRIX IS NOT STRONGLY NONSING')
IER=I
RETURN
END

```

INPUT PARAMETERS

N = 100 SEGMENTS
 L = .47000 WAVELENGTHS
 A = .00500 WAVELENGTHS

FIRST ROW OF IMPEDANCE MATRIX Z(1,N)

N	REAL	IMAGINARY	
1	-3.7077354E 0	1.3292525E 5	
6	-3.7004581E 0	-3.1099197E -3	
11	-3.6762423E 0	-4.3794510E -2	
16	-3.6362100E 0	-1.3827604E -2	
21	-3.5807025E 0	-6.2208773E -1	
26	-3.5102238E 0	-3.4051417E -1	
31	-3.4254281E 0	-2.1043779E -1	
36	-3.3270940E 0	-1.4076802E -1	
41	-3.2161212E 0	-9.9253023E -2	
46	-3.0935175E 0	-7.2439429E -2	
51	-2.9603874E 0	-5.4004493E -2	
56	-2.8179189E 0	-4.0693520E -2	
61	-2.6673696E 0	-3.0706081E -2	
66	-2.5100518E 0	-2.2986110E -2	
71	-2.3473177E 0	-1.6882066E -2	
76	-2.1805437E 0	-1.1979006E -2	
81	-2.0111146E 0	-7.9952716E -3	
86	-1.8404086E 0	-4.7396833E -3	
91	-1.6697817E 0	-2.0754298E -3	
96	-1.5005532E 0	9.7914246E -3	

CURRENT VECTOR I(N)			
N	REAL	IMAGINARY	
1	1.2423271E -3	-5.4686438E -4	
6	3.2532785E -3	-1.3818655E -3	
11	5.8296498E -3	-2.8684541E -3	
16	6.6899289E -3	-2.6858456E -3	
21	8.8181647E -3	-3.8234319E -3	
26	9.2231882E -3	-3.3132956E -3	
31	1.8235584E -2	-3.4687881E -3	
36	1.1833953E -2	-3.4813235E -3	
41	1.1686299E -2	-3.3359889E -3	
46	1.1943624E -2	-2.9984341E -3	
51	1.2848478E -2	-2.3718673E -3	
56	1.1895277E -2	-3.8884781E -3	
61	1.1518392E -2	-3.3788629E -3	
66	1.8892817E -2	-3.4988893E -3	
71	1.8849795E -2	-3.4487937E -3	
76	8.9961888E -3	-3.2658522E -3	
81	7.7447318E -3	-2.9498932E -3	
86	6.3882528E -3	-2.5862547E -3	
91	4.6914498E -3	-1.9368344E -3	
96	2.8678654E -3	-1.2258823E -3	

The program uses a block toeplitz subroutine which is called after statement 200. After this call statement, the input impedances and far-field pattern are calculated. The magnitude of the input impedance is given by ZMAG and its phase by ZPHASE. The terminal current is given by IMAG. The far-field values are stored in the complex quantity E.

Some sample output data are given after the program listing and corresponds to that in Fig. 7-24b.

```

PROGRAM XIXI
C MOMENT METHOD (PIECEWISE SINUSOIDS) PROGRAM FOR ARRAY OF
C EQUALLY SPACED, IDENTICAL, PARALLEL, LINEAR DIPOLES. THE
C ARRAY CONFIGURATION MAY BE LINEAR (IND=1) OR CIRCULAR (IND=2)
REAL L, L1, L2, L3, L4, L5, L6, L7, L8, L9, L10, L11, L12, L13, L14, L15, L16, L17, L18, L19, L20, L21, L22, L23, L24, L25, L26, L27, L28, L29, L30, L31, L32, L33, L34, L35, L36, L37, L38, L39, L40, L41, L42, L43, L44, L45, L46, L47, L48, L49, L50, L51, L52, L53, L54, L55, L56, L57, L58, L59, L60, L61, L62, L63, L64, L65, L66, L67, L68, L69, L70, L71, L72, L73, L74, L75, L76, L77, L78, L79, L80, L81, L82, L83, L84, L85, L86, L87, L88, L89, L90, L91, L92, L93, L94, L95, L96, L97, L98, L99, L100, L101, L102, L103, L104, L105, L106, L107, L108, L109, L110, L111, L112, L113, L114, L115, L116, L117, L118, L119, L120, L121, L122, L123, L124, L125, L126, L127, L128, L129, L130, L131, L132, L133, L134, L135, L136, L137, L138, L139, L140, L141, L142, L143, L144, L145, L146, L147, L148, L149, L150, L151, L152, L153, L154, L155, L156, L157, L158, L159, L160, L161, L162, L163, L164, L165, L166, L167, L168, L169, L170, L171, L172, L173, L174, L175, L176, L177, L178, L179, L180, L181, L182, L183, L184, L185, L186, L187, L188, L189, L190, L191, L192, L193, L194, L195, L196, L197, L198, L199, L200, L201, L202, L203, L204, L205, L206, L207, L208, L209, L210, L211, L212, L213, L214, L215, L216, L217, L218, L219, L220, L221, L222, L223, L224, L225, L226, L227, L228, L229, L230, L231, L232, L233, L234, L235, L236, L237, L238, L239, L240, L241, L242, L243, L244, L245, L246, L247, L248, L249, L250, L251, L252, L253, L254, L255, L256, L257, L258, L259, L260, L261, L262, L263, L264, L265, L266, L267, L268, L269, L270, L271, L272, L273, L274, L275, L276, L277, L278, L279, L280, L281, L282, L283, L284, L285, L286, L287, L288, L289, L290, L291, L292, L293, L294, L295, L296, L297, L298, L299, L300, L301, L302, L303, L304, L305, L306, L307, L308, L309, L310, L311, L312, L313, L314, L315, L316, L317, L318, L319, L320, L321, L322, L323, L324, L325, L326, L327, L328, L329, L330, L331, L332, L333, L334, L335, L336, L337, L338, L339, L340, L341, L342, L343, L344, L345, L346, L347, L348, L349, L350, L351, L352, L353, L354, L355, L356, L357, L358, L359, L360, L361, L362, L363, L364, L365, L366, L367, L368, L369, L370, L371, L372, L373, L374, L375, L376, L377, L378, L379, L380, L381, L382, L383, L384, L385, L386, L387, L388, L389, L390, L391, L392, L393, L394, L395, L396, L397, L398, L399, L400, L401, L402, L403, L404, L405, L406, L407, L408, L409, L410, L411, L412, L413, L414, L415, L416, L417, L418, L419, L420, L421, L422, L423, L424, L425, L426, L427, L428, L429, L430, L431, L432, L433, L434, L435, L436, L437, L438, L439, L440, L441, L442, L443, L444, L445, L446, L447, L448, L449, L450, L451, L452, L453, L454, L455, L456, L457, L458, L459, L460, L461, L462, L463, L464, L465, L466, L467, L468, L469, L470, L471, L472, L473, L474, L475, L476, L477, L478, L479, L480, L481, L482, L483, L484, L485, L486, L487, L488, L489, L490, L491, L492, L493, L494, L495, L496, L497, L498, L499, L500, L501, L502, L503, L504, L505, L506, L507, L508, L509, L510, L511, L512, L513, L514, L515, L516, L517, L518, L519, L520, L521, L522, L523, L524, L525, L526, L527, L528, L529, L530, L531, L532, L533, L534, L535, L536, L537, L538, L539, L540, L541, L542, L543, L544, L545, L546, L547, L548, L549, L550, L551, L552, L553, L554, L555, L556, L557, L558, L559, L560, L561, L562, L563, L564, L565, L566, L567, L568, L569, L570, L571, L572, L573, L574, L575, L576, L577, L578, L579, L580, L581, L582, L583, L584, L585, L586, L587, L588, L589, L590, L591, L592, L593, L594, L595, L596, L597, L598, L599, L600, L601, L602, L603, L604, L605, L606, L607, L608, L609, L610, L611, L612, L613, L614, L615, L616, L617, L618, L619, L620, L621, L622, L623, L624, L625, L626, L627, L628, L629, L630, L631, L632, L633, L634, L635, L636, L637, L638, L639, L640, L641, L642, L643, L644, L645, L646, L647, L648, L649, L650, L651, L652, L653, L654, L655, L656, L657, L658, L659, L660, L661, L662, L663, L664, L665, L666, L667, L668, L669, L670, L671, L672, L673, L674, L675, L676, L677, L678, L679, L680, L681, L682, L683, L684, L685, L686, L687, L688, L689, L690, L691, L692, L693, L694, L695, L696, L697, L698, L699, L700, L701, L702, L703, L704, L705, L706, L707, L708, L709, L710, L711, L712, L713, L714, L715, L716, L717, L718, L719, L720, L721, L722, L723, L724, L725, L726, L727, L728, L729, L730, L731, L732, L733, L734, L735, L736, L737, L738, L739, L740, L741, L742, L743, L744, L745, L746, L747, L748, L749, L750, L751, L752, L753, L754, L755, L756, L757, L758, L759, L760, L761, L762, L763, L764, L765, L766, L767, L768, L769, L770, L771, L772, L773, L774, L775, L776, L777, L778, L779, L780, L781, L782, L783, L784, L785, L786, L787, L788, L789, L790, L791, L792, L793, L794, L795, L796, L797, L798, L799, L800, L801, L802, L803, L804, L805, L806, L807, L808, L809, L810, L811, L812, L813, L814, L815, L816, L817, L818, L819, L820, L821, L822, L823, L824, L825, L826, L827, L828, L829, L830, L831, L832, L833, L834, L835, L836, L837, L838, L839, L840, L841, L842, L843, L844, L845, L846, L847, L848, L849, L850, L851, L852, L853, L854, L855, L856, L857, L858, L859, L860, L861, L862, L863, L864, L865, L866, L867, L868, L869, L870, L871, L872, L873, L874, L875, L876, L877, L878, L879, L880, L881, L882, L883, L884, L885, L886, L887, L888, L889, L890, L891, L892, L893, L894, L895, L896, L897, L898, L899, L900, L901, L902, L903, L904, L905, L906, L907, L908, L909, L910, L911, L912, L913, L914, L915, L916, L917, L918, L919, L920, L921, L922, L923, L924, L925, L926, L927, L928, L929, L930, L931, L932, L933, L934, L935, L936, L937, L938, L939, L940, L941, L942, L943, L944, L945, L946, L947, L948, L949, L950, L951, L952, L953, L954, L955, L956, L957, L958, L959, L960, L961, L962, L963, L964, L965, L966, L967, L968, L969, L970, L971, L972, L973, L974, L975, L976, L977, L978, L979, L980, L981, L982, L983, L984, L985, L986, L987, L988, L989, L990, L991, L992, L993, L994, L995, L996, L997, L998, L999, L1000

```

G.8 MOMENT METHOD PROGRAM FOR AN ARRAY OF EQUALLY SPACED, PARALLEL DIPOLES

The computer program listed in this appendix will compute the pattern (in azimuth) of an array of vertical (i.e., z-directed) linear dipoles with equal spacing (only). The array may be either linear or circular. The resulting generalized impedance matrix is block toeplitz.

The program employs the piecewise sinusoid in the Galerkin formulation described in Section 7.5.3. The dipoles may have lumped loads as described in Section 7.9.1. If only far-field patterns are needed, the number of expansion functions does not have to be large (e.g., NP \approx 5 per dipole).

The program as given here is set up to analyze a 12-dipole linear array with $\lambda/2$ spacing between dipoles. The dipoles are all $\lambda/2$ in length and have a radius of 0.0001 λ . To change the array configuration, it is necessary to change some of the following parameters.

- A = dipole radius in wavelengths
- L = dipole length in wavelengths
- NW = number of dipoles
- NP = number of piecewise sinusoids per dipole
- SPACE = dipole to dipole spacing in wavelengths
- IND = 1 for a linear array, 2 for a circular array
- ZLOAD = value of the terminal load impedance (may be zero)

```

100 ZZ(INDEXZ)=INGRLK(NINT,ZMM,ZM,ZMP,ZNM,ZN,ZNP,D)
200 ZMM=ZMP-DZ
    MP=((NP*NP)+1.01)/2.
    ZZ(MP)=ZZ(MP)+7LOAD
C CALL THE BLOCK TOEPLITZ SUBROUTINE
    CALL BLTSOL(ZZ,V,PS,NW,NP,44)
C COMPUTE INPUT IMPEDANCES AND FAR FIELD PATTERN(Z= 0 PLANE)
    DO 300 I5=1,NW
        AF(I5)=(0.,0.)
    DO 300 I4=1,NP
        INDEXV=I4+(I5-1)*NP
        IF(I4.EQ.NP/2+1)IZ(I5)=-CEXP(-B*J*X(I5)*COS(PHIOR))
    2/V(INDEXV)
300 AF(I5)=AF(I5)+V(INDEXV)
    DO 400 I7=1,361
        PHI=(I7-1)*DEGRAD
        E(I7)=(0.,0.)
    DO 400 I6=1,NW
        IF(IND.EQ.1)E(I7)=E(I7)+AF(I6)*CEXP(J*B*X(I6)*COS(PHI))
400 IF(IND.EQ.2)E(I7)=E(I7)+AF(I6)*CEXP(J*B*R*COS(PHI-(I6-1.)
    2*PHIS))
C CALL PLOT ROUTINE FOR FAR-FIELD PATTERN (OPTIONAL)
    WRITE(6,10)NW,NP,L,A,SPACE
10 FORMAT(1H,20X,'INPUT PARAMETER'//1H,22X,'NW='I3/1H,22X
    2'NP='I3/1H,22X,'L='F8.5/1H,22X,'A='F8.5/1H,22X
    3'SPACE='F8.5///1H,2X,'N',7X,'XN',9X,'YN',7X
    4,'ZMAG',7X,'ZPHASE',6X,'INORM'//)
    IMAX=0
    DO 500 I8=1,NW
        ZMAG(I8)=CABS(IZ(I8))
        S2=REAL(IZ(I8))
        S1=AIMAG(IZ(I8))
        ZPHASE(I8)=RADDEG*ATAN2(S1,S2)
        IMAG(I8)=1./ZMAG(I8)
500 IF(IMAG(I8).GT.IMAX)IMAX=IMAG(I8)
    DO 600 I9=1,NW
        IMAG(I9)=IMAG(I9)/IMAX
600 WRITE(6,20)I9,X(I9),Y(I9),ZMAG(I9),ZPHASE(I9),
    2IMAG(I9)
20 FORMAT(1H,I3,5F11.3)
    STOP
    END
C THIS SUBROUTINE USES SIMPSON'S RULE TO NUMERICALLY
C INTEGRATE FOR IMPEDANCE ELEMENTS USING EQUATION (7-60)
    COMPLEX FUNCTION INGRK(NINT,ZMM,ZM,ZMP,ZNM,ZN,ZNP,D)
    COMPLEX K1,K2,S1,S2,HALF1,HALF2,INGRL1,INGRL2
    COMMON/CNSTNS/J,B2,A2,B
    H1=(ZM-ZMM)/NINT
    H2=(ZMP-ZM)/NINT
    H102=0.5*H1
    H202=0.5*H2
    S1=(0.,0.)
    S2=S1
    CALL KERNEL(K1,K2,ZMM,ZM,ZMP,ZNM,ZN,ZNP,ZMM+H102,
    2ZM+H202,D)
    HALF1=K1
    HALF2=K2
    NINTM1=NINT-1
    DO 100 I=1,NINTM1
        Z1=ZMM+I*H1
        Z2=ZM+I*H2
        CALL KERNEL(K1,K2,ZMM,ZM,ZMP,ZNM,ZN,ZNP,Z1,Z2,D)
        S1=S1+K1
        S2=S2+K2
    CALL KERNEL(K1,K2,ZMM,ZM,ZMP,ZNM,ZN,ZNP,Z1+H102,Z2+
    2H202,D)
    HALF1=HALF1+K1
    100 HALF2=HALF2+K2
    INGR1=4.*HALF1+2.*S1
    INGR2=4.*HALF2+2.*S2

```

```

    CALL KERNEL(K1,K2,ZMM,ZM,ZMP,ZNM,ZN,ZNP,ZMM,ZM,D)
    INGR1=INGRL1+K1
    INGR2=INGRL2+K2
    CALL KERNEL(K1,K2,ZMM,ZM,ZMP,ZNM,ZN,ZNP,ZM,ZMP,D)
    INGR1=H1*(INGRL1+K1)/6.
    INGR2=H2*(INGRL2+K2)/6.
    INGRK=INGRL1+INGRL2
    RETURN
    END
C THIS SUBROUTINE COMPUTES VALUES OF INTEGRAND IN
C EQUATION (7-60)
    SUBROUTINE KERNEL(K1,K2,ZMM,ZM,ZMP,ZNM,ZN,ZNP,Z1,Z2,D)
    COMPLEX K1,K2,J
    COMMON/CNSTNS/J,B2,A2,B
    D2=D*D
    Z12=Z1*Z1
    Z22=Z2*Z2
    DZM=ZMP-ZM
    DZN=ZNP-ZN
    RNM1=SQRT(D2+(Z1-ZNM)*(Z1-ZNM))
    RN1=SQRT(D2+(Z1-ZN)*(Z1-ZN))
    RNP1=SQRT(D2+(Z1-ZNP)*(Z1-ZNP))
    RNM2=SQRT(D2+(Z2-ZNM)*(Z2-ZNM))
    RN2=SQRT(D2+(Z2-ZN)*(Z2-ZN))
    RNP2=SQRT(D2+(Z2-ZNP)*(Z2-ZNP))
    K1=30.*J*(CEXP(-J*B*RNM1)/RNM1-2.*COS(B*DZN)*CEXP(-J*B*RN1)
    2/RN1+CEXP(-J*B*RNP1)/RNP1)/SIN(B*DZM)
    K2=30.*J*(CEXP(-J*B*RNM2)/RNM2-2.*COS(B*DZN)*CEXP(-J*B*RN2)
    2/RN2+CEXP(-J*B*RNP2)/RNP2)/SIN(B*DZM)
    K1=K1*SIN(B*(Z1-ZMM))/SIN(B*DZM)
    K2=K2*SIN(B*(Z2-ZM))/SIN(B*DZM)
    RETURN
    END
    SUBROUTINE BLTSOL(Z,V,PS,NW,NP,IENTRY)
    COMPLEX Z(1),V(1),PS(1)
    DIMENSION IA(2)
    GO TO (41,42,43,44),IENTRY
44 CONTINUE
    IRET=0
    GO TO 1
    SUBROUTINE SOLVE FOR I THE MATRIX EQUATION V=ZI WHERE Z IS
    C ASYMMETRIC BLOCK-TOEPLITZ MATRIX OF ORDER NW*NP. EACH BLOCK IS
    C OF ORDER NP AND AN NW XNW PARTITIONING IS USED
    C V IS A SPECIFIED VECTOR OF LENGTH NW*NP. ON RETURN FROM BLTSOL
    C I IS STORED IN PLACE OF V
    C PS IS AN ARRAY FOR SCRATCH STORAGE.
    C STORAGE REQUIREMENTS ARE
    C Z(NW*NP**2) (I.E.,THE FIRST ROW OF NP X NP BLOCKS)
    C Z MATRIX IS FILLED BY COLUMNS, I.E.,Z((J-1)*NP+I)=Z(I,J)
    C V(NW*NP)
    C PS((2*NW+1)*NP**2) (FOR TEMPORARY STORAGE)
    C BOTH NP AND NW MUST BE GREATER THAN OR EQUAL TO 2.
    C ALL ARRAYS ARE COMPLEX.
    C CONTENTS OF Z ARE DESTROYED.
    C ENTRY (IENTRY) POINTS ARE AS FOLLOWS..
    C (1)= LINSET(Z,PS,NW,NP) FACTORIZES THE Z MATRIX-STEPS I AND IF.
    C (2) NEWRHS (V) MUST BE PRECEDED BY A CALL TO LINSET. CAN CALL
    C THIS ENTRY POINT A NUMBER OF TIMES TO SOLVES FOR CURRENT FOR
    C DIFFERENT V BUT THE SAME Z FACTORED BY INITIAL CALL TO LINSET.
    C (3) NEWFAC(Z,PS,NW,NP) CALLED TO RESET ADDRESSES. MUST BE CALLED
    C IF PS ARRAY, NW,NP ARE STORED ON TAPE AND REREAD FOR SUBSEQUENT
    C CALLS TO NEWRHS.
    C (4) BLTSOL(Z,V,PS,NW,NP) EQUIVALENT TO CALLS TO LINSET AND NEWRHS.
    C FACTORED ARRAY REMAINS FOR POSSIBLE REUSE BY FURTHER CALLS TO
    C NEWRHS OR PS ARRAY CAN BE SAVED ON TAPE FOR LATER USE.
    C ENTRY LINSET(Z,PS,NW,NP)

```

```

41 CONTINUE
   IRET=1
   GO TO 1
C   ENTRY NEWFAC(Z,PS,NW,NP)
42 CONTINUE
   N=NW-1
   N2=NP**2
   I=NW*N2+N2+1
   J=N2+1
   IF(MOD(N,2))2,2,3
C   N EVEN
2   IPHI=J-N2
   IPSI=I
   GO TO 4
C   N ODD
3   IPHI=I-N2
   IPSI=J
4   RETURN
C   ENTRY POINT IF A PREVIOUS CALL MADE TO BLTSOL AND NOW ONLY
C   SPECIFY A NEW RHS
C   ENTRY NEWRHS
43 CONTINUE
   GO TO 68
C   CALC DEL(-1) AND PS((0),0)
1   N=NW-1
   IF(NW.LT.2)GO TO 100
   IF(NP.LT.2)GO TO 101
   N2=NP*NP
   DO 5 I=1,N2
   WRITE(8,-)I,Z(I)
5   PS(I)=Z(I)
   CALL LINEQ(PS,NP)
   CALL MATMLT(PS,Z(N2+1),PS(N2+1),NP)
   IA(1)=START ADDRESS IN PS ARRAY OF PS((M-1),0)
C   IA(2)=START ADDRESS IN PS ARRAY OF PS((M),0)
C   IA(1N2)=START ADDRESS IN PS ARRAY OF DEL((M-1)
C   IA(2)-N2=START ADDRESS IN PS ARRAY OF DEL(M-1)
C   IST+I=2*NW*N2+1=START ADDRESS OF ADDITIONAL SCRATCH AREA
   IA(1)=N2+1
   IA(2)=NW*N2+N2+1
   IST=2*NW*N2
   MZ=N2+N2+1
   MM=0
C   ITERATE ON M=1,2,...N. FOR M=N, ONLY CALC DEL(M-1)
DO 45 M=1,N
   IO=IA(1)+MM
   MM=MM+N2
   I1=IA(2)+MM
C   IO IS START ADDRESS OF PS((M-1),M-1)
C   I1 IS START ADDRESS OF PS((M),M)
C   CALC DEL(M-1)
   CALL MATMLT(PS(IO),PS(IO),PS(IST+1),NP)
   IJ=IST
   DO 20 J=1,NP
   DO 20 I=1,NP
   IJ=IJ+1
   PS(IJ)=-PS(IJ)
20  IF(I.EQ.J)PS(IJ)=PS(IJ)+1.
   CALL LINEQ(PS(IST+1),NP)
   ID=IA(1)-N2
   ID1=IA(2)-N2
   CALL MATMLT(PS(IST+1),PS(ID),PS(ID1),NP)
   IF(M.EQ.N)GO TO 50
C   CALC PS((M),M)
   MZZ=MZ
   MS=IA(1)

```

```

   IJ=IST
   DO 25 I=1,N2
   IJ=IJ+1
   PS(IJ)=Z(MZZ)
25  MZZ=MZZ+1
   MZZ=MZ-N2
   DO 30 IS=1,M
   CALL TRMMLT(PS(MS),Z(MZZ),PS(IST+1),NP)
C   TRMMLT ACCUMULATES -TRANSP(PS(MS))*Z(MZZ)
   MS=MS+N2
30  MZZ=MZZ-N2
   MZ=MZ+N2
   CALL MATMLT(PS(ID1),PS(IST+1),PS(I1),NP)
C   CALC PS((M),R) FOR R=0,1,...M-1. (IR=R)
   IOR=IA(1)
   I1R=IA(2)
   IMR=IO
   DO 40 IR=1,M
   CALL MATMLT(PS(IMR),PS(I1),PS(IST+1),NP)
   IMR=IMR-N2
   IJ=IST
   DO 40 I=1,N2
   PS(I1R)=PS(IOR)-PS(IJ+1)
   IJ=IJ+1
   I1R=I1R+1
   IOR=IOR+1
40  I=IA(1)
   IA(1)=IA(2)
   IA(2)=I
C   HAVE FINISHED ITERATION ON PS. NOW PUT PHI(R) INTO PS(IA(2))
50  IPHI=IA(2)-N2
   IPSI=IA(1)
   IOR=IA(1)
   I1R=IA(2)
   DO 60 I=1,N
   CALL MULTTR(PS(IPHI),PS(IOR),PS(I1R),NP)
   IOR=IOR+N2
60  I1R=I1R+N2
C   PUT PHI(-1) IN PS(IPHI)
   J=IPHI
   DO 65 I=1,N2
   PS(J)=-PS(J)
65  J=J+1
C   NOW HAVE PHI(S), S=-1,0,1,...N-1 STARTING AT PS(IPHI)
C   AND   PSI(S), S=0,1,...N-1 STARTING AT PS(IPSI)
C   FROM A AND B IN Z ARRAY
   IF(IRET.NE.0)RETURN
68  IB=NW*NP+1
   IC=1
   J=2*NW*NP
   DO 70 I=1,J
   Z(I)=(0.,0.)
   IV=1
   DO 80 J=1,NW
   NR=NW-J+1
   I1S=IPHI
   I2S=IPHI+N*N2
   IVS=IV
   DO 75 I=1,NR
   JENTRY=1
   CALL MATVCA(PS(I1S),V(IVS),Z(IC),NP,JENTRY)
   CALL MATVCA(PS(I2S),V(IVS),Z(IB),NP,JENTRY)
   I1S=I1S+N2
   I2S=I2S+N2
75  IVS=IVS+NP
   IV=IV+NP

```

```

      IC=IC+NP
80  IB=IB+NP
C   NOW CALCULATE I IN V LOCATIONS.
      J=NW*NP
      DO 85 I=1,J
85  V(I)=-Z(I)
      IV=NP+1
      IC=1
      IB=IV+J
      DO 95 IR=1,N
      IIS=IPSI
      IIS=(N-1)*N2+IPSI
      ICS=IC
      IBS=IB
      DO 90 IS=1,IR
      JENTRY=1
      CALL MATVCA(PS(IIS),Z(ICS),V(IV),NP,JENTRY)
      JENTRY=2
      CALL MATVCA(PS(IIS),Z(ICS),V(IV),NP,JENTRY)
      IIS=IIS+N2
      IIS=IIS-N2
      ICS=ICS-NP
90  IBS=IBS-NP
      IV=IV+NP
      IC=IC+NP
95  IB=IB+NP
      GO TO 99
100 WRITE(6,1000)NW
101 WRITE(6,1001)NP
1000 FORMAT(///10X,27HILLEGAL CALL TO BLTSOL. NW, I6)
1001 FORMAT(///10X,27HILLEGAL CALL TO BLTSOL. NP=,I6)
99  RETURN
END
C   INVERSION OF COMPLEX MATRIX C, OF ORDER LL. INVERSE IS RETURNED IN
C   PLACE OF C
      SUBROUTINE LINEQ(C,LL)
      COMPLEX C(1),STOR,STO,ST,S
      DIMENSION LR(77)
      COMPLEX X
      CABQ(X)=REAL(X)*REAL(X)+AIMAG(X)*AIMAG(X)
      DO 20 I=1,LL
      LR(I)=I
20  CONTINUE
      M1=0
      DO 18 M=1,LL
      K=M
      DO 2 I=M,LL
      K1=M1+I
      K2=M1+K
      IF(CABQ(C(K1))-CABQ(C(K2)))2,2,6
6   K=I
2   CONTINUE
      LS=LR(M)
      LR(M)=LR(K)
      LR(K)=LS
      K2=M1+K
      STOR=C(K2)
      J1=0
      DO 7 J=1,LL
      K1=J1+K
      K2=J1+M
      STO=C(K1)
      C(K1)=C(K2)
      C(K2)=STO/STOR
      J1=J1+LL
7   CONTINUE

```

```

      K1=M1+M
      C(K1)=1./STOR
      DO 11 I=1,LL
      IF(I-M)12,11,12
12  K1=M1+I
      ST=C(K1)
      C(K1)=(0.,0.)
      J1=0
      DO 10 J=1,LL
      K1=J1+I
      K2=J1+M
      C(K1)=C(K1)-C(K2)*ST
      J1=J1+LL
10  CONTINUE
11  CONTINUE
      M1=M1+LL
18  CONTINUE
      J1=0
      DO 9 J=1,LL
      IF(J-LR(J))14,8,14
14  LRJ=LR(J)
      J2=(LRJ-1)*LL
21  DO 13 I=1,LL
      K2=J2+I
      K1=J1+I
      S=C(K2)
      C(K2)=C(K1)
      C(K1)=S
13  CONTINUE
      LR(J)=LR(LRJ)
      LR(LRJ)=LRJ
      IF(J-LR(J))14,8,14
8   J1=J1+LL
9   CONTINUE
      RETURN
      END
C   SUBROUTINE MATMLT(A,B,C,NP)
      CALCULATES C=A*B. A,B,C ARE NP X NP MATRICES OF COMPLEX NUMBER.
      COMPLEX A(1),B(1),C(1),D
      IJ=0
      L=1
      DO 15 J=1,NP
      DO 10 I=1,NP
      IJ=IJ+1
      D=(0.,0.)
      KJ=L
      IK=I
      DO 5 K=1,NP
      D=D+A(IK)*B(KJ)
      IK=IK+NP
5   KJ=KJ+1
10  C(IJ)=D
15  L=L+NP
      RETURN
      END
C   SUBROUTINE TRMMLT(A,B,C,NP)
      ACCUMULATES IN C -TRANS P(A)*B
      COMPLEX A(1),B(1),C(1),D
      IJ=0
      L=1
      DO 15 J=1,NP
      M=1
      DO 10 I=1,NP
      IJ=IJ+1
      D=(0.,0.)
      KI=M

```

```

KJ=L
DO 5 K=1,NP
D=D+A(KI)*B(KJ)
KI=KI+1
5 KJ=KJ+1
M=M+NP
10 C(IJ)=C(IJ)-D
15 L=L+NP
RETURN
END
SUBROUTINE MULTTR(A,B,C,NP)
CALCULATES C=A*TRANSPOSE(B)
COMPLEX A(1),B(1),C(1),D
IJ=0
DO 10 J=1,NP
DO 10 I=1,NP
IJ=IJ+1
D=(0.,0.)
IK=I
JK=J
DO 5 K=1,NP
D=D+A(IK)*B(JK)
IK=IK+NP
JK=JK+NP
5 C(IJ)=D
10 RETURN
END
SUBROUTINE MATVCA(A,B,C,N,JENTRY)
POSITIVE ACCUMULATION OF A*B IN C, WHERE A IS AN N X N MATRIX
B IS AN N-VECTOR, C IS AN N-VECTOR. ALL ARE COMPLEX
COMPLEX A(1),B(1),C(1),D
GO TO (32,33),JENTRY
32 IGO=1
GO TO 1
33 CONTINUE
NEGATIVE ACCUMULATION - SYMBOLS AS ABOVE
IGO=2
DO 10 J=1,N
D=(0.,0.)
IJ=J
DO 5 I=1,N
D=D+A(IJ)*B(I)
5 IJ=IJ+NP
GO TO (6,7),IGO
6 C(J)=C(J)+D
GO TO 10
7 C(J)=C(J)-D
10 CONTINUE
RETURN
END

```

INPUT PARAMETER

```

NW= 12
NP= 5
L= 0.50000
A= 0.00010
SPACE= 0.50000

```

N	XN	YN	ZMAG	ZPHASE	INORM
1	-2.750	0.000	137.142	22.772	1.000
2	-2.250	0.000	170.822	20.875	0.803
3	-1.750	0.000	176.438	15.464	0.777
4	-1.250	0.000	170.084	12.902	0.806
5	-0.750	0.000	163.760	12.917	0.837
6	-0.250	0.000	160.597	14.044	0.854
7	0.250	0.000	160.244	15.339	0.856
8	0.750	0.000	161.925	16.427	0.847
9	1.250	0.000	165.529	17.132	0.829
10	1.750	0.000	171.673	16.975	0.799
11	2.250	0.000	180.566	14.436	0.760
12	2.750	0.000	183.893	3.838	0.746

G.9 DIFFRACTION COEFFICIENT COMPUTER PROGRAM

The subroutine listing given below will compute the diffraction coefficients D_{\perp} and D_{\parallel} presented in Section 9.5 for the wedge of interior angle $(2-n)\pi$. The subroutine will also compute the slope diffraction coefficients associated with the perpendicular and parallel cases. The latter slope diffraction coefficient is discussed in Section 9.8.

To use the subroutine, it is only necessary to know the calling parameters in line 1, which are

DS = diffraction coefficient $D_{\parallel}(L, \phi, \phi')$
 DH = diffraction coefficient $D_{\perp}(L, \phi, \phi')$
 DPS = slope diffraction coefficient for the parallel case
 DPH = slope diffraction coefficient for the perpendicular case
 R = distance parameter L
 PH = angle ϕ
 PHP = angle ϕ'
 BO = angle γ_0
 FN = n of the interior wedge angle $(2-n)\pi$

As an example of the use of subroutine DW, consider the E -plane analysis of the horn antenna in Section 9.6. In writing a "main program" to analyze the horn antenna we would call, for example, DW (X, DPER, X, X, RL, PHI, 0.0, 90.0, 2.0) where X is a variable not used in the program. We must supply the subroutine with RL and PHI, and it will return DPER.

The user of subroutine DW may verify the statement listing by calculating the diffracted field in Fig. 9-16.


```

SUBROUTINE DW(DS,DH,DPS,DPH,R,PH,PHP,BO,FN)
C *** WEDGE DIFFRACTION AND SLOPE DIFFRACTION COEFFICIENT ***
C *** FOR THE SOFT AND HARD B.C. ***
COMPLEX DIN,DIP,DPM,DPP,DS,DH,DPS,DPH
CALL DI(DIN,R,BETN,BO,FN)
CALL DI(DIP,R,BETP,BO,FN)
CALL DP(DPP,R,BETP,BO,FN)
DS=(D.,D.)
DH=DIN
DPS=DPM
DPH=(D.,D.)
RETURN
CONTINUE
BETP=PH+PHP
CALL DI(DIP,R,BETP,BO,FN)
CALL DP(DPP,R,BETP,BO,FN)
DS=DIN+DIP
DPS=DPM+DPP
DPH=DPN+DPP
RETURN
END
SUBROUTINE DIR(DIR,R,BET,BO,FN)
C *** INCIDENT (BET=PH-PHP) OR REFLECTED (BET=PH+PHP) ***
C *** PART OF WEDGE DIFFRACTION COEFFICIENT ***
COMPLEX TOP,COM,EX,UUPI,UNPI,FA,DIR
DATA PI,TP1,DPR/3.14159265,6.2831853,57.29577958/
ANG=BET/DPR
SBO=SIN(BO/DPR)
TOP=CEXP(CMPLX(D.,-PI/4.))
DEM=4.*TP1*FN*SBO*SBO
COM=TOP/DEM
DNS=(PI+ANG)/(2.*FN*PI)
SGN=SIGN(1.,DNS)
N=FIX(ABS(DNS)+D.5)
DN=SGN*N
A=ABS(1.*COS(ANG-2.*FN*PI*DN))
BOTL = 2.*SQR(ABS(R*A))
EX=CEXP(CMPLX(D.,TP1*R*A))
CALL FRNELS (C,S,BOTL)
C=SQR(PI/2.*D.)*(S-B-C)
S= SQR(PI/2.*D.)*(S-B.5)
FPA=TP1*R*(CMPLX(D.,2.))+4.*SQR(ABS(TPI*R*A))*EX*CMPLX(C,S))
RAG=(PI+ANG)/(2.*FN)
TSIN=SIN(RAG)
TS=TSIN*TSIN
IF(TS.GT.1.E-5) GO TO 442
CSCA=-2.*FN*FN*COS(ANG-TP1*FN*DN)/COS((PI+ANG)/FN)
GO TO 443
CSCA=A/TS
UNPI=COM*CSCA*FPA
DIR=UUPI+UNPI
RETURN
END
SUBROUTINE DIRS(C,S,XS)
THIS IS THE FRESNEL INTEGRAL SUBROUTINE WHERE THE INTEGRAL IS FROM

```

542 123 442 443 444 445 446 447 448 449 450 451 452 453 454 455 456 457 458 459 460 461 462 463 464 465 466 467 468 469 470 471 472 473 474 475 476 477 478 479 480 481 482 483 484 485 486 487 488 489 490 491 492 493 494 495 496 497 498 499 500

```

RAG=(PI-ANG)/(2.*FN)
TSIN=SIN(RAG)
TS=ABS(TSIN)
IF(TS.GT.1.E-5) GO TO 542
COTA= SQR(2.*D.)*FN*SIN(ANG/2.*D.-FN*PI*DN).LT.(D.*D) COTA=-COTA
IF(COS(ANG/2.*D.-FN*PI*DN).LT.(D.*D) COTA=-COTA
GO TO 123
UNPI=COM*COTA*FA
DIR=UUPI+UNPI
RETURN
END
SUBROUTINE DIRS(C,S,XS)
THIS IS THE FRESNEL INTEGRAL SUBROUTINE WHERE THE INTEGRAL IS FROM

```

```

C      U=0 TO XS. THE INTEGRAND IS EXP(-J*PI/2.*U*U),AND THE OUTPUT IS
C      C(XS)-J*S(XS).
      DIMENSION A(12),B(12),CC(12),D(12)
      DATA A/1.595769148,-0.000001702,-6.888568854,-0.000576361,6.928691
*902,-0.016098657,-3.050485660,-0.075752419,0.850663701,-0.0256390
*1,-0.150230960,0.034404779/
      DATA B/-0.000000033,4.255387524,-0.000092810,-7.780020400,-0.00952
*0895,5.075161298,-0.138341947,-1.363729124,-0.403349276,0.7022220
*6,-0.216195929,0.019547031/
      DATA CC/0.,-0.024933975,0.000003936,0.005770956,0.000689892,-0.009
*497136,0.011948809,-0.006748873,0.000246420,0.002102967,-0.001217
*30,0.000233939/
      DATA D/0.199471140,0.000000023,-0.009351341,0.000023006,0.00485146
*6,0.001903218,-0.017122914,0.029064067,-0.027928955,0.016497308,-
*.005598515,0.000000000/
      DATA PI/3.14159265/
      IF(XS.LE.0.0) GO TO 414
      X=XS
      X = PI*X*X/2.0
      FR=0.0
      FI=0.0
      K=13
      IF(X-4.0) 10,40,40
10      Y=X/4.0
20      K=K-1
      FR=(FR+A(K))*Y
      FI=(FI+B(K))*Y
      IF(K-2) 30,30,20
30      FR=FR+A(1)
      FI=FI+B(1)
      C=(FR*COS(X)+FI*SIN(X))*SQRT(Y)
      S=(FR*SIN(X)-FI*COS(X))*SQRT(Y)
      RETURN
40      Y=4.0/X
50      K=K-1
      FR=(FR+CC(K))*Y
      FI=(FI+D(K))*Y
      IF(K-2) 60,60,50
60      FR=FR+CC(1)
      FI=FI+D(1)
      C=0.5+(FR*COS(X)+FI*SIN(X))*SQRT(Y)
      S=0.5+(FR*SIN(X)-FI*COS(X))*SQRT(Y)
      RETURN
414      C=-0.0
      S=-0.0
      RETURN
      END

```

The above diffraction program has been used extensively by one of the authors at the Ohio State University ElectroScience Laboratory where it was written over a period of years by the laboratory staff.

INDEX

- Active impedance, 155
- Antenna beam solid angle, 35
- Aperture antenna, 375
- Aperture efficiency, 395
- Archimedean spiral antenna, 285
- Array:
 - arbitrarily configured, 164-165
 - binomial, 147-151
 - circular, 350-354
 - collinear, 134-135
 - conformal, 109
 - Dolph-Chebyshev, 151, 537-542
 - feeding of, 165-167
 - linear, *see* Linear array
 - parallel element, 138-141, 342, 349-350
 - phased, 108, 160-167, 349-356
 - planar, 108, 354-355
 - superdirective, 134
- Array antenna, 108
- Array-element factor, 165
- Array factor, 109, 110-111, 135, 164

- Babinet's principle, 283
- Backscatter, 453
- Balun, 217-218
- Bandwidth, 260
- Beam broadening, 161

- Beam solid angle, 35
- Beamwidth, 30, 128
- Beverage antenna, 240
- Biconical antennas, 270-278
- Binomial array, 147-151
- Boundary conditions, 6, 7
- Bowtie antenna, 288
- Broadband antenna, 193, 239, 260-261
- Broadside antenna, 30

- Capacitor-plate antenna, 81
- Cardioid pattern, 115-116
- Cassegrain reflector antenna, 430-433
- Collinear array, 134-135
- Collinear dipoles, 155
- Collocation, 321
- Communication links, 60-62
- Conductivity, 6, 563
- Conformal array, 109
- Corner reflector antenna, 437
- Corporate feed of an array, 165
- Cosine-tapered line source, 184-185
- Creeping wave, 499
- Current density:
 - electric, 5
 - magnetic, 6
 - surface, 6, 7

Current element, 13

Diffraction, 458

Dipole:

- folded, 205-212
- full-wave, 197
- half-wave, 84-87, 196, 315
- ideal, 13-17, 81
- short, 50-52, 80, 313-314, 319
- sleeve, 280-281
- straight wire, 193-203
- top-hat loaded, 81
- vee, 204

Dirac delta function, 11, 565

Directive gain, 34

Directivity:

- definition of, 36
- Hansen-Woodyard increased, 130-134
- linear array, 141-145
- uniform line source, 180-182, 190

Discone antenna, 274-278

Dolph-Chebyshev array, 151, 537-542

Driving point impedance, 154

Effective aperture, 61

Effective isotropically radiated power (EIRP), 62

Effective length of an antenna, 65

Effective permeability, 102

Effective receiving aperture, 65

Efficiency:

- aperture, 395
- radiation, 38, 48-52, 395

Electrically small antenna, 79

Element factor, 28

Element pattern, 135, 137-138, 164

Endfire antenna, 30

Endfire array:

- Hansen-Woodyard, 130-134, 143, 265
- ordinary, 130, 139-141, 143

Equiangular spiral antenna, 284-287

Equivalence principle, 375-384

Equivalent currents, 309, 492

Fan beam, 31

Far-field region, 17, 22-25

Far zone, *see* Far-field region

Field probe, 41, 69

Fields, 4-6

Folded dipole, 205-212

Frequency-independent antenna, 281

Frequency scanning, 165

Friis transmission formula, 60

Frill generator, 337

Full-wave dipole, 197

Gain, 37, 334, 392-397

Galerkin's method, 319, 321, 323-332

Geometrical optics, 447-454

Geometrical theory of diffraction, 460, 469

Grating lobe, 123

Ground plane:

- imperfect, 229-238, 489-492
- perfect, 87-94

Half-power beamwidth, 30

Half-wave dipole, 84-87, 196, 315

Hansen-Woodyard endfire array, 130-134, 143, 265

Hansen-Woodyard increased directivity, 130-134

Helical antennas, 261-270

Horn antennas, 397-415, 479-481

Huygen's principle, *see* Equivalence principle

Ideal dipole, 13-17, 81

Impedance:

- active, 155
- antenna, 17, 47-53
- driving point, 154
- intrinsic, 16, 22
- matrix, 313
- mismatch, 65
- mutual, 154-160

Impedance matching, 52-53, 212-216

Interferometer, 161

Isotropic source, 33, 110

Linear array:

- beamwidth, 128-129
- Dolph-Chebyshev, 151, 537-542
- excitation of, 349-350
- general properties, 108-123
- Hansen-Woodyard endfire, 130-134, 143, 265
- main beam scanning of, 128, 160-167
- nonuniformly excited, 145-154
- ordinary endfire, 130, 139-141, 143
- unequally spaced, 151-153
- uniformly excited, 124-145

Linear phase, 161

Line source, 19, 26, 173-189, 522-530, 543-550

Log-periodic antennas, 287-303

Log-periodic dipole array, 294-303, 345-349

Long-wire antenna, 239

Loop antenna:

- circular, 259
- small, 99-104
- square, 244-251

Loop-stick antenna, 102

Magnetic moment, 101

Main beam, 29

Main lobe, *see* Main beam

Maximum effective aperture, 57

Maxwell's equations, 2, 4-6

Measurement:

- field intensity, 69-71
- gain, 39-40
- mutual impedance, 155-160
- pattern, 44-47

Method of moments, 306

Minor lobe, 29

Monopole, 92-94, 278, 489-492, 502-509

Mutual coupling, 154, 164, 349-356

Mutual impedance, 154-160

Near-field region, 17

Omnidirectional pattern, 19

Open-sleeve dipole, 280-281

Ordinary endfire array, 130, 139-141, 143

Parabolic reflector antenna, 397, 422-436, 482-485

Parallel dipoles, 155

Parallel element array, 138-141, 342, 349-350

Parallel feed of an array, 165

Pattern, *see* Radiation Pattern

Pattern factor, 28

Pattern multiplication, 134-141, 164

Pencil beam, 31

Permeability, 6, 102

Permittivity, 6

Phased array, 108, 160-167, 349-356

Physical optics, 381, 454-458

Planar array, 108, 354-355

Pocklington's integral equation, 307-310

Point-matching, 312, 321

Point source, 110

Polarization, 53-57

Polarization mismatch, 65-69

Potential:

- scalar, 10
- vector, 9

Power gain, *see* Gain

Power pattern, 28-29

Poynting's theorem, 7-8

Poynting vector, 7

Prime-focus reflector antenna, 422-430, 482-485

Principle of pattern multiplication, 137

Pyramidal horn antenna, 397, 398, 411-415

Q, 104-105, 134

Radar, 63-64

Radar cross section, 63, 335, 453, 457

Radiated power, 17

Radiation efficiency, 38, 48-52, 395

Radiation fields, 17

Radiation intensity, 33

Radiation pattern, 17-19, 27, 46

Radiation resistance, 48, 200-201

Ray optics, 447-454

Reaction, 40, 321

Reciprocity, 40-44

Reflector antennas, 422-440, 482-485

Rhombic antenna, 242-244, 259

Sampling method, 526-530, 534-535

Scanning:

- frequency, 165
 - of pattern main beam, 160-167
- Scattering, 332-336, 344-345, 365-370
- Sectoral horn antennas, 398-411, 479-481
- Series feed of an array, 165
- Short dipole, 50-52, 80, 313-314, 319
- Shunt matching, 215-216
- Side lobe, 29
- Side lobe level, 29
- Similar array elements, 136
- Sleeve antennas, 278-281
- Slice generator, 336
- Slope diffraction, 488, 518
- Slot antenna, 485-489
- Small loop antenna, 99-104
- Space feed of an array, 165
- Spiral antennas, 281-287
- Square loop antenna, 244-251
- Staggered dipoles, 155
- Superdirective array, 134
- Supergain, 134

Supergain ratio, 134

Taylor line source, 543-550

Toeplitz matrices, 340-343

Top-hat loaded dipole antenna, 81

Transmission-line loaded antenna, 81-82

Traveling-wave wire antenna, 239-244

Umbrella-loaded monopole, 94

Uniform line source, 26, 174-184

Uniform progressive phase, *see* Linear
phase

Uniform theory of wedge diffraction, 472

Vector potential, 9

Vee dipole, 204

Vee, traveling-wave, 242, 259

Wave antenna, 240

Wave equation, 10-11

Weighted residuals, 315

Wire-grid model, 356-365

Wood's anomaly, 356

Woodward-Lawson sampling method, 526-530,
534-535

Yagi-Uda antenna, 218-228

UNIVERSIDAD NACIONAL AUTÓNOMA DE MEXICO

DEPARTAMENTO DE BIBLIOTECAS

BIBLIOTECA CENTRAL

TEGUCHI, D. C. Presidente